Transactions of the ASME®

Transactions of the ASME, Journal of Heat Transfer (ISSN 0022-1481) is published bi-monthly (Feb., Apr., June, Aug., Oct., Dec.) by The American Society of Mechanical Engineers, Three Park Avenue, New York, NY 10016. Periodicals postage paid at New York, NY and additional mailing offices. POSTMASTER: Send address changes to Transactions of the ASME, Journal of Heat Transfer, c/o THE AMERICAN SOCIETY OF MECHANICAL ENGINEERS, 22 Law Drive, Box 2300, Fairfield, NJ 07007-2300.
CHANGES OF ADDRESS must be received at Society headquarters seven weeks before they are to be effective. Please send old label and new address.
STATEMENT from By-Laws. The Society shall not be responsible for statements or opinions advanced in papers or ... printed in its publications (B7.1, Para. 3), **COPYRIGHT**
 INDEXED by Applied Mechanics Reviews and Engineering Information, Inc. Canadian Goods & Services Tax Registration #126148048.

Journal of Heat Transfer

Published Bimonthly by The American Society of Mechanical Engineers

VOLUME 124 • NUMBER 1 • FEBRUARY 2002

TECHNICAL PAPERS

(Contents continued on inside back cover)

This journal is printed on acid-free paper, which exceeds the ANSI Z39.48-1992 specification for permanence of paper and library materials. ♾™
♻ 85% recycled content, including 10% post-consumer fibers.

Journal of Heat Transfer Volume 124, Number 1 FEBRUARY 2002

TECHNICAL NOTES

ANNOUNCEMENTS

Heat Transfer in Rotating Narrow Rectangular Ducts With Heated Sides Parallel to the *r-z* Plane

Fred T. Willett
Mem. ASME
Power Technology Incorporated,
P.O. Box 232,
Rexford, NY 12148
e-mail: frdwillett@aol.com

Arthur E. Bergles
Professor Emeritus,
Rensselaer Polytechnic Institute,
Troy, NY 12180
e-mail: abergles@aol.com

In gas turbine blade design, a variety of channel shapes and orientations are used in the cooling circuit. Most of the rotating channel heat transfer research to date has considered channels of square or round cross-sections. This research characterizes the effect of rotation on fully developed turbulent convective heat transfer in ducts of narrow cross-section (height-to-width aspect ratio of 1:10). Experiments were conducted using ducts of narrow cross-section, oriented such that the long sides of the duct cross-section are perpendicular to the direction of blade tangential velocity (parallel to the r-z plane). In the experiment, a high-molecular-weight gas (Refrigerant-134A) at ambient pressure and temperature conditions was used to simulate coolant-to-wall density ratios that match engine conditions. Thin foil heaters were used to produce a uniform heat flux at the long sides of the duct; the narrow sides were unheated. Duct Reynolds numbers were varied up to 31,000; rotation numbers were varied up to 0.11. The test results show the effect of rotation and aspect ratio on duct leading and trailing side heat transfer. The results provide insight into the effect of rotation (Coriolis) in the absence of buoyancy effects. Comparisons with previously reported results are presented to show the effect of cross-section shape on rotating channel heat transfer. [DOI: 10.1115/1.1418370]

Keywords: Channel Flow, Forced Convection, Heat Transfer, Rotating, Turbines

Introduction

The demand for more power, whether it be thrust from an aircraft engine or shaft horsepower from an industrial gas turbine, provides incentive for gas turbine manufacturers to continually seek improvements in gas turbine performance. Turbine performance can be increased by raising the turbine inlet temperature. It can also be increased by decreasing the amount of air from the compressor that is dedicated to turbine cooling. In general, turbine blades, in order to survive in higher performance turbines, must either be made from superior materials or have superior cooling designs, or both. Insufficiently cooled blades are subject to oxidation, creep rupture, and, in extreme cases, melting.

The heat transfer in a rotating heated channel is a complex phenomenon. The action of rotation on the coolant results in a non-uniform distribution of the heat transfer coefficient at any cross-section. Numerical solutions are not yet reliable or accurate enough for use in design. Experimental data are required to help gain a better understanding of the effects of rotation on heat transfer in a heated channel.

The cooling passage configuration studied in this research is a smooth-walled rectangular passage with a 1:10 aspect ratio, oriented such that the long sides of the duct cross-section are perpendicular to the direction of blade tangential velocity (parallel to the *r-z* plane). Only radially-outward flow is considered. This combination of cooling passage cross-section geometry and orientation is unlikely to be found in a cooled gas turbine blade, except in an unconventional design, for example, perimeter-cooled. However, there are some benefits to studying this configuration. One clear benefit is for comparison with channel cross-sections of similar geometry, but oriented at oblique angles to the *r-z* plane (Willett and Bergles [1]). The results of this study are also of benefit to the developers and users of computational fluid dynamics (CFD) software, as it provides a unique, complex, test case to enable code validation and refinement. Another benefit of this case is its value as a new lower bound on duct aspect ratio. The open literature contains very little information on rotational effect in rectangular ducts. The smallest aspect ratio researched, and with published leading and trailing-side results, is 1:2, from Kuo and Hwang [2].

Figure 1 describes the rotation-induced forces acting on radially outward-flowing coolant in a heated channel. The buoyancy force is governed by both the centrifugal force acting on the fluid and the density gradient in the fluid. The density gradient is a function of the difference in temperatures of the fluid near the heated walls and the fluid in the core of the passage.

Mori et al. [3] investigated the Coriolis effect, studying flow in round tubes both experimentally and analytically. Wagner et al. [4] investigated both Coriolis and buoyancy effects in their work, which used square passages and non-dimensional flow parameters typical of gas turbine blades. Later work by Johnson and Wagner [5] studied the effects of rotation on inward flow as well as outward flow. Soong et al. [6], and later Kuo and Hwang [2] expanded the investigation of secondary flow effects due to rotation by considering smooth-walled rectangular ducts, and concluded that aspect ratio is a critical parameter. They observed that the greatest Coriolis effect occurs in square ducts, i.e., an aspect ratio of 1:1.

Zhang et al. [7] experimented with a three-pass serpentine circuit with turbulators oriented normal to the flow, concluding that the normalized Nusselt number is insensitive to Reynolds-number variation. The effects of rotation they observed were consistent with the work of Wagner and Johnson [4]. Further work on two-pass cooling channels was done by Han et al. [8,9] who considered the effect of uneven wall temperature in a square, smooth-walled passage. A three-pass, smooth-walled, serpentine passage was studied by Mochizuki et al. [10] who noted the strong three-dimensional structure in the flow through the 180 deg bends.

Parsons et al. [11,12] investigated the effect of model orientation and wall heating condition on heat transfer in a rotating two-pass square channel. Dutta et al. [13] considered the effects of orientation and rotation on heat transfer in a smooth triangular-shaped passage. Morris and Chang et al. [14], and Park and Lau

Contributed by the Heat Transfer Division for publication in the JOURNAL OF HEAT TRANSFER. Manuscript received by the Heat Transfer Division January 3, 2001; revision received June 12, 2001. Associate Editor: M. L. Hunt.

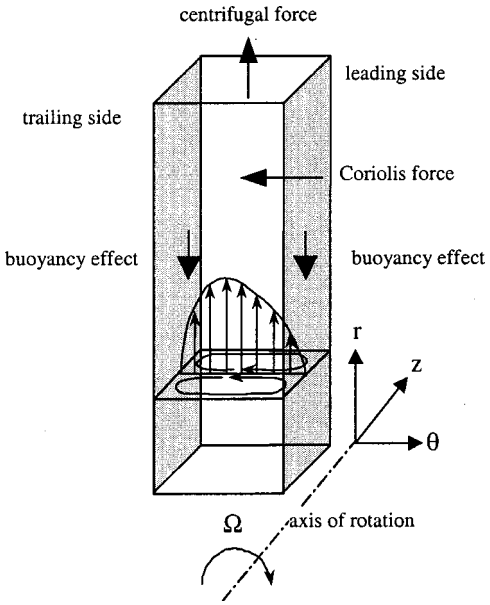

Fig. 1 Outward flowing channel in rotation

[15] attempted to uncouple the buoyancy and Coriolis effects, using extrapolation of experimental data to the implied zero-buoyancy condition and naphthalene sublimation experiments, respectively. Willett [16] presents a more detailed summary of the previous work.

Test Apparatus

Rotational Test Rig. The test facility consisted of a rotor and stator enclosed in a closed loop system using R-134a as the test fluid. The refrigerant was supplied as a gas to the test sections to be evaluated. The use of a high-molecular-weight gas, e.g., a refrigerant, means that the dimensionless parameters relevant to gas turbine operating conditions can be matched at ambient pressure and relatively low rotational speeds. A diagram of the test rig is given in Fig. 2.

The test sections, or ducts, were installed in a 622 mm [24.5 inch] diameter rotor. The rotor was constructed of mahogany and framed by an aluminum disk. The duct coolant was fed through the rotor via a rotating union and a radial supply passage in the disk. An inlet plenum was used to connect the supply tube to the rotor with an *O*-ring seal. Two inlet screens were used in the plenum to provide a uniform velocity at the inlet to the test duct. The inlet plenum was made of aluminum and was fitted into the supply tube at the inlet to the test duct. The inlet gas temperature was measured between the two inlet screens. The duct inlet was located at a radius of 168 mm [6.61 inches]. Figure 3 shows the rotor and test section before installation into the rig.

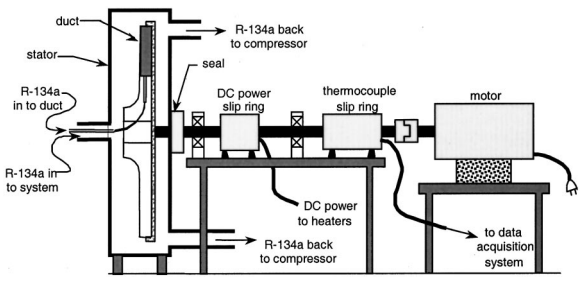

Fig. 2 Rotating test rig diagram

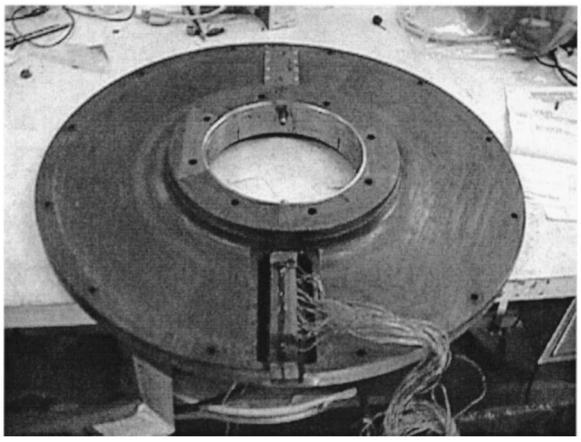

Fig. 3 Rotor disk with test duct ready for installation

Test Sections. The duct was a two-piece construction and was made of mahogany. The flow passage in the test section was created by removing material from one half of the section, then cementing the two halves together. The external dimensions of the test section are 26.7 mm×24.1 mm [1.05 inches×0.95 inches], which allows it to fit in the inlet plenum. Continuous thin (0.013 mm, 0.0005 in.) film nickel-based alloy heaters were attached to the wide sides of the duct. The heaters have a very thin polymer film backing, which prevents the foil from tearing easily, but more importantly, electrically insulates the foil from the thermocouples. A specially formulated epoxy cement was used to fasten the polymer backing of the heaters to the walls of the duct. This very thin layer of epoxy provided additional electrical insulation for the thermocouples. The narrow sides of the duct were not heated. The heated length of the duct was 114.3 mm [4.50 inches]. The two pieces of the duct were cemented together with gasket cement and wrapped with tape to prevent leaks. The flow area of the duct was 2.03 mm×20.3 mm [0.08 in.×0.80 in.]; the hydraulic diameter was 3.69 mm [0.145 in.].

Instrumentation and Data-Acquisition. The duct was instrumented with Type-*K* thermocouples. The insulated thermocouple beads were in contact with the back of the heater. The thermocouple wires were 0.25 mm [0.010 in.] diameter and were covered with 0.15 mm [0.006 in.] thick insulation. The thermocouples were fed through the duct wall, perpendicular to the heater surface. The thermocouples were connected to a slip ring, which allowed transmission of data from rotational frame to stationary frame. One side of the duct was well instrumented; the other side had only three thermocouples, used for measuring heater temperature and regulating the power to the heaters. The total number of thermocouples was limited by the slip ring capacity. A total of twenty-five thermocouples was used on the well-instrumented side, eleven in the developing region and fourteen in the fully developed region. An additional thermocouple was placed on the outer wall of the test section. Because of the limited number of slip ring channels available, leading side and trailing side data could not be obtained simultaneously. The test rig was operated in both forward and reverse rotation to obtain data for both sides. Figure 4 describes the test duct.

A program written using commercially available software enabled continuous readout of the data. The data were displayed on the computer screen in a virtual instrument format configured especially for the experiment. The user could write the data from the virtual instrument to a file command. Flow levels were set manually using a flow gage and monitored by the program. Rotating speed was measured with a tachometer and was set by the test operator using a variable-speed electric motor. Electric current to the heaters was controlled by the user via a DC power supply and

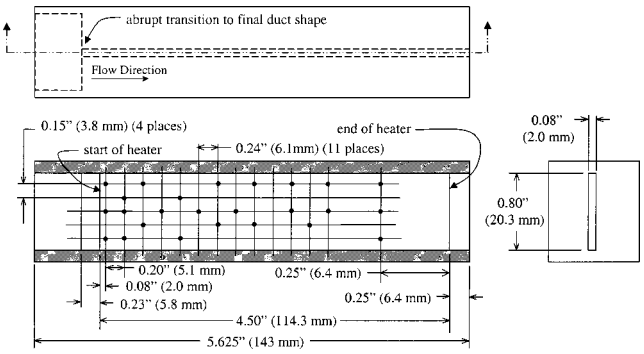

Fig. 4 Test duct and thermocouple locations

displayed along with the other data. Heat input to the test section was entirely from resistance heating; the same current was supplied to both heated sides of the duct. The uniform-heat-flux boundary condition was applied on two sides of the duct. Uniform heat flux is a reasonable first-order representation of the heat transfer in an actual turbine blade. The nickel-based alloy heaters have a very low temperature coefficient of resistance (TCR), so the resistance is relatively constant over the range of operation, however, a correction was made to the resistance for the calculation of heat input to the duct. The known or measured quantities for this experiment were (1) the heat into the test-section, (2) the R-134a flow rate, (3) the wall temperature, (4) the R-134a inlet temperature, (5) the fluid properties, and (6) the duct geometry.

The heat transfer coefficient is defined as

$$h = \frac{Q_{\text{in}} - Q_{\text{loss}}}{A(T_w - T_b)}. \tag{1}$$

In the experiment described here, Q, T_w, and A are known. T_b can be calculated knowing the inlet temperature and the heat supplied to the heaters. With the calculated value of T_b, the local heat transfer coefficient can be determined at any thermocouple location. Q_{loss}, the heat lost from the heaters by conduction out of the test section, was determined using temperatures measured at the outside wall of the test section and a two-dimensional finite-element model of the test section. Because the test section material has high thermal resistance, this loss is small, between 5 percent and 10 percent of the total heat supplied by the heaters, depending on test conditions. A second two-dimensional finite element analysis was used to determine the temperature measurement error due to thermocouple lead-wire conduction. The temperature correction ranged from 1.7 to 5.6°C [3 to 10°F], depending on heat input.

The duct-average heat transfer coefficient can also be determined for each heated wall. When determining the duct-average heat transfer coefficient, only the fully developed region is considered. In this experiment, it is expected that the flow be fully developed after ten hydraulic diameters from the duct inlet. The duct-average heat transfer coefficient is based on average temperatures, i.e.,

$$\overline{h} = \frac{Q_{\text{in}} - Q_{\text{loss}}}{A(T_w - T_b)}. \tag{2}$$

The average Nusselt number is calculated as

$$\overline{\text{Nu}} = \frac{\overline{h} d_h}{k}. \tag{3}$$

The Nusselt number is normalized to the Nusselt number for fully developed turbulent flow in a smooth duct as correlated by Dittus and Boelter/McAdams,

$$\text{Nu}_0 = 0.023\,\text{Re}^{0.8}\,\text{Pr}^{0.4}. \tag{4}$$

Table 1 Precision and bias limits for experimental parameters

Parameter	Bias	Precision	Units
Current	0	1.5E-02	amps
Heater Resistance	7.6E-04	0	ohms
T_{wall}	3.57E+00	1.55E+00	K
T_{cool}	3.57E+00	5.09E-01	K
$T_{outer\ wall}$	3.57E+00	2.06E+00	K
k_{R134a}	6.7E-06	3.7E-06	W/mK
d_H	1.9E-02	0	cm
Pr	6.1E-03	7.6E-04	
Cross-Section Area	3.4E-02	0	cm^2
Viscosity	8.9E-08	2.3E-08	kg/m-s
Mass Flow	0	1.7E-05	kg/s
Wall Δx	1.9E-02	0	cm
Heater Area	1.3E+00	0	cm^2

A series of tests were conducted, with the duct in a static, i.e., non-rotating, condition to validate the use of this correlation for the 1:10 aspect ratio duct. The static tests were conducted for Reynolds numbers of 10,000, 20,000, 30,000, 40,000, and 50,000. The stationary duct results were compared to the values predicted by the Dittus/Boelter/McAdams correlation (Rohsenow and Choi [17]) and were found to correlate well; the value of R^2 calculated was 98.3 percent. These results validate not only the use of the Dittus/Boelter/McAdams correlation for normalization, but also the use of hydraulic diameter as a characteristic length for the 1:10 aspect ratio duct. Additional data were taken to validate the assumption of fully developed flow for $L/d_H > 10$. The developing heat transfer data were compared with the results of Boelter, Young and Iversen as reported by Kays and Crawford [18], for air flowing in a circular tube with constant surface temperature. The results from the present experiment are reported by Willett [16] and match well with the previous results.

The duct-averaged normalized Nusselt number is calculated as

$$\frac{\overline{\text{Nu}}}{\text{Nu}_0} = \frac{\overline{\text{Nu}}}{\frac{1}{n}\Sigma_{i=1}^{n}(\text{Nu}_0)_i}, \tag{5}$$

where n is the number of thermocouples in the section of the duct over which the average is taken and $(\text{Nu}_0)_i$ is the calculated smooth, non-rotating, duct Nusselt number corresponding to the thermocouple location. The variation in Nu_0 with axial distance is quite small, and is due to the dependence of viscosity and Prandtl number on bulk fluid temperature.

Normalized Nusselt number was studied as a function of both rotation number and buoyancy number. Rotation number was controlled by adjusting the mass flow through the duct. Buoyancy number was controlled by adjusting mass flow and wall temperature. Three rotational speeds were used: 800, 1400, and 2400 RPM.

An uncertainty analysis was performed using the method described by Kline and McClintock [19]; the resultant experimental uncertainty in normalized Nusselt number was calculated to be ± 11 percent. The precision limit of Nu/Nu_0 is ± 5 percent; the bias limit is ± 10 percent. Table 1 contains estimates of precision and bias limits for the individual parameters. The largest sources of uncertainty were temperature measurement and measurement of heater area. Willett [16] describes the apparatus, procedure, and data reduction in greater detail.

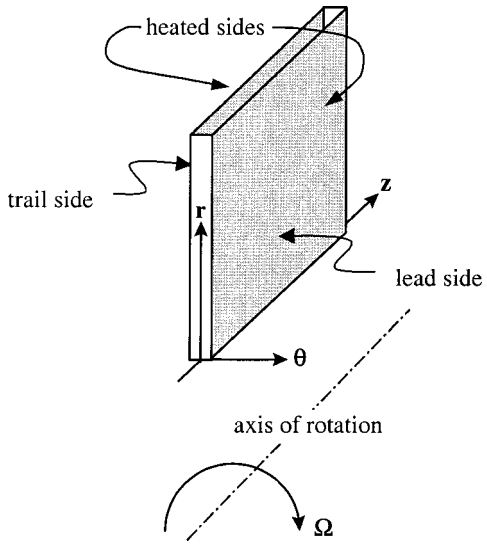

Fig. 5 The 1:10 aspect ratio duct oriented parallel to the *r-z* plane

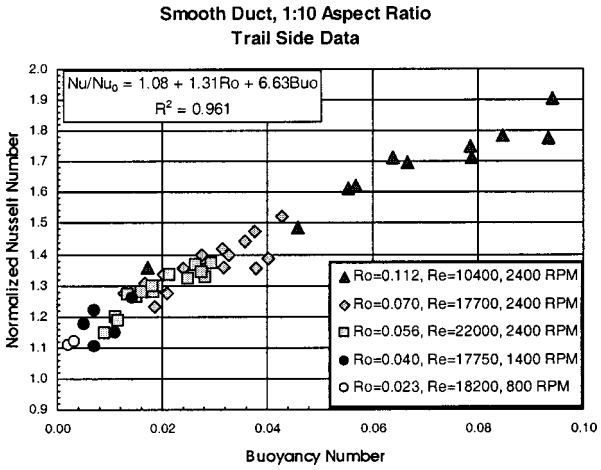

Fig. 6 Trailing-side Nu/Nu_0 versus buoyancy number for the smooth duct parallel to the *r-z* plane (uncertainty=±11 percent)

Smooth Duct With Heated Sides Oriented Parallel to the *r-z* Plane. Data were collected to assess heat transfer on both the leading and trailing sides of a smooth duct of 1:10 aspect ratio oriented parallel to the *r-z* plane. A schematic of the duct is shown in Fig. 5.

The Coriolis forces due to rotation generate secondary flows and produce a complicated three-dimensional flow and heat transfer distribution. The Coriolis force acts perpendicular to the flow direction. Secondary flows, produced by interaction of viscous forces and Coriolis forces, develop in the plane perpendicular to the flow direction.

The Coriolis force also has an effect on velocity profile, with the core flow shifting in the direction of the Coriolis force. In radially outward flow, this shift is towards the trailing side of the duct. The work of Moore, as reported in Hajek et al. [20], clearly demonstrated this shift in a rotating square (aspect ratio=1) duct.

An excellent discussion of the flow behavior in a rotating radial-outflow channel was published by Wagner et al. [4] and is pertinent to the present study. On the leading side, the boundary layer thickens as a result of the Coriolis force. The trailing-side boundary layer is thinner and turbulence is increased, contributing to higher heat transfer. Moreover, the secondary flows in the transverse direction bring cooler fluid from the core towards the trailing-side wall and increase heat transfer. The leading-side heat transfer is reduced, as the thicker boundary layer acts to stabilize the flow, so turbulent mixing is reduced. Also, the secondary flow patterns are such that warmed fluid is returned to the leading side, reducing heat transfer.

Flow in a rotating channel is further complicated by the buoyancy effect. In a radially outward flowing duct, the buoyancy force acts counter to the flow direction. These opposing forces create a strong shear gradient and generate additional turbulence, which results in increased heat transfer. When the Coriolis effect is taken into account, it follows that the buoyancy effect will be greater on the trailing side. The density gradient is steeper on the trailing side than on the leading side due to the movement of cooler core flow towards the trailing side and away from the leading side.

Trailing-Side Data for Smooth Duct With Heated Sides at 0 deg to the *r-z* Plane. Data for the trailing side of the duct were collected at three different values of rotation number. The three sets of data are shown together in Fig. 6; normalized Nusselt number is plotted as a function of buoyancy number.

The increase in heat transfer at the trailing side is due to the Coriolis-driven cross-flow, which impinges cooler fluid on the trailing-side wall. With increasing buoyancy number, there is an increase in the tendency towards counterflow near the wall, which destabilizes the shear layers and increases turbulent mixing near the wall, resulting in continuously increasing normalized Nusselt number. When rotation number is held constant, increasing the bulk-to-wall density ratio, which, in practical terms, means increasing the wall temperature, increases the buoyancy number. At lower rotation number, the increase in bulk-to-wall density ratio has a more dramatic effect on normalized Nusselt number, as indicated by the higher slope.

A regression analysis was conducted for the entire set of trailing-side data. Buo was found to be a significant factor, as was Ro. The regression equation for the data is

$$Nu/Nu_0 = 1.08 + 1.31\ Ro + 6.63\ Buo \tag{6}$$

confirming the slight effect of rotation number observed in Fig. 6. The coefficient of determination for the regression equation is 0.961, indicating a good fit of the equation to the data.

From this analysis, it can be concluded that both buoyancy number and rotation number influence the heat transfer coefficient on the trailing side wall, but that, for the range of rotation and buoyancy numbers tested, buoyancy number has a stronger effect. As expected, the leading coefficients for both buoyancy number and rotation number are positive. The constant term, 1.08, is close to 1, as expected, i.e., in the absence of rotation and buoyancy, the Nusselt number is that of a smooth duct as correlated by Dittus and Boelter/McAdams. This gives some insight into the effect of rotation number, as the normalized Nusselt number cannot physically approach 1.0 at very low buoyancy numbers, because the rotation (Coriolis) effect is still present. Morris and Chang et al. [13] reported similar findings in their investigation of rotational effects on convective heat transfer in a round tube. While rotational effects can be studied in the absence of buoyancy using, for example, the naphthalene sublimation technique, there has been no method proposed for studying the buoyancy effect in the absence of rotation.

Because buoyancy number is a function of rotation number (recall that $Buo \sim Ro^2$), it is difficult to separate the relative contributions to buoyancy of centrifugal force and density gradient. Another way of presenting the data is to use the density ratio, $\Delta\rho/\rho$, where

$$\frac{\Delta\rho}{\rho} = \frac{\rho_b - \rho_w}{\rho_b}, \tag{7}$$

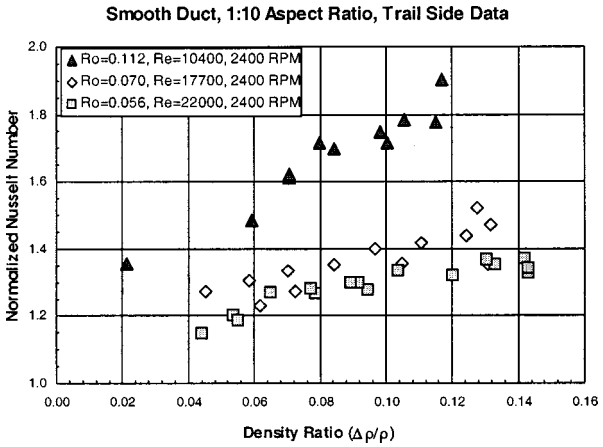

Fig. 7 Trailing-side Nu/Nu_0 density ratio for the smooth duct parallel to the *r-z* plane (uncertainty=±11 percent)

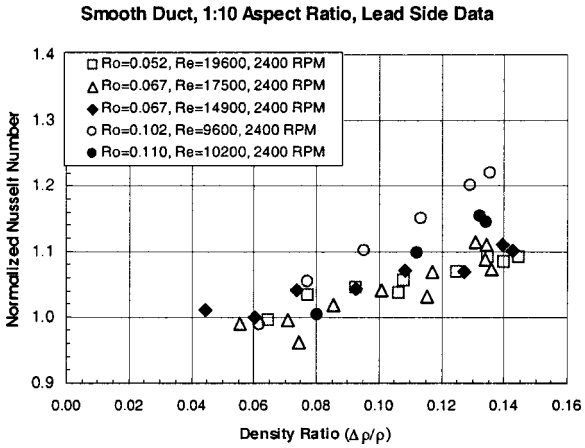

Fig. 9 Trailing-side Nu/Nu_0 density ratio for the smooth duct parallel to the *r-z* plane (uncertainty=±11 percent)

and ρ_w is the density of R-134a taken at the measured wall temperature. Figure 7 presents the normalized Nusselt number plotted as a function of density ratio for data taken at 2400 RPM. The data, when extrapolated to a density ratio of zero, again show the effect of rotation in the absence of buoyancy. The intercept value of Nu/Nu_0 is greater than 1.0 for the three rotation numbers studied and, as expected, increases as rotation number is increased, consistent with Eq. 6. The slope of the regression curves also increases with increasing rotation number, showing the increased importance of density ratio at higher rotation numbers.

Leading-Side Data for Smooth Duct With Heated Sides Parallel to the *r-z* Plane. Data at different ranges of rotation number were collected for the leading side and are shown together in Fig. 8. As above, normalized Nusselt number is plotted as a function of buoyancy number, where buoyancy number is defined as $Buo=Gr/Re^2$. The slopes of the data indicate intercepts of less than 1.0 for all values of rotation number studied, demonstrating again the effect of rotation. As rotation number is increased, the intercept is seen to decrease, an indication of the Coriolis effect isolated from the buoyancy effect. As was the case for the trailing side, this is explained physically by the effect of rotation, as the normalized Nusselt number cannot physically approach 1.0 at very low buoyancy numbers because the rotation (Coriolis) effect is still present.

In a square duct, previous researchers have observed a transition rotation number, marking the large-scale development of Coriolis-induced secondary flow cells and increased leading-side heat transfer. Wagner et al. [4] reported a transition rotation number of 0.2. At the leading side of the square duct, for values of rotation number less than the transition value, normalized Nusselt number decreases with increasing Ro. In the 1:10 aspect ratio duct, the sides are in such close contact that these cells develop at low Ro, so the initial decrease in Nu/Nu_0 with increasing Ro is not seen. When a regression analysis was conducted for the entire set of leading-side data, using the form of Eq. 6, the fit was not very good, as $R^2=0.76$. However, the constant term was close to 1.0 and the coefficient for Ro was negative, both as expected.

Figure 9 presents the normalized Nusselt number plotted as a function of density ratio for data taken at 2400 RPM. In general, it is observed that the effect of buoyancy, as indicated by the slope of the data, is greater for higher rotation numbers. The intercept value of Nu/Nu_0 is less than 1.0 for the rotation numbers studied and, as expected, decreases as rotation number is increased, demonstrating the effect of rotation alone.

Comparison With Previous Research. While most of the work of other researchers has concentrated on square ducts, there are some data for round, rectangular, and even triangular ducts. The present research concerns a duct of 1:10 aspect ratio, which is substantially different from any rectangular duct studied in previous research. Aspect ratio is defined in Fig. 10. Kuo and Hwang [2] investigated a duct with an aspect ratio of 1:2. This is the smallest aspect ratio described in the open literature for which leading side and trailing side data are reported separately. A comparison of the present research with the prior research into rotational effects on heat transfer in square ducts is given in Figs. 11 and 12. Figure 11 shows collected data for normalized Nusselt number, i.e., Nu/Nu_0, versus buoyancy number for the leading side of the duct. The data from the present study do not approach the extreme values observed for the square ducts. Also, the data for the 1:10 aspect ratio duct do not show the large reduction in normalized Nusselt number at buoyancy numbers between 0 and 0.6 observed by the previous researchers. Figure 12 shows a plot of normalized Nusselt number versus buoyancy number for the

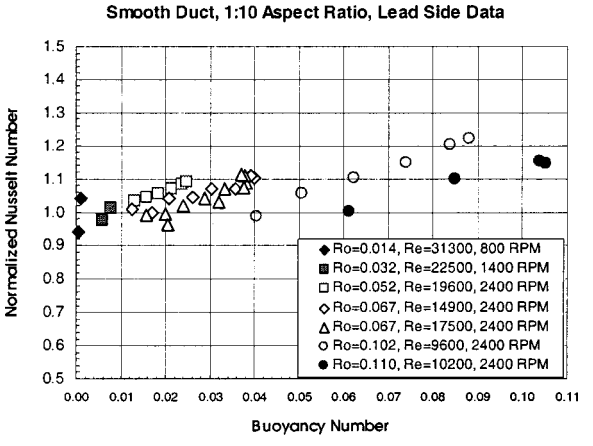

Fig. 8 Trailing-side Nu/Nu_0 buoyancy number for the smooth duct parallel to the *r-z* plane (uncertainty=±11 percent)

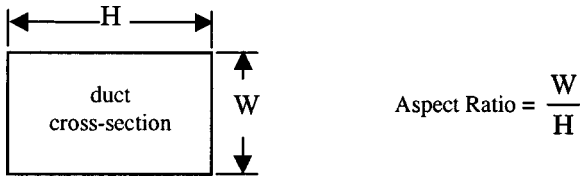

Fig. 10 Definition of aspect ratio

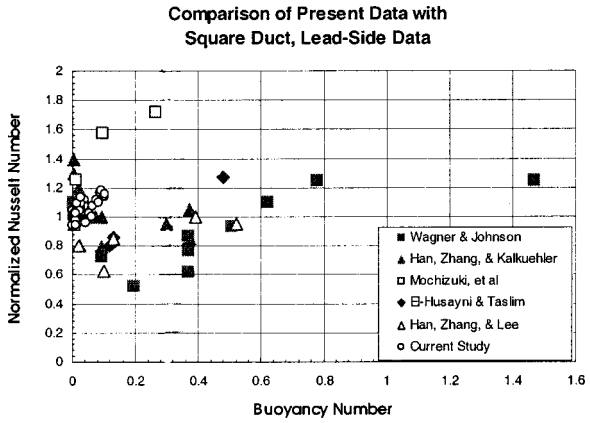

Fig. 11 Comparison of present leading-side data with leading-side data for square ducts (uncertainty of new data=±11 percent)

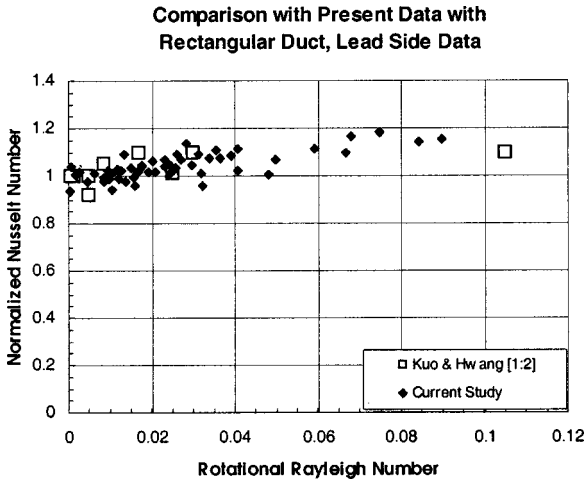

Fig. 13 Comparison of present duct leading-side data with leading-side data for a 1:2 aspect ratio rectangular duct (uncertainty of new data=±11 percent)

trailing side of the duct. Again, the data from the present study do not approach the extreme values observed for the square ducts. However, the data follow the same trend, i.e., a sharp increase in normalized Nusselt number with increasing buoyancy number.

The difference in heat transfer characteristics between the square and 1:10 aspect ratio rectangular ducts is due to the difference in duct geometry and the relative proximity of the heated sides of the duct to one another. In the narrow, 1:10 aspect ratio, duct, the secondary flow effects due to Coriolis and buoyancy forces are much less segregated than in the square duct. As buoyancy number increases, there is more transverse mixing in the duct, resulting in increased heat transfer on the leading side and decreased heat transfer on the trailing side, relative to the square duct.

Figures 13 and 14 compare the data of the present study with the data of Kuo and Hwang [2], described in their study of rotational effects on heat transfer in a 1:2 aspect ratio duct. Kuo and Hwang used rotational Rayleigh number, not buoyancy number, to characterize their data. Rotational Rayleigh number is defined as

$$\mathrm{Ra}^* = \frac{\mathrm{Ro}^2\,\mathrm{Re}^2\,R_m(T_w - T_b)\mathrm{Pr}}{d_h T_b}. \tag{8}$$

Figure 13 shows the leading side data. The range of rotational Rayleigh number covered in the current study is nearly the same as that of Kuo and Hwang [2]. The data trends for the two rectangular duct shapes are similar, showing a slight heat transfer enhancement with increasing Ra*, and no pronounced heat transfer degradation as was seen in the square ducts. The Coriolis force gradient is reduced compared to the square duct, resulting in less heat transfer degradation on the leading side and, as seen above, less heat transfer enhancement on the trailing side. Figure 14 shows the trailing side data. Again, the data trends are similar. The measured heat transfer enhancement in the 1:10 aspect ratio duct is less than that observed in the 1:2 aspect ratio duct, although the difference is not as pronounced as seen in the square duct comparison. In fact, the results of the present study are within 10 percent (the experimental uncertainty) of the results reported by Kuo and Hwang [2]. As discussed above, increasing duct aspect ratio reduces the segregation of secondary flow effects. In particular, the Coriolis effect on trailing side heat transfer is diminished with increasing duct aspect ratio. The results demonstrate the influence of heated wall spacing and duct aspect ratio on rotational heat transfer. Turbulent mixing near the walls, due to secondary-flow cell formation and the buoyancy effect, has a stronger influence on heat transfer coefficient than velocity profile distortion. Comparison of the present results with the results reported for a duct of 1:2 aspect ratio suggests that the limit of aspect ratio effect for a rectangular duct in rotation is reached close to an aspect ratio of 1:2.

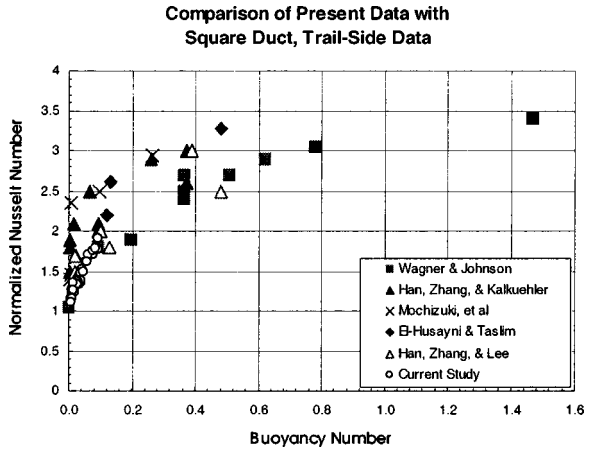

Fig. 12 Comparison of present trailing-side data with trailing-side data for square ducts (uncertainty of new data=±11 percent)

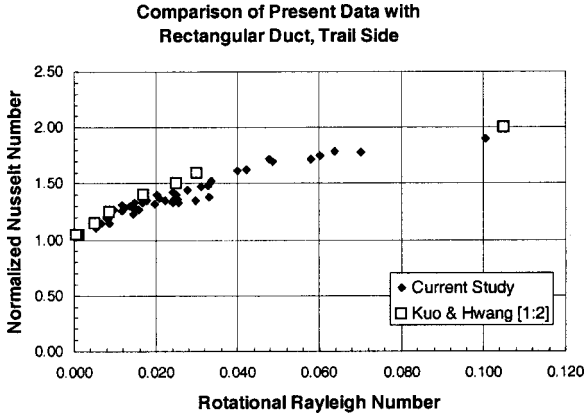

Fig. 14 Comparison of present duct trailing-side data with trailing-side data for a 1:2 aspect ratio rectangular duct (uncertainty of new data=±11 percent)

Conclusions

This research has expanded the range of available experimental data for convective heat transfer in rotating heated ducts. The passage aspect ratio makes this data set unique. The results of this research are useful in their present form, and can also be used for validation of computational models. Summarizing the conclusions,

1. Trailing-side heat transfer coefficient is found to increase monotonically with buoyancy number at constant rotation number.
2. Extrapolation of trailing-side normalized Nusselt number to Buo=0 at constant rotation number yields a normalized Nusselt number greater than 1.0 in all cases and shows an increasing trend with increasing Ro. The extrapolation provides insight into the effect of rotation (Coriolis) effects in the absence of buoyancy effects.
3. Trailing-side Nu/Nu_0 can be correlated to Buo and Ro, with a good fit over the range of experimental conditions.
4. Leading-side heat transfer coefficient is found to increase monotonically with buoyancy number at constant rotation number.
5. Extrapolation of leading-side normalized Nusselt number to Buo=0 at constant rotation number yields a normalized Nusselt number less than 1.0 in all cases and shows an decreasing trend with increasing Ro. The extrapolation provides insight into the effect of rotation (Coriolis) effects in the absence of buoyancy effects.
6. Leading side and trailing side heat transfer behavior, as described by the relationship between normalized Nusselt number and rotational Rayleigh number, is the same in a 1:10 aspect ratio duct as in a 1:2 aspect ratio duct.

Acknowledgments

This effort has benefited greatly from technical discussions with Mr. Fred Staub of GE's Corporate Research and Development Center. The authors also gratefully acknowledge the support of Mr. Karl Hardcastle, also of GE CR&D, during the data-gathering phase of this research. The rotating test rig used for this research is located at GE's Corporate Research and Development Center. Dr. Norm Shilling, Dr. Kent Cueman and Mr. Gene Kimura graciously made the rig available for this work; their interest and encouragement is much appreciated.

Nomenclature

R_m = mean duct radius
Ra^* = rotational Rayleigh number, $(=Ro^2\,Re^2\,R_m(T_{wall}-T_{bulk})Pr/d_hT_{bulk})$
Ro = rotation number $(=\Omega d_H/V)$
Ω = rotational speed

References

[1] Willett, F. T., and Bergles, A. E., 2000, "Heat Transfer in Rotating Narrow Rectangular Ducts with Heated Sides Oriented at 60 deg to the *r-z* Plane," ASME Paper No. 2000-GT-224.
[2] Kuo, C. R., and Hwang, G. J., 1994, "Aspect Ratio Effect on Convective Heat Transfer of Radially Outward Flow in Rotating Rectangular Ducts," 5th International Symposium on Transport Phenomena and Dynamics of Rotating Machinery, Kaanapali, Hawaii.
[3] Mori, Y., Fukada, T., and Nakayama, W., 1971, "Convective Heat Transfer in a Rotating Radial Circular Pipe," Int. J. Heat Mass Transf., **14**, pp. 1807–1824.
[4] Wagner, J. H., Johnson, B. V., and Hajek, T. J., 1989, "Heat Transfer in Rotating Passages with Smooth Walls and Radial Outward Flow," ASME Paper No. 89-GT-272.
[5] Johnson, B. V., Wagner, J. H., and Kopper, F. C., 1990, "Heat Transfer in Rotating Serpentine Passages with Smooth Walls," ASME Paper No. 90-GT-331.
[6] Soong, C. Y., Lin, S. T., and Hwang, G. J., 1991, "An Experimental Study of Convective Heat Transfer in Radially Rotating Rectangular Ducts," ASME J. Heat Transfer, **113**, pp. 604–611.
[7] Zhang, N., Chiou, J., Fann, S., and Yang, W.-J., 1993, "Local Heat Transfer Distribution in a Rotating Serpentine Rib-Roughened Flow Passage," ASME J. Heat Transfer, **115**, pp. 560–567.
[8] Han, J. C., Zhang, Y.-M., and Kalkuehler, K., 1993, "Uneven Wall Temperature Effect on Local Heat Transfer in a Rotating Two-Pass Square Channel With Smooth Walls," ASME J. Heat Transfer, **115**, pp. 912–920.
[9] Han, J. C., Zhang, Y.-M., and Lee, C. P., 1994, "Influence of Surface Heating Condition on Local Heat Transfer in a Rotating Square Channel With Smooth Walls and Radial Outward Flow," ASME J. Turbomach., **116**, pp. 149–158.
[10] Mochizuki, S., Takamura, J., Yamawaki, S., and Yang, W.-J., 1994, "Heat Transfer in Serpentine Flow Passages With Rotation," ASME J. Turbomach., **116**, pp. 133–140.
[11] Parsons, J. A., Han, J. C., and Zhang, Y., 1995, "Effect of Model Orientation and Wall Heating Condition on Local Heat Transfer in a Rotating Two-Pass Square Channel with Rib Turbulators," Int. J. Heat Mass Transf., **38**, pp. 1151–1159.
[12] Parsons, J. A., Han, J. C., and Zhang, Y., 1994, "Wall Heating on Local Heat Transfer in a Rotating Two-Pass Square Channel with 90 deg Rib Turbulators," Int. J. Heat Mass Transf., **37**, pp. 1411–1420.
[13] Dutta, S., Han, J.-C., and Lee, C. P., 1995, "Experimental Heat Transfer in a Rotating Triangular Duct: Effect of Model Orientation," Int. J. Heat Mass Transf., **117**, pp. 1058–1061.
[14] Morris, W. D., and Chang, S. W., May 1998, "Heat Transfer in a Radially Rotating Smooth-Walled Tube," Aeronaut. J., **102**, pp. 277–285.
[15] Park, C. W., and Lau, S. C., 1998, "Effect of Channel Orientation on Local Heat (Mass) Transfer Distributions in a Rotating Two-Pass Square Channel With Smooth Walls," ASME J. Heat Transfer, **120**, pp. 624–632.
[16] Willett, F. T., 1999, "An Experimental Study of the Effects of Rotation on Convective Heat Transfer in Smooth and Pin Fin Ducts of Narrow Cross-Section," Ph.D. thesis, Rensselaer Polytechnic Institute, Troy, NY.
[17] Rohsenow, W. M., and Choi, H., 1962, *Heat, Mass and Momentum Transfer*, Prentice-Hall, NJ, pp. 192–193.
[18] Kays, W. M., and Crawford, M. E., 1980, *Convective Heat and Mass Transfer*, McGraw-Hill, NY.
[19] Kline, S. J., and McClintock, F. A., 1953, "Describing Uncertainties in Single-sample Experiments," Mech. Eng. (Am. Soc. Mech. Eng.), p. 3.
[20] Hajek, T. J., Wagner, J. H., Johnson, B. V., Higgins, A. W., and Steuber, G. D., 1991, "Effects of Rotation on Coolant Passage Heat Transfer," *Volume 1—Coolant Passages with Smooth Walls*, NASA Contractor Report 4396.

Numerical Simulation of Laminar Flow and Heat Transfer Over a Blunt Flat Plate in Square Channel

Hideki Yanaoka
Associate Professor
e-mail: yanaoka@cc.hirosaki-u.ac.jp
Department of Intelligent Machines and System Engineering,
Hirosaki University, Bunkyo-cho 3,
Hirosaki 036-8561, Japan

Hiroyuki Yoshikawa
Research Associate

Terukazu Ota
Professor

Department of Machine Intelligence and Systems Engineering,
Tohoku University, Aramaki-Aoba 01,
Aoba-ku, Sendai 980-8579, Japan

Three-dimensional simulations of laminar separated and reattached flow and heat transfer over a blunt flat plate in a square channel are presented. Numerical calculations of Navier-Stokes equations and energy equation are carried out using the finite difference method. Results of three-dimensional calculation are compared with two-dimensional ones and effects of the side walls are described. It is clarified from the present results that the reattachment length increases with an increase of Reynolds number and the flow in the recirculation region becomes three-dimensional. The reattachment line is curved by the side wall effects. Two-dimensionality of the flow is reduced as Reynolds number increases. The horseshoe-vortex formed near the side walls has great effects upon the heat transfer in the redeveloping flow region. The separated shear layer around the center of plate becomes unstable with a further increase of Reynolds number and the vortices are periodically shed from the reattachment flow region. Such vortices exhibit a hairpin-like structure and greatly influence the heat transfer. [DOI: 10.1115/1.1420715]

Keywords: Heat Transfer, Separated and Reattached Flow, Blunt Flat Plate, DNS

Introduction

Separated and reattached flow occurs in various fluids engineering aspects resulting in a reduction of their performance and efficiency, and also their vibration and noise. Accordingly, it is expected that an occurrence of such the flow is suppressed. On the other hand, heat and mass transfer increase by strong mixing processes existing in the separated and reattached flow. There have been numerous experimental and numerical works on such complicated flow and heat transfer problems.

It may be considered that a blunt flat plate treated in the present study is one of the simplest models of a separated and reattached flow [1–8]. However, the flow structure is very complicated and the previous experimental works are conducted under a condition of turbulent flow, and studies at low Reynolds number are few. Lane and Loehrke [9], Ota et al. [10] and Sasaki and Kiya [11] performed visualization studies on such the flow at low Reynolds number. The reattachment length increases with an increase of Reynolds number. The flow is found to be steady until Reynolds number 325 by Lane and Loehrke, 270 by Ota et al., and 320 by Sasaki and Kiya, respectively. The separated shear layer becomes unstable, rolls up with a further increase of Reynolds number, and subsequently the flow becomes turbulent and three-dimensional. It has been shown in above works that the transition to turbulent flow occurs at relatively low Reynolds number.

Tafti and Vanka [6,7] analyzed unsteady behaviors of the separated shear layer over a blunt flat plate at Reynolds number 1000, which is included in the turbulent flow regime, and Tafti [12] made an analysis for the vortical dynamics and scalar transport. Djilali [13] carried out two-dimensional calculations of laminar flow and heat transfer and reported that the reattachment length decreases with an increase of blockage ratio. The present authors [8] performed two-dimensional analysis of a separated and reattached flow and heat transfer over a blunt flat plate at Reynolds number 1000 and simulated qualitative characteristics of turbulent flow. Further, three-dimensional calculations were carried out at Reynolds numbers 1000 and 5000 [14,15]. It is clarified that the hairpin-like vortices are shed from the reattachment region and have great effects upon the heat transfer. Periodic boundary condition on the spanwise boundary is employed in such the three-dimensional analysis.

On the other hand, there usually exist side walls in the experiments and the horseshoe-vortex is formed around the plate and the side wall. It is found that such a horseshoe-vortex generated by three-dimensional separation brings about high heat transfer [16–18]. However, the relationship between flow structure and heat transfer has not been clarified yet. Accordingly, clarifications of details of the flow and heat transfer over a blunt flat plate in a channel are very important. Further, three-dimensional measurements of such a complicated flow are not easy to be conducted. Especially, experiments on three-dimensional heat transfer are difficult, and the numerical analysis may be appropriate for understanding details of the heat transfer mechanism.

From this point of view, the purpose of present study is to numerically predict the steady and also unsteady three-dimensional laminar flow and heat transfer over a blunt flat plate in a square channel in order to investigate influences of side walls upon them as comparing with two-dimensional results, and to clarify the horseshoe-vortex around the plate and the side walls and also its effects upon the heat transfer. Further, the periodic shedding of hairpin-like vortices from the reattachment region and its influences upon heat transfer are investigated.

Fundamental Equations and Numerical Procedures

Figure 1 represents the flow configuration, coordinate system and main physical parameters. A blunt flat plate of thickness H is located at the center of a channel of $10H \times 10H$. Fundamental equations analyzed in the following are the continuity, momentum and energy ones for three-dimensional unsteady flow of incompressible viscous fluid with constant properties.

$$\nabla \cdot \mathbf{u} = 0 \tag{1}$$

Contributed by the Heat Transfer Division for publication in the JOURNAL OF HEAT TRANSFER. Manuscript received by the Heat Transfer Division November 15, 1999; revision received August 21, 2001. Associate Editor: R. Douglass.

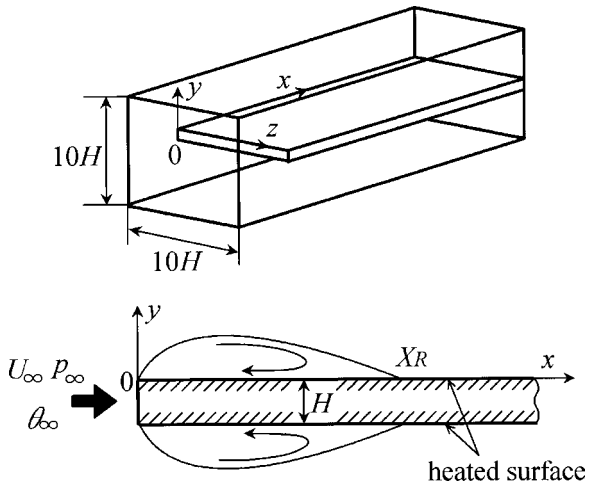

Fig. 1 Flow configuration and coordinate system

$$\mathbf{u}_t+(\mathbf{u}\cdot\nabla)\mathbf{u}=-\nabla p+\frac{1}{\mathrm{Re}}\nabla^2\mathbf{u} \tag{2}$$

$$\theta_t+(\mathbf{u}\cdot\nabla)\theta=\frac{1}{\mathrm{Re\,Pr}}\nabla^2\theta, \tag{3}$$

where space coordinates $\mathbf{x}$, fluid velocity $\mathbf{u}$, pressure p and temperature θ are non-dimensionalized by $\mathbf{x}^*=\mathbf{x}/H$, $\mathbf{u}^*=\mathbf{u}/U_\infty$, $p^*=p/\rho U_\infty^2$ and $\theta^*=\lambda(\theta-\theta_\infty)/(q_wH)$, respectively. The superscript * denotes non-dimensional quantities, and is neglected in the above equations. The numerical method is almost the same as our previous one [8]. The SMAC method [19] is applied in the present study.

$$\frac{\hat{\mathbf{u}}-\mathbf{u}^n}{\Delta t}=-(\mathbf{u}\cdot\nabla)\mathbf{u}-\nabla p+\frac{1}{\mathrm{Re}}\nabla^2\mathbf{u} \tag{4}$$

$$\frac{\mathbf{u}^{n+1}-\hat{\mathbf{u}}}{\Delta t}=-\nabla\phi \tag{5}$$

$$p^{n+1}=p^n+\phi \tag{6}$$

$$\nabla^2\phi=\frac{1}{\Delta t}\nabla\cdot\hat{\mathbf{u}}, \tag{7}$$

where $\hat{\mathbf{u}}$ denotes the prediction velocity, ϕ pressure correction, and superscript n the time level. The prediction velocity is obtained from Eq. (4), and the Poisson equation (7) for pressure correction is solved. Using this pressure correction, the velocity and pressure are corrected by Eqs. (5) and (6), respectively so that the continuity equation is satisfied. After that, the temperature is obtained by Eq. (3).

The finite difference forms of above equations are obtained by the implicit Euler backward method in steady flow and by the Crank-Nicholson method in unsteady flow for the time differentials, respectively. As for the space difference, the fifth-order upwind difference is applied for the convection terms in order to make clear the dynamics of vortices [20]. For example, $u\partial u/\partial x$ is discretized on the uniform grid system with mesh size Δx as follows:

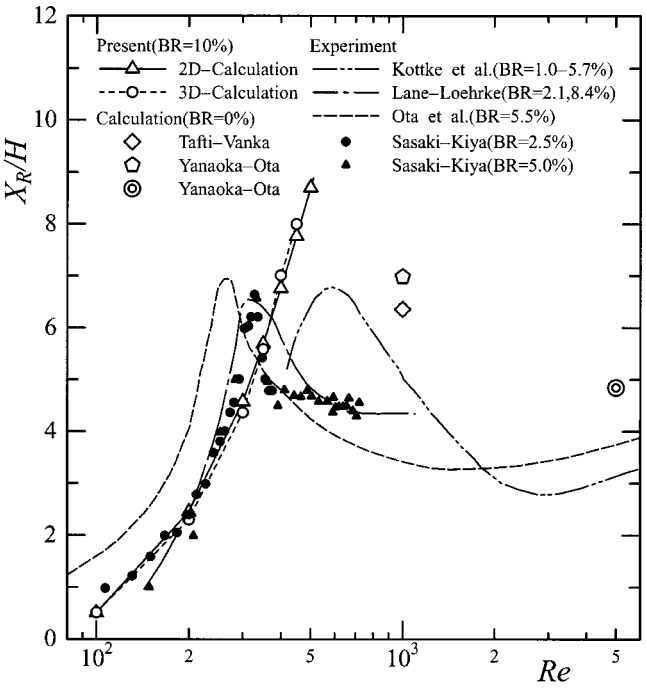

Fig. 2 Comparison of reattachment length on channel center

$$u\left.\frac{\partial u}{\partial x}\right|_{x_i}=\begin{cases}u_i\dfrac{-6u_{i+2}+60u_{i+1}+40u_i-120u_{i-1}+30u_{i-2}-4u_{i-3}}{120\Delta x} & ;u_i>0\\ u_i\dfrac{4u_{i+3}-30u_{i+2}+120u_{i+1}-40u_i-60u_{i-1}+6u_{i-2}}{120\Delta x} & ;u_i<0\end{cases} \tag{8}$$

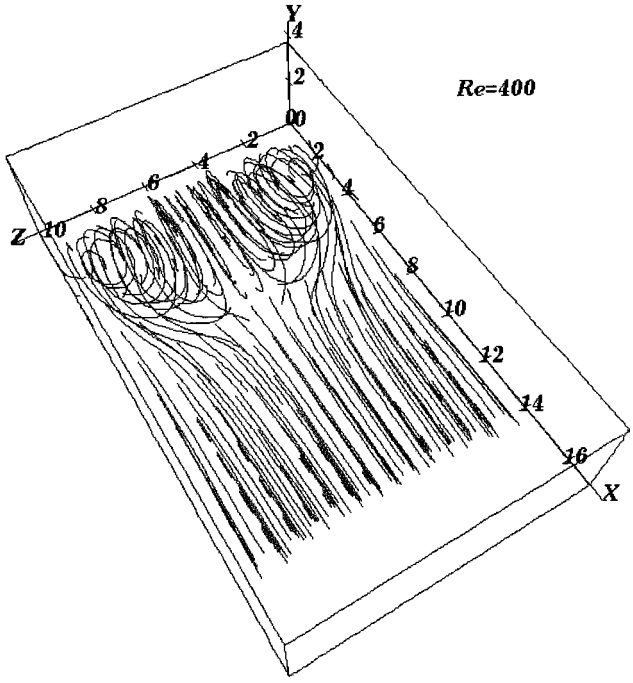

Fig. 3 Streamlines (Re=400)

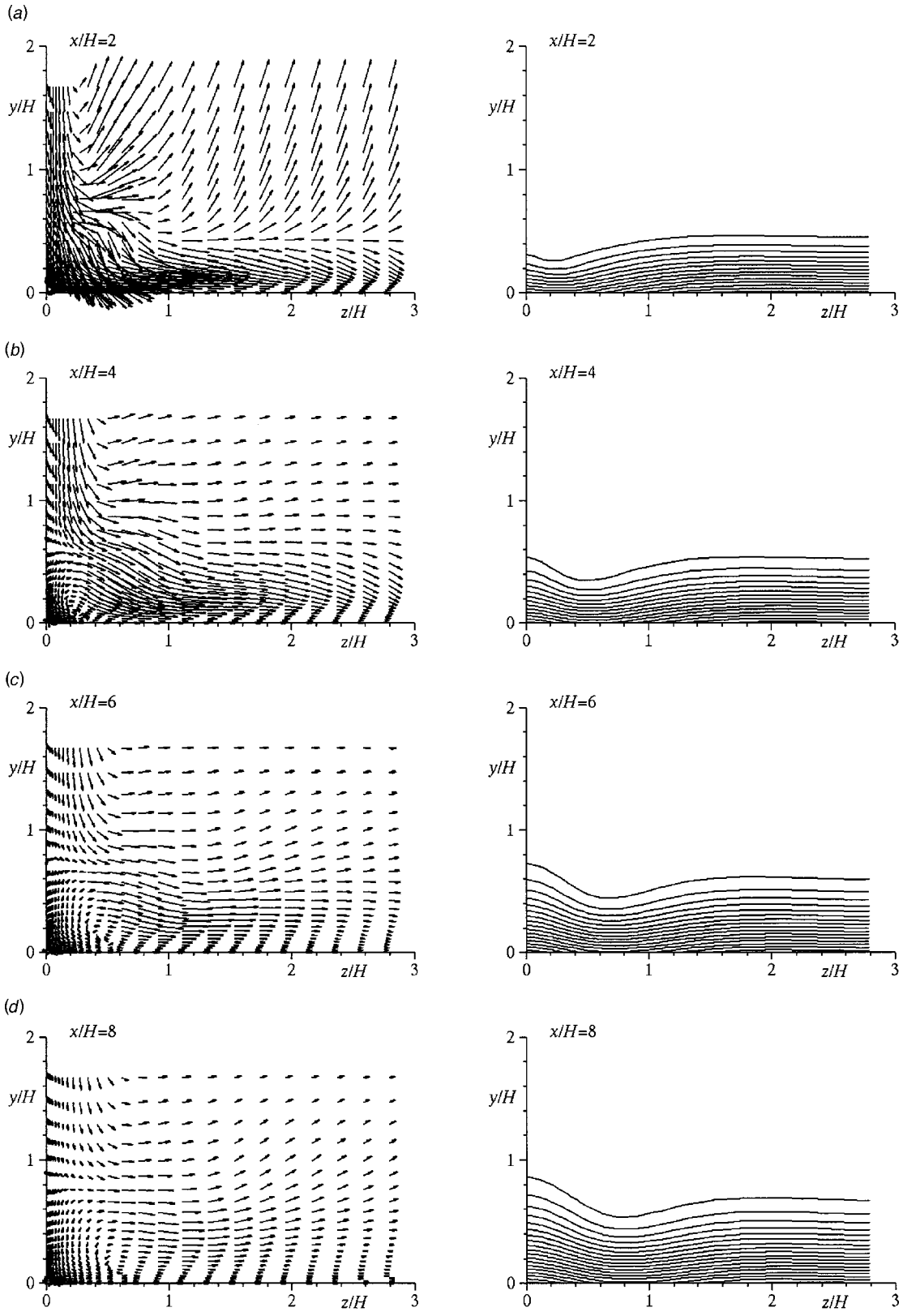

Fig. 4 Velocity vectors (left) and temperature contours (right) (Re=200). Contour interval is 0.025 from 0.025 to 0.75.

The diffusion terms are obtained by the fourth-order central difference; For example,

$$\left.\frac{\partial^2 u}{\partial x^2}\right|_{x_i} = \frac{-u_{i+2}+16u_{i+1}-30u_i+16u_{i-1}-u_{i-2}}{12\Delta x} \tag{9}$$

The other terms are discretized using the second-order central difference scheme. Lagrange polynomial is used to obtain coefficients in the difference forms so that the present numerical method is applied to non-uniform grid systems.

The computational region extends from $-5H$ to $20H$ in the

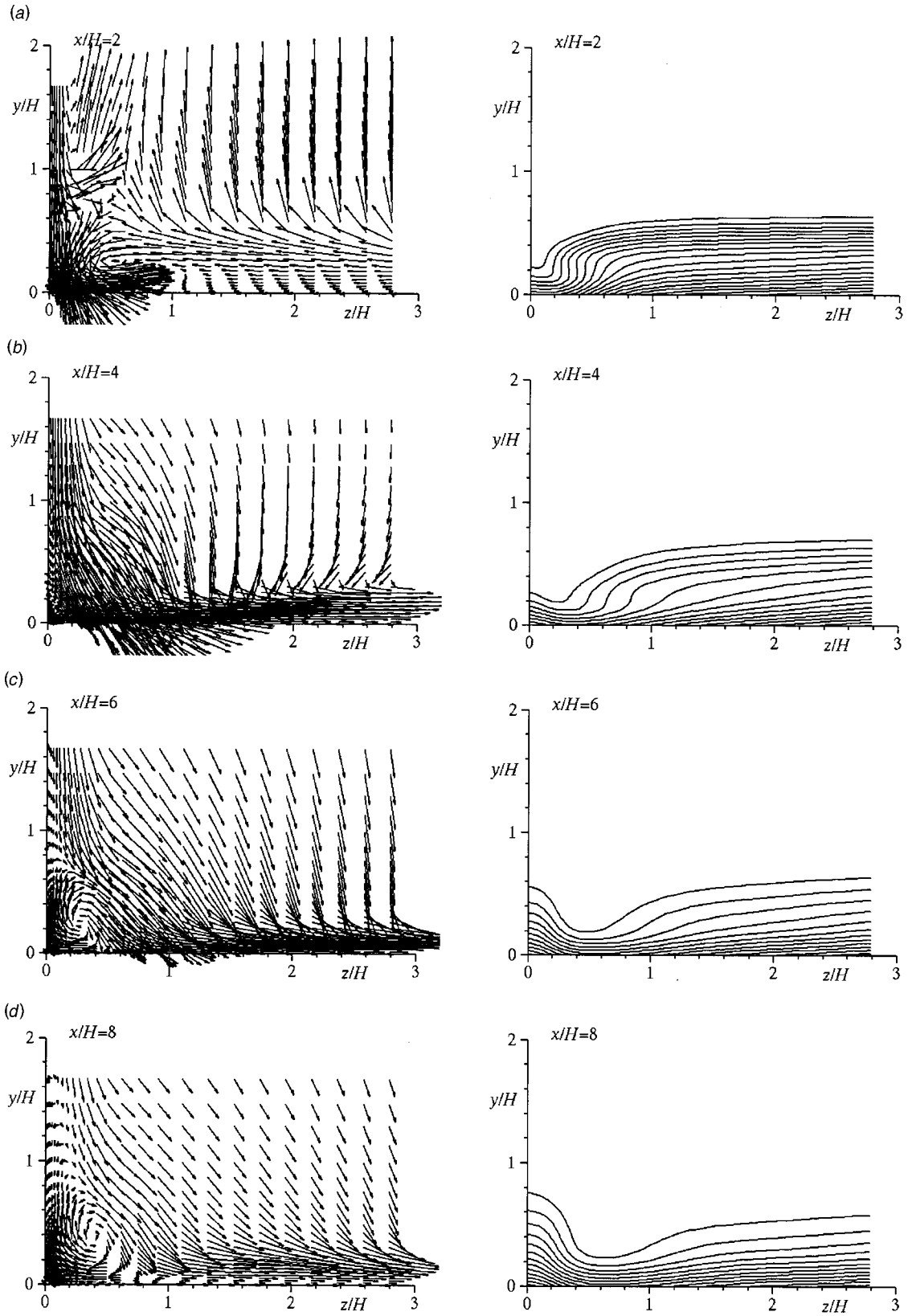

Fig. 5 Velocity vectors (left) and temperature contours (right) (Re=400). Contour interval is 0.025 from 0.025 to 0.75.

x-direction, $-0.5H$ to $4.5H$ in the y-direction and 0 to $10H$ in the z-direction. The blockage ratio, BR, in the present study is 0.10 and the aspect ratio is 10, whose values are selected with referring previous experimental works [1,3–5]. The boundary layer developing on the side wall may influence the horseshoe-vortex, suggesting that the inlet location is important. In the experimental studies, the distance between the nozzle exit and the leading edge of the testing plate is usually not long. Furthermore, the grid number increases as the length between the nozzle exit and the plate leading edge increases, and it results in an increase of computa-

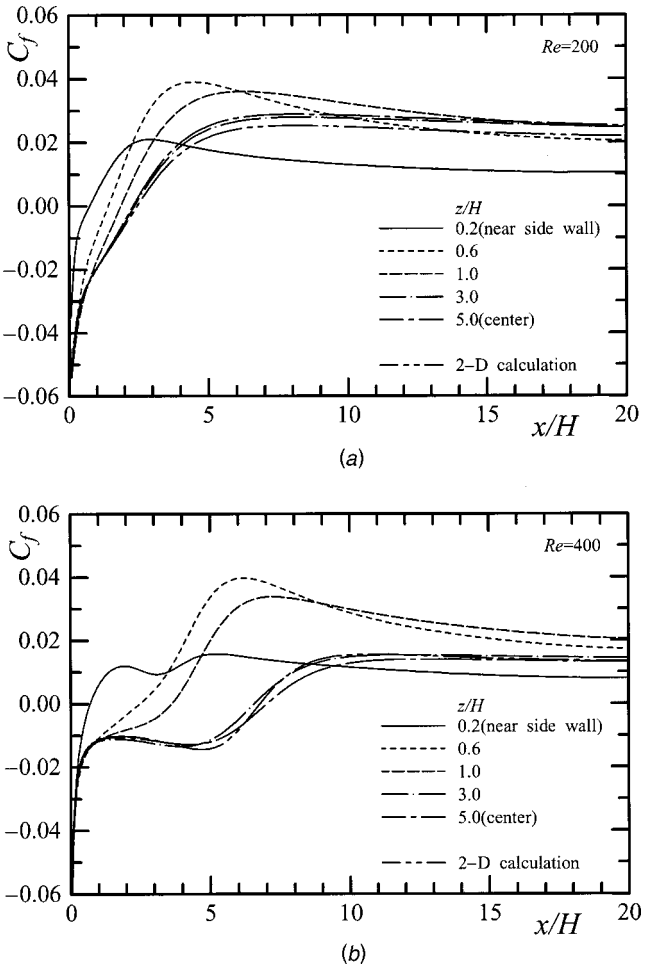

Fig. 6 (*a*) Surface friction coefficient (Re=200); and (*b*) surface friction coefficient (Re=400)

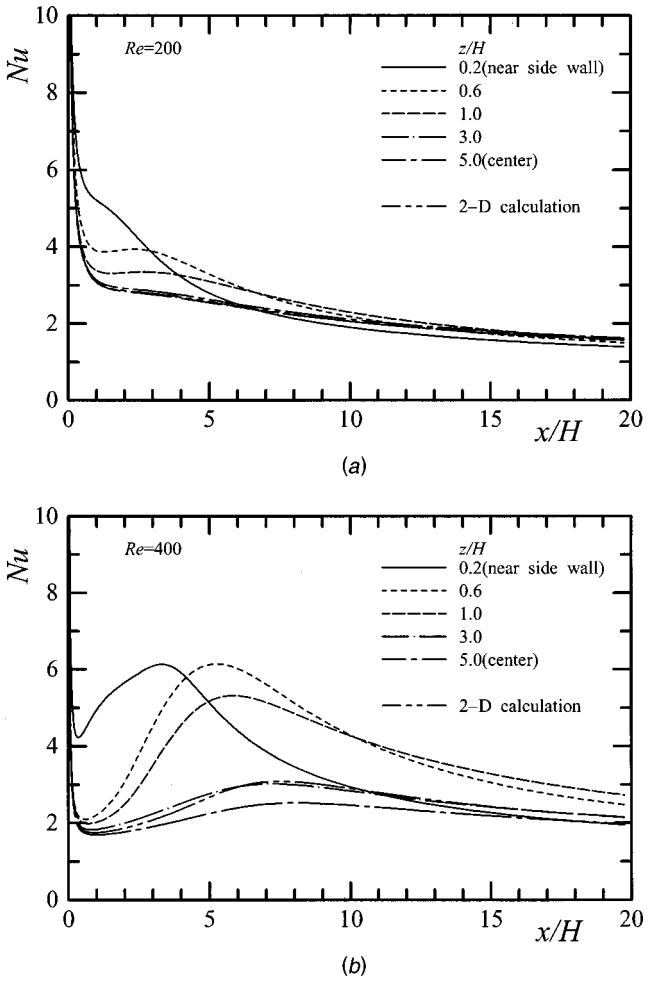

Fig. 7 (*a*) Nusselt number distribution (Re=200); and (*b*) Nusselt number distribution (Re=400)

tional work. As considering such the situations, the inlet location is assumed at $x=-5H$ in the present study.

The boundary conditions are as follows. As for the velocity, the uniform velocity profile at the inlet and the no-slip condition on the walls are assumed. At the outlet, the zero gradients are used. The symmetrical flow is presumed on the center line upstream of the leading edge, since it is confirmed that the flow in the upper and lower spaces is symmetric through the preliminary calculations on the entire flow field. As for the temperature, it is assumed to be uniform at the inlet, and the plate surface is heated under a uniform heat flux, though the leading edge of the plate and the side walls are adiabatic. The second derivative is assumed zero at the outlet and the symmetric condition is used on the center line upstream of the plate. As for the initial conditions, the uniform velocity and uniform temperature are assumed over the entire flow field.

The computational grids of 165×90, 250×120 and 329×179 for two-dimensional calculations and 165×90×71 for three-dimensional ones are generated by using the orthogonal coordinates with non-uniform spacing so that the grid space is fine near the walls and the recirculation region. The grid dependency of the present numerical results is confirmed by two-dimensional calculations since its confirmation by three-dimensional calculations is not economical. The maximum difference of Nusselt number at Reynolds number Re=550 between each computational grids is compared. The difference is found to be 1.1 percent between grids of 165×90 and 250×120, and 3.2 percent between grids of 165×90 and 329×179. It is found that the grid dependency is small until Re=550. Results of the surface friction and pressure coefficients also exhibit a similar trend. Accordingly, results using the grid of 165×90 are mainly represented in the following. As for three-dimensional calculations, the computational grid of 165×90×71 is used, in which a minimum grid spacing is about 0.01 *H* near the plate surface and the side walls.

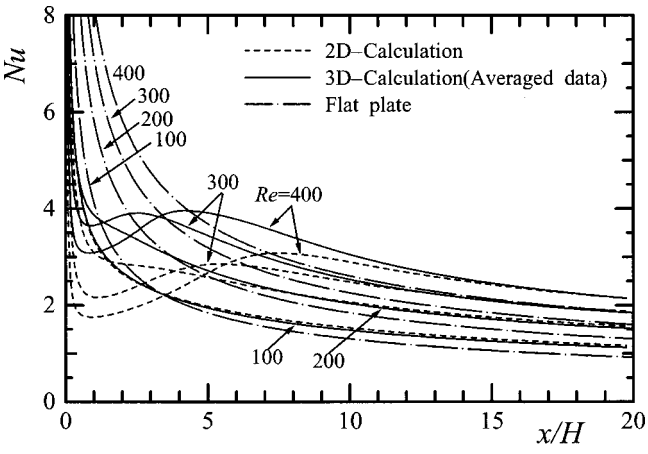

Fig. 8 Nusselt number averaged over spanwise direction

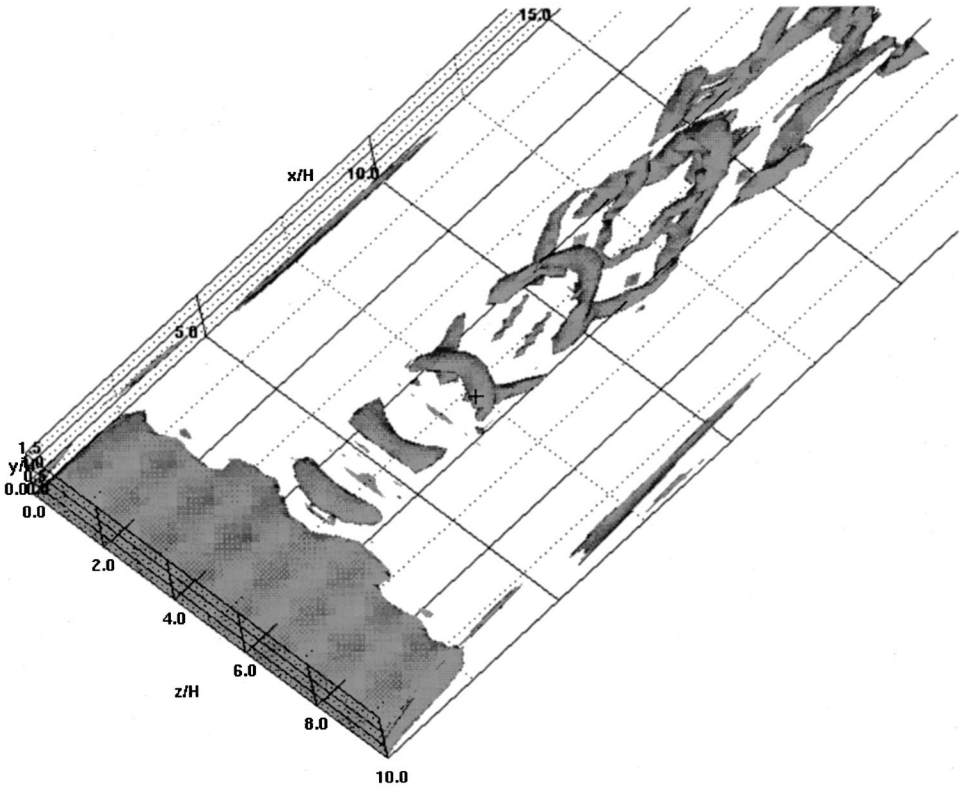

Fig. 9 Isosurface of curvature of equi-pressure surface (Re=450, T=20)

The numerical calculations are performed on the flow in a Reynolds number range from Re=100 to 550 for two-dimensional calculations and Re=100 to 450 for three-dimensional ones under Prandtl number Pr=0.7. As for the flow at Re=450 in three-dimensional analysis, the flow becomes unsteady. Accordingly the sampling of data is performed after the flow becomes periodically. The sampling time is $100\,H/U_\infty$ and sampling size is 20,000 for the mean quantities. The sampling frequency of velocity, pressure, and temperature variations is $100\,U_\infty/H$, which corresponds to about 400 times of vortex shedding frequency. The sampling time is $100\,H/U_\infty$ and sampling size is 10,000 for these instantaneous data. In the following, the starting time of sampling is presented as $T=0$.

Numerical Results and Discussion

Figure 2 presents a variation of the reattachment length X_R on the channel center with Reynolds number Re as comparing with previous experimental results by flow visualization. X_R is defined as the location of zero surface friction coefficient in the present results. The flow is found to be unsteady at Re=600 and 450 in two and three-dimensional calculations, respectively. The result at Re=450 in three-dimensional calculation is time averaged one. Three-dimensional results agree well with two-dimensional ones and the reattachment length increases with an increase of Reynolds number. However, the transition from the steady flow to unsteady one occurs at lower Reynolds number in the three-dimensional analysis. This may be due to side wall effect which brings about an increase of flow instability resulting in the three-dimensional flow in the recirculation region. The present critical Reynolds number at which the flow becomes unsteady is higher than the previous experimental results. The difference of critical Reynolds number between the numerical and experimental results is mainly caused by the flow state of free stream. Present calculations are performed for an ideal condition of zero turbulence intensity, while some turbulence exists in the experiments and its intensity is in a range of 0.1 to 2.0 percent [9,11,21] The reattachment point and critical Reynolds number are very sensitive to the turbulence intensity in the transition region, and the scatter of data is not small in the experimental works [10,11]. It is found from Fig. 2 that the transition of flow occurs at higher Reynolds numbers in the numerical calculations of zero turbulence intensity. Present authors [14,15] have calculated the flow over a blunt flat plate in a free stream at Reynolds number 1000 and 5000, in which the numerical scheme is essentially the same as the present one. These results show that the reattachment length decreases at higher Reynolds numbers in the transition region, as included in Fig. 2. The reattachment length X_R/H is about 7 and 5, respectively. The difference between the numerical and experimental results slightly increases with an increase of Reynolds number. This difference may be due to the effect of blockage ratio. Djilali [13] has shown that the reattachment length decreases with an increase of blockage ratio in his numerical study.

The flow in the channel center region is two-dimensional at low Reynolds number, and becomes three-dimensional with an increase of Reynolds number. The streamlines at Re=400 are shown in Fig. 3. The flow is found to be steady but rotate spirally in the recirculation region and reattach parabolically to the plate surface along the spanwise direction, which is caused by the side walls. It is clear that the flow is three-dimensional except in the neighborhood of the plate center.

Figures 4 and 5 represent the velocity vectors and temperature distributions near the side wall in the $y-z$ plane at Re=200 and 400, respectively. It is found from these figures that the downward flow exists around the side wall at both Reynolds numbers. The thermal boundary layer is suppressed by this downward flow and is thinner than that near the channel center, and it results in an increase of heat transfer therein. One part of the downward flow moves to the channel center, the other streams along the side wall, and then the horseshoe-vortex is generated. It is observed that a large scale horseshoe-vortex exists at $x/H=3$ for Re=200 and $x/H=5$ for Re=400 and it grows to the downstream. High Nusselt number near the side wall in the upstream region is caused by

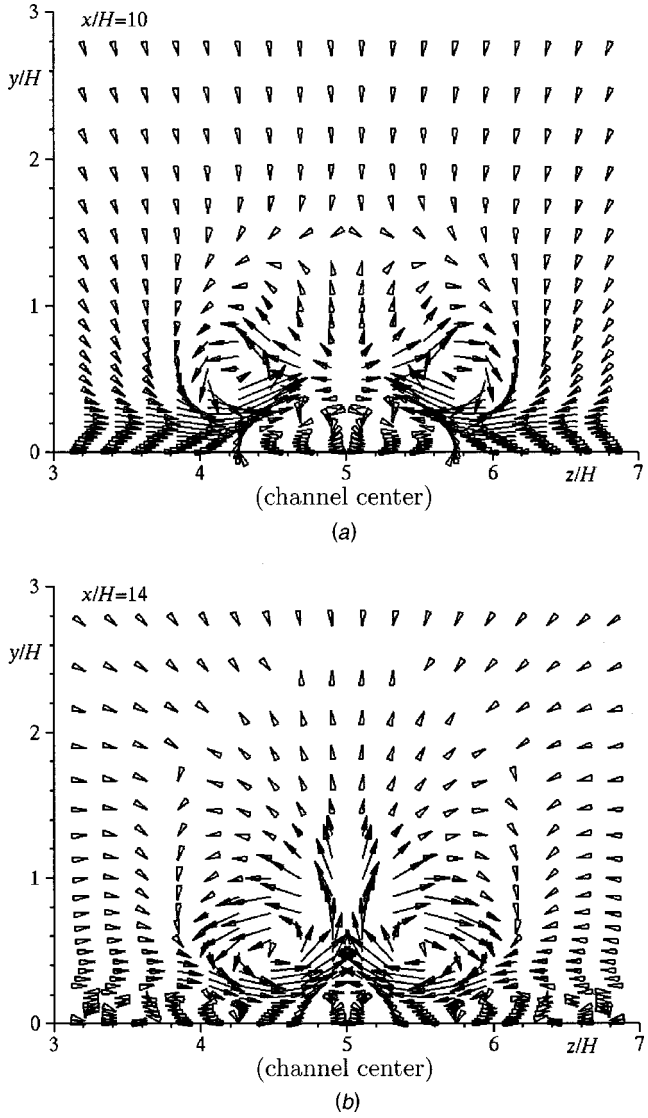

Fig. 10 Velocity vectors (Re=450, $T=20$; (*a*) $x/H=10$; (*b*) $x/H=14$)

this thin thermal boundary layer suppressed by the downward flow and the influence of the horseshoe-vortex upon Nusselt number increases to the downstream. As for $x/H=8$, the horseshoe-vortex at Re=200 is already diffused and weakens. However, the vortex structure at Re=400 is found to be clearer and stronger than that at Re=200 so that high Nusselt number is maintained to the downstream. It is found from these figures that the fluid mass heated on the plate surface is ejected into the free stream by the rotating motion of this vortex and it entrains the outer cold fluid into the plate surface resulting in a thin thermal boundary layer. As for Re=400, the flow from the channel center to the side wall exists at $x/H=1\sim2$ because the flow inside the recirculation region spirally recirculates, as previously shown in Fig. 3. However, Nusselt number increases from the channel center to the side wall as shown later in Fig. 7. This is due to the downward flow generated by an impingement of flow to the side wall and also the two-dimensionality of flow near the channel center.

Figures 6 and 7 present spanwise variations of the *x*-wise surface friction coefficient and Nusselt number at Re=200 and 400, respectively. Results of two-dimensional calculations are included in these figures for comparison. It is clear that the difference between two- and three-dimensional results for the surface skin friction coefficient and also Nusselt number is relatively small near the channel center at both Re=200 and 400, but increases greatly near the side walls. The surface friction coefficient attains a peak value near the side wall. Such a characteristic variation may be originated from the fact that the velocity near the side wall is increased by the horseshoe-vortex compared to that at the center and this vortex structure also increases the streamwise velocity. Spanwise variation becomes great with an increase of Reynolds number as shown in Fig. 6(*b*).

Nusselt number at Re=200 in the neighborhood of the side wall steeply decreases to the downstream independently of the spanwise location. Its value on the channel center monotonically decreases to the down-stream and the spanwise variation is small, which indicates that the temperature on the plate surface is almost two-dimensional except near the side wall at Re=200. Results at Re=400 show maxima at some location and its location shifts to the downstream compared to that at Re=200 because the reattachment of flow moves to the downstream with an increase of Reynolds number. The location of maximum Nusselt number shifts to the upstream from the channel center to the side wall. This may be due to the three-dimensionality of flow reattachment. Nusselt number near the side wall is higher than that on the channel center, which is caused by the horseshoe-vortex. That is, the horseshoe-vortex increases the streamwise velocity and causes higher velocity to the plate surface in the neighborhood of the side wall. Further, the rotation of this vortex structure entrains the fluid mass heated on the plate surface into the main stream outside the boundary layer. Its effect increases with an increase of Reynolds number.

Figure 8 shows the Nusselt number averaged over the spanwise direction, as comparing with results of the two-dimensional simulation for the blunt flat plate and the similarity solution for laminar heat transfer on a flat plate without separation [22], which is given as follows using the present nomenclature.

$$\mathrm{Nu}=0.464\mathrm{Pr}^{1/3}\sqrt{\mathrm{Re}}/\sqrt{x} \tag{10}$$

Present two and three-dimensional results are lower than similarity solution near the leading edge, but becomes higher downstream of the reattachment point, which is caused by the effect of flow acceleration in the channel. The difference between two and three-dimensional results is large in the recirculation region but decreases to the downstream. The strong downward flow exists near the side wall and causes higher Nusselt number for three-dimensional flow compared to that for two-dimensional one.

Present numerical results for the unsteady three-dimensional flow at Re=450 are illustrated in the following. The large-scale vortices are generated and shed to the downstream in this flow. In the present study for visualizing the skeleton structure of flow, the isosurface of curvature of equi-pressure surface is used. Figure 9 shows the isosurface of curvature of equi-pressure surface at time $T=20$. The process of generation and growth of hairpin-like vortices is observed from this figure. It is clearly illustrated that the hairpin-like vortices in row exist on the channel center downstream of the reattachment region. These vortices are generated by the instability of separated shear layer described later. The head of hairpin-like vortices moves away from the plate surface to the downstream, their leg elongates, and then the streamwise vortices are generated. In the previous studies using the periodic boundary condition on the spanwise boundary [14,15], the hairpin-like vortices exist periodically in the spanwise direction. However, only one hairpin-like vortex is shed on the channel center because of the side walls in the present study. The spanwise scale of these hairpin-like vortices is about $2H$ as clearly shown in the figure. The unsteadiness of the horseshoe-vortex is not observed in the present study.

The velocity vectors in the $y-z$ plane at $x/H=10$ and 14 are shown in Fig. 10. The time is the same as in Fig. 9. The hairpin-like vortices exist at $x/H=10$ and 14, resulting in a vortex pair of counter-rotation. It is found that the vortex at $x/H=14$ is larger as suggesting the vortex growing to the downstream.

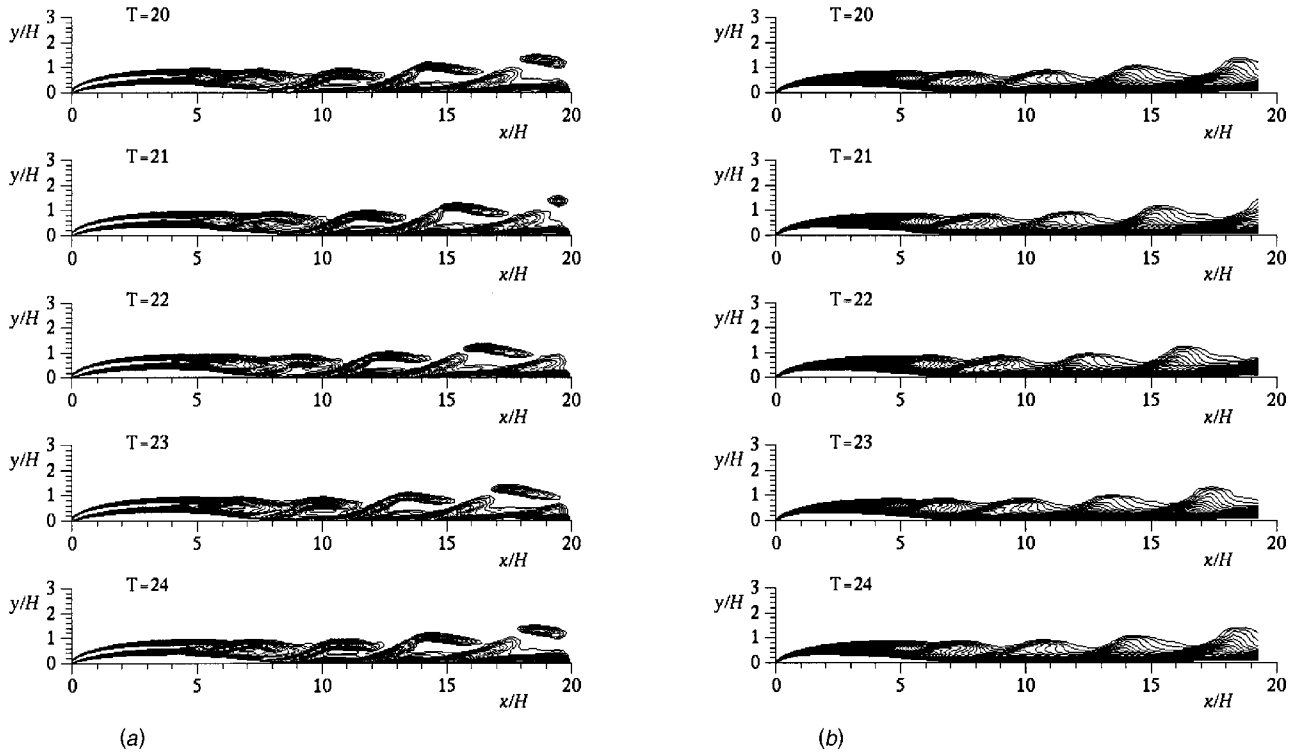

Fig. 11 (*a*) Time variations of spanwise vorticity contours on channel center (Re=450) (contour interval is 0.2 from −5.0 to −0.4); and (*b*) time variations of temperature contours on channel center (Re=450) (contour interval is 0.01 from 0.02 to 0.3)

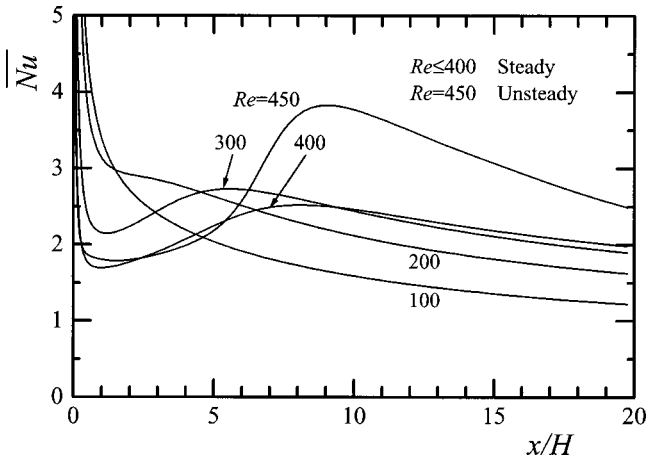

Fig. 12 Time averaged Nusselt number distribution (Re=450)

Time variations of the spanwise vortices and temperature distributions at the channel center are shown in Fig. 11. As for the result at $T=20$, the separated shear layer rolls up around $x/H=7$. The shed hairpin-like vortices incline to the plate surface at a point downstream of the reattachment one $x/H=8$. These vortices flow to the downstream with time, and its shedding frequency is estimated to be about $0.25U_\infty/H$. Such a phenomena of the instability of separated shear layer is also observed by Sasaki-Kiya [11] with the flow visualization. On the other hand, the temperature gradients near the reattachment region is large since the separated shear layer impinges onto the wall, resulting an increase of heat transfer therein. Further, it is found that the shed hairpin-like vortices entrain the heated fluid mass to the free stream.

The time averaged Nusselt number at Re=450 on the channel center is compared with the results for steady flow in Fig. 12. Results at Re=100 and 200 decrease monotonically to the downstream. Nusselt number at Re>200 reaches maximum near the reattachment point. The location of maximum Nusselt number exists slightly downstream of the reattachment point. Nusselt number for the unsteady flow increases greatly as compared with that of steady flow at lower than Re=400. This may be due to the impingement of the vortices generated by the rolling up of the separated shear layer onto the plate surface. Further, Nusselt number in the downstream is very high as suggesting great effects of the shed vortices.

Concluding Remarks

Numerical calculations of a separated and reattached flow and heat transfer over a blunt flat plate in a square channel are carried out at Re=100~550 in two-dimensional flow and at Re=100~450 in three-dimensional one for Pr=0.7. The main results obtained are as follows.

1 The reattachment length on the plate center increases with an increase of Reynolds number, and the present three-dimensional results agree well with the two-dimensional ones. However, the transition to unsteady flow in the three-dimensional flow occurs at lower Reynolds number by the side wall effect.

2 The flow inside the recirculation region spirally recirculates, as resulting in the parabolic flow reattachment along the spanwise direction. At higher Reynolds number, the hairpin-like vortices are periodically shed from the reattachment region originated from the instability of the separated shear layer. These vortices incline to the plate surface and flow out in row on the channel center. The fluid mass heated on the wall is entrained into the free stream by these vortices.

3 The horseshoe-vortex in the neighborhood of the side wall grows to the downstream with an increase of Reynolds number.

The fluid mass heated on the wall is entrained into the main stream by such the vortices. This vortex structure has great effects upon heat transfer.

4 Nusselt number becomes maximum near the side wall because of the parabolic reattachment of flow. The horseshoe-vortex causes an increase of the streamwise velocity and also the transverse one near the side wall. These flow brings about a great increase of Nusselt number near the side wall than the channel center.

Acknowledgment

The authors acknowledge that the present calculations were conducted using the CRAY-C916 at the Institute of Fluid Science, Tohoku University.

Nomenclature

C_f = surface friction coefficient $=\tau_w/(\rho U_\infty^2/2)$
H = plate thickness
Nu = Nusselt number $=\alpha H/\lambda$
p = pressure
Pr = Prandtl number
q_w = heat flux
Re = Reynolds number $=U_\infty H/\nu$
t = time
T = non-dimensional sampling time
$\mathbf{u}$ = velocity vector (u,v,w)
U_∞ = velocity of upstream uniform flow
$\mathbf{x}$ = coordinates (x,y,z)
X_R = reattachment length
α = heat transfer coefficient $=q_w/(\theta_w-\theta_\infty)$
θ = temperature
λ = thermal conductivity
ν = kinematic viscosity
ρ = density
τ_w = wall friction stress
ϕ = pressure correction

Subscript

w = wall
∞ = upstream uniform flow

Superscript

$-$ = time averaged result

References

[1] Ota, T., and Kon, N., 1974, ''Heat Transfer in the Separated and Reattached Flow on a Blunt Flat Plate,'' ASME J. Heat Transfer, **96**, pp. 459–462.
[2] Nishiyama, H., Ota, T., and Sato, K., 1988, ''Temperature Fluctuations in a Separated and Reattached Turbulent Flow over a Blunt Flat Plate,'' Wärme-Stroffübertragung, **23**, pp. 275–281.
[3] Kiya, M., and Sasaki, K., 1983, ''Structure of a Turbulent Separation Bubble,'' J. Fluid Mech., **137**, pp. 83–113.
[4] Cherry, N. J., Hillier, R., and Latour, M. E. M. P., 1984, ''Unsteady Measurements in a Separated and Reattaching Flow,'' J. Fluid Mech., **144**, pp. 13–46.
[5] Djilali, N., and Gartshore, I. S., 1991, ''Turbulent Flow around a Bluff Rectangular Plate. Part I: Experimental Investigation,'' ASME J. Fluids Eng., **113**, pp. 51–59.
[6] Tafti, D. K., and Vanka, S. P., 1991, ''A Numerical Study of Flow Separation and Reattachment on a Blunt Plate,'' Phys. Fluids A, **3**, No. 7, pp. 1749–1759.
[7] Tafti, D. K., and Vanka, S. P., 1991, ''A Three-Dimensional Numerical Study of Flow Separation and Reattachment on a Blunt Plate,'' Phys. Fluids A, **3**, No. 12, pp. 2887–2909.
[8] Ota, T., and Yanaoka H., 1993, ''Numerical Analysis of a Separated and Reattached Flow over a Blunt Flat Plate,'' *Proceedings of the 5th International Symposium on Computational Fluid Dynamics*, Vol. 3, pp. 423–428.
[9] Lane, J. C., and Loehrke, R. I., 1980, ''Leading Edge Separation from a Blunt Plate at Low Reynolds Number,'' ASME J. Fluids Eng., **102**, pp. 494–496.
[10] Ota, T., Asano, Y., and Okawa, J., 1981, ''Reattachment Length and Transition of the Separated Flow Over Blunt Flat Plates,'' Bull. JSME, **24**, No. 192, pp. 941–947.
[11] Sasaki, K., and Kiya, M., 1991, ''Three-Dimensional Vortex Structure in a Leading-Edge Separation Bubble at Moderate Reynolds Numbers,'' ASME J. Fluids Eng., **113**, pp. 405–410.
[12] Tafti, D. K., 1993, ''Vorticity Dynamics and Scalar Transport in Separated and Reattached Flow on a Blunt Plate,'' Phys. Fluids A, **5**, No. 7, pp. 1661–1673.
[13] Djilali, N., 1994, ''Forced Laminar Convection in an Array of Stacked Plates,'' Numer. Heat Transfer, Part A, **25**, pp. 393–408.
[14] Yanaoka, H., and Ota, T., 1996, ''Three-Dimensional Numerical Simulation of Separated and Reattached Flow and Heat Transfer over Blunt Flat Plate,'' Trans. Jpn. Soc. Mech. Eng., Ser. B, **62B**, pp. 1111–1117.
[15] Yanaoka, H., and Ota, T., 1996, ''Three-Dimensional Numerical Simulation of Separated and Reattached Flow and Heat Transfer over Blunt Flat Plate at High Reynolds Number,'' Trans. Jpn. Soc. Mech. Eng., Ser. B, **62B**, pp. 3439–3445.
[16] Baker, C. J., 1979, ''The Laminar Horseshoe Vortex,'' J. Fluid Mech., **95**, pp. 347–367.
[17] Goldstein, R. J., and Karni, J., 1984, ''The Effect of a Wall Boundary Layer on Local Mass Transfer From a Cylinder in Crossflow,'' ASME J. Heat Transfer, **106**, pp. 260–267.
[18] Tan, C. S., 1989, ''A Multi-Domain Spectral Computation of Tree-Dimensional Laminar Horseshoe Vortex Flow Using Incompressible Navier-Stokes Equations,'' J. Comput. Phys., **85**, pp. 130–158.
[19] Amsden, A. A., and Harlow, F. H., 1970, ''A Simplified MAC Technique for Incompressible Fluid Flow Calculations,'' J. Comput. Phys., **6**, pp. 322–325.
[20] Rai, M. M., and Moin, P., 1991, ''Direct Simulations of Turbulent Flow Using Finite-Difference Schemes,'' J. Comput. Phys., **96**, pp. 15–53.
[21] Kottke, V., Blenke, H., and Schmidt, K. G., 1977, ''Einfluß von Anstrompröfil und Turbulenzintensität auf die Umströmung längsangeströmter Platten endlicher Dicke,'' Waerme- Stoffuebertrag., **10**, pp. 159–174.
[22] Lighthill, M. J., 1950, ''Contributions to the Theory of Heat Transfer Through a Laminar Boundary Layer,'' Proc. R. Soc. London, Ser. A, **202**, pp. 359–377.

Convection Induced by a Cusp-Shaped Magnetic Field for Air in a Cube Heated From Above and Cooled From Below

Masayuki Kaneda
Interdisciplinary Graduate School of Engineering Sciences,
Kyushu University, Kasuga koen 6-1,
Kasuga 816-8580, Japan

Toshio Tagawa

Hiroyuki Ozoe
e-mail:ozoe@cm.kyushu-u.ac.jp

Institute of Advanced Material Study,
Kyushu University, Kasuga koen 6-1,
Kasuga 816-8580, Japan

Magnetizing force, which acts in a magnetic field of steep gradient, was applied to air in a cube heated from above and cooled from below, and with the four vertical walls thermally insulated. A four-poles magnet was installed to apply the cusp-shaped magnetic field to air in the cubic enclosure. A simple model equation was derived for magnetizing force and numerically computed for the system. Without a magnetic field, the conduction was stable, but under the magnetizing force a strong downward flow occurred from the center of the top heated plate and the average Nusselt number attained $Nu=1.17$ at $Ra=10^5$ and $\gamma=0.5$, which is equivalent to a temperature difference of 4 [°C] between the top and bottom walls under a maximum magnetic induction of 0.9 [T] inside a cube of $(0.064)^3$ [m^3] heated from above. The flow visualization experiment with hot incense smoke proved the downward flow from the top hot plate. [DOI: 10.1115/1.1418369]

1 Introduction

In 1847, Faraday [1] reported the movement of a soap bubble containing O_2 gas toward a center of a strong magnet pole. The paramagnetism of oxygen gas is known to be due to the parallel spin of two outer-shell electrons of the molecule. Pauling et al. [2] developed an oxygen gas analyzer based on this characteristic. However, this characteristic was neglected for many years until the recent development of a superconducting magnet providing strong magnetic induction of 10 Tesla or more for possible industrial usage. Wakayama and coworkers [3–7] have been very active in finding various interesting phenomena, such as the jet stream of nitrogen gas into air (Wakayama jet) in a steeply decreasing magnetic field, or enhancement of combustion flames, and sustaining flames under micro-gravity. Braithwaite et al. [8] reported the enhancement or suppression of the heat transfer rate through a shallow liquid layer (paramagnetic liquid) heated from below and cooled from above under a strong magnetic field. The average Nusselt number assumed a larger or smaller value than the gravitational natural convection heat transfer rate depending on the direction of the magnetizing force. Kitazawa and coworkers [9–12] also have been active in finding interesting phenomena, such as floating of a water droplet, a magnetically curved fluid surface and enhanced dissolution rate of oxygen gas into water. The present work reports the enhancement of conductive heat transfer by convection upon application of magnetic field gradient.

2 Derivation of Magnetizing Force Model

Bai et al. [7] gave the magnetizing force for air as follows:

$$\mathbf{f}_m=\frac{\mu_m}{2}\chi_{O_2}(\theta)Y_{O_2}\rho\nabla H^2. \tag{1}$$

This can be rephrased with magnetic induction **b** as follows:

$$\mathbf{f}_m=\frac{\rho\chi_{O_2}Y_{O_2}}{2\mu_m}\nabla b^2=\frac{\rho\chi Y}{2\mu_m}\nabla b^2. \tag{2}$$

Here, $\chi=\chi_{O_2}$, $Y=Y_{O_2}$ were employed for abbreviation. This can be included as an additional external force in the Navier-Stokes equation as follows:

$$\rho\frac{D\mathbf{u}}{Dt}=-\nabla p+\mu\nabla^2\mathbf{u}+\frac{\rho\chi Y}{2\mu_m}\nabla b^2+\rho\mathbf{g}. \tag{3}$$

At the reference state of the isothermal state, $\theta=\theta_0$, $p=p_0$, $\rho=\rho_0$ and $\chi=\chi_0$, there will be no convection and Eq. (3) becomes

$$0=-\nabla p_0+\frac{\rho_0\chi_0 Y}{2\mu_m}\nabla b^2+\rho_0\mathbf{g}. \tag{4}$$

When there is a temperature distribution in a fluid, convection will occur due to the difference in the magnetic susceptibility and density in the buoyancy term. Pressure p can be represented as the summation of p_0 at the isothermal state and p', the pressure difference due to the perturbed state, as follows:

$$p=p_0+p'. \tag{5}$$

Subtracting Eq. (4) from (3) gives

$$\rho\frac{D\mathbf{u}}{Dt}=-\nabla p'+\mu\nabla^2\mathbf{u}+\frac{(\rho\chi-\rho_0\chi_0)Y}{2\mu_m}\nabla b^2+(\rho-\rho_0)\mathbf{g}. \tag{6}$$

Since magnetic susceptibility of oxygen gas χ is inversely proportional to the absolute temperature θ, we get,

$$\chi=\frac{C}{\theta}, \tag{7}$$

where C is a constant.

By a Taylor expansion around a static state,

$$\rho\chi=(\rho\chi)_0+\left(\frac{\partial(\rho\chi)}{\partial\theta}\right)_0(\theta-\theta_0)+\ldots \tag{8}$$

$$\frac{\partial\rho}{\partial\theta}=\frac{\partial}{\partial\theta}\left(\frac{p}{R\theta}\right)=-\frac{\rho}{\theta}\cong-\rho\beta, \tag{9}$$

where $\beta\cong1/\theta$ were used for an ideal gas, $p=\rho R\theta$.

$$\frac{\partial(\rho\chi)}{\partial\theta}=\frac{\partial\rho}{\partial\theta}\chi+\rho\frac{\partial\chi}{\partial\theta}=-\rho\beta\chi+\rho\left(-\frac{C}{\theta^2}\right)=-2\rho\beta\chi \tag{10}$$

Contributed by the Heat Transfer Division for publication in the JOURNAL OF HEAT TRANSFER. Manuscript received by the Heat Transfer Division November 7, 2000; revision received June 12, 2001. Associate Editor: R. L. Mahajan.

Then, we get

$$\rho \frac{D\mathbf{u}}{Dt} = -\nabla p' + \mu \nabla^2 \mathbf{u} - \frac{\rho_0 \beta \chi_0 Y}{\mu_m} (\theta - \theta_0) \nabla b^2 - \rho_0 \beta (\theta - \theta_0) \mathbf{g}. \tag{11}$$

With the Boussinesq approximation, physical properties are constant at $\theta = \theta_0$, and then

$$\frac{D\mathbf{u}}{Dt} = -\frac{1}{\rho_0} \nabla p' + \nu_0 \nabla^2 \mathbf{u} - \frac{\beta \chi_0 Y}{\mu_m} (\theta - \theta_0) \nabla b^2 - \beta (\theta - \theta_0) \times \begin{pmatrix} 0 \\ 0 \\ -g \end{pmatrix}. \tag{12}$$

The equation of continuity, the energy equation and Biot-Savart's law for magnetic induction complete the model equations as follows:

$$\nabla \cdot \mathbf{u} = 0 \tag{13}$$

$$\frac{D\theta}{Dt} = \alpha \nabla^2 \theta \tag{14}$$

$$\mathbf{b} = -\frac{\mu_m i}{4\pi} \int \frac{\mathbf{r} \times d\mathbf{s}}{r^3}. \tag{15}$$

These can be non-dimensionalized by the method of Hellums and Churchill [13] as follows:

$$\nabla \cdot \mathbf{U} = 0 \tag{16}$$

$$DT/D\tau = \nabla^2 T \tag{17}$$

$$D\mathbf{U}/D\tau = -\nabla P + \mathrm{Pr} \nabla^2 \mathbf{U} + \mathrm{Ra}\ \mathrm{Pr}\ T \left[-\gamma \nabla B^2 + \begin{pmatrix} 0 \\ 0 \\ 1 \end{pmatrix} \right] \tag{18}$$

$$\mathbf{B} = -\frac{1}{4\pi} \oint \frac{\mathbf{R} \times d\mathbf{S}}{R^3} \tag{19}$$

These are the model equations for the present problem of an ideal gas (paramagnetic fluid) in magnetic and gravitational fields. Dimensionless variables are defined in Nomenclature. Characteristic dimensionless variables are as follows:

$$\mathrm{Ra} = g\beta(\theta_h - \theta_c) l^3/(\alpha \nu), \quad \mathrm{Pr} = \nu/\alpha, \quad \gamma = \chi_0 Y b_a^2/(g \mu_m l).$$

Initial condition is a conduction state at $\tau < 0$ is as follows: $U = V = W = 0$, $T = Z - 0.5$ $(0 \leqslant Z \leqslant 1)$.

Boundary conditions are as follows:

$$U = V = W = 0 \quad \text{on the wall}$$

$$T = -0.5 \quad \text{at } Z = 0$$

$$T = 0.5 \quad \text{at } Z = 1$$

$$\partial T/\partial Y = 0 \quad \text{at } Y = 0,1$$

$$\partial T/\partial X = 0 \quad \text{at } X = 0,1$$

The above equations were approximated with finite difference equations for staggered grids and numerically computed by the HSMAC method [14].

3 Computed Results

The effect of magnetizing force is known to be dependent on the magnetic field and two and four-coil systems were considered. The effect of magnetizing force alone would be clear in the absence of gravity, and the non-gravitational field was therefore numerically studied at first.

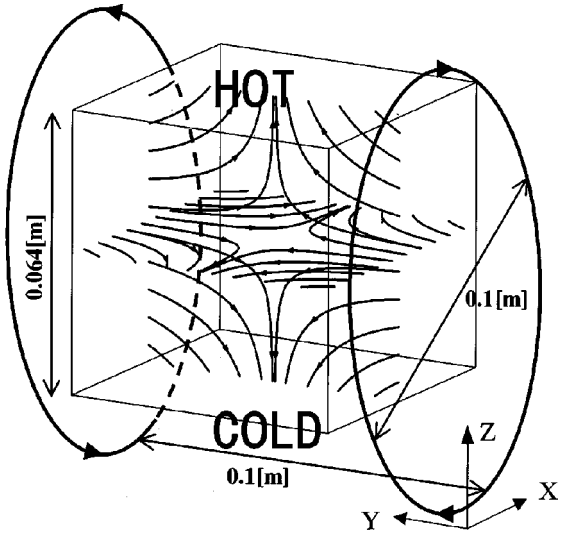

Fig. 1 Schematic drawing of magnetic field with two coils at opposing side walls

3.1 Effect of Computational Grid Numbers. On the effect of computational grid numbers, sample computations were carried out for representative cases at $\mathrm{Ra} = 10^5$, $\gamma = 0.5$ and four coils system with 30^3, 40^3, and 50^3 grids. The average Nusselt number on the top heated plate was 1.176 for grids 30^3, 1.167 for grids 40^3 and 1.163 for grids 50^3. The effect of grid numbers on the Nusselt number is about 0.3 percent and 40^3 grids were employed in the subsequent computations.

3.2 Two Coils Without Gravity Field. Figure 1 shows the schematics of the present system with two coils at two opposing side walls to produce a cusp-shaped magnetic field. The air in the cube is heated from above and cooled from below. Usually gravitational force works in the minus Z-direction. However, it is zero in this section. Lines with arrows in the cube indicate magnetic field lines. The north poles of the magnets are set at the center of the opposing walls, and the maximum strength of magnetic induction occurs at the center of these side walls, with the minimum strength ($\cong$zero) at a core center of the cubic enclosure. Figure 2 shows transient responses of the average Nusselt number at the hot and cold walls. The transient computations are at $(\gamma \mathrm{Ra}) = 0.5 \times 10^5$, $\mathrm{Pr} = 0.71$ and $g = 0$. The convergence is apparent. Dimensional equivalence for air at 1 [atm] and 300 [K] with $\chi_{\mathrm{air}} = \chi_0 Y = 3.2 \times 10^{-7}$ [m^3/kg] is $b_a = 1.13$ [T], $l = 0.064$ [m] and

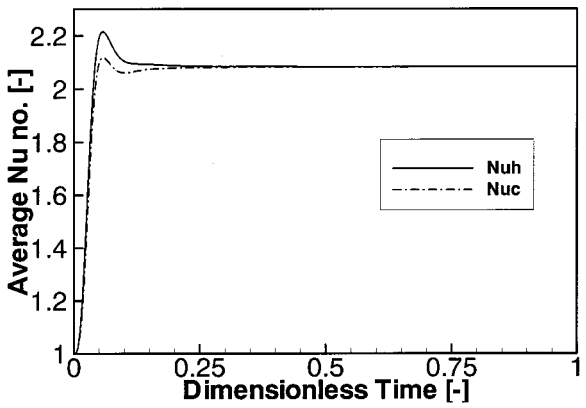

Fig. 2 Transient numerical responses of the average Nusselt number at the top hot plate (Nuh) and bottom cold plate (Nuc)

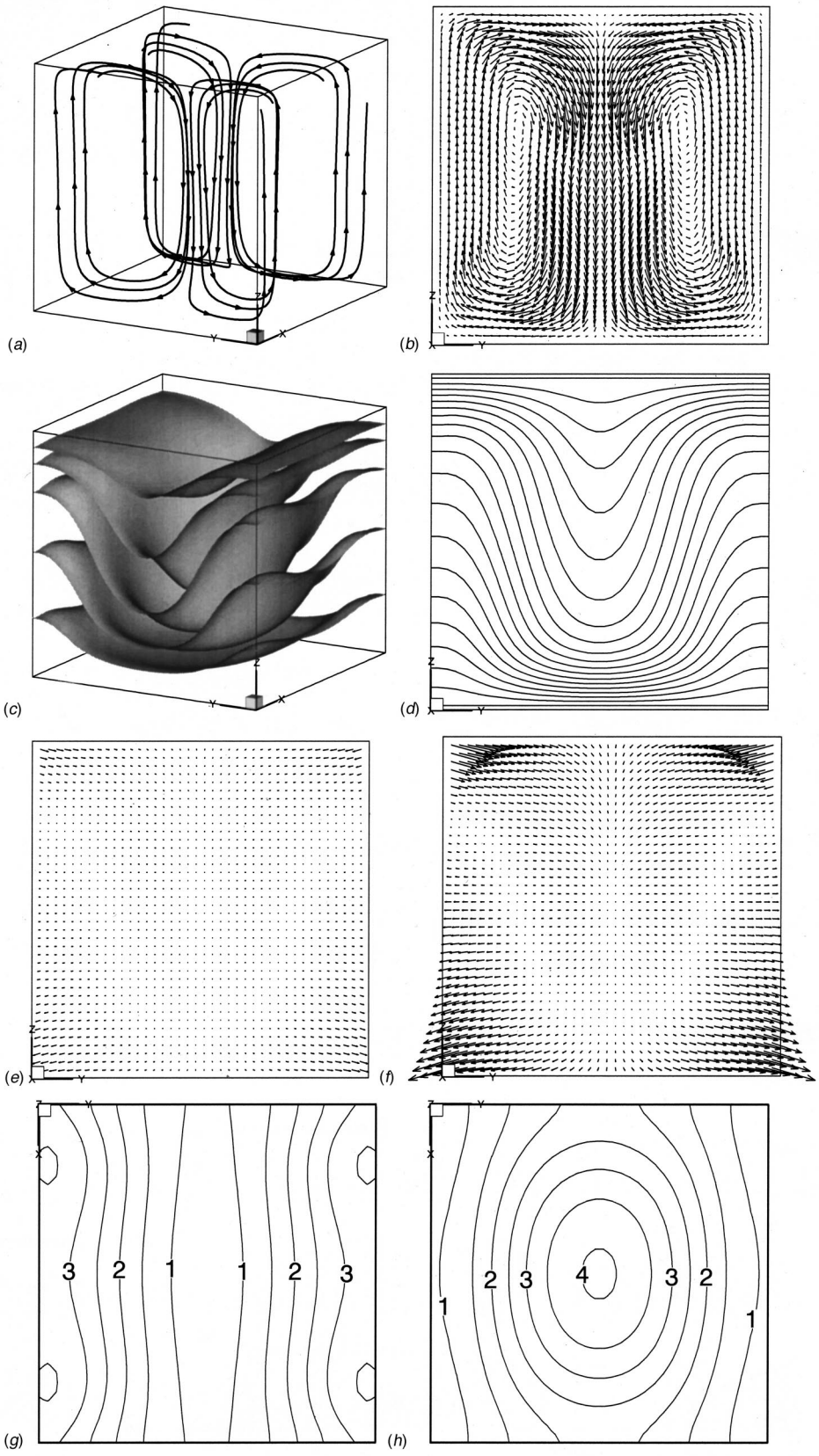

Fig. 3 Summary of computed results for the two coils at opposing side walls and non-gravity field at γRa$=0.5\times10^5$, Pr$=0.71$, and $g=0$: (*a*) streak lines of four particles; (*b*) velocity vectors in a vertical plane of $X=0.5$; (*c*) a perspective view of isotherms; (*d*) isothermal contours in a vertical plate of $X=0.5$; (*e*) magnetizing force vectors of $-\gamma\mathrm{Ra}\,\mathrm{Pr}\,T\nabla B^2$ (the scale is the same as in Figs. 5(*e*) and 6(*e*); (*f*) magnetizing force vectors in (*e*) enlarged five times; (*g*) contour maps of local Nusselt numbers on the top hot plate; and (*h*) contour maps of local Nusselt numbers on the bottom cold plate.

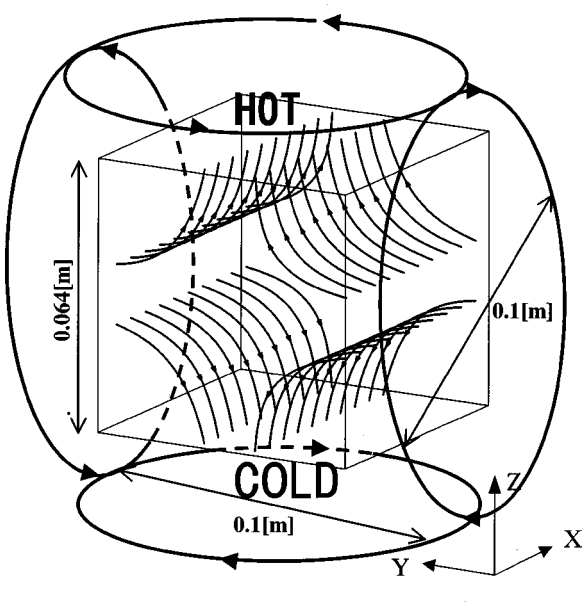

Fig. 4 Schematic of the magnetic field with four coils

$\theta_h - \theta_c = 4.06\,[\mathrm{K}]$. Figure 3 shows a summary of computed result. Figure 3(*a*) shows streak lines of four particles. Hot air proceeds downward to the cold bottom, driven by a magnetizing force. Figure 3(*b*) shows velocity vectors in a vertical cross section at $X=0.5$. Figure 3(*c*) shows a perspective view of isothermal planes. Figure 3(*d*) shows isothermal contours in a vertical cross section at $X=0.5$. It is apparent that downward flow starts from the center of the top plane. Figure 3(*e*) represents magnetizing force vectors on the same scale as in other cases presented hereafter (Figs. 5(*e*), 6(*e*)). Figure 3(*f*) shows the same vectors enlarged five times. Driving force is downwards from a top hot plate and is diverging near the bottom cold plate. The local Nusselt number shows contrasting contours at the top hot plate (*g*) and bottom cold plate (*h*). These shapes correspond with the isothermal contours in (*c*) and (*d*). The average Nusselt number is 2.08 for air in this magnetizing force field.

3.3 Four Coils Without Gravity Field. Four coils can provide a definite quasi-two-dimensional magnetic field as schematically shown in Fig. 4. Magnetic field vectors are from two vertical side walls to the top and bottom walls. Figure 5 summarizes the computed result for the present system at $(\gamma\mathrm{Ra}) = 0.5\times 10^5$ and $\mathrm{Pr}=0.71$ but at $g=0$. Figure 5(*a*) shows multi-particle streak lines. The flow is mainly downward from the center of the top hot plate. Figure 5(*b*) shows velocity vectors in a vertical cross section at $X=0.5$. Downward flow is very strong from $Y=0.5$ near the hot top plate. Figure 5(*c*) and (*d*) show isothermal contours. Figure 5(*e*) and (*f*) show driving force vectors of magnetizing force in a perspective view and in a plane of $X=0.5$. Figure 5(*g*) and (*h*) show local Nusselt numbers at the top hot plate and bottom cold plate, respectively. The profile at the bottom plate suggests that an almost two-dimensional hot plume hits the bottom plate. On the other hand, two cold plumes flow along the side walls toward the top plate. The average Nusselt number is 2.55 on the hot wall. That at the cold wall is 2.54, suggesting that more convergence required in the computation. These results clarify the effect of magnetizing force in the cube with hot and cold plates. In the following, the additional effect of gravity force is considered for the same system.

3.4 Four Poles With Normal Gravity Field. The effect of the standard acceleration due to gravity, i.e., $g=9.806\,[\mathrm{m/s^2}]$, is added in the minus *Z*-coordinate for the system described in the previous section. Figure 6(*a*) shows streak lines of four particles. The quasi-two-dimensional mode is similar to Fig. 5(*a*) but simpler. Streaks appear to proceed weakly toward the core between the upper and lower regions. This is a little clearer in the velocity vectors in Fig. 6(*b*) in a vertical plane at $X=0.5$. The velocity vectors are generally weaker than those of Fig. 5(*b*), especially in the lower region. Figure 6(*c*) and (*d*) show isothermal contours in a perspective view and in a vertical cross section at $X=0.5$. Generally, convection is much weaker than that at $g=0$. Figure 6(*e*) and (*f*) show the magnetizing force term $-\gamma\mathrm{Ra}\,\mathrm{Pr}\,T\nabla B^2$ and that combined with the gravity field, $-\gamma\mathrm{Ra}\,\mathrm{Pr}\,T\nabla B^2 + (0,0,\mathrm{Ra}\,\mathrm{Pr}\,T)^T$, in a vertical cross section at $X=0.5$. In the upper half of the cube, the temperature T is positive, the gravitational buoyancy force works in the positive *Z*-direction (upward) and the downward vectors in (*e*) decrease. On the other hand, dimensionless temperature T is negative near the cold bottom plate and the buoyant force term becomes negative, increasing the downward vectors in comparison with (*e*). This suggests that the lower cold fluid is suppressed to the lower plate. The upper hot fluid also receives less force that the magnetizing force minus the gravitational buoyant force. This gravitational buoyant force works to stagnate the convection due to the thermal boundary condition of heating from above. However, as seen in Fig. 6(*f*), horizontal and centripetal magnetizing forces are apparent along the top plate to convect the air toward the center of the top plate. This appears to be strong enough to drive the hot fluid downward from the center of the top plate. In total, the magnetizing force minus gravitational force results in weaker convection than in the non-gravitational case in Section 3.3. This is due to the stabilizing effect of temperature stratification due to heating from above in the gravitational field. Figure 6(*g*) and (*h*) show the local Nusselt number at the hot and cold plates, respectively. The magnitudes are much less than those in Fig. 5(*g*) and (*h*). The average Nusselt number also decreases to 1.17, less than half of the non-gravity case.

Table 1 shows the converged average Nusselt numbers computed. In the gravity field of $g=9.806\,[\mathrm{m/s^2}]$, the increase in the Rayleigh number from 10^3 to 10^5 increased average Nusselt number from 1.001 to 1.167 at $\gamma=0.5$. This suggests that convection is generated, and the heat transfer rate is increased with the increase in the temperature difference upon heating from above and cooling from below under the magnetizing force field plus the gravity field for air in a cube. The increase in the magnetic strength from $\gamma=0.1$ to $\gamma=1.0$ at $\mathrm{Ra}=10^5$ also increased the average Nusselt number from 1.005 to 1.631. The above result reveals the enhancement of heat transfer rate from conduction to the convection state by the application of magnetizing force.

The magnetic susceptibility χ_{O_2} is proportional to the inverse of the temperature. This suggests that the fluid at higher temperature has smaller magnetic susceptibility: fluid hotter than the reference temperature (θ_0, or $T=0$) receives a smaller magnetizing force. This means that hotter fluid is repelled from the larger magnetic field toward the smaller, as seen in Figs. 3(*a*), 5(*a*), and 6(*a*). In case of two magnetic poles, magnetic strength is the weakest in the plain of $Y=0.5$ ($0\leqslant X\leqslant 1$, $0\leqslant Z\leqslant 1$). In case of four poles, the weakest part is along the line of $Y=Z=0.5$ ($0\leqslant X\leqslant 1$). On the other hand, fluid colder than the reference temperature has larger magnitude of magnetic susceptibility and is attracted to the location of largest magnetic induction, the center of the bottom plate. However, mass balance requires its return to the upper part of the cube, and a weak rising flow is generated along the side walls at $Y=0$ and 1.

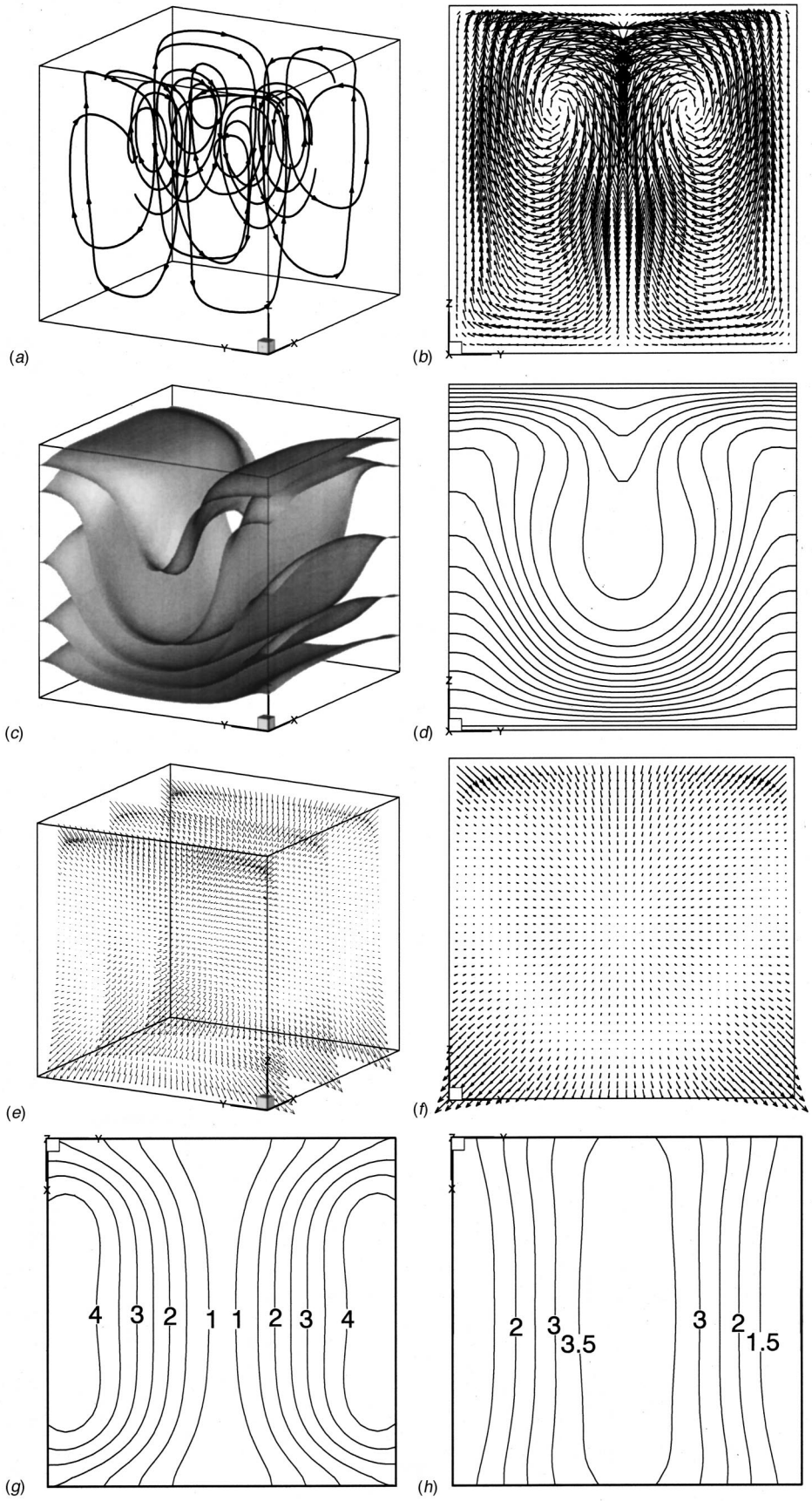

Fig. 5 Summary of the computed result with four coils and non-gravity field at γRa=0.5 $\times 10^5$, Pr=0.71 and g=0. Except for (*e*), (*a*) to (*h*) are the same as those of Fig. 3. Figure 5(*e*) is a perspective view of magnetizing force vectors in three vertical planes at X=0.15, 0.5 and 0.85.

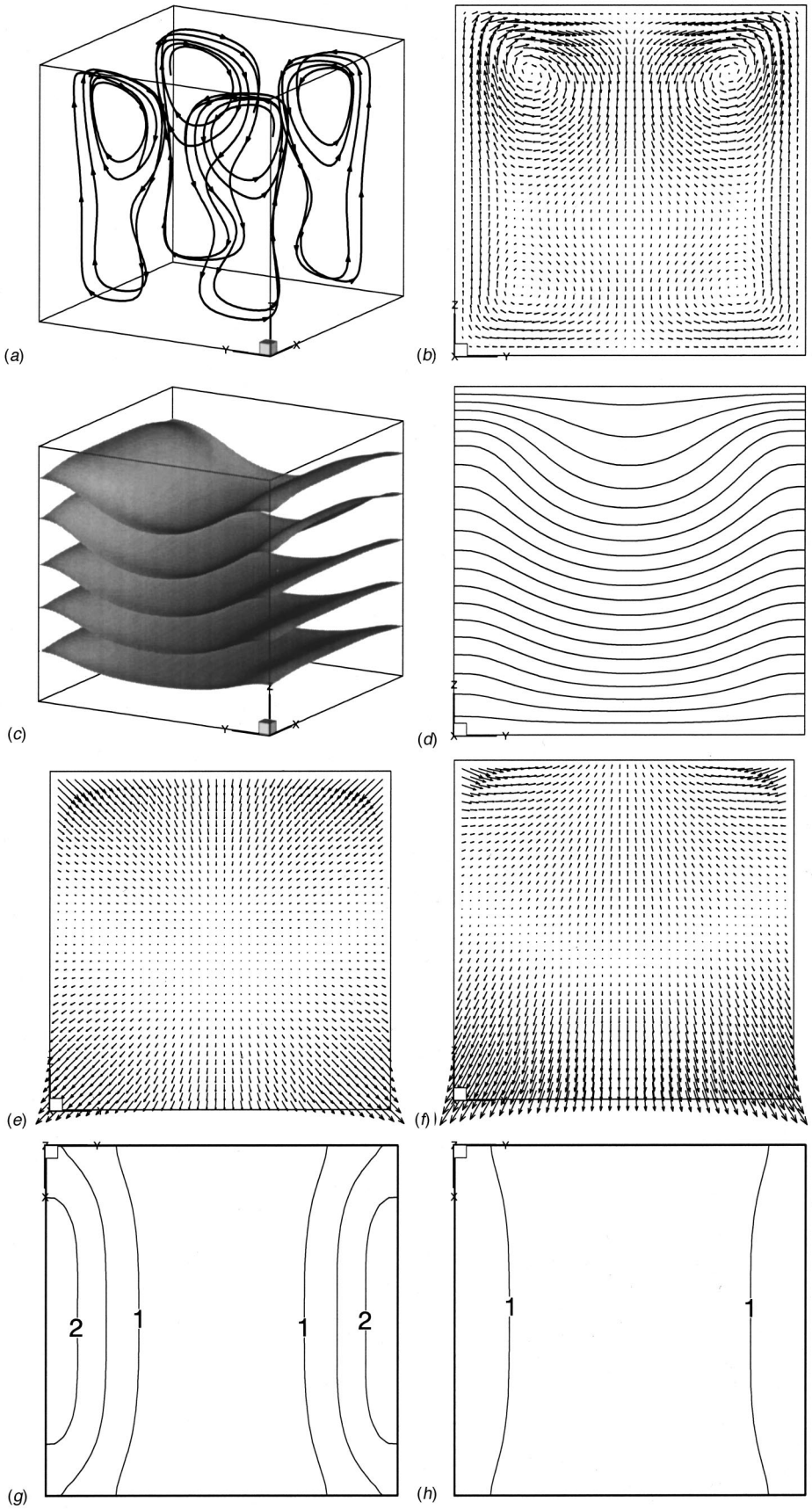

Fig. 6 Summary of the computed result with four coils and the gravity field at γ=0.5, Ra =10^5 and Pr=0.71. Except for (*e*) and (*f*), (*a*) to (*h*) are the same as those of Fig. 3. Figure 6(*e*) shows magnetizing force vectors at X=0.5. Figure 6(*f*) shows the magnetizing and buoyancy forces in a vertical plane of X=0.5. Figure 6(*g*) and (*h*) are the same as those of Fig. 3.

Table 1 Computed Nusselt numbers

g [m/s^2]	Coils	γ	Ra	Nu_{hot}
0	2	0.5	10^5	2.084
0	4	0.5	10^5	2.553
9.806	4	0.5	10^3	1.001
9.806	4	0.5	10^4	1.034
9.806	4	0.1	10^5	1.005
9.806	4	0.5	10^5	1.167
9.806	4	1.0	10^5	1.631

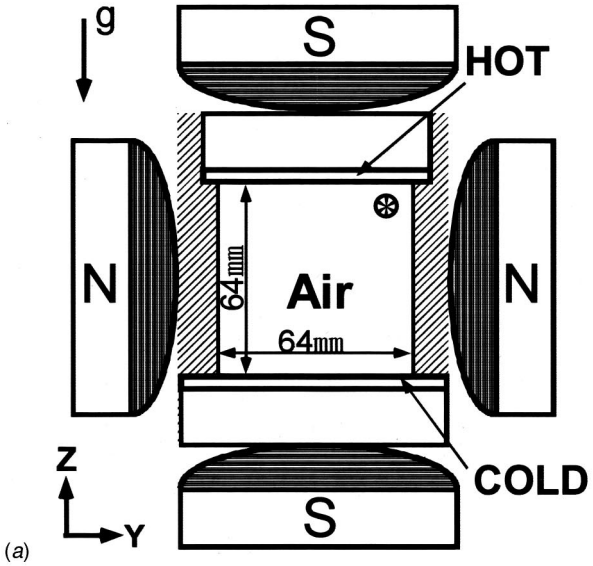

(*a*)

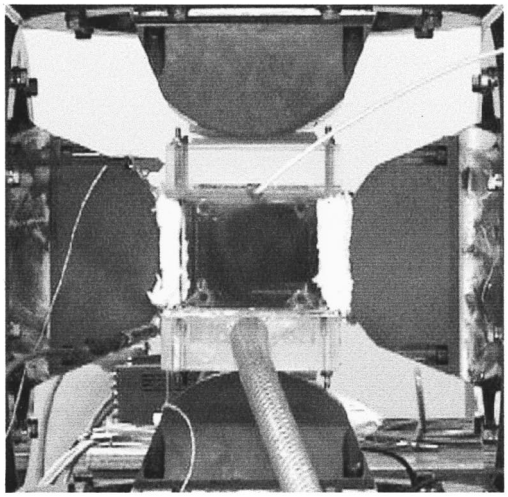

(*b*)

Fig. 7 Schematics of experimental setup: (*a*) schematic side view of the four electromagnets and the experimental cube located in the center; and (*b*) photograph of the side view of the experimental magnets and air box.

Table 2 Experimental conditions

$l=0.064[m]$, $T_h=45[°C]$, $T_c=13[°C]$, $\chi_{air}=3.2\times10^{-7}[m^3/kg]$ and Max. $b=1.01[T]$ correspond to $\gamma=0.402[-]$ and $Ra=7.89\times10^5[-]$.

Top and bottom plates are made of copper plate. Four side plates are made of plexiglass and thermally insulated.

4 Experimental Flow Visualization

Figure 7 shows schematic of the four-pole electromagnet (Tecno Electric Industry Co., Ltd), which supplies a magnetic field of as much as 1 Tesla in the square bore of 120×120 mm^2. In this bore, a cubic experimental box of 0.064 [m] inside length was placed. The top plate of the box was electrically heated, and the bottom plate was water-cooled by running water through a constant temperature bath. Other conditions are listed in Table 2. Figure 7(*b*) shows a photograph of the experimental box in place. Figure 8 shows flow visualization. Figure 8(*a*) shows three consecutive pictures of incense smoke inserted through a small hole at top right of the cube for a non-magnetic case. The smoke (white) diffuses from the top right corner into other parts of the cube. Figure 8(*b*) shows three consecutive pictures under a magnetic field. Smoke moves from the right top corner along the top plate toward the center, from where it travels down to the bottom cold plate, then diffuses to both sides. This behavior resembles that predicted by the numerical computation, that the hot fluid is driven downward from the center of the top hot plate. And the cold air near the bottom cold plate is attracted by the large magnetic field there and does not convect upwards extensively but stagnates over the bottom plate. These observations were confirmed in repeated experiments under different conditions.

The velocity of incense smoke at 1.01 [T] and $T_h-T_c=32$ [K] in a cubic enclosure was approximately 1.26 [cm/s] from a series of video screen. The dimensionless condition is $Ra=7.89\times10^5$ and $\gamma=0.402$. Computed maximum velocity at $\gamma=0.5$ and $Ra=10^5$ was 14.76 [–] which corresponds to 0.51 [cm/s]. To compare with experimental conditions, a further computation for $\gamma=0.5$ and $Ra=8\times10^5$ was carried out to get the maximum velocity 52.93 [–] which corresponds to 1.81 [cm/s]. These numerical values are almost the same magnitude as the experimental values to support present computations.

5 Conclusions

Magnetizing force was applied to the stagnant conduction state of air in a cube heated from above and cooled from below. The magnetic field is cusp-shaped, with the south poles at the top and bottom walls of the experimental box and the north poles at two opposing side walls. The magnetizing force is modeled to reflect the temperature dependence of magnetic susceptibility of oxygen gas and is included in the Navier-Stokes equation. Finite difference numerical computation suggested that the heat transfer rate increases from $Nu=1$ to 1.17 at $Ra=10^5$ and $\gamma=0.5$, which is equivalent to a magnetic induction of 1.13 [T] for a temperature difference of 4 [°C] in a cube of air of 0.064 [m] sides. The convection mode under a magnetizing force is as follows. Hot fluid near the top plate is repelled downward to the core center of the cube, where the magnitude of the magnetic induction is almost zero in the cusp-shaped magnetic field employed in the present system. This characteristic was more apparent for the non-gravitational test computation presented herein. Experimental flow visualization in a similar system revealed the downward flow from the center of the hot top plate, supporting the present model and numerical computation.

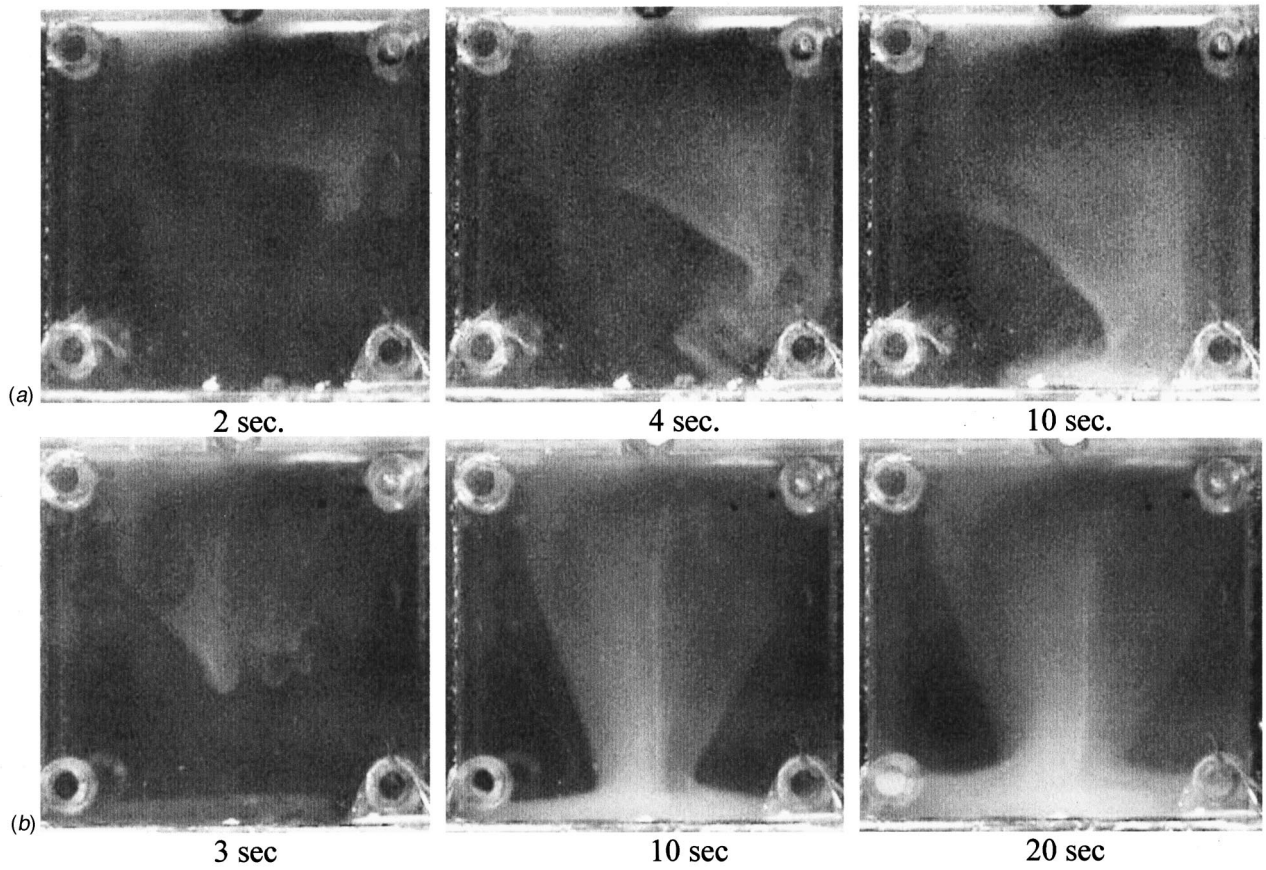

Fig. 8 Flow visualization with incense smoke. Three consecutive photographs at $T_h - T_c = 32$ [K]: (*a*) non-magnetic field; and (*b*) cusp-shaped magnetic field with the maximum magnetic induction of 1.0 [T].

Nomenclature

$\mathbf{B}$ = $\mathbf{b}/b_a$, [−]
$\mathbf{b}$ = magnetic induction (b_x, b_y, b_z), [T=Wb/m^2=V·s/m^2]
b_a = $\mu_m i/l$, [Wb/m^2]
l = length of a cubic enclosure, [m]
$\mathbf{f}_m$ = magnetizing force defined in Eq. (1), [N/m^3]
g = acceleration coefficient of gravity, [m/s^2]
Gr = Grashof number=$\{g\beta(\theta_h - \theta_c)l^3\}/\nu^2$, [−]
$\mathbf{H}$ = magnetic field=$\mathbf{b}/\mu_m$, [A/m]
i = electric current in a coil, [A]
P = p'/p_a, [−]
p = pressure, [N/m^2]
p_0 = reference pressure without convection of gas, [N/m^2]
p' = perturbed pressure due to convection, [N/m^2]
p_a = $\rho_0(\alpha/l)^2$, [N/m^2]
Pr = Prandtl number=ν/α, [−]
r = radial coordinate of a coil, [m]
R = universal gas constant, [J/kg·K]
Ra = Rayleigh number=Gr·Pr, [−]
$\mathbf{s}$ = circumferential length of a coil, [m]
$\mathbf{S}$ = $\mathbf{s}/l$, [−]
t = time, [s]
t_a = l^2/α, [s]
T = $(\theta - \theta_0)/(\theta_h - \theta_c)$, [−]
$\mathbf{U}$ = $\mathbf{u}/u_a$, [−]
$\mathbf{u}$ = velocity vector (u, v, w), [m/s]
u_a = α/l, [m/s]
Y_{O_2} = mass fraction of oxygen at some reference state (air) $=Y$, [−]
α = thermal diffusivity of gas, [m^2/s]
β = volumetric coefficient of expansion of gas due to temperature difference, [1/K]
θ = temperature, [K]
γ = $\chi_{O_2} Y_{O_2} b_a^2/(g\mu_m l)$, [−]
μ = viscosity of gas, [Pa·s]
μ_m = magnetic permeability, [H/m]
ν = kinematic viscosity of gas=μ/ρ_0, [m^2/s]
ρ = density of gas, [kg/m^3]
ρ_0 = density of gas at a reference state of no convection, [kg/m^3]
τ = t/t_a, [−]
χ_{air} = magnetic susceptibility of air=$\chi_{O_2} Y_{O_2}$, [m^3/kg]
χ_{O_2} = magnetic susceptibility of oxygen=χ, [m^3/kg]

References

[1] Faraday, M., 1847, "On the Diamagnetic Condition of Flame and Gases," Phil. Mag. S. 3, No. 210, p. 401.
[2] Pauling, L., Wood, R. E., and Sturdivant, J. H., 1946, "An Instrument for Determining of Partial Pressure of Oxygen in a Gas," J. Am. Chem. Soc., **68**, p. 795.
[3] Wakayama, N. I., 1991, "Behavior of Flow Under Gradient Magnetic Fields," J. Appl. Phys., **69**, No. 4, pp. 2734–2736.
[4] Wakayama, N. I., 1991, "Effect of a Decreasing Magnetic Field on the Flow of Nitrogen Gas," Chem. Phys. Lett., **185**, No. 5–6, pp. 449–451.
[5] Wakayama, N. I., 1993, "Magnetic Promotion of Combustion in Diffusion Flames," Combust. Flame, **93**, No. 3, pp. 207–214.
[6] Wakayama, N. I., Ito, H., Kuroda, Y., Fujita, O., and Ito, K., 1996, "Magnetic Support of Combustion in Diffusion Flames Under Mico Gravity," Combust. Flame, **107**, No. 1–2, pp. 187–192.
[7] Bai, B., Yabe, A., Qi, J., and Wakayama, N. I., 1999, "Quantitative Analysis of Air Convection Caused by Magnetic-Fluid Coupling," AIAA J., **37**, No. 12, pp. 1538–1543.
[8] Braithwaite, D., Beaugnon, E., and Tournier, R., 1991, "Magnetically Con-

trolled Convection in a Paramagnetic Field,'' Nature (London), **354**(6349), pp. 134–136.
[9] Ikezoe, Y., Hirota, N., Nakagawa, J., and Kitazawa, K., 1998, ''Making Water Levitate,'' Nature (London), **393**, pp. 749–750.
[10] Ikezoe, Y., Hirota, N., Sakihama, T., Mogi, K., Uetake, H., Homma, T., Nakagawa, J., Sugawara, H., and Kitazawa, K., 1998, ''Acceleration Effect on the Rate of Dissolution of Oxygen in a Magnetic Field, (in Japanese),'' Journal of Japan Institute of Applied Magnetics, **22**, No. 4-2, pp. 821–824.
[11] Uetake, H., Nakagawa, J., Hirota, N., and Kitazawa, K., 1999, ''Nonmechanical Magnetothermal Wind Blower by a Superconducting Magnet,'' J. Appl. Phys., **85**, No. 8, pp. 5735–5737.
[12] Nakagawa, J., Hirota, N., Kitazawa, K., and Shoda, M., 1999, ''Magnetic Field Enhancement of Water Vaporization,'' J. Appl. Phys., **86**, No. 5, pp. 2923–2925.
[13] Hellums, J. D. and Churchill, S. W., 1964, ''Simplification of the Mathematical Description of Boundary and Initial Value Problem,'' AIChE J., **10**, pp. 110–114.
[14] Hirt, C. W., Nichols, B. D., and Romero, N. C., 1975, ''A Numerical Solution Algorithm for Transient Fluid Flows,'' Technical Report, Los Alamos Scientific Laboratory, LA-5852.

Determination of Planck Mean Absorption Coefficients for HBr, HCl, and HF

S. P. Fuss
ASME Mem.,
Bureau of Alcohol, Tobacco, and Firearms,
Fire Research Laboratory,
Rockville, MD 20850

A. Hamins
Building and Fire Research Laboratory,
National Institute of Standards and Technology,
Gaithersburg, MD 20899-8663

The Planck mean absorption coefficient, a_p, has been calculated for HBr, HCl, and HF over a temperature range from 300 K–2300 K using data from the 1996 edition of the HITRAN molecular database. Plots of a_p versus temperature showed monotonically decreasing behavior over this temperature range, with peak values at 300 K of 45.9 (atm-m)$^{-1}$, 5.3 (atm-m)$^{-1}$, and 1.95 (atm-m)$^{-1}$ for HF, HCl, and HBr, respectively. The magnitude of these values suggests that HBr, HCl, and HF can significantly impact calculations of radiative transfer in flames containing these species. Two sets of additional calculations were performed for CO to validate the methodology used for calculation of a_p for HBr, HF, and HCl. In the first approach, which employed the narrow band model RADCAL, the calculation procedure was similar to that of the present calculations. The second approach utilized tabulated values of the integrated intensity for each CO band and an average value of the Planck function within each band. Results from the three methods showed general agreement. Polynomial expressions are provided as fits to a_p as a function of temperature for HBr, HCl, HF, and CO. [DOI: 10.1115/1.1416689]

Keywords: Absorption, Combustion, Participating Media, Properties, Radiation

Introduction

In large-scale fires, radiation is the dominant mode of heat transfer [1]. In non-sooting and moderately sooting fires, the participation of heated gases and soot, through absorption and emission of infrared radiation, plays a significant role in radiative exchange. The Planck mean absorption coefficient, a_p, characterizes radiative emission in the source term of the generalized energy equation for an absorbing/emitting (non-scattering) medium [2]. Because it is a function only of the local temperature, a_p can be conveniently tabulated and efficiently used in complex radiative heat transfer calculations. The Planck mean absorption coefficient, a_p, is defined as

$$a_p = \frac{\int_{\Delta\omega} \kappa_\omega E_{\omega,b} d\omega}{\sigma T^4}. \quad (1)$$

To calculate a_p from Eq. (1), the spectral absorption coefficient, κ_ω, for a gas or gas mixture, is needed as a function of temperature. In the more general case of a scattering medium, the absorption coefficient is replaced by the extinction coefficient, β_ω as follows:

$$\beta_\omega = \kappa_\omega + \sigma_\omega, \quad (2)$$

where σ_ω is the scattering coefficient. However, for a gas, scattering is typically neglected and the extinction coefficient is equivalent to the absorption coefficient. The radiative properties, including κ_ω, of molecular combustion species such as H_2O, CO_2, and CO have been relatively well characterized. A narrow band model (RADCAL) was developed which evaluates Eq. (1) for relevant combustion species including CO_2, H_2O, CO, CH_4, and soot [3]. Alternatively, Abu-Romia and Tien [4] presented a method for calculating a_p that is based on a simplified narrow band approach. This approach utilizes the integrated intensity of individual gas bands that can be determined independently and tabulated. This method has the advantage that it is easily implemented for cases in which the integrated intensity is a known function of temperature. Tien [5] presented results based on this model for CO_2, H_2O, N_2O, NH_3, SO_2, CH_4, CO, and NO. Grosshandler and Thurlow [6] extended this method to derive an expression for a_p based on the equivalence ratio for flames burning H_2, CO, CH_3OH, and CH_4 in air, and lean regions of other generic flames.

Radiative transfer involving species such as HBr, HCl, and HF has not been studied extensively. These species are found in flames inhibited by halogenated compounds and are also present in incinerators. They are difficult species to study experimentally due to their corrosive nature. Halogenated compounds are widely used as fire suppression agents. HCl is a stable combustion product that attains near equilibrium concentrations in inhibited hydrocarbon flames [7]. The same behavior can be expected for HF. Calculations have shown that HF and HBr can achieve local mass fraction levels on the order of 5 percent and 10 percent, respectively, in CF_3Br inhibited CH_4/air counterflow flames [8]. While the production of CF_3Br (Halon 1301) has been halted due to its adverse effects on stratospheric ozone, it is still widely used as a fire suppressant. Additionally, heptafluoropropane and other halogenated species are considered viable alternatives to CF_3Br in some applications. While these agents inhibit flames primarily through chemical effects, heat loss to the surroundings by radiative emission can also influence extinction. Radiation can be particularly significant in weakly strained flames [9]. Therefore, it is important to characterize the radiative properties of HF and HBr so that flame emission can be modeled more accurately.

The Planck mean absorption coefficient can be used to characterize radiative emission from gases of any optical thickness [2] and is thus a useful parameter, particularly since it can be determined a priori. The aim of this study was to calculate a_p for HBr, HCl, and HF for use in simplified flame models [10] using spectral data previously measured [11].

Methodology

The absorption coefficient for a single spectral line can be expressed as the product of line intensity (S), line shape (g), and the concentration of absorbing molecules (N) [12]

$$\kappa_\omega = S \cdot g(\omega - \omega_0) \cdot N, \quad (3)$$

Contributed by the Heat Transfer Division for publication in the JOURNAL OF HEAT TRANSFER. Manuscript received by the Heat Transfer Division September 26, 2000; revision received May 4, 2001. Associate Editor: J. P. Gore.

where ω is the wave number (cm^{-1}) and ω_o denotes the center of an absorbing line. The concentration can be related to temperature through the ideal gas law

$$N = N_L \cdot \left(\frac{296}{T} \right), \tag{4}$$

where N_L is Loschmidts' number ($N_L = 2.479 \cdot 10^{19}$ molecules/cm^3/atm at 296 K)[1]. The Lorentz line shape, which is generally used for applications at atmospheric pressure and moderate temperatures, was used. This profile has the form

$$g(\omega - \omega_0) = \frac{(\gamma_p / \pi)}{(\omega - \omega_0)^2 + \gamma_p^2}, \tag{5}$$

where γ_p is the pressure-broadened line half width at half maximum (HWHM)

$$\gamma_p = \Gamma \cdot \left(\frac{296}{T} \right)^n P_t . \tag{6}$$

P_t is the total pressure and Γ is the air broadened half width parameter $(atm\text{-}cm)^{-1}$. In the case of broadened lines, the absorption coefficient is obtained by summing contributions from overlapping adjacent lines [5].

A program was written to calculate the absorption coefficient according to Eqs. (3)–(6) using data from the 1996 edition of the HITRAN molecular database [11]. Calculations were performed for each gas over the spectral range from 0 cm^{-1}–8500 cm^{-1}, which included the fundamental and first overtone bands corresponding to vibration-rotation transitions, in addition to pure rotational bands that appear in the far-IR. The latter of these transitions are significant only at temperatures below approximately 600 K. Table 1 lists the spectral ranges that contain absorption bands for each molecule, along with the corresponding band centers. Calculations were performed from 300 K to 2300 K, a range of temperatures appropriate for combustion calculations.

In addition to HBr, HCl, and HF, calculations were performed for CO to validate the methodology and accuracy of the program through comparison with results from two narrow band approaches. Reviews of radiation band models are available in the literature [2,5]. One study utilized RADCAL [3], a narrow-band model that solves the equation of radiative transfer for a nonhomogeneous, absorbing and emitting mixture of gases and soot. The CO model employed by RADCAL is from Malkmus and Thompson [13] who applied the anharmonic oscillator model to calculate emissivity for temperatures as high as 7000 K using band integrated intensity measurements [14]. This model includes only the fundamental CO band, neglecting rotational and overtone bands. Neglecting the contribution of the rotational band between 0 cm^{-1}–200 cm^{-1} was justified by considering its intensity. The contribution of this band can be significant at low temperatures, however for CO its intensity is a factor of 10^3 lower than the fundamental band and the contribution to a_p is less than 0.5 percent. However, the first overtone band is more significant, particularly at higher temperatures where the contribution to a_p is on the order of 1–2 percent. This can be seen by comparing values of band integrated intensity in Table 1 [11].

The second approach was that of Abu-Romia and Tien [4], who utilized the Elsasser narrow band model to derive a general expression for the Planck mean absorption coefficient

$$a_p = \frac{\int_0^\infty \kappa_\omega E_{\omega,b} d\omega}{\sigma T^4} = \sum_j \frac{\overline{E_{b,j}} \alpha_j}{\sigma T^4}. \tag{7}$$

In this expression, the summation is over any bands that make a significant contribution to the absorption coefficient. The approximation is made that the blackbody emissive power varies linearly across each absorption band so that the value evaluated at the band center, ($\overline{E_{b,j}}$), can be used. The only required parameter is the temperature dependent integrated intensity, α_j, which characterizes absorption for each band. Tien [5] compiled a list of values for combustion related species, however more recent measurements are available for CO [15]. Alternatively, values can be obtained from HITRAN [11] at 296 K and scaled to higher temperatures [16].

[1]The policy of the National Institute of Standards and Technology is to use metric units of measurement in all its publications. However, in the field for which this document is written, certain non-metric units are much more widely used and familiar so the conventional units of the field will be used for greater clarity.

Table 1 Spectral parameters for each molecule based on [11]. The top row in each molecular category represents data for a rotational transition. The middle and bottom rows represent the fundamental and first overtone vibration-rotation bands, respectively.

Molecule	Spectral Bands of Absorption Lines, cm^{-1}	Band Center, cm^{-1}	Integrated Intensity at T = 296 K α (atm^{-1} cm^{-2})
HF	41 – 625		1394.45
	3269 – 4369	3960	389.64
	6999 – 7995	7749	12.30
HBr	16 – 383		117.23
	2123 – 2791	2559	35.37
	4593 – 5164	5027	0.39
HCl	20 – 438		262.40
	2399 – 3161	2885	155.35
	5159 – 5830	5666	3.52
CO	3 – 190		0.46
	1795 – 2317	2143	250.36
	3836 – 4361	4260	1.97

Results

Validation of Methodology. Figure 1 compares the CO calculations performed in this study with results from the narrow band approaches discussed previously. The calculations that were performed in this study using Eqs. (1) and (3)–(6) are labeled ''This Study''. The values of a_p determined from RADCAL and fit to a 4th order polynomial [17] are labeled ''RADCAL Fit''. Data calculated from Eq. (7) based on [5,18] is expanded in Fig. 1 as ''Integrated Intensity [5,18]''. An estimate of α from HITRAN at $T = 296$ K is given in Table 1. A plot of a_p based on Eq. (7), with α taken from Table 1 [11], is shown in Fig. 1 and labeled ''Integrated Intensity [11]''. Only the fundamental and first overtone bands were considered for the data labeled ''Integrated Intensity [5,18]'' and ''Integrated Intensity [11]''.

The temperature dependence of α for the calculations using Eq. (7) was taken from Breeze et al. [16]. It is worth emphasizing that a_p values from Eq. (7) are based on independent measurements of the CO integrated intensity, α [11,18] and a wide range of values can be found in the literature [18]. Recent measurements, how-

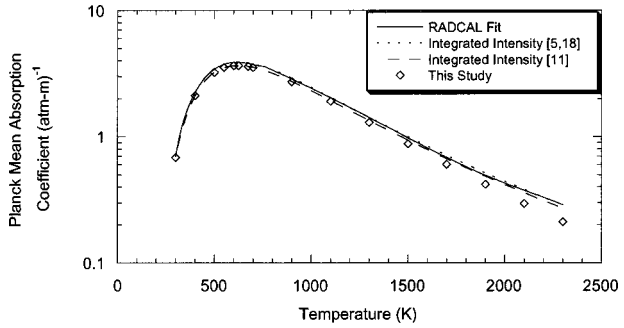

Fig. 1 Calculated values of Planck mean absorption coefficient for CO. Values calculated in the present study using Eqs. (1) and (3)–(6) are labeled "Present Study". Data labeled "RADCAL Fit" is a polynomial expression from [17]. Data labeled "Integrated Intensity [5,18]" and "Integrated Intensity [11]" are calculated using Eq. (7) with data from [5,18] and [11], respectively.

ever, show better agreement. Adjusting the value of α for the 2143 cm^{-1} CO band from Table 1 [11] to a temperature of 273 K yields $\alpha\,(273)=271.5\ atm^{-1}\ cm^{-2}$. This falls within the range given in [18] and is less than 3 percent below the value prescribed in [15].

The agreement between calculations shown in Fig. 1 is quite good considering the range of data sources. The difference in values predicted by Eq. (7) stems from the use of α values from more than one source. The Planck mean absorption coefficient calculated using Eqs. (1), (3)–(6) is 28 percent lower than the value predicted by Eq. (7) using HITRAN data [11] at a temperature of 2300 K. However, flame temperatures between 1200 K–1500 K are found in many applications [1], and over this range the agreement between methods is within 6 percent. Calculations using HITRAN at 2300 K were not appreciably different from those using its high temperature analog, HITEMP [19].

Discussion of HBr, HCl, HF, and CO calculations. Figure 2 shows the Planck mean absorption coefficient for HBr, HCl, HF, and CO, calculated over a temperature range from 300 K–2300 K using data from the 1996 edition of the HITRAN molecular database. HF has the highest a_p value throughout the range $300\ K \leqslant T \leqslant 2300\ K$. The relative magnitude of a_p can be predicted by examining the integrated intensity values for each absorption/emission band in Table 1; HF has the highest α value in each range. The plots of a_p for HBr, HCl, and HF all have the same general feature, a monotonic decrease with increasing temperature, which is different than that of CO. This is due to the fact that HBr, HCl, and HF each have significant rotational bands located between 0 cm^{-1}–700 cm^{-1}, while the CO band in this range is a factor of 10^3 less intense than its fundamental band. At low temperatures, absorption bands at small wave number locations are significant. At progressively higher temperatures, bands centered at larger wave number positions become dominant due to the shift in emissive power in Eq. (7). This is shown in Fig. 3, which plots the transmittance of the absorption bands for each molecule at room temperature between 0 cm^{-1}–6000 cm^{-1}. Also shown in this figure are plots of the normalized blackbody emissive power, $E_{\lambda,b}/\sigma T^4$, for temperatures of 300 K, 700 K, and 1100 K.

Uncertainties in line intensity and line width are generally near 5 percent and 10 percent, respectively, in the HITRAN database [20]. Furthermore, tunable diode laser measurements of HF and HBr have shown deviations from HITRAN data that are outside of this range for these species [21,22]. However, it has been estimated that the accuracy of spectrally integrated irradiance is better than that for individual lines [20].

Sample Application. The Planck mean absorption coefficient for CO_2 is a factor of 4 to 5 times higher than that of H_2O and

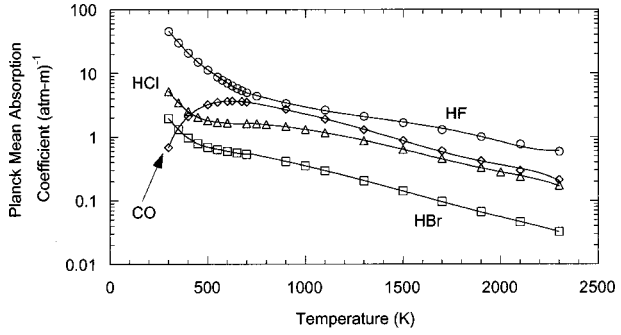

Fig. 2 Calculated values of Planck mean absorption coefficient for HBr, HCl, HF, and CO. Calculations are based on Eqns. (1) and (3)–(6) with data from the 1996 edition of the HITRAN molecular database [11]. The following symbols are used to identify individual species: HBr (□), HCl (△), HF (○), and CO (◇). Polynomial expressions from Eq. (8) are represented by solid lines through the points.

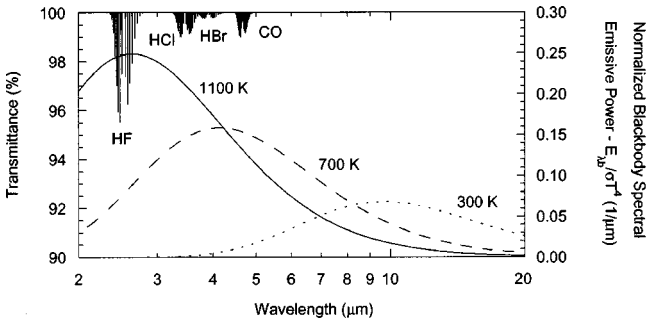

Fig. 3 Spectral transmittance, τ_λ, of the rotational and fundamental vibration-rotation HBr, HCL, HF, and CO bands for the condition $T=300$ K is plotted on the left vertical axis. The spectral blackbody emissive power, normalized by σT^4, is plotted on the right vertical axis for temperatures of 300 K, 700 K, and 1100 K.

10–15 times higher than that of CO over the temperature range 1100 K–2300 K. Throughout this range, however, a_p values for HF and HCl are comparable to those for CO. Additionally, Masri [8] reports that HF and HBr mass fractions are comparable to CO_2 and H_2O in CF_3Br inhibited flames. Therefore, the inclusion of HBr, HCl, and HF in radiative emission calculations of inhibited hydrocarbon flames may be significant.

To estimate the impact of HF and HBr on total flame emission, a homogeneous volume of heated products in a CF_3Br inhibited CH_4/air counterflow flame [8] was considered. The results showed that, for optically thin conditions, HF and HBr were found to account for approximately 7 percent and 1 percent, respectively, of the total flame emission. The a_p values for HCl lie between those of HF and HBr, so a similar contribution might be expected from HCl emission in incinerator or flame applications.

Polynomial Fit to Data. Polynomial expressions were fit to the HBr, HCl, HF, and CO data over two temperature regimes: $300\ K \leqslant T \leqslant 700\ K$ and $700\ K \leqslant T \leqslant 2300\ K$. These are shown in Fig. 3 as solid lines through the points. The expressions were of the form:

$$a_p = \sum_{n=0}^{4} a_n T^n \tag{8}$$

Table 2 lists values of the coefficients a_n. The r^2 correlation coefficient for each polynomial was 0.999 or better. The maximum difference between the calculated a_p values and polynomial values was 7 percent, with an average difference of less than 1 percent.

The effect of spectral overlap between absorption bands was not included in these fits. Significant overlap does exist between the HF fundamental at 3960 cm^{-1} and the H_2O and CO_2 bands nearby. At 300 K there is negligible overlap between the fundamental HCl and HBr bands; however, at higher temperatures as these bands broaden the overlap will increase and possibly spread into the range of the CO_2 band at 2350 cm^{-1}. Water lines in the

Table 2 Values of the polynomial coefficients to be used with Eq. (8)

a_n in Eq. 8		HF	HBr	HCl	CO
a_0	300 K – 700 K	435.74	20.583	56.261	6.2773
	700 K – 2300 K	21.322	1.3211	0.3090	6.2016
a_1	300 K – 700 K	-2.7099	-1.3398×10^{-1}	-3.6651×10^{-2}	-8.0223×10^{-2}
	700 K – 2300 K	-4.3028×10^{-2}	-1.3603×10^{-3}	5.9271×10^{-3}	-1.8068×10^{-3}
a_2	300 K – 700 K	6.6504×10^{-3}	3.4124×10^{-4}	9.3093×10^{-4}	3.2405×10^{-4}
	700 K – 2300 K	3.7464×10^{-5}	3.8057×10^{-7}	-8.0002×10^{-6}	-4.9650×10^{-6}
a_3	300 K – 700 K	-7.4327×10^{-6}	-3.8865×10^{-7}	-1.0569×10^{-6}	-4.6257×10^{-7}
	700 K – 2300 K	-1.5053×10^{-8}	3.0545×10^{-11}	3.6388×10^{-9}	3.5195×10^{-9}
a_4	300 K – 700 K	3.1531×10^{-9}	1.6594×10^{-10}	4.5099×10^{-10}	2.2200×10^{-10}
	700 K – 2300 K	2.2591×10^{-12}	-1.9485×10^{-14}	-5.6193×10^{-13}	-6.5751×10^{-13}

0–400 cm^{-1} region overlap with HF, HBr, and HCl lines in this range. Additionally, at higher temperatures, the overlap of H_2O with overtone bands of HF, HBr, and HCl will increase. These effects are usually negligible in optically thin conditions [2,17] and no correction was derived to accommodate band overlap.

Conclusions

Values of the Planck mean absorption coefficient have been calculated for HBr, HCl, HF, and CO based on data from the 1996 edition of the HITRAN molecular database. For temperature conditions where a_p is significant ($a_p > 0.5\ atm^{-1}\,m^{-1}$), the values of a_p for CO compare favorably with those from two narrow band models. Polynomial expressions were provided based on fits to a_p versus temperature data. The inclusion of HBr, HCl, and particularly HF, can significantly contribute to emission calculations for fire suppression or incinerator scenarios where halogenated compounds are present.

Acknowledgments

This research was partially supported by the NASA Microgravity Research Division through Contract No. C-32066-T (NIST) with Dr. Sandra L. Olson serving as Technical Monitor.

Nomenclature

a_p = Planck mean absorption coefficient $(atm\text{-}m)^{-1}$
α = band integrated intensity $(atm^{-1}\text{-}cm^{-2})$
β_ω = extinction coefficient $(atm\text{-}cm)^{-1}$
σ_ω = scattering coefficient $(atm\text{-}cm)^{-1}$
S = line intensity (cm/molecule)
P = pressure (atm)
T = temperature (K)
$E_{\omega b}$ = blackbody emissive power $(W/m^2/\mu m)$
g = line shape function (cm)
Γ = air broadened half width parameter $(cm\text{-}atm)^{-1}$
n = air-broadening temperature coefficient
N = concentration $(molecules/cm^3/atm)$
κ_ω = absorption coefficient $(atm\text{-}cm)^{-1}$
γ = pressure broadened line half width (cm^{-1})
ω = wave number (cm^{-1})
σ = Stefan-Boltzmann constant $(W/m^2/K^4)$

References

[1] DeRis, J., 1979, "Fire Radiation-A Review," *Seventeenth Symposium (International) on Combustion/The Combustion Institute*, pp. 1003–1015.
[2] Siegel, R., and Howell, J. R., 1992, *Thermal Radiation Heat Transfer*, Hemisphere Publishing, Washington.
[3] Grosshandler, W. L., 1993, "RADCAL: A Narrow-Band Model for Radiation Calculations in a Combustion Environment," NIST Technical Note 1402, National Institute of Standards and Technology, Gaithersburg MD.
[4] Abu-Romia, M. M., and Tien, C. L., 1967, "Appropriate Mean Absorption Coefficients for Infrared Radiation of Gases," ASME J. Heat Transfer, **89**, pp. 321–327.
[5] Tien, C. L., 1968, "Thermal Radiation Properties of Gases," *Advances in Heat Transfer*, Irvine, T. F., and Hartnett, J. P., eds., Academic Press, New York, **5**, pp. 253–324.
[6] Grosshandler, W. L., and Thurlow, E. M., 1992, "Generalized State-Property Relations for Nonluminous Flame Absorption Coefficients," ASME J. Heat Transfer, **114**, pp. 243–249.
[7] Yang, M. H., Hamins, A., and Puri, I. K., 1994, "The Structure of Inhibited Counterflowing Nonpremixed Flames," Combust. Flame, **107**, pp. 107–122.
[8] Masri, A. R., 1994, "Chemical Inhibition of Nonpremixed Flames of Hydrocarbon Fuels with CF_3Br," Combust. Sci. Technol., **96**, pp. 189–212.
[9] Maruta, K., Masaharu, Y., Hongsheng, G., Yiguang, J., and Niioka, T., 1998, "Extinction of Low-Stretched Diffusion Flame in Microgravity," Combust. Flame, **112**, pp. 181–187.
[10] Choi, M. Y., Hamins, A., Rushmeier, H., and Kashiwagi, T., 1994, "Simultaneous Optical Measurement of Soot Volume Fraction, Temperature, and CO_2 in Heptane Pool Fire," *Twenty-Fifth Symposium (International) on Combustion/The Combustion Institute*, pp. 1471–1480.
[11] Rothman, L. S., Rinsland, C. P., Goldman, A., Massie, S. T., Edwards, D. P., Flaud, J. M., Perrin, A., Camy-Peyret, C., Dana, V., Mandin, J. Y., Schroeder, J., McCann, A., Gamache, R. R., Wattson, R. B., Yoshino, K., Chance, K. V., Jucks, K. W., Brown, L. R., Nemtchinov, V., and Varanasi, P., 1998, "The HITRAN Molecular Spectroscopic Database and HAWKS (HITRAN Atmospheric Workstation): 1996 Edition," J. Quant. Spectrosc. Radiat. Transf., **60**, pp. 665–710.
[12] *HITRAN-PC User's Manual*, 1994, The University of South Florida, Tampa, FL.
[13] Malkmus, W., and Thomson, A., 1961, "Infrared Emissivity of Diatomic Gases for the Anharmonic Vibrating-Rotator Model," J. Quant. Spectrosc. Radiat. Transf., **2**, pp. 17–39.
[14] Benedict, W. S., and Plyler, E. K., 1954, "High-Resolution Spectra of Hydrocarbon Flames," *Energy Transfer in Hot Gases*, NBS Circular No. 523, Washington, D.C., p. 57–73.
[15] Varghese, P. L., and Hanson, R. K., 1980, "Tunable Infrared Diode Laser Measurements of Line Strengths and Collision Widths of $^{12}C\ ^{16}O$ at Room Temperature," J. Quant. Spectrosc. Radiat. Transf., **24**, pp. 479–489.
[16] Breeze, J. C., Ferriso, C. C., Ludwig, C. B., and Malkmus, W., 1965, "Temperature Dependence of the Total Integrated Intensity of Vibrational-Rotational Band Systems," J. Chem. Phys., **42**, No. 1, pp. 402–406.
[17] http://www.ca.sandia.gov/tdf/Workshop/Submodels.html
[18] Breeze, J. C., and Ferriso, C. C., 1965, "Integrated Intensity Measurements on the Fundamental and First Overtone Band Systems of CO Between 2500° and 5000°K," J. Chem. Phys., **43**, No. 9, pp. 3253–3258.
[19] Rothman, L. S., Wattson, R. B., Gamache, R. R., Goorvitch, D., Hawkins, R. L., Selby, J. E. A., Camy-Peyret, C., Flaud, J.-M., Goldman, A., and Schroeder, J., "HITEMP, the High-Temperature Molecular Spectroscopic Database," J. Quant. Spectrosc. Radiat. Transf., in preparation.
[20] Pinnock, S., and Shine, K. P., 1998, "The Effects of Changes in HITRAN and Uncertainties in the Spectroscopy on Infrared Radiance Calculations," J. Atmos. Sci., **55**, pp. 1950–1964.
[21] Chou, S., Baer, D. S., and Hanson, R. K., 1999, "Spectral Intensity and Lineshape Measurements in the First Overtone Band of HF Using Tunable Diode Lasers," J. Mol. Spectrosc., **195**, pp. 123–131.
[22] Chou, S., Baer, D. S., and Hanson, R. K., 1999, "High-Resolution Measurements of HBr Transitions in the First Overtone Band Using Tunable Diode Lasers," J. Mol. Spectrosc., **200**, pp. 138–142.

The Full-Spectrum Correlated-*k* Distribution for Thermal Radiation From Molecular Gas-Particulate Mixtures

Michael F. Modest
Fellow ASME
e-mail: mfm6@psu.edu

Hongmei Zhang
Mem. ASME

Dept. of Mechanical Engineering,
Penn State University,
University Park, PA 96802

A new Full-Spectrum Correlated-k Distribution has been developed, which provides an efficient means for accurate radiative transfer calculations in absorbing/emitting molecular gases. The Full-Spectrum Correlated-k Distribution can be used together with any desired solution method to solve the radiative transfer equation for a small number of spectral absorption coefficients, followed by numerical quadrature. It is shown that the Weighted-Sum-of-Gray-Gases model is effectively only a crude implementation of the Full-Spectrum Correlated-k Distribution approach. Within the limits of the Full-Spectrum Correlated-k Distribution model (i.e., an absorption coefficient obeying the so-called "scaling approximation"), the method is exact. This is demonstrated by comparison with line-by-line calculations for a one-dimensional CO_2-N_2 gas mixture as well as a two-dimensional CO_2-H_2O-N_2 gas mixture with varying temperature and mole fraction fields.
[DOI: 10.1115/1.1418697]

Keywords: Combustion, Gaseous, Radiation

Introduction

Radiative heat transfer in gases has important applications from combustion systems to modeling atmospheric processes. The magnitude of radiative heat fluxes can have profound effects on combustion performance and environmental impact. Radiative heat transfer calculations in combustion gases may be loosely grouped into the following three methods (in order of decreasing complexity): (1) line-by-line calculations; (2) band models; and (3) global models.

Line-by-line calculations are the most accurate to date, but they require vast amounts of computer resources. This is undesirable even with the availability of powerful supercomputers, since radiative calculations are only a small part of a sophisticated fire/combustion code. Many studies have been devoted to narrow and wide band models, such as the Malkmus narrow band model, the correlated-*k* (CK) model and many others. The CK method is based on the fact that inside a spectral band $\Delta\eta$, which is sufficiently narrow to assume a constant Planck function, the precise knowledge of each line position is not required for the computation [1–7]. In this paper the CK approach is extended to the whole spectrum by defining a Planck function weighted cumulative *k*-distribution function.

The most common global method is the so-called Weighted-Sum-of-Gray-Gases model. The concept of the WSGG approach was first presented by Hottel and Sarofim [8] within the framework of the zonal method. The method could be applied to arbitrary geometries with varying absorption coefficients, but was limited to nonscattering media confined within a black-walled enclosure. Modest [9] has shown that this model may be generalized for use with any arbitrary solution method. In this method the nongray gas is replaced by a number of gray gases, for which the heat transfer rates are calculated independently by solving the RTE with weighted emissive powers for each of the gray gases. The total heat flux is then found by adding the fluxes of all gray gases. The different absorption coefficient κ_i and emissive power weight factor for each gas are found from total emissivity data.

Denison and Webb [10–15] have improved on the WSGG model and have developed the Spectral-Line-Based Weighted-Sum-of-Gray-Gases (SLW) model based on detailed spectral line data. They also extended the SLW model to nonisothermal and nonhomogeneous media by introducing a cumulative distribution function of the absorption coefficient, calculated over the whole spectrum and weighted by the Planck function. The absorption distribution function (ADF) approach [16–18] is almost identical to the SLW model and differs from the SLW only in the calculation of the gray-gas weights. These weights are chosen in such a manner that emission by an isothermal gas is rigorously predicted for actual spectra. This method has been further generalized [17] by introducing fictitious gases (ADFFG) employing a joint distribution function that separates the κ_η into two or more fictitious gases, and is designed to be more suitable for the treatment of nonhomogeneous media.

In this paper, the Full-Spectrum Correlated-*k* Distribution approach is developed based on Weighted-Sum-of-Gray-Gases arguments. This approach provides a smoother—and, therefore, more easily integrated—set of weight functions than the ADF method. Through these arguments the Weighted-Sum-of-Gray-Gases model is shown to be simply a crude implementation of the FSCK (Full-Spectrum Correlated-*k* Distribution) developed here. Therefore, it is clear that the WSGG method, like the correlated-*k* approach, is not limited to black-walled enclosures without scattering [9], but can accommodate gray walls as well as gray scattering particles. This is also shown through direct WSGG arguments.

Theoretical Formulation

Consider an absorbing/emitting medium inside a black enclosure. For simplicity, we will first assume here that the medium does not scatter, and that it consists primarily of molecular combustion gases (such as H_2O and CO_2 mixed in air) with their thousands of spectral lines, plus perhaps some non-scattering particles, such as soot, all enclosed by opaque black walls. However,

Contributed by the Heat Transfer Division for publication in the JOURNAL OF HEAT TRANSFER. Manuscript received by the Heat Transfer Division November 28, 2001; revision received June 1, 2001. Associate Editor: J. P. Gore.

this approach is also valid for gray scattering and/or gray walls, which will be shown later. For such a situation the radiative equation of transfer (RTE) is given by [19]

$$\frac{dI_\eta}{ds}=\kappa_\eta(I_{b\eta}-I_\eta), \tag{1}$$

where I_η is the spectral intensity varying along a path s, η is wavenumber, $I_{b\eta}$ the Planck function, and κ_η is the spectral absorption coefficient, which (besides wavenumber) depends on local temperature T, pressure p and mole fractions $\underline{x}$. This is the starting point to make line-by-line calculations. The formal solution to Eq. (1) is [19]

$$I_\eta(s)=I_{bw\eta}e^{-\int_0^s\kappa_\eta ds''}+\int_0^s I_{b\eta}(T(s'))e^{-\int_{s'}^s\kappa_\eta ds''}\kappa_\eta(s')ds', \tag{2}$$

where the subscript w denotes a value at the wall. Integrated over the entire spectrum this becomes [9]

$$\begin{aligned}I(s)&=\int_0^\infty I_\eta d\eta\\&=I_{bw}[1-\alpha(T_w,0\to s)]\\&\quad+\int_0^s I_b(s')\frac{\partial\alpha}{\partial s'}(T(s'),s'\to s)ds',\end{aligned} \tag{3}$$

where

$$\alpha(T,s'\to s)=\frac{1}{I_b(T)}\int_0^\infty I_{b\eta}(T)[1-e^{-\int_{s'}^s\kappa_\eta ds''}]d\eta \tag{4}$$

is the total absorptivity for a gas column $s'\to s$ for irradiation from a blackbody source at temperature T. We will now assume that the commonly used ''scaling approximation'' applies, i.e., that spectral and spatial dependence of the absorption coefficient are separable,

$$\kappa_\eta(\eta,T,p,\underline{x})=k_\eta(\eta)u(T,p,\underline{x}). \tag{5}$$

This approximation is used, for example, in the popular Curtis-Godson approximation to calculate narrow band absorptivities for nonhomogeneous paths [20], and in correlated-k models applied to nonhomogeneous atmospheres [3,21]. While a good approximation for soot, its accuracy is more limited for molecular gases: if we assume spectral lines of Lorentz shape we get [19]

$$\kappa_\eta(\eta,T,p,\underline{x})=\sum_j\frac{S_j}{\pi}\frac{b_j}{(\eta-\eta_j)^2+b_j^2}, \tag{6}$$

where η_j is the spectral position of the center of the j^{th} line, b_j is the line's half width at half height, and S_j is the line's intensity. In order for Eq. (5) to hold, we need all b_j to be constant (usually fairly true if total pressure is constant) and all S_j to have the same spatial dependence (the S_j depend only on temperature and density of the absorbing species). Equation (5) has been shown to give very accurate results in atmospheric applications, even for strong variations in total pressure [2,21], but—due to hot lines with strongly different temperature dependence of the line intensities—may become less accurate in the presence of fields with extreme temperature variations [4,6,22]. Moreover, the line intensities are directly proportional to the partial pressure of the absorbing gas. Thus, in gas mixtures with locally varying mole fraction ratios, Eq. (5) is also certain to be violated.

Sticking Eq. (5) into Eqs. (2) and (4) yields

$$I_\eta(s)=I_{bw\eta}e^{-k_\eta X(0,s)}+\int_0^s I_{b\eta}(s')e^{-k_\eta X(s',s)}k_\eta u(s')ds', \tag{7}$$

$$\alpha(T,s'\to s)=\frac{1}{I_b(T)}\int_0^\infty I_{b\eta}[1-e^{k_\eta X(s',s)}]d\eta, \tag{8}$$

where

$$X(s',s)=\int_{s'}^s u(s'')ds''. \tag{9}$$

In the k-distribution method it is recognized that—over a small spectral interval over which $I_{b\eta}$ may be assumed constant—the absorption coefficient attains the same value many times. If the medium is homogeneous [i.e., $\kappa_\eta=\kappa_\eta(\eta)$ only], and even in a nonhomogeneous medium if Eq. (5) applies, the absorption coefficient may be reordered into a monotonically increasing function without loss of accuracy. For a narrow spectral interval we then write for the narrow band transmissivity $\overline{\tau}_\eta$

$$\overline{\tau}_\eta=\frac{1}{\Delta\eta}\int_{\Delta\eta}e^{-k_\eta X}d\eta=\int_0^\infty e^{-kX}f(k)dk=\int_0^1 e^{-k(g)X}dg, \tag{10}$$

where the cumulative k-distribution

$$g(k)=\int_0^k f(k)dk \tag{11}$$

is an equivalent, nondimensional wavenumber. In Eq. (10) the integration can be switched from η to k_η, since for each η there is only a single value of k_η (but many different η for each k_η).

A similar argument can be applied to the entire spectrum. Defining a fractional Planck function as

$$i(T,\eta)=\frac{1}{I_b(T)}\int_0^\eta I_{b\eta}d\eta, \tag{12}$$

it is obvious that $i(T,0)=0$ and $i(T,\infty)=1$, i.e., the fractional Planck function is monotonically increasing with $0\leqslant i\leqslant 1$. Equation (8) can then be rewritten as

$$\alpha(T,s'\to s)=1-\tau(T,s'\to s)=1-\int_0^1 e^{-k_\eta(i)X(s',s)}di. \tag{13}$$

We note there is only one value of k_η for each value of i (but many values of i for a single value of k_η). Thus, we may reorder Eq. (13) in the same way as Eq. (10), leading to

$$\tau=\int_0^1 e^{-k_\eta(i)X}di=\int_0^\infty e^{-kX}f(T,k)dk=\int_0^1 e^{-k(T,g)X}dg. \tag{14}$$

Here, g is no longer an equivalent wavenumber, but an equivalent fractional Planck function. Note that, since i is a function of temperature, so is k, i.e. $k=k(T,g)$. Since we would like to be able to use arbitrary methods for the solution of the radiative transfer problem, employing the simplified $k-g$ relation of Eq. (14) (rather than $k_\eta-\eta$), the temperature dependence of $k(T,g)$ is rather inconvenient. Following Modest [9] we desire a form, which, upon substitution into Eq. (3), can be shown to reduce back to the original RTE, Eq. (1). We will, therefore, carry out one more reordering step to modify Eq. (14) to

$$\tau=\int_0^1 e^{-k(T,g)X}dg=\int_0^1 a(T,g_{\text{ref}})e^{-k(T_{\text{ref}},g_{\text{ref}})X}dg_{\text{ref}}, \tag{15}$$

where $k(T_{\text{ref}},g_{\text{ref}})$ is the $k-g$ distribution evaluated at a reference temperature T_{ref}, i.e., we have moved the temperature dependence from the exponent (in k) to a base function a. How this is done is best understood by looking at Fig. 1, which shows two typical k-distributions for T_{ref} (the reference temperature) and some other temperature T. Both functions have identical values for $k=k_{\min}$ at $g=0$ (the minimum absorption coefficient across the spectrum, usually zero), and $k=k_{\max}$ at $g=1$ (the maximum absorption co-

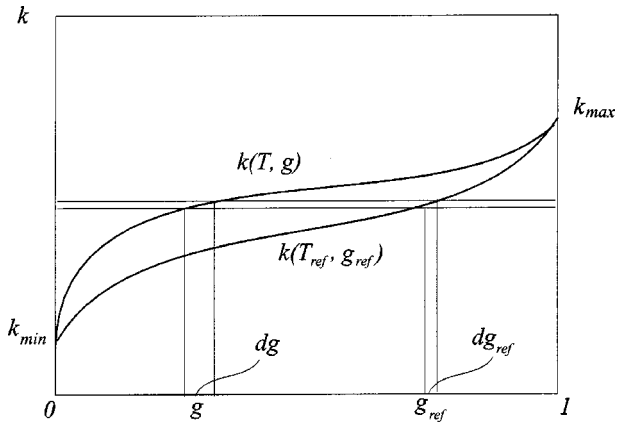

Fig. 1 The weight function *a*, obtained from *k*-distributions at different temperatures

efficient across the spectrum); for each value of k the corresponding value for g is simply shifted. Now setting $k(T,g) = k(T_{\text{ref}},g_{\text{ref}})$, and differentiating leads to

$$dg = \frac{\partial k(T_{\text{ref}},g_{\text{ref}})/\partial g_{\text{ref}}}{\partial k(T,g)/\partial g} dg_{\text{ref}} = \frac{f[T,k(g)]}{f[T_{\text{ref}},k(g_{\text{ref}})]} dg_{\text{ref}} = a(T,g_{\text{ref}}) dg_{\text{ref}}, \tag{16}$$

where we have arbitrarily set $a(T_{\text{ref}},g_{\text{ref}}) \equiv 1$ at the reference condition.

For simplicity of notation we will, from now on, drop the subscript "ref" from g_{ref}, as well as the argument T_{ref} from $k(T_{\text{ref}},g_{\text{ref}})$, which then is simply written as $k(g)$. Substituting Eq. (15) into Eq. (3), and noting that

$$\frac{\partial \alpha}{\partial s'} = -\frac{\partial \tau}{\partial s'} = \int_0^1 a(T,g) e^{-k(g)X(s',s)} k(g) \frac{\partial X}{\partial s'} dg = -\int_0^1 a(T,g) e^{-k(g)X} k(g) u(s') dg,$$

we obtain

$$I(s) = I_{bw} \int_0^1 a(T_w,g) e^{-kX(0,s)} dg + \int_0^s I_b(s') \int_0^1 a[T(s'),g] e^{-k(g)X(s',s)} k(g) u(s') dg ds'. \tag{17}$$

If we now introduce a new "spectral" intensity $I_g(s)$, we get

$$I(s) = \int_0^1 I_g(s) dg = \int_0^1 \left\{ [a(T_w,g) I_{bw}] e^{-kX(0,s)} + \int_0^s [a(T(s'),g) I_b(s')] \times e^{-kX(s',s)} ku(s') ds' dg. \right. \tag{18}$$

Comparing with Eq. (7) we find that I_g satisfies the general RTE, Eq. (1), subject to the same boundary conditions, but for a spectrally-integrated, gray case with the Planck function replaced by a weighted value, $[aI_b]$:

$$\frac{dI_g}{ds} = k(g) u(s) ([aI_b] - I_g), \quad 0 \leqslant g \leqslant 1. \tag{19}$$

What remains to be done is to solve the gray medium RTE, Eq. (19), by any arbitrary solution method for a small number of gray absorption coefficients $k(g)$ (since k is a smooth, monotonic function in g), followed by numerical quadrature over I_g. In the correlated-k approach this is generally done by Gaussian quadrature, since this gives a high degree of accuracy with relatively few RTE evaluations. The most primitive (and least accurate) quadrature scheme would be the use of the trapezoidal rule; i.e.,

$$\int_0^1 I_g dg \simeq \sum_{i=1}^n I_g(k(g_i)) \Delta g_i; \quad \sum_{i=1}^n \Delta g_i = 1, \tag{20}$$

which would imply

$$\alpha = 1 - \tau = \int_0^1 a(T,g)(1 - e^{-k(g)X}) dg \simeq \sum_{i=1}^n A_i(T)(1 - e^{-k_i X}), \quad A_i = \int_{\Delta g_i} a dg, \tag{21}$$

which is commonly known as the "Weighted-Sum-of-Gray-Gases" (WSGG) method. Therefore, the Weighted-Sum-of-Gray-Gases method, while a very powerful method in itself, is effectively only a crude implementation of the Full-Spectrum Correlated-k approach presented here. Nevertheless, the WSGG method as presented in Eq. (21) was a considerable improvement over the previous state-of-the-art, which allowed only cumbersome and inaccurate application to inhomogeneous media [9,13,14].

Alternative Development. Equation (19) can also be derived directly from the spectral RTE, also including gray scattering and gray boundaries. Under the scaling approximation, the spectral RTE is then given by [19]

$$\frac{dI_\eta}{ds} = k_\eta u I_{b\eta} - (k_\eta u + \sigma_s) I_\eta + \frac{\sigma_s}{4\pi} \int_{4\pi} I_\eta(\hat{s}') \Phi(\hat{s},\hat{s}') d\Omega', \tag{22}$$

where σ_s is the scattering coefficient and $\Phi(\hat{s},\hat{s}')$ is the scattering phase function. In its most general form, Eq. (22) is subject to the boundary condition [19]

$$\text{at a wall,} \quad I_\eta = I_{w\eta} = \epsilon_w I_{bw\eta} + (1 - \epsilon_w) \frac{1}{\pi} \int_{\hat{\mathbf{n}}\cdot\hat{\mathbf{s}} \leq 0} I_\eta |\hat{\mathbf{n}} \cdot \hat{\mathbf{s}}| d\Omega, \tag{23}$$

where $I_{w\eta}$ is the spectral intensity leaving the enclosure wall, due to (diffuse gray) emission and/or (diffuse gray) reflection, ϵ_w is the emissivity of the wall, and $\hat{\mathbf{s}}$ and $\hat{\mathbf{n}}$ are unit vectors for direction and the surface normal (pointing out of the wall), respectively.

A redistributed RTE is obtained by multiplying Eq. (22) by $\delta(k - k_\eta)/f(T_{\text{ref}},k)$, where $\delta(k - k_\eta)$ is the *Dirac-delta* function and

$$f(T_{\text{ref}},k) = \frac{1}{I_b} \int_0^\infty I_{b\eta}(T_{\text{ref}}) \delta(k - k_\eta) d\eta = \int_0^1 \delta(k - k_\eta) di \tag{24}$$

is the Planck-function-weighted k-distribution at the reference temperature, as already given in Eq. (14). Note that integrating the *Dirac-delta* function across a single occurrence of $k = k_\eta$ yields

$$\int \delta(k - k_\eta) d\eta = \int \delta(k - k_\eta) \frac{d\eta}{dk_\eta} dk_\eta = \left| \frac{d\eta}{dk_\eta} \right|. \tag{25}$$

Integrating the so-multiplied Eq. (22) across the spectrum, and assuming gray scattering properties yields the desired form

$$\frac{dI_g}{ds} = kuaI_b - (ku+\sigma_s)I_g + \frac{\sigma_s}{4\pi}\int_{4\pi} I_g(\hat{s}')\Phi(\hat{s},\hat{s}')d\Omega', \tag{26}$$

where

$$I_g = \int_0^\infty I_\eta \delta(k-k_\eta)d\eta \Big/ f(T_{\text{ref}},k), \tag{27a}$$

$$a = \frac{1}{I_b}\int_0^\infty I_{b\eta}\delta(k-k_\eta)d\eta \Big/ f(T_{\text{ref}},k) = f(T,k)/f(T_{\text{ref}},k), \tag{27b}$$

subject to the boundary condition

$$\text{at a wall,} \quad I_g = I_{wg} = \epsilon_w[a_g I_b](T_w) + (1-\epsilon_w)\frac{1}{\pi}\int_{\hat{\mathbf{n}}\cdot\hat{\mathbf{s}}<0} I_g|\hat{\mathbf{n}}\cdot\hat{\mathbf{s}}|d\Omega. \tag{28}$$

This reordering process requires that any factors accompanying radiative intensity I_η—with the exception of k_η itself—must be independent of wavenumber; i.e., like any global model the FSCK method is limited to gray surfaces and/or gray scattering properties.

Evaluation of Weight Function *a*. Note that expressing the transmissivity in terms of the correlated-*k* distribution $f(T,k)$ (second formulation in Eq. (14)) also satisfies the RTE, replacing the $[aI_b]$ in Eq. (19) by $[f(T,k)I_b]$, in which case the resulting intensity has to be integrated over *k*-space, i.e., $I=\int_0^\infty I_k dk$ [17]. The advantage of the present formulation—besides demonstrating the equivalence between *k*-distribution and the WSGG model—is the fact that the weight function $a(T,g)$ is much smoother and better behaved than the *k*-distribution, and thus requires fewer quadrature points (i.e., gray-gas evaluations) for the accurate determination of full spectrum results such as heat flux. It remains to determine the $k(T,g)$ distributions for a given gas mixture followed by transformation to $k(T_{\text{ref}},g_{\text{ref}})$, i.e., the evaluation of the $a(T,g_{\text{ref}})$. This can be done in a number of ways, the two most extreme ones being calculation from (i) total emissivity (transmissivity) data, and (ii) from line-by-line data such as the HITRAN [23,24] or HITEMP [25] databases. In this paper, we will limit our consideration to high-resolution databases.

HITRAN92 [23] has been used successfully in meteorological applications, but is known to be inaccurate for combustion scenarios since many hot lines are missing in that database. HITRAN96 [24] has remedied this problem to some extent and may now be used with confidence for up to 600K, although many hot lines are still missing. Very recently, HITEMP [25] has become available for carbon dioxide and water vapor and should be accurate for up to 1000 K. However, it has many times the number of spectral lines than HITRAN96, requiring substantially more computer time, and is limited to carbon dioxide and water vapor mixtures. In either case $k(T,g)$ is determined from Eqs. (14) or (24) for a fixed reference condition. Recall that the temperature dependence in $k(T,g)$ originates from the fractional Planck function *i*, *not* from the absorption coefficient, which is evaluated at the reference condition (which remains fixed). The transformation function $a(T,g)$ is best determined by ratioing the slopes of the (preferably slightly smoothened) *g* distribution functions for the actual and the reference temperature for the same *k*, since *a* may have discontinuities if $f(T,k)/f(T_{\text{ref}},k)$ is employed (since the *f* may have singularities, albeit at identical *k*-values). Once the correlated-*k* distribution and the weight function have been determined, the temperature and additional pressure dependence given by the function $u(T,p,\underline{x})$ in Eq. (5) must be postulated and/or determined in some optimal way.

There are several different ways to obtain $k(T,g)$ from line-by-line data as described in several papers [2,3,21,26]. We prefer the following method, which is simple, quick, adaptive and particularly well-suited for full-spectrum calculations: the spectrum $0\leqslant\eta<\infty$ is subdivided into *N* equal subintervals, and $N+1$ equally spaced spectral locations. Similarly, the *k*-range is subdivided into *J* ranges (because of the large order-of-magnitude range of the absorption coefficient, the *k*-range is subdivided equally on a $\log_{10}k$-basis). A set of temperatures T_i can be considered simultaneously. A scan is now made over the $N+1$ spectral locations, the local value of *k* is calculated, and the j^{th} *k*-bin for the i^{th} temperature T_i is incremented by the corresponding fractional Planck function if $k_j\leqslant k<k_{j+1}$, i.e., $I_{b\eta}\delta\eta$, with a resolution fine enough that $I_{b\eta}(T_i)$ is constant across $\delta\eta$. At the end of the scan all bin values are multiplied by $\pi/\sigma T_i^4$, after which they reflect the calculated values for $f(T,k_j)\delta k_j$ and the cumulative *k*-distribution for each temperature follows from

$$g(T,k_j) = \sum_{j'=1}^{j} f(T,k_{j'})\delta k_j = g(T,k_{j-1}) + f(T,k_j)\delta k_j. \tag{29}$$

Note that the number of *k*-bins as well as temperature bins can be made arbitrarily large without any appreciable increase in computation time. While that may result in empty bins, the $g(T,k)$ distribution would simply remain constant for adjacent *j*-values. After each scan the number of *N* is doubled, resulting in *N* additional knot points, and *N* additional *k*-values are calculated and placed in the $f(T,k_j)$ bins, until such time when the g_j no longer change beyond some criterion. Note also that, in the limit of $\delta k\to 0$, $\delta\eta\to 0$, it follows that $f(T,k)\to\infty$ wherever k_η is maximum or minimum, resulting in small discontinuities for $a(T,k)$ at these points. Thus, the smoothness of *f* and *a* are strongly affected by the numerical implementation.

By making a transformation from $f(k)dk$ to the weight function $a(T,g)dg$ it was hoped to obtain a smoothened function for easier quadrature (similar to the transformation from $f(k)dk$ to dg, with $k(g)$ being a much smoother function than $f(k)$). This is demonstrated for two extreme temperatures in Fig. 2(*a*), showing $f(T_{\text{cold}},k)$, $f(T_{\text{hot}},k)$, and $a(T_{\text{cold}},k)$, using the hot gas temperature as the reference state. The corresponding $k(T,g)$, together with $a(T_{\text{cold}},g)$ are shown in Fig. 2(*b*). While the weight function $a(T,g)$ is not as smooth as the $k(T,g)$ function, *a* is considerably better behaved than the $f(T,k)$: high frequency oscillations are reduced from approximately 25 percent of maximum to about 5 percent (as discussed earlier, maxima of *f* and, therefore, *a*, depend on the numerical implementation; values given are for our present calculations). Low frequency oscillations are also much less severe. As the temperature moves closer to the reference value, *a* becomes progressively smoother (hovering around an average value of $a=1$). Therefore, accurate numerical quadrature of Eq. (20) becomes relatively easy. Efficient quadrature can be further improved by smoothing the weight function through

$$\int_0^1 a(g)\phi(k(g))dg = \int_0^1 \frac{1}{\Delta g}\int_{\Delta g} a(g')\phi(k(g'))dg'dg \simeq \int_0^1 \overline{a}(g)\phi(k(g))dg, \tag{30}$$

where

$$\overline{a} = \frac{1}{\Delta g}\int_{\Delta g} a(g')dg' \tag{31}$$

since $k(g)$ is essentially constant across a small interval Δg. In this expression $\phi(k)$ is any function that depends on *g* through the function $k(T,g)$, such as I_g. The smoothened weight function $\overline{a}$ is also indicated in Fig. 2(*b*) along with typical quadrature points used in later examples. Also indicated are typical step values k_i for the WSGG trapezoidal integration.

Scaling of Absorption Coefficient. The FSCK method is exact as compared to LBL calculations that use the same scaled

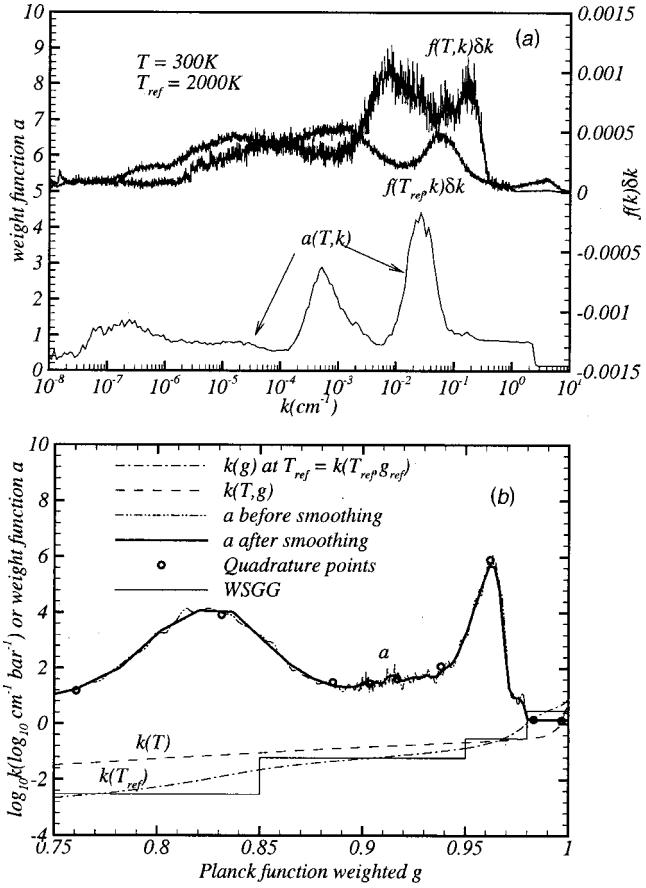

Fig. 2 (*a*) Comparison of *k*-distributions at different temperatures and the weight function *a*, (*b*) Planck function weighted cumulative *k*-distribution *g*, and the weight function *a*

absorption coefficient. Errors arise only from the fact that actual gas mixtures do not obey the scaling approximation. Therefore, optimal scaling methodology is extremely important for the accuracy of the FSCK method, although this remains somewhat of a black art. While the FSCK method is, in principle, valid for arbitrary gas mixtures, we will limit ourselves here to systems with constant total pressure, which reduces the determination of a scaled absorption coefficient distribution from a line-by-line database to two steps. First, a reference condition must be chosen. Assuming constant total pressure throughout, it appears natural to take a volume average as the reference mole fraction distribution, or

$$\underline{x}_{\mathrm{ref}}=\frac{1}{V}\int_V \underline{x}\,dV. \tag{32}$$

Choosing an optimal reference temperature is less obvious; different possibilities are listed and discussed as follows:

Maximum Temperature in System.

$$T_{\mathrm{ref}}=T_{\mathrm{hot}} \tag{33a}$$

Minimum Temperature in System.

$$T_{\mathrm{ref}}=T_{\mathrm{cold}} \tag{33b}$$

Volume Averaged Temperature.

$$T_{\mathrm{ref}}=\frac{1}{V}\int_V T\,dV \tag{33c}$$

Planck Mean Temperature.

$$(\kappa_P T^4)_{\mathrm{ref}}=\frac{1}{V}\int_V \kappa_P T^4\,dV \tag{33d}$$

Emission Weighted Temperature.

$$T_{\mathrm{ref}}=\frac{\int_V T[4\sigma\kappa_P(T,p,\underline{x})T^4]dV+\int_A T[\epsilon\sigma T^4/\pi]dA}{\int_V[4\sigma\kappa_P(T,p,\underline{x})T^4]dV+\int_A[\epsilon\sigma T^4/\pi]dA} \tag{33e}$$

Since at the reference state the absorption coefficient is set to coincide with that of the database, an intermediate temperature may be expected to do better than choosing the maximum (Eq. (33*a*)) or minimum temperatures (Eq. (33*b*)) as the reference temperature, such as a spatially averaged temperature (Eq. (33*c*)). However, straight volume averaging neglects local variations in mole fractions, as well as the fact that emission from hot regions often dominates the radiative field. Therefore, using a Planck mean temperature (based on overall emitted energy) or an emission-weighted temperature can be expected to give better results. The performance of different reference temperatures will be tested later within this paper.

Once a reference state has been established, an appropriate spatial variation function $u(T,p,\underline{x})$ must be found. If we assume constant total pressure throughout the system and neglect pressure effects on the line half widths b_j (generally a good approximation for systems with roughly constant total pressure), then spectral lines become temperature and pressure dependent through only the line intensities S_j, which, for a linear absorption coefficient, is linearly proportional to the partial pressure of the absorbing gas, times a function of temperature only.

Since radiative heat fluxes from a layer are governed by emission rates attenuated by self absorption, the scaling function for a gas mixture with only one participating gas $u(T,x)$ is found here from the implicit relation

$$\int_0^\infty I_{b\eta}(T_{\mathrm{em}})\exp[-\kappa_\eta(T,x)L_m]d\eta = \int_0^\infty I_{b\eta}(T_{\mathrm{em}})\exp[-k_\eta u(T,x)L_m]d\eta, \tag{34}$$

where $k_\eta=\kappa_\eta(T_{\mathrm{ref}},x_{\mathrm{ref}})$ and L_m is the mean beam length of the volume under consideration. Note that there are two temperatures involved in Eq. (34), an emission temperature T_{em} and the reference temperature T_{ref}. Using an emission temperature different from T_{ref} may give better results, but will involve a larger amount of precalculations and interpolations. For simplicity, one may consider the use of the reference temperature also as the emission temperature. For optically thin situations, Eq. (34) ensures that the scaling produces the correct Planck-mean absorption coefficient at all locations (weighted by T_{em}). For optically thick situations, Eq. (34) ensures that the scaling produces the correct heat flux escaping a layer with a thickness of L_m. For gas mixtures with more than one participating gas specie, we use here an assumed shape of

$$u(T,\underline{x})=\sum_{n=1}^{N} x_n u_n(T), \tag{35}$$

where $x_n u_n(T)$ is the scaling function for the n^{th} gas specie and is evaluated, independently for each specie, using Eq. (34). This simplification has the disadvantage that it neglects line overlap between species (in the function of optimal scaling parameters only, *not* in the heat transfer calculations). It has the advantage that the volumetric scaling function can be databased independently for each specie.

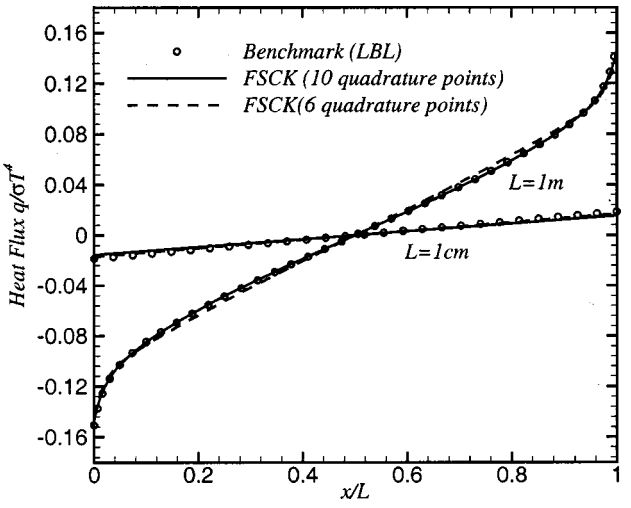

Fig. 3 Local radiative flux in an isothermal N_2–CO_2 mixture (T=1500 K, p=1 bar, x_{CO_2}=0.1, L=1 cm and L=1 m) bounded by cold, black walls

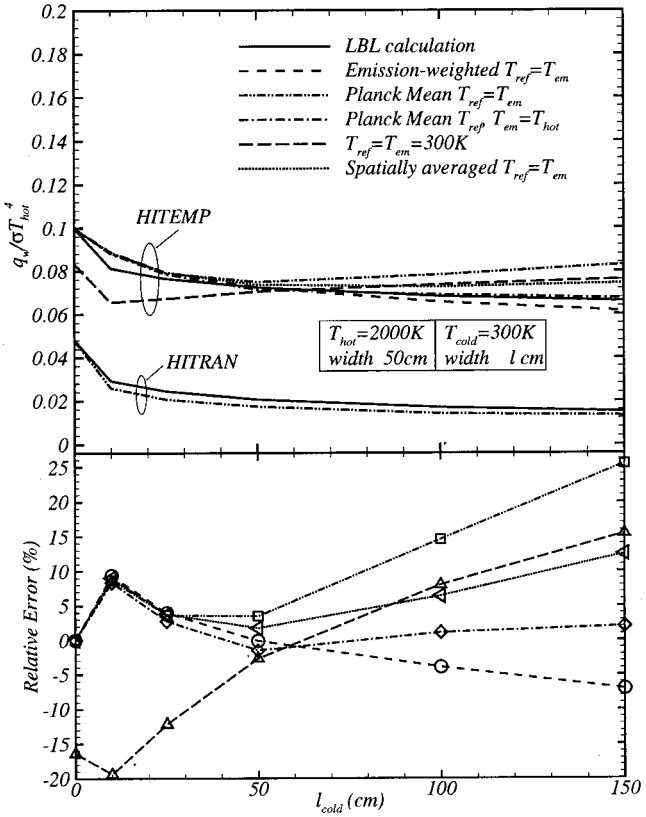

Fig. 4 Radiative flux exiting from the cold column of a two-column CO_2-nitrogen mixture at different temperatures (T_{hot}=2000 K, l_{hot}=50 cm; T_{cold}=300 K, l_{cold} variable; uniform p=1 bar, x_{CO_2}=0.1, cold and black walls) using HITEMP and HITRAN96 databases; the relative errors shown are for HITEMP results

Sample Calculations

The validity of the present model, its application to non-black walls and scattering media, and its limitations due to the scaling approximation will be shown through a number of relatively simple one-dimensional examples in which CO_2-N_2 mixtures confined between two infinite parallel walls are considered. Also, a two-dimensional practical combustion problem will be studied to test the model, with more than one participating gas coexisting in a cylindrical axisymmetric combustion chamber. The P_1 approximation is employed in the following examples, since it is a popular method with reasonable levels of effort and accuracy. Since the FSCK method is a spectral model that can be used with any RTE solution method, comparison of the LBL benchmark with FSCK demonstrates the accuracy of the FSCK method as long as the same RTE solver is employed in both cases. Any other solution method than the P_1 approximation would also be acceptable. The HITEMP as well as HITRAN96 databases are used in the following calculations to validate the new approach, and methods to determine optimally scaled absorption coefficients will be discussed.

One-Dimensional Slab. First an isothermal medium confined between two parallel, cold and black plates is considered. Since the medium is homogeneous, the *k*-distribution at only one temperature is needed, i.e., at the temperature of the medium, so that $a \equiv 1$ in this case. The medium is a nitrogen-carbon dioxide mixture at 1500 K, 1 bar total pressure, with a 10 percent mole fraction of CO_2. Using the HITEMP database for the evaluation of absorption coefficients, benchmark line-by-line results are compared in Fig. 3 with the Full-Spectrum Correlated-*k* Distribution (FSCK) method for two slab widths demonstrating that the FSCK method is indeed exact for homogeneous media. Using 10 Gaussian quadrature points, the FSCK results essentially coincide with the LBL results (for which approximately 600,000 quadrature points were needed). Using only 6 quadrature points shows slight discrepancies for optically thick cases ($L=1$ m). Similar to LBL calculations, more accurate results can be obtained by using more quadrature points. Within numerical accuracy, the wall heat flux predicted by the FSCK is exact for the homogeneous and isothermal case.

Taine et al. [22] have shown that the scaling approximation may produce substantial errors when radiation emitted in a hot region travels through a cold layer, since (i) *k*-distributions always sort absorption coefficients according to magnitude (assuming that this produces consistent wavenumber sorting), while (ii) in strongly non-isothermal media this ordering consistency is violated by "hot lines," which have large absorption coefficients at high temperatures, while being essentially negligible at low temperatures. We will consider two types of non-isothermal media. First, we will look at the extreme case of an isothermal hot layer adjacent to an isothermal cold layer. This extreme test will allow us to find out optimum ways to determine accurately scaled absorption coefficient distributions from the HITEMP database. Figure 4 shows the radiative heat flux arriving at the cold black wall of a N_2-CO_2 mixture with a step in temperature. Pressure and CO_2 mole fraction are constant throughout at 1 bar and 10 percent, respectively. The hot layer is at $T=2000$ K and has a fixed width of 50 cm, while the cold layer is at 300 K, and is of varying width. The LBL results obtained from both the HITEMP and the HITRAN96 databases are compared with various scaling approximations. Note that heat fluxes predicted from the HITEMP database are more than double (no cold layer) to five-fold (thick cold layer) of those predicted from the HITRAN96 database: while the HITRAN96 database can be used with confidence up to about 600 K [27], for temperatures beyond that level it appears to be missing many hot lines, which are estimated in the HITEMP database. Since FSCK requires quadrature over a single monotonically increasing function and needs about 10 quadrature points, while LBL calculations require about 1 million quadrature points, the FSCK method will greatly speed up the calculations. In this example, based on a well-established absorption coefficient database for both FSCK and LBL, the FSCK calculations required less than 0.05 second (10 quadrature points) on an SGIO200 (single processor R10000 at 150 MHz), while the LBL calculations required 25 minutes, or a factor of approximately 100,000:1.

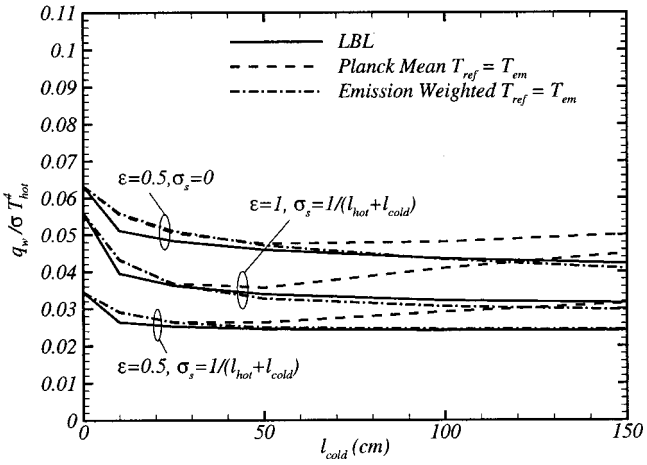

Fig. 5 Same as Fig. 4, but for medium bounded by gray walls as well as for gray scattering media

From Fig. 4 it can be seen that using two temperature scaling (T_{hot} as T_{em} in Eq. (34), plus a Planck mean reference temperature) gives the best results with a maximum error of only 8 percent. In this problem, the emission weighted temperature is very close to the hot temperature of 2000 K and, using it for both T_{em} and T_{ref}, gives a maximum error of 9 percent. Using the spatially averaged temperature and the cold temperature (300 K) as T_{ref} and T_{em} gives maximum errors of 13 percent and 19 percent, respectively. Using the Planck mean temperature for both T_{ref} and T_{em} produces a maximum error of 25 percent for this extreme temperature case because, with increasing cold layer, the Planck-mean reference temperature moves closer to the cold temperature, greatly overpredicting emission from the hot layer. Although producing large errors in this extreme example, we feel that the Planck mean temperature, together with the emission-weighted temperature, are the best choices for reference temperature. As will be shown later, Planck mean and emission-weighted temperatures are actually very close in more realistic combustion systems.

Denison and Webb [11] have already shown that the WSGG method is applicable to gray boundaries. To demonstrate that the FSCK method and, therefore, also the WSGG method is equally valid not only for media bounded by gray walls, but also for (gray) scattering media, heat fluxes through the mixture of the previous example were also calculated for the cases of gray walls (ϵ=0.5), the addition of a gray scattering medium (scattering coefficient $\sigma_s = 1/(l_{\text{hot}} + l_{\text{cold}})$), and the combination of both. The choice of σ_s here is arbitrary, and is chosen to give an optical thickness of unity, where one would expect scattering to have the largest effects. Representative calculations using line-by-line calculations together with the scaled absorption coefficient confirmed that the FSCK method produces exact results (for the scaled absorption coefficient), even in the presence of non-black walls and gray scattering. In all cases using the emission-weighted temperature as the reference value gave again the most accurate results. Inspection of Fig. 5 shows that with the presence of a nonblack wall the heat flux to the wall is reduced and the maximum relative error remains approximately the same. The influence of scattering and combined effects are also shown in Fig. 5. Qualitatively, the trends remain the same, with maximum errors at $l_{\text{cold}} = 10$ cm of 9.5 percent and 10.4 percent, respectively. Again, HITEMP results as compared to HITRAN96 results are higher by a factor of 2 (no cold layer) to about 6 (thick cold layer).

The previous examples with a step change in temperature were designed to be a worst-case scenario, i.e., to understand the limits of the scaling approximation, and as a tool to find methods to determine optimum scaling parameters for a gas mixture. One-dimensional nitrogen-carbon dioxide mixtures with smoothly

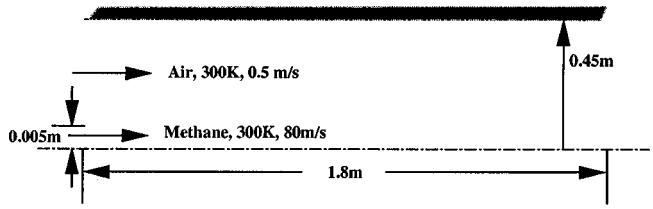

Fig. 6 Geometry of the cylindrical combustor

varying temperature and/or mole fraction profiles, such as one may expect to occur in actual combustion applications, make LBL and FSCK results virtually coincide [28].

Two-Dimensional Gas Mixtures. The model will now be tested further by applying it to a practical combustion problem. A mixture of combustion products (i.e., CO_2 and H_2O) as well as fuel (i.e., CH_4) in a cylindrical axisymmetric geometry is studied, as shown in Fig. 6. A small nozzle at the center of the combustor introduces methane at high speed and ambient air enters the combustor coaxially at a lower speed. Fuel and air mix and are allowed to react using a simple eddy dissipation reaction model. The liner wall is assumed black and insulated, and its temperature is equal to the local gas temperature. Since fuel is injected from the inlet together with cold air, temperatures near the inlet are relatively low (≅300 K). The combustion reaction produces a bell-shaped flame sheet with high downstream outlet temperatures. Temperature levels inside the chamber range from 300 K to around 1700 K, as shown in Fig. 7(*a*). The mole fraction distri-

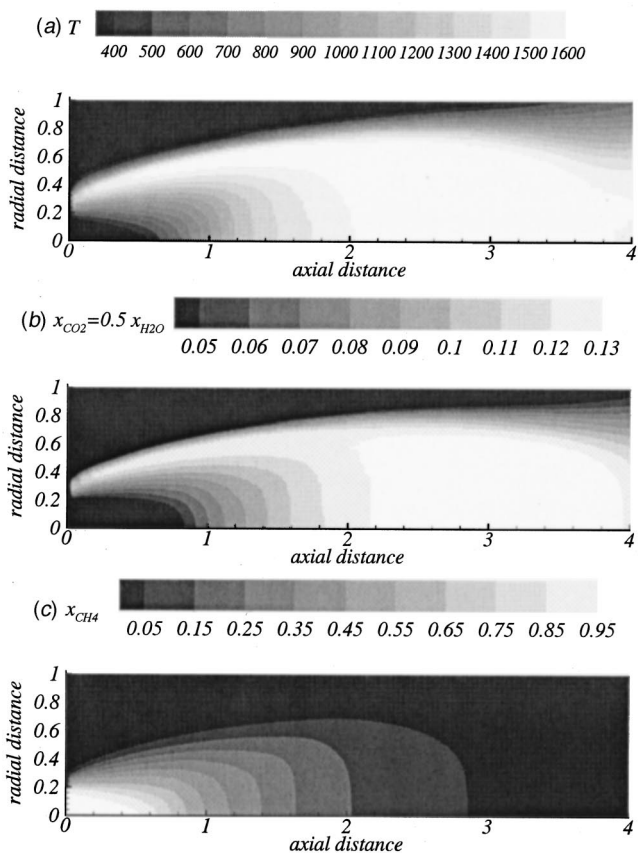

Fig. 7 Temperature and mole fraction distribution in a two-dimensional cylindrical combustion chamber, (*a*) temperature distribution; (*b*) mole fraction distribution of CO_2 and H_2O; and (*c*) mole fraction distribution of CH_4 (gas mixtures with methane and without methane are both considered).

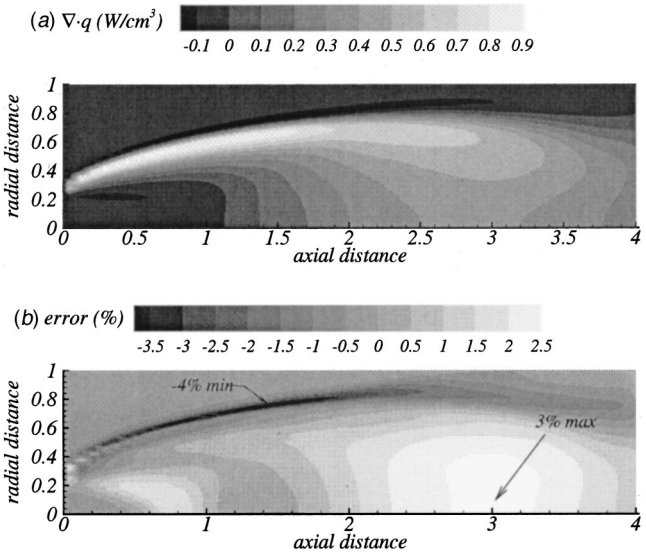

Fig. 8 Two-dimensional cylindrical combustion chamber with a gas mixture containing CO_2 and H_2O: (*a*) LBL calculations for the radiative heat source $\nabla\cdot\mathbf{q}$ (W/cm^3); (*b*) relative error of FSCK results, $(\nabla\cdot q_{\mathrm{LBL}}-\nabla\cdot q_{\mathrm{FSCK}})/\nabla\cdot q_{\mathrm{LBL,max}}$.

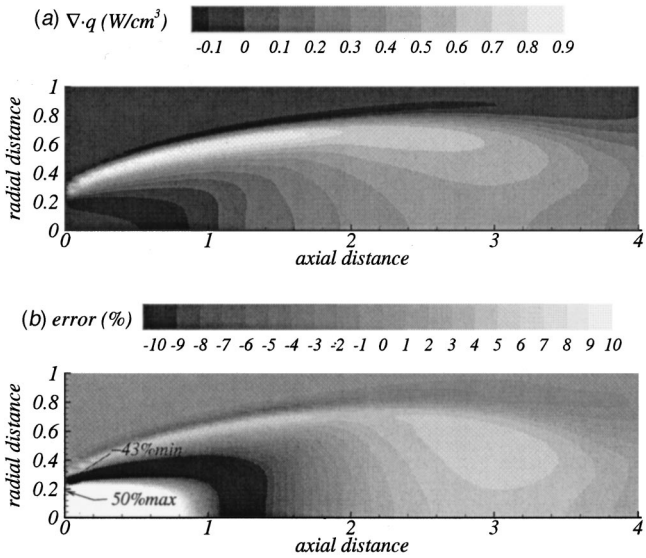

Fig. 9 Two-dimensional cylindrical combustion chamber with a gas mixture containing CO_2, H_2O and CH_4: (*a*) LBL calculations for the radiative heat source $\nabla\cdot\mathbf{q}$ (W/cm^3); (*b*) relative error of FSCK results, $(\nabla\cdot q_{\mathrm{LBL}}-\nabla\cdot q_{\mathrm{FSCK}})/\nabla\cdot q_{\mathrm{LBL,max}}$.

bution of the combustion products basically follows the pattern of the temperature change, as shown in Fig. 7(*b*), with $x_{H_2O}=2x_{CO_2}$ everywhere (using a simple global reaction for methane). The fuel, on the other hand, has large mole fractions near the inlet where it has not yet been consumed, and is barely present beyond where combustion has taken place, as shown in Fig. 7(*c*). LBL calculations were carried out as a benchmark. Since three emitting and absorbing gases coexist in this chamber (in this case, methane, carbon dioxide and water vapor), the FSCK approach needs now to be applied to a gas mixture of more than one participating gas. In the following calculations, the reference and emission temperatures in Eq. (34) are taken as the Planck mean temperature. Choosing the emission weighted temperature from Eq. (33*e*) instead, yields essentially the same results, since both temperatures are very close to each other.

We will first consider the case of CO_2 and H_2O being the only radiatively participating gases, with the temperature distribution shown in Fig. 7(*a*) and mole fraction distribution shown in Fig. 7(*b*). Although the mole fractions of the combustion products vary throughout the volume, the mole fraction ratios of CO_2 to H_2O is 0.5 everywhere. The radiative heat source $\nabla\cdot\mathbf{q}$ determined from LBL calculations for this case is shown in Fig. 8(*a*) and the relative error of the FSCK method with respect to the LBL benchmark, defined as

$$\text{error(percent)}=\frac{\nabla\cdot\mathbf{q}_{\mathrm{LBL}}-\nabla\cdot\mathbf{q}_{\mathrm{FSCK}}}{\nabla\cdot\mathbf{q}_{\mathrm{LBL,max}}}\times 100 \qquad (36)$$

is shown in Fig. 8(*b*). It can be seen that the maximum errors are around -4 percent across the sharp gradients just outside the flame sheet, and $+3$ percent in the hot downstream section. Thus, one may conclude that the FSCK method predicts heat transfer rates very well in situations where gases have constant ratios of mole fraction. In this problem, the CPU time required for LBL calculations is about 60 h, while that for the FSCK method is 5 sec.

Next we consider the same mixture of CO_2 and H_2O, but will also include the radiative participation of CH_4. Since methane, as the fuel, has large mole fractions only near the inlet as shown in Fig. 7(*c*), the gases in the mixture no longer have the same mole fraction ratio throughout the combustion chamber. Again, LBL calculations are carried out as a benchmark and are shown in Fig. 9(*a*). The distribution of the radiative heat source differs from the previous problem only in the inlet region because of the presence of CH_4. Shown in Fig. 9(*b*), the maximum error of the FSCK approach now increases to 50 percent in the inlet region with its mole fraction discontinuity, although the error remains well below 10 percent throughout most of the combustion chamber. It can be seen that non-constant ratios of mole fraction of participating gases have a big effect on the accuracy of the method, since at one location gas ''*a*'' may be prominent, and gas ''*b*'' at another, causing severe breakdown of absorption coefficient scaling. To overcome this problem we have also developed a multi-scale FSCK method [29].

Summary and Conclusions

A Full-Spectrum Correlated-*k* Distribution (FSCK) has been developed, which—within its limitations (gray walls, gray scattering, spectral absorption coefficient obeying the scaling approximation)—allows very efficient ''exact'' evaluation of radiative fluxes for arbitrary molecular gas mixtures, using any desired RTE solver. Nongray surfaces and/or nongray scattering would require a multi-band approach (rather than full-spectrum). It has been shown that the popular Weighted-Sum-of-Gray-Gases (WSGG) method is simply a crude implementation of the FSCK method; therefore, it is implied that the WSGG method can also be applied to gray enclosures as well as gray scattering media. Limitations of the scaling approximation have also been investigated and procedures to find optimally scaled distributions have been discussed. Comparison of results using the HITRAN96 and HITEMP databases shows that, beyond 1000 K, HITEMP radiative fluxes are several times larger than those from HITRAN, thus indicating the application limits of HITRAN96.

Acknowledgments

The authors gratefully acknowledge the financial support of the National Science Foundation under the contract CTS-9615009. Temperature and mole fraction profiles for the axisymmetric combustion problem in Fig. 7 were provided by Mr. G. Li.

Nomenclature

A = weight function for WSGG method

a = weight function for FSCK method
b = line half-width, cm^{-1}
f = k-distribution function, cm
g = cumulative k-distribution
I = radiative intensity, W/m^2sr
i = fractional Planck function
k = absorption coefficient variable, cm^{-1}
k_η = spectral absorption coefficient at reference state, cm^{-1}
l = geometric length, m
L_m = mean beam length, m
p = pressure, bar
q = radiative heat flux, W/m^2
S = line intensity, cm^{-2}
s, s' = distance along path, m
T = temperature, K
u = spatial dependence function for absorption coefficient
V = Volume, m^3
X = weighted path length, m
$x, \underline{x}$ = mole fraction, mole fraction vector

Greek Symbols

α = absorptivity
ϵ = emissivity
η = wavenumber, cm^{-1}
Φ = scattering phase function
κ = absorption coefficient, cm^{-1}
Ω = solid angle, sr
σ_s = scattering coefficient, cm^{-1}
τ = transmissivity

Subscripts

0 = reference condition
b = blackbody emission
em = emission
i = gray gas in WSGG
j = line or bin
P = Planck mean
w = wall
η = spectral

References

[1] Goody, R., West, R., Chen, L., and Crisp, D., 1989, "The Correlated-*k* Method for Radiation Calculations in Nonhomogeneous Atmospheres," J. Quant. Spectrosc. Radiat. Transf., **42**, No. 6, pp. 539–550.

[2] Lacis, A. A., and Oinas, V., 1991, "A Description of the Correlated-*k* Distribution Method for Modeling Nongray Gaseous Absorption, Thermal Emission, and Multiple Scattering in Vertically Inhomogeneous Atmospheres," Journal of Geophysical Research, **96**, No. D5, pp. 9027–9063.

[3] Fu, Q., and Liou, K. N., 1992, "On the Correlated-*k* Distribution Method for Radiative Transfer in Nonhomogeneous Atmospheres," J. Atmos. Sci., **49**, No. 22, pp. 2139–2156.

[4] Rivière, Ph., Soufiani, A., and Taine, J., 1992, "Correlated-*k* and Fictitious Gas Methods for H_2O Near 2.7 μm," J. Quant. Spectrosc. Radiat. Transf., **48**, pp. 187–203.

[5] Rivière, Ph., Scutaru, D., Soufiani, A., and Taine, J., 1994, "A New CK Data Base Suitable From 300 K to 2500 K for Spectrally Correlated Radiative Transfer in CO_2-H_2O-Transparent Gas Mixtures," in *Proceedings of the 10th International Heat Transfer Conference*, ed., G. F., Hewitt, Taylor & Francis, London.

[6] Rivière, Ph., Soufiani, A., and Taine, J., 1995, "Correlated-*k* and Fictitious Gas Model for H_2O Infrared Radiation in the Voigt Regime," J. Quant. Spectrosc. Radiat. Transf., **53**, pp. 335–346.

[7] Soufiani, A., and Taine, J., 1997, "High Temperature Gas Radiative Property Parameters of Statistical Narrow-Band Model for H_2O, CO_2 and CO, and Correlated-*k* Model for H_2O and CO_2," Int. J. Heat Mass Transf., **40**, No. 4, pp. 987–991.

[8] Hottel, H. C., and Sarofim, A. F., 1967, *Radiative Transfer*, McGraw-Hill, New York.

[9] Modest, M. F., 1991, "The Weighted-Sum-of-Gray-Gases Model for Arbitrary Solution Methods in Radiative Transfer," ASME J. Heat Transfer, **113**, No. 3, pp. 650–656.

[10] Denison, M. K., and Webb, B. W., 1993, "An Absorption-Line Blackbody Distribution Function for Efficient Calculation of Total Gas Radiative Transfer," J. Quant. Spectrosc. Radiat. Transf., **50**, pp. 499–510.

[11] Denison, M. K., and Webb, B. W., 1993, "A Spectral Line Based Weighted-Sum-of-Gray-Gases Model for Arbitrary RTE Solvers," ASME J. Heat Transfer, **115**, pp. 1004–1012.

[12] Denison, M. K., and Webb, B. W., 1994, "*k*-Distributions and Weighted-Sum-of-Gray Gases: A Hybrid Model," in *Tenth International Heat Transfer Conference*, Taylor & Francis, London, pp. 19–24.

[13] Denison, M. K., and Webb, B. W., 1995, "The Spectral-Line-Based Weighted-Sum-of-Gray-Gases Model in Nonisothermal Nonhomogeneous Media," ASME J. Heat Transfer, **117**, pp. 359–365.

[14] Denison, M. K., and Webb, B. W., 1995, "Development and Application of an Absorption Line Black-Body Distribution Function for CO_2," Int. J. Heat Mass Transf., **38**, pp. 1813–1821.

[15] Denison, M. K., and Webb, B. W., 1995, "The Spectral-Line Weighted-Sum-of-Gray-Gases Model for H_2O/CO_2 Mixtures," ASME J. Heat Transfer, **117**, pp. 788–792.

[16] Rivière, Ph., Soufiani, A., Perrin, Y., Riad, H., and Gleizes, A., 1996, "Air Mixture Radiative Property Modelling in the Temperature Range 10000-40000 K," J. Quant. Spectrosc. Radiat. Transf., **56**, pp. 29–45.

[17] Pierrot, L., Rivière, Ph, Soufiani, A., and Taine, J., 1999, "A Fictitious-Gas-Based Absorption Distribution Function Global Model for Radiative Transfer in Hot Gases," J. Quant. Spectrosc. Radiat. Transf., **62**, pp. 609–624.

[18] Pierrot, L., Soufiani, A., and Taine, J., 1999, "Accuracy of Narrow-Band and Global Models for Radiative Transfer in H_2O, CO_2, and H_2O-CO_2 Mixtures at High Temperature," J. Quant. Spectrosc. Radiat. Transf., **62**, pp. 523–548.

[19] Modest, M. F., 1993, *Radiative Heat Transfer*, McGraw-Hill, New York.

[20] Goody, R. M., and Yung, Y. L., 1989, *Atmospheric Radiation—Theoretical Basis*, 2nd ed., Oxford University Press, New York.

[21] Goody, R., West, R., Chen, L., and Crisp, D., 1989, "The Correlated-*k* Method for Radiation Calculations in Nonhomogeneous Atmospheres," J. Quant. Spectrosc. Radiat. Transf., **42**, pp. 539–550.

[22] Taine, J., and Soufiani, A., 1999, "Gas IR Radiative Properties: From Spectroscopic Data to Approximate Models," in *Advances in Heat Transfer*, **33**, Academic Press, New York, pp. 295–414.

[23] Rothman, L. S., Gamache, R. R., and Tipping, R. H. et al., 1992, "The HITRAN Molecular Database: Editions of 1991 and 1992," J. Quant. Spectrosc. Radiat. Transf., **48**, No. 5/6, pp. 469–507.

[24] Rothman, L. S., Rinsland, C. P., Goldman, A., Massie, S. T., Edwards, D. P., Flaud, J. M., Perrin, A., Camy-Peyret, C., Dana, V., Mandin, J. Y., Schroeder, J., McCann, A., Gamache, R. R., Wattson, R. B., Yoshino, K., Chance, K. V., Jucks, K. W., Brown, L. R., Nemtchinov, V., and Varanasi, P., 1998, "The HITRAN Molecular Spectroscopic Database and HAWKS (HITRAN Atmospheric Workstation): 1996 Edition," J. Quant. Spectrosc. Radiat. Transf., **60**, pp. 665–710.

[25] Rothman, L. S., Camy-Peyret, C., Flaud, J.-M., Gamache, R. R., Goldman, A., Goorvitch, D., Hawkins, R. L., Schroeder, J., Selby, J. E. A., and Wattson, R. B., 2000, "HITEMP, the High-Temperature Molecular Spectroscopic Database," J. Quant. Spectrosc. Radiat. Transf., to appear.

[26] Arking, A., and Grossman, K., 1972, "The Influence of Line Shape and Band Structure on Temperatures in Planetary Atmospheres," J. Atmos. Sci., **29**, pp. 937–949.

[27] Modest, M. F., and Bharadwaj, S., 2001, "High-Resoultion, High-Temperature Transmissivity Measurements and Correlations for Carbon Dioxide-Nitrogen Mixtures," in *Proceedings of the ICHMT 3rd International Symposium on Radiative Transfer*, Antalya, Turkey.

[28] Modest, M. F., and Zhang, H., 2000, "The Full-Spectrum Correlated-*k* Distribution and Its Relationship to the Weighted-Sum-of-Gray-Gases Method," in *Proceedings of the 2000 IMECE*, **HTD-366-1**, Orlando, FL, ASME, New York, pp. 75–84.

[29] Modest, M. F., and Zhang, H., 2002, "A Multi-Level Full-Spectrum Correlated-*k* Distribution for Radiative Heat Transfer in Inhomogeneous Gas Mixtures," J. Quant. Spectrosc. Radiat. Transf., in print.

An Investigation of the Breakup of an Evaporating Liquid Film, Falling Down a Vertical, Uniformly Heated Wall

Mohamed S. El-Genk
e-mail: mgenk@unm.edu

Hamed H. Saber

Institute for Space and Nuclear Power Studies
and Chemical and Nuclear Eng. Dept.,
The University of New Mexico,
Albuquerque, NM 87131

The breakup of an evaporating, thin liquid film falling down a vertical, uniformly heated wall is of interest in many applications. Analytical expressions are developed for predicting the thickness of an evaporating liquid film and the corresponding wetting rate at breakup, which are in good agreement with experimental data for water. These expressions, derived from minimizing the total energy of a stable liquid rivulet forming immediately following the film breakup, required solving for the rivulet profile and the two-dimensional velocity field in the rivulet. The total energy of the rivulet is the sum of the kinetics energy of the liquid, the surface energies at the liquid-vapor and the solid-liquid interfaces, and those due to evaporation and the thermocapillary force along the liquid-vapor interface. The liquid film thickness at breakup is a function of Marangoni number, vapor Reynolds number, liquid and vapor properties, equilibrium contact angle of the liquid with underlying wall material, and the wall thermal conductance $<3\times10^4$ *W/m*^{2}*K. For a wall conductance* $<3\times10^4$ *W/m*^{2}*K, the film thickness at breakup, when the wall is heated uniformly at its inner surface, is higher than when the wall is heated at its outer surface, but both are identical when the wall conductance* $\geqslant3\times10^4$ *W/m*^{2}*K. The contribution of the equilibrium contact angle diminishes, but the thickness of the liquid film at breakup increases, as the wall heat flux increases.* [DOI: 10.1115/1.1420712]

1 Introduction

The flow of an evaporating thin liquid film, flowing down a vertical or an inclined heated surface is encountered in many energy and thermal processing applications. Examples include distillation and brewery industry, closed two-phase thermosyphons (CTPTs) for waste heat recovery and redundant heat exchangers, wet columns, cooling towers, thin liquid film heat exchangers, application of thin films onto computer microchips, and cooling of nuclear fuel elements following a loss-of-coolant accident (LOCA). The conditions for an evaporating liquid film to break up into a series of stable liquid rivulets, leaving the underlying surface partially dry, are important to these applications.

The breakup of continuous liquid films flowing down on heated and non-heated vertical walls have been observed experimentally [1–4] (Fig. 1(*a*)). It occurs when the liquid flow reaches a Minimum Wetting Rate (MWR), beyond which a continuous, thin liquid film cannot be maintained on the underlying wall. The film thickness at breakup is referred to here as the Minimum Liquid Film Thickness (MLFT).

Several approaches, based on either the Force Balance (FB) at a stagnation point or the Minimum Total Energy (MTE) of a stable liquid rivulet, forming following the film breakup, have been proposed for predicting the MLFT and MWR for a non-evaporating film, falling down a vertical wall. The FB criterion [5] determines the MLFT from the balance of the inertia and surface tension forces at a stagnation point of a leading edge of the liquid film after breakup (Fig. 1(*a*)). The MWR is then obtained from the momentum balance, far upstream of the stagnation point, based on the Nusselt theory approximation. The predictions of the MWR by the FB criterion [5] are 40–70 percent higher than measurements and of the MLFT are ~30 percent higher than those determined from the measured MWRs [6].

The MTE criterion, as applied to a stable, non-evaporating rivulet, forming following the breakup of a liquid film, derives an expression for the MLFT through minimizing the total energy of the rivulet. The corresponding MWR is then determined using the Nusselt theory approximation, as in the force balance criterion. The total energy of a non-evaporating rivulet is the sum of the kinetic energy of the liquid and the surface energies at the Liquid-Vapor (L-V) and the Liquid-Solid (L-S) interfaces. The former requires knowledge of the velocity field in the rivulet and the latter requires knowledge of the rivulet profile. The reported expressions of the MLFT and MWR by various investigators [7–10] have been inconsistent, due to several simplifying assumptions. These include a zero-order approximation of the liquid velocity within the rivulet and assuming that the rivulet profile, $\phi(x)$, is a part of a circle or deriving an expression for it based on the zero-order liquid velocity approximation.

For the breakup of an evaporating liquid film, falling down a vertical heated wall, very little work has been reported [11–13]. Hsu et al. [11] have conducted experiments to determine the MLFT of an evaporating water film, falling down on the inside of a vertical glass tube. The glass tube with 11.0 mm inside diameter, was uniformly heated on the outside using a thin, electrically conductive metallic thin film. The metallic film was transparent, thus did not limit visual observation of the falling liquid film on the inner surface of the tube.

Zuber and Staub [12] have used the FB criterion to derive expressions for the MLFT and MWR of an evaporating liquid film using the same methodology as Hartely and Murgatroyd [5]. However, they added to the force balance the thermocapillary force resulting from the temperature gradient developing along the L-V interface, and the thrust caused by the evaporating molecules from the L-V interface. They approximated the profile of the liq-

Contributed by the Heat Transfer Division for publication in the JOURNAL OF HEAT TRANSFER. Manuscript received by the Heat Transfer Division January 3, 2001; revision received August 3, 2001. Associate Editor: G. P. Peterson.

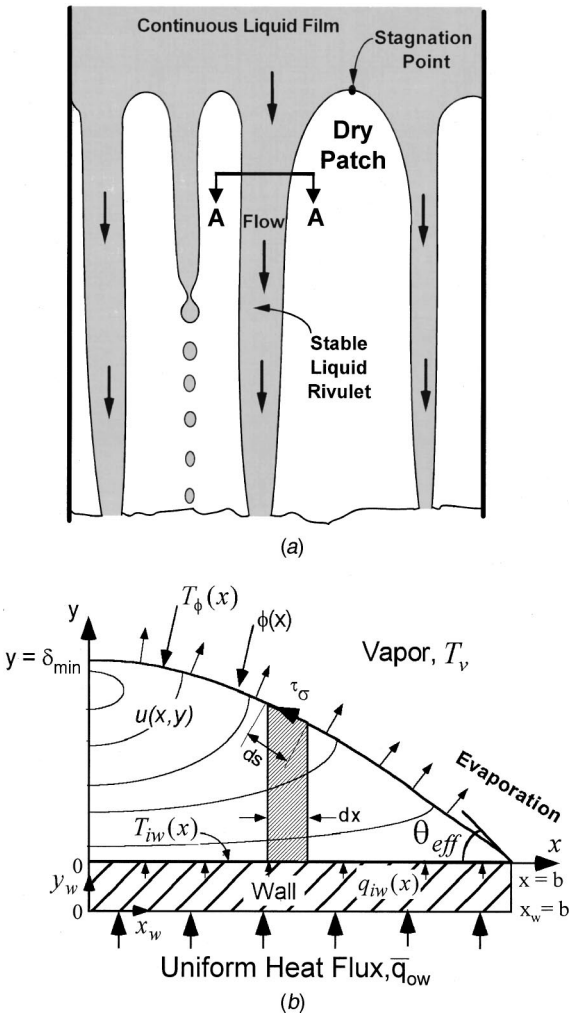

Fig. 1 Breakup of an evaporating liquid film, falling down a vertical, uniformly heated wall: (*a*) observed breakup of a falling, evaporating liquid film [3]; and (*b*) cross-section area of the stable, evaporating liquid rivulet at A-A.

uid film at the stagnation point by a wedge, having an angle equal to the equilibrium contact angle of the liquid with the wall, θ_o, at zero heat flux. Other simplifying assumptions included neglecting the effect of evaporation at L-V interface, assuming the thickness of the falling liquid film is uniform and equals that far upstream of the stagnation point. These assumptions limited the applicability of the derived expressions to very low wall heat flux or low evaporation rate. Zuber and Staub [12] also neglected the effect of axial conduction in the underlying heated wall, which contributes to the significant evaporation at the triple interface lines of the liquid rivulet, $x=\pm b$ (Fig. 1). The derived expressions for the MLFT and MWR by Zuber and Staub [12] deviated from the data for evaporating water films [11,13] by +20 percent to −55 percent and by +60 percent to −75 percent, respectively. When the wall heat flux is zero, these expressions are the same as those of Hartely and Murgatroyd [5], for a non-evaporating liquid film.

Fujita and Ueda [13] have conducted experiments to determine MLFT and MWR for an evaporating water film, falling down on the outside of a uniformly heated, stainless steel tube. The reported measurements of the MWR were for the incipient breakup of the film and for a film breakup and the formation of a stable dry patch (Fig. 1(*a*)). The stainless steel tubes used in the experiment, 16.0 mm outside diameter, 1.0 mm wall thickness, and 600 or 1000 mm long, were heated by applying an electrical potential across.

In addition, Fujita and Ueda [13] solved the continuity and the momentum equations of the falling liquid film, assuming an approximate temperature profile in the film. They equated the inertia and the thermocapillary forces and derived an expression for the MLFT. They neglected the acceleration within the falling liquid film, the flow velocity component normal to the wall and at the L-V interface, and the change in the liquid film thickness due to evaporation. The derived expression for the MLFT by Fujita and Ueda [13] underestimates their own data and that of Hsu et al. [11] by more than 85 percent.

Recently, El-Genk and Saber [6] have shown that solving for the two-dimensional, liquid velocity in the rivulet, $u(x,y)$, and using it to obtain the rivulet profile, significantly enhanced the comparison of the MTE criterion with the experimental data for the breakup of non-evaporating liquid films. The calculated thickness of a non-evaporating liquid rivulet, at its plane of symmetry, has also been shown to be the same as that of the measured liquid film thickness at breakup [6]. The derived expressions for the MLFT and MWR, which predicted to within ±10–20 percent the data for non-evaporating falling films of water and glycerol-water mixtures on glass, stainless steel, copper, and Perspex, are given, respectively, as

$$\Delta_{\min,o}=(1-\cos\theta_o)^{0.22},$$

and

$$\Gamma_{\min,o}=0.67\Delta_{\min,o}^{2.83}+0.26\Delta_{\min,o}^{9.51}. \quad (1)$$

This paper extends the work of El-Genk and Saber [6] to evaporating liquid films, flowing down uniformly heated vertical walls (Fig. 1(*a*)), and derives expressions for the MLFT and MWR. These expressions are applicable to when the wall is heated at either the outer or the inner surface. For the former, the present analysis accounts for the axial heat conduction in the wall and quantify the effects of the wall thickness and thermal conductivity on the values of MLFT and MWR. The two-dimensional velocity field in the liquid rivulet, $u(x,y)$, obtained using the Ritz method, is used to solve for the profile of the liquid rivulet, $\phi(x)$, and the effective contact angle, θ_{eff}, at the triple interface line of the rivulet, $x=\pm b$ (Fig. 1(*b*)). The predictions of the MLFT and MWR are compared with the reported data for water films [11,13].

2 Problem Description

Consider a stable, liquid rivulet flowing down a vertical wall (Fig. 1(*a*)), subject to a constant heat flux, either at the wall inner surface ($y=0$), q_{iw}, or at the wall outer surface ($y=-\delta_w$), q_{ow} (Fig. 1(*b*)). The rivulet is formed, following the breakup of an evaporating liquid film. Since the thickness of the rivulet near its triple interface line ($x=\pm b$) is infinitesimally small (Fig. 1(*b*)), the local evaporation flux is significantly greater [14] than at the center plane, $x=0$. The thermocapillary force, which is proportional to the gradient of the liquid surface tension with respect to temperature along the L-V interface, causes a persistent contraction of the rivulet and is highest near the triple interface line. In addition, the departing vapor molecules from the L-V interface develop thrust in the perpendicular direction to the interface (Fig. 1(*b*)). The thermocapillary force and vapor thrust depend not only on the local evaporation flux and the change in T_ϕ along the L-V interface, but also on the liquid rivulet profile, $\phi(x)$, and the velocity field in the rivulet, $u(x,y)$.

The total energy of the evaporating liquid rivulet is the sum of the liquid kinetic energy, the interfacial energies at L-S and L-V interfaces, and those caused by the thermocapillary force and the vapor thrust. The evaluation of the liquid kinetic energy requires knowledge of the velocity field within the liquid rivulet, $u(x,y)$, as well as of the rivulet profile, $\phi(x)$. The interfacial energy at the L-V and L-S interfaces require knowledge of the temperature distributions along the L-V interface, T_ϕ, and along the L-S interface, $T_{iw}(x)$.

3 Heat Transfer in Liquid Rivulet

Owing to the small thickness of the liquid rivulet (<0.5 mm) and to the low thermal conductivity of the liquid, the temperature profile in the liquid rivulet is expressed as

$$T(x,y)=T_{iw}(x)-(T_{iw}(x)-T_{\phi}(x))\,\frac{y}{\phi(x)}, \tag{2}$$

where

$$T_{\phi}(x)=T_v+R_{\rm int}\,q_{iw}(x), \tag{3}$$

and the interfacial resistance, $R_{\rm int}$, is given [15,16] as

$$R_{\rm int}=\frac{1}{a\rho_g h_{fg}^2}[(2\pi\Re T_v^3)/M]^{1/2}. \tag{4}$$

When the wall is heated uniformly at its inner surface, $q_{iw}(x)$ is a known quantity. However, when the wall is heated at its outer surface, $q_{iw}(x)$ is determined from the solution of the two-dimensional, steady-state heat conduction equation in the wall and the heat balance at the L-S interface. The accommodation coefficient, a in Eq. (4) is taken equal to 0.04 [15,16].

4 Heat Conduction in the Wall

The two-dimensional heat conduction equation in the wall (Fig. 1(*b*)):

$$\partial^2T(x_w,y_w)/\partial x_w^2+\partial^2T(x_w,y_w)/\partial y_w^2=0, \tag{5}$$

is solved subject to the following boundary conditions:

$$(a)\,\frac{\partial T(0,y_w)}{\partial x_w}=0,\quad (b)\,\frac{\partial T(b,y_w)}{\partial x_w}=0,$$

$$(c)\,\frac{\partial T(x_w,0)}{\partial y_w}=-q_{ow}/k_w,$$

and

$$(d)\,\frac{\partial T(x_w,\delta_w)}{\partial y_w}=-(h_{eq}(x)/k_w)(T(x_w,\delta_w)-T_v). \tag{6}$$

The wall thermal conductivity is taken constant, since the change in temperature across the wall is only a few degrees, but evaluated at the mean temperature of the wall. The second boundary condition reflects the fact that for a uniformly heated wall, at the liquid film breakup and immediate formation of stable rivulets, the lateral heat flow in the underlying wall is zero, as before the film breaks up. In Eq. (6*d*), the local heat transfer coefficient $h_{eq}(x)$ can be expressed as

$$h_{eq}(x)=\left[\frac{\phi(x)}{k_1}+R_{\rm int}\right]^{-1}. \tag{7}$$

Using the method of separation of variables, the temperature distribution in the wall is

$$T(x_w,y_w)=T_v+\frac{q_{ow}}{h_{eq}}[1+(\overline{h}_{eq}/k_w)(\delta_w-y_w)]+B_0\left(\frac{k_w}{h_{eq}}\right)+\sum_{n=1}^{\infty}\frac{2B_n\cos n\pi(1-x_w/b)\cosh n\pi(y_w/b)}{\frac{\overline{h}_{eq}}{k_w}\cosh n\pi(\delta_w/b)+\frac{n\pi}{b}\sinh n\pi(\delta_w/b)}, \tag{8}$$

where,

$$B_0=\frac{1}{b}\int_0^b f(x_w)dx_w,\quad B_n=\frac{1}{b}\int_0^b f(x_w)\cos\frac{n\pi}{b}x_w dx_w, \tag{9a}$$

$$f(x_w)=(\overline{h}_{eq}/k_w-h_{eq}(x_w)/k_w)(T(x_w,\delta_w)-T_v), \tag{9b}$$

and

$$\overline{h}_{eq}=\frac{1}{b}\int_0^b h_{eq}(x)dx. \tag{9c}$$

The wall temperature along the L-S interface is given by substituting $y_w=\delta_w$ in Eq. (8):

$$T_{iw}(x_w)=T_v+\frac{q_{ow}}{h_{eq}}+B_0\left(\frac{k_w}{h_{eq}}\right)+\sum_{n=1}^{\infty}\frac{2B_n\cos n\pi(1-x_w/b)\cosh n\pi(\delta_w/b)}{\frac{\overline{h}_{eq}}{k_w}\cosh n\pi(\delta_w/b)+\frac{n\pi}{b}\sinh n\pi(\delta_w/b)}. \tag{10a}$$

Similarly, the wall heat flux at the L-S interface, $q_{iw}(x_w)$ is

$$q_{iw}(x_w)=q_{ow}-\sum_{n=1}^{\infty}\frac{2B_n k_w\frac{n\pi}{b}\cos n\pi(1-x_w/b)\sinh n\pi(\delta_w/b)}{\frac{\overline{h}_{eq}}{k_w}\cosh n\pi(\delta_w/b)+\frac{n\pi}{b}\sinh n\pi(\delta_w/b)}. \tag{10b}$$

The residual function $f(x_w)$, (Eq. 9*b*), is determined using an iterative procedure, and used to evaluate the heat flux and temperature at L-S interface and $\overline{h}_{eq}$. When the wall is heated uniformly at its inner surface, the wall temperature at the L-S interface is

$$T_{iw}(x)=T_v+q_{iw}\left(\frac{\phi(x)}{k_l}+R_{\rm int}\right). \tag{11}$$

5 Total Energy of Liquid Rivulet

The total energy of a stable, evaporating liquid rivulet is the sum of the liquid kinetic energy, the interfacial energies at L-S and L-V interfaces, and those due to the thermocapillary force and vapor thrust at L-V interface. The first two have been dealt with elsewhere [6] and will not be repeated here due to space limitation. The infinitesimal thermocapillary energy of the rivulet can be written as

$$de_s=\left(\int_{s=0}^{s}\frac{\partial\sigma_{LV}}{\partial s}ds\right)\sqrt{1+(d\phi(x)/dx)^2}dx, \tag{12}$$

and the energy induced by evaporation at L-V interface can be expressed as

$$de_e=2\left(\int_0^s\rho_g\left(\frac{q_n(x)}{\rho_g h_{fg}}\right)^2\frac{\rho_l-\rho_g}{\rho_l}ds\right)\frac{d\phi(x)/dx}{\sqrt{1+(d\phi(x)/dx)^2}}dx. \tag{13}$$

The total energy of the liquid rivulet can now be written in a dimensionless form as

$$E_{\rm tot}=2\int_{X=0}^{1}\left(\frac{15}{2}\Delta^5\left[\int_{Y=0}^{\Phi(X)}U^2(X,Y)dY\right]+\left[\frac{\sigma_{LV}}{\sigma_R}\sqrt{1+\varepsilon^2\Phi'^2(X)}+\frac{\sigma_{SV}}{\sigma_R}-\frac{\sigma_{LV}}{\sigma_R}\cos\theta_{\rm eff}\right]+F_s(X)\sqrt{1+\varepsilon^2\Phi'^2(X)}+F_e(X)\frac{2\varepsilon\Phi'(X)}{\sqrt{1+\varepsilon^2\Phi'^2(X)}}\right)dX, \tag{14}$$

where

$$F_s(X)=\frac{\Delta}{\mathrm{Pr}_l}\left(\frac{l_s}{\delta^*}\right)\int_{X=0}^{X}\mathrm{Ma}(X)\Phi'(X)dX, \tag{15a}$$

and

$$F_e(X)=\frac{\Delta}{\varepsilon}\left(\frac{l_s}{\delta^*}\right)\left(\frac{\rho_l-\rho_g}{\rho_g}\right)\int_{X=0}^{X}\mathrm{Re}_v^2(X)\sqrt{1+\varepsilon^2\Phi'^2(X)}dX. \tag{15b}$$

For a non-evaporating liquid rivulet, the last two terms in Eq. (14) are zero, and the effective contact angle, $\theta_{\mathrm{eff}}=\theta_o$ [6]. In Eq. (15*a*), Marangoni number, Ma, is defined as:

$$\mathrm{Ma}(X)=(((d\sigma_{LV}/dT)_{LV}(\partial T/\partial y)_{LV})/(\mu_l\alpha_l/\delta^{*2})), \tag{16}$$

which upon substituting for $(\partial T/\partial y)_{LV}$ from Eq. (2) becomes

$$\mathrm{Ma}=(((-d\sigma_{LV}/dT)_{LV}(q_{iw}(x)/k_l))/(\mu_l\alpha_l/\delta^{*2})). \tag{17}$$

The vapor Reynolds number, Re_v, in Eq. (15*b*) is defined as

$$\mathrm{Re}_v=((q_n(x)\delta^*)/h_{fg}\mu_l), \tag{18}$$

where

$$q_n(x)=\frac{\phi'(x)q_{x,LV}}{\sqrt{1+\phi'^2(x)}}+\frac{q_{y,LV}}{\sqrt{1+\phi'^2(x)}}. \tag{19}$$

Substituting $q_{x,LV}=-k_l(\partial T/\partial x)_{LV}$ and $q_{y,LV}=-k_l(\partial T/\partial y)_{LV}$ from Eq. (2) gives

$$q_n(x)=\left(\frac{1}{\sqrt{1+\phi'^2(x)}}\right)\times\left[q_{iw}(x)-\phi'(x)\left(k_l\frac{dT_\phi(x)}{dx}+\phi'(x)q_{iw}(x)\right)\right]. \tag{20}$$

Liquid Flow Rate in Liquid Rivulet

The dimensionless liquid volumetric flow rate in the rivulet is expressed as

$$Q=\int_0^1 Q'dX,\quad \text{where}\quad Q'=2\left(\int_{Y=0}^{\Phi}U(X,Y)dY\right). \tag{21}$$

The velocity distribution in the rivulet, $U(X,Y)$, required to evaluate E_{tot} (Eq. 14) and Q' (Eq. 21), is obtained using the Ritz method as detailed in [6], and summarized below.

6 Velocity Distribution in Liquid Rivulet

The velocity distribution, $u(x,y)$ in the liquid rivulet and the rivulet profile, $\phi(x)$ are determined from solving the continuity and the momentum equations of the liquid in the rivulet:

$$\frac{\partial v}{\partial x}+\frac{\partial w}{\partial y}=0, \tag{22a}$$

$$\rho_l\left(v\frac{\partial v}{\partial x}+w\frac{\partial v}{\partial y}\right)=-\frac{\partial p_l}{\partial x}+\mu_l\frac{\partial^2 v}{\partial y^2}, \tag{22b}$$

$$\rho_l\left(v\frac{\partial w}{\partial x}+w\frac{\partial w}{\partial y}\right)=-\frac{\partial p_l}{\partial y}+\mu_l\frac{\partial^2 w}{\partial y^2}, \tag{22c}$$

and

$$0=\mu_l\left(\frac{\partial^2 u}{\partial x^2}+\frac{\partial^2 u}{\partial y^2}\right)+\rho_l g. \tag{22d}$$

In addition to assuming that the liquid is Newtonian and incompressible, Eqs. (22*a*)–(22*d*) assume that since the aspect ratio of the liquid rivulet, ε, is much smaller than unity, $\partial^2 v/\partial x^2$ and $\partial^2 w/\partial x^2$ are $\ll\partial^2 v/\partial y^2$ and $\partial^2 w/\partial y^2$, respectively, and are neglected. Also, the velocity components v and w in x and y directions, respectively, are small compared to that in z-direction, u. For a non-evaporating liquid rivulet, both $v(x,y)$ and $w(x,y)$ are zero, reducing Eqs. (22*b*) and (22*c*) to $\partial p_l/\partial x=0$ and $\partial p_l/\partial y=0$, respectively [6].

Equation (22*d*) is solved for the dimensionless velocity $U(X,Y)$ using the Ritz method [17] as detailed in [6], which is expressed as

$$U(X,Y)=\sum_{i=1}^{m}c_i\cos\frac{(2i-1)\alpha}{2}X\sin i\alpha Y. \tag{23}$$

For a non-evaporating rivulet, when the damping coefficient, $\alpha=0.05$, only the first three terms ($m=3$) in Eq. (23) were sufficient to accurately describe the velocity field [6]. Equation (22*b*) can be rewritten in an integral form as

$$\frac{d}{dx}\int_{y=0}^{\phi}(v^2-vv_\phi)dy+\frac{dv_\phi}{dx}\int_{y=0}^{\phi}v\,dy=-\frac{1}{\rho_l}\int_{y=0}^{\phi}\frac{\partial p_l}{\partial x}dy+\frac{\mu_l}{\rho_l}\left.\frac{\partial v}{\partial y}\right|_\phi-\frac{\mu_l}{\rho_l}\left.\frac{\partial v}{\partial y}\right|_{y=0}. \tag{24}$$

In this equation, v_ϕ is the liquid velocity in the x-direction at the L-V interface, and $\partial p_l/\partial x$ is given [19,20] as

$$\frac{\partial p_l}{\partial x}=-\sigma_{LV}\frac{dk(x)}{dx}-k(x)\frac{d\sigma_{LV}}{dT_\phi}\frac{dT_\phi}{dx}+\frac{dp_d}{dx}+\frac{d}{dx}\rho_g\frac{\rho_l-\rho_g}{\rho_l}\left(\frac{q_n(x)}{\rho_g h_{fg}}\right)^2. \tag{25}$$

The local curvature of the liquid rivulet profile can be expressed as

$$k(x)=\frac{\phi''(x)}{(1+\phi'^2(x))^{3/2}};\quad \text{or in dimensionless form,}\quad K(X)=\frac{\varepsilon^2\Phi''(X)}{(1+\varepsilon^2\Phi'^2(X))^{3/2}}. \tag{26}$$

The disjoining pressure [20,21] is given as

$$p_d=-A/\phi^3(x). \tag{27}$$

The dispersion or Hamaker constant, A, depends on the wall and the liquid properties. For an evaporating liquid meniscus, Hallinan et al. [22] have used $A=10^{-21}$ J, which has also been indicated by Stephan and Busse [14]. Thus, in this work a value of $A=10^{-21}$ J is used.

The liquid velocity in the x-direction within the rivulet, $v(x,y)$ is represented by a cubic polynomial [23] as

$$v(x,y)=a_1+a_2Y(1-Y)+a_3Y^3,\quad \text{where}\quad Y=y/\phi(x). \tag{28}$$

The coefficients in Eq. (28) are determined from substituting the boundary conditions

$$v(x,y=0)=0,\quad v(x,\phi(x))=v_\phi,$$

and

$$\mu_l\left.\frac{\partial^2 v(x,y)}{\partial y^2}\right|_{y=0}=\frac{\partial p_l}{\partial x}. \tag{29}$$

The pressure gradient, $\partial p_l/\partial x$, is given by Eq. (25) and v_ϕ is determined from the balance of the momentum fluxes the L-V interface:

$$\mu_l\left.\frac{\partial v(x,y)}{\partial y}\right|_{y=\phi(x)}=\frac{d\sigma_{LV}}{dx}=\left(\frac{d\sigma_{LV}}{dT_\phi}\right)\left(\frac{dT_\phi}{dx}\right). \tag{30}$$

Applying this condition to Eq. (28) gives a_1, a_2, a_3, and v_ϕ as

$$a_1=0,\quad a_2=-\frac{\phi^2(x)}{2\mu_l}\left(\frac{\partial p_l}{\partial x}\right),\quad a_3=v_\phi(x),$$

and

$$v_\phi(x) = -\frac{\phi^2(x)}{6\mu_l}\left(\frac{\partial p_l}{\partial x}\right) + \frac{\phi(x)}{3\mu_l}\left(\frac{d\sigma_{LV}}{dT_\phi}\right)\left(\frac{dT_\phi}{dx}\right). \quad (31)$$

Substituting Eq. (31) into Eq. (24) and rewriting results in a dimensionless form gives

$$\Phi(X)\frac{d}{dX}\left\{\Phi(X)\left(\frac{A_2^2}{30} - \frac{3V_\phi^2}{28} - \frac{A_2 V_\phi}{10}\right)\right\} + \Phi^2(X)\frac{dV_\phi}{dX}\left(\frac{A_2}{6} + \frac{V_\phi}{4}\right)$$
$$= -\Phi^2(X)\frac{\partial P_l}{\partial X} + \frac{\Delta^2}{\mathrm{Pr}_l}\mathrm{Ma}(X)\Phi(X)\Phi'(X) - \frac{A_2}{\varepsilon}. \quad (32)$$

In this equation,

$$\frac{\partial P_l}{\partial X} = -\Delta\frac{\delta^*}{l_s}\left(\frac{\sigma_{LV}}{\sigma_R}\right)\frac{dK(X)}{dX} - \frac{\Delta^2}{\mathrm{Pr}_l}K(X)\mathrm{Ma}(X)\Phi'(X)$$
$$+ \frac{dP_d}{dX} + \Delta^2\left(\frac{\rho_l - \rho_g}{\rho_g}\right)\frac{d}{dX}\{\mathrm{Re}_v^2(X)\}, \quad (33)$$

$$\frac{dP_d}{dX} = \frac{d}{dX}\left(-\frac{A\rho_l}{\Delta\delta^*\mu_l^2\Phi^3(X)}\right), \quad (34a)$$

$$A_2(X) = -\frac{\varepsilon}{2}\Phi^2(X)\frac{\partial P_l}{\partial X}, \quad (34b)$$

and

$$V_\phi(X) = -\frac{\varepsilon}{6}\Phi^2(X)\frac{\partial P_l}{\partial X} + \frac{\varepsilon}{3}\frac{\Delta^2}{\mathrm{Pr}_l}\mathrm{Ma}(X)\Phi(X)\Phi'(X). \quad (34c)$$

Rivulet Profile

Equation (32) is solved for the rivulet profile, $\Phi(X)$, subject to the boundary conditions

$$\Phi(X=0)=1, \quad \Phi'(X=0)=0,$$
$$\left.\frac{dK(X)}{dX}\right|_{X=0} = 0, \quad \text{or the curvature is minimum}$$
$$(\text{i.e., } \Phi'''(X=0)=0), \quad (35)$$
$$\Phi(X=1)=0, \quad \text{and} \quad \Phi'(X=1) = -\tan\theta_{\mathrm{eff}}/\varepsilon.$$

The obtained rivulet profile is similar to the one obtained by El-Genk and Saber [6] for a non-evaporating rivulet, except for using θ_{eff} instead of θ_o as follows:

$$\Phi(X) = 1 - \frac{1}{(1-\cos\theta_{\mathrm{eff}})}\left\{1 - \sqrt{1 - \left(\frac{X}{\varepsilon}\right)^2(1-\cos\theta_{\mathrm{eff}})^2}\right\}. \quad (36)$$

In this equation, $\theta_{\mathrm{eff}} = (\theta_o - \theta_e)$, and θ_e accounts for the contribution of liquid evaporation at the L-V interface (Fig. 1(*b*)). Therefore, the effective contact angle of the rivulet equals θ_o when the heat flux applied to the wall is zero (i.e., $\theta_e = 0$), but decreases below θ_o as the heat flux increases. The change in θ_e with the heat flux applied to the wall is discussed later in the results section (Eq. 56*b*).

The aspect ratio of the rivulet, ε, in Eq. (36) is given as follows:

$$\varepsilon = \left(\frac{1 - \cos\theta_o\cos\theta_e - \sin\theta_o\sin\theta_e}{1 + \cos\theta_o\cos\theta_e + \sin\theta_o\sin\theta_e}\right)^{1/2}. \quad (37)$$

This equation is the same as that for a non-evaporating rivulet [6], when substituting $\theta_e = 0$. In an integral form, Eq. (32) is written as

$$\int_{X=0}^{1}\left\{\Phi(X)\Phi'(X)\left(\frac{A_2 V_\phi}{10} - \frac{A_2^2}{30} - \frac{V_\phi^2}{7} - \frac{\Delta^2}{\mathrm{Pr}_l}\mathrm{Ma}(X)\right)\right.$$
$$\left. + \Phi^2(X)\left(\frac{1}{6}A_2\frac{dV_\phi}{dX} + \frac{1}{2}\frac{\partial P_l}{\partial X}\right)\right\}dX = 0. \quad (38)$$

Equations (37) and (38) are two transcendental equations in three unknowns, ε, $\Delta_{\min}$, and θ_e. Therefore, an additional equation is needed, which is obtained from the minimization of the total energy of the liquid rivulet, as discussed below.

7 Minimization of Total Energy

The condition for minimizing the total energy of the rivulet (Eq. 14) is given by the Euler equation [18]:

$$\frac{\partial\Psi}{\partial\Phi} = \frac{d}{dX}\left(\frac{\partial\Psi}{\partial\Phi'}\right), \quad \Phi' = d\Phi(X)/dX. \quad (39)$$

In this equation, Φ and Φ' are obtained from Eq. (36), and Ψ is given as

$$\Psi = E' + \lambda Q'. \quad (40)$$

The term $E' = dE_{\mathrm{tot}}/dX$ is given by Eq. (14), and Q' is obtained from substituting Eq. (23) into Eq. (21) and integrating with respect to Y, which gives:

$$Q' = 2\sum_{i=1}^{3}\frac{c_i}{i\alpha}\cos\frac{(2i-1)\alpha}{2}X[1 - \cos i\alpha\Phi(X)]. \quad (41)$$

In Eq. (40), the Lagrange multiplier, λ, is determined by first integrating Eq. (39) once as follows

$$\Psi - \Phi'\left(\frac{\partial\Psi}{\partial\Phi'}\right) = d, \quad (42)$$

and substituting for Ψ from Eq. (40) into Eq. (42), which gives

$$\frac{15}{2}\Delta^5\left[\sum_{i=1}^{3}\frac{c_i^2}{2}\cos^2\frac{(2i-1)\alpha}{2}X\left[\Phi(X) - \frac{1}{2i\alpha}\sin 2i\alpha\Phi(X)\right]\right.$$
$$+ 2\frac{c_1c_2}{\alpha}\cos\frac{\alpha}{2}X\cos\frac{3\alpha}{2}X\left[\frac{1}{2}\sin\alpha\Phi(X) - \frac{1}{6}\sin 3\alpha\Phi(X)\right]$$
$$+ 2\frac{c_1c_3}{\alpha}\cos\frac{\alpha}{2}X\cos\frac{5\alpha}{2}X\left[\frac{1}{4}\sin 2\alpha\Phi(X) - \frac{1}{8}\sin 4\alpha\Phi(X)\right]$$
$$+ 2\frac{c_2c_3}{\alpha}\cos\frac{3\alpha}{2}X\cos\frac{5\alpha}{2}X\left[\frac{1}{2}\sin\alpha\Phi(X)\right.$$
$$\left.\left. - \frac{1}{10}\sin 5\alpha\Phi(X)\right]\right] + \frac{\sigma_{LV}}{\sigma_R}(1+\varepsilon^2\Phi'^2)^{1/2} + \frac{\sigma_{SV}}{\sigma_R}$$
$$- \frac{\sigma_{LV}}{\sigma_R}\cos\theta_{\mathrm{eff}} + F_s(1+\varepsilon^2\Phi'^2)^{1/2} + F_e\frac{2\varepsilon\Phi'}{(1+\varepsilon^2\Phi'^2)^{1/2}}$$
$$+ \lambda\sum_{i=1}^{3}\frac{c_i}{i\alpha}\cos\frac{(2i-1)\alpha}{2}(1-X)[1 - \cos i\alpha\Phi(X)]$$
$$- \frac{\sigma_{LV}}{\sigma_R}\frac{\varepsilon^2\Phi'^2}{(1+\varepsilon^2\Phi'^2)^{1/2}} - F_s\frac{\varepsilon^2\Phi'^2}{(1+\varepsilon^2\Phi'^2)^{1/2}} - F_e\frac{2\varepsilon\Phi'}{(1+\varepsilon^2\Phi'^2)^{3/2}}$$
$$- \frac{\partial F_s}{\partial\Phi'}\Phi'(1+\varepsilon^2\Phi'^2)^{1/2} - \frac{\partial F_e}{\partial\Phi'}\frac{2\varepsilon\Phi'^2}{(1+\varepsilon^2\Phi'^2)^{1/2}}$$
$$+ \frac{1}{\sigma_R}\left(-\frac{d\sigma_{LV}}{dT}\right)\frac{dT_\phi}{dX}\frac{\Phi'}{\Phi''}(1+\varepsilon^2\Phi'^2)^{1/2} = d. \quad (43)$$

Then, the coefficients d and λ are evaluated by applying the boundary conditions given by Eq. (35) into Eq. (43), which yield

$$d=\frac{\sigma_{SV}}{\sigma_R}+F_s(X=1)\cos\theta_{\text{eff}}-2F_e(X=1)\sin^3\theta_{\text{eff}}+\left(\frac{\partial F_s}{\partial\Phi'}\right)_{X=1}\frac{\tan\theta_{\text{eff}}}{\varepsilon\cos\theta_{\text{eff}}}-2\left(\frac{\partial F_e}{\partial\Phi'}\right)_{X=1}\frac{\tan^2\theta_{\text{eff}}\cos\theta_{\text{eff}}}{\varepsilon},\tag{44a}$$

and

$$\lambda=-\frac{1}{\beta}\left(\frac{\sigma_{LV}(X=0)}{\sigma_R}(1-\cos\theta_{\text{eff}})+\frac{15}{2}\Delta^5\omega-F_s(X=1)\cos\theta_{\text{eff}}+2F_e(X=1)\sin^3\theta_{\text{eff}}-\left(\frac{\partial F_s}{\partial\Phi'}\right)_{X=1}\frac{\tan\theta_{\text{eff}}}{\varepsilon\cos\theta_{\text{eff}}}+2\left(\frac{\partial F_e}{\partial\Phi'}\right)_{X=1}\frac{\tan^2\theta_{\text{eff}}\cos\theta_{\text{eff}}}{\varepsilon}\right).\tag{44b}$$

In these equations,

$$\left(\frac{\partial F_s}{\partial\Phi'}\right)_{X=1}=-\frac{b}{\sigma_R}\left(-\frac{\partial\sigma_{LV}}{\partial T}\right)\left(\frac{q_{iw}(X=1)}{k_l}\right)\frac{\tan\theta_{\text{eff}}}{\Phi''(X=1)},$$

and

$$\left(\frac{\partial F_e}{\partial\Phi'}\right)_{X=1}=\frac{b}{\sigma_R}\left(\frac{\rho_g}{\rho_l}\right)(\rho_l-\rho_g)\times\left(\frac{q_{iw}(X=1)}{\rho_g h_{fg}}\right)^2\left(\frac{(1-\tan^2\theta_{\text{eff}})^2\cos\theta_{\text{eff}}}{\Phi''(X=1)}\right).\tag{44c}$$

The coefficients β and ω in Eq. (44*b*) are given as

$$\beta=\sum_{i=1}^{3}\frac{c_i}{i\alpha}(1-\cos i\alpha).\tag{45a}$$

$$\omega=\sum_{i=1}^{3}c_i^2\left(\frac{1}{2}-\frac{1}{4i\alpha}\sin 2i\alpha\right)+2\frac{c_1c_2}{\alpha}\left(\frac{1}{2}\sin\alpha-\frac{1}{6}\sin 3\alpha\right)+2\frac{c_1c_3}{\alpha}\left(\frac{1}{4}\sin 2\alpha-\frac{1}{8}\sin 4\alpha\right)+2\frac{c_2c_3}{\alpha}\left(\frac{1}{2}\sin\alpha-\frac{1}{10}\sin 5\alpha\right).\tag{45b}$$

Minimum Liquid Film Thickness

The following transcendental equation to be solved for $\Delta_{\min}$ is obtained from substituting Eq. (40) into Eq. (39) and rearranging the results for when $dK(X=0)/dX=0$:

$$a_6(\Delta_{\min}^5a_1+\lambda a_2)=a_5\left(\frac{15}{4}\Delta_{\min}^5a_4+\lambda a_3\right).\tag{46}$$

The coefficients a_1-a_6 are given as

$$a_1=\sum_i^3 c_i^2\left(2i\alpha\sin 2i\alpha+2\varepsilon^2\left(\frac{(2i-1)\alpha}{2}\right)^2\frac{1-\cos 2i\alpha}{1-\cos\theta_{\text{eff}}}\right)+2c_1c_2\left((3\alpha\sin 3\alpha-\alpha\sin\alpha)+10\varepsilon^2\left(\frac{\alpha}{2}\right)^2\frac{\cos\alpha-\cos 3\alpha}{1-\cos\theta_{\text{eff}}}\right)+2c_1c_3\left((4\alpha\sin 4\alpha-2\alpha\sin 2\alpha)+26\varepsilon^2\left(\frac{\alpha}{2}\right)^2\frac{\cos 2\alpha-\cos 4\alpha}{1-\cos\theta_{\text{eff}}}\right)+2c_2c_3\left((5\alpha\sin 5\alpha-\alpha\sin\alpha)+34\varepsilon^2\left(\frac{\alpha}{2}\right)^2\frac{\cos\alpha-\cos 5\alpha}{1-\cos\theta_{\text{eff}}}\right),$$

$$a_2=\sum_i^3 c_i\left(i\alpha\cos i\alpha+\varepsilon^2\left(\frac{(2i-1)\alpha}{2}\right)^2\frac{\sin i\alpha}{1-\cos\theta_{\text{eff}}}\right),$$

$$a_3=\sum_i^3 c_i\sin i\alpha,$$

$$a_4=\sum_i^3 c_i^2(1-\cos 2i\alpha)+2c_1c_2(\cos\alpha-\cos 3\alpha)+2c_1c_3(\cos 2\alpha-\cos 4\alpha)+2c_2c_3(\cos\alpha-\cos 5\alpha),$$

$$a_5=-\frac{5}{\sigma_R}\left(-\frac{\partial\sigma_{LV}}{\partial T}\right)\left(\frac{T''_\phi}{\Phi''}\right)_{X=0}+\frac{4}{\sigma_R}\left(-\frac{\partial\sigma_{LV}}{\partial T}\right)\left(\frac{T''_\phi\Phi'''}{\varepsilon^2\Phi''^4}\right)_{X=0}-\frac{4}{\sigma_R}\left(-\frac{\partial\sigma_{LV}}{\partial T}\right)(T''_\phi\Phi'')_{X=0}-\frac{1}{\sigma_R}\left(-\frac{\partial\sigma_{LV}}{\partial T}\right)\left(\frac{T'''_\phi}{\varepsilon^2\Phi''^3}\right)_{X=0}+5\frac{\Delta_{\min}}{\text{Pr}_l}\left(\frac{l_s}{\delta^*}\right)\text{Ma}(X=0)+2\frac{\Delta_{\min}}{\text{Pr}_l}\left(\frac{l_s}{\delta^*}\right)\left(\frac{\text{Ma}''}{\varepsilon^2\Phi''^2}\right)_{X=0}-4\Delta_{\min}\left(\frac{l_s}{\delta^*}\right)\left(\frac{\rho_l-\rho_g}{\rho_g}\right)\text{Re}_v^2(X=0)+16\frac{\Delta_{\min}}{\varepsilon^2}\left(\frac{l_s}{\delta^*}\right)\left(\frac{\rho_l-\rho_g}{\rho_g}\right)\times\left(\frac{\text{Re}_v\,\text{Re}''_v}{\Phi''^2}\right)_{X=0}-8\frac{\Delta_{\min}}{\varepsilon^2}\left(\frac{l_s}{\delta^*}\right)\left(\frac{\rho_l-\rho_g}{\rho_g}\right)\left(\frac{\text{Re}_v^2\Phi'''}{\Phi''^3}\right)_{X=0},$$

and

$$a_6=\frac{\sigma_{LV}(X=0)}{\sigma_R}+2\frac{\Delta_{\min}}{\varepsilon^2}\left(\frac{l_s}{\delta^*}\right)\left(\frac{\rho_l-\rho_g}{\rho_g}\right)\left(\frac{\text{Re}_v^2}{\Phi''}\right)_{X=0}\tag{47}$$

Equations (36), (37), (38), and (46) are solved for ε, Φ, θ_{eff} and $\Delta_{\min}$ using a multi-dimensional Newton-Raphson method. The MWR ($\Gamma_{\min}$) obtained from substituting $\Delta_{\min}$ into Eq. (21) is given as

$$\Gamma_{\min}=(15)^{3/5}(\Delta_{\min})^3\int_0^1\sum_{i=1}^{3}\frac{c_i}{i\alpha}\cos\frac{(2i-1)\alpha}{2}\times X(1-\cos i\alpha\Phi(X))dX.\tag{48}$$

When the heat flux applied to the wall is zero, $\theta_{\text{eff}}=\theta_o$, $a_5=0$, and $a_6=1$, reducing Eq. (46) to that for a non-evaporating liquid film [6] as

$$\Delta_{\min,o}=\left(a_2(1-\cos\theta_o)\Big/\left(\beta a_1-\frac{15}{2}\omega a_2\right)\right)^{1/5}.\tag{49}$$

This equation is in excellent agreement with Eq. (1), expressing $\Delta_{\min,o}$ solely in terms of the cosine of θ_o [6]. Owing to the complexity of Eqs. (46) and (48), the results were used to develop simpler expressions for $\Delta_{\min}$ and $\Gamma_{\min}$, in terms of Marangoni number, $\overline{\text{Ma}}$, modified vapor Reynolds number, $\overline{G}$, liquid Prandtl number, Pr_l, the characteristic liquid film thickness δ^*, and the characteristic length, l_s. The accuracy of these expressions are confirmed by comparing them in Fig. 4 with the calculated values obtained from solving Eqs. (46) and (48). The results are presented and discussed next.

8 Results and Discussion

In this section, the calculated profiles of and the velocity fields in evaporating liquid rivulets are presented as functions of the heat flux applied to the wall (Figs. 2 and 3). The developed expressions

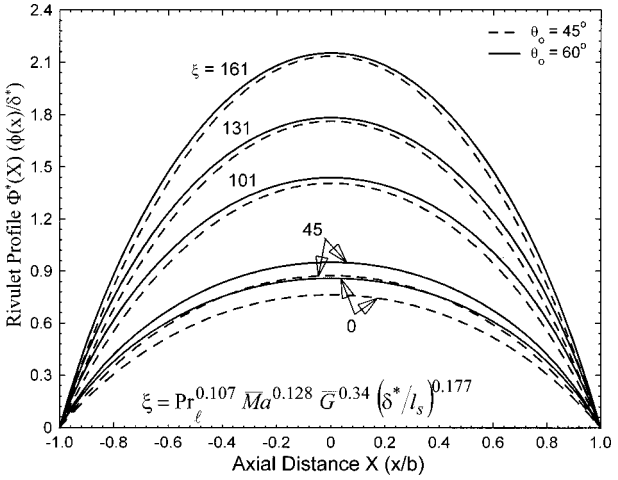

Fig. 2 Effect of the evaporation parameter, ξ on the profile of the liquid rivulet for θ_o=45 deg and 60 deg

for the MLFT and MWR (Eqs. 51*a* and 51*b*, respectively) are verified in Fig. 4 using Eqs. (46) and (48), respectively, for water, methanol, R-113, and ethanol, and compared with the experimental data for water films [11,13]. In addition, the effective contact angle, θ_{eff}, of the rivulet is expressed in terms of θ_o and the appropriate dimensionless quantities (Eq. 56). The results on the effects of θ_o, and the wall thermal conductance on both the MLFT and the MWR are also presented and discussed. Finally, representative values of the thickness of evaporating films of water and pentane at breakup, as functions of the applied heat flux are presented and compared. In addition, the corresponding values of the Marangoni number, Ma, and the modified vapor Reynolds number, $\bar{G}$, are given.

Rivulet Profile

Figure 2 shows the profiles of the liquid rivulet as a function of the evaporation parameter ξ, for θ_o=45 deg and 60 deg. This parameter is defined as

$$\xi = \text{Pr}_l^{0.107}\bar{\text{Ma}}^{0.128}\bar{G}^{0.34}(\delta^*/l_s)^{0.177}. \quad (50)$$

Thus, by definition ξ is proportional to the applied heat flux applied to the wall, raised to the power 0.553 (see nomenclature list for the definitions of $\bar{\text{Ma}}$ and $\bar{G}$). Equation (50) also indicates that the contribution of the evaporation at the L-V interrface, $\bar{G}$, to ξ, and, hence, to $\Delta_{\min}$, and $\Gamma_{\min}$, is highest followed by the liquid physical properties, (δ^*/l_s), the surface tension gradient along the L-V interface, Ma, and finally the liquid Prandtl number Pr_l.

The thickness of the rivulet at its plane of symmetry, $X=0$, is the same as the liquid film thickness at breakup or MLFT [6]. As Fig. 2 indicates, for a given θ_o, increasing ξ raises the profile of the rivulet, including the MLFT. The profiles for ξ=0, are those of non-evaporating rivulets. The results delineated in Fig. 2 also show that increasing θ_o, raises the profile of the rivulet at low ξ, but slightly at high ξ.

Velocity Field in Liquid Rivulet

Figures 3(*a*)–3(*d*) present the contour lines of the velocity field in the rivulet, for different values of the applied heat flux at the inner surface of the wall, $\bar{q}_{iw}$ (or ξ) when θ_o=45 deg. A close examination of these figures reveals that the highest velocity within the rivulet occurs at the plane of symmetry, $X=0$, and close to the L-V interface. Increasing the wall heat flux (or ξ), increases the velocity of the liquid in the rivulet, as a direct result of rising the rivulet profile (Fig. 2) and the decreasing liquid viscosity due to the higher wall temperature at the L-S interface. For example, the highest velocity in the non-evaporating rivulet (ξ=0) in Fig. 3(*a*) is ~0.26 compared to ~0.3375, 1.4, and 2.1 in an evaporating rivulet when ξ=45, 131, and 161, respectively (Figs. 3(*b*)–3(*d*).

Developed Expressions for MLFT and MWR

The obtained expressions for $\Delta_{\min}$ and $\Gamma_{\min}$, are compared with Eqs. (46) and (48), respectively. When a high heat flux is applied uniformly at the inner surface of the wall (or L-S interface), $\bar{q}_{iw}$, such that ξ>125, $\Delta_{\min}$ and $\Gamma_{\min}$ are solely dependent on ξ (Eq. 50)

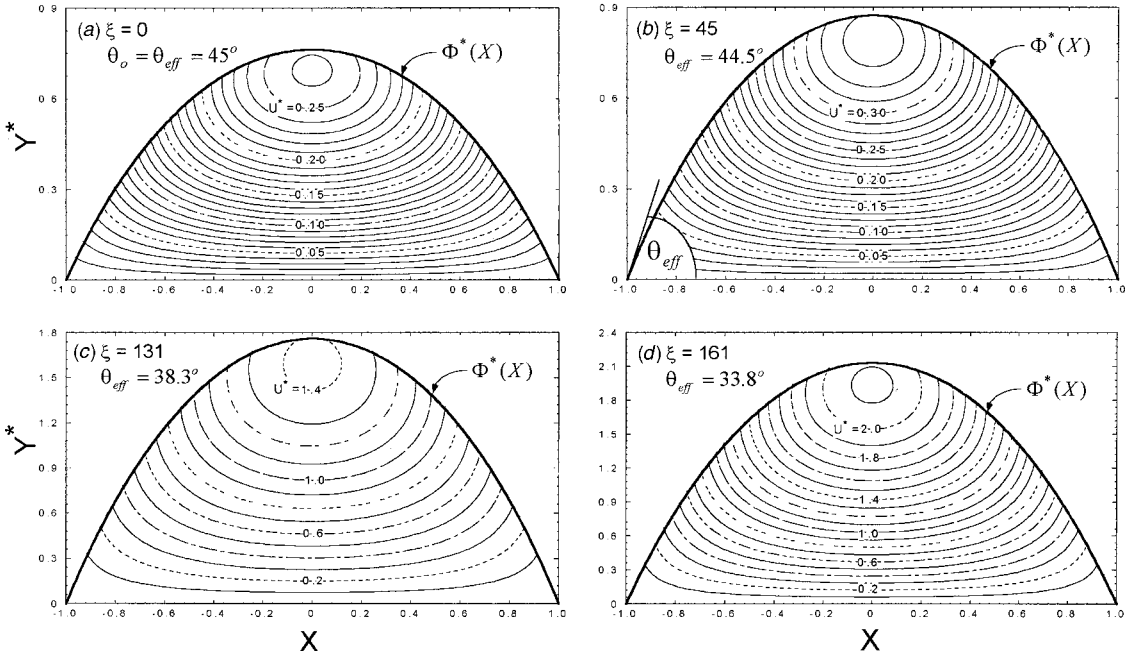

Fig. 3 Comparisons of calculated velocity contours within stable evaporating liquid rivulet for θ_o=45 deg

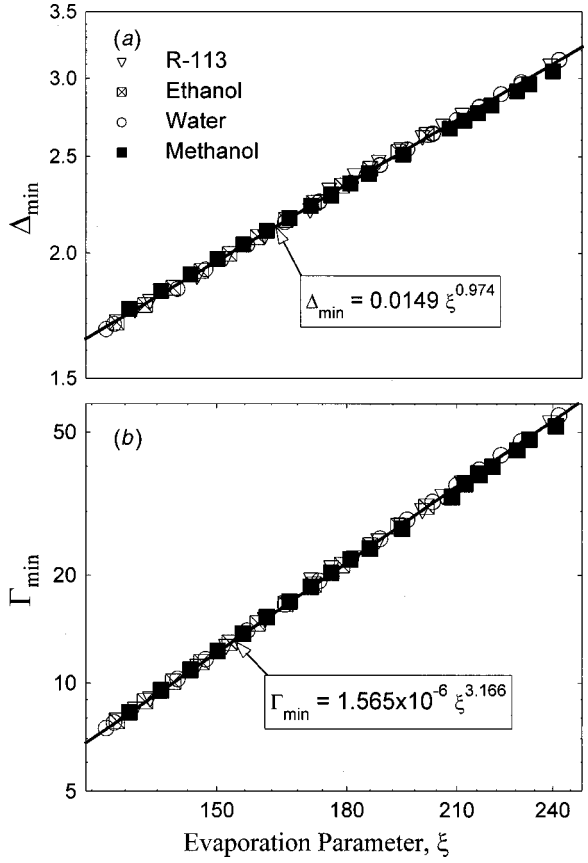

Fig. 4 Developed expressions for MLFT and MWR for different liquids, when the wall is uniformly heated at its inner surface

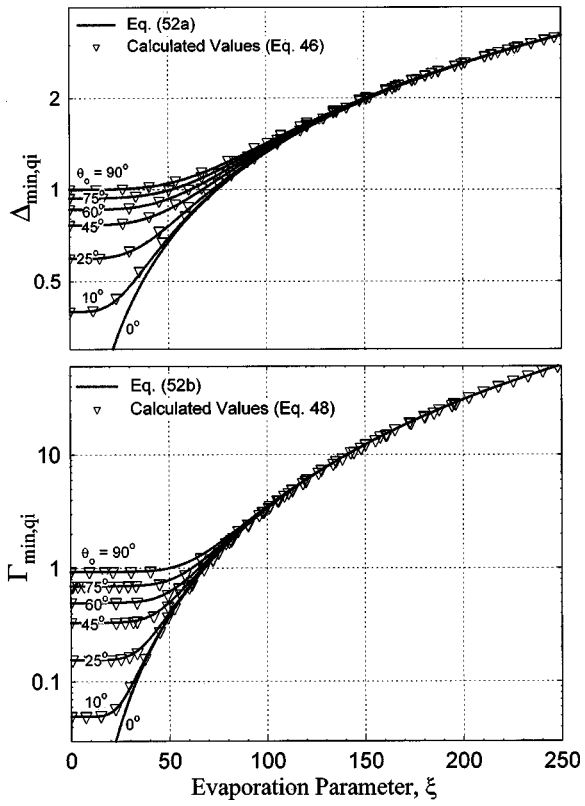

Fig. 5 Comparison of calculated values of the MLFT and MWR with developed expressions for a uniformly heated wall at its inner surface

[Figs. 4(*a*) and 4(*b*)], thus independent of the equilibrium contact angle of the liquid with the underlying wall material, θ_o. The obtained expressions (represented by the solid lines in Figs. 4(*a*) and 4(*b*)) for $\xi > 125$:

$$\Delta_{min} = 0.0149\xi^{0.974}, \tag{51a}$$

and

$$\Gamma_{min} = 1.565\times 10^{-6}\xi^{3.166}, \tag{51b}$$

which are in excellent agreement with Eqs. (46) and (48), respectively. The symbols in Figs. 4(*a*) and 4(*b*) represent the calculated values obtained from solving Eqs. (46) and (48), respectively, for different liquids. When the applied heat flux is zero, however, the liquid film thickness at breakup, $\Delta_{min,o}$, and the corresponding wetting rate, $\Gamma_{min,o}$ [6] have been shown to depend solely on θ_o (Eq. 1). Therefore, in order to capture the smooth increase in the values of MLFT and MWR, and the diminishing effect of θ_o with increasing ξ (or the applied heat flux at the inner surface of the wall) a power law expression is used to fit the calculated values using equations (46) and (48), for $\xi \geqslant 0$ in terms of Δ_{min} and $\Delta_{min,o}$, and in terms of Γ_{min} and $\Gamma_{min,o}$, respectively, as

$$\Delta_{min,qi} = [(\Delta_{min,o})^4 + (\Delta_{min})^4]^{1/4}, \tag{52a}$$

and

$$\Gamma_{min,qi} = [(\Gamma_{min,o})^2 + (\Gamma_{min})^2]^{1/2}. \tag{52b}$$

As shown in Figs. 5(*a*) and 5(*b*), these expressions are in excellent agreements with Eqs. (46) and (48), respectively, for all values of the applied heat flux (or $\xi \geqslant 0$).

Effect of the Wall Thermal Conductance

The results presented in Fig. 6, are for the ratio η versus the wall thermal conductance, (k_w/δ_w). Figure 6 indicates that η, the ratio of the liquid film thickness at breakup when the heat flux is applied at the outer surface of the wall, to that when the same heat flux is applied at the inner surface of the wall, is solely dependent on the wall conductance, and changes insignificantly with the properties of the liquids. The insert in Fig. 6, plots η versus the wall thermal conductivity for different values of the wall thickness (0.5 mm to 10 mm) and for different liquids. The results clearly show that η is independent of the thermal conductance of the wall $> 3\times 10^4$ W/m^{2}K, or of the wall thickness when the thermal conductivity of the wall in excess of 400 W/mK (e.g., copper). Conversely, at lower thermal conductivity of the wall material, η decreases as the wall thickness increases. This dependence, however, gradually diminishes as the wall thermal conductivity increases. Therefore, when the wall is heated on the outside and its thermal conductance is less than 3×10^4 W/m^{2}K (or $k_w < 400$ W/mK), η is less than unity, for the same applied heat flux. For these conditions, the axial heat conduction in the wall reduces the net heat flow at the L-S interface near the middle of the liquid rivulet, $X = 0$, decreasing the evaporation heat flux at L-V interface and resulting in a lower values for the MLFT and the MWR. To account for the effect of thermal conductance of the wall, the values of Δ_{min}, and Γ_{min} when the heat flux is applied at the wall outer surface are obtained from multiplying equations (51*a*) and (51*b*) by η and $\eta^{3.25}$, respectively (Fig. 6) as:

$$\Delta_{min} = \eta(0.0149\xi^{0.974}), \tag{53a}$$

and

$$\Gamma_{min} = \eta^{3.25}(1.565\times 10^{-6}\xi^{3.166}), \tag{53b}$$

where,

$$\eta = [1 - \exp(-0.783(k_w/\delta_w)^{0.182})]^2. \tag{54}$$

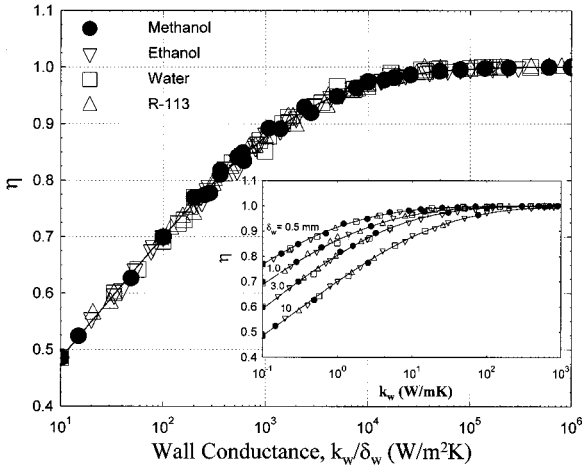

Fig. 6 Effect of the wall thermal conductance and thickness on the MLFT for different liquids

Similar to Eqs. (52*a*) and (52*b*), when the wall is heated uniformly at its outer surface, the MLFT and MWR for $\xi \geqslant 0$, can be calculated using the following power law expressions:

$$\Delta_{\min,qo} = [(\Delta_{\min,o})^4 + (\Delta_{\min})^4]^{1/4}, \tag{55a}$$

and

$$\Gamma_{\min,qo} = [(\Gamma_{\min,o})^2 + (\Gamma_{\min})^2]^{1/2}. \tag{55b}$$

Comparison With Experimental Data

Figures 7(*a*) and 7(*b*) compare the present predictions of the MLFT and MWR at the breakup of the liquid film, with the data

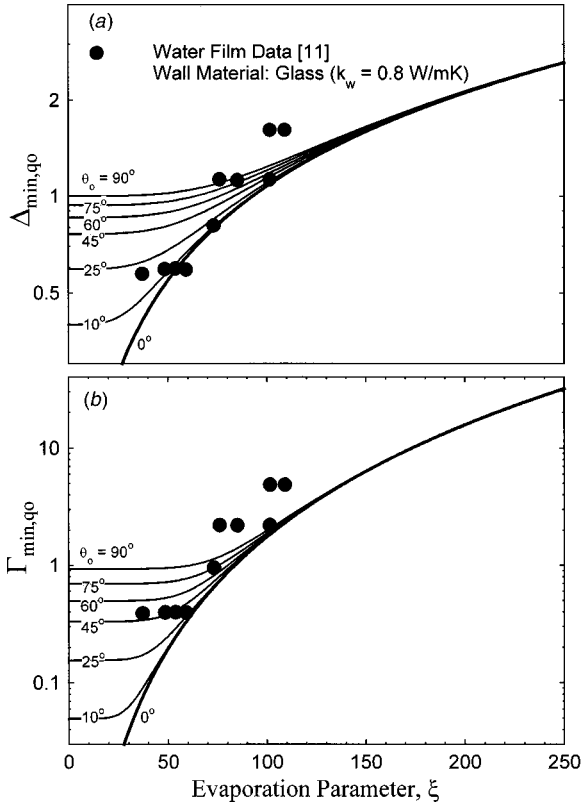

Fig. 7 Comparison of the present predictions of MLFT and MWR with experimental data of Hsu et al. [11]

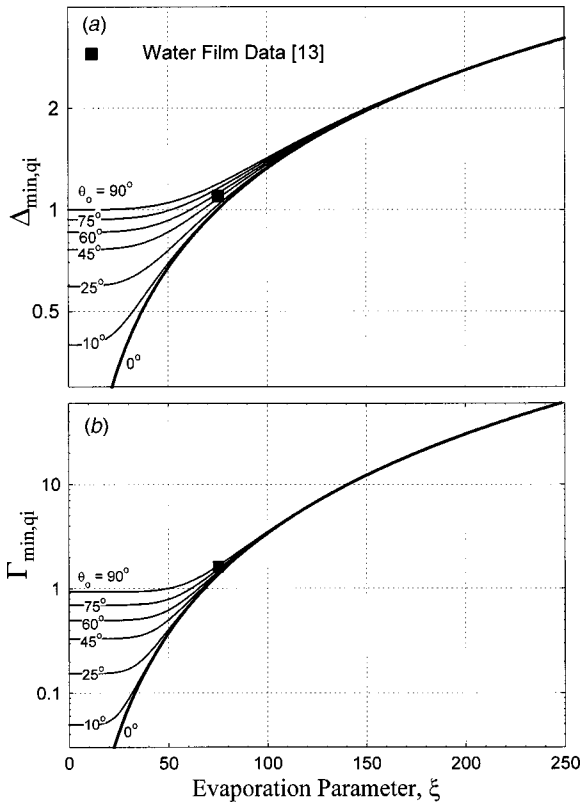

Fig. 8 Comparison of the present predictions of MLFT and MWR with experimental data of Fujita and Ueda [13]

reported by Hsu et al. [11], for a water film falling on the inside of a glass tube that was heated uniformly at its outer surface. Owing to the large scattering in the data, the comparison is nonconclusive. For example, the data indicate the same MLFT and MWR at two and three different values of ξ, or the wall heat flux. Nonetheless, the comparison of the present calculations (Eqs. 55*a* and 55*b*) with the data for $\xi < 100$ are reasonable.

Figures 8(*a*) and 8(*b*) compare the present predictions (or Eqs. 52*a* and 52*b*) with the single data point of Fujita and Ueda [13] for an evaporating water film falling down a stainless steel wall heated on the inside surface. Fujita and Ueda [13] have reported many other data that could not be used in this comparison, because the equilibrium contact angle, θ_o, and the location at which the film breakup occurred, were not reported. The results in these figures and in Figs. 7(*a*) and 7(*b*) show that the effect of the equilibrium contact angle, θ_o, on MLFT and MWR become increasingly more pronounced, the lower is ξ, or the wall heat flux. Conversely, the effect of the equilibrium contact angle gradually decreases as the wall heat flux increases, and diminishes completely when $\xi \geqslant 150$. At zero heat flux, or $\xi = 0$, the values of the MLFT and MWR in Figs. 7 and 8 are the same as those reported by El-Genk and Saber [6] for the breakup of a non-evaporating liquid film (Eq. 1).

Effective Contact Angle

Owing to the large evaporation heat flux at the solid-liquid-vapor triple line of the liquid rivulet, $X = 1$ (Fig. 1(*b*)), the effective contact angle, θ_{eff}, changes with the applied heat flux to the wall. This angle, measured between the tangent to the rivulet profile at $X = 1$ and the L-S interface, is given as the difference between the following two quantities:

$$\theta_{\text{eff}} = \theta_o - \theta_e\,. \tag{56a}$$

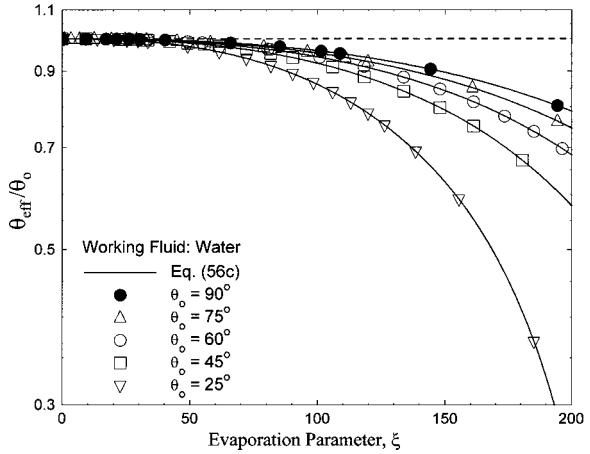

Fig. 9 Effect of the equilibrium contact angle, θ_o and the evaporation parameter, ξ on the effective contact angle, θ_{eff} of the liquid rivulet

The second term on the right hand side (Eq. 56*a*) accounts for the contributions of evaporation at the L-V interface, and is expressed in terms of the modified vapor Reynolds number, $\bar{G}$, the Marangoni number, Ma, and the liquid and vapor properties, as a function of the vapor pressure above the rivulet. The calculations based on the solution of Eq. (46) in conjunction with Eq. (37), and delineated in Fig. 9 show that θ_e can also be expressed solely in terms of the evaporation parameter ξ (Eq. 50) as

$$\theta_e(\text{deg}) = 4.38\times10^{-5}\xi^{2.45}, \tag{56b}$$

and, hence, θ_{eff} can be expressed in terms of θ_o and the evaporation parameter ξ, as

$$\theta_{\text{eff}}(\text{deg}) = \theta_o(\text{deg}) - 4.38\times10^{-5}\xi^{2.45}. \tag{56c}$$

As delineated in Fig. 9, $\theta_{\text{eff}} \simeq \theta_o$ when $\xi \leqslant 20$, but decreases exponentially as ξ increases. For $\xi > 20$, decreasing the equilibrium contact angle decreases θ_{eff} and increase its drop rate with the evaporation heat flux, or ξ. For example, for a typical equilibrium contact angle of water on stainless steel of ~60 deg, θ_{eff} could decrease by ~20 percent to ~48 deg at ξ~165. For same value of ξ and $\theta_o = 25$ deg, θ_{eff} could decrease by as much as 60 percent to 15 deg. Figs. 3(*a*)–3(*d*) show that for $\theta_o = 45$ deg, increasing the evaporation rate, or ξ, decreases the effective contact angle θ_{eff}. At zero heat flux $\theta_{\text{eff}} = \theta_o$ (Fig. 3(*a*), while at ξ=45, 131, and 161, θ_{eff} decreases, respectively, to 44.5 deg, 38.3 deg, and 33.8 deg (Figs. 3(*b*)–3(*d*)).

Results for Water and Pentane

As indicated earlier, the present results for the breakup of an evaporating liquid film, falling down a vertical wall, when the wall is heated uniformly either at its inner or outer surface are formulated in terms of a number of dimensionless groups. These groups, which are all lumped in a single dimensionless parameter, ξ, include the Marangoni number, Ma, the modified vapor Reynolds number, $\bar{G}$, the liquid Prandtl number, Pr_l, and the characteristic liquid film thickness δ^*, and characteristic length, l_s. Therefore, in order to easily quantify the individual contribution to the MLFT of $\bar{G}$ and Ma, which are directly associated with the applied heat flux, results for water and pentane are presented in Figs. 10(*a*) and 10(*b*), for $\theta_o = 45$ deg and $T_v = 333$ K. Table 1 compares the properties of the two liquids, which affect the breakup of the film. These figures indicate that when the heat flux applied uniformly at the inner surface of the wall is 10^5 W/m^2, the film at breakup would be about 0.52 mm for water versus only 0.29 mm for pentane. At this heat flux, ξ, Ma, and $\bar{G}$ for water are

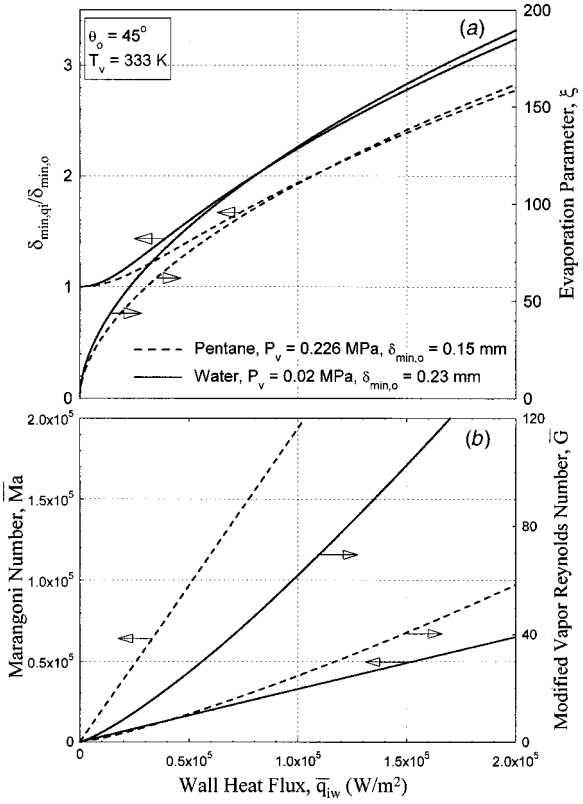

Fig. 10 Comparison of the values of the liquid film thickness at breakup for water and pentane at $T_v = 333$ K and $\theta_o = 45$ deg versus the wall heat flux

Table 1 Comparison of water and pentane properties at $T_v = 333$ K

Liquid	Property				
	$(\delta^*/h_{fg}\mu_l)$	(ρ_l/ρ_v)	$(\delta^{*2}Cp_l/\nu_l k_l^2)$	$(-d\sigma_{LV}/dT)$	(δ^*/l_s)
Water	$2.66\text{x}10^{-7}$	5761	1847	$1.77\text{x}10^{-4}$	84,841
Pentane	$3.377\text{x}10^{-6}$	95	19155	$1.01\text{x}10^{-4}$	47,407

129.4, 3.3×10^4, and 61.4, respectively, while for pentane, they are 110.3, 1.9×10^5 and 24.6, respectively. These results indicate that at $\bar{q}_{iw} = 10^5$ W/m^2, although the MLFT for water is about 79 percent higher than that for pentane, Ma for the latter is more than five times of that for water, while $\bar{G}$ is only 40 percent of that for water. The high values of $\bar{G}$ for water in comparison with pentane at the same wall heat flux, are caused by the higher values of the product of $(\delta^* h_{fg}\mu_l)$ and (ρ_l/ρ_v) (Table 1). Conversely, the high values of Ma for pentane are because of the values of the product of $(-d\sigma/dT)$ and $(\delta^{*2}Cp_l/\nu_l k_l^2)$ are higher than those for water (Table 1). At the wall heat flux of 10^5 W/m^2, the evaporation parameter, ξ, for water is only 17 percent higher than for pentane because (δ^*/l_s) for water is much greater than for pentane (Table 1). The results in Figs. 10(*a*) and 10(*b*) also show that while the liquid film thickness for both water and pentane increased almost at the same rate with the wall heat flux, Ma increased much faster than $\bar{G}$ as the wall heat flux increased.

9 Summary and Conclusions

The minimum total energy criterion (MTE) is used to obtain expressions for the MLFT and the corresponding MWR at the breakup of an evaporating liquid film, falling down a vertical,

uniformly heated wall. In addition to minimizing the total energy of a stable rivulet, forming following the liquid film breakup, the obtained rivulet profile and the two-dimensional velocity field within the rivulet are used in formulating the total energy of the rivulet. The thickness of the liquid rivulet at its plane of symmetry is the same as that of the liquid film at breakup [6]. Results indicated that at high wall heat flux, MLFT and MWR are independent of the equilibrium contact angle of the liquid with the underlying wall, θ_o, and depends solely on the dimensionless evaporation parameter expressed in terms of Ma, G, and the liquid and vapor properties (Eq. 50). Conversely, at a low wall heat flux, the MLFT and MWR depend on both the evaporation parameter and the equilibrium contact angle. They decrease gradually with decreasing the heat flux, approaching the values for non-evaporating liquid film at zero heat flux.

Results also showed that MLFT and MWR, when the heat flux is applied at the inner surface of the wall, are the same as when the heat flux is applied at the outer surface of the wall, but only when the wall conductance $>3\times10^4$ W/m^{2}K (or the wall thermal conductivity >400 W/m K). For these conditions, the MLFT and MWR are independent of the wall thickness. However, at a lower wall thermal conductance (or low wall thermal conductivity) the values of MLFT and MWR, when the heat flux is applied at the wall inner surface are higher than when the wall is heated at its outer surface, at same heat flux. The difference between these values increases as the wall thermal conductivity decreases and/or the wall thickness increases.

The effective contact angle of the rivulet, θ_{eff}, also changes as a function of the evaporation parameter, the equilibrium contact angle, and the conductance of the wall, when heated at its outer surface. As the wall heat flux increases, θ_{eff} decreases and both MLFT and MWR increase. At a zero wall heat flux, $\theta_{\text{eff}}=\theta_o$. The present expressions for the MLFT and MWR are in reasonable agreement with the limited data found in the literature for the breakup of evaporating water films, falling down vertical, uniformly heated wall at either the inner or the outer surface.

Acknowledgment

This research is funded by the University of New Mexico's Institute for Space and Nuclear Power Studies.

Nomenclature

a = accommodation coefficient (Eq. 4)
a_1-a_6 = coefficient (Eq. 47)
b = rivulet half-width [m]
c = Ritz coefficient (Eq. 23)
d = coefficient (Eq. 44a)
e = energy [J m^{-1}]
E = dimensionless energy ($e/(\sigma_{LV}b)$)
g = acceleration of gravity [m s^{-2}]
G = Modified vapor Reynolds number $(\overline{q}_{iw}\delta^*/h_{fg}\mu_l)^{1.25}(\rho_l/\rho_v)$ (Eq. 50)
h = heat transfer coefficient [W m^{-2} K]
h_{fg} = latent heat of vaporization [J kg^{-1}]
k = thermal conductivity [W m^{-1} K^{-1}], curvature (Eq. 26) [m^{-1}]
K = dimensionless curvature of rivulet profile (Eq. 26)
l_s = characteristic length ($\mu_l^2/(\rho_l\sigma_R)$) [m]
M = molecular weight [kg mole^{-1}]
Ma = Marangoni number, (Eq. 17)
Ma = Marangoni number (Eq. 50) $(-(d\sigma_{LV}/dT)(\overline{q}_{iw}/k_l)(\delta^{*2}Cp_l/(\nu_l k_l)))$
p = pressure [N m^{-2}]
P = dimensionless pressure ($p_l/(\mu_l^2/(\delta_{\min}^2\rho_l))$)
Pr$_l$ = Prandtl number ($\mu_l Cp_l/k_l$)
q = heat flux [W m^{-2}], flow rate [m^3 s^{-1}]
$\overline{q}$ = uniform heat flux [W m^{-2}]
q_n = heat flux normal to L-V interface [W m^{-2}] (Eq. 19)
Q = dimensionless flow rate ($q\mu_l/(\rho_l g b\delta_{\min}^3)$)
Re$_v$ = vapor Reynolds number (Eq. 18)
s = length along rivulet profile [m]
T = temperature [K]
u = liquid velocity in z-direction [m s^{-1}]
U = dimensionless velocity ($u\mu_l/(g\rho_l\delta_{\min}^2)$)
U^* = dimensionless velocity ($u\mu_l/(g\rho_l\delta^{*2})$)
v = liquid velocity in x-direction [m s^{-1}]
V = dimensionless velocity ($v/(\mu_l/(\delta_{\min}\rho_l))$)
w = liquid velocity in y-direction [m s^{-1}]
W = dimensionless velocity ($w/(\mu_l/(\delta_{\min}\rho_l))$)
x = coordinate along wall surface [m]
X = dimensionless distance (x/b)
y = coordinate normal to surface [m]
Y, Y^* = dimensionless height ($y/\delta_{\min}$), (y/δ^*)
z = coordinate in direction of liquid flow [m]

Greek Symbols

α = thermal diffusivity [m^2 s^{-1}], damping coefficient (Eq. 23)
β = coefficient (Eq. 45a)
δ = liquid film thickness, thickness, rivulet profile $\phi(x)$ [m]
δ^* = characteristic film thickness $(15\mu_l^2\sigma_R/(\rho_l^3 g^2))^{0.2}$ [m]
Δ = dimensionless liquid film thickness (δ/δ^*)
ε = aspect ratio ($\delta_{\min}/b$) (Eq. 37)
η = correction factor for effect of the wall conductance (Eq. 54)
Ψ = dimensionless parameter (Eq. 39)
γ = wetting rate per unit perimeter $(\rho_l q/2b)$ [kg m^{-1} s^{-1}]
γ^* = characteristic wetting rate per unit perimeter $(\rho_l\mu_l\sigma_{LV}^3/g)^{1/5}$
Γ = dimensionless wetting rate (γ/γ^*)
λ = Lagrange multiplier (Eq. 44b)
ϕ = rivulet profile [m]
Φ = dimensionless profile ($\phi(x)/\delta_{\min}$) (Eq. 36)
Φ^* = dimensionless profile ($\phi(x)/\delta^*$)
θ = contact angle [deg]
ω = coefficient (Eq. 45b)
$\Re$ = universal gas constant (8314.3 J kg-mole^{-1}K^{-1})
ρ = density [kg m^{-3}]
μ = dynamic viscosity [N s m^{-2}]
ν = kinematic viscosity [m^2 s^{-1}]
σ = surface tension [N m^{-1}]
ξ = evaporation parameter (Eq. 50)

Subscripts

e = evaporation
eff = effective
i,iw = wall inner surface
k = kinetic energy
l = liquid
min = minimum, or at rivulet plane of symmetry
n = normal to L-V interface
o = equilibrium
ow = wall outer surface
R = reference
qi = isoflux inner wall for entire range of ξ
qo = isoflux outer wall for entire range of ξ
sat = saturation
tot = total
v,g = vapor
w = wall
ϕ,LV = at liquid-vapor interface

Abbreviations

FB = force balance
L-S = liquid-solid interface
L-V = liquid-vapor interface
MLFT = minimum film thickness
MTE = minimum total energy
MWR = minimum wetting rate

References

[1] Ponter, A. B., Davies, G. A., Ross, T. K., and Thornley, P. G., 1967, ''The Influence of Mass Transfer on Liquid Film Breakdown,'' Int. J. Heat Mass Transf., **10**, pp. 349–359.

[2] Munakata, T., Watanabe, K., and Miyashita, K., 1975, ''Minimum Wetting Rate on Wetted-Wall Column,'' J. Chem. Eng. Jpn., **8**, No. 6, pp. 440–444.

[3] Andros, F. E., 1980, ''Heat Transfer Characteristics of the Two-Phase Closed Thermosyphon (Wickless Heat Pipe) Including Direct Flow Observation,'' Ph.D. dissertation, Arizona State University, Tempe, AZ.

[4] Roesler, S., and Groll, M., 1992, ''Flow Visualization and Analytical Modeling of Interaction Phenomena in Closed Two-Phase Flow Systems,'' *Proc. 8th Int. Heat Pipe Conf.*, Beijing, China, Institute of Engineering Thermophysics, Chinese Academy of Sciences, pp. 26–32.

[5] Hartely, D. E., and Murgatroyd, W., 1964, ''Criteria for the Break-up of Thin Liquid Layers Flowing Isothermally over Solid Surface,'' Int. J. Heat Mass Transf., **7**, pp. 1003–1015.

[6] El-Genk, M. S., and Saber, H. H., 2001, ''Minimum Thickness of a Flowing Down Liquid Film on a Vertical Surface,'' Int. J. Heat Mass Transf., **44**, pp. 2809–2825.

[7] Hobler, T., 1964, ''Minimum Surface Wetting,'' *Chemia Stosow.*, **2B**, pp. 145–159.

[8] Bankoff, S. G., 1971, ''Minimum Thickness of a Draining Liquid Film,'' Int. J. Heat Mass Transf., **14**, pp. 2143–2146.

[9] Mikielewicz, J., and Moszynski, J. R., 1976, ''Minimum Thickness of a Liquid Film Flowing Vertically Down a Solid Surface,'' Int. J. Heat Mass Transf., **19**, pp. 771–776.

[10] Doniec, A., 1991, ''Laminar Flow of a Liquid Rivulet Down a Vertical Solid Surface,'' Can. J. Chem. Eng., **69**, pp. 198–202.

[11] Hsu, Y. Y., Simon, F. F., and Lad, J. F., 1965, ''Destruction of a Thin Liquid Film Flowing Over a Heating Surface,'' Chem. Eng. Prog., Symp. Ser., **57**, No. 61, pp. 139–152.

[12] Zuber, N., and Staub, F. W., 1966, ''Stability of Dry Patches Forming in Liquid Films Flowing Over Heated Surfaces,'' Int. J. Heat Mass Transf., **9**, pp. 897–905.

[13] Fujita, T., and Ueda, T., 1978, ''Heat Transfer to Falling Liquid Films and Film Breakdown—I, Subcooled Liquid Films,'' Int. J. Heat Mass Transf., **21**, pp. 97–108.

[14] Stephan, P. C., and Busse, C. A., 1992, ''Analysis of the Heat Transfer Coefficient of Grooved Heat Pipe Evaporator Walls,'' Int. J. Heat Mass Transf., **35**, No. 2, pp. 383–391.

[15] Guo, Z. X., and El-Genk, M. S., 1994, ''Liquid Microlayer Evaporation During Nucleate on the Surface of a Flat Composite Wall,'' Int. J. Heat Mass Transf., **37**, No. 11, pp. 1641–1655.

[16] Hsu, Y. Y., and Graham, R. W., 1976, *Transport Processes in Boiling and Two-Phase Systems*, McGraw-Hill, New York.

[17] Reddy, J. N., 1984, *An Introduction to the Finite Element Method*, McGraw-Hill, New York.

[18] Forry, M. J., 1968, *Variational Calculus in Science and Engineering*, McGraw-Hill, New York.

[19] Mirzamoghadam, A., and Catton, I., 1988, ''A Physical Model of the Evaporating Meniscus,'' ASME J. Heat Transfer, **110**, pp. 201–207.

[20] Khrustalev, D., and Faghri, A., 1995, ''Heat Transfer During Evaporation on Capillary—Grooved Structures of Heat Pipes,'' ASME J. Heat Transfer, **117**, pp. 740–747.

[21] Kim, I. Y., and Wayner, P. C., 1996, ''Shape of an Evaporating Completely Wetting Extended Meniscus,'' J. Thermophys. Heat Transfer, **10**, No. 2, pp. 320–325.

[22] Hallinan, K. P., Chebaro, H. C., Kim, S. J., and Chang, W. S., 1994, ''Evaporation from an Extended Meniscus for Nonisothermal Interfacial Conditions,'' J. Thermophys. Heat Transfer, **8**, No. 4, pp. 709–716.

[23] Adams, J. A., and Rogers, D. F., 1973, *Computer—Aided Heat Transfer Analysis*, McGraw-Hill, New York.

Numerical Simulation of Bubble Merger Process on a Single Nucleation Site During Pool Nucleate Boiling

G. Son
Department of Mechanical Engineering,
Sogang University,
Seoul, 121-742, Korea

N. Ramanujapu

V. K. Dhir

Mechanical and Aerospace
Engineering Department,
University of California, Los Angeles,
Los Angeles, CA 90095

A bubble merger process on a single nucleation site has been investigated by numerically solving the equations governing conservation of mass, momentum and energy in the vapor and liquid phases. The vapor-liquid interface is captured by a level set method which can easily handle breaking and merging of the interface. The level set method is modified to include the effects of phase change at the interface and contact angle at the wall. Also, the evaporative heat flux from the thin liquid film that forms underneath a growing bubble attached to the wall is incorporated in the analysis. Based on the numerical simulations, the effect of bubble merger on vapor removal rate, flow field and heat transfer has been quantified. The bubble merger pattern predicted numerically has been found to compare well with the experimental observations. [DOI: 10.1115/1.1420713]

Keywords: Boiling, Bubble Growth, Heat Transfer, Two-Phase

Introduction

Despite extensive studies of nucleate boiling, a fundamental understanding of dynamics including the growth, departure and merger of vapor bubbles observed during nucleate boiling is lacking in the literature. In most of the previous studies, the modeling of bubble dynamics has been overly simplified and the flow and temperature fields influenced by the bubble motion have not been analyzed correctly.

Recently, several efforts have been made to numerically simulate bubble growth and departure associated with partial nucleate boiling. Lee and Nydahl [1] computed the bubble growth on a horizontal surface using a numerical mapping method. Although Lee and Nydahl solved numerically the momentum and energy equations, they had to assume that the bubble remained hemispherical in shape during its growth. Obtaining the bubble shape as part of the solution, Welch [2] carried out more generalized computations of vapor bubble growth. However, his method was not extended for configurations with large interfacial distortion or change in topology such as observed during bubble departure. Son et al. [3] simulated a growing and departing bubble on a horizontal surface by incorporating the effect of phase change in the level set formulation. The level set method was earlier developed by Sussman et al. [4] for solving incompressible two-phase flows with large density ratios. In this method, the interface is implicitly captured by the level set function defined as a signed distance from the interface. Thus, this method can handle the bubble departure process. Son et al. [3] included the effect of microlayer evaporation in the analysis as well.

Only a few studies have been reported in the literature for bubble merger, which is one of the fundamental phenomenon related to the transition from partial to fully developed nucleate boiling. Gaertner [5] observed from a photographic study of fully developed nucleate boiling that merger of bubbles in the vertical direction led to formation of vapor columns whereas merger of bubbles in the horizontal direction led to development of mushroom type bubbles. The mushroom type bubbles were supported by vapor stems connecting the vapor mass to the heater surface. Lay and Dhir [6] used the concept of vapor stems in predicting fully developed nucleate boiling heat flux. However, the physical processes leading to formation of vapor columns and mushroom type bubbles and their departure is not yet understood well. The objectives of this study are to perform a complete simulation of bubble merger and to quantify the effect of bubble merger on the flow and temperature fields adjacent to the heater surface. In this work, we focus only on the bubble merger in the vertical direction on a single nucleation site.

Contributed by the Heat Transfer Division for publication in the JOURNAL OF HEAT TRANSFER. Manuscript received by the Heat Transfer Division February 15, 2001; revision received August 16, 2001. Associate Editor: M. K. Jensen.

Numerical Formulation

In analyzing the bubble growth and merger on a single nucleation site, the computational domain, following the work of Son et al. [3], is divided into micro and macro regions as shown in Fig. 1. The macro region consists of the bubble and the liquid surrounding the bubble whereas the micro region contains the liquid film that forms underneath the bubble. The liquid film thickness varies from the mesh size to the order of molecular size. As such, the computational domain is divided into the macro and micro regions and the microlayer analysis is incorporated into numerical simulation for the macro region. In carrying out the analysis the process is assumed to be axisymmetric and flows are taken to be laminar. The fluid properties including density, viscosity and thermal conductivity are assumed to be constant in each phase.

Lubrication theory for the microlayer has been used and validated by a number of investigators in the literature [6,7]. The equation of mass conservation in the microlayer is written as

$$\frac{\partial \delta}{\partial t} = v_l - q/\rho_l h_{fg}. \tag{1}$$

In Eq. (1), the liquid velocity normal to the vapor-liquid interface, v_l, is obtained from the continuity equation as

$$v_l = -\frac{1}{r}\frac{\partial}{\partial r}\int_o^\delta r u_l dy. \tag{2}$$

The momentum equation for the microlayer is written as

$$\frac{\partial p_l}{\partial r} = \mu_l \frac{\partial^2 u_l}{\partial y^2}. \tag{3}$$

The energy conservation equation for the film yields

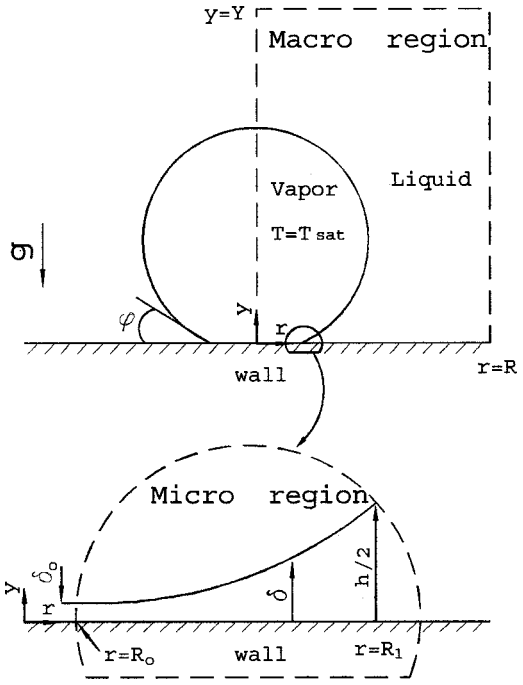

Fig. 1 Macro and micro regions used in numerical simulation

$$q = k_l(T_w - T_{\text{int}})/\delta. \tag{4}$$

Using modified Clausis Clayperon equation [7], the evaporative heat flux is written as

$$q = h_{ev}[T_{\text{int}} - T_v + (p_l - p_v)T_v/\rho_l h_{fg}], \tag{5}$$

where

$$h_{ev} = (2/\pi R_v T_v)^{0.5}\rho_v h_{fg}^2/T_v; \quad T_v = T_{\text{sat}}(p_v). \tag{6}$$

The pressures in the vapor and liquid phases are related [6] as

$$p_l = p_v - \sigma\kappa - \frac{A}{\delta^3} + \frac{q^2}{\rho_v h_{fg}^2}, \tag{7}$$

where σ was taken to be a function of temperature, and A is the dispersion constant relating disjoining pressure to the film thickness. In Eq. (7), the second term on the right hand side accounts for the capillary pressure, the third term for the disjoining pressure and the last term originates from the recoil pressure. The curvature of the interface is defined as

$$\kappa = \frac{1}{r}\frac{\partial}{\partial r}\left[r\frac{\partial\delta}{\partial r} \Big/ \sqrt{1+\left(\frac{\partial\delta}{\partial r}\right)^2}\right]. \tag{8}$$

The combination of the mass, momentum, and energy equations for the microlayer yields

$$\delta''' = f(\delta, \delta' \delta'' \delta'''), \tag{9}$$

where $'$ denotes $\partial/\partial r$.

The boundary conditions for the above equation are as follows:

At $r=R_o$,

$$\delta = \delta_o; \quad \delta' = \delta''' = 0, \tag{10}$$

where δ_o is of the order of molecular size [6]. We used $\delta_o = 6 \times 10^{-10}$ m.

At $r=R_1$,

$$\delta = h/2; \quad \delta' = \tan\varphi; \quad \delta'' = 0, \tag{11}$$

where $h/2$ is the distance to the first computational node for the level set function, ϕ, from the wall and φ is an apparent contact angle that is measurable experimentally. In implementing the above boundary conditions the radius R_1 was determined from the solution of macro region. For a given contact angle, the microlayer formulation, Eq. (9), is integrated using six boundary conditions, Eqs. (10) and (11), under the condition that the dispersion constant and R_o are unknown.

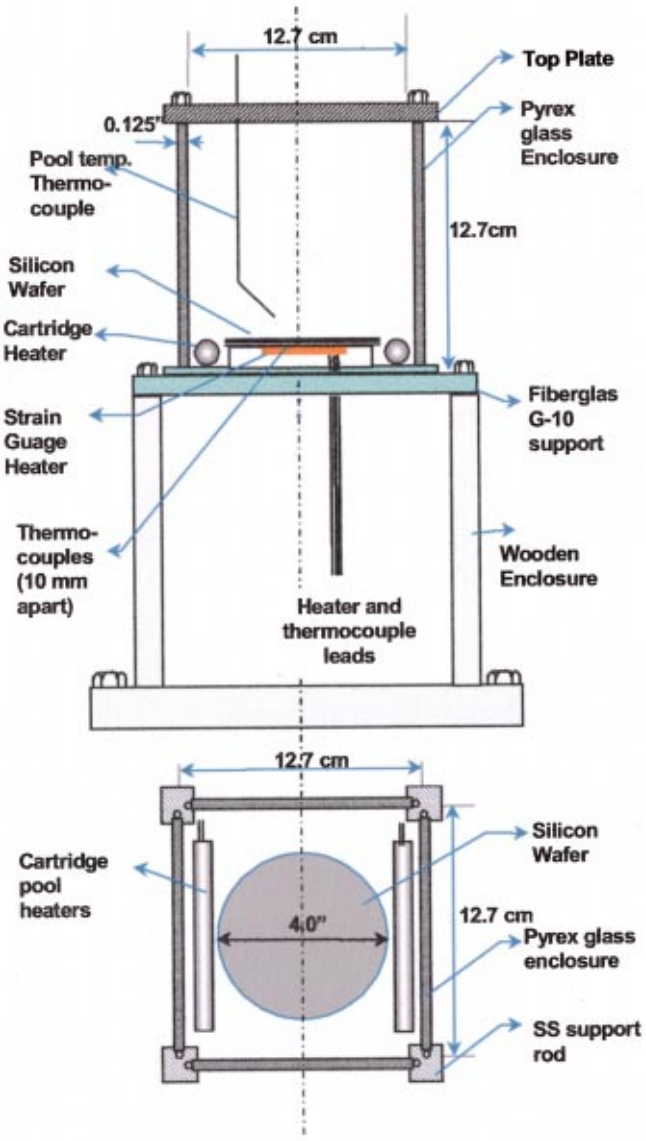

Fig. 2 Schematic of the experimental apparatus

For numerically analyzing the macro region, the level set formulation modified by Son et al. [3] to accommodate the effect of phase change is used. The interface separating the two phases is captured by ϕ which is defined as a signed distance from the interface. The negative sign is chosen for the vapor phase and the positive sign for the liquid phase. The equations governing conservation of momentum, energy and mass for the vapor-liquid region are written as

$$\rho\left(\frac{\partial\mathbf{u}}{\partial t} + \mathbf{u}\cdot\nabla\mathbf{u}\right) = -\nabla p + \rho\mathbf{g} - \rho\beta_T(T - T_{\text{sat}})\mathbf{g} - \sigma\kappa\nabla H + \nabla\cdot\mu\nabla\mathbf{u} + \nabla\cdot\mu\nabla\mathbf{u}^T \tag{12}$$

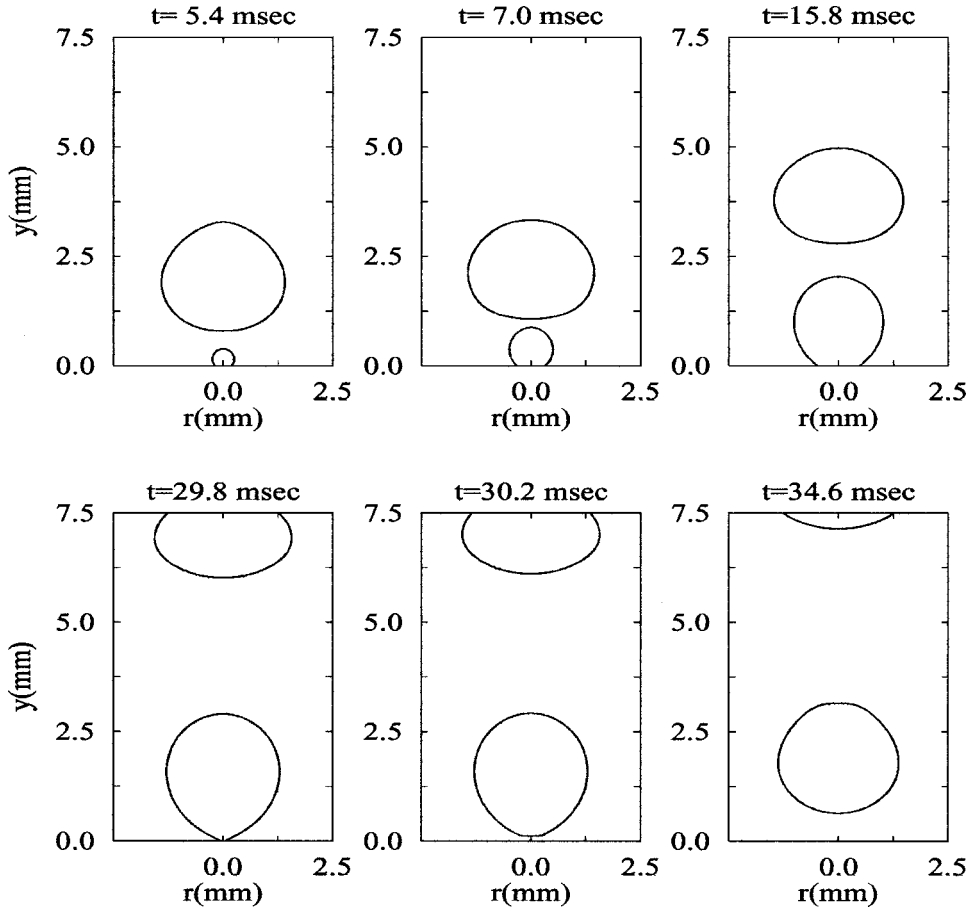

Fig. 3 Bubble growth pattern for $\Delta T=10$ K and $\tau_w=4.8$ msec

$$\rho c_{pl}\left(\frac{\partial T}{\partial t}+\mathbf{u}\cdot\nabla T\right)=\nabla\cdot k\nabla T \quad \text{for } H>0$$
$$T=T_{\text{sat}}(p_v) \quad \text{for } H=0 \tag{13}$$

$$\nabla\cdot\mathbf{u}=\frac{\mathbf{m}}{\rho^2}\cdot\nabla\rho+\dot{V}_{\text{micro}}, \tag{14}$$

where

$$\rho=\rho_v+(\rho_l-\rho_v)H$$
$$\mu^{-1}=\mu_v^{-1}+(\mu_l^{-1}-\mu_v^{-1})H$$
$$k^{-1}=k_l^{-1}H$$
$$H=1 \quad \text{if } \phi\geqslant+1.5h$$
$$=0 \quad \text{if } \phi\leqslant-1.5h$$
$$=0.5+\phi/(3h)+\sin[2\pi\phi/(3h)]/(2\pi) \quad \text{if } |\phi|\leqslant 1.5h,$$

where h is a grid spacing. The volume source term included in Eq. (14) due to liquid-vapor phase change is derived from the conditions of the mass continuity and energy balance at the interface:

$$\mathbf{m}=\rho(\mathbf{u}_{\text{int}}-\mathbf{u})=k\nabla T/h_{fg}. \tag{15}$$

In Eq. (14), $\dot{V}_{\text{micro}}$ is obtained from the microlayer solution as

$$\dot{V}_{\text{micro}}=\int_{R_o}^{R_1}\frac{k_l(T_w-T_{\text{int}})}{\rho_v h_{fg}\delta\Delta V_{\text{micro}}}rdr, \tag{16}$$

where ΔV_{micro} is a vapor-side control volume near the micro region. In the level set formulation, the level set function, ϕ, is advanced and reinitialized as

$$\frac{\partial\phi}{\partial t}=-\mathbf{u}_{\text{int}}\cdot\nabla\phi \tag{17}$$

$$\frac{\partial\phi}{\partial t}=\frac{\phi_o}{\sqrt{\phi_o^2+h^2}}(1-|\nabla\phi|), \tag{18}$$

where ϕ_o is a solution of Eq. (17).

The boundary conditions for the governing equations for the macro region are as follows:

At the Wall ($y=0$)

$$u=v=0, \quad T=T_w, \quad \frac{\partial\phi}{\partial y}=-\cos\varphi \tag{19}$$

At the Planes of Symmetry ($r=0, R$)

$$u=\frac{\partial v}{\partial r}=\frac{\partial T}{\partial r}=\frac{\partial\phi}{\partial r}=0 \tag{20}$$

At the Top of Computational Domain (Free Surface, $y=Y$)

$$\frac{\partial u}{\partial y}=\frac{\partial v}{\partial y}=\frac{\partial\phi}{\partial y}=0, \quad T=T_{\text{sat}} \tag{21}$$

The convergence test for grid resolutions using mesh sizes of 52 μm, 26 μm, and 13 μm was made in the earlier study of a growing and departing bubble on a horizontal surface [3]. As the mesh points increase, the relative difference of the bubble growth rates between successive mesh sizes becomes small. For 26 μm and 13 μm mesh sizes, the difference of the bubble growth periods is less than two percent. Also, the bubble shapes at departure

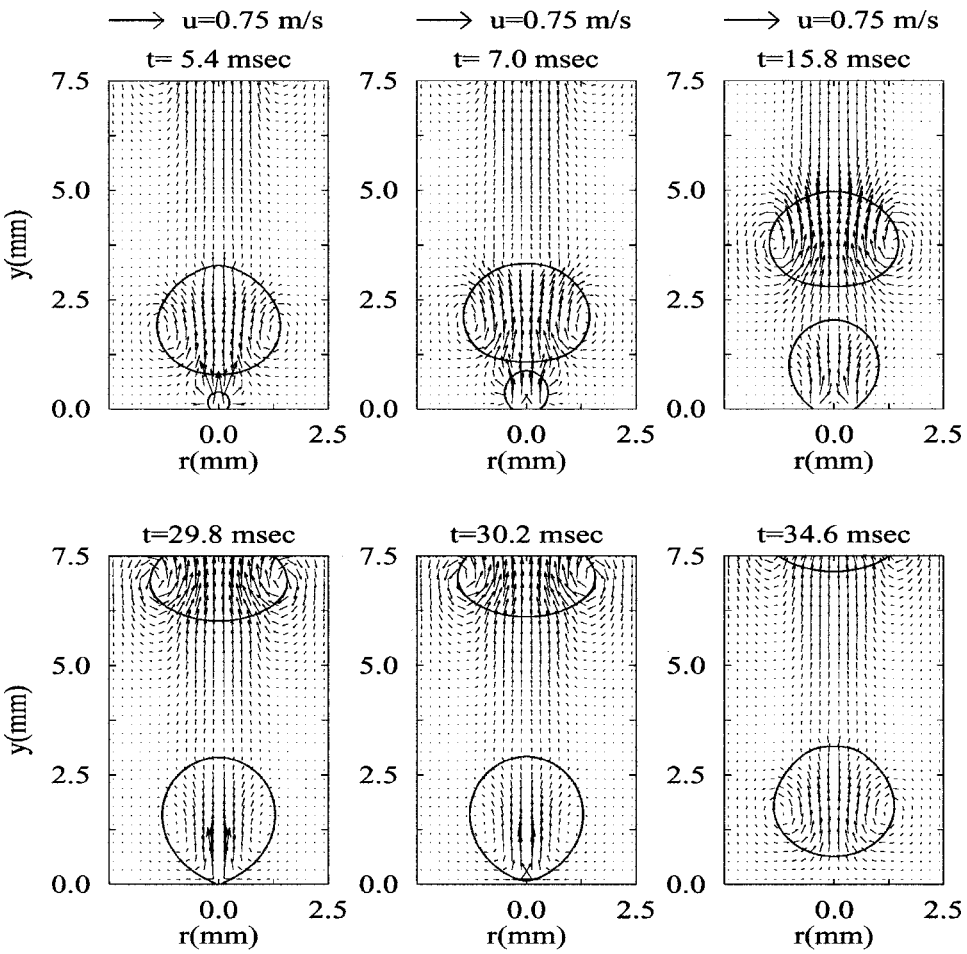

Fig. 4 Flow fields during bubble growth and detachment for $\Delta T = 10$ K and $\tau_w = 4.8$ msec

for the two finest grids have shown insignificant differences. Therefore, most of computations in this study are performed on 26 μm mesh size to save the computing time without losing the accuracy of numerical results. During the computations, time steps were chosen to satisfy the CFL condition, $\Delta t \leq h/(|u|+|v|)$. This was done because of the explicit treatment of the convection terms and the condition that the numerical results should not change if the time steps are halved. An appropriate time step was approximately 8×10^{-3} msec. Also, in our previous study [3], the departure bubble sizes and growth periods predicted from numerical simulation were validated by comparing with the experimental data.

Experiments

Figure 2 shows the experimental apparatus used in this work. The boiling surface is made up of a mirror-polished 100 silicon wafer. The wafer has a diameter of 10.16 cm and a single square cavity with a size of 10 μm and a depth of 20 μm was micromachined at the center. The back surface of the wafer is heated with strain gauge thin film heaters connected to a DC power supply. Each strain gauge heater is 11 mm$\times$6.5 mm with a 6.5 mm$\times$6.5 mm heated portion with the remaining area being used for soldering leads. Thermocouples were placed at various locations on the back of the wafer to measure the surface temperature of the wafer. All measured temperatures were acquired using a data acquisition system running at 16 Bit precision. The uncertainty in measured temperatures is $\pm$0.2 K. The liquid in the pool could be maintained at a desired temperature using two cartridge heaters provided on either sides of the wafer. In this work, no attempt was made to experimentally determine the surface heat flux on the area surrounding the nucleation site. The heat input to the strain gauge heaters was controlled so that a desired temperature could be obtained on the area surrounding the cavity. The observed temperature did not vary by more than $\pm$0.5 K during the experiments.

Before an experiment was conducted the test surface was thoroughly cleaned with isopropanol followed by methanol. The test fluid used in the experiments was deionized water. The quality of water was measured and tabulated before the experiment using an ION probe. The test fluid was then vigorously boiled for 2 to 3 hours to remove any dissolved air in the liquid. The static contact angle was measured using sessile drop method and was found to be about 50 deg.

The degassed deionized water was cooled to room temperature and was introduced into the test chamber. The pool cartridge heaters were then switched on and the liquid was allowed to heat up to the saturation temperature. The wafer, being in contact with the liquid, also heated up with the test fluid. After the pool reached a steady value at the saturation temperature corresponding to the ambient pressure (1 atm.), strain gauge heaters at the back of the wafer were switched on. The power input to the strain gauge heaters was increased in small increments and the wafer surface was allowed to reach a steady state. This increase was continued until nucleation was visible on a particular site on the surface. At the point the auxiliary heaters were switched off and the imposed liquid motion was allowed to subside. The bubble growth, departure and merger processes were recorded on a HiSIS 2000 CCD Camera operating at 1020 frames per second.

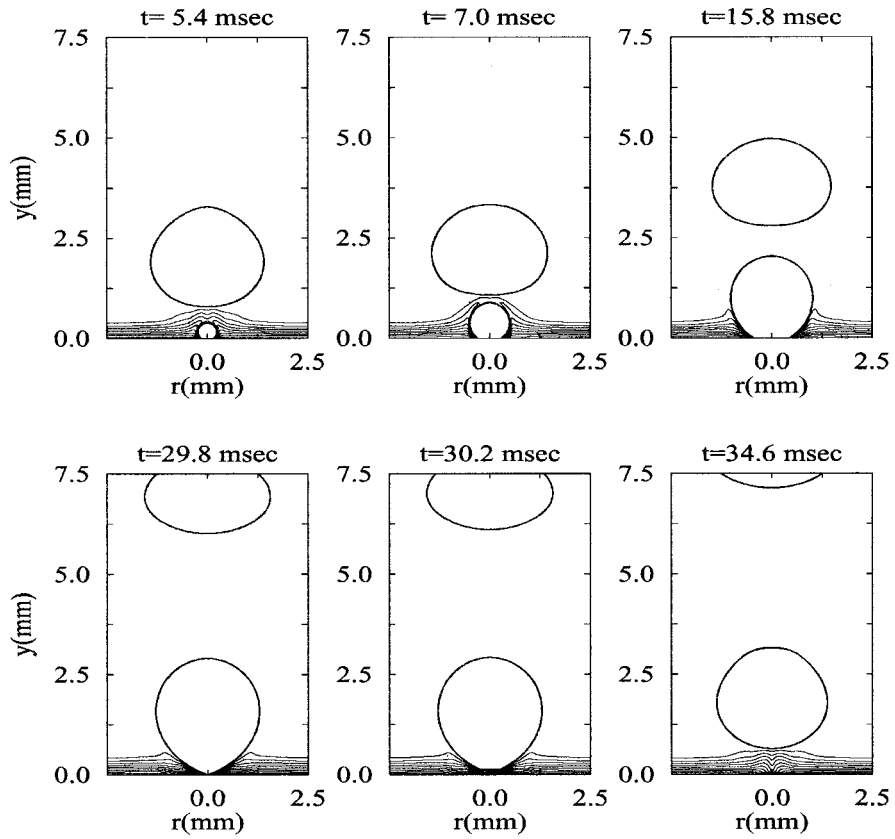

Fig. 5 Temperature fields with temperature interval of 1 K for $\Delta T = 10$ K and $\tau_w = 4.8$ msec

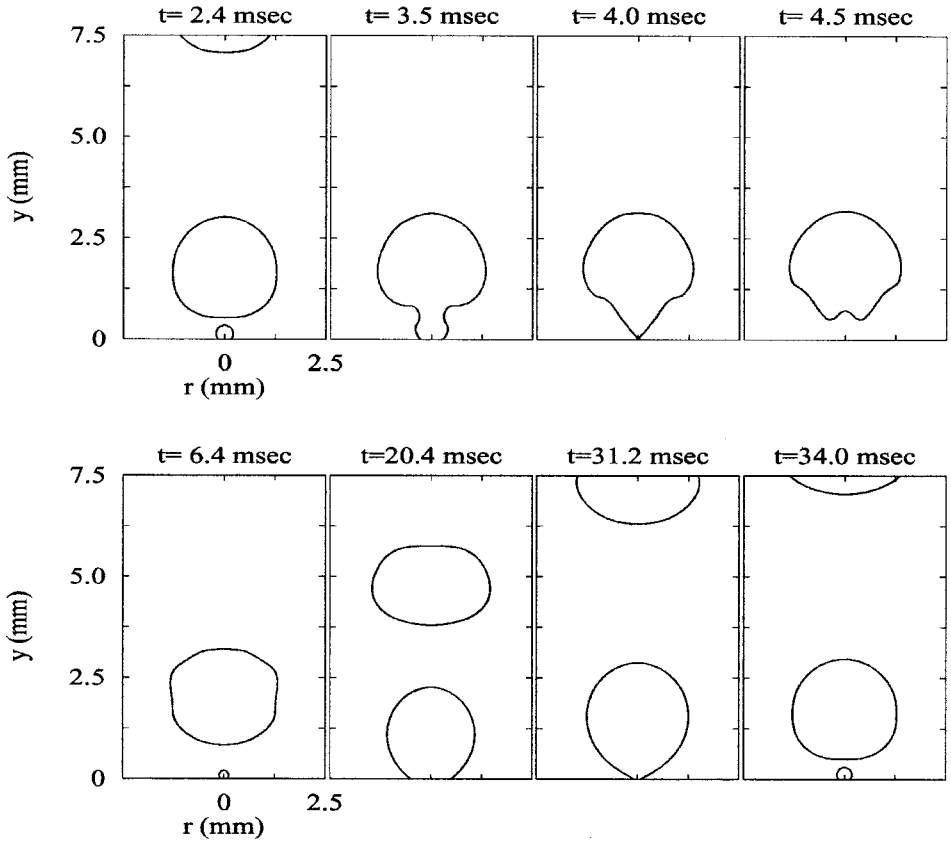

Fig. 6 Bubble growth and merger pattern for $\Delta T = 10$ K and $\tau_w = 2.4$ msec

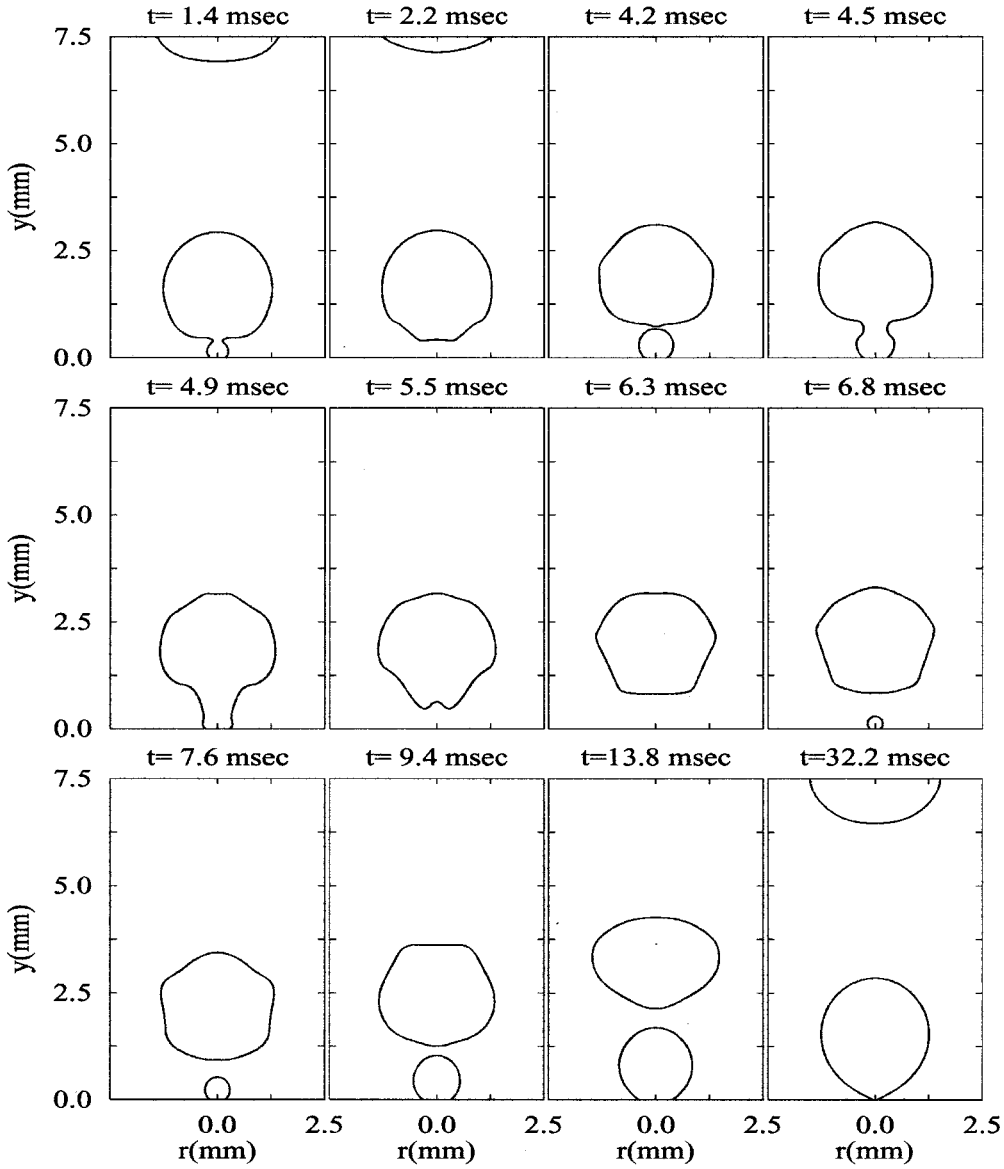

Fig. 7 Bubble growth and dmerger pattern for $\Delta T = 10$ K and $\tau_w = 1.28$ msec

Results and Discussion

In carrying out numerical simulations, the properties of water at 1 atm are used. Also, the contact angle is chosen to be 38 deg, which corresponds to a dispersion constant of -8.5×10^{-21} J from the microlayer analysis. The contact angle of 38 deg was used in most of our previous numerical simulations on a growing and departing bubble on a horizontal surface [3]. The dependence of bubble growth on surface wettability was shown in the previous paper. Computations were made for three different contact angles of 25 deg, 30 deg and 38 deg. As the contact angle increases, the bubble growth period increases. Also, the bubble diameter at departure becomes larger as the contact angle increases. However, the bubble volume at departure divided by the growth period is nearly identical within 1 percent deviation, regardless of the contact angles. As such the results obtained from numerical simulations with contact angle of 38 deg should not be materially different from those obtained from the experiments in which the contact angle was 50 deg.

During numerical simulations of bubble growth and merger process, the waiting period is one of the important parameters affecting the bubble merger pattern. The waiting period for an extremely small cavity (10 μm) is practically zero in the present study under the assumption that the wall temperature remains constant. In most experiments, a constant heat flux condition is applied. As such the wall temperature decreases momentarily when the cold pool liquid fills the area vacated by the departing bubble. The liquid layer and the heater surface have to be heated to a temperature necessary to initiate the next bubble. The waiting period decreases with wall superheat and can be predicted when a conjugate problem involving conduction in the solid is solved simultaneously with the flow and temperature field in the liquid. In the present work, the waiting period, τ_w, is varied parametrically because we did not solve the conjugate problem.

Figure 3 shows the bubble growth pattern during one cycle for $\Delta T = 10$ K and $\tau_w = 4.8$ msec. The calculation was carried out in the computational domain of $(R,Y) = (2.5\text{ mm}, 10\text{ mm})$. When the domain was increased from $R = 2.5$ mm up to $R = 5.0$ mm, the bubble departure diameter and the bubble growth period were increased by less than two percent. Thus beyond $R = 2.5$ mm, the computational domain size has little effect on the bubble dynamics. Initial thickness of the thermal layer is assumed to be that predicted for turbulent natural convection on the upward facing

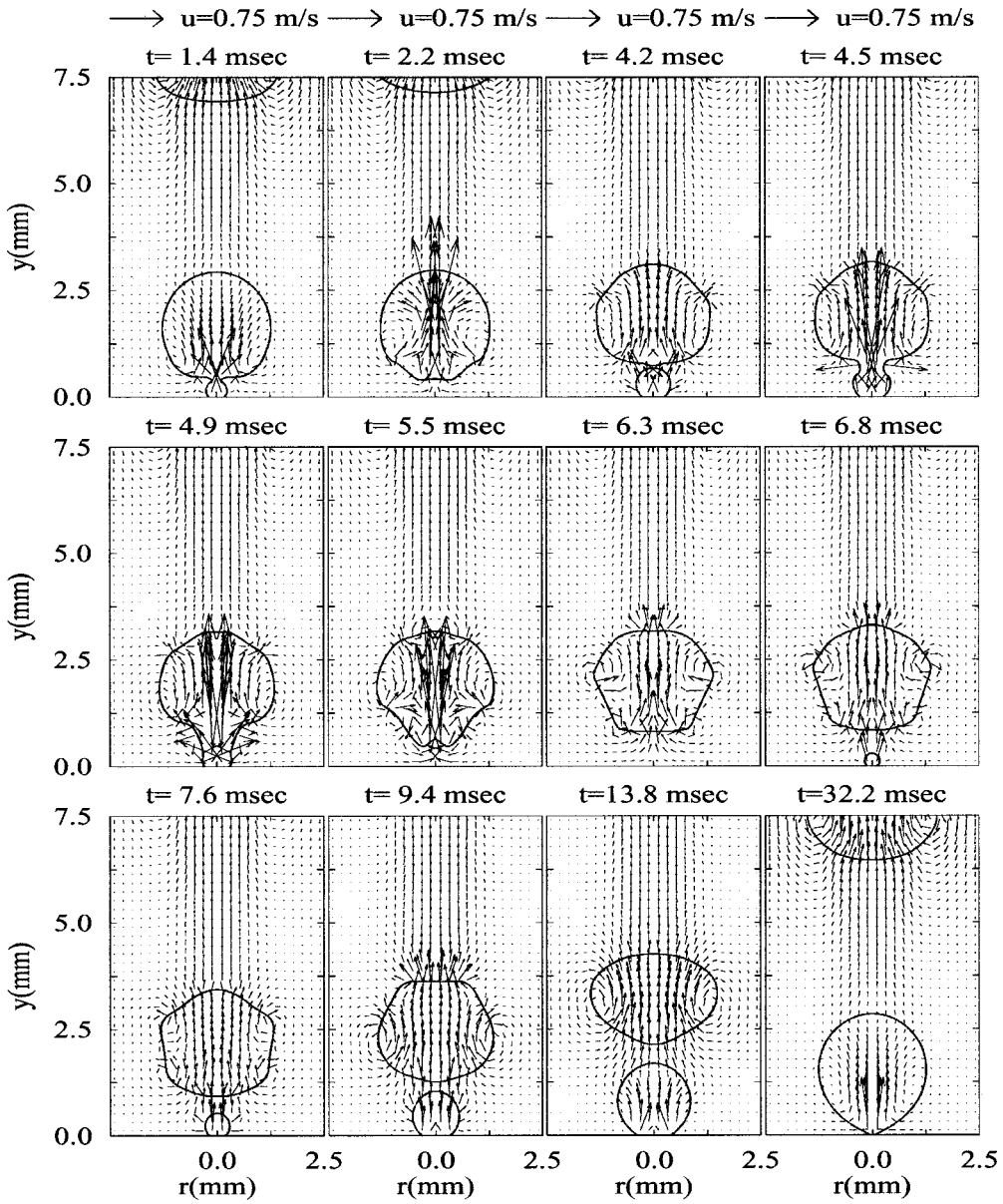

Fig. 8 Flow fields during bubble growth, detachment and merger for $\Delta T = 10$ K and $\tau_w = 1.28$ msec

heated surface. It is seen that a small bubble attached to the wall grows while the previously departed bubble rises in the pool. As the attached bubble grows, the base of the bubble expands and then shrinks until the bubble finally departs from the wall. During the waiting period, the boiling surface is entirely covered with liquid and is devoid of any bubbles. A small bubble serving as nucleus for the next cycle is placed on the heater surface after the end of the waiting period, which is an external parameter in the present computation as mentioned earlier. The initial radius of the bubble was chosen to be four times of the mesh size irrespective of the wall superheat. It is found that for $\tau_w = 4.8$ msec or greater a bubble growing on the wall surface does not merge with the previously departed bubble. In practice the waiting period for a given cavity will decrease as the wall superheat is increased, hence the process will shift from single to merged bubbles as wall superheat is increased.

The flow and temperature fields associated with the growth and departure of a single bubble are plotted in Figs. 4 and 5. Initially the liquid around a bubble attached to the wall is seen to be pushed out by the growing bubble. The bubble growth results from heat input from the superheated liquid layer surrounding the bubble including the micro region. Subsequently, the bubble grows out of the thermal boundary layer and the liquid flow is radially inward near the bubble base as the bubble departs. Also, it is seen from Fig. 5 that after the bubble detachment a thermal boundary layer begins to form under the departed bubble and develops as the bubble rises in the pool. The bubble shape, bubble growth rate, bubble diameter at departure and bubble growth period predicted from the numerical simulations were compared by Son et al. [3] with data from experiments. An excellent agreement was found between predictions and the data.

When the waiting period is decreased to 2.4 msec, bubble merger occurs as demonstrated in Fig. 6. With the reduction in waiting period prior to bubble initiation, the distance between the bubble growing on the wall and the previously departed bubble decreases so that two bubbles merge in the vertical direction at $t = 3.5$ msec. Thereafter, the lower portion of the merged bubble springs up quickly due to the restoring force of surface tension. This leads to the formation of a wall jet and a dimple at the bottom of the merged bubble at $t = 4.5$ msec. This also accelerates

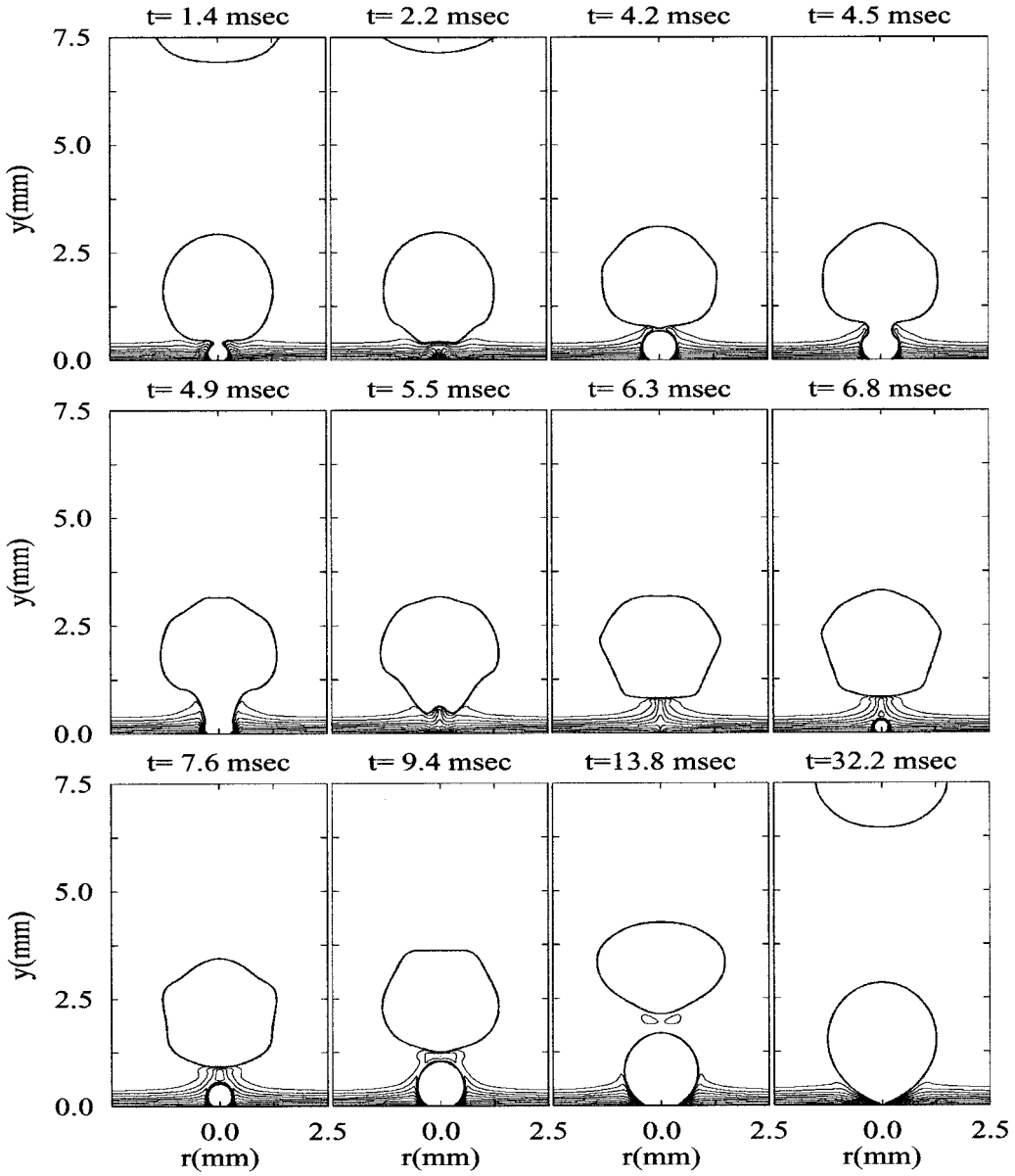

Fig. 9 Temperature fields with temperature interval of 1 K for $\Delta T = 10$ K and $\tau_w = 1.28$ msec

the bubble away from the wall such that the departed bubble cannot be caught by the succeeding bubble growing on the wall. After this interruption, the merger process repeats all over again. As τ_w is further reduced to 1.28 msec, bubble merger occurs twice during one cycle at $t = 1.4$ msec and $t = 4.5$ msec as shown in Fig. 7. After the departure of the merged bubble at 5.5 msec, the bubble merger process is interrupted until a single bubble grows on the surface and departs. Thereafter the merger process begins all over ($t > 32.2$ msec). This indicates that for a given wall superheat the type of bubble merger pattern depends on the waiting period. For a given size cavity, the waiting period decreases with increase in wall superheat. Thus because of distribution of different size cavities on a particular surface, bubble merger will be observed to occur at varying wall superheats. The merger of bubbles in the vertical direction gives appearance of the formation of a vapor column at $t = 4.9$ msec, the configuration of which is consistent with the observation of Gaertner [5].

Figure 8 shows the flow field influenced by the bubble merger as well as bubble growth and departure processes corresponding to the bubble merger case. During the bubble merger process, the vapor in the lower portion of the merged bubble is sucked into the upper portion due to the restoring force of surface tension. This causes very high velocities inside the bubble and a high velocity wall jet under the departing bubble. While the merged bubble rises in the pool, it is seen that the bubble shape changes continuously and this induces several vortical structures near the bubble interface. The temperature field during the bubble merger process is plotted in Fig. 9. It is observed that for 5.5 msec$\leq t \leq$7.6 msec the isotherms near $r = 0$ follow the merged bubble departing from the wall whereas the isotherms near the edge of the computational domain ($r = R$) are not much influenced by the bubble motion. The rising isotherms under the bubble are reflective of the very high velocity induced by the departure of the merged bubble.

Figure 10 presents the effect of bubble growth and merger on Nusselt number based on the area average heat flux at the wall during two consecutive cycles. Figure 10(*a*) is for a single bubble whereas Figs. 10(*b*) and 10(*c*) are for merger of two and three consecutive bubbles respectively. For a single bubble, the Nusselt number initially increases with the expansion of the bubble base underneath which the microlayer evaporation occurs. Thereafter, the Nusselt number decreases as the bubble base shrinks during the bubble detachment period. For the bubble merger cases, the

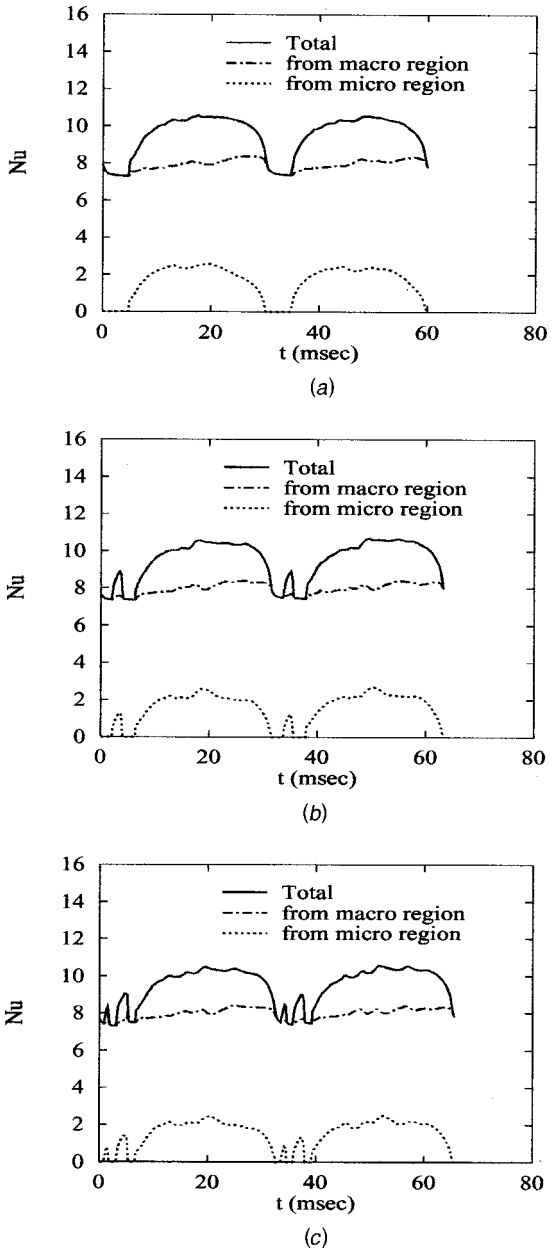

Fig. 10 Variation of Nusselt number with time for $\Delta T = 10$ K and three different waiting periods: (*a*) $\tau_w = 4.8$ msec; (*b*) $\tau_w = 2.4$ msec; and (*c*) $\tau_w = 1.28$ msec

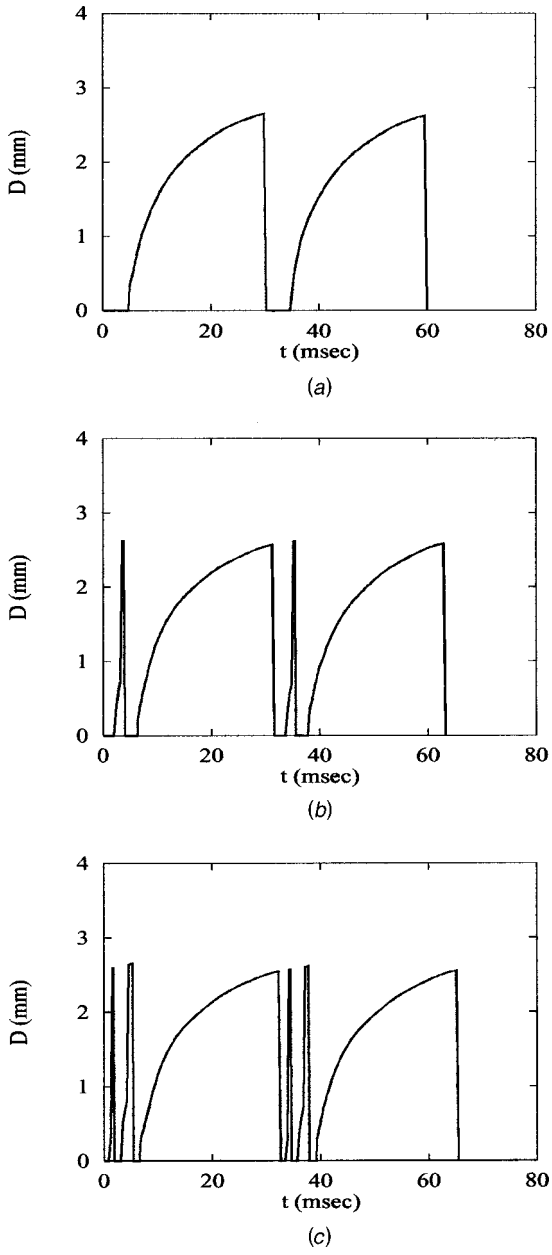

Fig. 11 Variation of bubble diameter with time for $\Delta T = 10$ K and three different waiting periods: (*a*) $\tau_w = 4.8$ msec; (*b*) $\tau_w = 2.4$ msec; and (*c*) $\tau_w = 1.28$ msec

Table 1 Effect of bubble merger on the heat transfer and vapor removal rate

ΔT (K)	τ_w (msec)	Nu_{total}	Nu_{micro}	D_d (mm)	τ_{total} (msec)	$\dot{V}_{removal}$ $(10^{-7}\ m^3/sec)$	Nu_{evap}
10	4.8	9.58	1.66	2.64	29.7	3.28	8.30
10	2.4	9.56	1.59	2.63	31.6	3.03	7.67
10	1.28	9.52	1.55	2.63	32.9	2.91	7.36

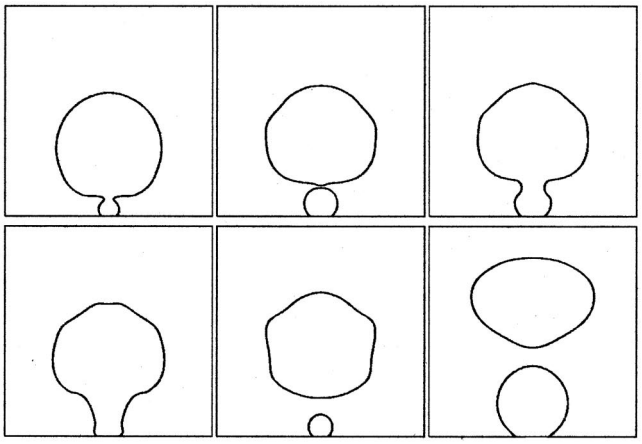

(*a*)

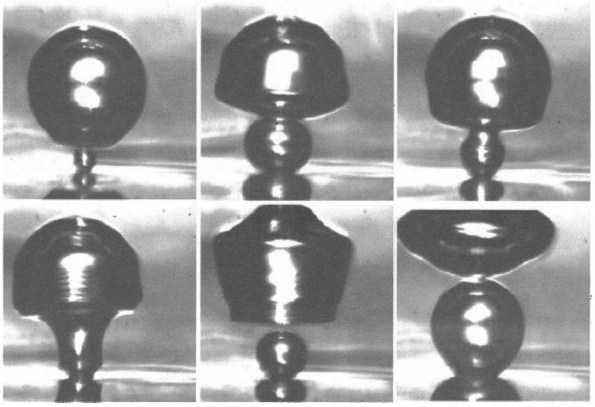

(*b*)

Fig. 12 Comparison of bubble merger patterns on a single nucleation site for $\Delta T=10$ K obtained from (*a*) numerical simulation with $\tau_w=1.28$ msec and (*b*) experiment

curve for Nusselt number has small peaks as shown in Fig. 10(*b*) and 10(*c*). This is caused by the fact that a bubble nucleating on the heater surface can not grow uninhibitedly because of the merger with the previously departed bubble. Thus, during the periods with the small peaks in the Nusselt number, the expansion of the bubble base that accompanies high heat removal rate is limited by the bubble merger. However, during the subsequent bubble growth period the curves are similar to each other regardless of the number of bubble mergers. The time and area-averaged Nusselt numbers are listed in Table 1. It is seen that the Nusselt number based on the heat flux from the microlayer, Nu_{micro}, contributes about 15~20 percent to the Nusselt number, Nu_{total}, based on the total heat flux. Also, Nu_{micro} and Nu_{total} are found to be not much influenced by the bubble growth and merger pattern.

The diameter of a bubble having a volume equal to the volume of the merged bubble attached to the wall is plotted in Fig. 11(*a*), (*b*), and (*c*) for waiting periods of 4.8, 2.4, and 1.28 msec respectively. The bubble diameter at departure and the total period, τ_{total}, including the waiting period are listed in Table 1. The sharp peak in bubble diameter as shown in Fig. 11(*b*) and (*c*) is reflective of the increase in the vapor volume due to the merger of a small bubble growing on the wall with the previously departed bubble. The bubble diameters at departure are almost the same for three different waiting periods but the total period increases as the waiting period decreases and the number of bubble mergers increases before the cycle is disrupted. Thus, the vapor removal rate ($\dot{V}_{removal}$) defined as the bubble volume at departure over the total period tends to slightly decrease with decrease in τ_w or with bubble merger as listed in Table 1. This indicates that the merger of bubbles does not enhance vapor (or heat) transfer rate from the wall. The Nusselt number based on the evaporative heat flux associated with the bubble, Nu_{evap}, can be calculated from the energy balance at the interface or from the vapor production rate. From Table 1, the fraction of total heat dissipated at the wall that is utilized for the bubble growth, Nu_{evap}/Nu_{total}, is about 77~87 percent.

In Fig. 12 a comparison of the shapes of merged bubbles predicted from the numerical simulation is made with those observed in the experiments. It is seen that bubble shapes calculated numerically are in excellent agreement with those observed experimentally.

Figure 13 shows the bubble merger pattern when the wall superheat, ΔT, is increased to 15 K. The calculation is carried out in the computational domain of $(R,Y)=(2.5\,\text{mm}, 15.0\,\text{mm})$. In a given cycle the bubble merger occurs much more often than for $\Delta T=10$ K because the vapor generation rate increases with the wall superheat. After four sequential bubble mergers, a tall vapor column forms on the wall at $t=35.5$ msec and then departs. The departed vapor column undergoes several configurational changes as a result of interfacial tension and the surrounding flow field before acquiring a spherical shape. For $38.1\,\text{msec}\leqslant t \leqslant 54.7\,\text{msec}$, a single bubble grows on the surface and departs without merging with the previously departed vapor column. Thereafter the new cycle of the bubble merger process starts at $t=54.7$ msec. It is interesting to see that at $t=61.4$ msec a small liquid droplet is entrapped into the vapor column during the bubble merger process. The apperarance of droplet is caused by the fact that two bubbles start to contact off the axis of symmetry ($r>0$) rather than at $r=0$ during the merger process. At $t=64.5$ msec, the departed large bubble begins to touch the symmetry plane ($r=R$). This also implies the possibility of bubble merger in the horizontal direction. The computations were terminated at that moment because the horizontal bubble merger cannot be simulated from the two-dimensional model.

The vapor removal rate for single bubble case as well as that for bubble merger cases as a function of wall superheat is presented in Fig. 14. Over the limited range of wall superheats it is found that the vapor removal rate predicted numerically increases almost linearly with the wall superheat regardless of the merger of bubbles. The data from experiments are also plotted in the figure and show a linear increase in vapor removal rate as well. However, in comparison to the experimental data, the vapor removal rates obtained from the numerical simulations match well at low wall superheats but tend to be under predicted by about 32 percent at the highest wall superheat. The steep increase in vapor removal rate with the wall superheat as observed during nucleate boiling on surfaces with many cavities is thus not caused by the bubble merger in the vertical direction but it may be caused by the bubble merger in the horizontal direction resulting from increased nucleation site density.

Conclusions

1 A complete numerical simulation of bubble dynamics including the growth, departure and merger of bubbles on a single nucleation site has been performed successfully.
2 From the numerical simulation, the total wall heat flux and the bubble diameter at departure are observed to be not much influenced by the bubble merger pattern. However, the vapor removal rate tends to slightly decrease as the waiting period decreases and bubble merger occurs.
3 At a wall superheat of 10 K the evaporative heat flux utilized for the bubble growth is found to be about 77~87 percent of the total heat flux from the wall supporting the computational domain.

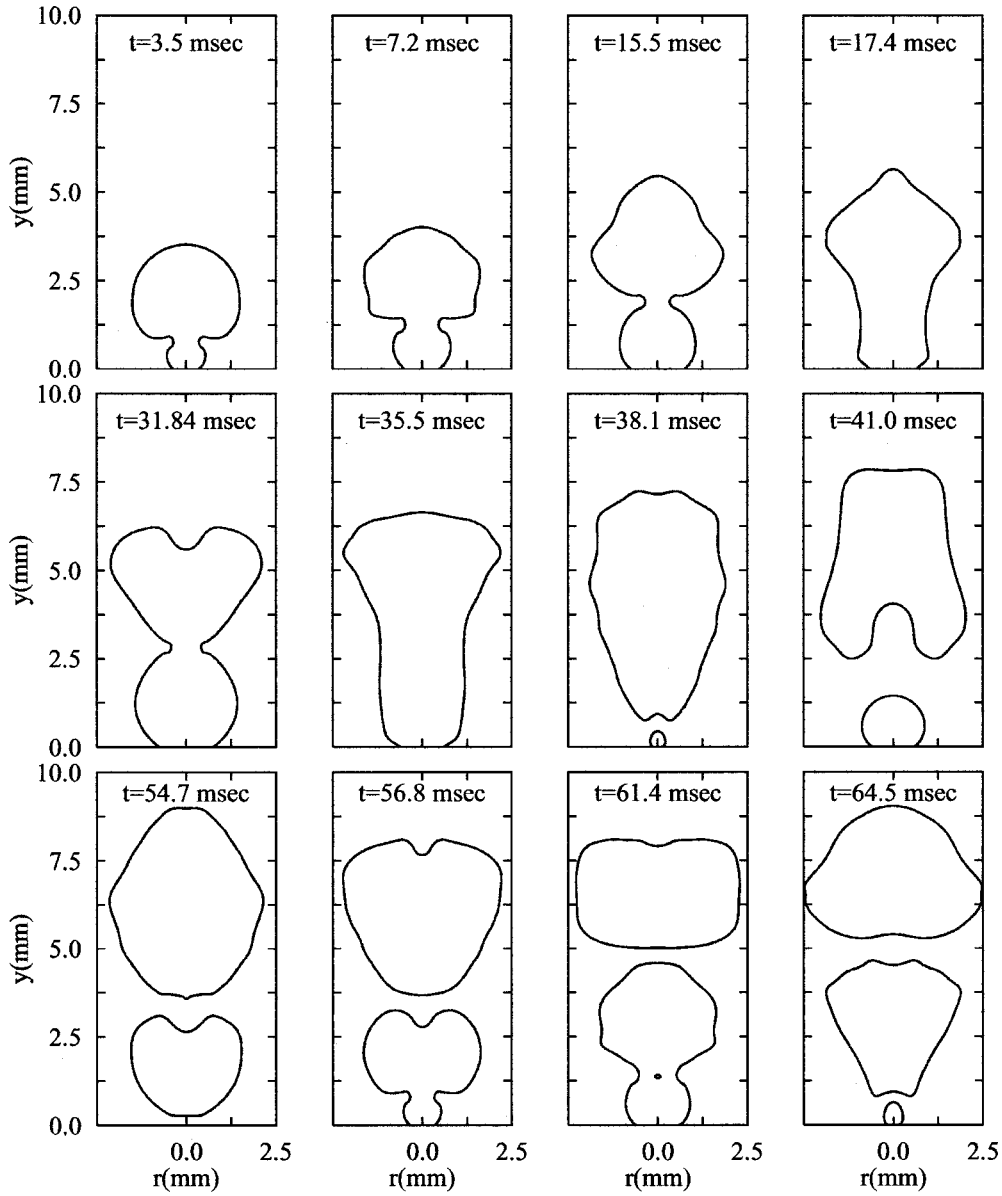

Fig. 13 Bubble growth and merger pattern for $\Delta T = 15$ K and $\tau_w = 1.28$ msec

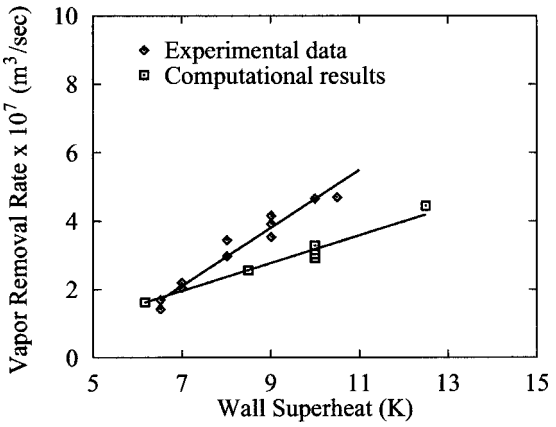

Fig. 14 Dependence of vapor removal rate on the wall superheat

4 The bubble merger pattern predicted from the numerical simulations compares well with that observed in the experiments.
5 Over the limited range of wall superheats investigated the vapor removal rate increases almost linearly with the wall superheat regardless of the bubble merger in the vertical direction.

Acknowledgment

This work received support from NASA under the Microgravity Fluid Physics Program.

Nomenclature

A = dispersion constant
c_p = specific heat at constant pressure
D = equivalent bubble diameter
D_d = bubble diameter at departure

$\mathbf{g}$ = gravity vector
H = step function
h = grid spacing for the macro region
h_{ev} = evaporative heat transfer coefficient
h_{fg} = latent heat of evaporation
k = thermal conductivity
$\mathbf{m}$ = mass flux vector defined in Eq. (15)
Nu = Nusselt number, $q\sqrt{\sigma/g(\rho_l-\rho_v)}/k_l\Delta T$
p = pressure
q = heat flux
R = radius of computational domain
R_o = radius of dry region beneath a bubble
R_1 = radial location of the interface at $y=h/2$
R_v = gas constant
r = radial coordinate
T = temperature
t = time
ΔT = temperature difference, T_w-T_{sat}
$\mathbf{u}$ = velocity vector, (u,v)
$\mathbf{u}_{\text{int}}$ = interfacial velocity vector
$\dot{V}_{\text{micro}}$ = rate of vapor volume production from the microlayer
ΔV_{micro} = control volume near the micro region
Y = height of computational domain
y = vertical coordinate
β_T = coefficient of thermal expansion
δ = liquid film thickness
δ_o = nonevaporating liquid film thickness
κ = interfacial curvature
μ = dynamic viscosity
ρ = density
σ = surface tension
τ = period
ϕ = level set function
φ = contact angle

Subscripts

int = interface
l, v = liquid, vapor
sat, w = saturation, wall or waiting

References

[1] Lee, R. C., and Nydahl, J. E., 1989, ''Numerical Calculation of Bubble Growth in Nucleate Boiling From Inception Through Departure,'' ASME J. Heat Transfer, **111**, pp. 474–479.
[2] Welch, S. W. J., 1998, ''Direct Simulation of Vapor Bubble Growth,'' Int. J. Heat Mass Transf., **41**, pp. 1655–1666.
[3] Son, G., Dhir, V. K., and Ramanujapu, N., 1999, ''Dynamics and Heat Transfer Associated With a Single Bubble During Nucleate Boiling on a Horizontal Surface,'' ASME J. Heat Transfer, **121**, pp. 623–631.
[4] Sussman, M., Smereka, P., and Osher, S., 1994, ''A Level Set Approach for Computing Solutions to Incompressible Two-Phase Flow,'' J. Comput. Phys., **114**, pp. 146–159.
[5] Gaertner, R. F., 1965, ''Photographic Study of Nucleate Pool Boiling on a Horizontal Surface,'' ASME J. Heat Transfer, **87**, pp. 17–29.
[6] Lay, J. H., and Dhir, V. K., 1995, ''Shape of a Vapor Stem During Nucleate Boiling of Saturated Liquids,'' ASME J. Heat Transfer, **117**, pp. 394–401.
[7] Wayner, P. C., Jr., 1992, ''Evaporation and Stress in the Contact Line Region,'' *Proceedings of The Engineering Foundation Conference On Pool and External Flow Boiling*, V. K. Dhir and A. E. Bergles, eds., Santa Barbara, CA, pp. 251–256.

Bubble Behavior and Nucleate Boiling Heat Transfer in Saturated FC-72 Spray Cooling

Daniel P. Rini

Ruey-Hung Chen
e-mail: chenrh@pegasus.cc.ucf.edu

Louis C. Chow

Department of Mechanical, Materials and Aerospace Engineering, University of Central Florida, Orlando, FL 32816-2450

Bubble behavior during saturated FC-72 spray cooling was experimentally investigated. A heater previously used for pool boiling was used to allow direct comparison. The results are analyzed to reveal the interaction between bubbles and impinging droplets. The following are presented: (1) the importance of secondary nuclei entrained by impingement droplets, (2) the role of impinging droplets on bubble parameters such as growth, diameter at puncture, lifetime, life cycle and bubble number density, and (3) the relative contribution of nucleation, especially that of secondary nuclei, to the heat transfer. It is concluded that increasing the droplet flux increases the number of secondary nuclei, helps to lower surface temperature for a given heat flux, increases the overall heat transfer coefficient, and increases heat transfer due to both nucleate boiling and enhanced convection. Increasing the droplet flux also shortens the bubble growth time (i.e., resulting in earlier bubble removal) and life cycle. However, increasing the droplet flux (and, therefore, secondary nucleation) for each of the three heat flux values does not affect the percentage of either nucleate or convection heat transfer. This suggests that both the nucleate and convection heat transfer are enhanced, as a result of increased secondary nuclei and turbulent mixing due to the impinging droplets. [DOI: 10.1115/1.1418365]

Introduction

A spray cooling system consists of liquid droplets generated by pressure- or air-assisted atomizers that impinge on a heated surface. Traditionally, spray was used to cool highly heated surfaces, such as those in steel mills, where film cooling rather than nucleate boiling dominates. Recent applications of spray cooling include high heat flux removal from surfaces while maintaining low surface superheats, such as for electronic cooling. In this application, a significant portion of heat transfer is due to nucleate boiling heat transfer. Several events occur in spray cooling. First, the impacting droplets puncture and remove the vapor bubble (or the nucleus). The bubble size at puncture is usually smaller than that allowed under pool boiling conditions. Secondly, a thin liquid film may form on the heated surface within which nucleation takes place. Finally, air or vapor is entrained by the droplets into the thin liquid film, thus forming the so-called secondary nuclei [1–4]. The heat transfer mechanism is believed to consist of three key mechanisms: nucleate boiling due to both surface and secondary nuclei, convective heat transfer, and direct evaporation from the surface of the liquid film [5]. However, the relative contributions of these three mechanisms are not known. It is essential to understand the mechanisms and their contributions to designing effective cooling strategies.

The following observations have been made as a result of reported experimental studies. Spray cooling has been shown to yield a heat flux approximately an order of magnitude higher than pool boiling using the same liquid. For example, spray cooling using water is capable of a critical heat flux (CHF) of approximately 1000 W/cm^2, compared to approximately 120 W/cm^2 by pool boiling (see, for example, [5]). In the case of liquid nitrogen (LN_2), the values of CHF of pool boiling and spray cooling are approximately 16 W/cm^2 and 160 W/cm^2, respectively [6,7]. For FC-72, the values of CHF of pool boiling and spray cooling are approximately 20–30 W/cm^2 [8,9] and 100 W/cm^2 [10], respectively. Due to the high heat flux, the heat transfer coefficient in spray cooling is also higher than that in pool boiling. Surface characteristics, such as roughness, may play a role in determining the heat transfer coefficient, but it generally does not significantly affect the value of CHF [11,12]. A correlation for CHF was proposed, which successfully collapsed data over a wide range of liquids [5,7]. It was also found that increasing the droplet flux (N) beyond a certain value does not help to extend CHF [5,7,13]. The reason for this existence of a limit on CHF is not well known.

The enhanced heat flux due to spray cooling finds useful applications in electronic cooling [10,13]. As the circuit density and clock speed of microprocessors seem to be forever increasing, the need for removing heat dissipation from future desktop computers calls for more efficient cooling techniques than the conventional single-phase fan and immersion/pool boiling. Other advantages of spray cooling over pool boiling include the elimination of hysteresis of boiling incipience. Such hysteresis is frequently observed in pool boiling of highly wetting liquids such as FC-72 [14–17]. The ability to eliminate the hysteresis has important implications for electronic cooling, as temperature overshoot and fluctuation resulting from the hysteresis may cause deterioration in device performance.

Due to the above-mentioned desirability, spray cooling has been a subject of study over the past three decades (see, for example, review in [5]). In these studies, efforts were made to gain understanding of the heat transfer mechanisms and the parametric effects of the spray and droplets. Kopchikov et al. [18] found that the CHF using a water spray was approximately 600 W/cm^2, without specifying spray characteristics. In this work, no differentiation was made among the relative contributions of the three heat transfer mechanisms. Nucleating bubbles were found to grow beyond the thickness (up to 300 μm) of the liquid film. It was also found that the spray characteristics did not effectively affect the heat transfer process, probably because at this stage bubbles were likely to rupture. How droplets punctured vapor bubbles and how the puncturing affected the heat transfer process were not known.

In pool boiling, evidence suggests that bubbles lasting beyond the period of microlayer evaporation are not effective in removing heat from the heated surface [19,20]. Moore and Mesler [19] used a flush-mounted thermocouple to measure heater surface temperature beneath growing bubbles in water pool boiling conditions. Knowing that the surface temperature varied with time as a con-

Contributed by the Heat Transfer Division for publication in the JOURNAL OF HEAT TRANSFER. Manuscript received by the Heat Transfer Division November 1, 2000; revision received June 5, 2001. Associate Editor: T. Avedisian.

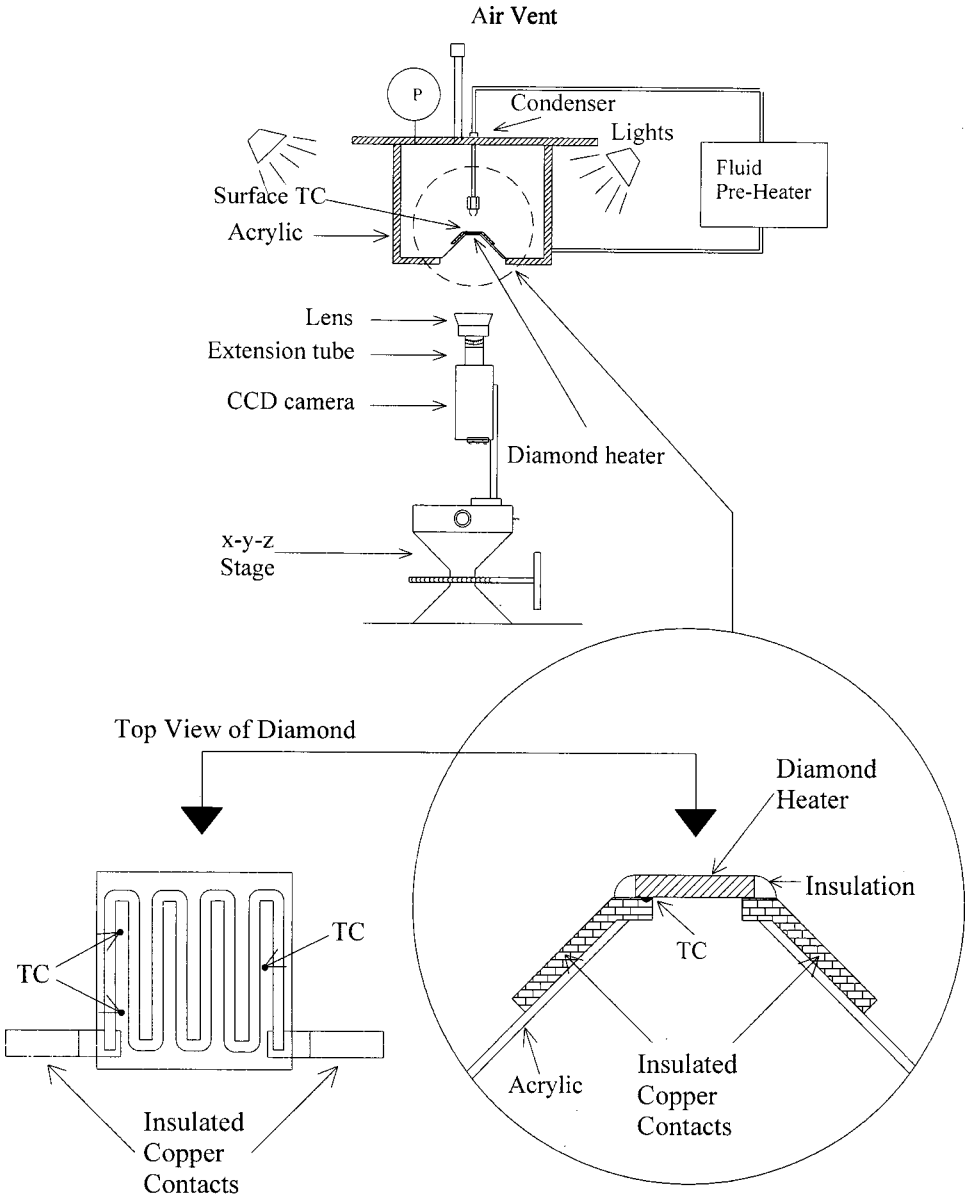

Fig. 1 Schematic of experimental setup

sequence of microlayer evaporation, they carried out a heat conduction analysis over the area beneath a bubble to extract the local heat transfer rate. Based on the known parameters at a heater-average heat flux of about 42.5 W/cm^2, the heat flux over the surface area under a bubble can be calculated. The local heat flux thus found is approximately 315 W/cm^2, compared to CHF of water pool boiling, which is 100–120 W/cm^2. This result demonstrates the important contribution from microlayer evaporation to the total heat flux from the heater surface. Once the microlayer is evaporated, the surface temperature increases due to the local dry-out and the efficiency of heat removal is substantially reduced. Since the period of microlayer evaporation is commonly an order of magnitude shorter than the bubble lifetime [19–22], the heat removal would be most effective during the early stage of bubble growth. The results of Kopchikov et al.'s investigation [18] suggest ineffective puncturing and removal of bubbles in spray cooling, as the 600 W/cm^2 value of CHF is significantly lower than 1000 W/cm^2 reported by others. Therefore, it is of interest to investigate how bubble puncturing will increase heat flux, both near and below CHF.

When sufficient water spray was supplied and nucleate boiling was vigorous within the thin liquid film, Monde [23] found the value of CHF to range from 45 W/cm^2 to approximately 800 W/cm^2 as the flow rate was increased (Fig. 12 in [23]). It is expected that a large quantity of water droplets may promote the puncturing of bubbles and enhancement of CHF. Mudawar and coworkers have addressed effects of the liquid flow rate, with CHF increased by increasing the amount of liquid arriving at the heater surface [24,25]. For a given spray nozzle, increasing the

Table 1 FC-72 properties at one atmospheric pressure

Specific heat	1.1 kJ/kgK
Surface tension	0.012 N/m
Density	1680 kg/m^3
Heat of vaporization	87.91 kJ/kg
Boiling point	56°C

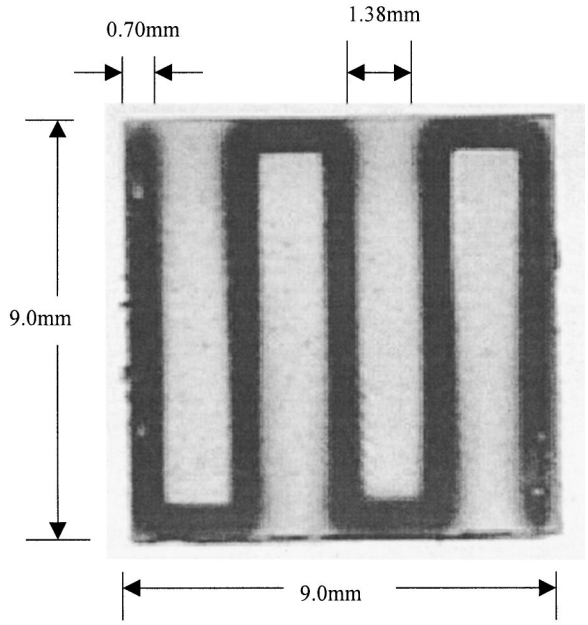

Fig. 2 Photo of the heater and heater pattern, with relevant dimensions

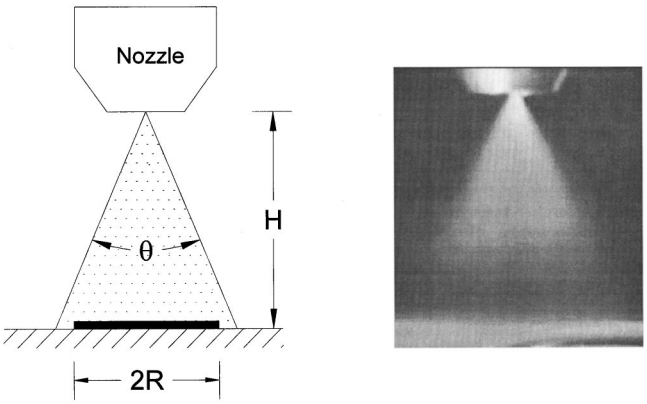

Fig. 3 Photo and legends of spray dimensions

liquid flow rate is accompanied by an increased number of droplets. It causes more frequent bubble puncturing and increases the number of secondary nuclei, enhancing heat fluxes and CHF.

Toda [26], using water "mist" droplets with diameters ranging from 80 μm to 146 μm and droplet velocity in the range of approximately 40–70 m/s, found CHF to be in the neighborhood of 300 W/cm^2. This value of CHF is larger than that of pool boiling and smaller than that of some reported values for spray cooling (i.e., $\approx$1000 W/cm^2). Toda [26] attributed the heat transfer to the direct evaporation from the thin liquid film formed by the impacting liquid droplets. This was because near CHF *no* nucleate boiling was observed within the thin liquid film and the value of CHF was limited by the liquid supply [26]. The value of 300 W/cm^2, however, falls within the range of CHF values found by Monde [23]. The value of CHF in Toda's experiment can be expected to increase with increased flow rate. Toda also observed a linear $q''-\Delta T$ relationship with no subcooling, from the low temperature regime ($\Delta T \approx 3°C$) to CHF ($\Delta T \approx 40°C$), as can be seen in Figs. 7–9 in [26]. This result suggests that heat is conducted through the thin liquid film, followed by direct evaporation from the liquid-vapor surface. It can be concluded that thin-film heat transfer may significantly contribute to the overall heat flux in spray cooling with nucleation and that nucleate boiling (and bubble opuncturing) should further enhance CHF.

Thus, a combination of direct evaporation from the thin liquid layer from its surface and early removal/puncture of vapor bubble is desirable for efficient cooling. However, the relative contributions of these two mechanisms has not been investigated to the knowledge of the authors. More recent investigations of spray cooling are concentrated on parametric effects. They were reviewed by Chow et al. [5]. Furthermore, the role that secondary nuclei play in heat transfer is not yet known. It is expected to become more important as the droplet flux is increased because more air or vapor will be entrained into the liquid film and possibly brought near the heater surface.

The above reported wide range of CHF values in spray cooling (e.g., approximately 600 W/cm^2–1000 W/cm^2 using water) appears to be dependent on several spray parameters. They suggest a need to further understand the details of droplet-bubble interaction and formation of secondary nuclei and the role they play in removing bubbles from the heated surface.

This study used a semi-transparent synthetic diamond (transmittance $\approx$70 percent in the visible wavelength range) heater to allow visualization of the growth of bubbles (surface and secondary) and the impact of droplets on bubble behavior. The contribution from nucleate boiling was calculated based on the bubble cycle, density and size, as was previously done for pool boiling using a similar experimental set-up. The contribution of direct evaporation from the liquid film and convection was also estimated. To the authors' knowledge, this study is the first attempt to determine the relative contributions of the three heat transfer mechanisms during spray cooling. The results should provide useful information for design engineers in selecting spray parameters to properly cool a heater surface. The present study is confined to the spray conditions below the Leidenfrost temperature. The reader is referred to a recent review article by Yao [27] for spray cooling above the Leidenfrost temperature.

Experiment

The experimental setup (shown in Fig. 1) and procedure are similar to those reported in an earlier study on FC-72 pool boiling [9]. The FC-72 liquid is an inert fluoro-carbon fluid manufactured by 3M Corporation. It is known for its low dielectric constant and is desirable for cooling electronic devices. Its properties can be found in [28] and those of interest to this study are listed in Table 1. The synthetic diamond heater was 1 cm$\times$1 cm$\times$0.05 cm in dimensions with a thin-film Ni-Cr resistor as the heat source (shown in Fig. 2). The film of Ni-Cr (an alloy of 60 percent nickel and 40 percent chromium) was deposited onto the underside of the heater as described in Rini et al. [9]. The diamond heater rested on a pyramid-shaped platform, as shown in Fig. 1. The measured electric resistance of the resistor pattern was 1000 Ω. Because this resistance was much greater than those in the electrical circuit connected to the experiment, the power dissipation therefore occurred primarily within the resistor pattern, which served the purpose of the heater design. The upper side of the diamond was the heat transfer surface, which always faced vertically upward and was in contact with the FC-72 liquid throughout the experimental investigation. The resistor pattern was designed so that the temperature variations on the heat transfer surface were found to be less than 1.0°C (see [9] for details). The heater surface temperature (T_w) was measured as described below. A T-type thermocouple (TC) with a 0.5 mm bead was attached to the underside of the heater and was in contact with the acrylic support, which has a much smaller value of thermal conductivity than the diamond. Therefore, the TC accurately read the temperature of the lower side of the heater. For a heat flux equal to 60 W/cm^2, the temperature on the heat transfer (i.e., wetted) surface was estimated to be

Table 2 Spray droplet parameters

Nozzle	Pressure (psig)	d_{20} (μm)	d_{32} (μm)	N (1/cm^{2}s)*	Q_i (cm^3/s)
TG0.3	20.0	93.0	113.0	2,088,000	1.66
TG0.4	40.0	83.0	104.0	4,443,000	3.08
TG0.6	40.0	78.0	102.0	8,249,000	5.63

* Equation (2).

0.2 K lower than the temperature measured by the TC. This is based on the thermal conductivity (1500 W/m.K) and the thickness (0.5 mm) of the diamond.

The heat flux was supplied by a power source with a capacity of 2000 volts and 300 mA. As shown in [9], the power loss to the air trapped within the pyramid upon which the heater rested is no more than 0.012 W/cm^2 and that loss through other parts of the heater and the electric connection to the Ni-Cr pattern was essentially negligible.

The casing of the test section was made of acrylic so that visualization from all angles was possible (Fig. 1). A large aluminum plate covered the top of the casing, acting as a condenser. The aluminum plate had a venting valve that was open to the room air during the degassing phase of the experiment (discussed below). Air is lighter than the FC-72 vapor and would exit the chamber through the open valve. The valve was then closed to seal the chamber and the chamber pressure was regulated at one atmospheric pressure, which was monitored by the reading of a pressure gauge.

The FC-72 liquid was circulated in a closed loop (Fig. 1). It was heated to saturation conditions (56°C at 1 atm in this study) before entering the spray nozzle. Three pressure-atomizing nozzles (manufactured by Spray Systems Co.) were selected for this study, TG0.3, TG0.4, and TG0.6. All of these are full-cone spray nozzles, made of No. 303 stainless steel. Fig. 3 depicts the appearance of a typical spray and a sketch of relevant dimensions of the spray and its relative position to the heater. Since the heater is a 1 cm×1 cm square, only part of the liquid issued from the nozzle landed on the heater. The relative position of the nozzle to the heater was always such that spray characteristics were uniform across and over the heater surface. These spray characteristics included droplet velocity (v), number density (n), surface mean diameter (d_{20}) and Sauter mean diameter (d_{32}). The relative position was determined by trial-and-error. All average values of spray parameters of interest were within 5 percent over the heater surface. Due to the uniformity of the spray, the fraction of the liquid landing on the heater (Q_i) can be determined by the following equation, according to geometric consideration:

$$\frac{Q_i}{Q}=\frac{1}{1-\cos\frac{\theta}{2}}\left[1-\frac{1}{((1+(R/H)^2)^{1/2})}\right], \tag{1}$$

where Q is the total flow rate at the nozzle exit. To quantify the impact of droplets on bubble behavior, the droplet number flux (N) had to be determined. As shown in [7],

$$N=6Q_i/\pi d_{32}d_{20}^2. \tag{2}$$

Three nozzles (designated as TG0.3, TG0.4 and TG0.6) were used to produce the desired spray conditions, listed in Table 2. It is noted from Table 2 that the values of d_{32} fall within a narrow range (107 μm±5 percent) and should be considered to be constant throughout this study. The values of d_{20} were also found to be in a narrow range of 78–93 μm. Again, the values of N in Table 2 were calculated using Eq. (2). The flow rate, Q_i, in Table 2, was calculated using Eq. (1). The density (ρ_l) and latent heat (h_{fg}) of the FC-72 liquid at its boiling temperature are 1680 kg/m^3 and 87.9×10^3 J/kg, respectively (shown in Table 1 along with other thermophysical properties). For Q_i equal to 1.66 cc/s a heat flux of 246 W/cm^2 from the heater surface would be required to completely vaporize the liquid flow. The near CHF heat flux in this study was found to be only slightly higher than 80 W/cm^2. Thus, the liquid flow rates used in this investigation were always in excess and are not in the regime described by Monde [23], where the value of CHF was limited by liquid flow rate. During the experiment, the Ni-Cr heater pattern was damaged if q'' was increased further beyond 80 W/cm^2 due to a rapid increase in surface temperature. Therefore, no experimental run was recorded beyond 80 W/cm^2.

Gases are known to dissolve in FC-72 easily. Before taking data for each experimental run, procedures similar to those described in Ref. [9] were taken for degassing. During the degassing phase, the pre-heater would heat the fluid while the fluid was sprayed through the pressure atomizer. At the same time, the diamond heater was heated with a heat flux 30 W/cm^2, which was sufficient to cause vigorous boiling. This setting would be maintained for 60 minutes, when all fluid used was boiled for a sufficiently long time. A procedure described in [29] was then adopted to analyze the extent of dissolved gases for the same experimental set-up [9]. It was concluded that the effect of dissolved gas was negligible after this procedure. It is noted that the liquid was held at 56 °C throughout the data acquisition phase.

A microscopic lens system in conjunction with a high-speed camera was used to observe the bubble behavior. The framing rate was up to 8000/s with a shutter speed of 1/80,000th of a second. The results of the high-speed photography were played at a much slower rate to extract data of bubble size, bubble lifetime, and the waiting time. Figures 4(*a*) and 4(*b*) help to demonstrate how bubble parameters were experimentally determined. Figure 4(*a*) is a sample still frame from the high-speed video. Due to the turbulent nature of the liquid film, the bubble image was not clearly or easily seen. To enhance the bubble image, an image processing technique, a Sobel filter in MATLAB, was used. It filtered out noise and enhanced the edge of the bubble, with the result shown in Figure 4(*b*). The images were enlarged 250 times on a screen so that 1 mm on the screen was equal to 4 μm in true bubble size. A caliper was used to measure the bubble diameter so that the true diameter could be calculated. The spatial uncertainty was therefore approximately 4 μm. Since the average bubble diameter at the end of its lifetime was about 200 μm, the uncertainty in bubble size measurement was about 2 percent. These procedures were also used to determine the bubble size vs. time and the bubble site density (n_b). The bubble size reported here was an average value of more than 100 bubbles at the point of time of

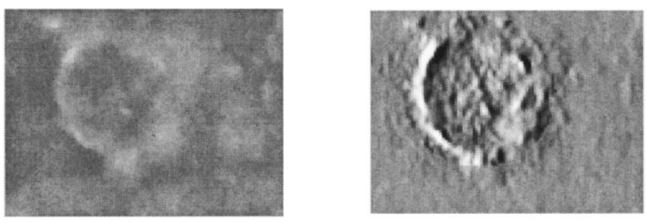

(*a*) (*b*)

Fig. 4 (*a*) Still image of a bubble from high-speed video; (*b*) enhanced image of the still image by using a Sobel filter technique

Table 3 Experimental bubble parameters and heat fluxes

$q'' = 40$ W/cm^2	TG0.3 nozzle	TG0.4 nozzle	TG0.6 nozzle
N (experimental, 1/cm^{2}s)	2,088,000	4,443,000	8,249,000
N_{cal} (= $1/[\pi d_p^2 \tau/4]$, 1/cm^{2}s), Eq. (4)	1,860,000	4,390,000	6,170,000
d_p (μm)	282	205	181
τ (ms)	0.86 (50 % of τ_{cyc})	0.69 (50 % of τ_{cyc})	0.44 (44 % of τ_{cyc})
τ_w (ms)	0.80	0.70	0.63
$\tau_{w,cal}$ (=$4/[\pi d_p^2 N]$, ms), Eq. (3)	0.76	0.69	0.47
$\tau_{cyc} = \tau + \tau_w$ (ms)	1.68	1.39	1.07
n_b (1/cm^2)	1,000	2,400	2,610
T_w (°C)	65.0	63.0	62.0
Nucleate Heat Transfer (W/cm^2)	18.0	20.0	19.0
$q'' = 50$ W/cm^2			
	TG0.3 nozzle	TG0.4 nozzle	TG0.6 nozzle
N (experimental, 1/cm^{2}s)	2,088,000	4,443,000	8,249,000
N_{cal} (= $1/[\pi d_p^2 \tau/4]$, 1/cm^{2}s), Eq. (4)	1,930,000	5,570,000	10,700,000
d_p (μm)	268	202	175
τ (ms)	0.92 (53 % of τ_{cyc})	0.56 (44 % of τ_{cyc})	0.39 (38 % of τ_{cyc})
τ_w (ms)	0.80	0.70	0.63
$\tau_{w,cal}$ (=$4/[\pi d_p^2 N]$, ms), Eq. (3)	0.84	0.71	0.50
$\tau_{cyc} = \tau + \tau_w$ (ms)	1.72	1.26	1.02
n_b (1/cm^2)	1,400	2,900	2,990
T_w (°C)	67.0	65.5	63.0
Nucleate Heat Transfer (W/cm^2)	24.0	25.0	21.0
$q'' = 60$ W/cm^2			
	TG0.3 nozzle	TG0.4 nozzle	TG0.6 nozzle
N (experimental, 1/cm^{2}s)	2,088,000	4,443,000	8,249,000
N_{cal} (= $1/[\pi d_p^2 \tau/4]$, 1/cm^{2}s), Eq. (4)	1,670,000	5,770,000	10,300,000
d_p (μm)	282	195	174
τ (ms)	0.96 (56 % of τ_{cyc})	0.58 (53 % of τ_{cyc})	0.41 (45 % of τ_{cyc})
τ_w (ms)	0.75	0.50	0.50
$\tau_{w,cal}$ (=$4/[\pi d_p^2 N]$, ms), Eq. (3)	0.76	0.70	0.51
$\tau_{cyc} = \tau + \tau_w$ (ms)	1.71	1.08	0.91
n_b (1/cm^2)	1,600	3,500	4,040
T_w (°C)	69.5	67.0	66.0
Nucleate Heat Transfer (W/cm^2)	30.0	32.0	31.0

interest (e.g., at puncturing, at each time step during bubble growth, ... etc.). The value of n_b was the averaged result of over 100 images taken at 1 mm×1 mm areas throughout the heater. In practice, the replay of a series of video images similar to that shown in Figure 4(*a*) could be more clearly seen than the still frame. The growth and departure of bubbles could then be seen from the replay. Due to the framing rate, the temporal resolution and the uncertainty were 0.125 ms. A typical bubble was punctured between the fifth and the sixth frames (i.e., between 0.625 ms and 0.75 ms).

The playback of the high-speed video record also helped to qualitatively identify secondary nuclei, as described below. It is assumed that the secondary nuclei did not become attached to the surface and would flow with the speed of the liquid flow. The typical fluid velocity assuming a uniform flow was estimated to be 20–38 cm/s for nozzle conditions in Table 2. In contrast, the velocity associated with the surface nuclei should be equal to zero or small compared to the fluid velocity due to the unsteadiness of the turbulent flow field. As N was increased from 2.1×10^6/cm^{2}s to 8.2×10^6/cm^{2}s (i.e., from TG0.3 to TG0.6), the speed with which bubbles moved was found to increase. Furthermore the number of bubbles moving with high speed also increased with increasing N. These results suggest that the number of secondary nuclei increase with the number flux of the liquid droplets. It is cautioned that the velocity with secondary nuclei movement varied over a wide range, as there is a velocity distribution within the thin liquid layer and the secondary nuclei might penetrate at different depth into the layer.

Results and Discussion

Secondary Nucleation. The importance of secondary nucleation is discussed here based on the bubble parameters shown in Table 3. It is noted that all values of droplet and bubble parameters in Table 3 are averages from many observations, as discussed in the Experiment section. First of all, it is useful to check whether the bubble number density agrees with some fundamental findings of pool boiling studies. Referring to Table 3, one finds that for each of the three nozzles (i.e., three given values of N), as T_w was increased, n_b increased. For example, as T_w was increased from 62°C to 66°C under the same spray conditions generated by the TG0.6 nozzle, n_b increased from 2610/cm^2 to 4044/cm^2. Similar observations can be made for the other two nozzles. This agrees with the pool boiling result that the nucleation site density increases with surface superheat. Nevertheless, these values of n_b are significantly higher than those found in pool boiling using the same liquid, FC-72 [9]. This increase over pool boiling is believed to result from secondary nucleation, as discussed in the following.

It is noted from Table 3 that as N was increased for a given value of q'', the bubble density (n_b) increased. For $q''=40$ W/cm^2, as N was increased from approximately 2.1×10^6/cm^{2}s to 8.2×10^6/cm^{2}s, the value of n_b increased by a factor of approximately 2.5 from 1000/cm^2 to 2600/cm^2. Similar factors of increase can be seen for $q''=50$ W/cm^2 and 60 W/cm^2 (Table 3). It is further noted from Table 3 that, for a given value of q'', as N was increased from approximately 2.1×10^6/cm^{2}s to 8.2×10^6/cm^{2}s, the surface superheat (ΔT) decreased by 3–4K for the three values of heat flux. It is well known for pool boiling that n_b is a strong increasing function of ΔT. The present results seem contradictory because n_b increased with decreasing ΔT. The reason for this is that for a given q'', increasing N leads to an increase in n_b and h, and thus lowers ΔT. This can only be explained by secondary nucleation. The importance of secondary nucleation has been suggested for thin film boiling [1] and spray

cooling [5]. However, the relative numbers of the surface and secondary nuclei have not been quantified.

In a previous study of FC-72 pool boiling on the same heater [9], the nucleation site density at a surface temperature of 68°C and with $q''=10\ \mathrm{W/cm^2}$ was found to be approximately $900/\mathrm{cm^2}$. For the TG0.4 nozzle with $q''=60\ \mathrm{W/cm^2}$ and similar surface temperature (67°C), the bubble density n_b was approximately $3500/\mathrm{cm^2}$. If T_w determines n_b, then the value of n_b in spray cooling should be approximately the same as that in pool boiling. The result suggest the importance of secondary nuclei brought into the thin liquid film by spray droplets.

For $q''=60\ \mathrm{W/cm^2}$, the bubble density in fact increased from approximately $1600/\mathrm{cm^2}$ to $4040/\mathrm{cm^2}$ as N was increased from $2.1\times10^6/\mathrm{cm^2s}$ to $8.2\times10^6/\mathrm{cm^2s}$ and as T_w decreased from 69°C to 66°C (Table 3). It is believed that as N was increased, the number of secondary nuclei also increased. For further evidence, consider $T_w=63$°C. At this temperature, the TG0.4 nozzle with $q''=40\ \mathrm{W/cm^2}$ and the TG0.6 nozzle with $q''=50\ \mathrm{W/cm^2}$ generated a bubble density of $2400/\mathrm{cm^2}$ and $2990/\mathrm{cm^2}$, respectively. Again, a larger N ($8.2\times10^6/\mathrm{cm^2s}$) generated a larger n_b ($2990/\mathrm{cm^2}$). Comparing the TG0.3 nozzle with $q''=50\ \mathrm{W/cm^2}$ and the TG0.4 nozzle with $q''=60\ \mathrm{w/cm^2}$ (i.e., T_w was the same at 67°C, although coincidental), one finds the larger N ($4.4\times10^6/\mathrm{cm^2s}$ versus $2.1\times10^6/\mathrm{cm^2s}$) to generate a larger n_b ($3500/\mathrm{cm^2}$ versus $1400/\mathrm{cm^2}$). Such increases in n_b with T_w fixed while N was increased are mostly due to the increase in secondary nuclei. It should be noted, however, that n_b does not increase proportionally with N.

The value of n_b is not only a function of N, either. Depending on the thermal environment that a secondary nucleus is in, it may not grow or may even collapse. Consider the case of TG0.6 nozzle (i.e., N is fixed at $8.2\times10^6/\mathrm{cm^2s}$). As q'' was increased from 40 $\mathrm{W/cm^2}$ to 60 $\mathrm{W/cm^2}$, n_b increased from 2610 to 4040. Note that for the corresponding change in q'', T_w increased from 62.0 K to 66.0 K. With $T_w=66.0$ K, the thermal environment is expected to be more favorable for secondary nuclei, especially the smaller ones, to survive and grow and, thus, for a larger value of n_b. This reasoning is qualitative since the turbulent temperature field within the liquid film is not known at the present time.

The effects of N on n_b can further be illustrated in the following. It is noted from Table 3 that a large T_w or a large N can yield high values of n_b. For TG0.3 nozzle, as T_w was increased from 65°C to 69.5°C (as a result of increasing the heat flux), n_b increased from $1000/\mathrm{cm^2}$ to $1600/\mathrm{cm^2}$. Similar observations can be made for the other two nozzles. Such increases in n_b can be attributed to the increased active surface nucleation sites, as a result of increase in T_w, and the favorable thermal environment, as just discussed above. While keeping q'' fixed, n_b increased as N was increased, although T_w was decreased (see each case of the three heat fluxes in Table 3). Such increases in n_b cannot result from an increase in activation of surface sites, as a decreased T_w would suggest otherwise. It can be concluded that n_b increases with increasing N and that in the present study increasing N can more than compensate the effect of decreasing T_w.

The following describes the estimation of the fraction of the bubbles that are caused by secondary nucleation. Results of Table 3 were used. The estimation is then compared with the results by direct observation of moving bubble by the high-speed photography described in the Experiment section. In the above-mentioned pool boiling study [9], $n_b=900/\mathrm{cm^2}$ at $T_w=68$°C. This bubble site density of pool boiling is due entirely to surface nucleation. By comparison, the percentage of secondary nuclei of the present study can be estimated for similar surface temperatures. For example, consider the TG0.6 nozzle with $q''=60\ \mathrm{w/cm^2}$. Under this condition, $T_w=66$°C, the density of surface nuclei is expected to be less than $900/\mathrm{cm^2}$ while the total bubble density is $4040/\mathrm{cm^2}$ (see Table 3). Thus, secondary nuclei comprised at least 80 percent of all the observed bubbles because with $T_w=66$°C, fewer than 900 of the 4040 bubbles are surface nuclei.

More estimations can be done by comparing the conditions of the TG0.3 nozzle with $T_w=67$°C and the TG0.4 nozzle with $T_w=67$°C (again, see Table 3). The former has $n_b=1400/\mathrm{cm^2}$ while the latter has $3500/\mathrm{cm^2}$. At $T_w=67$°C, the number of surface nuclei should be smaller than $900/\mathrm{cm^2}$ found for pool boiling with $T_w=68$°C. One can say that the percentage of the bubbles due to secondary nucleation for the TG0.4 nozzle with $T_w=67$°C is at least 74 percent (i.e., 2600/3500).

The playback of the high-speed video record, described in the Experiment section, qualitatively supports above estimation. It can therefore be concluded that secondary nuclei can account for as much as 74 percent and 80 percent of all nuclei in spray cooling using TG0.4 and TG0.6 nozzles, respectively. Similarly, the fraction for TG0.3 can be estimated to be approximately 40 percent using Table 3.

During the course of this study, cold experiment without heating the heater was conducted. Under this condition, bubbles observed were generated by the spray droplets impacting the liquid film and were therefore ''secondary'' nuclei. However, these bubbles did not grow in size as in the heat transfer experiment.

Bubble Growth. The typical average bubble size versus time for $q''=40\ \mathrm{W/cm^2}$, 50 $\mathrm{W/cm^2}$, and 60 $\mathrm{W/cm^2}$ is shown in Figure 5(*a*), 5(*b*), and 5(*c*), respectively. Substantial scatter of the data can be seen, as indicated by the error bars in these figures, which represent ± one standard deviation within the mean bubble diameter. This is believed to be due to the experimental uncertainty and the turbulent temperature field resulting from the impact of randomly arriving droplets. The averaged growth shown by the solid lines in Fig. 5 was similar to that in pool boiling; the solid line is a curve fit of $t^{1/2}$, which was also observed in FC-72 pool boiling in an earlier study [9]. This suggests that the bubble growth in spray cooling is also in the heat transfer-controlled regime. According to this scaling, the longer a bubble lasts, the more heat it will remove from the nucleation site, as the bubble volume scales as $t^{3/2}$. More importantly, the bubble removes heat at an increasing rate that scales as $t^{1/2}$ (i.e., the time derivative of $t^{3/2}$). It was noted earlier that the bubble number density in spray cooling is significantly larger than in pool boiling for similar surface superheat. Spray cooling therefore yields larger heat fluxes than pool boiling.

It is interesting to note that the bubble growth rate in spray cooling is comparable to that in pool boiling. Referring to Figures 5(*a*), 5(*b*), and 5(*c*), the average bubble size is 200 μm for $t\approx0.5$ ms. In pool boiling using the same liquid, experimental setup, and heater, a similar result was obtained for $q''=4\ \mathrm{W/cm^2}$ (Fig. 8 in Ref. [9]).

The Heat Transfer Curve. The q'' versus ΔT curve using the three spray nozzles is shown in Fig. 6. It can be seen that the slope of the curve (i.e., the heat transfer coefficient h) increases with N, with the TG0.6 nozzle providing the largest N and h. Similarly, values of CHF for the three spray nozzles are in the descending order of TG0.6, TG0.4, and TG0.3, equaling 80 $\mathrm{W/cm^2}$, 70 $\mathrm{W/cm^2}$, and 67 $\mathrm{W/cm^2}$, respectively. At CHF, h_c for the three nozzles can be found to be approximately 64,000 $\mathrm{W/m^2K}$, 58,300 $\mathrm{W/m^2K}$, and 51,500 $\mathrm{W/m^2K}$. The results of Fig. 6 indicate that increasing N helps to remove heat from the surface more efficiently, i.e., the same amount of heat is removed at a smaller surface superheat. This trend and the heat transfer mechanisms will be further discussed below.

Bubble Puncturing by Spray Droplets. Table 3 shows the bubble diameter at puncture (d_p), bubble lifetime (τ), waiting time (τ_w), bubble site density (n_b), surface superheat, and heat transfer due to nucleate boiling using three different nozzles (i.e., three values of droplet number flux) under three values of heat

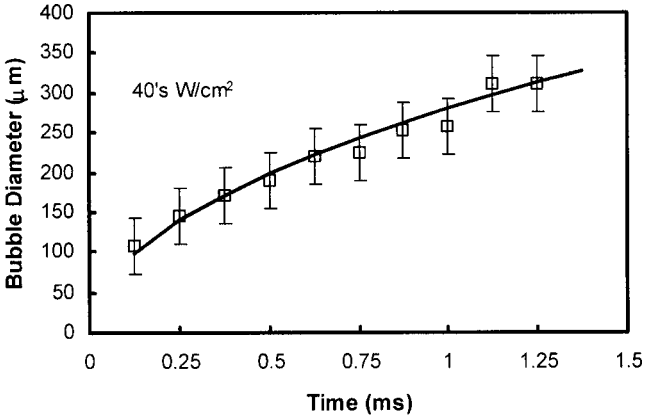

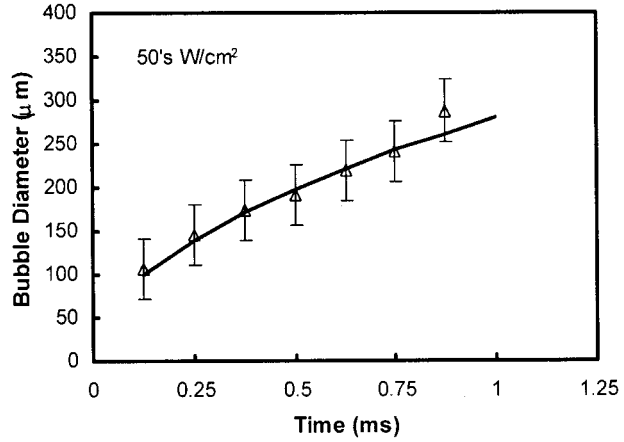

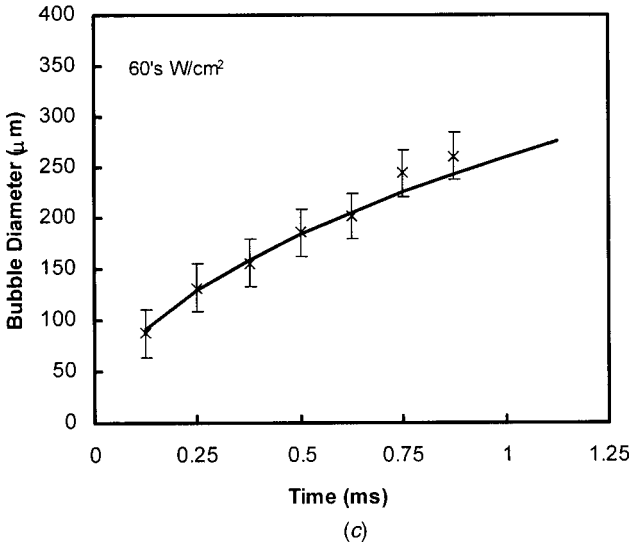

Fig. 5 Bubble size versus time for (*a*) 40 W/cm^2, (*b*) 50 W/cm^2, and (*c*) 60 W/cm^2. Note that the error bars denote one standard deviation and that the curves represent $t^{1/2}$ scaling.

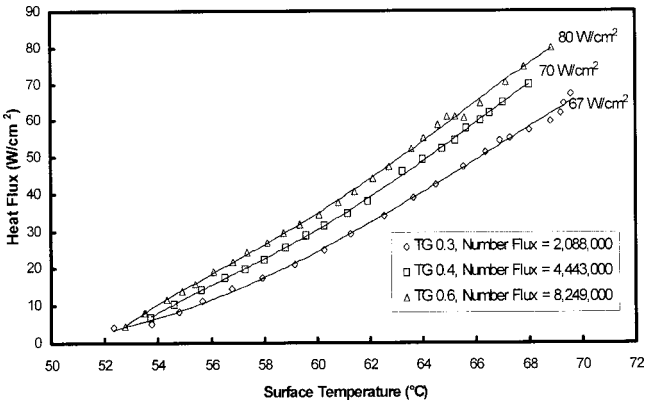

Fig. 6 Heat transfer curves for three heat fluxes. Note that the values of CHF are 67 W/cm^2, 70 W/cm^2, and 80 W/cm^2 for $N=2.1\times10^6$/cm^{2}s, 4.4×10^6/cm^{2}s, and 8.2×10^6/cm^{2}s, respectively.

flux. It is noted that the values of d_p, τ, and τ_w are averaged results from tracking several hundred bubbles for each of the nine combinations of the nozzle and q''. The bubble lifetime (τ) is the period spanning from the inception of a bubble to its disappearance by puncturing, while τ_w is time spent from its disappearance until the next inception on the same site. The life cycle of a bubble (τ_{cyc}) can be defined as the time lapse between inceptions of two consecutive bubbles on the same nucleation site. Therefore, $\tau_{cyc}=\tau+\tau_w$. It is noted that no differentiation was made between the surface and the secondary nuclei in reporting d_p, τ, and τ_w. From Table 3, the following observations can be made.

For a given value of q'', as N was increased, both d_p and τ decreased. Take the case of $q''=40$ W/cm^2 (shown in Table 3) for example. As N was increased from approximately 2.1×10^6/cm^{2}s to 8.2×10^6/cm^{2}s, the values of d_p and τ decreased from 282 μm to 181 μm and 0.86 ms to 0.44 ms, respectively. Decreases in d_p and τ while increasing N also can be observed for $q''=50$ w/cm^2 and 60 W/cm^2, as seen in Table 3. These results are expected because a larger N means more droplets arriving at the heater surface and leads to more frequent puncturing of bubbles per unit time. Values of τ listed in Table 3 are more than an order of magnitude smaller than that during pool boiling using the same liquid on the same heater. In pool boiling with q'' at 1/3 and 1/2 of the CHF, the bubble lifetime τ is approximately 17 ms and 6 ms, respectively [9].

The value of τ_{cyc} also decreases with increasing N. For example, consider $q''=40$ W/cm^2. As N was increased from 2.1×10^6/cm^{2}s to 8.2×10^6/cm^{2}s, τ_{cyc} decreased from 1.68 ms to 1.07 ms. Similar decreases in τ_{cyc} as a result of increasing N also can be seen for $q''=50$ W/cm^2 and 60 W/cm^2. A cross examination of values of τ_{cyc} in Table 3 reveals that they are nearly equal for a given N, within the experimental uncertainty. The values of τ_{cyc} for $N=2.1\times10^6$/cm^{2}s and 8.2×10^6/cm^{2}s are approximately 1.68 ms and 1.02 ms, respectively, while that for $N=4.4\times10^6$/cm^{2}s is somewhat more spread out, between 1.08 ms and 1.39 ms. Combined with the above observations, it can be concluded that (1) spray droplets play an important role in bubble growth dynamics, and (2) that they significantly shorten the lifetime, the waiting time and the life cycle of a bubble compared to those in pool boiling.

The waiting time in spray cooling decreases with T_w, as opposed to pool boiling in which it increases as T_w decreases [30]. As discussed earlier, many of the nuclei observed are secondary nuclei. They are brought into the liquid film and near the heater surface by impinging droplets, unlike the surface nuclei in pool boiling. As N was increased, the number of secondary nuclei increased while T_w decreased (see Table 3) due to the enhanced turbulent cooling. Consider $q''=60$ W/cm^2 for example. As N is increased from 2.1×10^6/cm^{2}s to 8.2×10^6/cm^{2}s, τ_w decreases from 0.75 ms to 0.41 ms. The bubbles are not generated due to surface superheat, but are introduced by impinging droplets; the frequency of bubble generation increases with N. If one assumes that each droplet entrains one secondary nucleus, then the frequency with which secondary nuclei arrives at an area is equal to

that occupied by a bubble at puncture (i.e., $\pi d_p^2/4$), is equal to $\{N(\pi d_p^2/4)\}$. Therefore, the time it takes for the arrival of a secondary nuclei over the area ($\pi d_p^2/4$) is

$$\tau_{w,\mathrm{cal}} = 4/(\pi N d_p^2). \tag{3}$$

Values of $\tau_{w,\mathrm{cal}}$ are listed in Table 3. The agreement with the experimental results of τ_w is very encouraging. This suggests that the waiting time thus defined in spray cooling is different from that in pool boiling. In pool boiling, the waiting time is that period during which the rewetting fluid acquires the necessary superheat to start a nucleus after the bubble departs from the immediate past cycle. In spray cooling, the secondary nuclei were brought into the liquid layer at a statistically averaged time interval. It should be noted that each droplet might bring more than one secondary nucleus into the liquid film. However, some (or even all) of them may not survive and grow because of the unfavorable local condition, as discussed above. Therefore, some droplets may in effect not entrain any nucleus, as it cannot be observed during the experiment. Further studies are warranted to quantitatively resolve this issue.

Impinging droplets played a major role in puncturing the bubble, as demonstrated by the following analysis. Assuming that that each droplet hits and punctures one bubble, the number of droplets arriving at the heater surface is equal to

$$N_{\mathrm{cal}} = 4/(\pi d_p^2 \tau). \tag{4}$$

The results of N_{cal} (also shown in Table 3) are within approximately ± 25 percent of those experimentally determined values of N. It is reasonable to say that some bubbles rupture without droplet action (e.g., bubbles that have grown beyond the free surface of the liquid film and rupture by themselves [5]), resulting in overestimation of the droplet number flux. On the other hand, some droplets may impinge on the liquid film without rupturing any bubbles and the droplet number flux would thus be underestimated. These two opposing factors appear to have canceling effects, resulting in the encouraging agreement.

As a consequence of the above analyses, it can be concluded that the impinging droplet plays an important role in determining the lifetime and other characteristics of bubbles. It is thus expected to play a role in determining the heat flux, especially that part which depends on nucleation.

Contributions of Various Heat Transfer Mechanisms. The above results suggest that as n_b is increased, CHF and h_c increase. Since secondary nuclei make up the majority of nucleating bubbles, it is desirable to determine whether nucleate boiling is the dominant factor in spray cooling that ultimately decides the total heat flux, at values near or less than that of CHF. Knowing n_b, τ_{cyc}, and d_p, the amount of the liquid vaporized per unit time and per unit area and, therefore, the heat flux can be calculated. The results are shown in Table 3.

It can be seen from Table 3 that as q'' was increased from 40 W/cm^2 to 60 W/cm^2, the contribution from nucleate boiling remained around 50 percent. Besides nucleate boiling, convection heat transfer (as a result of fluid flow across the heater and off its edge) and direct evaporation from the liquid surface account for the rest of the heat flux. These two latter modes of heat transfer also should combine to contribute 50 percent to q''. This finding suggests that for the present study, further increasing N beyond 2.1×10^6/cm^{2}s does not help to increase the relative contribution by nucleate boiling. This might remain true near CHF, as indicated by the result of $N=2.1\times10^6$/cm^{2}s and $q''=60$ W/cm^2 (i.e., TG0.3 nozzle, for which CHF equals 67 W/cm^2; see Fig. 6).

It is worth mentioning that both the surface and secondary nuclei contribute to the heat transfer. As discussed earlier, both types of bubbles grow to similar sizes and should therefore contribute a similar amount of heat transfer on a per bubble basis. Since the secondary nuclei constitute up to 85 percent of all bubbles, they may therefore contribute as much as 40 percent of the total heat flux. As CHF is approached and N is further increased, the contribution from secondary nucleation is expected to increase. However, the present results would suggest that secondary nucleation would most likely contribute no more than 50 percent to the total heat flux. A possible explanation for the fixed contribution by nucleate boiling and the other two modes is given as follows.

As N is increased, both τ and d_p decreased. Since $d \propto t^{1/2}$, $d_p \propto \tau^{1/2}$ and the vapor volume when punctured is $\propto \tau^{3/2}$. Therefore, as N is increased, the phase-change heat transfer due to each bubble over its lifetime decreases. However, this decrease is compensated by the increased n_b as a result of increasing N. Turbulent mixing and h are also enhanced as N is increased. However, this enhancement may be counteracted by the decrease in T_w as a result of the impinging droplets. Therefore, the net heat transfer due to convection and to direct evaporation remains relatively constant as N is varied by a factor of four.

The relative contribution of convection heat transfer and the direct evaporation is not known. However, they may be estimated as follows. For the current purpose, it is relevant to compare the time scales of conduction and flow over the heater surface. The molecular conduction time scale (τ_{cond}) across the thin liquid film is $\tau_{\mathrm{cond}} \approx \delta^2/\alpha_l$, where δ is the film thickness and α_l is the thermal diffusivity of the FC-72 liquid ($\alpha_l = k_l/\rho_l C_{p,l} \approx 3 \times 10^{-8}$ m^2/s, where $k_l = 5.5\times10^{-2}$ W/mK, $\rho_l = 1680$ kg/m^3, and $C_{p,l} = 1100$ J/kgK are the thermal conductivity, density, and heat capacity of the FC-72 liquid, respectively). δ is calculated as $Q_i/(Pv)$, where Q_i, P, and v are the volume flow rate over the heater surface, the perimeter of heater (i.e., 3.6 cm as shown in Fig. 2), and the fluid velocity within the liquid film, respectively. The velocity was determined from the high-speed photography as the velocity of the bubbles. The velocities and liquid film thickness were approximately (20 cm/s, 212 μm), (29 cm/s, 297 μm), and (38 cm/s, 409 μm) for TG0.3, TG0.4, and TG0.6 nozzles, respectively. Therefore, $\tau_{\mathrm{cond}} \approx 1.5$ seconds, 2.95 seconds, and 5.58 seconds for TG0.3, TG0.4, and TG0.6 nozzles, respectively. Due to the strong mixing caused by droplet impingement, the effective (or turbulent) thermal conductivity, k_{eff}, can be as much as 40 times of the molecular (or laminar) value. Therefore, $\tau_{\mathrm{cond,eff}} \approx 0.04-0.14$ seconds.

The residence time scale (τ_{res}) is determined by the flow velocity within the liquid film. Since the half width of the heater is 0.5 cm, $\tau_{\mathrm{res}} \approx 0.025$ seconds, 0.017 seconds, and 0.013 seconds for TG0.3, TG0.4 and TG0.6 nozzles, respectively. When the conduction and residence time scales are of the same order of magnitude the contributions from these two modes are expected to be equally important. In the present study, as the flow rate was increased (as the nozzle was varied from TG0.3 to TG0.4, and then to TG0.6), the relative contribution from the conduction mode decreased. For the TG0.3 nozzle, the time scales are indeed on the same order (0.04 seconds vs. 0.025 seconds). The residence time scale is an order of magnitude smaller than that of conduction for the TG0.6 nozzle (0.013 sec versus 0.14 sec). For the TG0.6 nozzle the time required for the fluid to be convected is more than 10 times shorter than that required for the heat to be conducted to the free surface of the liquid film for direct evaporation.

The importance of secondary nucleation in contributing to the heat transfer can further be revealed by cross-examining the results of Fig. 6 and of Table 3. The heat transfer curve is not a unique function of T_w, unlike pool boiling over a given surface. It depends on the value of N. As shown in Fig. 6, for a given value of T_w, there are three values of q''; similarly, for a given value of q'', there are three values of T_w. For a given value of q'' in Fig. 6, T_w increases as N is decreased. As can be seen from Table 3, as N is decreased from 8.2×10^6/cm^{2}s to 2.1×10^6/cm^{2}s, T_w increases from 63.0 K to 67.0 K. Such a q''-T_w relation is not found in pool boiling, except possibly in the regime of hysteresis.

The above analysis should be considered qualitative. Further investigations are needed to obtain quantitative results. For example, the values of δ and k_{eff} need to be experimentally deter-

mined, which is not a trivial task and is not within the scope of the present study [31].

How Important is Early Bubble Removal? Increasing N shortens bubble cycle time (τ_{cyc}) and reduces the fraction of the cycle period for bubble growth (i.e., τ), as discussed above. Therefore, increasing N promotes early bubble removal. According to the finding in Refs. [19–22] (i.e., pool boiling studies), early bubble removal from the heater surface takes advantage of the efficient heat transfer by microlayer evaporation while avoids local dry-out at the later stage of bubble growth that reduces the efficiency. It was speculated that by removing bubbles early with spray droplets, heat transfer could be enhanced. However, present results do not appear to support such speculations. Present results suggest that the relative contribution of nucleate boiling as a result of bubble puncturing was not enhanced by early bubble removal, which is achieved by increasing the droplet flux (N). This is probably because secondary nuclei, unlike surface nuclei, do not attach to the heater surface. As they grow, no local dry-out results.

Because the majority of the nuclei are secondary, to increase n_b requires an increase in N. An increase in N enhances turbulent mixing that leads to enhancement of convection and direct evaporation heat transfer, as discussed earlier. An increase in N also leads to the puncturing of bubbles at smaller sizes at earlier stages of their growth. Consequently, it deprives the bubble's opportunity of achieving even higher rates of heat removal, but this was compensated by an increase in n_b, as discussed above. The overall effect of increasing N, therefore, should result in an increase in q'' for a given T_w. The present experiment was conducted by keeping q'' fixed while varying N. The result was a decrease in T_w, as mentioned earlier. This suggests no direct benefits of early bubble removal, but that increasing N increase the heat transfer coefficient.

The growth of secondary nuclei bears resemblance to bubble growth in extensive liquid pool, as suggested by the $t^{1/2}$ scaling of bubble diameter. A surface nucleus, whose growth depends on microlayer evaporation, also follows the $t^{1/2}$ scaling. For pool boiling, such a scaling ceases to hold when the microlayer dries out, followed by the ineffective vapor phase conduction. Typically, microlayer evaporation lasts over a period approximately 1/10 of the bubble lifetime (τ) [19–22]. The value of τ in FC-72 pool boiling is of the order of 17 ms [9]. Therefore, the surface nuclei would have to be removed approximately 1–2 ms after inception so that the locally dry area can be rewetted to enhance heat transfer. Bubbles in the present spray cooling investigation had a lifetime τ shorter than 1 ms (see Table 3), satisfying the early removal requirement. However, because there is no dry-out due to the secondary nucleation, no direct benefit of early bubble removal is seen, as mentioned above.

Since there is no microlayer dry-out mechanism for secondary nuclei, it appears advantageous for them to grow indefinitely to take full advantage of the increasing evaporation rate, which also scales as $t^{1/2}$. However, in spray cooling bubbles can be ruptured either upon reaching the free surface or by droplet impingement. In the present study, τ was found to be in the range of 0.4 ms to 0.7 ms, which is substantially shorter than that in pool boiling. As a consequence, increasing N acts to counter the benefits of increased n_b, resulting in a relatively constant contribution from nucleate boiling (at the above-mentioned 50 percent). This may help explain results from previous studies that CHF in spray cooling reaches a limit even if one continues to increase N beyond some critical value [5,7,13]. Although the dry-out mechanism does not exist for secondary nuclei, this comparison should serve to show that bubbles are removed in the present spray cooling prematurely. In fact, removing the secondary nuclei (by puncturing) at any stage of their growth should be considered premature. However, there does not appear to be an easy way to prolong the lifetime of as many secondary bubbles as possible without increasing N.

Concluding Remarks

Heat transfer mechanisms in spray cooling of a thin diamond heater by highly wetting FC-72 liquid were experimentally investigated. The FC-72 liquid was under saturated conditions at the nozzle exit. The following conclusions can be drawn.

1. The number of secondary nuclei was found to depend on the droplet flux (N) and the heater surface temperature (T_w). As much as 85 percent of the nuclei observed in the present study belong to this category under high heat flux (about 3/4 of CHF) conditions. Increasing N for a given heat flux leads to an increase in n_b. The concept of bubble waiting time (τ_w) in pool boiling is not applicable in spray cooling. The waiting time in spray cooling was found to be directly related to N.
2. Increasing N leads to the early removal of bubbles (surface and secondary). As N is increased, both the bubble cycle and lifetime are shortened. However, the fractional contribution of nucleate boiling to the total heat flux appeared to remain constant with increased N, at approximately 50 percent, in spite of the increasing bubble-removing ability. The accompanying effects with increasing N may be the increase of the heat transfer by convection and direct evaporation heat transfer as turbulent mixing is enhanced.
3. Early removal of bubbles does not lead to enhanced heat flux under the present experimental conditions, unlike what pool boiling results would suggest. This is believed due to the absence of microlayer dry-out phenomenon in secondary nucleation, which dominated over surface nucleation in the present spray cooling study.

Acknowledgment

This research has been supported by the National Science Foundation (NSF) Division of Chemical and Thermal Systems (Grant numbers CTS-9813959 and CTS-9616344). Mr. Phil Tuma of 3M Corporation assisted in providing the FC-72 fluid. Dr. Kurt Lin helped with processing the images in Fig. 4.

Nomenclature

CHF = critical heat flux
C_{pl} = Specific heat of liquid
d = bubble diameter
d_p = bubble diameter at puncture
d_{20} = surface-mean diameter
d_{32} = Sauter-mean diameter
h = convection heat transfer coefficient
h_c = convection heat transfer coefficient at CHF
h_{fg} = heat of evaporation
k_l = thermal conductivity of liquid
N = droplet flux
n = droplet number density
n_b = nucleation site density
Pr_l = Prandtl number of liquid
q'' = heat flux
P = perimeter of heater
Q = liquid flow rate at spray nozzle exit
Q_i = liquid flow rate on heater surface
t = time
T_{sat} = saturation temperature of liquid
T_w = surface temperature
T_∞ = liquid temperature far away from heater surface
v = droplet speed

Greek Symbols

α_l = thermal diffusivity of liquid
δ = liquid layer thickness
θ = half angle of spray cone
ρ_v = density of vapor

ρ_l = density of liquid
τ = bubble life time
τ_w = bubble waiting time
τ_{cyc} = bubble life cycle ($=\tau+\tau_w$)
τ_{cond} = conduction time scale
τ_{res} = residence time scale
ΔT = surface superheat ($=T_w-T_{sat}$)

References

[1] Mesler, R., and Mailen, G., 1977, ''Nucleate Boiling in Thin Liquid Films,'' AIChE J., **23**, pp. 954–957.
[2] Sigler, J., and Mesler, R., 1990, ''The Behavior of the Gas Film Formed Upon Drop Impact With a Liquid Surface,'' J. Colloid Interface Sci., **134**, pp. 459–474.
[3] Esmailizadeh, L., and Mesler, R., 1986, ''Bubble Entrainment With Drops,'' J. Colloid Interface Sci., **110**, pp. 561–573.
[4] Mesler, R., 1982, ''Research on Nucleate Boiling,'' *Chem. Eng. Education*, pp. 152–156.
[5] Chow, L. C., Sehembey, M. S., and Pais, M. R., 1997, ''High Heat Flux Spray Cooling,'' Annu. Rev. Heat Transfer, **8**, pp. 291–318.
[6] Nguyen, D., Chen, R.-H., and Chow, L. C., 2000, ''Effects of Heater Orientation and Confinement on Liquid Nitrogen Pool Boiling,'' J. Thermophys. Heat Transfer, **14**, pp. 109–111.
[7] Sehmbey, M. S., Chow, L. C., Hahn, O. J., and Pais, M. R., 1995, ''Effect of Spray Characteristics on Spray Cooling With Liquid Nitrogen,'' J. Thermophys. Heat Transfer, **9**, pp. 757–765.
[8] Chang, J. Y., and You, S. M., 1997, ''Boiling Heat Transfer Phenomena From Microporous and Porous Surfaces in Saturated FC-72,'' Int. J. Heat Mass Transf., **40**, pp. 4437–4447.
[9] Rini, D. P., Chen, R.-H., and Chow, L. C., 2001, ''Bubble Behavior and Heat Transfer Mechanism in FC-72 Pool Boiling,'' Exp. Heat Transfer, **14**, No. 1, pp. 27–44.
[10] Estes, K. A., and Mudawar, I., 1995, ''Comparison of Two-Phase Electronic Cooling Using Free Jets and Sprays,'' ASME J. Electron. Packag., **117**, pp. 323–332.
[11] Pais, M. R., Chow, L. C., and Mahefkey, E. T., 1992, ''Surface Roughness and Its Effects on the Heat Transfer Mechanism in Spray Cooling,'' ASME J. Heat Transfer, **114**, pp. 211–219.
[12] Sehmbey, M. S., Pais, M. R., and Chow, L. C., 1992, ''Effect of Surface Material Properties and Surface Characteristics in Evaporative Spray Cooling,'' J. Thermophys. Heat Transfer, **6**, pp. 505–512.
[13] Sehmbey, M. S., Chow, L. C., Hahn, O. J., and Pais, M. R., 1995, ''Spray Cooling of Power Electronics at Cryogenic Temperatures,'' J. Thermophys. Heat Transfer, **9**, No. 1, pp. 123–128.
[14] You, S. M., Simon, T. W., Bar-Cohen, A., and Hong, Y. S., 1995, ''Effects of Dissolved Gas Content on Pool Boiling of a Highly Wetting Fluid,'' ASME J. Heat Transfer, **117**, pp. 687–692.
[15] You, S. M., Simpson, T. W., and Bar-Cohen, A., 1997, ''Pool Boiling Heat Transfer With an Array of Flush-Mounted Square Heaters on a Vertical Surface,'' ASME J. Heat Transfer, **119**, pp. 17–25.
[16] Anderson, T. M., and Mudawar, I., 1989, ''Microelectronic Cooling by Enhanced Pool Boiling of a Dielectric Fluorocarbon Liquid,'' ASME J. Heat Transfer, **111**, pp. 752–759.
[17] Reed, S. J., and Mudawar, I., 1999, ''Elimination of Boiling Incipience Temperature Drop in Highly Wetting Fluids Using Spherical Contact With a Flat Surface,'' Int. J. Heat Mass Transf., **42**, pp. 2439–2454.
[18] Kopchikov, I. A., Veronin, G. I., Kolach, T. A., Labuntsov, D. A., and Lebedev, P. D., 1969, ''Liquid Boiling in a Thin Film,'' Int. J. Heat Mass Transf., **12**, 791–896.
[19] Moore, F. D., and Mesler, R. B., 1961, ''The Measurement of Rapid Surface Temperature Fluctuations During Nucleate Boiling of Water,'' AIChE J., **7**, pp. 620–624.
[20] Yu, C. L., and Mesler, R., 1977, ''A Study of Nucleate Boiling Near the Heat Flux Through Measurement of Transient Surface Temperature,'' Int. J. Heat Mass Transf., **20**, pp. 827–840.
[21] Cooper, M. G., and Lloyd, A. J. P., 1969, ''The Microlayer in Nucleate Pool Boiling,'' Int. J. Heat Mass Transf., **12**, pp. 895–913.
[22] Cooper, M. G., 1969, ''The Microlayer and Bubble Growth in Nucleate Pool Boiling,'' Int. J. Heat Mass Transf., **12**, pp. 915–933.
[23] Monde, M., 1979, ''Critical Heat Flux in the Saturated Forced Convection Boiling on a Heated Disk With Impinging Droplets,'' Heat Transfer-Jpn. Res., **8**, pp. 54–64.
[24] Mudawar, I., and Estes, K. A., 1996, ''Optimizing and Predicting CHF in Spray Cooling of a Square Surface,'' ASME J. Heat Transfer, **118**, pp. 672–670.
[25] Estes, K. A., and Mudawar, I., 1995, ''Correlating of Sauter Mean Diameter and Critical Heat Flux for Spray Cooling of Small Surface,'' Int. J. Heat Mass Transf., **38**, pp. 2985–2996.
[26] Toda, S., 1972, ''A Study of Mist Cooling (1st Report: Investigation of Mist Cooling),'' Heat Transfer-Jpn. Res., **1**, pp. 54–64.
[27] Yao, S. C., 1994, ''Dynamics of Heat Transfer of Impacting Sprays,'' Annu. Rev. Heat Transfer, **5**, pp. 351–382.
[28] *Product Manual*, 98-0212-0282-9, 1997, 3M Corporation.
[29] You, S. M., Simon, T. W., Bar-Cohen, A., and Hong, Y. S., 1995,''Effects of Dissolved Gas Content on Pool Boiling of a Highly Wetting Fluid,'' ASME J. Heat Transfer, **117**, pp. 687–692.
[30] Carey, V. P., 1992, *Liquid-Vapor Phase-Change Phenomena*, Taylor and Francis, PA, p. 202.
[31] Yang, J., Chow, L. C., and Pais, M. R., 1992, ''Liquid Film Thickness and Topography Determination Using Fresnel Diffraction and Holography,'' Exp. Heat Transfer, **5**, pp. 239–252.

Turbulent Subcooled Boiling Flow—Experiments and Simulations

R. P. Roy
Fellow ASME
e-mail: roy@asu.edu

S. Kang

J. A. Zarate

Arizona State University,
Department of Mechanical and
Aerospace Engineering,
Tempe, AZ 85287-6106

A. Laporta
Electricité de France,
Departement Transferts Thermiques et
Aerodynamique,
Chatou, France

Experiments and simulations were carried out in this investigation of turbulent subcooled boiling flow of Refrigerant-113 through a vertical annular channel whose inner wall only was heated. The measurements used, simultaneously, a two-component laser Doppler velocimeter for the liquid velocity field and a fast-response cold-wire for the temperature field, and a dual-sensor fiberoptic probe for the vapor fraction and vapor axial velocity. In the numerical simulation, the two-fluid model equations were solved by the solver ASTRID developed at Electricité de France. Wall laws for the liquid phase time-average axial velocity and temperature were developed from the experimental data, and the turbulent Prandtl number in the liquid was determined from the wall laws. The wall laws and turbulent Prandtl number were used in the simulations. The wall heat transfer model utilized the measured turbulent heat flux distribution in the liquid. Results from the simulations were compared with the measurements. Good agreement was found for some of the quantities while the agreement was only fair for others. [DOI: 10.1115/1.1418698]

Keywords: Boiling, Flow, Turbulence, Two-Phase

Introduction

Turbulent boiling flow occurs in many important engineering equipment—for example, steam generators, nuclear reactors, and refrigeration systems. To improve the design and performance of these equipment, models of high fidelity must be available. Development of such models is possible only if the structure of the flow and the transport processes are understood well. Fundamental experiments can provide this understanding.

In turbulent subcooled boiling flow, the vapor phase is typically dispersed as bubbles in the liquid phase. The bubbles are generated at and depart from heated surfaces (channel walls) whose temperature is sufficiently higher than the local saturation temperature of the fluid. The turbulence plays crucial roles in the spatial distribution of the bubbles and in the transports of momentum and thermal energy in the liquid.

Previous fundamental experimental studies of subcooled bubbly boiling flow include those by Jiji and Clark [1], Dix [2], and Delhaye et al. [3]. A limited amount of information regarding the turbulent velocity and thermal fields in the flow can be found in Roy et al. [4,5]. There have been numerous experimental studies of the turbulent velocity field in isothermal bubbly gas-liquid flow—for example, Marié [6], Lance and Bataille [7], and Grossetéte [8].

The two-fluid model (Ishii [9], Drew [10], Dykhuizen et al., [11]) is an important tool for simulating turbulent boiling flow. In the model, each phase satisfies the conservation equations for mass, momentum, and thermal energy. The phases are coupled at the interface by the balance relations for mass, momentum, and thermal energy, Delhaye [12]. Closures must also be provided for a multitude of quantities. They include the turbulent stresses and turbulent thermal energy flux in the phases, the transfer rates of mass, momentum, and thermal energy at the interface, and the wall laws for time-average liquid velocity and temperature.

A turbulence model for two-phase dispersed flow was reported by Bel F'dhila and Simonin [13]. Turbulence in the continuous phase was predicted by a k-ε model in which additional terms were introduced in the two equations to account for the interaction between the phases. The dispersed phase turbulence was modeled by extending Tchen's theory on the dispersion of particles in homogeneous turbulence. Lopez de Bertodano et al. [14] reported on a k-ε model of turbulence for the liquid phase in isothermal bubbly air-water flow. In this model, the turbulent momentum diffusivity was calculated by linearly superposing the shear-induced and bubble-induced diffusivities.

More recently, Morel and Bestion [15] conducted a study of the multidimensional two-fluid model. A scaling analysis of the mass and momentum conservation equations, and of the k and ε equations was performed. Based on this analysis, equations for k and ε were proposed.

The liquid velocity boundary conditions in isothermal bubbly gas-liquid flow simulations have typically been based on the velocity wall law for single-phase flow in the absence of such a law for the gas-liquid flow. Marié et al. [16], observed that the viscous layer, the logarithmic region, and the wake region exist in turbulent bubbly air-water flow. The authors also suggested that the von Karman constant in the velocity wall law would be the same as for single-phase flow and that only the additive term would be different.

We have carried out experiments, modeling, and simulation of turbulent subcooled bubbly boiling flow through a vertical concentric annular channel. Only the inner wall of the channel was heated, creating a flow regime sufficiently downstream in the channel similar to that shown in Fig. 1. The measurements were made in this regime. The work is reported in the following arrangement: first, the experimental setup and the measurement instrumentation are described; next, the two-fluid model equations, key closure relations, and the CFD solver are described; and finally, the experimental and simulation results are presented and compared.

The Experimental Facility

Refrigerant-113 (R-113) was the working fluid in the experiments.

The Test Section. Figure 2 shows, schematically, the *measurement section* of the 3.66 m long annular channel. The inner tube of the channel is of 304 stainless steel (i.d.=14.60 mm, o.d. =15.78 mm). The outer tube of the 0.521 m long measurement section is made of optical quality quartz (i.d.=38.02 mm, o.d.

Contributed by the Heat Transfer Division for publication in the JOURNAL OF HEAT TRANSFER. Manuscript received by the Heat Transfer Division February 9, 2001; revision received July 9, 2001. Associate Editor: D. B. R. Kenning.

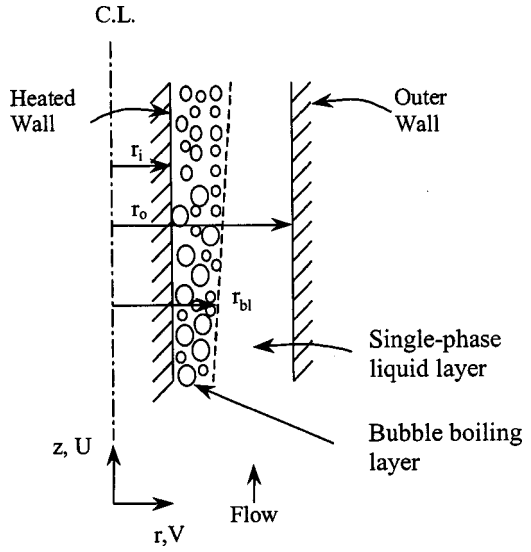

Fig. 1 Subcooled boiling flow in a vertical annular channel—the boiling layer and the all-liquid layer

=42.02 mm). The *measurement plane (m.p.)* was located 0.424 m (≈19 hydraulic diameters) downstream of the measurement section entrance, this entrance in turn being 1.56 m downstream of the beginning of the 2.75 m heated length. The inner stainless tube could be heated over the latter length by direct current. A 0.91 m unheated section was provided upstream of the heated length.

An anodized aluminum box with flat front and back quartz windows and a glass side window served as a jacket around a 15 cm length of measurement section with the m.p. located at about the box mid-height. The box was filled with liquid R-113 to alleviate laser beam refraction at the outer wall of the quartz tube.

The Laser Doppler Velocimeter. The two-component LDV system (TSI) consisted of a 100 mW Argon-Ion laser and a fiberoptic probe with 50 mm beam spacing and a backscatter light detector. A 130 mm focal length transmitting lens was used for the measurements reported here. This focal length is considerably shorter than the 261 mm length used for the measurements reported in Roy et al. [5]. In isothermal flow of liquid R-113, the LDV measuring volume was calculated to be an ellipsoid with minor axes (in the *r-z* plane) about 55 μm long and major axis (perpendicular to the *r-z* plane) about 290 μm long. The two beam pairs functioned in the coincidence mode, the window being in the 100–200 μs range (its value depending upon the fluid local axial velocity). The smaller measuring volume in the present set-up along with the appropriate coincidence window yielded better measurement of the streamwise turbulent shear stress in the liquid phase compared to that reported in Roy et al. [5]. The effects of measuring volume (m.v.) size and coincidence window on turbulence measurement has been reported by Kang et al. [17].

A three-dimensional traverse mechanism with a rotating stage served as the LDV probe mount. To locate the measuring volume at desired positions in the annulus, a beam steering mechanism was used with guidance from a beam tracing algorithm. Two types of seed particles were used in the fluid, separately: 3–7 μm diameter white nylon particles, and 8–12 μm diameter hollow glass spheres, their Stokes numbers being $\sim 10^{-4}$ and $\sim 10^{-3}$, respectively. No distinction was found between the liquid velocity measurements with the two types of seed particles. However, when the cold-wire was inserted into the flow, the nylon seed particles tended to adhere to the wire since they softened in the boiling fluid. As such, the hollow glass spheres were used as seed particles for all measurements in which velocity and temperature were measured simultaneously.

The Cold-Wire. A 3.8 μm diameter tungsten wire measured the fluid temperature field. While the total wire length was 0.9 mm, only the 0.3 mm bare center segment was the active (temperature-sensing) length, the two side segments (each 0.3 mm long) having been coated with a 5 μm thick copper layer, Fig. 3. The wire was operated by a Temperature Module (TSI 1040), which fed a small constant current to the wire from a regulated power supply. The output signal was amplified by a Pacific Instruments amplifier prior to data acquisition.

The temporal response of the cold-wire in a particular fluid flow depends upon the thermal inertia of the wire, heat conduction from its ends to the relatively massive support prongs, and transport properties of the fluid. Wroblewski and Eibeck [18] suggested an analytical method to compensate for the first two effects. Adopting a similar approach, we employed an active phase-lead circuit for thermal inertia compensation and introduced a constant gain to correct for the end conduction. The time constant of the compensated cold-wire was measured *in situ* in single-phase liquid R-113 flow at the velocities of our interest and found to be 0.30 ± 0.02 ms (Kang et al. [19]).

Depending upon whether vapor or liquid surrounds the cold-wire at any particular time, it senses the corresponding phase temperature. Thus, when in the boiling layer, it becomes necessary to extract information about the individual phase temperatures from the signal. One method of doing this is to construct a PDF of the signal, then separate the PDF into two PDFs, one for the liquid phase and the other for the vapor phase (Roy et al. [4]). This was done with the cold-wire signal and good results were obtained. A second method is described briefly in the following paragraph.

Simultaneous Measurement of Local Velocity and Temperature in the Liquid. Several issues needed to be considered for this measurement. One was that the spanwise length of the LDV measuring volume and the cold-wire active length should be approximately equal. Another was the juxtaposition of the LDV m.v. and the active length of the cold-wire. They must be sufficiently close to provide the correct cross-correlation between the velocity and temperature fluctuations but, at the same time, not interfere with each other. Referring to Fig. 3, if the LDV m.v. is placed too close to the cold-wire, the latter will be felt by the m.v. as an obstruction to the flow and at least the mean axial velocity will become lower. A lesser problem (in the sense that this occurs at even smaller separation distance) is the heat-up of the cold-wire by the laser beams. In our case, an axial separation distance of 0.25 mm was found to be a good choice. For low velocity flows, it is also important to consider the time delay incurred by the fluid in flowing from the LDV m.v. location to the cold-wire location (200–500 μs for the present experiments). A delay circuit was introduced to provide the appropriate time delay in the temperature time series data. A multi-channel interface and a 16-bit data acquisition board were then used to acquire the velocity-temperature data simultaneously. The velocity and temperature data corresponding to the liquid phase were separated from the vapor phase data by means of a circuit designed to tag the Doppler bursts due to the vapor bubbles on the basis of the burst pedestal amplitude, Roy et al. [5]. The velocity-temperature data rate ranged from a low of about 30 per minute adjacent to the inner wall (high bubble population region) to a high of approximately 6000 per minute at the outer edge of the boiling layer. At each measurement location three data files were acquired, each file either 15 minutes long or containing 12,000 data points (whichever came first).

This simultaneous measurement technique was validated in heated single-phase liquid flow, Kang et al. [19], prior to its use in subcooled boiling flow.

The Two-Sensor Fiberoptic Probe. Measurements of the local vapor phase residence time fraction, time-average axial velocity, and bubble diameter were performed by means of this probe. The probe (Photonetics) featured two fiberoptic sensors whose tips had a characteristic size of 50 μm and were 1.78 mm apart.

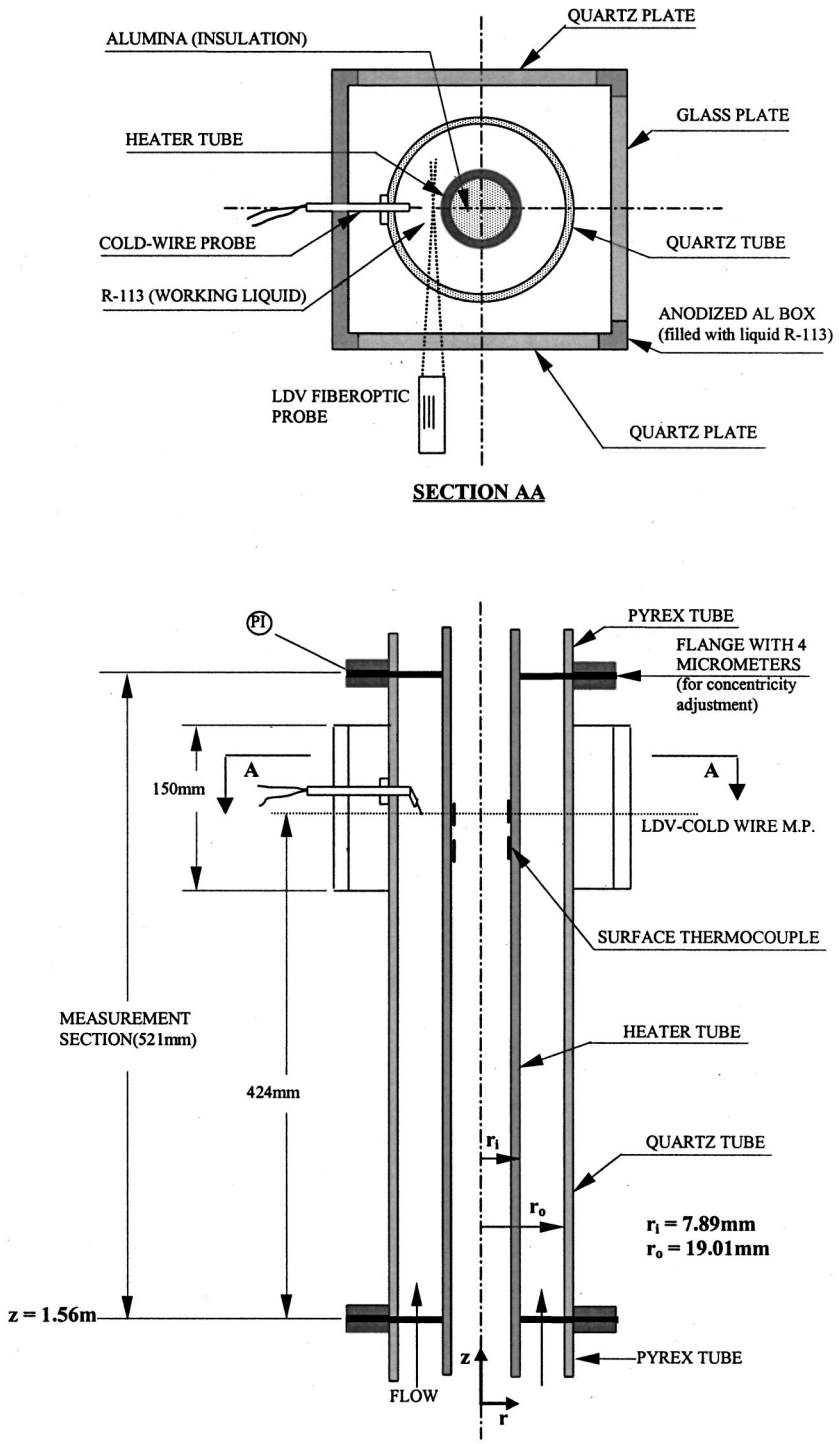

Fig. 2 The measurement section

Typical sensor signals were described in Roy et al. [4]. For each of the present measurements, a sampling time interval of 50 μs was used and 20,000 data points were acquired per sensor.

Selection of an optimal baseline (or threshold) voltage for the sensor signal is an important consideration. This was done in accordance with Cartellier [20]:

$$\frac{V_{\text{baseline}}-V_L}{V_G-V_L}=\left[1+\frac{\Sigma_{i=1}^{N}t_{mi}}{\Sigma_{i=1}^{N}t_{di}}\right]^{-1}, \tag{1}$$

where t_{mi} and t_{di} are the rise and fall times of the voltage pulse due to a vapor bubble. A value of 0.25 was chosen for this ratio based on scrutiny of the probe signals.

Other System Measurements. The dissolved air content of R-113 must be measured since air is highly soluble in liquid R-113 and its influence can be significant in boiling flow experiments. Prior to each experiment, degassing of the liquid inventory was performed and the residual air content measured by an Aire-

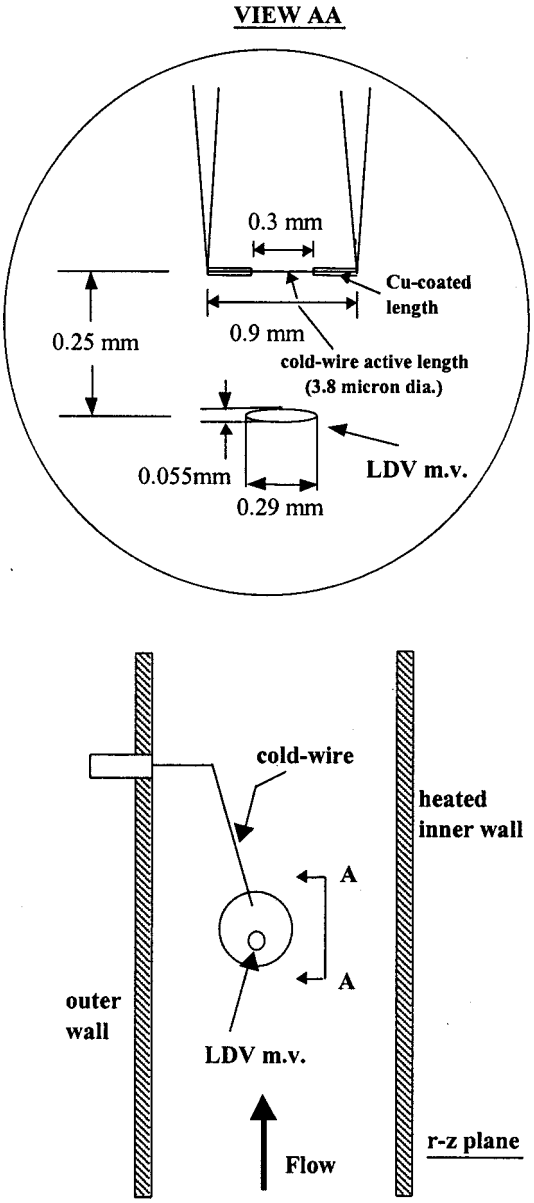

Fig. 3 Positioning of the cold-wire with respect to the LDV measuring volume

Ometer (Seaton-Wilson). For the experiments reported here, the residual air partial pressure was approximately 8 kPa out of a total pressure of 277 kPa at the measurement plane.

The pressure at the measurement plane was monitored by a test gauge (Omega, 0-1200 kPa range, 1.4 kPa resolution). The volumetric flow rate of liquid R-113 at the test section inlet was measured by a turbine flow meter (EG & G Flow Technology).

The Models and Simulation Approach

Two-Fluid Model

Conservation Equations. The local time-averaged conservation equations for phase *k*, neglecting temporal fluctuations in its density, are per unit volume of fluid:

Mass.

$$\frac{\partial(\alpha_k\rho_k)}{\partial t}+\frac{\partial(\alpha_k\rho_k\overline{U}_{k,j})}{\partial x_j}=\Gamma_k\,. \tag{2}$$

$\overline{U}_{k,j}$ is the time-average velocity (*j* component) of phase *k*. In the remainder of this paper, we have used *average* to indicate *time-average*.

Momentum.

$$\alpha_k\rho_k\frac{\partial\overline{U}_{k,i}}{\partial t}+\alpha_k\rho_k\overline{U}_{k,j}\frac{\partial\overline{U}_{k,i}}{\partial x_j}=-\alpha_k\frac{\partial\overline{P}_k}{\partial x_i}+\frac{\partial[\alpha_k(\tau_{k,ij}+\tau^T_{k,ij})]}{\partial x_j}+\alpha_k\rho_k g_i+I_{k,i}+\Gamma_k\overline{U}_{k,i}\,. \tag{3}$$

In this equation, $\overline{P}_k$, $\tau_{k,ij}$, and $\tau^T_{k,ij}=-\rho_k\overline{(u_iu_j)}_k$ are, respectively, the average thermodynamic pressure and the viscous and turbulent stress tensors. Also,

$$I_{k,i}+\overline{U}_{k,i}\Gamma_k=I'_{k,i}+(\overline{U}_{k,i}-\overline{U}_{\sigma,i})\Gamma_k\,, \tag{4}$$

where $I'_{k,i}$ represents the interfacial forces due to viscous and pressure effects acting on phase *k*, and $\overline{U}_{\sigma,i}$ is the average interface velocity. Assuming the magnitude of $(U_{k,i}-\overline{U}_{\sigma,i})$ to be small, it was neglected.

Thermal Energy.

$$\alpha_k\rho_k\frac{\partial\overline{H}_k}{\partial t}+\alpha_k\rho_k\overline{U}_{k,j}\frac{\partial\overline{H}_k}{\partial x_j}=-\frac{\partial(\alpha_k\overline{Q}_{k,j})}{\partial x_j}+\alpha_k\frac{\partial\overline{P}_k}{\partial t}+\frac{\partial[-\alpha_k\rho_k\overline{(hu_j)}_k]}{\partial x_j}+\Pi^H_k+\overline{H}_k\Gamma_k. \tag{5}$$

Here, $\overline{Q}_{k,j}=-\lambda_k\partial\overline{T}_k/\partial x_j$ is the average molecular thermal energy flux vector, $\rho_k\overline{(hu_j)}_k$ is the turbulent thermal energy flux (*j* component), and Π^H_k is the interfacial thermal energy transfer rate.

Interfacial Balance Conditions. The balance conditions for the exchanges of mass, momentum, and thermal energy between the liquid and vapor phases across the interface are well known and are not given here.

Closure Models.

Turbulent Stresses. The liquid phase turbulent stresses were modeled using the gradient transport approximation:

$$-\rho_L\overline{(u_iu_j)}_L=-\rho_L\left[-2\nu^t_L S_{L,ij}+\frac{2}{3}\delta_{ij}\nu^t_L S_{L,mm}+\frac{2}{3}\delta_{ij}k_L\right]. \tag{6}$$

Assuming that the stresses are the result of linear superposition of wall shear and bubble agitation effects, the turbulent momentum diffusivity, ν^t_L, was calculated as

$$\nu^t_L=\nu^t_{L,si}+\nu^t_{L,bi}\,. \tag{7}$$

The shear-induced diffusivity was obtained from the standard constitutive equation for single-phase turbulent flow:

$$\nu^t_{L,si}=C_\mu\frac{k^2_L}{\varepsilon_L}. \tag{8}$$

To calculate the bubble-induced diffusivity, the model of pseudo-turbulence proposed by Sato and Sekoguchi [21] was adopted:

$$\nu^t_{L,bi}=0.6\alpha_G D_b\overline{|\vec{u}_r|}, \tag{9}$$

where D_b is a representative vapor bubble diameter and $\overline{|\vec{u}_r|}$ is the average magnitude of the relative velocity vector. D_b was taken to be equal to the measured local most probable bubble diameter—the local Sauter mean diameter may be another option. If measurements are not available, a predictive correlation will have to be used.

The local vapor fraction appears as a multiplier on the right hand side of Eq. (9). The consequent steep radial profile of $\nu^t_{L,bi}$ near the heated inner wall occasionally gave rise to non-physical results—for example, for the average liquid temperature. To alle-

viate this problem, a local-average vapor fraction spanning three grid points was used in Eq. (9). A possible alternative would be to use a damping function for the bubble-induced diffusivity so that it decreases as the wall is approached. This function should be based on experimental measurement of near-wall axial turbulent shear stress in the liquid.

To determine $\nu^t_{L,si}$, the standard k-ε model of turbulence was adopted with interface-related terms added to each equation. The model equations are as follows:

Turbulent Kinetic Energy.

$$\alpha_L\rho_L\left[\frac{\partial k_L}{\partial t}+\overline{U}_{L,j}\frac{\partial k_L}{\partial x_j}\right]=\frac{\partial}{\partial x_j}\left[\alpha_L\left(\mu_L+\frac{\mu^t_L}{\sigma_k}\right)\frac{\partial k_L}{\partial x_j}\right]+\alpha_L P^k_L-\rho_L\alpha_L\varepsilon_L+\Pi^k_L \tag{10}$$

Dissipation Rate.

$$\alpha_L\rho_L\left[\frac{\partial \varepsilon_L}{\partial t}+\overline{U}_{L,j}\frac{\partial \varepsilon_L}{\partial x_j}\right]=\frac{\partial}{\partial x_j}\left[\alpha_L\left(\mu_L+\frac{\mu^t_L}{\sigma_\varepsilon}\right)\frac{\partial \varepsilon_L}{\partial x_j}\right]+\frac{\varepsilon_L}{k_L}[\alpha_L(C_{\varepsilon 1}P^k_L-C_{\varepsilon 2}\rho_L\varepsilon_L)+C_{\varepsilon 3}\Pi^k_L]. \tag{11}$$

Here, $P^k_L=-\rho_L(\overline{u_iu_j})_L\partial\overline{U}_{L,i}/\partial x_j$ is the production term, and Π^k_L is a source term due to liquid-vapor bubble interaction. The latter term was modeled as, Thai Van et al. [22]:

$$\Pi^k_L=\frac{\rho_G}{\rho_L+C_A\rho_L}\alpha_G\rho_L F_D[\overline{u_{L,i}u_{G,i}}-2k_L+\overline{U}_{d,i}\overline{U}_{r,i}], \tag{12}$$

where

$$F_D=\frac{3}{4}\frac{C_D}{D_b}|\vec{u}_r|. \tag{13}$$

$\overline{U}_{d,i}$ is a drift velocity, Simonin [23]. C_A, the added mass coefficient, was set equal to 0.5. The model of the covariance between the turbulent velocity fluctuations of the two phases, $\overline{u_{L,i}u_{G,i}}$, has been described by Thai Van et al. [22].

The values of the constants in the model are those that are used widely in the standard k-ε model for single-phase turbulent flow:

σ_k	σ_ε	C_μ	$C_{\varepsilon 1}$	$C_{\varepsilon 2}$
1.0	1.3	0.09	1.44	1.92

and $C_{\varepsilon 3}$ is equal to 1.2, Elgobashi and Abou-Arab [24].

The turbulent stresses in the vapor phase were also modeled using the gradient transport approximation:

$$-\rho_G(\overline{u_iu_j})_G=-\rho_G\left[-2\nu^t_G S_{G,ij}+\frac{2}{3}\delta_{ij}\nu^t_G S_{G,mm}+\frac{2}{3}\delta_{ij}k_G\right]. \tag{14}$$

The turbulent kinetic energy of the vapor phase, k_G, was calculated in terms of k_L. Additional details such as the determination of ν^t_G can be found in Bel F'dhila and Simonin [13].

Turbulent Thermal Energy Flux. For this closure, gradient transport was assumed and Reynolds analogy invoked between the transports of thermal energy and momentum:

$$\rho_k\overline{(hu_i)}_k=-\frac{\rho_k\nu^t_k}{\mathrm{Pr}^t_k}\frac{\partial\overline{H}_k}{\partial x_i}. \tag{15}$$

The basis for estimating the turbulent Prandtl number for the liquid phase, Pr^t_L, is stated later. For the vapor phase, a value of unity was prescribed for Pr^t_G.

The applicability of Reynolds analogy in turbulent bubbly boiling flow may be questioned. The alternative, of course, would be to provide separate equations for the turbulent thermal energy flux components.

Interfacial Momentum Transfer. $I'_{k,i}$ was modeled on the basis of the forces generated on a particle immersed in a fluid when there is a relative motion between the particle and the fluid. Only the drag, added mass, and turbulent pressure force were considered, Simonin and Viollet [25].

Interfacial Thermal Energy Transfer. The interfacial heat transfer coefficient on the liquid side, h_{IL}, was calculated by means of the Nusselt number correlation for bubble condensation suggested by Zeitoun et al. [26]:

$$\mathrm{Nu}_b=2.04\,\mathrm{Re}_b^{0.61}\,\alpha_G^{0.328}\,\mathrm{Ja}^{-0.308}. \tag{16}$$

Although Eq. (16) had been obtained for subcooled flow boiling of water, it should provide reasonable results for R-113 whose liquid phase molecular Prandtl number is of the same order of magnitude as that of water.

h_{IG} was not calculated explicitly. Instead, the vapor-side interfacial heat transfer rate per unit volume of fluid was calculated as

$$\frac{\alpha_G\rho_G C_{pG}(\overline{T}_G-\overline{T}_{\mathrm{sat}})}{\Delta t}, \tag{17}$$

where Δt is an appropriate time scale of the thermal energy exchange. The value of Δt was equated to the time step used in the time-marching solution scheme (this scheme is explained later). It should be noted here that in subcooled flow boiling the vapor-side interfacial heat transfer rate is typically considerably smaller than that on the liquid-side.

Interfacial Mass Transfer. Per unit volume of the fluid,

$$\Gamma_G=-\Gamma_L=\frac{1}{h_{fg}}\left[h_{IL}(\overline{T}_L-\overline{T}_{\mathrm{sat}})a_i+\frac{\alpha_G\rho_G C_{pG}}{\Delta t}(\overline{T}_G-\overline{T}_{\mathrm{sat}})\right], \tag{18}$$

where a_i, the interfacial area concentration, was approximated as $6\alpha_G/D_b$, D_b being the Sauter mean bubble diameter.

Wall Boundary Conditions.

Velocity Field. A new velocity wall law was used to impose the boundary conditions for $\overline{U}_L$, k_L, and ε_L at the channel inner wall. The law was developed, Zarate [27], on the basis of our experimental data and is

$$\overline{U}^+_L=1.8(\pm 0.25)\ln y^+ +5.9(\pm 1.0). \tag{19}$$

This relation is plotted in Fig. 4 along with the experimental data.

At the outer wall of the channel, the boundary conditions were in accordance with the standard single-phase velocity wall law for a pipe.

The wall boundary conditions for the vapor phase corresponded to zero radial gradient of its relative velocity with respect to the liquid, and of k_G and ε_G.

Heat Flux at Wall. A uniform heat flux, q''_W, was prescribed at the channel inner wall. The wall heat transfer model of Boree and Freydier [28], which is based on an earlier model due to Kurul and Podowski [29], was adopted. In the model, when boiling occurs, the wall heat flux is apportioned into three components: a vaporization heat flux, q''_V, which represents the heat transfer by conduction across a liquid microlayer under each nucleated vapor bubble; a quenching heat flux, q''_Q, which represents the transient heat conduction to the subcooled liquid that replenishes the space vacated by departed bubbles; and a forced convection heat flux to the liquid, q''_C, in areas of the wall not influenced by nucleating bubbles. Thus,

$$q''_W=q''_V+q''_Q+q''_C. \tag{20}$$

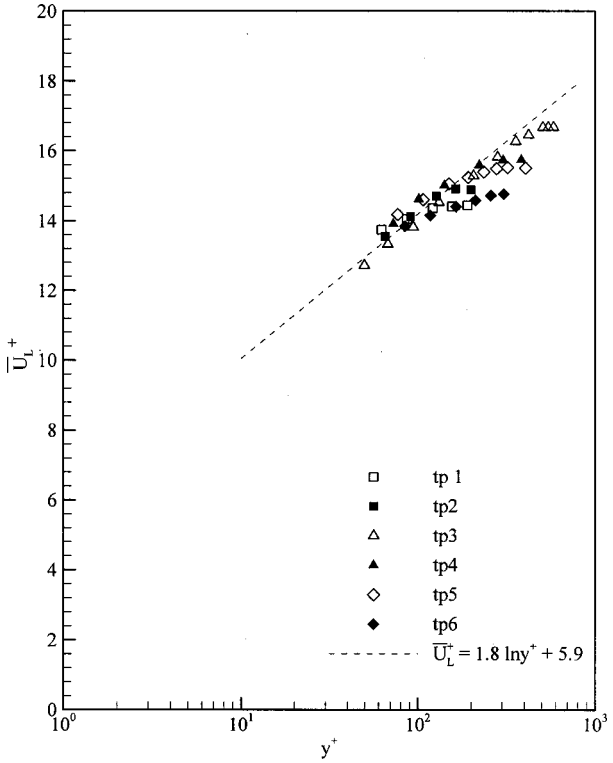

Fig. 4 Liquid axial velocity law for the inner wall

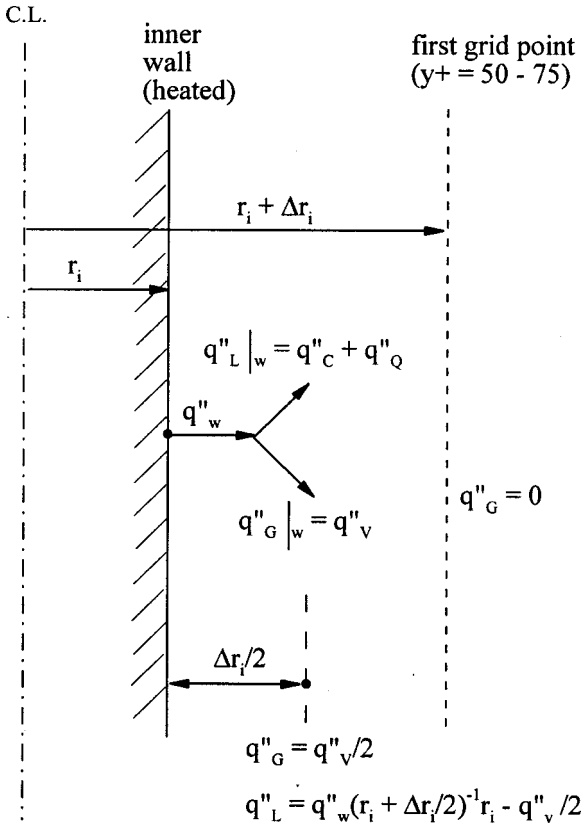

Fig. 5 The heat flux boundary condition

It should be noted that q''_Q and q''_C are transferred directly to the liquid phase.

In the present simulations, the heat flux boundary condition was imposed at a radial location mid-way between the inner wall and the first grid point away from the wall. The first grid point was typically at $R^*=0.047$, this corresponding to, depending on the experimental condition simulated, $y^+ \approx 50-75$. Our measurement of the radial component of the turbulent thermal energy flux in the liquid (this is presented later in the paper) led to the prescription that the vaporization portion of the thermal energy flux was essentially zero by $R^*=0.05$. Assuming a linear decrement away from the inner wall, the vaporization heat flux was set to (q''_V at wall)/2 at the mid-way point ($R^* \approx 0.024$) and the remainder of the thermal energy flux was applied to the liquid phase. This is shown schematically in Fig. 5.

The expression that was used to calculate the vaporization heat flux at the inner wall is

$$q''_V = f n v_B \rho_G h_{fg}, \tag{21}$$

where f is the bubble departure frequency, n is the bubble population per unit wall area (the active nucleation site density), and v_B is the bubble volume at detachment. The relations adopted for f and n are the same as in Kurul and Podowski [29].

Temperature Field. An inner wall law for the liquid phase average temperature was developed on the basis of our measurements. The wall heat flux was employed in defining the *friction temperature*. The wall temperature was calculated by means of a correlation proposed by Hasan et al. [30] on the basis of measurements in the same annular channel. The wall law is

$$T_L^+ = 1.95(\pm 0.15) \ln y^+ + 6.2(\pm 1.2). \tag{22}$$

This relation is plotted in Fig. 6 along with the experimental data.

Turbulent Prandtl Number in Liquid. The liquid phase turbulent Prandtl number, Pr_L^t, is needed for the calculation of turbulent thermal energy flux in the liquid, Eq. (15). Pr_L^t can be obtained by two methods: (i) it is equated to K/K_H, the ratio of the slope of the liquid temperature wall law to that of the liquid velocity wall law—in our case, this yields a value of 1.08 which is then taken to be constant across the annulus; and (ii) the relation

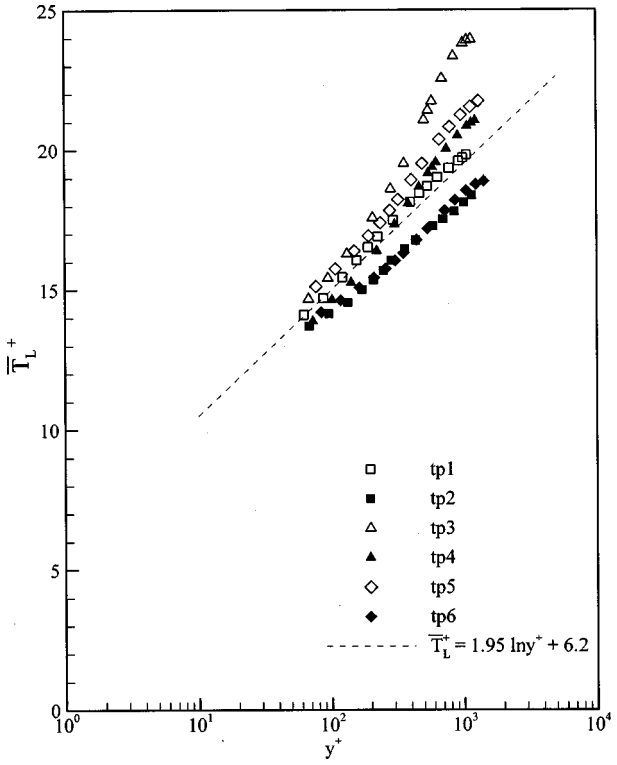

Fig. 6 Liquid temperature law for the inner wall

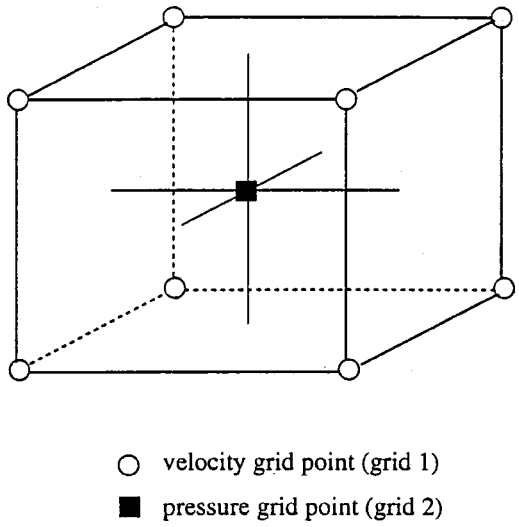

Fig. 7 Staggered grid used for discretization of the equations

$$\mathrm{Pr}_L^t = \frac{(\overline{uv})_L}{(\overline{vt})_L} \cdot \frac{\partial \overline{T}_L/\partial r}{\partial \overline{U}_L/\partial r} \tag{23}$$

can be used. Considerable care is needed in obtaining the radial gradients of $\overline{T}_L$ and $\overline{U}_L$ from the experimental data and the uncertainty in the value of Pr_L^t can be substantial. In contrast to the first method, local values of Pr_L^t are obtained. Also, the Pr_L^t values in the narrow radial zone delimited by the $(\overline{uv})_L = 0$ and $\partial \overline{U}_L/\partial r = 0$ locations will be indeterminate.

In the simulations whose results are presented in this paper, a uniform Pr_L^t value of 1.08 was used.

Inlet and Outlet Conditions. A channel length of 3.30 m was simulated of which the initial 0.91 m was unheated and the remaining 2.39 m heated. Uniform radial profiles were prescribed at the channel inlet for the liquid average axial velocity, average temperature, turbulent kinetic energy, and its dissipation rate. The conditions at the outlet were: $\partial\Phi/\partial z = 0$, where Φ is any flow variable except pressure. The outlet condition for pressure was $\partial^2 \overline{P}/\partial r \partial z = 0$.

Numerical Method. The CFD solver ASTRID developed at Electricité de France was used. In this solver, the conservation equations for mass, momentum, and thermal energy of the two phases, and the turbulence model equations of the liquid phase are discretized in space in a structured staggered grid with collocated arrangement of the velocity components. A combination of finite difference and finite volume methods is used. Pressure and vapor fraction are located at the pressure grid points—grid 2, Fig. 7. The vapor phase mass conservation equation and the pressure equation are solved using the finite volume method. All other variables are located on the velocity grid (grid 1). The equation for the latter variables are solved using the finite difference method.

The conservation equations for the two phases and the liquid phase turbulence model equations, in their discretized form, are solved in a time-marching scheme by the fractional step method (Yanenko [31], Kim and Moin [32]). The fractional step method splits an equation into two or more partial differential equations, which are solved individually at each time step. In the present cases, the maximum value of the Courant number, $\mathrm{Co} = \overline{U}\Delta t/\Delta x$, ranged from 0.15 to 0.28 for the liquid field and from 0.35 to 0.38 for the vapor field. The steady state solution was obtained via appropriately long (in time) simulation, the convergence criterion typically being

$$\frac{\Sigma(\psi^{n+1} - \psi^n)^2}{\Sigma(\psi^{n+1})^2} < 10^{-6}. \tag{24}$$

The *baseline* numerical simulations were carried out using 19 grid points in the radial direction, 166 grid points in the axial direction, and 3 grid points in the azimuthal direction. The axial grid points were equally spaced (0.02 m) as were the azimuthal grid points ($\pi/32$). The first radial grid point was usually located at a distance of 0.52 mm ($R^* = 0.047$ and $y^+ \approx 50-75$) from the inner wall and the distance between successive grid points was incremented away from the wall such that $(r_{j+1} - r_j)/(r_j - r_{j-1}) = 1.02$.

In the boiling length of the channel, from physical consideration, the distance of the first radial grid point from the inner wall was kept approximately equal to or slightly larger than the most probable bubble diameter in the region. The azimuthal grid spacing was of the same order of magnitude. Simulation results changed very little (by less than 1 percent) upon changing the radial grid spacing increment ratio to as much as 1.2. Refinement of the axial grid to 221 grid points resulted in insignificant changes in the results.

The simulations were performed in a CRAY C98 computer located at Electricité de France.

Results

The results of experiments and simulations are now presented concurrently to facilitate comparison between them. Table 1 contains the conditions of six subcooled boiling flow experiments and

Table 1 Conditions of six subcooled boiling flow experiments and the associated uncertainties

Parameter	*Experiment*						*Uncertainty*
	tp1	tp2	tp3	tp4	tp5	tp6	
Fluid mass velocity $(\mathrm{kg/m^2s})$	568	568	784	784	784	784	± 8
$U_{b,in}$ (m/s)	0.374	0.374	0.516	0.516	0.522	0.522	± 0.006
Re_{in}	22800	22800	31500	31500	34450	34450	± 350
R-113 pressure at m.p. (kPa)	269	269	269	269	269	269	± 1
Saturation temperature (°C)	80.5	80.5	80.5	80.5	80.5	80.5	± 0.3
Average liquid temperature at channel inlet (°C)	42.7	42.7	42.7	42.7	50.2	50.2	± 0.1
Inner wall heat flux ($\mathrm{W/m^2}$)	95000	116000	95000	116000	95000	116000	± 400

Table 2 Conditions of two single-phase liquid experiments and the associated uncertainties

Parameter	*Experiment*		*Uncertainty*
	sp1	sp2	
Fluid mass velocity (kg/m^2s)	568	784	± 8
$U_{b,in}$ (m/s)	0.374	0.516	± 0.006
Re_{in}	22800	31500	± 350
R-113 pressure at m.p. (kPa)	269	269	± 1
Average liquid temperature at channel inlet (°C)	42.7	42.7	± 0.1
Inner wall heat flux (W/m^2)	16000	16000	± 200

the associated uncertainties. Simulations were performed of the same six conditions. Table 2 shows the conditions of two heated single-phase liquid flow experiments whose results are compared with the boiling flow results. The estimated uncertainties in the measured velocity and thermal field quantities are given in Table 3. The uncertainty estimates are for 95 percent confidence.

The results are presented in the following sequence. First, the quantities that were measured as well as computed are shown, these being the vapor fraction, liquid average axial velocity, vapor average axial velocity, liquid turbulent kinetic energy, and liquid average temperature. Next, the quantities that were measured but not explicitly computed are presented, these being the liquid axial and radial turbulent intensities, liquid axial turbulent shear stress, liquid temperature fluctuation intensity, and liquid axial and radial turbulent heat fluxes. Finally, the measured vapor bubble most probable and Sauter mean diameters are shown for one experiment.

Table 3 Measurement uncertainties

Measured quantity	Uncertainty
α_G (nondim)	± 1 percent α_G when $\alpha_G < 10$ percent ± 2 percent α_G when $\alpha_G > 10$ percent
$\overline{U}_L$ (m/s)	± 4 percent of value when $R^* < 0.2$ ± 3 percent of value when $R^* > 0.2$
$\overline{U}_G$ (m/s)	± 6 percent of value
u'_L (m/s)	± 3 percent of value
v'_L (m/s)	± 4 percent of value
$\overline{(uv)}_L$ (m^2/s^2)	± 12 percent of value when $R^* < 0.2$ ± 10 percent of value when $R^* > 0.2$
$\overline{T}_L$ (°C)	± 1.0°C in boiling layer ± 0.5°C in all-liquid layer
t'_L (°C)	± 5 percent of value in boiling layer ± 3 percent of value in all-liquid layer
$\overline{T}_w$ (°C)	± 0.6°C
$\overline{(ut)}_L$ (m°C/s)	± 10 percent of value in boiling layer ± 6 percent of value in all-liquid layer
$\overline{(vt)}_L$ (m°C/s)	± 10 percent of value in boiling layer ± 7 percent of value in all-liquid layer

Figures 8(*a*)–(*c*) show the radial distribution of vapor fraction at the measurement plane. The trends that are observable in the data are reproduced fairly well by the simulations, particularly near the inner wall. The simulated boiling layer is somewhat thinner than the measured layer, except in the case of experiment tp3. This can happen if too high a vapor condensation rate is calculated in the outer part of the boiling layer.

The liquid average axial velocity radial distribution is shown in Figs. 9(*a*)–(*c*). As a reference, the measured average axial velocity distribution for heated single-phase liquid flow at the same mass flux is included in Figs. 9(*a*) and (*b*). Significant changes in the velocity distribution is brought about by boiling in all of the experiments except tp3 which had the thinnest boiling layer with the least vapor content. For all experiments except tp3, the liquid axial velocity inside the boiling layer increased markedly and there occurred, as anticipated from mass conservation consideration, a concomitant decrease in the liquid axial velocity outside the boiling layer. Additionally, there was a substantial shift of the maximum axial velocity location toward the inner wall. The velocity could not be measured close enough to the inner wall to allow determination of its radial gradient (and hence, the axial shear stress based on this gradient) very near the wall.

In each case, the simulation predicted a larger magnitude of the liquid average axial velocity in the region $0.05 < R^* < 0.3$. When integrated over the annulus, the liquid mass flow rate obtained from the simulated profile is between 1 to 3 percent (depending on the experiment) higher than the flow rate estimated from the measured profile. We note again that the simulated profile was utilized in the $0.8 \leqslant R^* \leqslant 1$ region when integrating the *measured* profile as no velocity measurement could be made in this region.

Figures 10(*a*)–(*c*) contain the radial distribution of the measured vapor bubble average axial velocity. This velocity distribution was measured for only four of the six experiments—tp1, tp3, tp4, and tp6. The thickness of the boiling layer and its vapor content clearly influence the distribution. For example, the boiling layer for tp3 is thin and its vapor content low and here, the measured velocity increases monotonically to the edge of the boiling layer. On the other hand, the tp6 boiling layer is thick and its vapor content high and the vapor axial velocity first increases and then decreases radially outward in the layer. Also, the velocity is higher when the vapor content in the layer is higher, Fig. 10(*b*). The corresponding radial distributions of the vapor phase average axial velocity predicted by simulations are also shown. While there is qualitative similarity between the measurements and the simulations, quantitative difference is apparent.

Figures 11(*a*)–(*c*) show the radial distribution of liquid turbulent kinetic energy. Since only the axial and radial turbulent intensities were measured, Figs. 12(*a*)–(*c*), it was necessary to estimate the azimuthal turbulent intensity in order to obtain the turbulent kinetic energy. This was done on the basis of the measurements of Brighton and Jones [33] in air flow through annular channels,

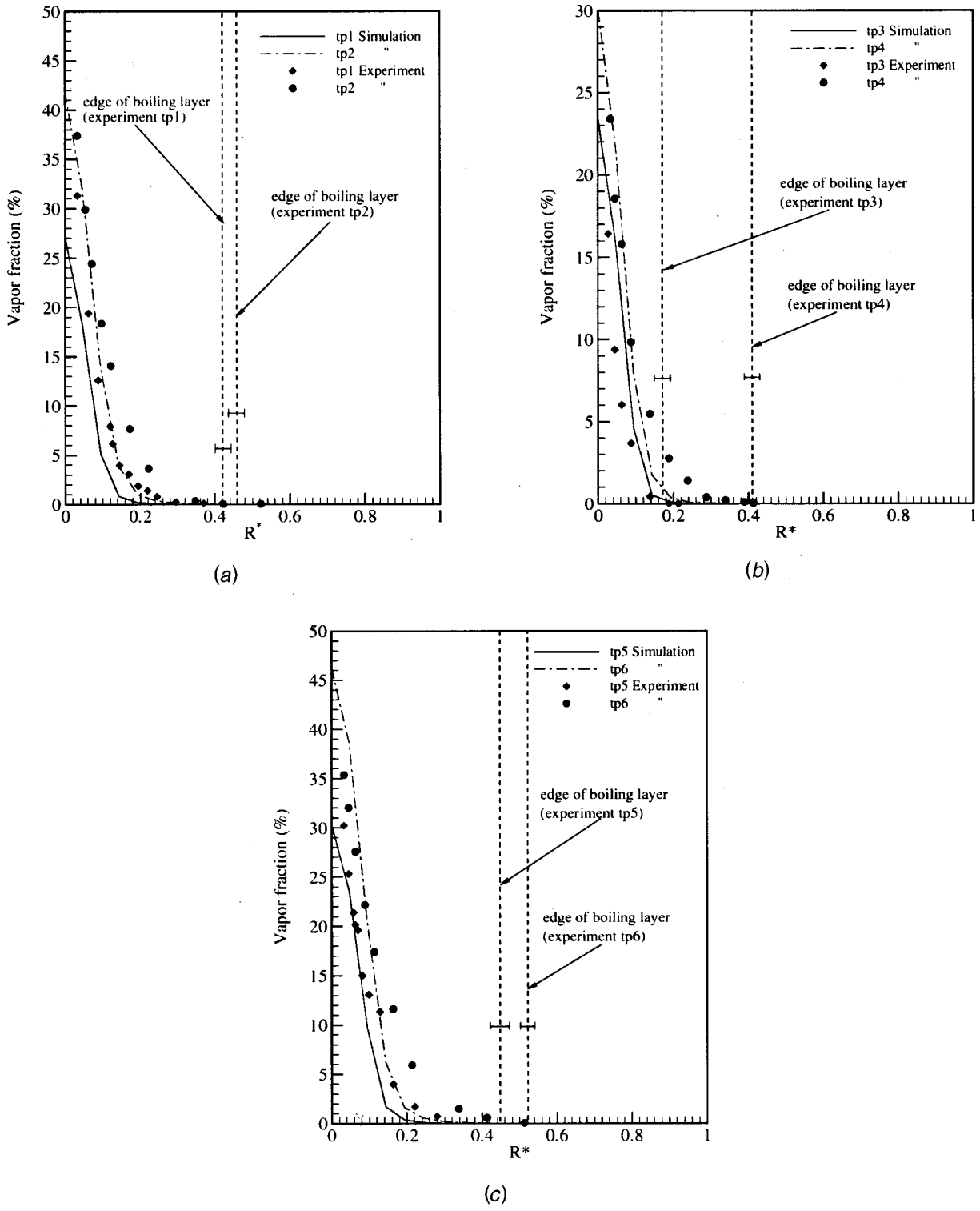

Fig. 8 Vapor fraction: (*a*) experiments tp1 and tp2; (*b*) experiments tp3 and tp4; and (*c*) experiments tp5 and tp6

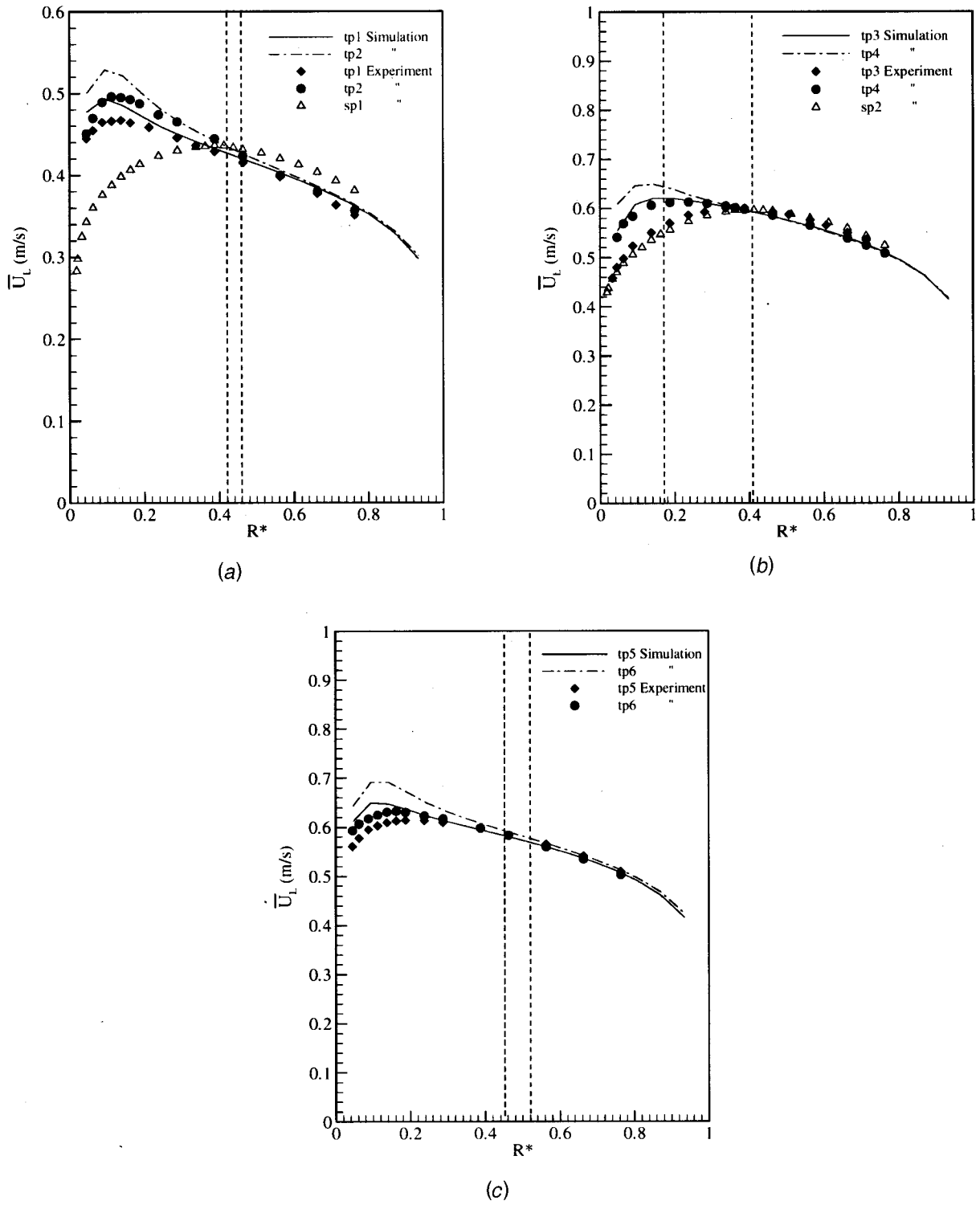

Fig. 9 Liquid average axial velocity: (*a*) experiments tp1, tp2, and sp1; (*b*) experiments tp3, tp4, and sp2; and (*c*) experiments tp5 and tp6

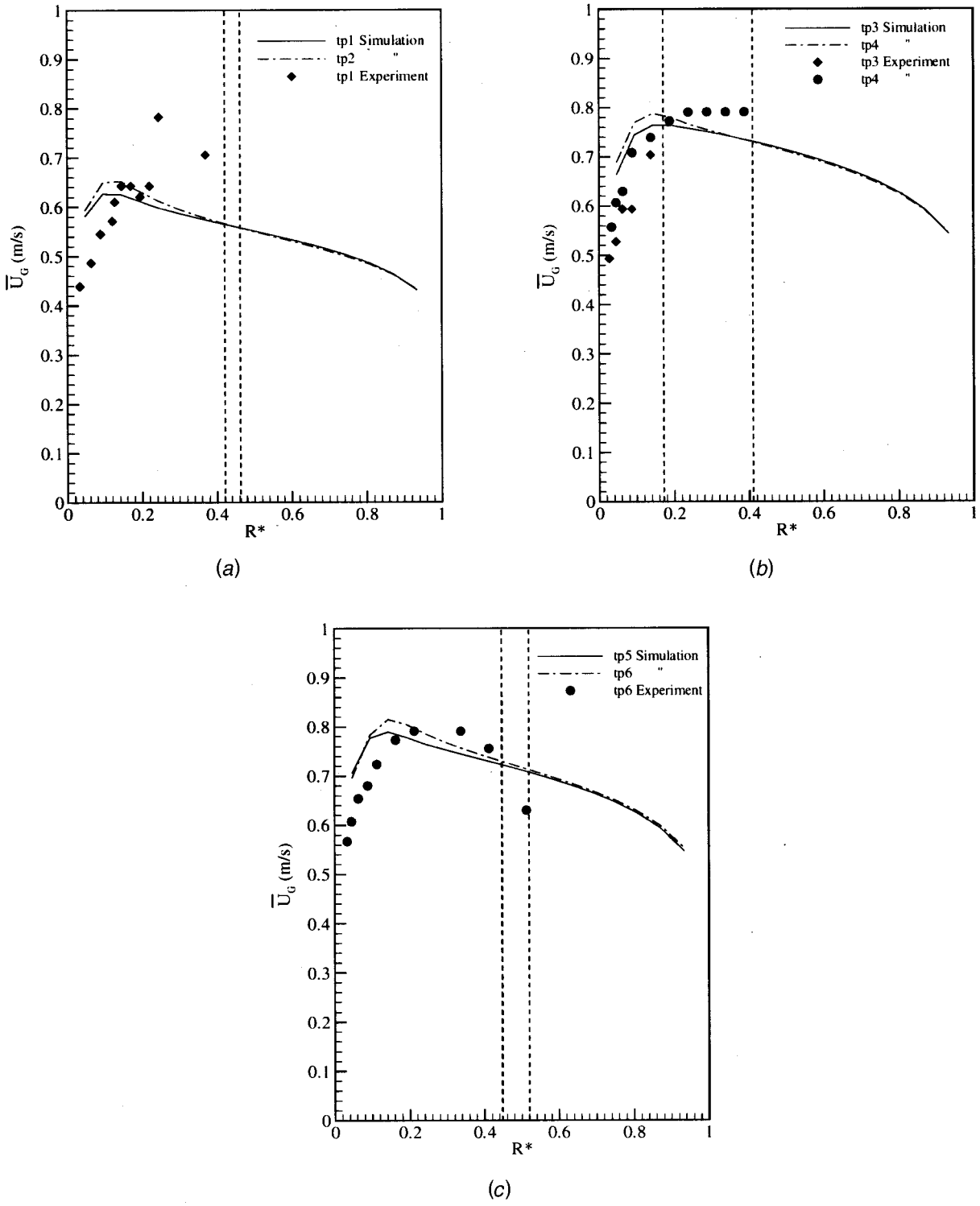

Fig. 10 Vapor bubble average axial velocity: (*a*) experiments tp1 and tp2; (*b*) experiments tp3 and tp4; and (*c*) experiments tp5 and tp6

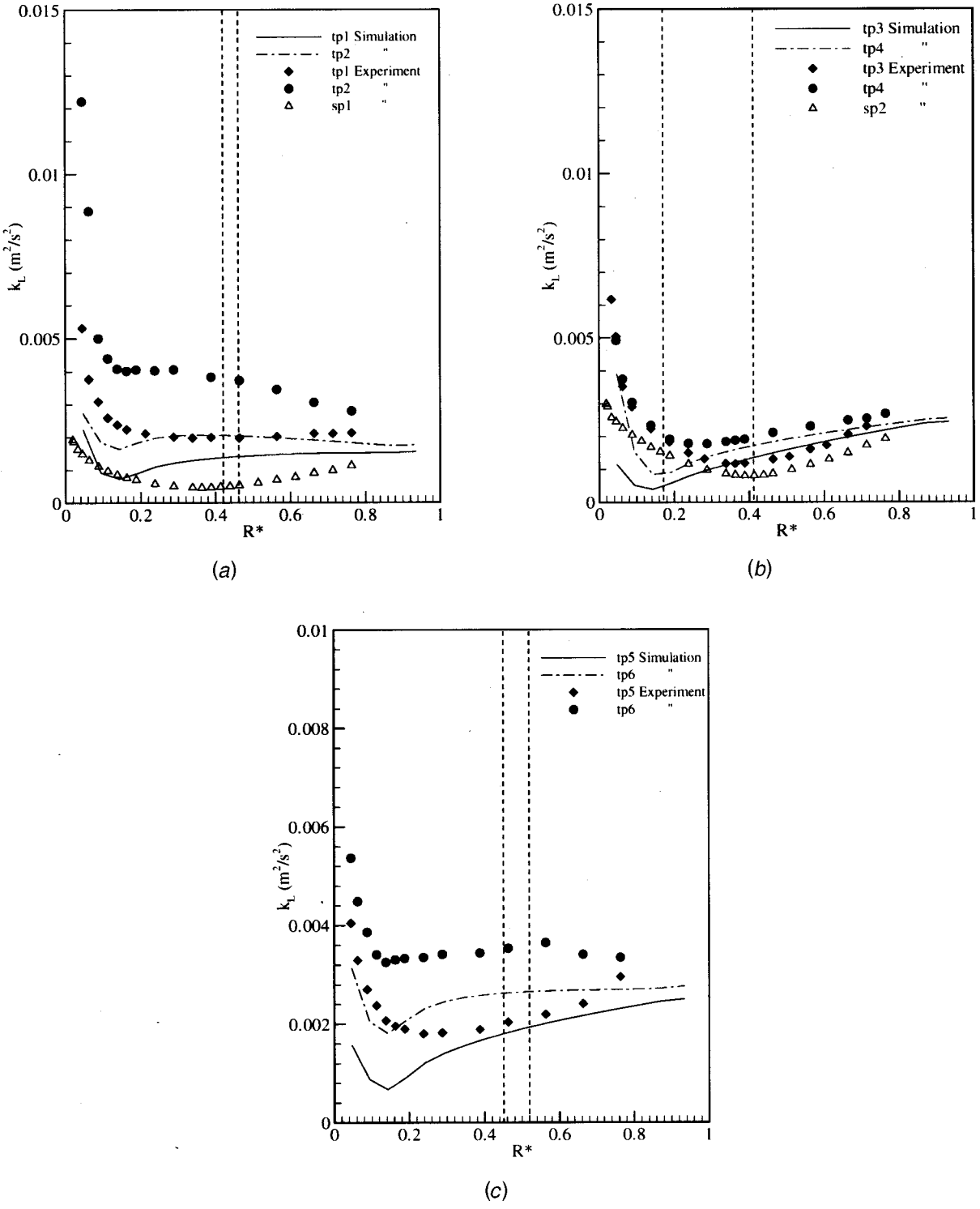

Fig. 11 Liquid turbulent kinetic energy: (*a*) experiments tp1, tp2, and sp1; (*b*) experiments tp3, tp4, and sp2; and (*c*) experiments tp5 and tp6

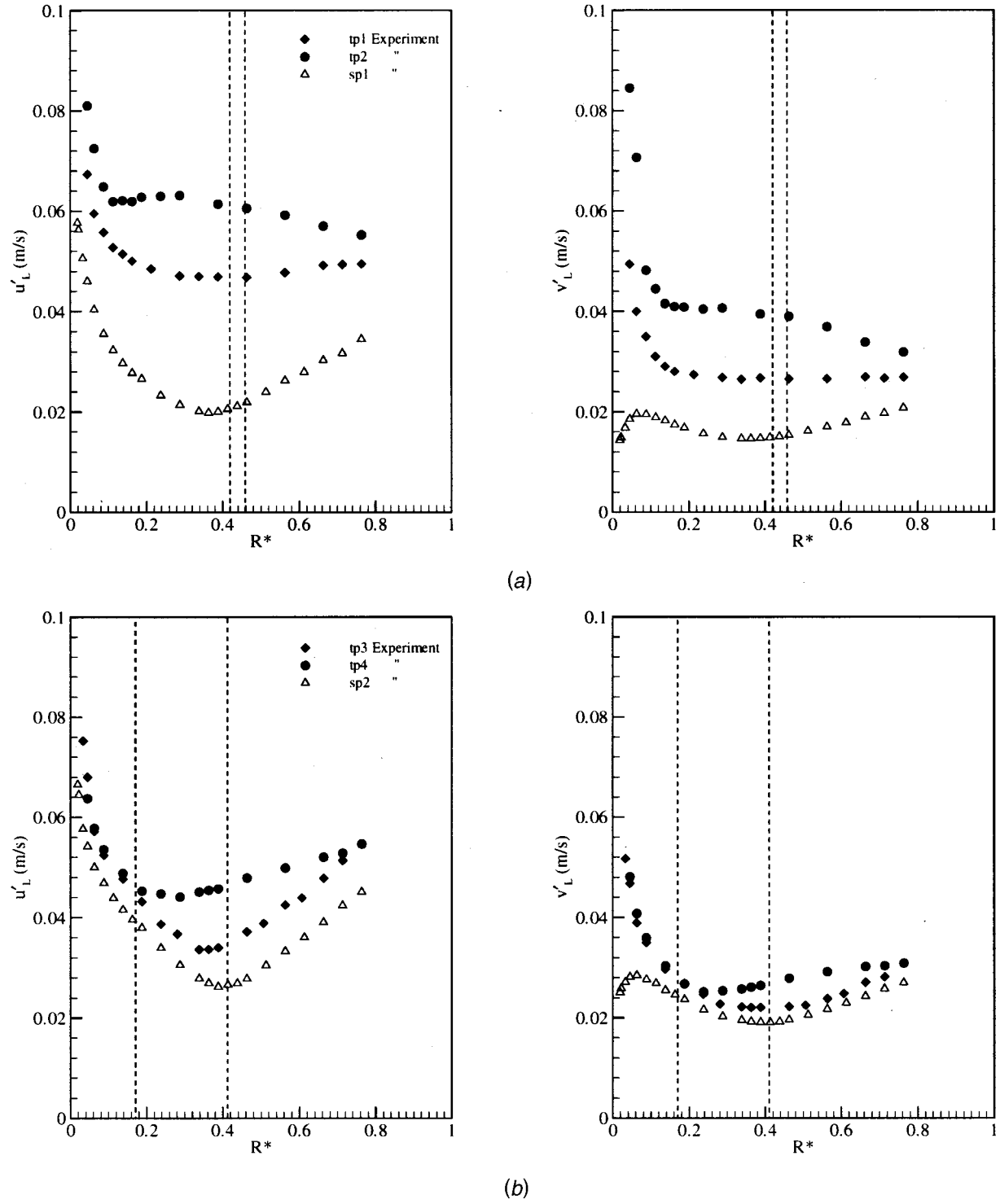

Fig. 12 Liquid velocity turbulent intensities: (*a*) experiments tp1, tp2, and sp1; (*b*) experiments tp3, tp4, and sp2; and (*c*) experiments tp5 and tp6

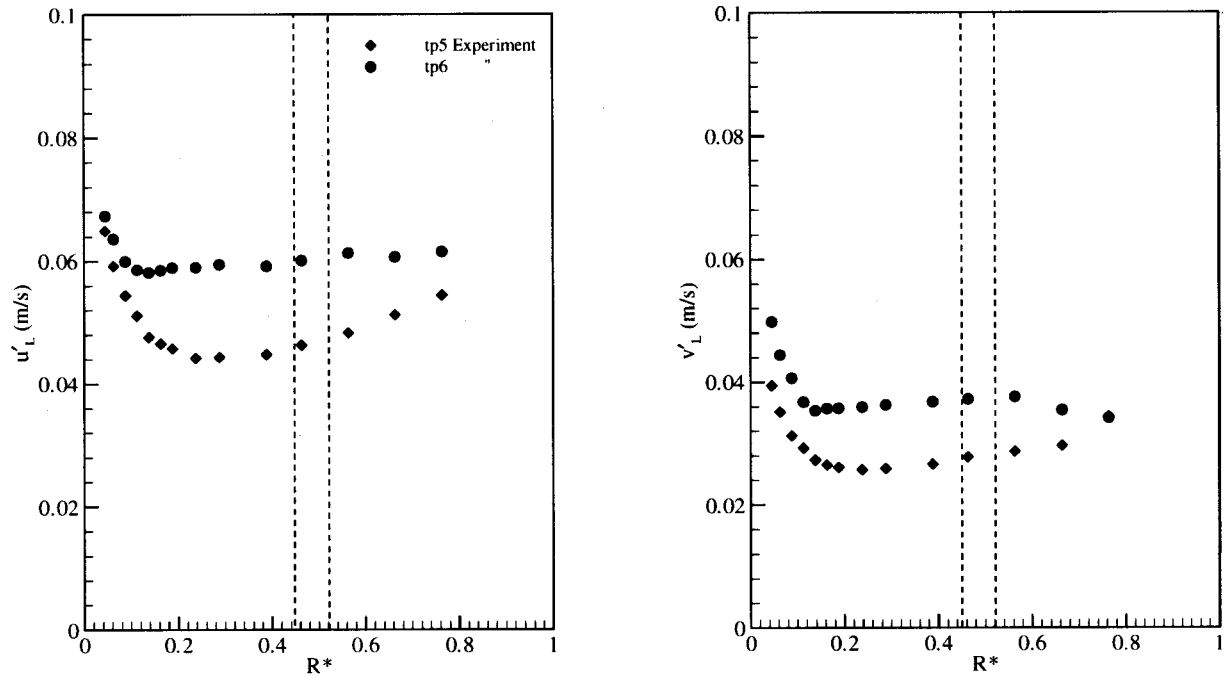

(*c*)

Fig. 12 (***Continued.***)

yielding $w'_L \approx 1.22 v'_L$. The experimental k_L was then equated to $(u'^2_L + 2.5 v'^2_L)/2$. However, this estimate of w'_L may not be appropriate for boiling flow.

It is apparent that a substantial increase in the liquid turbulent kinetic energy occurred within the boiling layer, especially near the inner wall. A major cause may be the increased turbulent kinetic energy production in the liquid near the inner wall as a result of higher mean shear (this is demonstrated later). The simulations underpredict k_L in all cases although there are qualitative similarities between the measured and simulated distributions. In the boiling layer, the characteristic turbulence length scale was estimated to be of the order of 0.5 mm, and the Kolmogorov length scale (microscale) of the order of 0.05 mm. The latter length scale was not resolved in our LDV measurements. The temperature microscale would be smaller by a factor of $1/\sqrt{\mathrm{Pr}_L}$, the Pr_L range for the present experiments being 4.8–6.8.

Additional comments on the turbulent intensity distribution reflecting our earlier measurements can be found in Roy et al. [5].

Figures [13](*a*)–(*c*) contain the measured radial distribution of $(\overline{uv})_L$ which is proportional to the axial turbulent shear stress in the liquid. The shift of the zero shear stress location toward the inner wall is substantial in all cases except tp3 which had the thinnest boiling layer with the least vapor content. The magnitude of $(\overline{uv})_L$ increased sharply as the inner wall was approached. It is clear that the wall shear stress in the boiling flows is larger than that in the corresponding (i.e., at same mass flux) single-phase heated liquid flows. Also, the tendency of the profiles to merge as the outer wall is approached is evident in Figs. 13(*a*) and (*b*).

The liquid average temperature distribution is shown in Figs. 14(*a*)–(*c*). The relatively large uncertainty of ± 1.0°C in the boiling layer should be borne in mind. The measured profiles became somewhat flatter in the inner part of the boiling layer at the higher wall heat flux (116,000 W/m^2)—this may have been due to the increased turbulent thermal diffusivity in the region caused by more pronounced vapor bubble activity. While measurement could not be made very close to the inner wall, it may be inferred from the plots that much of the temperature drop occurred across a thin region adjacent to the wall. The measured wall temperature changed only slightly with wall heat flux, this being typical of fully developed nucleate boiling with low subcooling. It can also be observed that the liquid remained subcooled quite close to the inner wall.

The calculated liquid average temperature distributions do not agree with the corresponding measured distributions in the inner region of the boiling layer. The calculated profiles are steeper and higher here. This contributed to a mismatch between the calculated and measured thermal energy balances of 1 to 3 percent (depending on the experiment) for the total heat input up to the measurement plane. The inner wall temperature is predicted well however, this being because the temperature wall law, Eq. (22), had been used.

The measured radial profile of liquid temperature fluctuation intensity is presented in Figs. 15(*a*)–(*c*). The intensity was substantially higher than in heated single-phase liquid flow. This was especially the case within the boiling layer with the increase persisting into the all-liquid region. We had suggested in an earlier paper, Roy et al. [4], that the liquid temperature fluctuation intensity in a boiling layer depends mainly on the local vapor fraction and the local liquid subcooling. The intensity should increase when the vapor fraction increases and when the liquid subcooling increases. Whether the intensity undergoes an increasing, flattening, or decreasing trend as the inner wall is approached depends upon the relative contributions of the two effects which will usually be opposite.

Figures 16(*a*)–(*c*) show the measured radial distribution of $(\overline{ut})_L$ which is proportional to the axial turbulent heat flux in the liquid. The distribution underwent the least change from the heated single-phase liquid flow distribution at the same mass flux in the case of experiment tp3—this experiment, of course, had the thinnest boiling layer with the smallest vapor content. In the case of the other experiments, the distribution changed dramatically—the correlation was positive and its magnitude large over most of the annulus and it experienced a sharp decrease near the inner wall crossing over (or tending to cross over) to a negative value. The radial location of zero-crossing is of interest as this reflects the altered radial profile of the liquid axial velocity. The $(\overline{ut})_L$

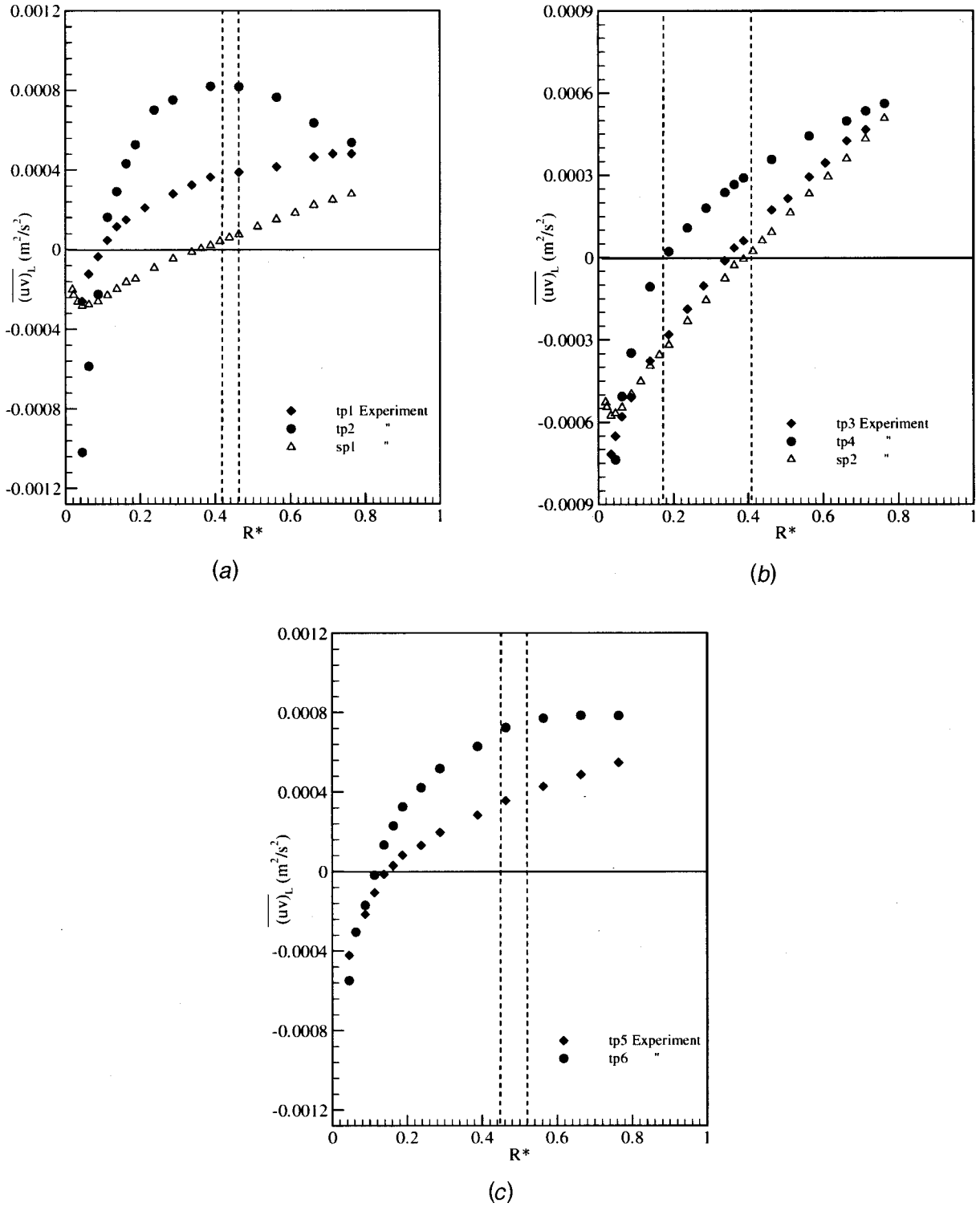

Fig. 13 Liquid axial turbulent shear stress: (*a*) experiments tp1, tp2, and sp1; (*b*) experiments tp3, tp4, and sp2; and (*c*) experiments tp5 and tp6

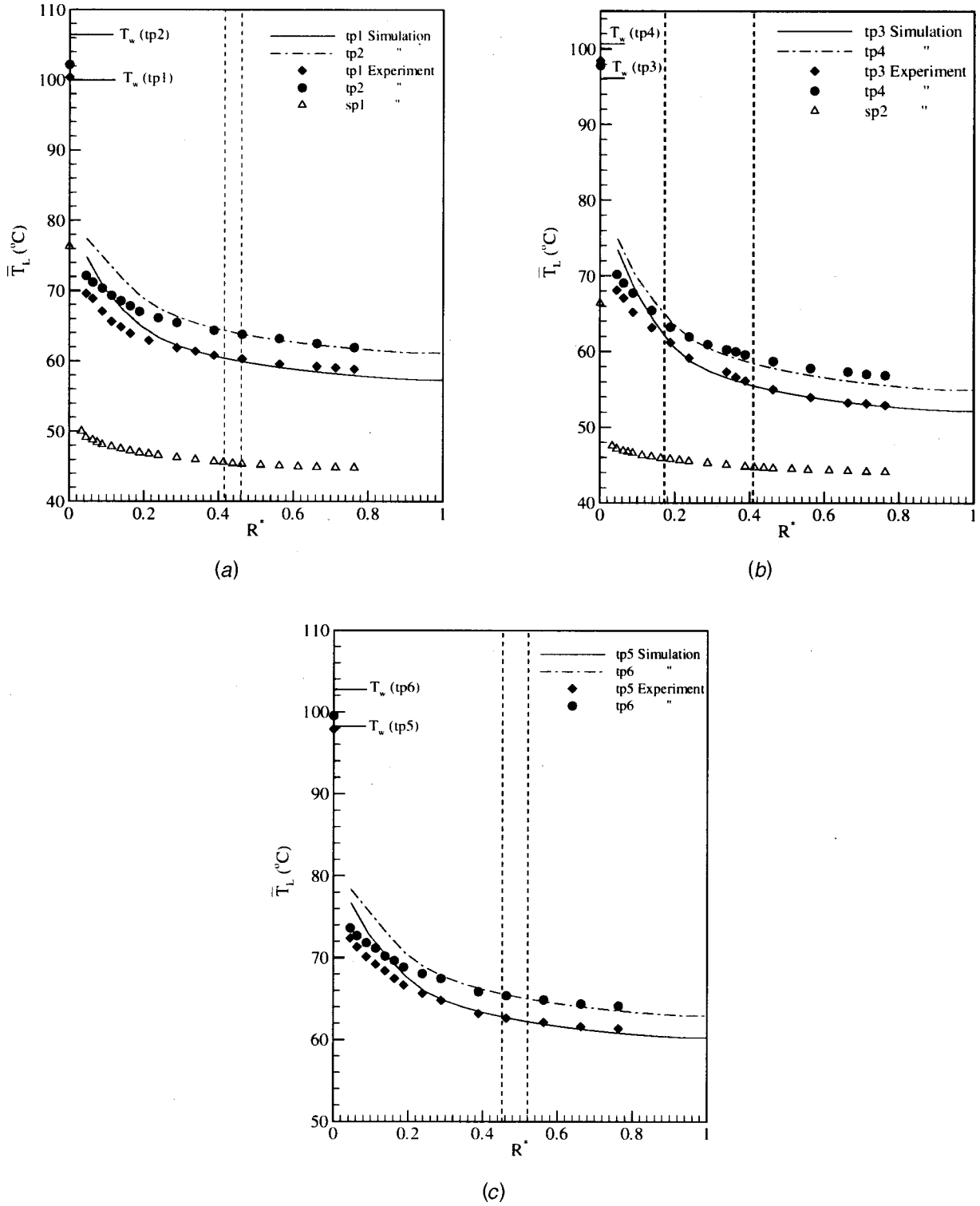

Fig. 14 Liquid average temperature: (*a*) experiments tp1, tp2, and sp1; (*b*) experiments tp3, tp4, and sp2; and (*c*) experiments tp5 and tp6

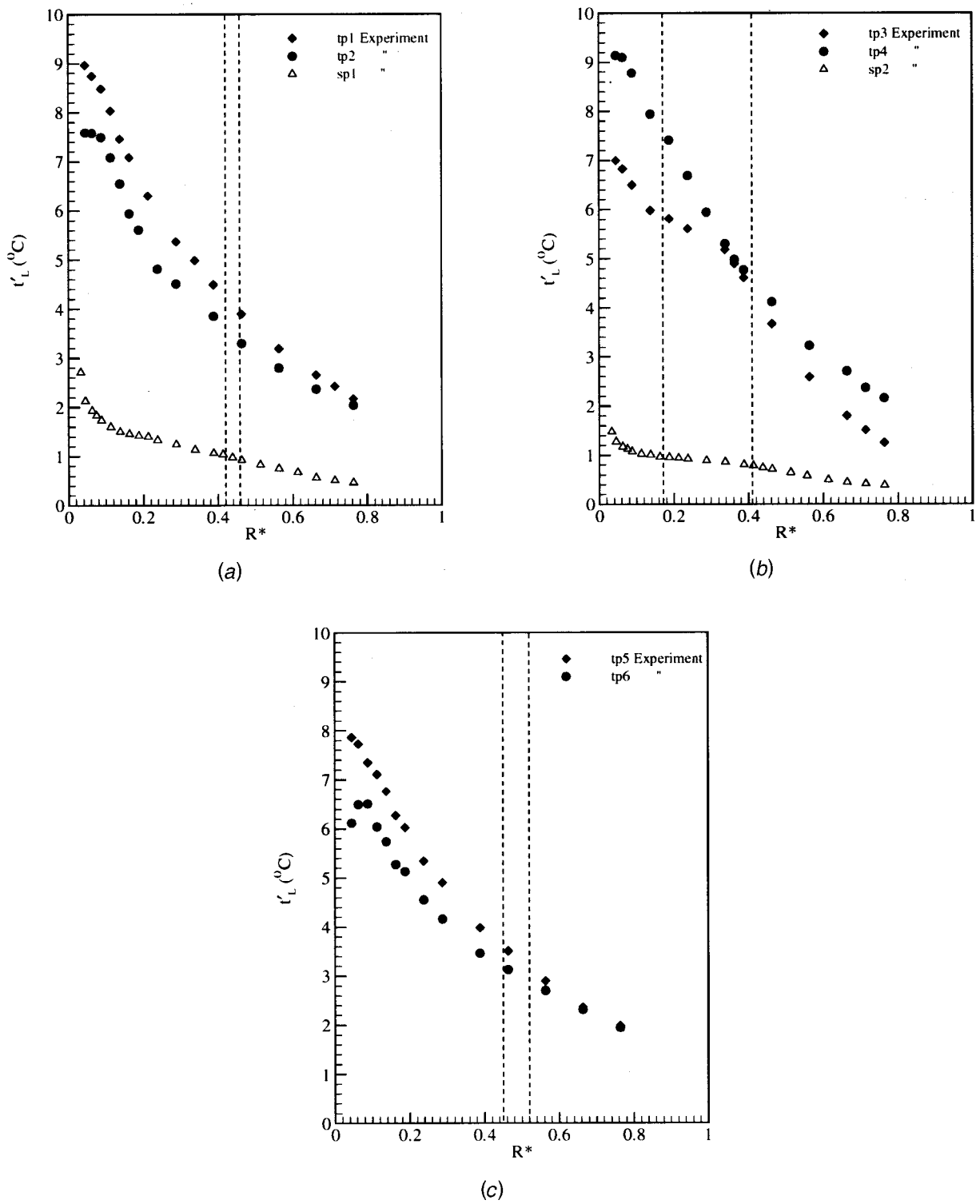

Fig. 15 Liquid temperature fluctuation intensity: (*a*) experiments tp1, tp2, and sp1; (*b*) experiments tp3, tp4, and sp2; and (*c*) experiments tp5 and tp6

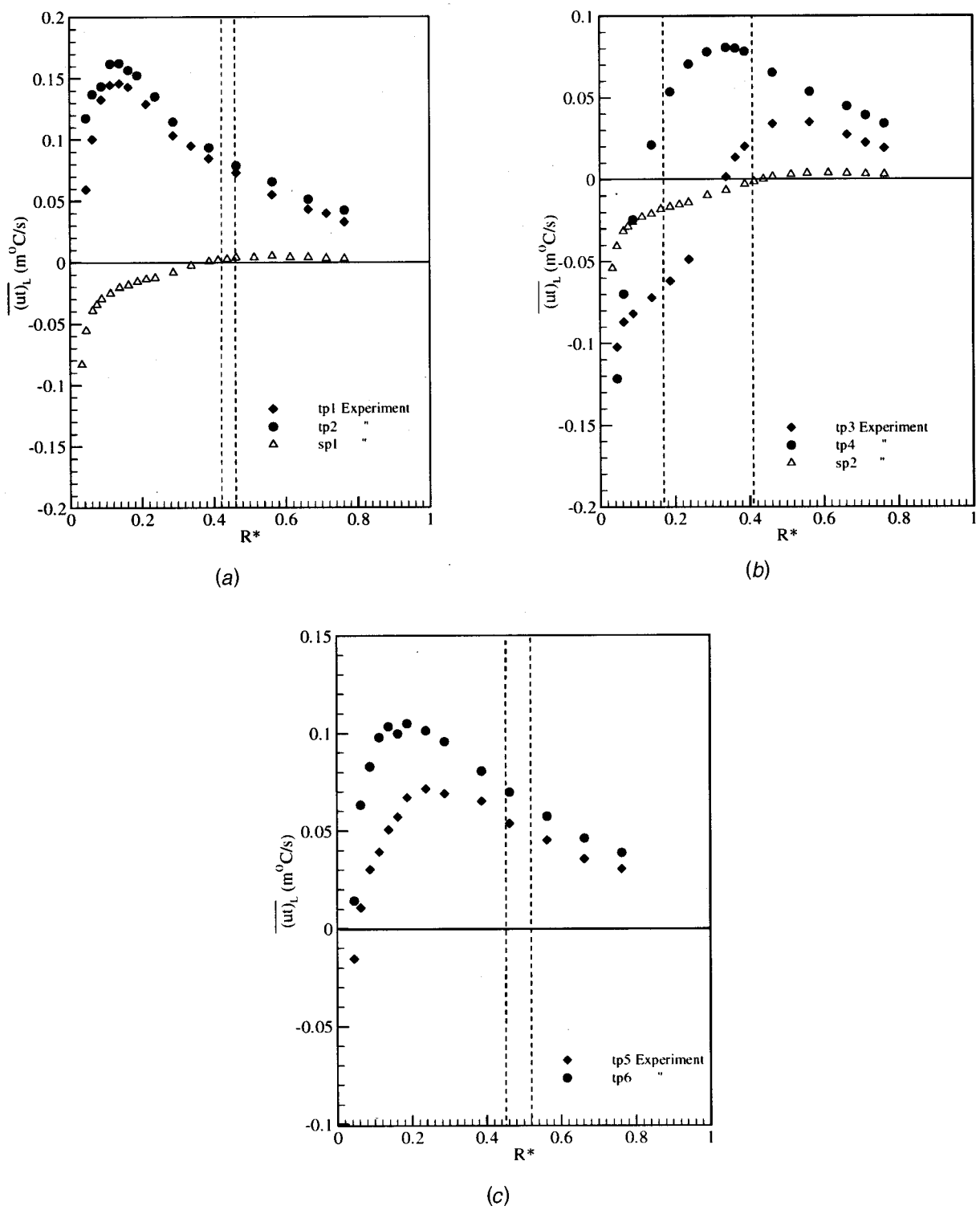

Fig. 16 Liquid axial turbulent heat flux: (*a*) experiments tp1, tp2, sp1; (*b*) experiments tp3, tp4, and sp2; and (*c*) experiments tp5 and tp6

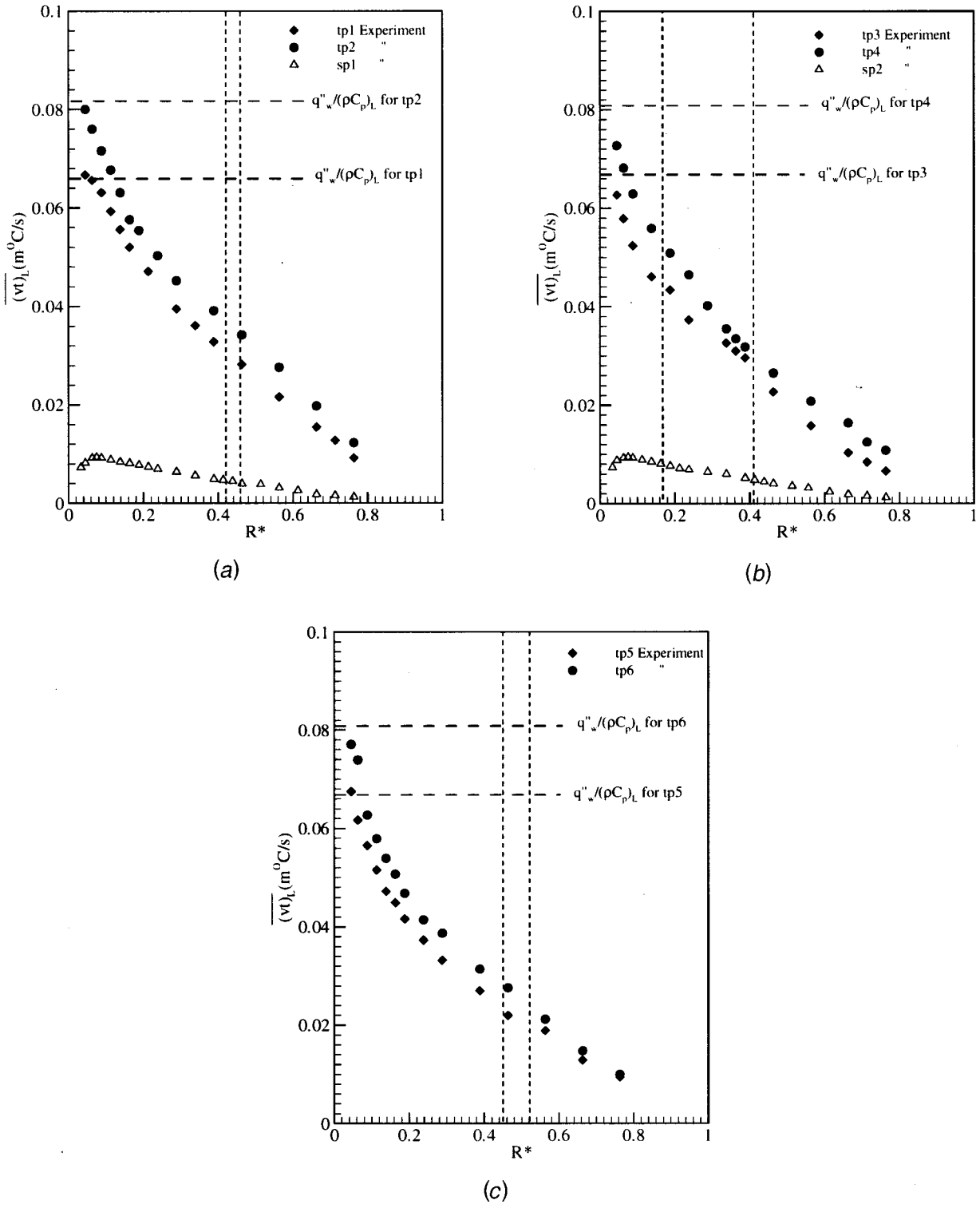

Fig. 17 Liquid radial turbulent heat flux: (*a*) experiments tp1, tp2, and sp1; (*b*) experiments tp3, tp4, and sp2; and (*c*) experiments tp5 and tp6

distribution underscores the difficulty of modeling the axial turbulent heat flux in the liquid using the gradient approximation and a turbulent thermal diffusivity.

Figures 17(*a*)–(*c*) show the measured radial distribution of $(\overline{vt})_L$ which is proportional to the radial turbulent heat flux in the liquid. The quantity $q''_W/(\rho C_p)_L$ is also shown for each experiment. Based on these we postulate that essentially all of the thermal energy supplied at the channel inner wall is transferred to the liquid by $R^* \approx 0.05$. As described earlier, this feature was utilized in the wall heat transfer model.

Finally, the measured radial distribution of the most probable vapor bubble diameter and the Sauter mean diameter for experiment tp6 are plotted in Fig. 18. The boiling layer was the thickest and its vapor content the largest for this experiment. The diam-

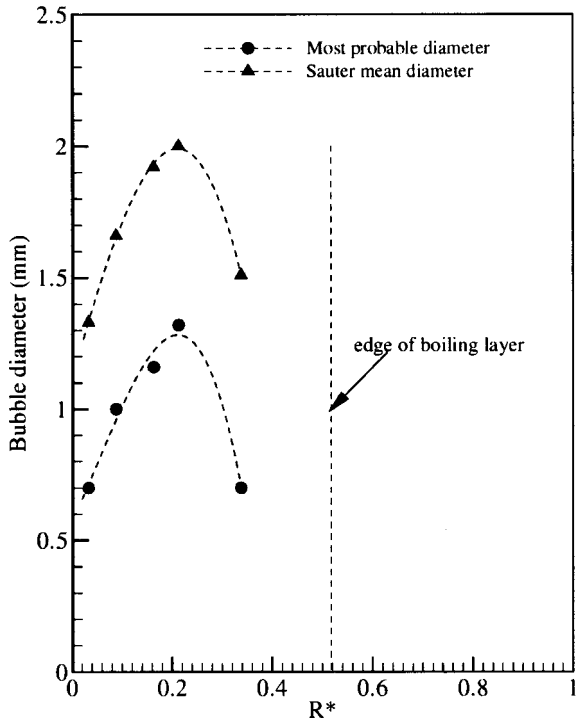

Fig. 18 Most probable and Sauter mean bubble diameters for experiment tp6

eters first increase away from the inner wall and then decrease. The increase could be due to bubble coalescence and the decrease due to vapor condensation. The substantial difference between the most probable and Sauter mean diameters for the experiment is caused by the shape of the bubble diameter probability density function (PDF) at each location. The diameter values could not be determined in the outer part of the boiling layer because the bubble detection rate was too low. As a result, meaningful bubble diameter PDF could not be constructed in this region.

Concluding Remarks

Key to accurate simulation of turbulent boiling flow are sound models of the physical processes that occur in them. Model building requires fundamental experiments designed to provide understanding of the processes. A part of the experimental data must also be set aside for validation of the simulation. These considerations motivated this study in which experiments, modeling, and simulations were carried out.

Velocity and thermal fields were measured in turbulent subcooled boiling flow of Refrigerant-113 through a vertical annular channel whose inner wall only was heated. Among the quantities measured were some of the turbulent stresses and heat fluxes in the liquid phase. Wall laws for the liquid average axial velocity and temperature were developed from the experimental data.

The two-fluid model equations were solved numerically to simulate the flow. A high Reynolds number k-ε model was used for the shear-induced part of the liquid turbulence. An existing model was utilized for the bubble agitation contribution to the turbulence. A turbulent Prandtl number was determined from the two wall laws and used in conjunction with Reynolds analogy to calculate the turbulent heat flux in the liquid. Whether the Reynolds analogy holds in boiling flow is open to question however.

The numerical simulation results were compared with measurements wherever possible. Reasonably good agreement was found for some flow field quantities while the agreement was at best fair for others.

Much work remains to be done. Among the work are: modeling of the thermal field without resorting to Reynolds analogy, modeling of the interfacial area distribution, and developing a near-wall model of turbulence along with a numerical method that permits fine gridding near heated walls where the vapor bubbles may be larger than the grid size. These objectives may be achievable through a judicious combination of experiments and modeling.

Acknowledgments

This work was partially funded by Electricité de France. Funding from the National Science Foundation, Thermal Transport and Thermal Processing Program and Electric Power Research Institute is also gratefully acknowledged.

Nomenclature

a_i = interfacial area concentration
$C_{\varepsilon 1}, C_{\varepsilon 2}, C_{\varepsilon 3}$ = model constants in the ε-equation
C_μ = model constant
C_p = specific heat of fluid at constant pressure
C_D = drag coefficient
D_b = bubble diameter
D_h = channel hydraulic diameter, $=2(r_o-r_i)$
g_i = i-component of acceleration due to gravity
h_{fg} = latent heat of vaporization
h_{IL} = heat transfer coefficient on the liquid side of the interface
Ja = Jacob number, $=C_{pL}(\overline{T}_{\rm sat}-\overline{T}_L)/h_{fg}$
k = turbulent kinetic energy per unit mass of fluid
Nu_b = Nussett number based on bubble diameter, $=h_{IL}D_b/\lambda_L$
$\overline{P}$ = time-average thermodynamic pressure
P^k = production rate of turbulent kinetic energy due to mean shear
Pr = molecular Prandtl number
Pr^t = turbulent Prandtl number
q''_W = wall heat flux
q''_C, q''_Q, q''_V = liquid convective, quenching, vaporization portion of the wall heat flux
r = radial coordinate
r_i, r_o = inner, outer radius of annulus
R^* = dimensionless radius, $=(r-r_i)/(r_o-r_i)$
Re = Reynolds number, $=\overline{U}_b D_h/\nu_L$
Re_b = bubble Reynolds number, $=(\overline{U}_G-\overline{U}_L)D_b/\nu_L$
S_{ij} = mean strain rate tensor, $=1/2(\partial\overline{U}_i/\partial x_j+\partial\overline{U}_j/\partial x_i)$
$\overline{T}$, $\overline{T}_b$ = time-average temperature, time-average bulk temperature of fluid
$\overline{T}_{wi}$ = time-average inner wall temperature
T^+ = dimensionless fluid temperature, $=(\overline{T}_{wi}-\overline{T})/T_\tau$
T_τ = friction temperature, $=q''_w/\rho C_p U_{\tau i}$
t = time; also, temperature fluctuation
t' = temperature fluctuation intensity
$\overline{U}_b$ = time-average bulk axial velocity
$\overline{U}_i$ = i-component of time-average local velocity
$\overline{U}^+$ = dimensionless axial velocity, $=\overline{U}_z/U_{\tau i}$
$U_{\tau i}$ = friction velocity at inner wall, $=(\tau_{wi}/\rho)^{1/2}$
u = axial velocity fluctuation
u_i = i-component of velocity fluctuation
u' = axial turbulent intensity
$\overline{ut}$ = axial turbulent heat flux (divided by ρC_p)
$\overline{u_i u_j}$ = turbulent stress tensor (divided by ρ)
$\overline{uv}$ = axial turbulent shear stress (divided by ρ)
v = radial velocity fluctuation

v' = radial turbulent intensity
V = fiberoptic sensor output voltage
$\overline{vt}$ = radial turbulent heat flux (divided by ρC_p)
x_i = coordinates
y = coordinate normal to the inner wall
y^+ = nondimensional inner wall normal coordinate, $=yU_{\tau i}/\nu$
z = axial coordinate

Greek Symbols

α_k = residence time fraction of phase k
δ_{ij} = Kronecker delta
ε = dissipation rate of k
$\mathbf{K}$, $\mathbf{K}_H$ = von Karman constant for velocity, for temperature
λ = thermal conductivity of fluid
μ = dynamic viscosity of fluid
μ^t = turbulent viscosity
ν = kinematic viscosity of fluid
ν^t = turbulent momentum diffusivity
ρ = density of fluid
σ_k = model constant in k-equation
σ_ε = model constant in ε-equation
τ_{ij} = viscous stress tensor
τ_{ij}^T = turbulent stress tensor
Γ_k = k-phase mass generation rate per unit volume of fluid

Subscripts

b = vapor bubble, also bulk fluid
G = vapor phase
in = channel inlet
i,o = annulus inner wall, outer wall
k = k-phase
L = liquid phase
r = relative
sat = saturation condition

References

[1] Jiji, L. M., and Clark, J. A., 1964, "Bubble Boundary Layer and Temperature Profiles for Forced Convection Boiling in Two-Phase Flow," ASME J. Heat Transfer, **86**, pp. 50–58.
[2] Dix, G. E., 1971, "Vapor Void Fraction for Forced Convection with Subcooled Boiling at Low Flow Rates," General Electric Report NEDO-10491.
[3] Delhaye, J. M., Semeria, R., and Flamand, J. C., 1973, "Void Fraction, Vapor and Liquid Temperatures; Local Measurements in Two-Phase Flow Using a Microthermocouple," ASME J. Heat Transfer, **95**, pp. 363–370.
[4] Roy, R. P., Velidandla, V., Kalra, S. P., and Peturaud, P., 1994, "Local Measurements in the Two-Phase Region of Turbulent Subcooled Boiling Flow," ASME J. Heat Transfer, **116**, pp. 660–669.
[5] Roy, R. P., Velidandla, V., and Kalra, S. P., 1997, "Velocity Field in Turbulent Subcooled Boiling Flow," ASME J. Heat Transfer, **119**, pp. 754–766.
[6] Marié, J. L., 1982, "Investigation of Two-Phase Bubbly Flows Using Laser-Doppler Anemometry," PCH, PhysicoChem. Hydrodyn., **4**, pp. 103–118.
[7] Lance, M., and Bataille, J., 1991, "Turbulence in the Liquid Phase of the Uniform Bubbly Air-Water Flow," J. Fluid Mech., **222**, pp. 95–118.
[8] Grossetéte, C., 1995, "Experimental Investigation and Preliminary Numerical Simulation of Void Profile Development in a Vertical Cylindrical Pipe," *Proceedings of Multiphase Flow Conference*, Vol. 2, Kyoto, Japan, A. Serizawa et al., eds.
[9] Ishii, M., 1975, *Thermo-Fluid Dynamic Theory of Two-Phase Flows*, 1st ed., Eyrolles, Paris, France.
[10] Drew, D. A., 1983, "Mathematical Modeling of Two-Phase Flow," Annu. Rev. Fluid Mech., **15**, pp. 261–291.
[11] Dykhuizen, R. C., Roy, R. P., and Kalra, S. P., 1986, "A Linear Time-Domain Two-Fluid Model Analysis of Dynamic Instability in Boiling Flow Systems," ASME J. Heat Transfer, **108**, pp. 100–108.
[12] Delhaye, J. M., 1974, "Jump Conditions and Entropy Sources in Two-Phase Systems. Local Instant Formulation," Int. J. Multiphase Flow, **1**, pp. 395–409.
[13] Bel F'dhila, R., and Simonin, O., 1992, "Eulerian Prediction of a Turbulent Bubbly Flow Downstream of a Sudden Pipe Expansion," *Proceedings of the Fifth Workshop on Two-Phase Flow Predictions*, Erlangen, Germany.
[14] Lopez de Bertodano, M., Lahey, R. T., Jr., and Jones, O. C., 1994, "Development of a k-ε Model for Bubbly Two-Phase Flow," ASME J. Fluids Eng., **116**, pp. 128–134.
[15] Morel, C., and Bestion, D., 1997, "Study About Turbulence Modeling in Steam-Water Two-Phase Flows," *ASME Fluids Engineering Division Summer Meeting*, New York, pp. 1–10.
[16] Marié, J. L., Moursali, E., and Tran-Cong, S., 1997, "Similarity Law and Turbulence Intensity Profiles in a Bubbly Boundary Layer at Low Void Fractions," Int. J. Multiphase Flow, **23**, pp. 227–247.
[17] Kang, S., Patil, B. K., and Roy, R. P., 2001, "Effects of Coincidence Window and Measuring Volume Size on Laser Doppler Velocimetry Measurement of Turbulence," Exp. Fluids, **30**, pp. 365–370.
[18] Wroblewski, D. E., and Eibeck, P. A., 1991, "A Frequency Response Compensation Technique for Cold Wires and Its Application to a Heat Flux Probe," Exp. Therm. Fluid Sci., **4**, pp. 452–463.
[19] Kang, S., Patil, B. K., Roy, R. P., and Zarate, J. A., 2001, "Isothermal and Turbulent Heated Upflow in a Vertical Concentric Annular Channel—Part I. Measurements," Int. J. Heat Mass Transf., **44**, No. 6, pp. 1171–1184.
[20] Cartellier, A., 1990, "Optical Probes for Local Void Fraction Measurements: Characterization of Performance," Rev. Sci. Instrum., **61**, No. 2, pp. 874–886.
[21] Sato, Y., and Sekoguchi, K., 1975, "Liquid Velocity Distribution in Two-Phase Bubble Flow," Int. J. Multiphase Flow, **2**, pp. 79–95.
[22] Thai Van, D., Minier, J., Simonin, O., Freydier, P., and Olive, J., 1994, "Multidimensional Two-Fluid Model Computation of Turbulent Dispersed Two-Phase Flows," *Numerical Methods in Multiphase Flows*, ASME FED-Vol. 185, pp. 277–291.
[23] Simonin, O., 1990, "Eulerian Formulation for Particle Dispersion in Turbulent Two-Phase Flows," M. Sommerfeld and D. Wennerberg, eds., *Proceedings of the Fifth Workshop on Two-Phase Flow Predictions*, Erlangen, Germany.
[24] Elgobashi, S., and Abou-Arab, T., 1983, "A Two-Equation Turbulence Model for Two-Phase Flows," Phys. Fluids, **26**, pp. 931–938.
[25] Simonin, O., and Viollet, P., 1989, "Numerical Study on Phase Dispersion Mechanisms in Turbulent Bubbly Flows," *Proceedings of the International Conference on Mechanics of Two-Phase Flows*, Taipei, Taiwan.
[26] Zeitoun, O., Shoukri, M., and Chatoorgoon, V., 1995, "Interfacial Heat Transfer Between Steam Bubbles and Subcooled Water in Vertical Upward Flow," ASME J. Heat Transfer, **117**, pp. 402–407.
[27] Zarate, J. A., 2000, "Numerical Simulation of Turbulent Heated Liquid and Subcooled Boiling Flows With Input From Experiments," Ph.D. thesis, Arizona State University, Tempe, AZ.
[28] Boree, J., and Freydier, P., 1993, "Boiling Water Flows. A Local Wall Heat Transfer Model for Use in Eulerian 3-D Computer Code," Second ASME-JSME International Conference on Nuclear Engineering, San Francisco, CA.
[29] Kurul, N., and Podowski, M. Z., 1990, "Multidimensional Effects in Forced Convection Subcooled Boiling," *Proceedings of the Ninth International Heat Transfer Conference*, Jerusalem, Vol. 2, pp. 21–26.
[30] Hasan, A., Roy, R. P., and Kalra, S. P., 1990, "Experiments on Subcooled Flow Boiling Heat Transfer in a Vertical Annular Channel," Int. J. Heat Mass Transf., **33**, pp. 2285–2293.
[31] Yanenko, N. N., 1971, *The Method of Fractional Steps*, 1st ed., Springer-Verlag, Berlin, Germany.
[32] Kim, J., and Moin, P., 1985, "Application of a Fractional-Step Method to Incompressible Navier-Stokes Equations," J. Comput. Phys., **59**, pp. 308–323.
[33] Brighton, J. A., and Jones, J., 1964, "Fully Developed Turbulent Flow in Annuli," ASME J. Basic Eng., **86**, pp. 835–844.

A Theoretical Study of Film Condensation in Horizontal Microfin Tubes

Hiroshi Honda
e-mail: hhonda@cm.kyushu-u.ac.jp

Huasheng Wang

Institute of Advanced Material Study,
Kyushu University,
Kasuga, Fukuoka 816-8580, Japan

Shigeru Nozu
Dept. of Systems Engineering,
Okayama Prefectural University,
Souja, Okayama 719-1197, Japan

A stratified flow model of film condensation in helically grooved, horizontal microfin tubes has been developed. The height of stratified condensate was estimated by extending the Taitel and Dukler model for a smooth tube to a microfin tube. For the upper part of the tube exposed to the vapor flow, laminar film condensation due to the combined effects of gravity and surface tension forces was assumed. For the lower part of the tube exposed to the stratified condensate flow, the heat transfer coefficient was estimated by an empirical equation for the internally finned tubes developed by Carnavos. The theoretical predictions of the circumferential average heat transfer coefficient by the present model and previously proposed annular flow model were compared with available experimental data for five tubes and five refrigerants. It was shown that the stratified flow model was applicable to wide ranges of mass velocity and quality as long as the vapor to liquid density ratio was larger than 0.05. Comparison was also made with the predictions of previously proposed empirical equations. [DOI: 10.1115/1.1421048]

Keywords: Condensation, Enhancement, Heat Transfer, Modeling, Two-Phase

Introduction

Horizontal microfin tubes have been commonly used for heat exchangers of refrigerators and air conditioners due to their superior heat transfer performance. Many experimental studies reporting on the effects of fin geometry, tube diameter, refrigerant, oil etc. on the condensation heat transfer and pressure drop of the microfin tubes have been published. The heat transfer enhancement factors as high as 3.0 (relative to a smooth tube) have been reported. Webb [1] and Newell and Shah [2] have given comprehensive reviews of relevant literature. As pointed out in these reviews, no theoretically based generalized method for predicting the condensation heat transfer coefficient is still available. Cavallini et al. [3,4], Shikazono et al. [5] and Kedzierski and Goncalves [6] have proposed empirical equations based on the extension of smooth tube models. Yang and Webb [7] proposed a semi-empirical model considering the combined effects of vapor shear and surface tension forces for axially grooved microfin tubes. Nozu and Honda [8] presented a detailed analysis of annular flow condensation in helically grooved microfin tubes. They considered the combined effects of vapor shear and surface tension forces but neglected the effect of gravity. For a high quality region where grooves between adjacent fins were not filled with condensate, the theoretical prediction of the heat transfer coefficient agreed with available experimental data for three tubes and four refrigerants to a mean absolute deviation of 15 percent. However, this theoretical model can not be applied to a low quality region where the effect of gravity is important.

The objective of the present study is to develop a stratified flow model of film condensation in helically grooved, horizontal microfin tubes that complements the previously developed annular flow model [8]. The theoretical predictions of the circumferential average heat transfer coefficient are compared with available experimental data for five refrigerants and five tubes. Comparison is also made with the predictions of the annular flow model and previously proposed empirical equations.

Contributed by the Heat Transfer Division for publication in the JOURNAL OF HEAT TRANSFER. Manuscript received by the Heat Transfer Division November 27, 2000; revision received August 14, 2001. Associate Editor: V. P. Carey.

Analysis

Physical Model. Figure 1 shows the physical model of stratified condensate flow in a helically grooved, horizontal microfin tube and coordinates. In Fig. 1(*a*), z_s denotes the height of stratified condensate measured from the tube bottom, and the coordinate z is measured vertically upward from the surface of stratified condensate. The angle φ is measured from the top of tube and φ_s denotes the angle below which the tube is filled with the stratified condensate. The tube surfaces at the angular portions of $0 \leqslant \varphi \leqslant \varphi_s$ and $\varphi_s \leqslant \varphi \leqslant \pi$ are denoted as region 1 and region 2, respectively. In the region just above the level of stratified condensate, condensate is retained in the groove between adjacent fins by the capillary effect. As a result, a relatively thick condensate film is formed in the groove. The angle below which the condensate is retained in the groove is denoted as the flooding angle φ_f. Figures 1(*c*) and 1(*d*) show the condensate profiles in the fin cross-sections for regions $0 \leqslant \varphi \leqslant \varphi_f$ and $\varphi_f \leqslant \varphi \leqslant \varphi_s$, respectively. The fin profile is assumed to be a trapezoid with round corners at the fin tip and fin root. The fin height and fin pitch are h and p, respectively, and the fin half tip angle is θ. The coordinate x is measured along the fin surface from the center of fin tip and y is measured vertically outward from the fin surface. The condensate on the fin surface is drained by the combined gravity and surface tension forces toward the fin root and then it flows down the groove by gravity. Thus the condensate film thickness δ is very small near the fin tip and it is relatively thick near the fin root. The effect of vapor shear force on the condensate flow on the fin surface is assumed to be negligible.

Height of Stratified Condensate. The height of stratified condensate is estimated by extending the Taitel and Dukler [9] model for a smooth tube to a microfin tube. The basic equation is written as

$$f_v \frac{\rho_v U_v^2}{2} \frac{S_v}{A_v} - f_l \frac{\rho_l U_l^2}{2} \frac{S_l}{A_l} + f_i \frac{\rho_v U_v^2}{2} \left(\frac{S_i}{A_v} + \frac{S_i}{A_l} \right) = 0, \qquad (1)$$

where f_v and f_l are the friction factors in regions 1 and 2, respectively, f_i is the interfacial friction factor, ρ_v and ρ_l are the densi-

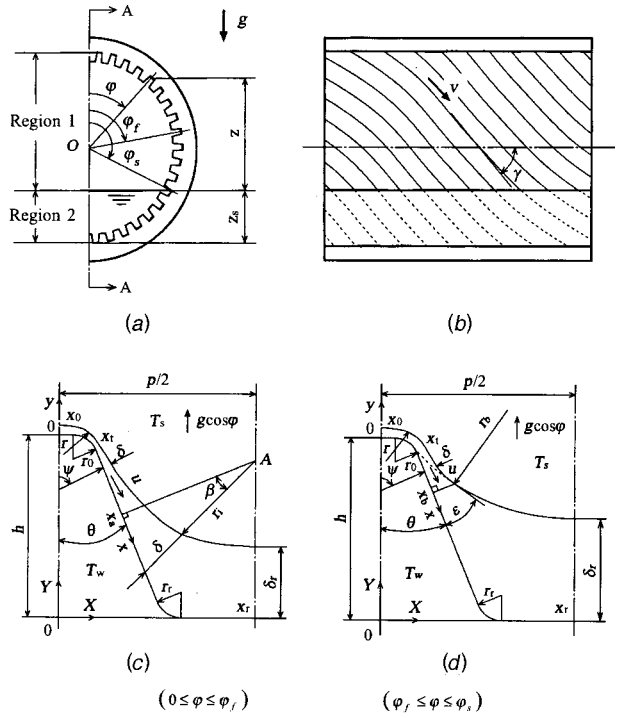

Fig. 1 Physical model and coordinates: (*a*) tube cross section; (*b*) A-A cross section; (*c*) fin cross section ($0 \le \varphi \le \varphi_f$); and (*d*) fin cross section ($\varphi_f \le \varphi \le \varphi_s$)

ties of vapor and condensate, respectively, U_v and U_l are the velocities of vapor and condensate, respectively, A_v and A_l are the cross sectional areas of the vapor space and condensate space, respectively, S_v and S_l are the perimeter lengths of regions 1 and 2, respectively, and S_i is the perimeter length of the interface. The values of f_v and f_l are estimated by an empirical equation for the internally finned tubes developed by Carnavos [10]. Thus the expressions for f_v and f_l are given by

$$f_v = 0.046\left(\frac{\rho_v d_v U_v}{\mu_v}\right)^{-0.2}\left(\frac{A}{A_n}\right)^{0.5}(\sec\gamma)^{0.75}, \tag{2}$$

$$f_l = 0.046\left(\frac{\rho_l d_l U_l}{\mu_l}\right)^{-0.2}\left(\frac{A}{A_n}\right)^{0.5}(\sec\gamma)^{0.75}. \tag{3}$$

The f_i is given by

$$f_i = 0.046\left(\frac{\rho_v d_v U_v}{\mu_v}\right)^{-0.2}, \tag{4}$$

where d_v and d_l are the equivalent diameters of the vapor space and liquid space given by $d_v = 4A_v/(S_v + S_i)$ and $d_l = 4A_l/S_i$, respectively, A is the actual cross sectional area of the tube, A_n is the nominal cross sectional area based on the fin root diameter d, and γ is the helix angle of the groove.

Equation (1) is written in dimensionless form as

$$(\overline{U}_v\,\overline{d}_v)^{-0.2}\overline{U}_v{}^2\left\{\frac{\overline{S}_v}{\overline{A}_v} + \left(\frac{A_n}{A}\right)^{0.5}(\cos\gamma)^{0.75}\left(\frac{\overline{S}_i}{\overline{A}_l} + \frac{\overline{S}_i}{\overline{A}_v}\right)\right\}$$
$$- X^2(\overline{U}_l\,\overline{d}_l)^{-0.2}\overline{U}_l{}^2\frac{\overline{S}_l}{\overline{A}_l} = 0, \tag{5}$$

where

$$\overline{A}_v = \frac{1}{4}\left[\left(\frac{A}{A_n}\right)\cos^{-1}(2\overline{z}_s - 1) - (2\overline{z}_s - 1)\{1 - (2\overline{z}_s - 1)^2\}^{1/2}\right],$$

$$\overline{A}_l = \frac{1}{4}\left[\left(\frac{A}{A_n}\right)\{\pi - \cos^{-1}(2\overline{z}_s - 1)\} + (2\overline{z}_s - 1)\{1 - (2\overline{z}_s - 1)^2\}^{1/2}\right],$$

$$\overline{d}_v = \frac{d_v}{d}, \quad \overline{d}_l = \frac{d_l}{d}, \quad \overline{S}_v = \varepsilon_a\cos^{-1}(2\overline{z}_s - 1),$$

$$\overline{S}_l = \varepsilon_a\{\pi - \cos^{-1}(2\overline{z}_s - 1)\}, \quad \overline{S}_i = \{1 - (2\overline{z}_s - 1)^2\}^{1/2},$$

$$\overline{U}_v = \frac{\overline{A}}{\overline{A}_v}, \quad \overline{U}_l = \frac{\overline{A}}{\overline{A}_l}, \quad X = \left(\frac{1-\chi}{\chi}\right)^{0.9}\left(\frac{\rho_v}{\rho_l}\right)^{0.5}\left(\frac{\mu_l}{\mu_v}\right)^{0.1}, \quad \overline{z}_s = \frac{z_s}{d},$$

ε_a is the surface area enhancement, and χ is the quality. The value of $\overline{z}_s$ is obtained by solving Eq. (5) iteratively.

Profile of Thick Condensate Film. In the angular portion $\varphi_f \le \varphi \le \varphi_s$ (Fig. 1(*d*)), the condensate velocity in the thick film is supposed to be very small. Thus its profile is approximated by a static meniscus that touches the fin flank (shown by a dotted line). Then the radius of curvature of the thick film r_b is given by

$$\frac{\sigma}{r_b} = (\rho_l - \rho_v)gz = \frac{(\rho_l - \rho_v)gd}{2}(\cos\varphi - \cos\varphi_s). \tag{6}$$

It is seen from Eq. (6) that $r_b = \infty$ at $z = 0$ ($\varphi = \varphi_s$), and r_b decreases first rapidly, and then gradually, with increasing z (decreasing φ). This means that $\delta_r = h$ at $\varphi = \varphi_s$ and δ_r decreases with decreasing φ.

Profile of Thin Condensate Film. In the thin film region $0 \le \varphi \le \varphi_f$, δ is assumed to be sufficiently smaller than h and p. Assuming a laminar flow, the momentum equation in the x-direction and in the direction along the groove are respectively written as

$$\mu_l\frac{\partial^2 u}{\partial y^2} - (\rho_l - \rho_v)g\sin\psi\cos\varphi = \frac{\partial P}{\partial x} \tag{7}$$

$$\mu_l\frac{\partial^2 v}{\partial y^2} + (\rho_l - \rho_v)g\sin\gamma\sin\varphi = 0, \tag{8}$$

where u and v are the velocity components in the x-direction and in the direction along the groove, respectively, ψ is the angle shown in Figs. 1(*c*) and 1(*d*), and P is the pressure difference between the condensate and vapor due to the surface tension effect. The boundary conditions are

$$u = v = 0 \quad \text{at } y = 0 \tag{9}$$

$$\partial u/\partial y = \partial v/\partial y = 0 \quad \text{at } y = \delta. \tag{10}$$

The P in Eq. (7) is given by

$$P = \sigma/r, \tag{11}$$

where σ is the surface tension, and r is the radius of curvature of the condensate surface in the fin cross-section. The expression for r is given by

$$\frac{1}{r} = -\frac{\partial^2\delta/\partial x^2}{\{1 + (\partial\delta/\partial x)^2\}^{3/2}} \quad \text{for } 0 \le x \le x_0 \text{ and } x_t \le x \le x_a \tag{12a}$$

$$\frac{1}{r}=\frac{\frac{1}{r_0}+\left(\frac{2}{r_0^2}+\frac{\delta}{r_0^3}\right)\delta+\frac{2}{r_0}\left(\frac{\partial\delta}{\partial x}\right)^2-\left(1+\frac{\delta}{r_0}\right)\left(\frac{\partial^2\delta}{\partial x^2}\right)}{\left\{\left(1+\frac{\delta}{r_0}\right)^2+\left(\frac{\partial\delta}{\partial x}\right)^2\right\}^{3/2}}$$

$$\text{for } x_0\leqslant x\leqslant x_t \tag{12b}$$

$$\frac{1}{r}=\frac{r_i^2+2(dr_i/d\beta)^2-r_i(d^2r_i/d\beta^2)}{\{r_i^2+(dr_i/d\beta)^2\}^{3/2}} \quad \text{for } x_a\leqslant x\leqslant x_r, \tag{12c}$$

where x_0 and x_t are the connecting points between the straight and round portions of the fin surface, x_a is the coordinate at the foot of the perpendicular from point A in Fig. 1(*c*), x_r is the mid point at the fin root, r_0 is the radius of curvature at the corner of the fin tip, r_i is the distance of the condensate surface measured from point A and β is the angle shown in Fig. 1(*c*). Equations (12*a*) and (12*c*) are the expressions for r in the Cartesian and polar coordinates, respectively. Equation (12*b*) is obtained from Eq. (12*c*) by putting $r_i=r_0+\delta$. The x_a is chosen so that point A is located in the vapor space. For $x_a<x\leqslant x_r$, δ is defined as shown in Fig. 1(*c*).

Since δ is very small, a linear temperature drop is assumed across the condensate film. Thus the heat flux q is written as

$$q=\lambda_l(T_s-T_w)/\delta, \tag{13}$$

where T_s and T_w are the saturation temperature of vapor and the wall temperature, respectively. Ignoring the effect of subcooling of the condensate film compared to the latent heat, q is related to the condensation mass flux m by the following equation:

$$q=h_{fg}m, \tag{14}$$

where m is given by

$$m=\rho_l\left(\frac{\partial}{\partial x}\int_0^\delta u\,dy+\frac{2\sin\gamma}{d}\frac{\partial}{\partial\varphi}\int_0^\delta v\,dy\right). \tag{15}$$

Substituting q and m given by Eqs. (13) and (15) into Eq. (14) yields

$$\rho_l\left(\frac{\partial}{\partial x}\int_0^\delta u\,dy+\frac{2\sin\gamma}{d}\frac{\partial}{\partial\varphi}\int_0^\delta v\,dy\right)=\frac{\lambda_l(T_s-T_w)}{h_{fg}\delta}. \tag{16}$$

Substituting the solutions of Eqs. (7) and (8) into Eq. (16) yields

$$-\frac{(\rho_l-\rho_v)g\cos\varphi}{3\nu_l}\frac{\partial}{\partial x}(\sin\psi\delta^3)-\frac{\sigma}{3\nu_l}\frac{\partial}{\partial x}\left\{\frac{\partial}{\partial x}\left(\frac{1}{r}\right)\delta^3\right\}+\frac{2(\rho_l-\rho_v)g\sin^2\gamma}{3\nu_l d}\frac{\partial}{\partial\varphi}(\sin\varphi\delta^3)=\frac{\lambda_l(T_s-T_w)}{h_{fg}\delta}. \tag{17}$$

The boundary conditions are

$$\partial\delta/\partial\varphi=0 \quad \text{at } \varphi=0 \tag{18}$$

$$\partial\delta/\partial x=\partial^3\delta/\partial x^3=0 \quad \text{at } x=0 \text{ and } x_r. \tag{19}$$

The second boundary condition in Eq. (19) indicates that $\partial P/\partial x=0$ at $x=0$ and x_r.

The solution of Eq. (17) subject to the boundary conditions (18) and (19) was obtained numerically by a finite difference scheme. Two different grid sizes with a finer grid at the tip and corner and a coarser grid at the side and fin root were chosen along x with a total of 51 to 117 grid points. The grid size in the φ-direction, $\Delta\varphi$, was chosen as $\pi/36$. In the numerical calculation, the unsteady term $\rho_l\partial\delta/\partial t=0$ was added to the left side of Eq. (17) and the solution was obtained as the steady-state solution of an unsteady condensate flow subject to an arbitrary initial distribution of δ. The calculation was started at $\varphi=0$ and proceeded in the φ-direction. For each φ, calculation was continued until the convergence criterion $|1-\delta_{i,j}^*/\delta_{i,j}|<10^{-4}$ and $|1-\delta_{i,j}^*/\delta_{i,j}|/\Delta\tau<0.01$ was satisfied, where $\delta_{i,j}^*$ and $\delta_{i,j}$ are the old and new values of δ at grid point (i,j), and $\Delta\tau=t\nu_l/p^2$ is the dimensionless time step. The solution differed from that corresponding to the convergence criterion $|1-\delta_{i,j}^*/\delta_{i,j}|<10^{-4}$ and $|1-\delta_{i,j}^*/\delta_{i,j}|/\Delta\tau<0.1$ by a maximum of 0.1 percent. The difference in the local δ value between the solutions for the number of grid points along x of 51 and 117 was less than 0.1 percent. The solution could be obtained for the whole range of φ except $\varphi=\pi$. However, this solution must be modified for the effect of condensate retention. According to the numerical results, $r(x_r,\varphi)$ increased monotonically with increasing φ. Comparison of $r(x_r,\varphi)$ and $r_b(\varphi)$ (given by Eq. (6)) revealed that $r_b(\varphi)\geqslant r(x_r,\varphi)$ near $\varphi=\varphi_s$. The difference between $r_b(\varphi)$ and $r(x_r,\varphi)$ decreased rapidly with decreasing φ and the two quantities crossed at some angle unless χ was too small. The angle $\varphi=\varphi_f$ was defined as the point where $r(x_r,\varphi)$ agreed with $r_b(\varphi)$.

For $\varphi_f\leqslant\varphi\leqslant\varphi_s$ where the condensate film is consisted of the thin film region near the fin tip and the thick film region near the fin root, the boundary conditions at the connecting point between the thin film and the thick film are given by

$$\partial\delta/\partial x=\tan\varepsilon, \quad r=-r_b \quad \text{at } x=x_b, \tag{20}$$

where ε is the angle shown in Fig. 1(*d*). The value of ε was assumed as $\pi/6$ for $x_b>(x_0+x_t)/2$ and $\pi/18$ for $x_b<(x_0+x_t)/2$. This was because the solution became unstable when $\varepsilon=\pi/6$ was assumed for a very small x_b. As described in the previous paper [8], the deviation in the calculated values of α_φ for $\varepsilon=\pi/6$ and $\pi/20$, obtained from Eq. (21), was less than 1 percent. The solution of Eq. (17) subject to the boundary conditions (20) was obtained numerically using the same scheme as for $0\leqslant\varphi\leqslant\varphi_f$.

Heat Transfer Coefficients. For region 1, the average heat transfer coefficient for the fin cross section α_φ is defined on the projected area basis as

$$\alpha_\varphi=\frac{2}{p}\int_0^{x_r}\alpha_x dx=\frac{2\lambda_l}{p}\int_0^{x_r}\frac{1}{\delta}dx, \tag{21}$$

where $\alpha_x=\lambda_l/\delta$ is the local heat transfer coefficient. The value of α_x becomes incorrect as δ increases, because the two-dimensional effect appears. However, the value of α_φ is not affected so much by the incorrect estimation of α_x in the thick film region, because the contribution of the thick film region is small. The average heat transfer coefficient for region 1, α_1, is defined on the projected area basis as

$$\alpha_1=\frac{1}{\varphi_s}\int_0^{\varphi_s}\alpha_\varphi d\varphi=\frac{2\lambda_l}{p\varphi_s}\int_0^{\varphi_s}\int_0^{x_r}\frac{1}{\delta}dx\,d\varphi. \tag{22}$$

In order to avoid difficulty associated with the analysis of heat transfer in region 2, α_2 is estimated using the following empirical equation for forced convection in internally finned tubes developed by Carnavos [10]:

$$\alpha_2=0.023\frac{\lambda_l}{d_l}\left(\frac{\rho_l d_l U_l}{\mu_l}\right)^{0.8}\mathrm{Pr}_l^{0.4}\left(\frac{A}{A_c}\right)^{0.1}\varepsilon_a^{0.5}(\sec\gamma)^3, \tag{23}$$

where $A_c=\pi(d-2h)^2/4$ is the core flow area.

Comparison of α_1 and α_2 revealed that $\alpha_1\geqslant\alpha_2$, which indicated that the wall temperature was not uniform around the tube. Thus the condensation temperature difference (T_s-T_{wk}) and the heat flux q_k for region k were obtained from

$$q_k=\left\{\frac{1}{\alpha_k}+\frac{d}{2\lambda_w}\ln\left(\frac{d_o}{d}\right)+\frac{1}{\alpha_c}\frac{d}{d_o}\right\}^{-1}(T_s-T_c)=\alpha_k(T_s-T_{wk})$$

$$k=1,\,2, \tag{24}$$

where d_o is the tube outside diameter, α_c is the coolant side heat transfer coefficient, T_{wk} is the inside tube wall temperature for region k. Then the circumferential average heat transfer coefficient at the tube inside surface α_m was obtained from

Table 1 Fin and tube dimensions

Tube designation			A	B	C	D	E
Outside diameter	d_o	mm	9.53	10.0	9.52	7.0	7.0
Fin root diameter	d	mm	8.44	8.48	8.88	6.50	6.49
Number of fins	n	-	47	60	60	50	60
Helix angle	γ	deg	20.0	18.0	18.7	18.0	18.0
Fin pitch *	p	mm	0.53	0.42	0.44	0.39	0.34
Fin height	h	mm	0.24	0.16	0.19	0.21	0.19
Fin half tip angle *	θ	deg	30.5	19.9	22.3	19.5	13.1
Curvature radius at corner of fin tip *	r_0	mm	0.074	0.015	0.025	0.008	0.030
Length of flat portion at fin tip *	x_0	mm	0.004	0.027	0.015	0.019	0.018
Area enhancement ratio	ε_a	-	1.49	1.52	1.51	1.71	1.78
Length of sub-section		mm	400	500	600	300	300
Authors			Nozu & Honda	Haraguchi	Hayashi	Miyara et al.	Miyara et al.

* dimension in a cross-section normal to groove

$$\alpha_m = q_m/(T_s - T_{wm}), \tag{25}$$

where

$$q_m = \{\varphi_s q_1 + (\pi - \varphi_s) q_2\}/\pi \tag{26}$$

$$T_s - T_{wm} = \{\varphi_s (T_s - T_{w1}) + (\pi - \varphi_s)(T_s - T_{w2})\}/\pi. \tag{27}$$

q_m and T_{wm} are the circumferential average heat flux and circumferential average wall temperature, respectively.

Comparison With Experiments and Discussion

Numerical predictions of the stratified flow model and the previously proposed annular flow model [8] and empirical equations are compared with available experimental data for five tubes and five fluids. Table 1 shows the dimensions of test tubes used in the previous studies [8, 11–13]. In these studies, the refrigerant and cooling water flowed counter-currently through a number of subsections in which the sectional-average heat transfer coefficients were measured. The local wall temperatures at the top, side(s) and bottom of each sub-section were measured by thin thermocouples embedded in the tube wall. Then the value of T_{wm} was obtained from the weighted average of the measured values making a small correction for radial wall conduction. The experimental data adopted were limited to those with the $T_s - T_{wm}$ value greater than 0.8 K and the temperature rise of cooling water in the sub-section ΔT_c greater than 0.6 K. The uncertainties associated with the measurements of $T_s - T_{wm}$ and ΔT_c are considered to be about 0.1 K and 0.05 K, respectively. Thus the uncertainty in the measured value of α_m is estimated to be about 15 percent or less. The uncertainty is supposed to be largest at the high quality region where the $T_s - T_{wm}$ value is smallest. The value of d was about 8.5 mm for tubes A-C and 6.5 mm for tubes D and E. The test fluids were R-11 for tube A, R-123, R-134a, and R-22 for tube B, R-134a for tube C, and R410A for tubes D and E. R410A (R32/R125=50/50 mass percent) is a near azeotropic mixture with a temperature glide of 0.11 K [14]. Thus the mass transfer resistance in the vapor phase may be neglected. The most significant difference in the physical properties among these fluids is the vapor density. Table 2 shows the vapor to liquid density ratios of these fluids at the experimental conditions.

Figure 2(*a*) shows examples of the numerical results of the condensate profile in the fin cross section for tube C. It is seen from Fig. 2(*a*) that the condensate profile changes very slowly in the region $0 \leqslant \varphi \leqslant \varphi_f$, whereas it changes rapidly in the region $\varphi_f \leqslant \varphi \leqslant \varphi_s$. It is also seen that the condensate profile has two solutions at $\varphi = \varphi_f$. The upper profile consists of the thin film region near the fin tip and the thick film region near the fin root, whereas the lower profile consists only of the thin film region. This is due to the simplifying assumption on the thick condensate film adopted in the present analysis. Figure 2(*b*) shows the distributions of the local heat transfer coefficient corresponding to Fig. 2(*a*). The α_x takes a very sharp peak at the corner of fin tip and decreases rapidly to a very small value as x increases.

Figures 3(*a*) and 3(*b*), respectively, show the distributions of α_φ and T_w that correspond to Fig. 2. The α_φ takes a maximum value at $\varphi = 0$ and decreases gradually with increasing φ in the region $0 \leqslant \varphi \leqslant \varphi_f$. It shows a small drop at $\varphi = \varphi_f$ due to the simplifying

Table 2 Vapor-to-liquid density ratios of test fluids

	R11	R123	R134a	R22	R410A
T_s °C	40	50	50	50	40
ρ_v / ρ_l	6.87×10^{-3}	9.33×10^{-3}	5.97×10^{-2}	8.00×10^{-2}	0.102

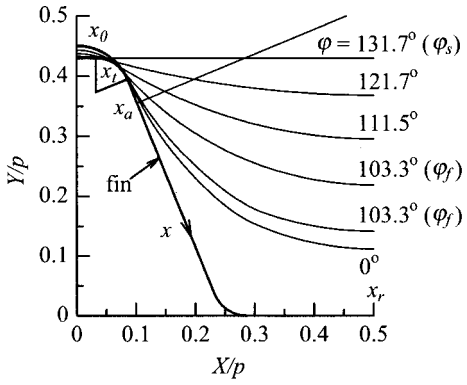

(*a*)

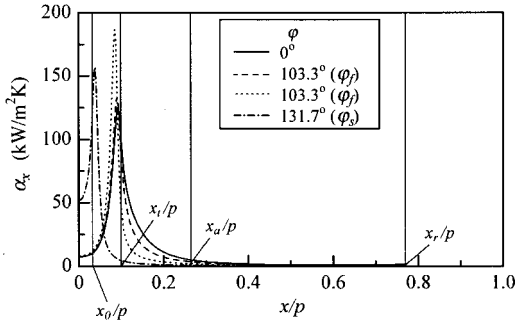

(*b*)

Fig. 2 Condensate profiles in fin cross-section (*a*) and distribution of local heat transfer coefficient (*b*); Tube C, $G = 98$ kg/m^2 s, $\chi = 0.72$

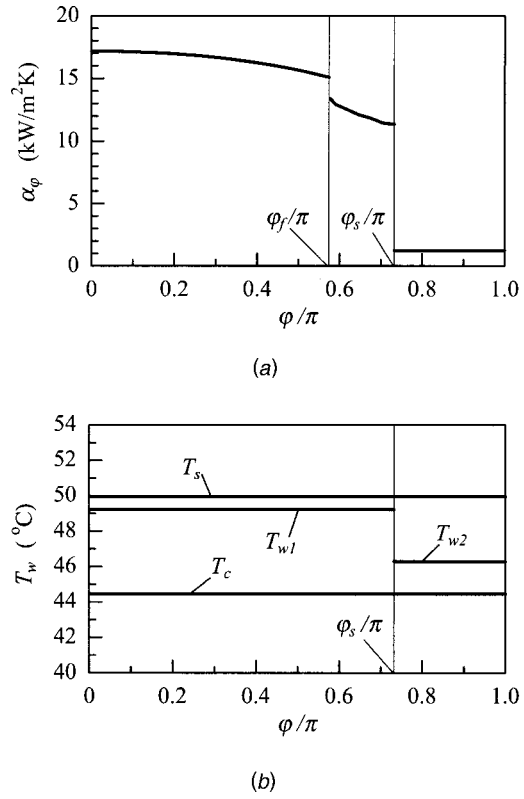

Fig. 3 Circumferential distributions of average heat transfer coefficient for fin cross-section (*a*) and tube wall temperature (*b*); Tube C, $G=98$ kg/m^2 s, $\chi=0.72$

assumption adopted and then decreases gradually with increasing φ in the region $\varphi_f \leqslant \varphi \leqslant \varphi_s$. It shows a large drop at $\varphi=\varphi_s$ and then takes a very small value in the region $\varphi_s \leqslant \varphi \leqslant \pi$. The large drop in α_φ at $\varphi=\varphi_s$ is due to the fact that the effect of curvature change of the condensate surface in the φ-direction is neglected in the theoretical analysis. As a result of a large difference in α_φ between regions 1 and 2, T_w takes a considerably different value in regions 1 and 2.

Figure 4 shows comparisons of the measured and predicted values of α_m for tube C. In this figure the results for two refrigerant mass velocities $G=102$ and 299 kg/m^{2}s are plotted on the

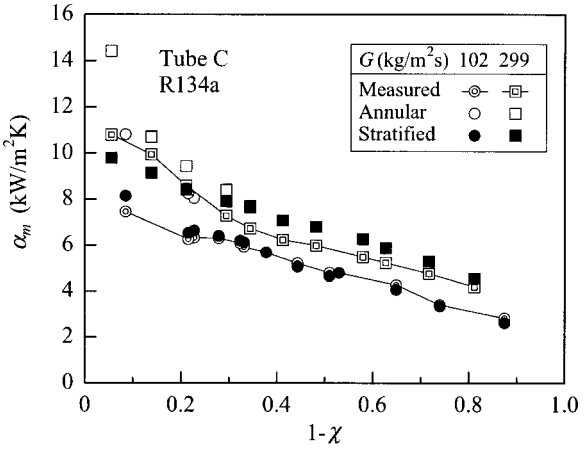

Fig. 4 Variation of circumferential average heat transfer coefficient with wetness fraction; comparison of measured and predicted values, Tube C

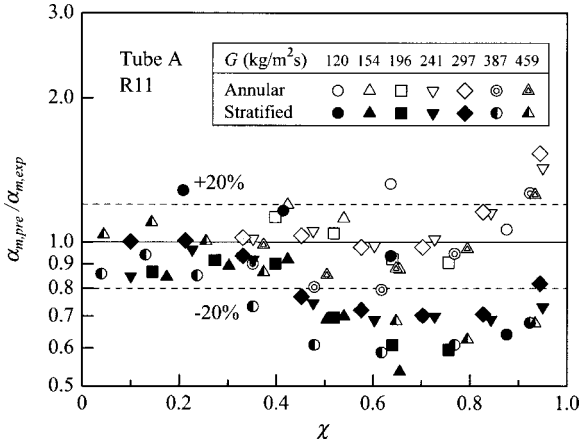

Fig. 5 Comparison of measured and predicted circumferential average heat transfer coefficients

coordinates of α_m versus the wetness fraction $1-\chi$. Generally, the measured α_m decreases monotonically as $(1-\chi)$ increases. The decrease is more significant for higher G and smaller $(1-\chi)$. The open and solid symbols show the predictions of the annular flow model [8] and the stratified flow model, respectively. The former is shown only for the high quality region where the grooves between adjacent fins are not flooded with condensate. The annular flow model predicts a higher α_m than the stratified flow model at small $(1-\chi)$. The difference between the two theoretical predictions decreases as $(1-\chi)$ increases. Comparison of the measured and predicted values reveals that the measured value agrees fairly well with the prediction of the stratified flow model for both cases of $G=102$ and 299 kg/m^{2}s. The agreement is better for $G=102$ kg/m^2 s. The annular flow model gives a higher α_m than the measured value and the difference is more significant for $G=102$ kg/m^2 s. If an appropriate turbulence model is introduced to the condensate flow, the annular flow model can be extended to the case where the grooves are completely flooded with the condensate. However, this kind of calculation predicts a very small α_m (about one half of the measured value or less). This is because the region near the fin tip with a very thin condensate film (see Fig. 2) does not exist any more.

Figures 5–11, respectively, show comparisons of the measured α_m values and theoretical predictions of the annular flow and stratified flow models for tubes A~E. In these figures the ratio of the predicted value $\alpha_{m,\mathrm{pre}}$ to the measured value $\alpha_{m,\mathrm{exp}}$, $\alpha_{m,\mathrm{pre}}/$

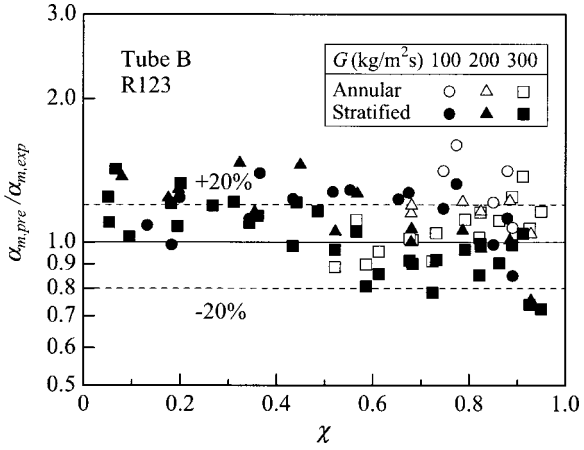

Fig. 6 Comparison of measured and predicted circumferential average heat transfer coefficients

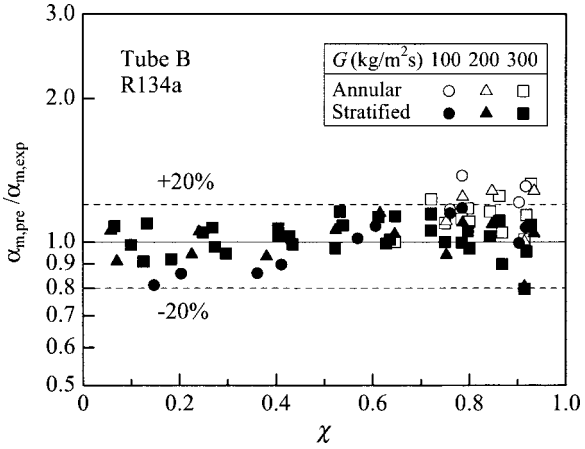

Fig. 7 Comparison of measured and predicted circumferential average heat transfer coefficients

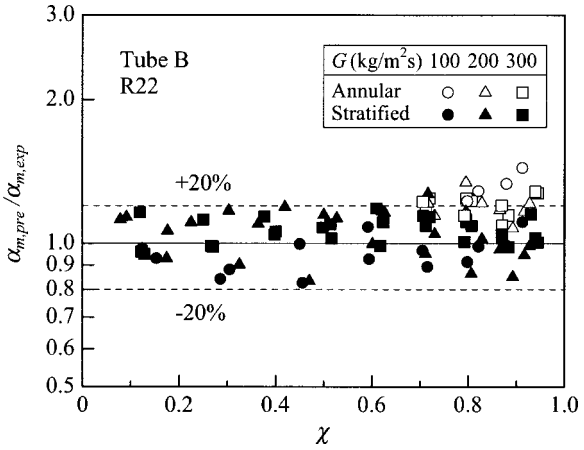

Fig. 8 Comparison of measured and predicted circumferential average heat transfer coefficients

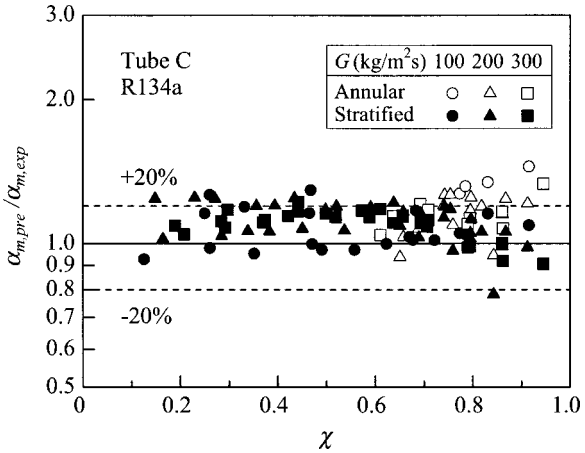

Fig. 9 Comparison of measured and predicted circumferential average heat transfer coefficients

$\alpha_{m,\exp}$, is plotted as a function of χ. Generally, the annular flow model predicts a considerably higher α_m than the measured value at high χ. This is probably due to the overestimation of the interfacial shear stress acting on the condensate film. The annular flow model needs to be modified regarding the method for estimating the interfacial shear stress. A better agreement ($\pm$20 percent) is obtained as χ decreases. However, as noted previously, this model is not applicable to the region where the grooves are completely flooded with condensate. In Fig. 5 for tube A with R11, most of the measured values agree within $\pm$20 percent with the higher of the two theoretical predictions. In Figs. 7 and 8 for tube B with R134a and R22, Fig. 9 for tube C with R134a, and Fig. 10 for tube D with R410A, most of the measured values agree within $\pm$20 percent with the predictions of the stratified flow model. In Fig. 6 for tube B with R123, most of the measured values agree within $\pm$20 percent with the predictions of the stratified flow model in the region of $0.5<\chi<1.0$. However, the predictions of the stratified flow model are 0 to 40 percent higher than the measured values in the region of $0<\chi<0.5$. In Fig. 11 for tube E with R-410A, most of the predictions of the stratified flow model are 0 to 30 percent higher than the measured values.

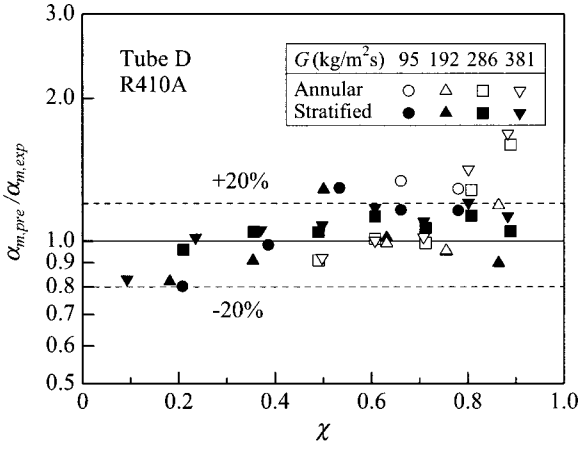

Fig. 10 Comparison of measured and predicted circumferential average heat transfer coefficients

Table 3 summarizes the results of assessment of the stratified flow model and previously proposed empirical equations [3,5,6,15]. In Table 3, the empirical equation for tubes with relatively large fin dimensions proposed by Luu and Bergles [15] is also included. The performance of the stratified flow model and each empirical equation was assessed in terms of the arithmetic mean error a.m. and the root-mean-square error r.m.s. defined as follows:

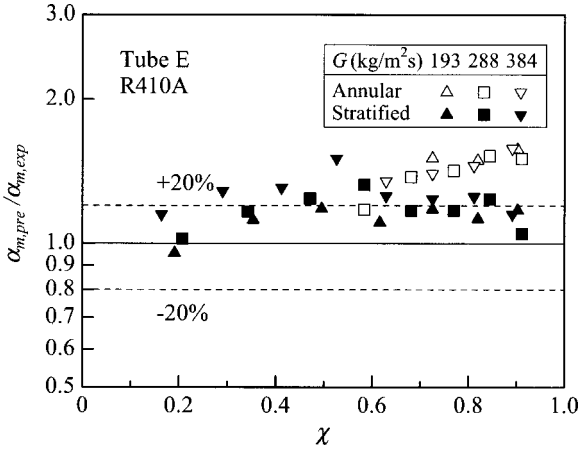

Fig. 11 Comparison of measured and predicted circumferential average heat transfer coefficients

Table 3 Performance of empirical equations and stratified flow model

				Luu-Bergles		Cavallini et al.		Kedzierski-Goncalves		Shikazono et al.		Stratified flow model	
Tube	Fluid	d, mm	N	a.m.	r.m.s.	a.m.	r.m.s.	a.m.	r.m.s.	a.m.	r.m.s.	a.m.	r.m.s.
A	R11	8.44	47	-40.5	43.7	-77.1	77.1	-39.9	41.7	-51.4	51.9	-19.2	25.2
B	R123	8.48	65	-22.5	29.3	-44.1	44.6	-14.8	19.1	-37.0	38.1	9.8	21.2
B	R134a	8.48	57	-32.0	35.0	-13.0	15.3	-23.2	24.8	-33.8	37.1	1.5	9.2
B	R22	8.48	66	-40.8	43.1	-3.6	13.2	-26.4	27.3	-28.5	32.2	3.4	10.7
C	R134a	8.88	78	-43.1	45.2	-12.8	15.5	-26.0	26.6	-28.9	30.8	9.2	13.7
D	R410A	6.50	26	-62.1	62.9	7.5	14.6	-20.2	23.5	-20.5	31.6	5.0	13.8
E	R410A	6.49	23	-56.8	57.6	48.9	52.2	-6.1	11.7	-12.4	22.0	19.1	22.0

N: Number of experimental data; a.m.: Arithmetic mean error (%); r.m.s.: Root-mean-square error (%).

$$\text{a.m.} = \frac{1}{N}\sum \frac{\alpha_{m,\text{pre}} - \alpha_{m,\text{exp}}}{\alpha_{m,\text{exp}}} \times 100\,\% \tag{28}$$

$$\text{r.m.s.} = \sqrt{\frac{1}{N}\sum \left(\frac{\alpha_{m,\text{pre}} - \alpha_{m,\text{exp}}}{\alpha_{m,\text{exp}}}\right)^2} \times 100\,\%, \tag{29}$$

where N is the number of data points. It is seen from Table 3 that the stratified flow model gives a better agreement with the measured value than the empirical equations for most cases, though there is a trend to overestimate α_m. The r.m.s. error is within 22.0 percent except for R-11 with small ρ_v/ρ_l (see Table 2). Considering a relatively large uncertainty (about 15 percent or less) in the measured α_m, the agreement may be considered satisfactory. This does not necessarily mean that the actual flow pattern is the stratified flow for all cases. However, the forgoing results suggest that the assumptions of laminar condensate flow in region 1 and turbulent condensate flow in region 2 adopted in the stratified flow model are satisfactory enough for the calculation of α_m. One of the reasons for the overestimation is the assumption of flat vapor-liquid interface adopted in the theoretical model. In the actual stratified flow, the interface is supposed to be curved due to the effects of surface tension and vapor shear forces. Thus the angle φ_s in Fig. 1(*a*) will be smaller than the case of flat interface. This will result in a decrease in the tube surface area in region 1 with much higher α_φ than that in region 2 (see Fig. 3(*a*)). As a result, the α_m value predicted by the modified stratified flow model taking account of the curvature effect will be smaller than the prediction of the present model. This effect will be more significant for tubes with smaller d and for the low χ region where the void fraction is small.

Conclusions

A stratified flow model of film condensation in helically-grooved, horizontal microfin tubes has been developed. The height of stratified condensate was determined by extending the Taitel and Dukler model for a smooth tube to a microfin tube. The friction factors at the upper and lower parts of the tube exposed to the vapor flow and condensate flow, respectively, were estimated by the Carnavos [10] equation for internally finned tubes. For the upper part of the tube, numerical calculation of laminar film condensation that considered the combined effects of gravity and surface tension forces was conducted. For the lower part of the tube, the heat transfer coefficient was estimated by the Carnavos [10] equation for forced convection in internally finned tubes. The predictions of the circumferential average heat transfer coefficient α_m by the present model, and previously proposed annular flow model and empirical equations were compared with available experimental data for five tubes and five refrigerants. The annular flow model predicted a considerably higher α_m than the measured value at high χ. This was probably due to the overestimation of the interfacial shear stress. A better agreement (within ± 20 percent) was obtained as χ decreased. However, this model predicted a considerably smaller α_m than the measured value (about one half or less) when the fins were completely flooded with condensate. The stratified flow model gave a better agreement with the measured values than the empirical equations for most cases, though there was a trend to overestimate α_m. The r.m.s. error was within 22.0 percent except for R-11 with small ρ_v/ρ_l. The overestimation was probably due to the effect of curved vapor-liquid interface, caused by the surface tension and vapor shear forces, which was neglected in the present analysis.

Nomenclature

A = actual cross-sectional area of tube
d = fin root tube diameter
d_l = equivalent diameter of liquid space ($=4A_l/S_i$)
d_o = tube outside diameter
d_v = equivalent diameter of vapor space ($=4A_v/(S_v+S_i)$)
f = friction factor
g = gravitational acceleration
G = refrigerant mass velocity
h = fin height
h_{fg} = specific enthalpy of evaporation
m = condensation mass flux
N = number of experimental data
n = number of fins
p = fin pitch
P = static pressure
Pr = Prandtl number
q = heat flux
r = radius of curvature of condensate surface in fin cross-section
r_0 = radius of curvature at corner of fin tip
r_b = radius of curvature of condensate surface in thick film region
r_i = distance of condensate surface measured from point A, Fig. 1
r_r = radius of curvature at corner of fin root
S = perimeter length
T = temperature
t = time
U = velocity in axial direction
u,v = velocity components in x-direction and along groove
x,y = coordinates, Fig. 1
x_b = coordinate at connecting point between thin and thick film regions, Fig. 1
x_a = coordinate at the foot of perpendicular from point A, Fig. 1
x_0, x_t = coordinates at connecting points between straight and round portions of fin, Fig. 1
x_r = mid point between adjacent fins

X,Y = coordinates, Fig. 1
z = vertical height measured from condensate surface, Fig. 1
z_s = height of stratified condensate

Greek Symbols

α = heat transfer coefficient
β = angle, Fig. 1
χ = mass quality
δ = condensate film thickness
ε = angle, Fig. 1
ε_a = surface area enhancement
γ = helix angle of groove
φ = angle measured from tube top
λ = thermal conductivity
μ = dynamic viscosity
ν = kinematic viscosity
θ = fin half tip angle
ρ = density
σ = surface tension
τ = dimensionless time
ψ = angle, Fig. 1

Subscripts

b = boundary of thin and thick film regions
c = coolant or coolant side
exp = measured value
f = flooding point
i = interface or grid point
j = grid point
l = liquid
m = circumferential average value
pre = predicted value
r = root of fin or mid point at fin root
s = saturation
v = vapor
w = wall
x = local value
φ = average value for fin cross-section
1 = region 1
2 = region 2

Superscript

$-$ = dimensionless quantity

References

[1] Webb, R. L., 1994, *Principles of Enhanced Heat Transfer*, chap. 14, John Wiley and Sons, New York.
[2] Newell, T. A., and Shah, R. K., 1999, ''Refrigerant Heat Transfer, Pressure Drop, and Void Fraction Effects in Microfin Tubes,'' *Proceedings of 2nd International Symposium on Two-Phase Flow and Experimentation*, Pisa, Italy, Vol. 3, pp. 1623–1639.
[3] Cavallini, A., Doretti, L., Klammsteiner, N., Longo, G. A., and Rosetto, L., 1995, ''Condensation of New Refrigerants Inside Smooth and Enhanced Tubes,'' *Proceedings of 19th International Congress of Refrigeration*, Vol. IV, pp. 105–114.
[4] Cavallini, A., Del Col, D., Doretti, L., Longo, G. A., and Rosetto, L., 1999, ''A New Computational Procedure for Heat Transfer and Pressure Drop during Refrigerant Condensation Inside Enhanced Tubes,'' Journal of Enhanced Heat Transfer, **6**, No. 1, pp. 441–456.
[5] Shikazono, N., Itoh, M., Uchida, M., Fukushima, T., and Hatada, T., 1998, ''Predictive Equation Proposal for Condensation Heat Transfer Coefficient of Pure Refrigerants in Horizontal Microfin Tubes,'' Transactions of JSME, **64**, pp. 196–203.
[6] Kedzierski, M. A., and Goncalves, J. M., 1999, ''Horizontal Convective Condensation of Alternative Refrigerants Within a Micro-Fin Tube,'' Journal of Enhanced Heat Transfer, **6**, No. 2–4, pp. 161–178.
[7] Yang, C. Y., and Webb, R. L., 1997, ''A Predictive Model for Condensation in Small Hydraulic Diameter Tubes Having Axial Microfins,'' ASME J. Heat Transfer, **119**, No. 4, pp. 776–782.
[8] Nozu, S., and Honda, H., 2000, ''Condensation of Refrigerants in Horizontal, Spirally Grooved Microfin Tubes: Numerical Analysis of Heat Transfer in Annular Flow Regime,'' ASME J. Heat Transfer, **122**, No. 1, pp. 80–91.
[9] Taitel, Y., and Dukler, A. E., 1976, ''A Model for Predicting Flow Regime Transitions in Horizontal and Near Horizontal Gas-Liquid Flow,'' AIChE J., **22**, No. 1, pp. 47–55.
[10] Carnavos, T. C., 1980, ''Heat Transfer Performance of Internally Finned Tubes in Turbulent Flow,'' Heat Transfer Eng., **4**, No. 1, pp. 32–37.
[11] Haraguchi, H., 1994, ''Studies on Condensation of HCFC-22, HFC-134a and HCFC-123 in Horizontal Tubes,'' Dr. Eng. thesis, Kyushu University.
[12] Hayashi, T., 1998, ''Enhancement of Condensation of HFC-134a in Horizontal Tubes,'' M. Eng. thesis, Kyushu University.
[13] Miyara, A., Nonaka, K., and Taniguchi, M., 2000, ''Condensation Heat Transfer and Flow Pattern Inside a Herringbone-Type Microfin Tube,'' Int. J. Refrig., **23**, No. 1, pp. 141–152; also private communication.
[14] Mclinden, M. O., Klein, S. A., Lemmon, E. W., and Peskin, A. P., 1998, NIST Thermodynamic and Transport Properties of Refrigerants and Refrigerant Mixtures—REFPROP, Version 6.0.
[15] Luu, M., and Bergle, A. E., 1980, ''Enhancement of Horizontal In-Tube Condensation of Refrigerant-113,'' ASHRAE Trans., **86**, Pt. 1, pp. 293–312.

Linear Instability Analysis of a Horizontal Two-Phase Flow in the Presence of Electrohydrodynamic Extraction Force

Y. Feng

J. Seyed-Yagoobi
e-mail: jayagoobi@mengr.tamu.edu

Electrohydrodynamics Laboratory,
Department of Mechanical Engineering,
Texas A&M University,
College Station, TX 77843-3123

The flow regimes associated with a horizontal internal two-phase (liquid-vapor) flow in the presence and absence of the electric field are investigated with the linear stability analysis. The momentum interchange due to the entrainment between the two phases is included in the analysis. The presence of the electric field promotes instability by providing the electrohydrodynamic (EHD) extraction force. Qualitative stability maps for the annular two-phase flow are provided with and without the electric field presence. Onset of the instability is compared with the experimental data and it is shown that the transition between the EHD-enhanced and EHD-suppressed convective boiling heat transfer is located near the annular-to-mist transition region. [DOI: 10.1115/1.1414132]

Keywords: Electric Fields, Heat Transfer, Instability, Phase Change, Stability, Two-Phase

1 Introduction

Electrohydrodynamic (EHD) phenomena, generated by the electric field coupled with the hydrodynamic flow, can be applied to enhance the heat transfer in the liquid-vapor channel flow. In the past ten years, a number of researchers, including Singh et al. [13,14], Bryan and Seyed-Yagoobi [1,2], Norris et al. [10], and Cotton et al. [4], have studied the effects of electric fields upon the flow patterns and the heat transfer in the liquid-vapor horizontal pipe flow. Their studies have provided a better understanding of the relation between the EHD extraction phenomenon and the two-phase flow. As indicated by Bryan and Seyed-Yagoobi [1,2] and Cotton et al. [4], the EHD force can enhance the convective boiling heat transfer as well as suppress it. The heat transfer enhancement with the electric field is considered as the result of the reduced thermal resistance in the liquid layer, secondary flow induced by the electric field, and/or the promotion of the turbulence. Various approaches have been used to predict the heat transfer with EHD, such as the dimensional analysis [4] and the axial flow momentum versus radial EHD pressure analysis [1]. However, due to the complicated nature of the two-phase flow coupled with the effects of the EHD force, it is rather difficult to determine the conditions under which the convective boiling heat transfer will be enhanced or suppressed.

According to Taitel and Dukler [16], the horizontal liquid-vapor channel flow in the absence of the electric field can be divided into five basic flow regimes: smooth stratified, wavy stratified, intermittent (slug/plug), annular with dispersed liquid (annular/mist), and dispersed bubble. Each regime has its own distinct characteristics with regards to the interface configuration, the pressure drop, and the heat transfer. As indicated by Quandt [11], the flow regime is the result of the influence of three fundamental forces: the axial pressure gradient, the gravitational attraction, and the interfacial surface tension. In the presence of the electric field, the EHD force will join these three forces to affect the two-phase flow. The coupling of the electric field and the flow field introduces new characteristics in the flow and the heat transfer, including the enhancement and suppression of the heat transfer.

Contributed by the Heat Transfer Division for publication in the JOURNAL OF HEAT TRANSFER. Manuscript received by the Heat Transfer Division October 13, 2000; revision received April 19, 2001. Associate Editor: D. Poulikakos.

In the presence of the electric field, the transition from the enhancement to the suppression could depend on many factors, such as the fluid mass flux, fluid properties, channel dimensions, and applied electric field. Currently, there is no capability to properly predict the enhancement or suppression of the heat transfer with the EHD extraction force in internal two-phase flows. Perhaps the relation between the heat transfer and the axial momentum/radial pressure ratio, suggested by Bryan and Seyed-Yagoobi [1], is the only tool that exists. However, this approach is not necessarily precise. Lack of the fundamental understandings becomes the obstacle for the future application of the EHD technique to effectively enhance and control the system performance. In this paper, the linear stability theory is used to qualitatively predict the flow regimes of a two-phase flow with and without the EHD extraction force in the horizontal channel. Based on the predicted flow regimes, the transition between the EHD-enhanced and EHD-suppressed convective boiling heat transfer is successfully predicted.

2 Linear Stability Analysis of Basic Liquid-Vapor Flow With and Without EHD Extraction Force

Consider a horizontal pipe, inside which the liquid flows around the vapor core and the liquid film thickness is uniform. At the center of the pipe there is an electrode, which is connected to the high voltage power supply, while the pipe is grounded. When the liquid and vapor flow along the pipe, they withstand the gravity, the EHD extraction force, and the interfacial surface tension as shown in Fig. 1 for an annular flow. The liquid-vapor flow will be stable and will remain at the annular regime as long as the forces are balanced. The annular flow may turn into the mist flow or change to the intermittent or wavy flow, if the forces are no longer balanced. In addition to the above forces, the momentum exchange between the liquid and vapor at the interface should be included for the accurate analysis of the interface instability.

To simplify the linear stability analysis, a simple two-dimensional liquid-vapor flow is considered as shown in Fig. 2. The liquid mainly lies in the upper region, which extends a_l above the nominal interface, while the vapor occupies the lower region, which extends a_v below the nominal interface. This configuration almost represents the liquid flow on the upper portion of the pipe as illustrated in Fig. 1. Note that in Fig. 1, the liquid at the top is

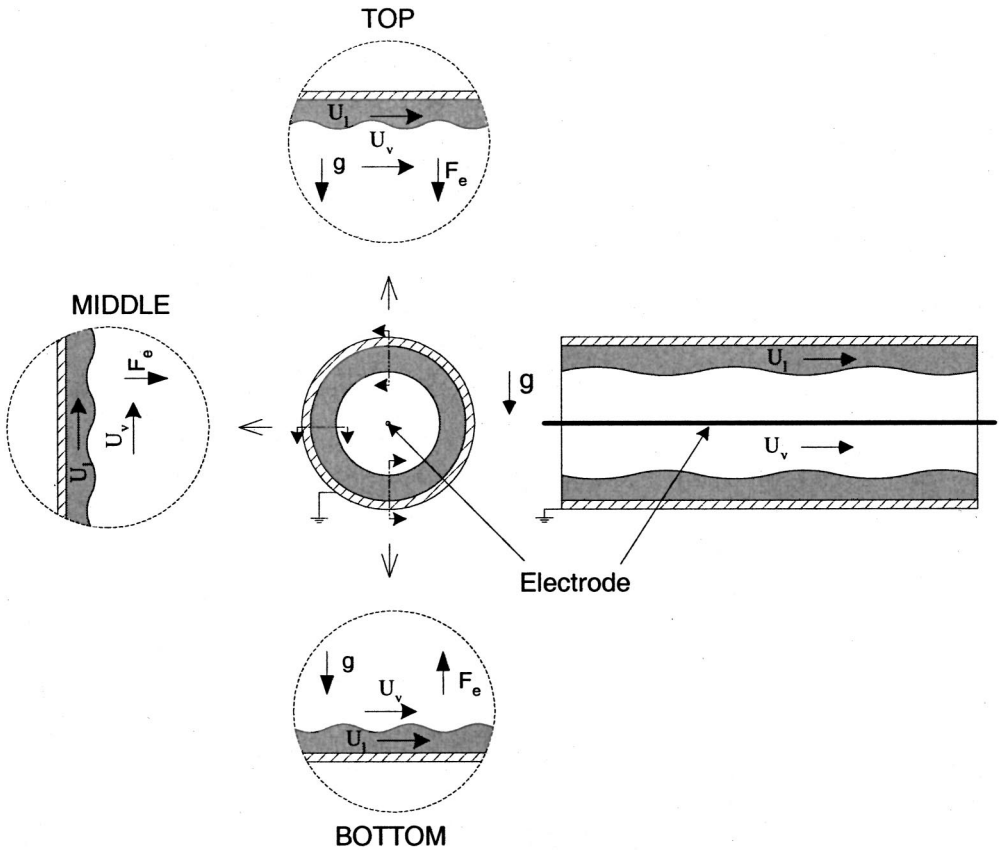

Fig. 1 Liquid-vapor annular flow in the presence of EHD extraction force

more susceptible to the combined gravity force and EHD extraction force (if present) destabilization than the liquid at the other locations. The instability of the two-phase flow always starts from the instability at the top. The liquid and vapor flows are also assumed incompressible and inviscid. The assumption of no viscosity is mainly for simplifying the analysis while the presence of viscosity would promote stability. Therefore, the results of the instability given in this paper are more conservative.

2.1 EHD Extraction Force. It is assumed that there is no net charge accumulation at the liquid/vapor interface when the electric field is applied to a two-phase flow through the high voltage electrode positioned below the liquid/vapor interface and the ground channel wall as shown in Fig. 2. The basic electric potential distribution satisfies the following electrostatics governing equations and boundary conditions:

$$\nabla^2\Phi_l=0, \quad 0<z\leq a_l, \quad \nabla^2\Phi_v=0, \quad -a_v\leq z<0$$

and

$$\Phi_l=\Phi_v \quad \text{at} \quad z=0$$

$$\varepsilon_l\frac{d\Phi_l}{dz}=\varepsilon_v\frac{d\Phi_v}{dz} \quad \text{at} \quad z=0$$

$$\Phi_l=0 \quad \text{at} \quad z=a_l$$

$$\Phi_v=V \quad \text{at} \quad z=-a_v.$$

The applied electric field adds a normal EHD extraction force on the interface, which tends to pull the liquid downwards. For a smooth interface, the presence of the EHD extraction force induces an interface pressure difference between the vapor and the liquid [9], which can be expressed as

$$\overline{P_l}-\overline{P_v}=f_{\text{EHD}}=\frac{1}{2}\varepsilon_l E_l^2-\frac{1}{2}\varepsilon_v E_v^2 \quad \text{at} \quad z=0,$$

where $E_l=-d\Phi_l/dz$ and $E_v=-d\Phi_v/dz$. Note that the electrostriction terms, for both the liquid and vapor phases, are not included in the above equation since the two phases are assumed to be incompressible.

2.2 Hydrodynamic Stability in the Presence of EHD Extraction Force. As indicated in Fig. 2, the main flow velocity is along the x-axis with the magnitude of U_l and U_v for the liquid and the vapor, respectively. With the initial perturbation in the form of Fourier component waves,

$$\delta_0(x,0)=\xi_0 e^{i\alpha x} \quad \text{where} \quad \alpha=2\pi/\lambda,$$

the basic two-phase flow is disturbed due to the wavy character of the interface. The subsequent position of the interface $\delta(x,t)$ has

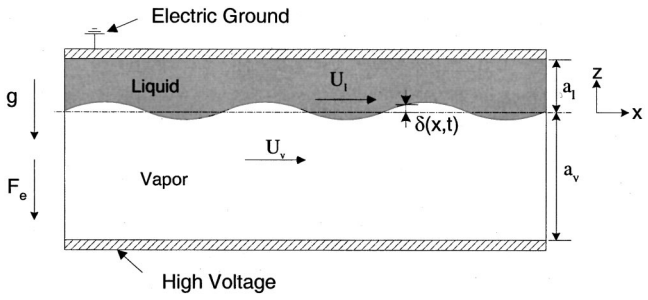

Fig. 2 Perturbed liquid-vapor flow in which the liquid overlays the vapor in the presence of EHD extraction force

the spatial variation similar to that of the initial perturbation and its temporal variation is oscillatory. Therefore, the subsequent position of the interface δ is postulated as

$$\delta(x,t)=\xi_0 e^{i\alpha x+\beta t}.$$

β in the above equation indicates the frequency. If β has a real positive part, the perturbation will be amplified.

The velocities and the pressure after the perturbation are expressed as

$$u=\begin{cases} U_l+u_l', & z>0 \\ U_v+u_v', & z<0 \end{cases} \qquad w=\begin{cases} w_l', & z>0 \\ w_v', & z<0 \end{cases}$$

$$P=\begin{cases} \overline{P}_l+P_l', & z>0 \\ \overline{P}_v+P_v', & z<0. \end{cases} \tag{1}$$

The potential after the perturbation is expressed as $\Phi+\phi'$, where $\phi'=\hat{\phi}(z)e^{i\alpha x+\beta t}$. Since the perturbed potential also satisfies the base Laplace equation, subtracting the corresponding base electric potential equation leads to

$$\nabla^2\phi_l'=0 \quad \text{and} \quad \nabla^2\phi_v'=0.$$

The boundary conditions for the above equations become

$$\delta\frac{d\Phi_v}{dz}+\phi_v'\cong\delta\frac{d\Phi_l}{dz}+\phi_l' \qquad \text{at} \quad z=0$$

$$\varepsilon_l\left(\delta\frac{d^2\Phi_l}{dz^2}+\frac{d\phi_l'}{dz}\right)\cong\varepsilon_v\left(\delta\frac{d^2\Phi_v}{dz^2}+\frac{d\phi_v'}{dz}\right) \qquad \text{at} \quad z=0$$

$$\phi_l'=0 \qquad \text{at} \quad z=a_l$$

$$\phi_v'=0 \qquad \text{at} \quad z=-a_v.$$

Solutions for ϕ' in the liquid and vapor regions, which satisfy the above boundary conditions, are

$$\phi_l'=\delta\frac{E_v|_{z=0}-E_l|_{z=0}}{\tanh(\alpha a_v)+\dfrac{\varepsilon_v}{\varepsilon_l}\tanh(\alpha a_l)}\cdot\frac{\sinh(\alpha z-\alpha a_l)}{\cosh(\alpha a_l)}\cdot\frac{\varepsilon_v}{\varepsilon_l}$$

where $0<z\leqslant a_l$ and

$$\phi_v'=\delta\frac{E_v|_{z=0}-E_l|_{z=0}}{\tanh(\alpha a_v)+\dfrac{\varepsilon_v}{\varepsilon_l}\tanh(\alpha a_l)}\cdot\frac{\sinh(\alpha z+\alpha a_v)}{\cosh(\alpha a_v)}$$

where $0>z\geqslant -a_v$.

After the perturbation, the EHD extraction force and the surface tension generate the following pressure difference at the interface:

$$\begin{aligned} P_l-P_v&=f_{\text{surf tension}}+f_{\text{EHD}} \\ &=\sigma\frac{(\partial^2\delta/\partial x^2)}{[1+(\partial\delta/\partial x)^2]^{3/2}}+\frac{1}{2}\varepsilon_l(E_l+e_l')^2-\frac{1}{2}\varepsilon_v(E_v+e_v')^2 \\ &\quad \text{at} \quad z=\delta \\ &\cong-\sigma\alpha^2\delta+\frac{1}{2}\varepsilon_l(E_l^2+2E_le_l')|_{z=0} \\ &\quad-\frac{1}{2}\varepsilon_v(E_v^2+2E_ve_v')|_{z=0} \end{aligned} \tag{2}$$

where $e_l'=-d\phi_l'/dz$ and $e_v'=-d\phi_v'/dz$.

In reality, if the interface is not smooth, the wavy liquid surface can affect the axial vapor flow even though the fluids are assumed to be inviscid. The wavy liquid surface changes the vapor flow path and results in the interaction between the two phases. A small amount of liquid will even be entrained in the vapor region in the form of liquid drops, when the relative velocity of the liquid and vapor phases is sufficiently large. Such interaction with the wavy interface leads to the momentum exchange between the phases.

The momentum exchange between the phases will generate more perturbations. Thus, the perturbation quantities u', w', and P' will be decomposed into two components as $u'=u_1'+u_2'$, $w'=w_1'+w_2'$, and $P'=P_1'+P_2'$. Here, u_1', w_1', and P_1' are generated solely due to the Kelvin-Helmholtz phenomenon, while u_2', w_2', and P_2' indicate the contribution of the momentum exchange between the liquid and vapor phases at the interface. Thus, instabilities due to the Kelvin-Helmholtz phenomenon and the momentum exchange are both considered in the analysis here. It is worth mentioning that the instability due to the momentum exchange follows the establishment of the wavy interface caused by the Kelvin-Helmholtz phenomenon. The perturbation components will be discussed separately and then they will be combined together to investigate the stability of the interface. Note that the electric perturbations remain as e_l' and e_v' and do not need to be separated into two components.

The momentum exchange in the presence of the entrainment results in the main vapor velocity perturbation, u_{v2}'. The entrainment rate is needed for the prediction of u_2'. Lopez de Bertodano et al. [7] theoretically obtained an expression for the entrainment rate by applying the model of Taylor [17] for growth of interfacial waves. They assumed that the entrainment rate is proportional to the liquid density multiplied by the average growth rate of the interfacial waves, which can be expressed as $\dot{\varepsilon}\propto\rho_l\overline{\delta\beta}$, where the interfacial wave growth rate is given as $\partial\delta/\partial t=\delta\beta$. This assumption applies to a single given wave as well. The corresponding relation can be expressed as $\dot{\varepsilon}\propto\rho_l\delta\beta$. Since the time scale of the interfacial wave is the inverse of the wave frequency and the local entrainment rate is defined as the entrained liquid mass versus the time, the local entrainment rate can also be expressed as $\dot{\varepsilon}\propto m_{\text{entr}}\beta$, where m_{entr} denotes the local entrained liquid mass per unit area. Thus, the local entrained liquid mass per unit area can be directly related to the interface position and the liquid density since $m_{\text{entr}}\propto\rho_l\delta$. In agreement with the above discussion, Russell and Lamb [12] concluded that the rate of entrained droplets depends on both the wave amplitude and the wave form.

When the liquid is entrained into the vapor layer in the form of the droplets, the corresponding interaction between the liquid droplets and the vapor layer affects the bulk vapor velocity. If the wavy portion of the liquid interface is entrained into the vapor layer, the amount of the local entrained liquid per unit area, m_{entr}, is proportional to $\rho_l\delta$, as justified by the above discussion. Based on the direct momentum balance between the entrained liquid droplets and the vapor layer, the bulk vapor velocity perturbation, u_2', can be estimated as

$$u_{v2}'\cong\frac{\rho_lU_l(U_v-U_l)}{\rho_vU_v}\cdot\frac{\delta}{a_v}.$$

In the above equation, it has been assumed that the entrained droplets reach vapor velocity upon the entrainment. Furthermore, the total entrainment of the liquid wave by the vapor was also assumed in the above equation. The entrainment of the vapor phase into the liquid phase was assumed to be negligible. These assumptions were necessary to make due to the lack of detailed information on the entrainment. Nevertheless, it should be emphasized that this analysis provides accurate qualitative results.

Assuming that the vapor follows the Bernoulli's equation, the corresponding vapor pressure perturbation due to u_2' becomes

$$P_{v2}'\cong-\rho_lU_l(U_v-U_l)\cdot\frac{\delta}{a_v}. \tag{3}$$

Since the momentum exchange in the presence of the entrainment mainly takes place in the vapor layer, P_{l2}' and u_{l2}' are neglected.

The z-directional bulk velocity perturbation, w_2', limited by the solid wall boundaries, is also assumed to be zero in both the liquid and vapor phases.

The analysis of the perturbations (u_1', w_1', and P_1') due to the Kelvin-Helmholtz phenomenon is similar to that of the classical Kelvin-Helmholtz case except that the liquid-vapor flow is of limited thickness. For the system considered here, it is plausible to expect that the spatial variations of u_1', w_1', and P_1' with x are similar to that of the initial perturbation, and that their temporal variations are oscillatory. Therefore, the perturbation quantities u_1', w_1', and P_1' are postulated as the following functional forms:

$$u_1'(x,z,t)=\hat{u}_1(z)e^{i\alpha x+\beta t}$$

$$w_1'(x,z,t)=\hat{w}_1(z)e^{i\alpha x+\beta t}$$

$$P_1'(x,z,t)=\hat{P}_1(z)e^{i\alpha x+\beta t}. \tag{4}$$

The linear stability analysis proceeds by substituting Eq. (1) into the governing continuity and momentum equations, subtracting the corresponding base flow equations, and neglecting products of perturbation quantities. If u_1', w_1', and P_1' are separated from u_2', and P_2' in the linearized governing equations, the resulting equations for the perturbation quantities u_1', w_1', and P_1' are as follows:

$$\frac{\partial u_1'}{\partial x}+\frac{\partial w_1'}{\partial z}=0$$

$$\rho\left[\frac{\partial u_1'}{\partial t}+U\left(\frac{\partial u_1'}{\partial x}\right)\right]=-\frac{\partial P_1'}{\partial x} \tag{5}$$

$$\rho\left[\frac{\partial w_1'}{\partial t}+U\left(\frac{\partial w_1'}{\partial x}\right)\right]=-\frac{\partial P_1'}{\partial z}. \tag{6}$$

Note that there are no electric terms in the above equations since it is assumed that there are no electric charges present within the fluids (as well as at the interface of the two phases) and that the electrostriction terms are negligible.

Differentiating Eq. (5) with respect to x and Eq. (6) with respect to z, adding them together, and substituting the continuity equation yield the Laplace equation for the perturbation pressure field

$$\nabla^2 P_1'=0. \tag{7}$$

Substituting Eq. (4) for P_1' into Eq. (7) yields the following equation for $\hat{P}_1$:

$$\frac{d^2\hat{P}_1}{dz^2}=\alpha^2\hat{P}_1. \tag{8}$$

Solutions for $\hat{P}_1$ in the liquid and vapor regions, which satisfy Eq. (8), are

$$\hat{P}_{l1}=A_l e^{\alpha z}+B_l e^{-\alpha z} \quad \text{where } 0<z\leqslant a_l$$

$$\hat{P}_{v1}=A_v e^{\alpha z}+B_v e^{-\alpha z} \quad \text{where } 0>z\geqslant -a_v.$$

Similarly, substituting $w_1'(x,z,t)=\hat{w}_1(z)e^{i\alpha x+\beta t}$ into Eq. (6) yields

$$\hat{w}_1(z)=-[\rho(\beta+i\alpha U)]^{-1}\left(\frac{d\hat{P}_1}{dz}\right).$$

Correspondingly, the relations for $\hat{w}$ in the liquid and vapor regions are

$$\hat{w}_{l1}(z)=-\alpha(A_l e^{\alpha z}-B_l e^{-\alpha z})[\rho_l(\beta+i\alpha U_l)]^{-1}$$
$$\text{where } 0<z\leqslant a_l$$

$$\hat{w}_{v1}(z)=-\alpha(A_v e^{\alpha z}-B_v e^{-\alpha z})[\rho_v(\beta+i\alpha U_v)]^{-1}$$
$$\text{where } 0>z\geqslant -a_v.$$

w_1' at the interface must be equal to

$$w_1'|_{z\to 0}=\frac{\partial\delta}{\partial t}+U\frac{\partial\delta}{\partial x}.$$

The above condition on both the vapor and liquid sides of the interface and the condition that $w_1'\to 0$ at the top and at the bottom of the channel are applied to determine A and B. Finally, the perturbation of pressure should be in the following forms:

$$P_{l1}'=\frac{\rho_l}{\alpha}(\beta+i\alpha U_l)^2\frac{\cosh(\alpha a_l-\alpha z)}{\sinh(\alpha a_l)}\delta \quad \text{where } 0<z\leqslant a_l$$

$$P_{v1}'=-\frac{\rho_v}{\alpha}(\beta+i\alpha U_v)^2\frac{\cosh(\alpha a_v+\alpha z)}{\sinh(\alpha a_v)}\delta \quad \text{where } 0>z\geqslant -a_v.$$

Since $P=\overline{P}+P_1'+P_2'$, the interface pressure difference can also be expressed as follows:

$$\begin{aligned}P_l-P_v&=\overline{P}_l-\overline{P}_v+P_{l1}'-P_{v1}'-P_{v2}'\\&=\frac{1}{2}\varepsilon_l E_l^2|_{z=0}-\frac{1}{2}\varepsilon_v E_v^2|_{z=0}-\rho_l g\delta+\rho_v g\delta\\&\quad+\frac{\rho_l}{\alpha}(\beta+i\alpha U_l)^2\coth(\alpha a_l)\delta\\&\quad+\frac{\rho_v}{\alpha}(\alpha+i\alpha U_v)^2\coth(\alpha a_v)\delta+\frac{\rho_l U_l(U_v-U_l)}{a_v}\delta.\end{aligned} \tag{9}$$

Combining Eqs. (2) and (9) leads to

$$\begin{aligned}&-\sigma\alpha^2\delta+\varepsilon_l E_l e_l'|_{z=0}-\varepsilon_v E_v e_v'|_{z=0}\\&\quad=-\rho_l g\delta+\rho_v g\delta+\frac{\rho_l}{\alpha}(\beta+i\alpha U_l)^2\coth(\alpha a_l)\delta\\&\qquad+\frac{\rho_v}{\alpha}(\beta+i\alpha U_v)^2\coth(\alpha a_v)\delta+\frac{\rho_l U_l(U_v-U_l)}{a_v}\delta.\end{aligned}$$

Solving the above equation for β results in the following equation:

$$\beta=-\frac{i\alpha[\rho_l U_l\coth(\alpha a_l)+\rho_v U_v\cdot\coth(\alpha a_l)]}{[\rho_l\coth(\alpha a_l)+\rho_v\coth(\alpha a_v)]}\pm\frac{\left\{\begin{array}{l}\alpha^2\rho_l\rho_v\coth(\alpha a_l)\coth(\alpha a_v)(U_v-U_l)^2\\+\alpha^2[\rho_l\coth(\alpha a_l)+\rho_v\coth(\alpha a_v)]\cdot\dfrac{(\varepsilon_l-\varepsilon_v)^2E_l|_{z=0}E_v|_{z=0}}{\varepsilon_l\tanh(\alpha a_v)+\varepsilon_v\tanh(\alpha a_l)}\\-[\rho_l\coth(\alpha a_l)+\rho_v\coth(\alpha a_v)]\cdot\left[\alpha^3\sigma+\dfrac{\rho_l U_l(U_v-U_l)}{a_v}\alpha-\alpha(\rho_l-\rho_v)g\right]\end{array}\right\}^{1/2}}{[\rho_l\coth(\alpha a_l)+\rho_v\coth(\alpha a_v)]}.$$

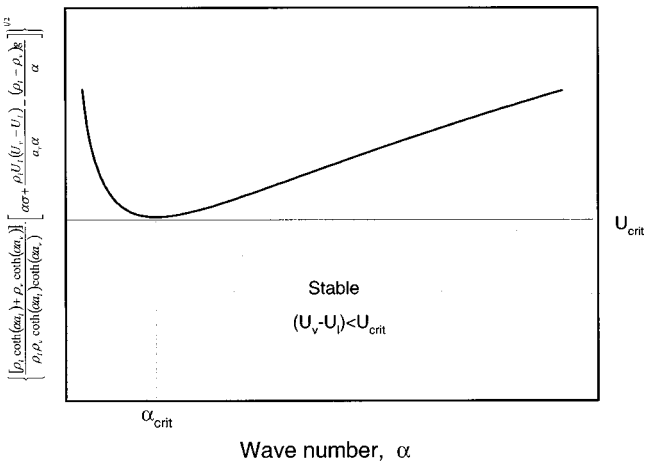

Fig. 3 Qualitative variation of stability criteria with wave numbers without EHD extraction force

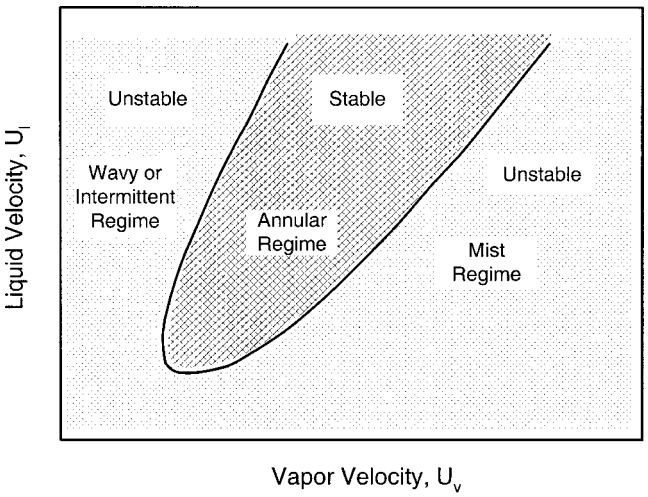

Fig. 4 Qualitative liquid-vapor flow stability map and the corresponding flow regimes with and without EHD extraction force

If there is no positive real part in β, the two-phase flow will be stable. Therefore, the following stability criterion is obtained:

$$(U_v-U_l)^2 \leqslant \frac{[\rho_l \coth(\alpha a_l)+\rho_v \coth(\alpha a_v)]}{\rho_l\rho_v \coth(\alpha a_l)\coth(\alpha a_v)} \cdot\left\{\left[\alpha\sigma+\frac{\rho_l U_l(U_v-U_l)}{\alpha a_v}-\frac{(\rho_l-\rho_v)g}{\alpha}\right] -(\varepsilon_l-\varepsilon_v)^2 E_l|_{z=0}E_v|_{z=0} \times\frac{1}{\varepsilon_l \tanh(\alpha a_v)+\varepsilon_v \tanh(\alpha a_l)}\right\}. \quad (10)$$

With the momentum exchange term removed, the above equation agrees with the electrohydrodynamic stability criterion described by Zahn and Melcher [19].

Near the interface, the magnitude of the electric field strength in the vapor phase, $E_v|_{z=0}$, is always greater than that of the electric field strength in the liquid phase, $E_l|_{z=0}$, since the vapor electric permittivity is smaller than the liquid electric permittivity. The sign of the electric term in the above equation is always negative, which indicates that the presence of electric field affects the base liquid-vapor flow by destabilizing the interface. As previously mentioned, the above linear analysis is based on the assumption that the fluids are inviscid. The omission of the viscosity will result in a conservative prediction of the stability criterion. The qualitative stability map corresponding to Eq. (10) will be discussed at the end of the following sub-section.

2.3 Hydrodynamic Stability in the Absence of EHD Extraction Force. In the absence of the electric field, Eq. (10) reduces to

$$(U_v-U_l)^2 \leqslant \frac{[\rho_l \coth(\alpha a_l)+\rho_v \coth(\alpha a_v)]}{\rho_l\rho_v \coth(\alpha a_l)\coth(\alpha a_v)} \cdot\left[\alpha\sigma+\frac{\rho_l U_l(U_v-U_l)}{a_v\alpha}-\frac{(\rho_l-\rho_v)g}{\alpha}\right]. \quad (11)$$

If the influence of the momentum exchange due to the entrainment is not taken into account (i.e., the middle term in the bracket on the right hand side of Eq. (11) is set to zero), then the above equation reduces to the classical instability criterion.

The above two stability criteria (Eqs. (10) and (11)) imply that the stability depends on the interactions of the interfacial surface tension, the gravity force, the momentum exchange, and the EHD extraction force (if present). In the absence of the electric field, if the relative velocity is small and the momentum exchange term is unable to overcome the influence of the gravity force, $[\rho_l U_l(U_v-U_l)/a_v-(\rho_l-\rho_v)g]$ in Eq. (11) remains negative. Since the noise from the surrounding environment is of all kinds of wave numbers, the right-hand side of Eq. (11) is unable to remain positive when the perturbations of all kinds of wave number are triggered by the noise. When the wave number, α, is small, the surface tension term can not counteract the momentum exchange and gravity terms. The liquid will become unstable and drain down to the bottom, indicating that the flow is gravity-controlled. When the relative velocity is high enough for the momentum exchange term to dominate the gravity, $[\rho_l U_l(U_v-U_l)/a_v-(\rho_l-\rho_v)g]$ in Eq. (11) becomes positive. Since the surface tension is positive, there exists a minimum value at the critical wave number, α_{crit}, for the term on the right side of Eq. (11), as shown in Fig. 3. Due to the complexity of Eq. (11), the critical wave number, α_{crit}, should be calculated numerically. If the corresponding $\{[\rho_l \coth(\alpha a_l)+\rho_v \coth(\alpha a_v)]/\rho_l\rho_v \coth(\alpha a_l)\coth(\alpha a_v)\cdot[\alpha\sigma+\rho_l U_l(U_v-U_l)/a_v\alpha-(\rho_l-\rho_v)g/\alpha]\}^{1/2}|_{min}$ at α_{crit}, named as U_{crit} here, is greater than the relative velocity, (U_v-U_l), the flow is stable. Otherwise, the perturbation may destabilize the flow. In the presence of the electric field, the EHD extraction force will tend to destabilize the liquid-vapor flow. Since the EHD extraction force term is always negative, the minimum value, U_{crit}, of the right hand side of Eq. (10) is lowered by the EHD extraction force term compared with that of Eq. (11).

A qualitative stability map for the liquid-vapor flow, with and without the EHD extraction force, is illustrated in Fig. 4 with the liquid and vapor velocities as the coordinates, The center shadow area indicates the stable region. The remaining area represents the unstable regions due to the insufficient relative velocity or the excessively high relative velocity. Physically, the stable region in Fig. 4 is considered as the annular flow regime, as the top liquid film remains above the vapor. The left unstable area indicates the intermittent or wavy regime, where the gravity force is dominant and pulls the liquid film down to the bottom. The right unstable area represents the mist region caused by the excessively high relative velocity, and the unstable liquid film will be broken into liquid drops and carried away by the vapor core.

3 Linear Stability Analysis of Pipe Liquid-Vapor Flow With and Without EHD Extraction Force

In this section the above analysis which was developed for a basic liquid-vapor flow is extended to include the horizontal two-phase flow in a pipe with and without the EHD extraction force.

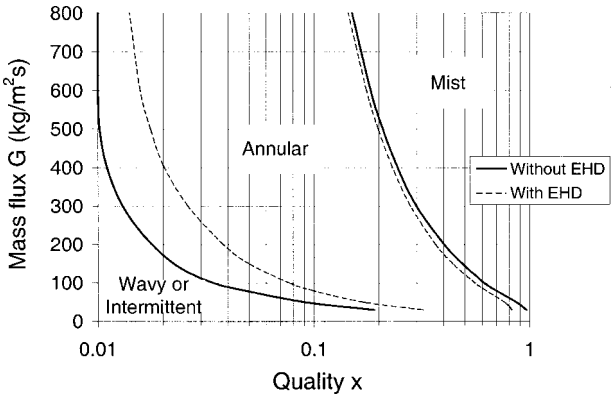

Fig. 5 Flow regime map for R-134a at $T_{sat}=5°C$ flowing inside a tube of $D=14$ mm with and without EHD extraction force

3.1 Pipe Liquid-Vapor Flow in the Presence of EHD Extraction Force. Currently, there are no guidelines available in the literature to predict the flow regime transitions in the presence of EHD force. Utilizing the results of the analysis given in Section 2.2, such guidelines are developed based on the linear stability analysis. When the electric field is applied through a high voltage electrode suspended in the vapor core and the ground pipe wall, the top of the horizontal annular two-phase pipe flow (see Fig. 1) will always be the most unstable position due to the gravity and the EHD extraction force. If the liquid film thickness is small compared with the pipe size, the top of the pipe flow can be analyzed as the basic liquid-vapor flow by neglecting the secondary curvature effects associated with the circumferential curvature of the pipe.

Based on the equations given in Section 2, and modifying Eq. (3) to take the pipe geometry into account

$$P'_{v2} \cong -2\rho_l U_l (U_v - U_l) \cdot \frac{\delta}{a_v},$$

where $a_v = R_i - R_e$ and $a_l = R_o - R_i$, the stability criterion for the pipe flow in the presence of the EHD extraction force can be expressed as

$$(U_v - U_l)^2 \leqslant \frac{[\rho_l \coth(\alpha a_l) + \rho_v \coth(\alpha a_v)]}{\rho_l \rho_v \coth(\alpha a_l)\coth(\alpha a_v)} \cdot \left\{ \left[\alpha\sigma + \frac{2\rho_l U_l (U_v - U_l)}{a_v \alpha} - \frac{(\rho_l - \rho_v) g}{\alpha} \right] - (\varepsilon_l - \varepsilon_v)^2 E_l|_{z=0} E_v|_{z=0} \times \frac{1}{\varepsilon_l \tanh(\alpha a_v) + \varepsilon_v \tanh(\alpha a_l)} \right\}. \quad (12)$$

Note that Eq. (12) is slightly different from Eq. (10).

If the mass flux, flow quality, and pipe diameter are given, the vapor and liquid velocities can be determined by the void fraction models provided by Lockhart and Martinelli [6]. Then, with the known liquid and vapor velocities, it is possible to predict the corresponding flow regime based on the linear stability analysis. As shown in Fig. 5, the annular-to-mist transition for the flow with EHD takes place at a lower quality compared to that without EHD, while the annular-to-intermittent transition for the flow with EHD takes place at a relatively higher quality. This is due to the fact that the EHD extraction force tends to destabilize the flow by pulling the interface towards the electrode in the pipe center.

The imposed EHD extraction force significantly affects the heat transfer as well as the hydrodynamic stability of the liquid-vapor flow. For most regimes, it is known that the EHD force can enhance the convective boiling heat transfer by reducing the thermal resistance in the liquid layer, inducing the EHD secondary flow, and/or promoting the turbulence. However, the EHD force is also able to cause the suppression of the convective boiling heat transfer under certain conditions. There exists a transition region for the convective two-phase heat transfer from EHD-enhanced to EHD-suppressed. Such region can be represented by the ratio of heat transfer coefficient with EHD and without EHD (i.e., h_{EHD}/h_0).

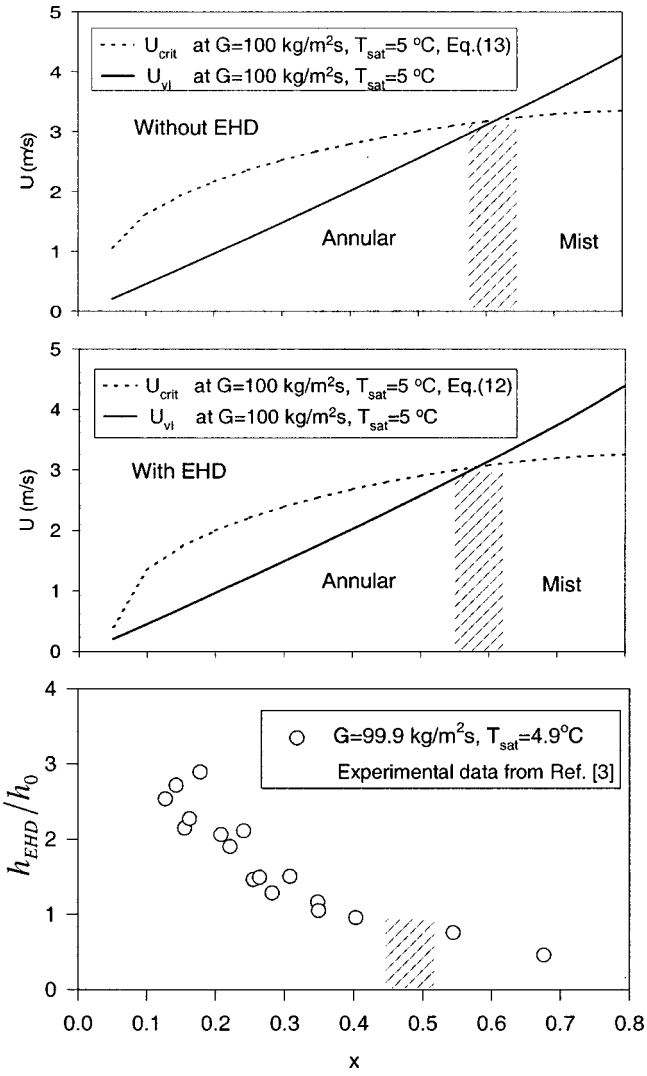

Fig. 6 Comparison of linear stability analysis and experimental convective boiling data for R-134a at $G \cong 100$ kg/m²s and $T_{sat} \cong 5°C$

Figures 6–9 present the critical velocity, U_{crit}, and the relative velocity, U_{vl}, at the applied voltages of 0 kV and 15 kV, and the corresponding h_{EHD}/h_0 experimental data for R-134a flowing through a tube of $D=14$ mm. The details of the experimental data are provided in Bryan [3]. Lockhart and Martinelli [6] void fraction model is used to predict the liquid and vapor velocities in the two-phase pipe flow. It is interesting that the transition of the heat transfer from enhancement to suppression always takes place near the annular-to-mist transition region. This observation can be explained as follows.

For the mist regime without EHD, liquid drops carried by the vapor flow along the pipe, hit the pipe wall randomly and wet the wall as a result. If there exists the EHD extraction force, the liquid drop will be attracted towards the electrode in the middle and the pipe can not be kept wet. Thus, EHD suppresses the heat transfer since no liquid remains on the pipe wall to be vaporized directly.

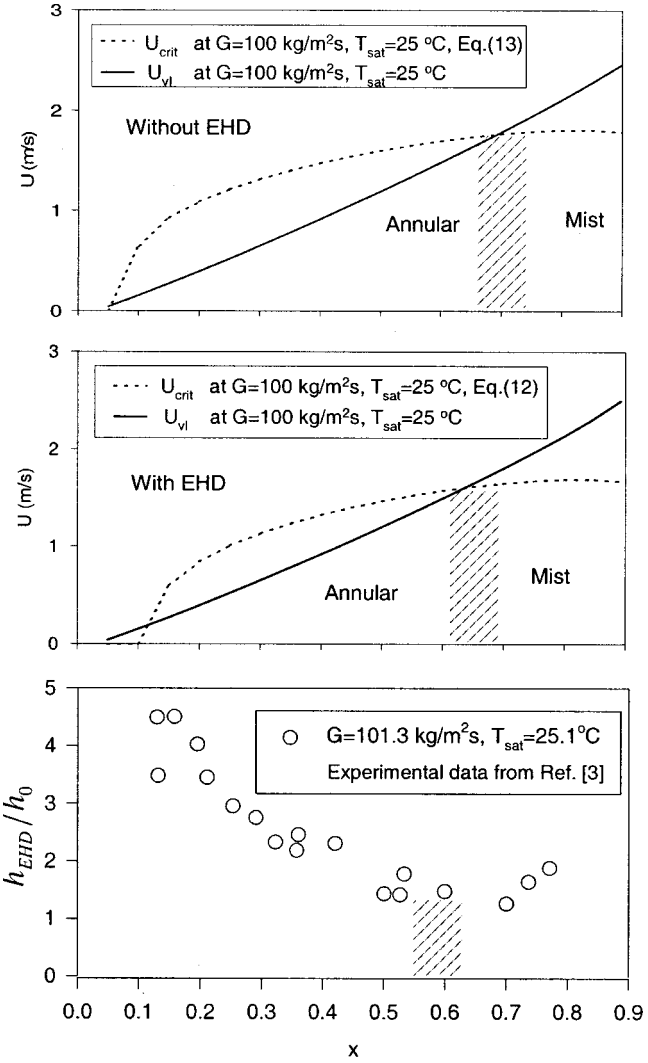

Fig. 7 Comparison of linear stability analysis and experimental convective boiling data for R-134a at $G \cong 100$ kg/m^{2}s and $T_{sat} \cong 25°C$

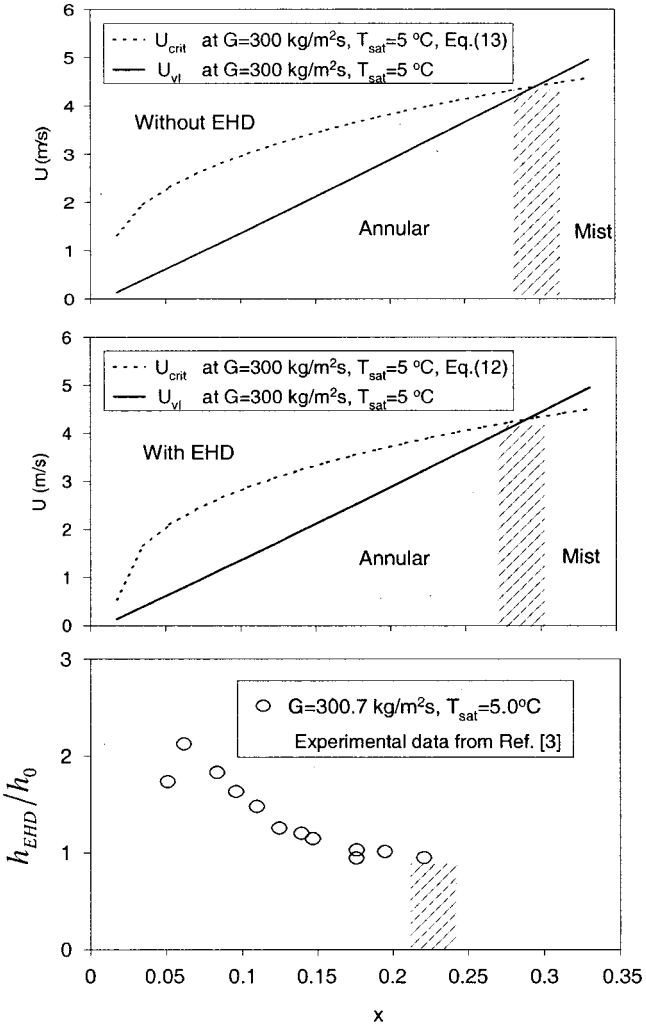

Fig. 8 Comparison of linear stability analysis and experimental convective boiling data for R-134a at $G \cong 300$ kg/m^{2}s and $T_{sat} \cong 5°C$

Furthermore, during the onset of the instability for the flow from the annular regime to the mist regime, the corresponding EHD effects on the heat transfer switch from the enhancement to the suppression, since the EHD extraction force promotes instability resulting in removal of liquid away from the heated wall. This is why the heat transfer transition from enhancement to suppression happens close to the flow regime transition region.

3.2 Pipe Liquid-Vapor Flow in the Absence of EHD Extraction Force. In the absence of the EHD extraction force, the stability criterion for the horizontal annular pipe flow becomes

$$(U_v - U_l)^2 \leqslant \frac{[\rho_l \coth(\alpha a_l) + \rho_v \coth(\alpha a_v)]}{\rho_l \rho_v \coth(\alpha a_l)\coth(\alpha a_v)} \cdot \left[\alpha\sigma + \frac{2\rho_l U_l (U_v - U_l)}{a_v \alpha} - \frac{(\rho_l - \rho_v) g}{\alpha}\right], \quad (13)$$

where $a_v = R_i$ and $a_l = R_o - R_i$. Similarly, the corresponding flow regime without the electric field can be predicted based on the linear stability analysis if the mass flux, flow quality, and pipe diameter are given.

A fixed Martinelli parameter is commonly used to separate the annular regime and the intermittent regime. Taitel and Dukler [16] applied $X_{tt} = 1.6$ for the adiabatic horizontal pipe flow and Kattan et al. [5] applied $X_{tt} = 0.34$ for the boiling pipe flows. However, Weisman et al. [18] recommended $1.9(U_{sv}/U_{sl})^{1/8} = \mathrm{Ku}^{0.2}\mathrm{Fr}^{0.18}$, in which the viscosity was not included, as the correlation for the transition to annular flow when the flow is adiabatic. Weisman et al. described that the above correlation indicated no effect of liquid viscosity and very small effects of liquid density and surface tension on the transition, which was confirmed by the observations. Figure 10 shows the various intermittent-annular transition boundaries in G-x map for R-134 at $T_{sat} = 35°C$ flowing through a horizontal tube of $D = 14$ mm. As illustrated in Fig. 10, the results of the linear stability analysis are close to the $X_{tt} = 1.6$ of Taitel and Dukler [16] and show a similar trend as Weisman et al.'s criterion [18]. Kattan et al.'s correlation [5] does not agree with the others, including the linear stability prediction, because of the presence of the heat transfer.

Soliman [15] suggested a modified Weber number to predict the mist-annular transition during condensation. The correlation is given as

$$\mathrm{We} = 2.45\,\mathrm{Re}_v^{0.64}\left(\frac{\mu_v^2}{\rho_v \sigma D}\right)^{0.3} \Big/ \phi_v^{0.4}, \quad \mathrm{Re}_l \leqslant 1250$$

and

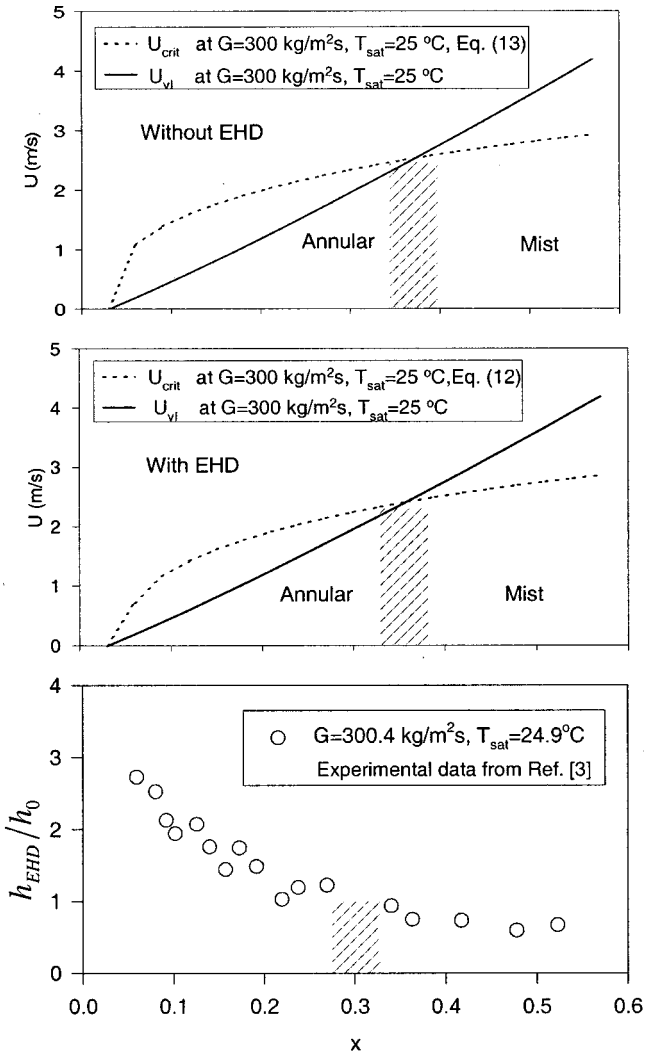

Fig. 9 Comparison of linear stability analysis and experimental convective boiling data for R-134a at $G \cong 300$ kg/m^{2}s and $T_{sat} \cong 25°C$

$$\mathrm{We} = 0.85\,\mathrm{Re}_v^{0.79}\left(\frac{\mu_v^2}{\rho_v \sigma D}\right)^{0.3}\left[\left(\frac{\mu_v}{\mu_l}\right)^2\left(\frac{\rho_l}{\rho_v}\right)\right]^{0.084}(X_{tt}/\phi_v^{2.55})^{0.157},$$

$$\mathrm{Re}_l > 1250.$$

Since the maps of Mandhane et al. [8], Taitel and Dukler [16], and Weisman et al. [18] did not include a distinct mist flow region, the linear stability analysis results are compared with the transition criteria of Soliman only. Figure 11 shows that the linear stability analysis has a similar trend as Soliman's correlation; however, disagreement also exists primarily due to the neglect of viscosity and heat transfer with the linear stability analysis presented in this paper. These comparisons show that the linear stability analysis developed here can qualitatively predict the two-phase regime transitions. The prediction can be further improved by incorporation of, for example, viscosity in the stability analysis.

4 Conclusions

The linear stability analysis presented in this paper for an internal two-phase (liquid-vapor) flow allowed for qualitative predictions of the flow regimes in the presence and absence of the EHD extraction force. Based on the predicted flow regimes, the EHD effects on the convective boiling heat transfer were predicted. The EHD extraction phenomenon can significantly enhance the convective boiling heat transfer. However, the presence of the EHD extraction force is also inclined to destabilize the vapor-liquid annular flow and to suppress the heat transfer under certain conditions. The stability analysis showed that the flow regime transitions were dependent on the interactions of the surface tension, the gravity, the liquid-vapor momentum exchange, and the EHD extraction force. Qualitative stability maps, in the presence and absence of the EHD extraction force, were provided based on the linear stability analysis. The resulting flow regime transition curves based on the onset of the instability provided the basic flow characteristics which agreed with the existing transition criteria. The experimental data showed that the heat transfer transition from enhancement to suppression, in the presence of the electric field, took place close to the annular-to-mist transition region.

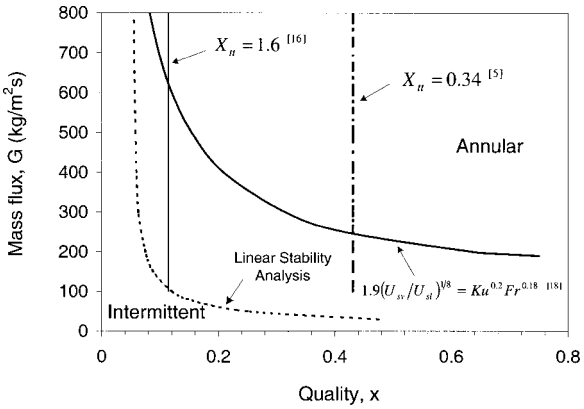

Fig. 10 Comparison of various intermittent—annular transition curves for R134a at $T_{sat} = 35°C$ flowing inside a tube of $D = 14$ mm without EHD extraction force

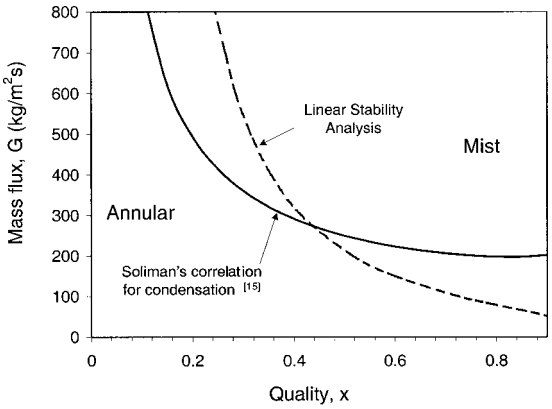

Fig. 11 Comparison of linear stability analysis and Soliman's correlation for R134a at $T_{sat} = 35°C$ flowing inside a tube of $D = 14$ mm without EHD extraction force

Acknowledgments

This work was partially supported by the NASA Microgravity Fluid Physics Program. The authors acknowledge the valuable technical contribution of Professor Markus Zahn at Massachusetts Institute of Technology.

Nomenclature

A = coefficient
a = thickness, m
B = coefficient
D = inner diameter, m

E = electric field strength, V/m
e' = electric field strength perturbation, V/m
F = force, N
Fr = Froude number, $U_{sv}^2/(gD)$
f = force per unit area, N/m^2
G = mass flux, kg/m^{2}s
g = acceleration of gravity, m/s^2
h = heat transfer coefficient, W/m^{2}s
Ku = Kutdelaze number, $U_{sv}\rho_v^{0.5}/[g(\rho_l-\rho_v)\sigma]^{0.25}$
m_{entr} = entrained liquid mass per unit area, kg/m^2
P = pressure, Pa

Greek Symbols

α = wave number, m^{-1}
β = frequency, Hz
δ = interfacial disturbance, m
ε = electric permittivity, F/m
$\dot{\varepsilon}$ = entrainment rate, kg/m^{2}s
Φ, ϕ = electric potentials, V

Subscripts

crit = critical
EHD = electrohydrodynamic
e = electrode or electric
fr = frictional
i = interface
l = liquid
o = pipe
sat = saturation
$\overline{P}$ = mean pressure, Pa
$\hat{P}$ = amplitude of pressure perturbation, Pa
P' = pressure perturbation, Pa
R = radius, m
Re = Reynolds number
T = temperature, °C
U, u = velocities in x-direction, m/s
u' = velocity perturbation in x-direction, m/s
We = modified Weber number
w' = velocity perturbation in z-direction, m/s
X_{tt} = turbulent/turbulent Martinelli parameter
x = x-axis coordinate or quality
z = z-axis coordinate
$\propto$ = proportional to
ϕ_v = two-phase multiplier $[(dP/dz)_{fr}/(dP/dz)_v]^{1/2}$
λ = wavelength, m
μ = dynamic viscosity, Ns/m^2
ρ = density, kg/m^3
σ = surface tension, N/m
ξ = disturbance amplitude, m
sl = superficial liquid velocity
sv = superficial gas velocity
v = vapor
vl = relative velocity of vapor and liquid phases
0 = initial or non-EHD
1 = caused by the momentum exchange
2 = caused by the wavy interface

References

[1] Bryan, J. E., and Seyed-Yagoobi, J., 2000, "Electrohydrodynamically Enhanced Convective Boiling: Relationship between Electrohydrodynamic Pressure and Momentum Flux Rate," ASME J. Heat Transfer, **122**, pp. 266–277.
[2] Bryan, J. E., and Seyed-Yagoobi, J., 2001, "Influence of Flow Regime and Heat Flux on Electrohydrodynamically Enhanced Convective Boiling," ASME J. Heat Transfer, **123**, pp. 355–367.
[3] Bryan, J. E., 1998, "Fundamental Study of Electrohydrodynamically Enhanced Convective and Nucleate Boiling Heat Transfer," Ph.D. dissertation, Texas A&M University, College Station, TX.
[4] Cotton, J. S., Chang, J. S., Shoukri, M., and Smith-Pollard, T., 2000, "Electrohydrodynamic (EHD) Flow and Convective Boiling Augmentation in Single-component Horizontal Annular Channels," *Proceedings of the ASME Heat Transfer Division of 2000 ASME International Mechanical Engineering Congress & Exposition*, **366-4**, pp. 177–184.
[5] Kattan, N., Thome, J. R., and Favrat, D., 1998, "Flow Boiling in Horizontal Tubes: Part 1—Development of a Diabatic Two-Phase Flow Pattern Map," ASME J. Heat Transfer, **120**, pp. 140–147.
[6] Lockhart, R. W., and Martinelli, R. C., 1949, "Proposed Correlation of Data for Isothermal Two-Phase, Two-Component Flow in Pipes," Chem. Eng. Prog., **45**, No. 1, pp. 39–48.
[7] Lopez de Bertodano, M. A., Assad, A., and Beus, S. G., 2001, "Experiments for Entrainment Rate of Droplets in the Annular Regime," Int. J. Multiphase Flow, **27**, pp. 685–699.
[8] Mandhane, J. M., Gregory, G. A., and Aziz, K., 1974, "A Flow Pattern Map for Gas-Liquid Flow in Horizontal Pipes," Int. J. Multiphase Flow, **1**, pp. 537–553.
[9] Melcher, J. R., 1981, *Continuum Electromechanics*, MIT Press, Cambridge, MA.
[10] Norris, C., Cotton, J. S., Shoukri, M., Chang, J. S., and Smith-Pollard, T., 1999, "Eletrohydrodynamic Effects on Flow Redistribution and Convective Boiling in Horizontal Concentric Tubes Under High Inlet Quality Conditions," ASHRAE Trans., **105**, No. 1, pp. 222–236.
[11] Quandt, E., 1963, "Analysis of Gas-Liquid Flow Patterns," *AIChE Annual Meeting*, Boston, MA.
[12] Russell, T. W. F., and Lamb, D. E., 1965, "Flow Mechanism of Two-Phase Annular Flow," Can. J. Chem. Eng., **43**, pp. 237–245.
[13] Singh, A., Ohadi, M. M., Dessiatoun, S., and Chu, W., 1994, "In-Tube Boiling Enhancement of R-123 Using the EHD Technique," ASHRAE Trans., **100**, No. 2, pp. 818–825.
[14] Singh, A., Ohadi, M. M., Dessiatoun, S., and Salehi, M., 1995, "In-Tube Boiling Enhancement of R-134a Utilizing the Electric Field Effect," *ASME/JSME Thermal Engineering Joint Conference*, Vol. **2**, pp. 215–223.
[15] Soliman, H. M., 1986, "The Mist-Annular Transition During Condensation and its Influence on the Heat Transfer Mechanism," Int. J. Multiphase Flow, **12**, No. 2, pp. 277–288.
[16] Taitel, Y., and Dukler, A. E., 1976, "A Model for Predicting Flow Regime Transitions in Horizontal and Near Horizontal Gas-Liquid Flow," AIChE J., **22**, No. 1, pp. 47–55.
[17] Taylor, G. I., 1963, "Generation of Ripples by Wind Blowing over a Viscous Fluid," The Scientific Papers of Sir Geoffrey Ingram Taylor, Vol. **3**, Cambridge University Press, pp. 244–254.
[18] Weisman, J., Duncan, D., Gibson, J., and Crawford, T., 1979, "Effects of Fluid Properties and Pipe Diameter on Two-Phase Flow Patterns in Horizontal Lines," Int. J. Multiphase Flow, **5**, pp. 437–462.
[19] Zahn, M., and Melcher, J. R., 1972, "Space-Charge Dynamics of Liquids," Phys. Fluids, **15**, pp. 1197–1206.

C. Tangthieng
Graduate Student

F. B. Cheung
Professor,
Fellow ASME,
e-mail: fxc4@psu.edu

Department of Mechanical
and Nuclear Engineering,
The Pennsylvania State University,
University Park, PA 16802

S. W. Shiah
Chairman,
Mem. ASME
Department of Naval Architecture
and Marine Engineering,
Chung Cheng Institute of Technology,
Tao-Yuan, Taiwan

Behavior of the Two-Phase Mushy Zone During Freeze Coating on a Continuous Moving Plate

The process of freeze coating of a binary substance on a chilled moving plate is studied theoretically with special emphasis on the behavior of the two-phase mushy zone. The flow and heat transfer in five separate regions of the system, i.e., the moving plate, the freeze coat, the two-phase packing region, the two-phase dispersed region and the molten substance region, are formulated mathematically to describe the freeze-coating process. A supplemental equation derived from a simplified phase diagram and an appropriate viscosity model are employed to complete the mathematical description of the two-phase mushy zone. The system of equations is solved by a combined analytical-numerical technique to determine the spatial variations of the solidus and liquidus fronts. Effects of seven controlling parameters, including the freeze coat-to-wall thermal ratio, the wall subcooling parameter, the molten substance superheating parameter, the Prandtl number, the Stefan number, the equilibrium partition ratio, and the packing limit fraction, on the behavior of the two-phase mushy zone and the freeze-coating process are determined.
[DOI: 10.1115/1.1420714]

Keywords: Coatings, Forced Convection, Solidification

Introduction

The freeze-coating process is a material manufacturing process that finds applications in electrical, chemical and thermal industries. In these applications, a chilled objected is fed through a bath of molten substance. Before entering the bath, the object is subcooled below the freezing point of the substance. As the object travels through the bath, the molten substance begins to solidify on the surface of the object, thus forming a thin layer of freeze coat. Depending on which type of materials the molten substance is made of, the freeze coat may have different functions. For a polymeric substance, the freeze coat may be applied for water resistance, corrosive protection, thermal insulation, electrical insulation, or fire retardation. For a binary metallic substance, on the other hand, the freeze coat may be applied for rust resistance, water resistance, or chemical protection.

The freeze-coating process has been investigated by many researchers. However, most of the previous studies have been restricted to the case of a pure substance in which the interface between the solidified layer and molten substance is sharp and isothermal. The early work of Kuiken [1] presented an analysis of freeze coat thickness by assuming the wall to be semi-infinite. Asymptotic solutions for small and large Prandtl numbers were obtained. Seeniraj and Bose [2] analyzed the process of freeze coating on a moving plate by assuming that the wall temperature was constant and the ambient liquid was saturated. Cheung [3,4] relaxed the assumptions made in [2] to account for the heat convection from a superheated liquid and the temperature variations within the wall. Rezaian and Poulikakos [5] examined the solidification on a moving isothermal boundary for molten substances having low and high Prandtl numbers. Mahmound [6] studied the process of freeze coating of a polymeric substance by assuming that the freezing point of the polymeric substance is sharp and isothermal. The problem was numerically solved by a finite-element method, and the temporal variation of the freeze coat thickness was graphically presented. Cheung and Cha [7] employed a finite-difference method to study the growth and decay of a freeze coat on an axially moving cylinder. An experimental verification of the theoretical analysis was also conducted by Cheung et al. [8], using a thin copper wire to simulate the moving cylinder and water to simulate the molten substance.

Most of the previous studies of the freeze-coating process were investigated for the case where the liquid is a pure substance. For the case of a binary mixture such as a metal alloy, however, solidification would take place over a range of temperature leading to the formation of a two-phase mushy zone. Thus far, the only study of the process of freeze coating of a binary alloy was by Stevens and Poulikakos [9]. They assumed that there was no advection effect in the two-phase mixture and the heat transfer in the mushy zone was by conduction only. The effects of a variety of dimensionless parameters were identified.

In this study, freeze coating of a binary mixture on a semi-infinite moving plate is investigated, taking full account of the flow and heat transfer in the two-phase mushy zone. Equations governing five separate regions of the freeze-coating system are formulated and solved by a combined analytical-numerical technique. Seven independent controlling parameters are identified and their effects on the behavior of the two-phase mushy zone and the freeze-coating process are determined.

Problem Formulation

A schematic of the freeze-coating system under consideration is illustrated in Fig. 1. A chilled semi-infinite plate at a constant velocity, U_o, is fed continuously into an inlet slit on an adiabatic wall at $x = 0$ through a bath of molten binary substance. The plate is cooled at a uniform temperature, T_o, before entering the bath whereas the ambient liquid in the bath is kept constant at temperature T_∞. The inlet plate temperature, T_o, is lower than the solidus temperature, T_1, of the binary substance whereas the bath temperature, T_∞, is higher than the liquidus temperature, T_2, of the binary substance, (i.e., $T_\infty > T_2 > T_1 > T_o$). As the plate enters the bath, a thin solidified layer or a freeze coat begins to form on the surface of the plate and continuously grows along the immersed distance. The freeze coat thickness δ_1 and the location δ_2 represent the isothermal contours of the solidus and liquidus temperatures, respectively.

Contributed by the Heat Transfer Division for publication in the JOURNAL OF HEAT TRANSFER. Manuscript received by the Heat Transfer Division December 4, 2000; revision received August 17, 2001. Associate Editor: V. P. Carey.

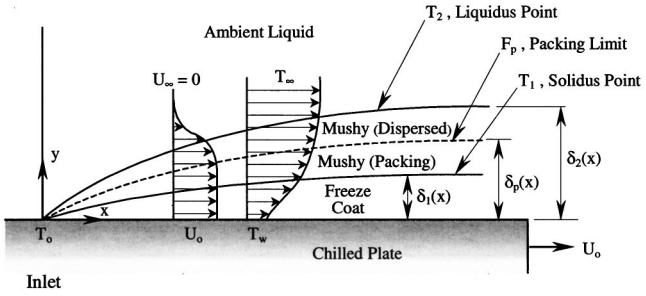

Fig. 1 Schematic of the freeze coating system under consideration

The region $\delta_1 \leqslant y \leqslant \delta_2$ for which the temperature is bounded by the solidus and liquidus points, is the two-phase mushy zone. For a binary system, the mushy zone can be divided into two distinct regions (see Fig. 2): the two-phase packing region and the two-phase dispersed region, based on the value of the mixture viscosity. When the solid fraction, F, in the mushy zone increases beyond a certain limit, which is called the packing limit, F_p, the dendrites start locking and packing to one another and form a rigid structure trapping the liquid inside [10,11]. The viscosity in this region asymptotically approaches infinity, acting as if it were a solid. This domain of solid-like structure is the two-phase packing region. On the other hand, if F is lower than F_p, the two-phase mixture is able to flow like a fluid. Based on experimental observation, the effect of force convection in the main flow can cause the dendritic structure in the mushy zone to break off [12]. The broken dendrites advected by the main flow may behave like dispersed particles suspending in the surrounding liquid. This region is referred to as the two-phase dispersed region.

To formulate the system of governing equations, a number of assumptions are made: (i) Both the molten substance and the two-phase dispersed regions behave as a Newtonian fluid. (ii) The flow is steady and laminar. Note that this is a preferred operating condition as the occurrence of transition to turbulent flow can cause a sudden decrease in the freeze coat thickness [13]. (iii) A boundary layer flow may be assumed in the molten substance and the two-phase dispersed regions. (iv) Physical properties of each phase are constant. The properties of the mushy zone are a result of the weighted average of the physical properties in each individual phase, except for the viscosity which requires a supplemental model. (v) Local thermodynamics equilibrium exists such that the solid fraction can be evaluated directly from the equilibrium phase diagram. (vi) In the two-phase dispersed region, the dispersed dendrites and the local liquid element travel at the same velocity.

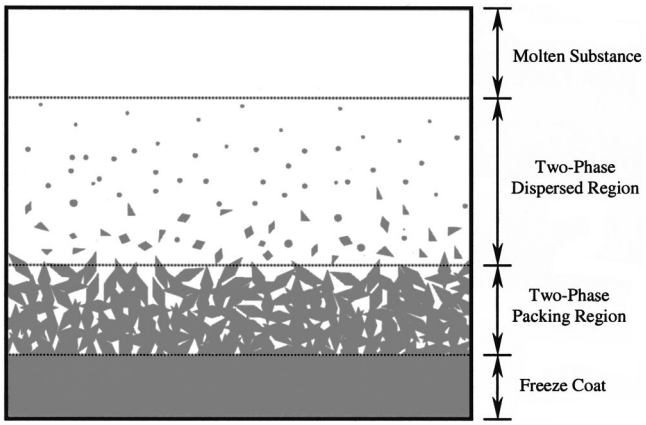

Fig. 2 Graphical representation of the two-phase packing region and the two-phase dispersed region

As a result, there are no dispersion flux terms appearing in the momentum and energy equation. A similar approach has been employed by Voller et al. [14]. (vii) The constituent concentration in the system remains the same during the freeze-coating process. This is equivalent to assume that the effect of macrosegregation is negligible, i.e., the local composition remains constant at the initial value. Note that for the freeze-coating process, the flow is predominantly forced convection. The behavior is different than that during alloy solidification under natural convection conditions [15,16]. According to experimental observation, the higher solute concentration rejected during solidification may be washed away by the main flow in the freeze-coating process [12,17]. Nevertheless, there could be appreciable relative velocities between the liquid and the solid phases in the two-phase packing region as well as in the two-phase dispersed region, which may result in some macrosegregation [18,19]. The extent of macrosegregation, however, would not be considered in the present study, as the main focus here is the growth of the solidified layer and the behavior of the two-phase mushy zone during the freezing coating process.

With the above assumptions the governing equations for each individual region can be written along with the appropriate boundary conditions as follows:

(i) Wall Region ($x \geqslant 0$ and $y \leqslant 0$)

$$\rho_w C_{P_w} U_o \frac{\partial T_w}{\partial x} = k_w \frac{\partial^2 T_w}{\partial y^2} \tag{1}$$

$$x = 0 : T_w = T_o \tag{2a}$$

$$y = 0 : T_w = T_s \quad \text{and} \quad k_w \frac{\partial T_w}{\partial y} = k_s \frac{\partial T_s}{\partial y} \tag{2b}$$

$$y \to -\infty : T_w = T_o \tag{2c}$$

(ii) Freeze-Coat Region ($x \geqslant 0$ and $0 \leqslant y \leqslant \delta_1$)

$$\rho_s C_{P_s} U_o \frac{\partial T_s}{\partial x} = k_s \frac{\partial^2 T_s}{\partial y^2} \tag{3}$$

$$x = 0 : \delta_1 = 0 \tag{4a}$$

$$y = 0 : T_s = T_w \quad \text{and} \quad k_s \frac{\partial T_s}{\partial y} = k_w \frac{\partial T_w}{\partial y} \tag{4b}$$

$$y = \delta_1 : T_s = T_1 \quad \text{and} \quad \frac{\partial T_s}{\partial y} = \frac{\partial T_{mp}}{\partial y} \tag{4c}$$

(iii) Two-Phase Packing Region ($x \geqslant 0$ and $\delta_1 \leqslant y \leqslant \delta_p$)

$$U_o \frac{\partial T_{mp}}{\partial x} = \alpha_m \frac{\partial^2 T_{mp}}{\partial y^2} + \frac{\Delta H_m}{C p_m} U_o \frac{\partial F}{\partial x} \tag{5}$$

$$x = 0 : \delta_p = 0 \tag{6a}$$

$$y = \delta_1 : T_{mp} = T_1 \quad \text{and} \quad \frac{\partial T_{mp}}{\partial y} = \frac{\partial T_s}{\partial y} \tag{6b}$$

$$y = \delta_p : T_{mp} = T_p \quad \text{and} \quad \frac{\partial T_{mp}}{\partial y} = \frac{\partial T_{md}}{\partial y} \tag{6c}$$

(iv) Two-Phase Dispersed Region ($x \geqslant 0$ and $\delta_p \leqslant y \leqslant \delta_2$)

$$\frac{\partial u_{md}}{\partial x} + \frac{\partial v_{md}}{\partial y} = 0 \tag{7}$$

$$u_{md} \frac{\partial u_{md}}{\partial x} + v_{md} \frac{\partial u_{md}}{\partial y} = \frac{\partial}{\partial y} \left(v_m \frac{\partial u_{md}}{\partial y} \right) \tag{8}$$

$$u_{md}\frac{\partial T_{md}}{\partial x}+v_{md}\frac{\partial T_{md}}{\partial y}=\alpha_m\frac{\partial^2 T_{md}}{\partial y^2}+\frac{\Delta H_m}{C_{P_m}}\left(u_{md}\frac{\partial F}{\partial x}+v_{md}\frac{\partial F}{\partial y}\right) \tag{9}$$

$$x=0:\delta_2=0 \tag{10a}$$

$$y=\delta_p:u_{md}=U_o,\quad v_{md}=0,\quad T_{md}=T_p\quad\text{and}\quad\frac{\partial T_{md}}{\partial y}=\frac{\partial T_{mp}}{\partial y} \tag{10b}$$

$$y=\delta_2:u_{md}=u_l,\quad\frac{\partial u_{md}}{\partial y}=\frac{\partial u_l}{\partial y},\quad v_{md}=v_l,\quad T_{md}=T_2\quad\text{and}\quad\frac{\partial T_{md}}{\partial y}=\frac{\partial T_l}{\partial y} \tag{10c}$$

(v) Molten Substance Region ($x\geq 0$ and $y\geq\delta_2$)

$$\frac{\partial u_l}{\partial x}+\frac{\partial v_l}{\partial y}=0 \tag{11}$$

$$u_l\frac{\partial u_l}{\partial x}+v_l\frac{\partial u_l}{\partial y}=v_l\frac{\partial^2 u_l}{\partial y^2} \tag{12}$$

$$u_l\frac{\partial T_l}{\partial x}+v_l\frac{\partial T_l}{\partial y}=\alpha_l\frac{\partial^2 T_l}{\partial y^2} \tag{13}$$

$$x=0:u_l=0\quad\text{and}\quad T_l=T_\infty \tag{14a}$$

$$y=\delta_2:u_l=u_{md},\quad v_l=v_{md},\quad\frac{\partial u_l}{\partial y}=\frac{\partial u_{md}}{\partial y},\quad T_l=T_2\quad\text{and}\quad\frac{\partial T_l}{\partial y}=\frac{\partial T_{md}}{\partial y} \tag{14b}$$

$$y\to\infty:u_l=0\quad\text{and}\quad T_l=T_\infty \tag{14c}$$

In the above formulation, the subscripts "*w*" refers to the wall region, "*s*" the freeze coat, "*mp*" the two-phase packing region, "*md*" the two-phase dispersed region, and "*l*" the molten substance region. The location δ_p is an unknown quantity corresponding to the packing limit F_p. The local temperature T_p at which $F=F_p$ is the packing limit isotherm. The right-hand side of Eqs. (1), (3), and (5) represents the advection terms due to the motion induced by the moving plate. The latent heat effect is included in the last term on the right-hand side of Eq. (5) whereas it is included in the last two terms on the right-hand side of Eq. (9). Since the two-phase packing region is forced to travel together with the plate and the freeze coat, the vertical velocity is absent and the latent heat effect is restricted to the axial direction only. In contrast, in the two-phase dispersed region, the entire flow field brings about the two-dimensional latent heat effect.

The continuous boundary conditions at the interface between each two adjacent regions result in a strong coupling of the equations governing the five distinct regions. To close the system of equations, an expression for the solid fraction must be specified in terms of the primary unknowns. Generally, the relation of the solid fraction to the local temperature of a binary substance can be graphically expressed by an equilibrium phase diagram. Following the approach of Flemings [20], the solidus and liquidus lines in the equilibrium phase diagram are assumed linear as shown in Fig. 3. Note that the equilibrium phase diagram of a binary substance can be categorized into many different regions based on the solubility of the constituents. If the value of the constituent concentration is between $C_{\min}$ and $C_{\max}$, the binary substance becomes partially soluble resulting in the formation of a eutectic structure during solidification. In the present study, the freeze-coating process is restricted to the isomorphous region given by the shaded regions in Fig. 3. An expression for the solid fraction in the isomorphous region can be derived by employing the level arm principle and the rule of similar triangle:

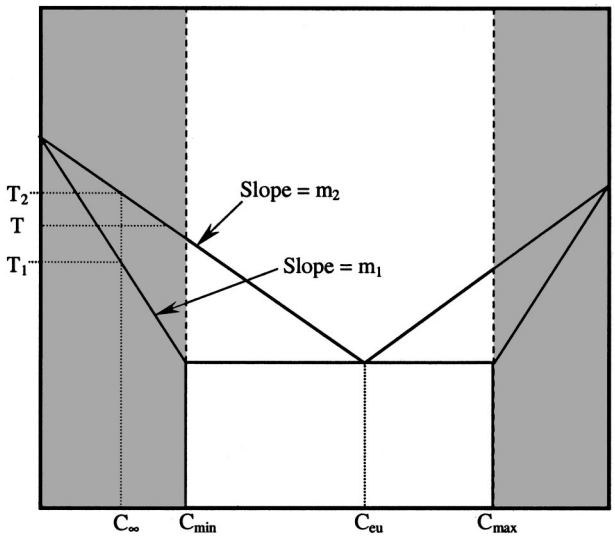

Fig. 3 The simplified equilibrium phase diagram

$$F=\frac{T_2-T_m}{(T_2-T_m)+\kappa(T_m-T_1)}, \tag{15}$$

where T_m is the local temperature of the two-phase mixture, and κ is the equilibrium partition ratio defined as the ratio of the slope of the liquidus line to that of the solidus line. From Eq. (15) it can be seen that the solid fraction is unity at the solidus line. It starts to decrease as the local temperature of the two-phase mushy zone is increased. When the local temperature reaches the liquidus point, the solid fraction becomes zero.

The properties of the two-phase packing and dispersed regions (represented by the subscript "*m*"), including the density, specific heat and thermal conductivity, are calculated by taking an average over the properties of the individual phases weighted by the local solid fraction:

$$\rho_m=\left[\frac{(1-F)}{\rho_l}+\frac{F}{\rho_s}\right]^{-1} \tag{16}$$

$$C_{P_m}=(1-F)C_{P_l}+FC_{P_s} \tag{17}$$

$$k_m=\frac{\rho_m}{\rho_l}(1-F)k_l+\frac{\rho_m}{\rho_s}Fk_s. \tag{18}$$

In order to minimize the number of parameters, the density, specific heat and thermal conductivity of the freeze coat and the molten substance are treated to be the same. As a result, these properties, as well as the thermal diffusivity, of the two-phase mushy zone are identical to those for the freeze coat and molten substance.

The viscosity, on the other hand, of the two-phase dispersed region is modeled as the viscosity of dispersions (assumption iv). An expression for the viscosity of dispersions was first presented by Einstein in 1906 [21]. Einstein analytically showed that for dilute concentration of dispersed spherical particles, the intrinsic viscosity had a value of 2.5. To include the effect of high concentration and maximum packing limit, the viscosity of dispersions can be written as follows:

$$\mu_m=\mu_l\left(1-\frac{F}{F_p}\right)^{-[\mu]F_c}. \tag{19}$$

In terms of the dynamics viscosity, the above expression becomes

$$v_m=v_l\left(1-\frac{F}{F_p}\right)^{-[\mu]F_c}, \tag{20}$$

where $[\mu]$ is the intrinsic viscosity and has a value equal to 2.5 according to Einstein's theory. In the above expression, F_p represents the maximum packing limit of solid fraction. Equation (19), which has been experimentally verified by Krieger [10] and theoretically derived by Krieger and Daugherty [22], is known as the Krieger-Daugherty Equation. In general, the value of F_p may vary from 0.5 to 0.75 depending on the structure of the two-phase mixture [23]. The local temperature $T_m = T_p$ at which $F = F_p$ can be determined by Eq. (15), and this temperature is called the packing limit isotherm. By using Eqs. (15) and (20) the system of equations for the two-phase dispersed region is mathematically closed.

Mathematical Analysis

A similarity analysis is invoked to transform the system of equations, i.e., Eqs. (1) to (20), to a set of ordinary differential equations, which can then be conveniently solved by a numerical technique. The following independent and dependent similarity variables are introduced:

(i) Wall Region

$$\eta_w = \frac{y}{\sqrt{\frac{\alpha_w x}{U_0}}}; \quad -\infty \leq \eta_w \leq 0 \quad \text{and} \quad \Theta_w = \frac{T_w - T_o}{T_1 - T_o}; \qquad 0 \leq \Theta_w \leq \Theta_w(0) \tag{21}$$

(ii) Freeze-Coat Region

$$\eta_s = \frac{y}{\delta_1}; \quad 0 \leq \eta_s \leq 1 \quad \text{and} \quad \Theta_s = \frac{T_s - T_o}{T_1 - T_o}; \qquad \Theta_w(0) = \Theta_s(0) \leq \Theta_s \leq 1 \tag{22}$$

(iii) Two-Phase Packing Region

$$\eta_{mp} = 1 + \frac{y - \delta_1}{\delta_2 - \delta_1}; \quad 1 \leq \eta_{mp} \leq \eta_p \qquad \text{and} \quad \Theta_{mp} = 1 + \frac{T_{mp} - T_1}{T_2 - T_1}; \quad 1 \leq \Theta_{mp} \leq \Theta_p \tag{23}$$

(iv) Two-Phase Dispersed Region

$$\eta_{md} = 1 + \frac{y - \delta_1}{\delta_2 - \delta_1}; \quad \eta_p \leq \eta_{md} \leq 2, \qquad f'_{md} = \frac{u_{md}}{U_o}; \quad f'_{md}(2) \leq f'_{md} \leq 1 \qquad \text{and} \quad \Theta_{md} = 1 + \frac{T_{md} - T_1}{T_2 - T_1}; \quad \Theta_p \leq \Theta_{md} \leq 2 \tag{24}$$

(v) Molten Substance Region

$$\eta_l = 1 + \frac{y}{\delta_2}; \quad 2 \leq \eta_l \leq \infty, \qquad f'_l = \frac{u_1}{U_o}; \quad 0 \leq f'_l \leq f'_l(2) = f'_{md}(2) \qquad \text{and} \quad \Theta_l = 2 + \frac{T_l - T_2}{T_\infty - T_2}; \quad 2 \leq \Theta_l \leq 3 \tag{25}$$

In the above transformation, η_p is the similarity variable at the location where the solid fraction reaches the packing limit. The solidus and liquidus line, δ_1 and δ_2, respectively, and the dimensionless packing limit isotherm are given by

$$\delta_1 = \sigma_1 \sqrt{\frac{\alpha_s x}{U_0}} \tag{26a}$$

$$\delta_2 = \sigma_2 \sqrt{\frac{\alpha_s x}{U_0}} \tag{26b}$$

$$\Theta_p = 1 + \frac{T_p - T_1}{T_2 - T_1}, \tag{26c}$$

where σ_1 and σ_2 are the solidus and liquidus constants. Note that σ_1 and σ_2 are treated as primary unknowns in this problem. The location of the packing limit can be defined in terms of the packing limit constant σ_p in a similar manner, i.e.,

$$\delta_p = \sigma_p \sqrt{\frac{\alpha_s x}{U_0}}. \tag{26d}$$

Once σ_1 and σ_2 are known, σ_p can be determined from Eqs. (23) and (26*d*) by setting $y = \sigma_p$ at $\eta_{md} = \eta_{md}$. This gives

$$\sigma_p = (\eta_p - 1)(\sigma_2 - \sigma_1) + \sigma_1. \tag{27}$$

By performing the similarity transformation, the system of equations can be transformed into the following similarity forms:

(i) Wall Region

$$\Theta''_w + \frac{\eta_w}{2}\Theta'_w = 0 \tag{28}$$

$$\eta_w = 0 : \Theta_w = \Theta_s \quad \text{and} \quad \Theta'_w = \frac{R_1}{\sigma_1}\Theta'_s \tag{29a}$$

$$\eta_w \to -\infty : \Theta_w = 0 \tag{29b}$$

(ii) Freeze-Coat Region

$$\Theta_s + \frac{\sigma_1^2 \eta_s}{2}\Theta'_s = 0 \tag{30}$$

$$\eta_s = 0 : \Theta_s = \Theta_w \quad \text{and} \quad \Theta'_s = \frac{\sigma_1}{R_1}\Theta'_w \tag{31a}$$

$$\eta_s = 1 : \Theta_s = 1 \quad \text{and} \quad \Theta'_s = \frac{\sigma_1}{\sigma_2 - \sigma_1}\frac{1}{R_2}\Theta'_{md} \tag{31b}$$

(iii) Two-Phase Packing Region

$$\Theta''_{mp} + \frac{(\sigma_2 - \sigma_1)^2}{2}\left(1 + \frac{\kappa}{Ste[(2 - \Theta_{mp}) + k(\Theta_{mp} - 1)]^2}\right) \times \left(\eta_{mp} - 1 + \frac{\sigma_1}{\sigma_2 - \sigma_1}\right)\Theta'_{mp} = 0 \tag{32}$$

$$\eta_{mp} = 1 : \Theta_{mp} = 1 \quad \text{and} \quad \Theta'_{mp} = \frac{\sigma_2 - \sigma_1}{\sigma_1} R_2 \Theta'_s \tag{33a}$$

$$\eta_{mp} = \eta_p : \Theta_{mp} = \Theta_p \quad \text{and} \quad \Theta'_{mp} = \Theta'_{md} \tag{33b}$$

(iv) Two-Phase Dispersed Region

$$f'''_{md} + \frac{(\sigma_2 - \sigma_1)^2}{2\,\mathrm{Pr}}\left(1 - \frac{F}{F_p}\right)^b \left(f_{md} f''_{md} + \left(\eta_p - 1 + \frac{\sigma_1}{\sigma_2 - \sigma_1}\right) f''_{md}\right) - \frac{b\kappa}{F_p[(2 - \theta_{mp}) + k(\theta_{mp} - 1)]^2}\left(1 - \frac{F}{F_p}\right)^{-1} \theta'_{md} f''_{md} = 0 \tag{34}$$

$$\Theta''_{md}+\frac{(\sigma_2-\sigma_1)^2}{2}\left(1+\frac{\kappa}{Ste[(2-\Theta_{md})+k(\Theta_{md}-1)]^2}\right)\times\left(f_{md}\Theta'_{md}+\left(\eta_p-1+\frac{\sigma_1}{\sigma_2-\sigma_1}\right)\Theta'_{md}\right)=0 \tag{35}$$

$$\eta_{md}=\eta_p: f_{md}=0,\quad f'_{md}=1,\quad \Theta_{md}=\Theta_p \quad \text{and} \quad \Theta'_{md}=\Theta'_{mp} \tag{36a}$$

$$\eta_{md}=2: f_{md}=\frac{\sigma_2}{\sigma_2-\sigma_1}f_l+\left(1-\eta_p-\frac{\sigma_1}{\sigma_2-\sigma_1}\right),\quad f'_{md}=f'_l,$$

$$f''_{md}=\frac{\sigma_2-\sigma_1}{\sigma_2}f''_l, \tag{36b}$$

$$\Theta_{md}=2 \quad \text{and} \quad \Theta'_{md}=\frac{\sigma_2-\sigma_1}{\sigma_2}R_3\Theta'_l$$

(v) Molten Substance Region

$$f'''_l+\frac{\sigma_2^2}{2\text{Pr}}f_l f''_l=0 \tag{37}$$

$$\Theta''_l+\frac{\sigma_2^2}{2}f_l\Theta'_l=0 \tag{38}$$

$$\eta_l=2: f_l=\frac{\sigma_2-\sigma_1}{\sigma_2}f_{md}-\left(1-\eta_p-\frac{\sigma_1}{\sigma_2-\sigma_1}\right)\frac{\sigma_2-\sigma_1}{\sigma_2},$$

$$f'_l=f'_{md}, \tag{39a}$$

$$f''_l=\frac{\sigma_2}{\sigma_2-\sigma_1}f''_{md},\quad \Theta_l=2 \quad \text{and} \quad \Theta'_l=\frac{\sigma_2}{\sigma_2-\sigma_1}\frac{1}{R_3}\Theta'_{md}$$

$$\eta_l\to\infty: f'_l=0 \quad \text{and} \quad \Theta_l=3 \tag{39b}$$

(vi) Supplemental Equation

$$F=\frac{2-\Theta_{md}}{(2-\Theta_{md})+\kappa(\Theta_{md}-1)} \tag{40a}$$

The supplemental equation can be used to determine the packing limit isotherm, Θ_p. At the location where the solid fraction reaches the packing limit fraction, the packing limit isotherm is

$$\Theta_p=\frac{2-2F_p+\kappa F_p}{1-F_p+\kappa F_p}. \tag{40b}$$

There are seven dimensionless parameters appearing in the above system of similarity equations. These parameters are the freeze-coat-to-wall thermal ratio R_1, the wall subcooling parameter R_2, the molten substance superheating parameter R_3, the Prandtl number of the molten substance Pr, the Stefan number Ste, the equilibrium partition ratio κ, and the exponent b in Eq. (34) that is directly proportional to the packing limit fraction F_p:

$$R_1=\sqrt{\frac{k_s\rho_s C_{P_s}}{k_w\rho_w C_{P_w}}},\quad R_2=\frac{T_1-T_o}{T_2-T_1},\quad R_3=\frac{T_\infty-T_2}{T_2-T_1} \tag{41}$$

$$\text{Pr}=\frac{\upsilon_l}{\alpha_l},\quad \text{Ste}=\frac{C_{P_m}(T_2-T_1)}{\Delta H_m},\quad \kappa=\frac{m_2}{m_1} \quad \text{and}$$

$$b=[\mu]F_p=2.5F_p.$$

Evidently, the freeze-coating process under consideration is controlled by these seven dimensionless parameters.

Solution Methodology

A closed-form solution for Θ_w and Θ_s can be obtained from Eqs. (28) and (30) by direct integration using the appropriate boundary conditions (Eqs. (29a–29b) and (31a–31b) respectively). This gives

$$\Theta_w=\frac{R_1}{R_1+\text{erf}(\sigma_1/2)}\left[1+\text{erf}\left(\frac{\eta_w}{2}\right)\right] \tag{42}$$

$$\Theta_s=\frac{R_1+\text{erf}\left(\frac{\sigma_1\eta_s}{2}\right)}{R_1+\text{erf}(\sigma_1/2)}. \tag{43}$$

The dimensionless temperature at the interface between the wall and the freeze-coat region, i.e., at $\eta_w=\eta_s=0$, is given by

$$\Theta_w(0)=\Theta_s(0)=\frac{R_1}{R_1+\text{erf}(\sigma_1/2)}. \tag{44}$$

The first derivative of Θ_s evaluating at $\eta_s=1$ can be determined from Eq. (43) as

$$\Theta'_s(1)=\frac{\sigma_1}{\sqrt{\pi}}\left[\frac{\exp(-\sigma_1^2/4)}{R_1+\text{erf}(\sigma_1/2)}\right]. \tag{45}$$

Applying the above equation to the flux condition (Eq. (31*b*)) yields

$$\Theta'_{md}(1)=\frac{(\sigma_2-\sigma_1)R_2}{\sqrt{\pi}}\left[\frac{\exp(-\sigma_1^2/4)}{R_1+\text{erf}(\sigma_1/2)}\right]. \tag{46}$$

For a given set of parameters, equations (32), (34), (35), (37), and (38) with the appropriate boundary conditions can be numerically solved by using the classical fourth-order Runge-Kutta method. To avoid the singularity point at $\eta_{md}=\eta_p$, the Taylor's series expansion is applied to the momentum equation for the two-phase dispersed region, Eq. (34). In so doing, the initial condition is set at $\eta_p+\Delta\eta_{md}$ instead of η_p, where $\Delta\eta_{md}$ is a small increment of η_{md}. In order to solve the remaining equations, the values of σ_1, σ_2, and $f''_{md}(\eta_p+\Delta\eta_{md})$ are first estimated. Thereafter the value of η_p can be obtained by numerically solving the heat conduction equation in the two-phase packing region using Eq. (46) as an initial condition. Once η_p is known, the momentum and energy equations for the two-phase dispersed and molten substance regions can be solved. The Secant iterative procedure is applied until the estimated values of σ_1, σ_2, and $f''_{md}(\eta_p+\Delta\eta_{md})$ match the boundary conditions given by Eqs. (36*b*) and (39*b*), i.e., $\Theta_{md}(2)=2$, $\Theta_l(\infty)=3$ and $f'_l(\infty)=0$. The solution is shown to converge under the prescribed tolerance of 10^{-5}.

Grid independency is also examined by setting the standard grid size at $\Delta\eta_{mp}=\Delta\eta_{md}=0.01$ and $\Delta\eta_l=0.02$ where the reference case ($R_1=1$, $R_2=10$, $R_3=1$, Pr=1, Ste=0.1, $\kappa=0.3$, $F_p=0.6$, $b=1.5$) is chosen to test the algorithm. With the grid size being increased by two and four times, the relative errors of the calculated values of σ_1 and σ_2 are less than 0.1 percent and 0.3 percent, respectively. On the other hand, as the grid size is decreased to one half of the standard grid size, the relative error is found to be less than 0.03 percent. This numerical accuracy is considered satisfactory for predicting the behavior of the freeze-coating process.

Results and Discussion

Numerical calculations have been made to determine the dependence of the solidus, packing limit and liquidus constants (σ_1, σ_p, and σ_2) on the controlling parameters. These three solidification constants characterize the behavior of the two-phase mushy zone. In practice, the wall subcooling parameter and the molten substance superheating parameter can be controlled by adjusting the inlet wall temperature and the ambient bath temperature, re-

spectively. On the other hand, the freeze-coat-to-wall thermal ratio, the Prandtl number, the Stefan number, the equilibrium partition ratio, and the packing limit fraction depend upon selection of the binary substance and wall material.

In this study, selected cases with various sets of values of the controlling parameters have been studied. Typical numerical results are depicted in Figs. 4 to 8. These results are obtained by varying the controlling parameters from the reference case. As expected, the liquidus constant is always greater than the solidus constant as the liquidus temperature, T_2, is higher than the solidus temperature, T_1. On the other hand, the packing limit constant lies between the values of the solidus and liquidus constants.

Figure 4 depicts the variations of the solidus, packing limit and liquidus constants with the freeze-coat-to-wall thermal ratio R_1 for different Stefan numbers. For a given Stefan number, σ_1, σ_p, and σ_2 decrease with increasing R_1. As the thermal conductivity and the heat capacity of the wall compared to those of the freeze coat become smaller, the cooling capacity of the wall is reduced, resulting in a slower freeze-coating process. Note that as the value of R_1 approaches zero, corresponding to an infinite heat capacity of the wall, σ_1, σ_p, and σ_2 asymptotically approach to constant values. On the other hand, for a given R_1, increasing the Stefan number causes σ_1, σ_p, and σ_2 to increase. Under the same cooling conditions, a thicker freeze coat is expected for a material with a larger Stefan number.

The variations of the solidus, packing limit and liquidus constants with the wall subcooling parameter for different freezecoat-to-wall thermal ratios are illustrated in Fig. 5. For a given thermal ratio, σ_1, σ_p, and σ_2 increase with increasing R_2. Physically, an increase in R_2 corresponds to a higher value of the degree of subcooling, leading to a thicker freeze coat. On the other hand, for a given subcooling parameter, σ_1, σ_p, and σ_2 increase as R_1 is decreased. For R_1 less than 0.01, the three solidification constants tend to approach their asymptotic values corresponding to those for an isothermal wall.

Figure 6 depicts the variation of the solidus, packing limit and liquidus constants with wall subcooling parameter for different Stefan numbers. In this firgure, R_1 is set equal to zero, corresponding to an isothermal wall. For a given Stefan number, σ_1, σ_p, and σ_2 increase with R_2, similar to the behavior shown in Fig. 5. Note that the values of σ_1, σ_p, and σ_2 for an isothermal wall with infinite heat capacity represent the upper limits for the three solidification constants. For a given R_2, σ_1, σ_p, and σ_2 increase with increasing Stefan number. Comparison of Figs. 4 and 6 indicates that σ_1, σ_p, and σ_2 are more sensitive to the change in the values of R_2 than that of R_1.

The variations of the solidus, packing limit and liquidus constants with the molten substance superheating parameters for different Prandtl numbers are illustrated in Fig. 7. For a given Prandtl number, σ_1, σ_p, and σ_2 decrease with increasing R_3. This is expected as more heat is convected from the liquid as the superheating parameter is increased, resulting in a slower freeze-coating process. Note that both σ_1 and σ_p vary with R_3 in a manner which are quite different than that of σ_2. As R_3 becomes smaller, both σ_1 and σ_p asymptotically approach to constant values whereas σ_2 continues to increase. For a given R_3, σ_1, σ_p, and σ_2 increase as the Prandtl number is decreased. It is known that the convective heat transfer coefficient decreases with a decrease in the Prandtl number. Thus at a smaller value of the Prandtl number, the rate of heat convected from the liquid is reduced, resulting in a thicker freeze coat layer. Note that for $\mathrm{Pr} \geqslant 10$, there is virtually no effect of the Prandtl number on σ_1, σ_p, and σ_2.

Figure 8 depicts the variation of the solidus, packing limit and liquidus constants with the molten substance superheating parameter for different Stefan numbers for the case of a large Prandtl number fluid, i.e., $\mathrm{Pr}=100$. For a given Stefan number, σ_1, σ_p, and σ_2 vary with R_3 in the same manner as those shown in Fig. 7. The asymptotic behavior of σ_1 and σ_p as R_3 approaches zero is

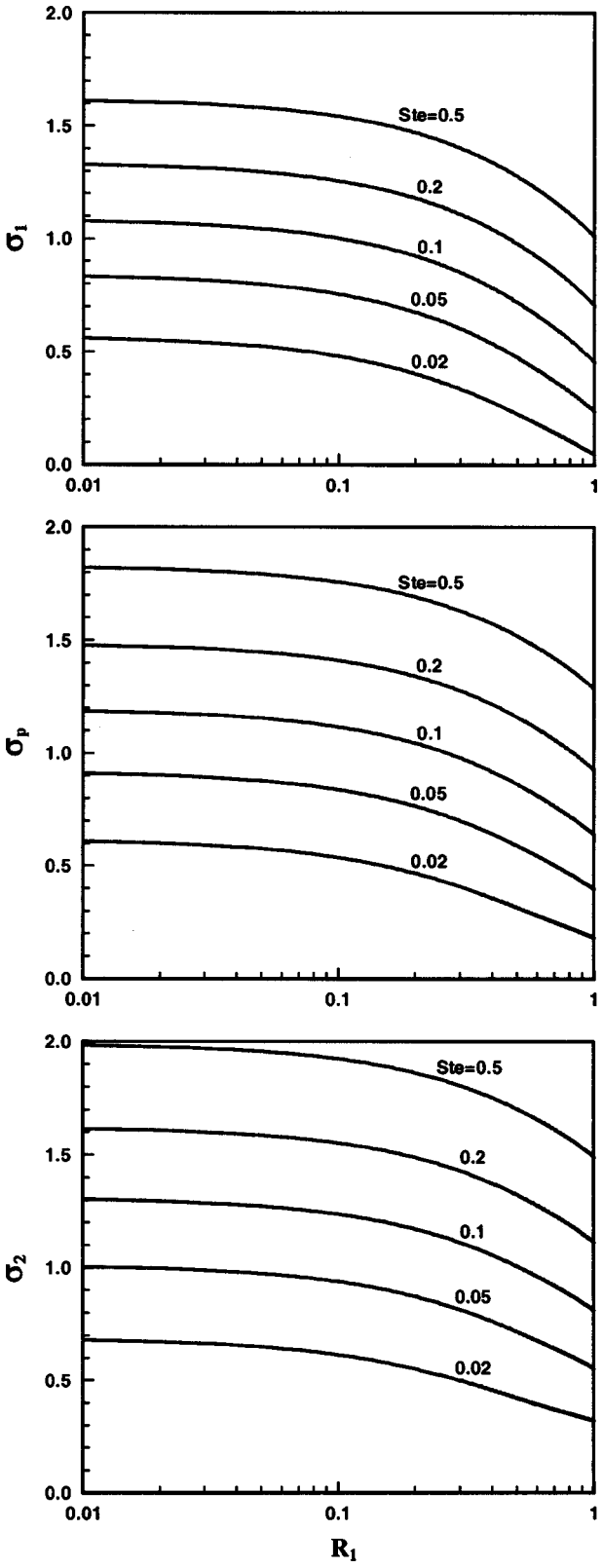

Fig. 4 Variations of the solidus, packing limit and liquidus constants with the freeze-coat-to-wall thermal ratio and the Stefan number ($R_2=10$, $R_3=1$, $\mathrm{Pr}=1$, $\kappa=0.3$, and $F_p=0.6$)

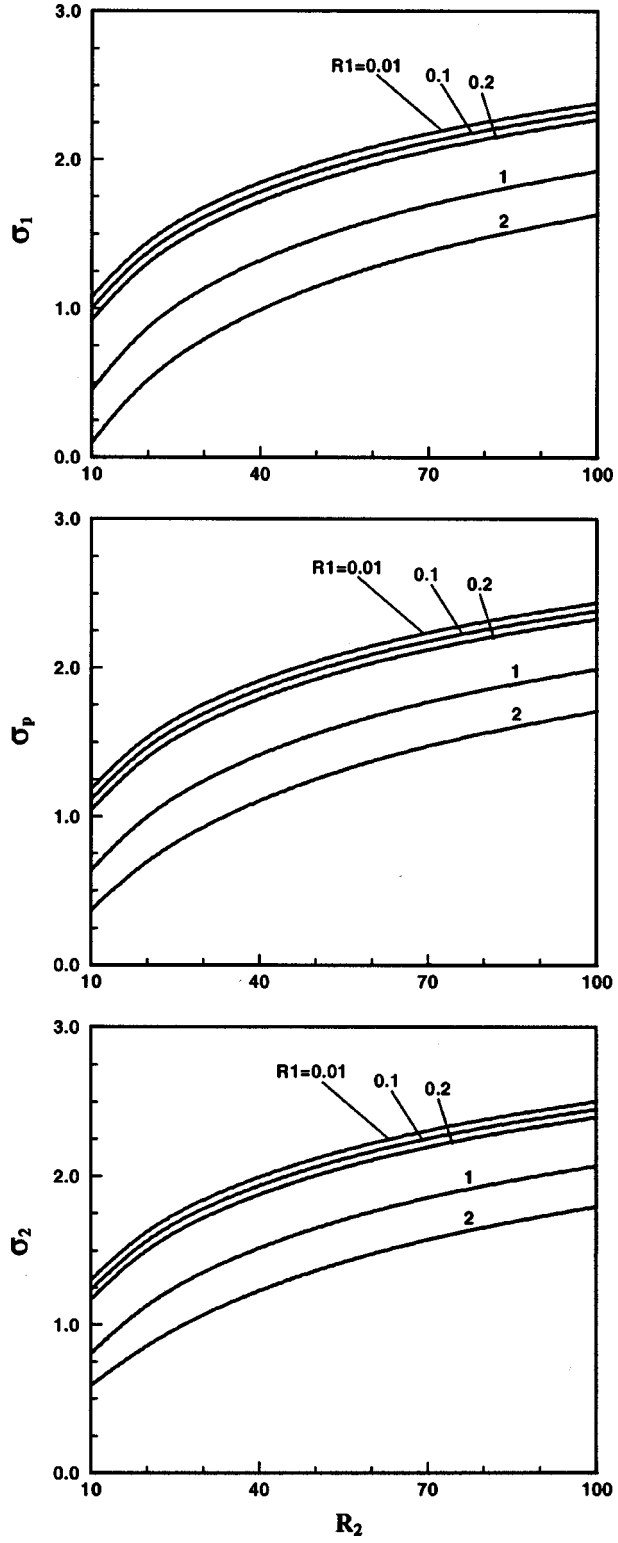

Fig. 5 Variations of the solidus, packing limit and liquidus constants with the wall subcooling parameter and the freeze-coat-to-wall thermal ratio (R_3=1, Pr=1, Ste=0.1, κ=0.3, and F_p=0.6)

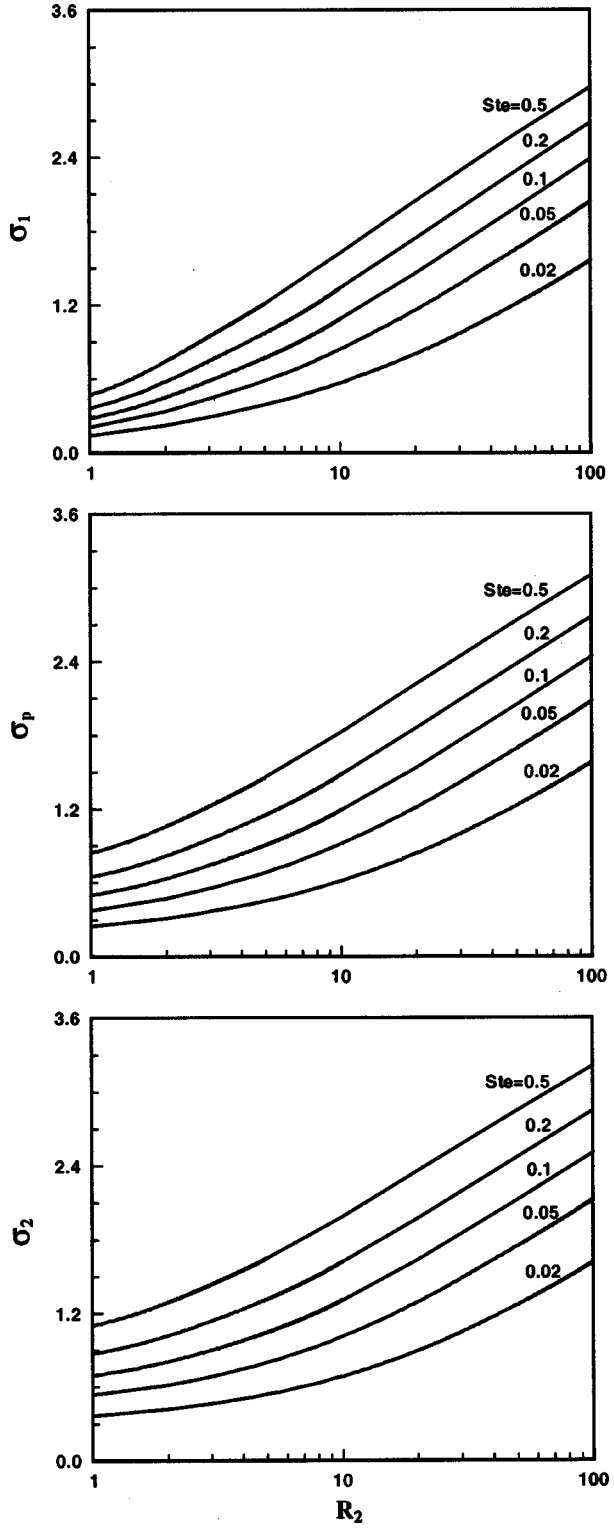

Fig. 6 Variations of the solidus, packing limit and liquidus constants with the wall subcooling parameter and the Stefan number for an isothermal wall (R_1=0, R_3=1, Pr=1, κ=0.3 and F_p=0.6)

observed for all Stefan numbers, but the same behavior is not observed for σ_2. Note that for Stefan number smaller than 0.02, σ_1 and σ_p appear to be quite insensitive to the change of R_3. This trend, however, is not true for the liquidus constant σ_2. Comparison of Figs. 6 and 8 shows that σ_1, σ_p, and σ_2 are more sensitive to the change in the values of R_2 than that of R_3.

The effects of the equilibrium partition ratio κ and the packing limit fraction F_p are presented in Tables 1 and 2, respectively. As the value of κ is increased from 0.1 to 0.5, σ_1 increases by less than 4 percent whereas σ_2 increases by almost 15 percent. On the

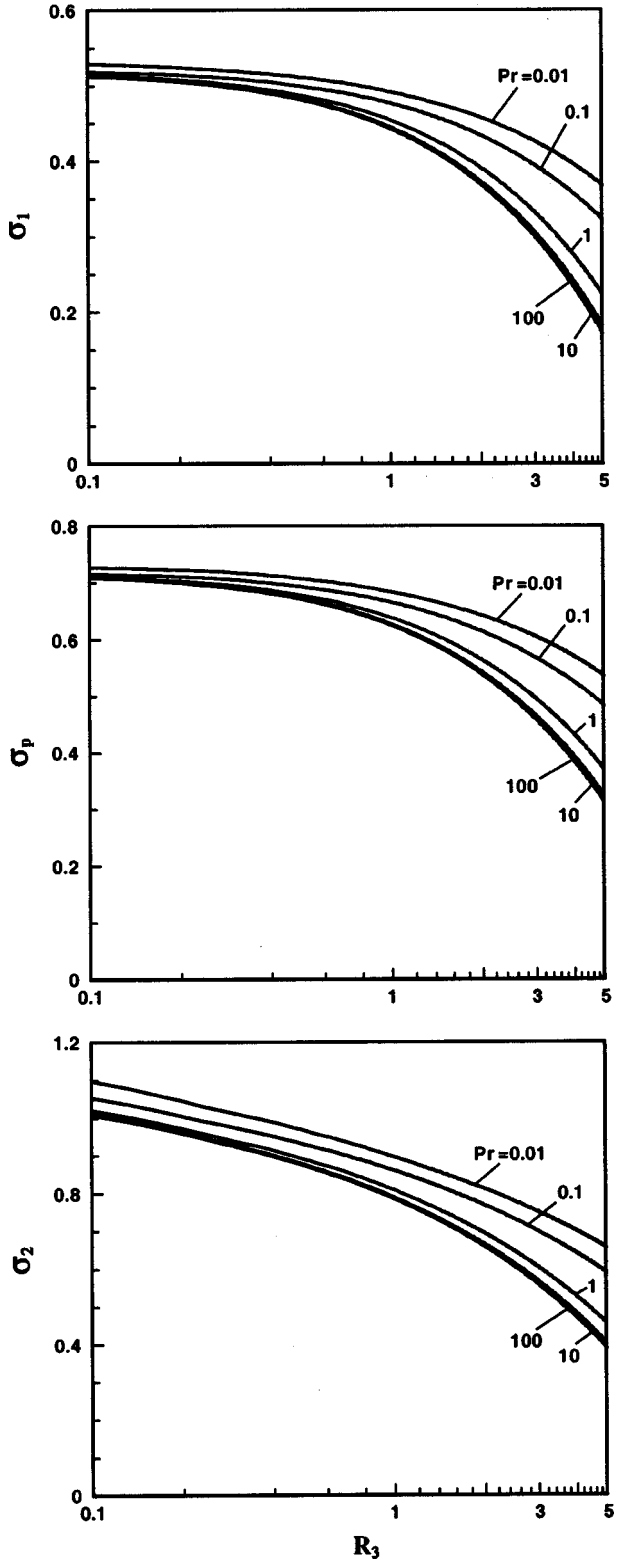

Fig. 7 Variations of the solidus, packing limit and liquidus constants with the molten substance superheating parameter and the Prandtl number (R_1=1, R_2=10, Ste=0.1, κ=0.3, and F_p=0.6)

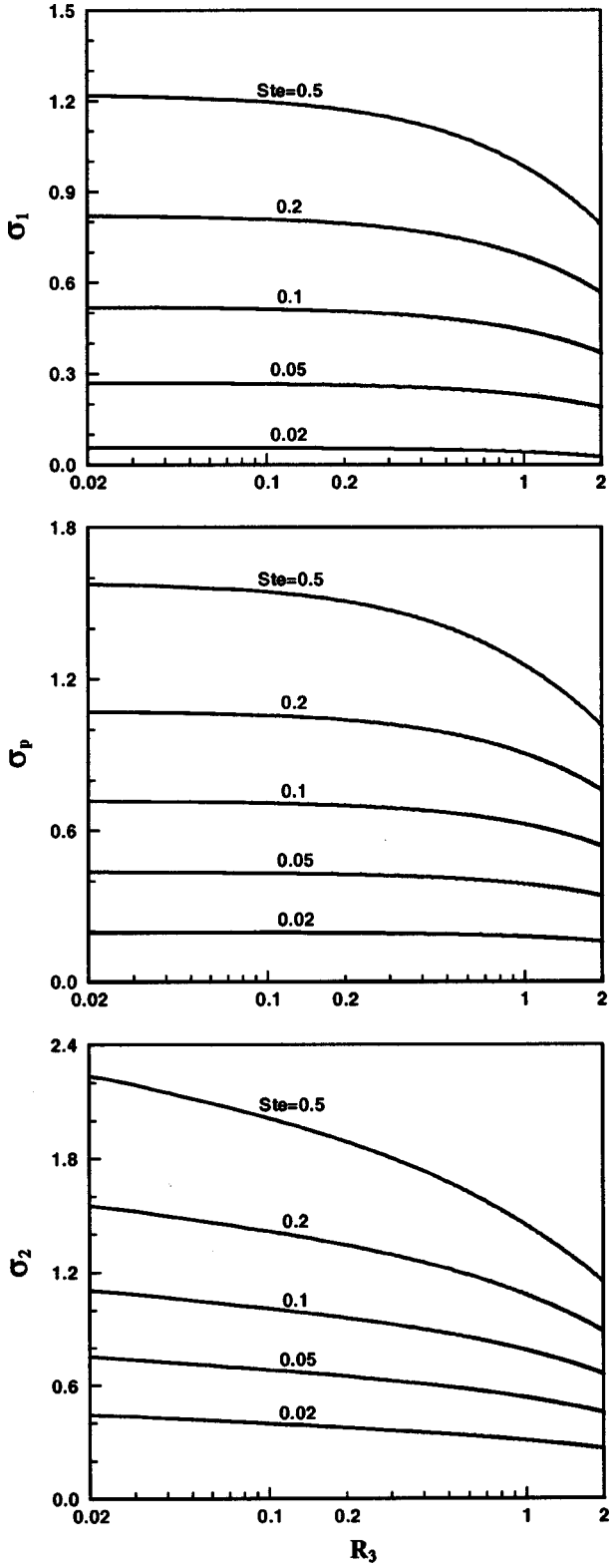

Fig. 8 Variations of the solidus, packing limit and liquidus constants with the molten substance superheating parameter and the Stefan number for the high Prandlt number case (R_1=1, R_2=10, Pr=100, κ=0.3, and F_p=0.6)

other hand, σ_p decreases by nearly 9 percent. Note from Eq. 40*b* that for a given F_p, the packing limit isotherm, Θ_p, decreases as κ is increased, thus resulting in a smaller value of σ_p. The solidus and liquidus constants are weak functions of the packing limit fraction, as shown in Table 2. As the value of F_p is increased from 0.5 to 0.75, σ_1 and σ_2 increase by less than 0.1 percent. In contrast, the value of σ_p decreases by almost 12 percent over the same range of F_p. The sensitivity of σ_p on F_p is due to the fact that the packing limit isotherm depends directly on the packing limit fraction, as given by Eq. (40*b*).

Table 1 The Solidus, packing limit and liquidus constants for various values of the equilibrium partition ratio ($R_1=1$, $R_2=10$, $R_3=1$, Pr=1, Ste=0.1, and $F_p=0.6$)

κ	σ_1	σ_p	σ_2
0.1	0.4458	0.6709	0.7427
0.2	0.4501	0.6539	0.7806
0.3	0.4544	0.6386	0.8097
0.4	0.4577	0.6259	0.8339
0.5	0.4606	0.6151	0.8547

Table 2 The solidus, packing limit and liquidus constants for various values of the packing limit fraction ($R_1=1$, $R_2=10$, $R_3=1$, Pr=1, Ste=0.1, and $\kappa=0.3$)

F_p	σ_1	σ_p	σ_2
0.50	0.4543	0.6670	0.8096
0.55	0.4543	0.6531	0.8096
0.60	0.4544	0.6386	0.8097
0.65	0.4545	0.6232	0.8099
0.70	0.4545	0.6065	0.8099
0.75	0.4546	0.5884	0.8100

Conclusions

A theoretical study of the process of freeze coating of a binary substance on a chilled moving plate has been preformed. Based on the results of this study, the following conclusions can be drawn:

1 The behavior of the two-phase mushy zone can be characterized by the solidus constant, the packing limit constant, and the liquidus constant. These three solidification constants, which represent the major unknowns of the problem, are functions of seven dimensionless parameters of the freeze-coating system. These parameters are the freeze-coat-to-wall thermal ratio, the wall subcooling parameter, the molten substance superheating parameter, the Prandtl number, the Stefan number, the equilibrium partition ratio, and the packing limit fraction.

2 As the Stefan number or the wall subcooling parameter is increased, the solidus constant, the packing limit constant, and the liquidus constant increase. On the other hand, the three solidification constants decrease as either the freeze-coat-to-wall thermal ratio, the molten substance superheating parameter, or the Prandtl number is increased. At a sufficiently large Prandtl number (i.e., $Pr \geqslant 10$), however, the three solidification constants appear to be independent of the Prandtl number. For small Stefan numbers ($Ste < 0.02$), the solidus constant and the packing limit constant are not sensitive to the variation of the molten substance superheating parameter.

3 For given values of the Prandtl number and Stefan number, the three solidification constants appear to be more sensitive to the variation in the wall subcooling parameter than to the variations in the freeze-coat-to-wall thermal ratio and the molten substance superheating parameter.

4 The three solidification constants approach asymptotically to constant values as the freeze-coat-to-wall thermal ratio R_1 approaches zero, corresponding to the case of an isothermal plate. Similarly, as the molten substance superheating parameter R_3 approaches zero, corresponding to the case of a saturated liquid, the solidus constant and the packing limit constant approach asymptotically to constant values. However, the liquidus constant continues to increase with decreasing value of the superheating parameter. Note that the maximum rate of freeze coating is obtained for the case of an isothermal plate ($R_1=0$) moving through a saturated binary substance ($R_3=0$).

5 Both the value of the packing limit constant and the liquidus constant change appreciably as the equilibrium partition ratio is varied from 0.1 to 0.5, which covers the range anticipated for most binary substances. On the other hand, the value of the solidus constant varies only slightly over this range. The packing limit constant tends to decrease as the packing limit fraction is increased. On the contrary, over the range considered in this study, both the solidus constant and liquidus constant appear to be insensitive to the variation of the packing limit fraction.

References

[1] Kuiken, H. K., 1977, "Solidification of a Liquid on Moving Sheet," Int. J. Heat Mass Transf., **20**, pp. 309–314.
[2] Seeniraj, R. V., and Bose, T. K., 1981, "Freeze-Coating on a Continuous Moving Sheet and an Axially Moving Cylinder," Warme Stoffubertrag, **15**, pp. 239–243.
[3] Cheung, F. B, 1985, "Analysis of Freeze Coating on a Non-Isothermal Moving Plate by a Perturbation Method," ASME J. Heat Transfer, **107**, pp. 549–556.
[4] Cheung, F. B., 1987, "Thermal Boundary Layer on a Continuous Moving Plate With Freezing," AIAA J. Thermophys & Heat Transfer, **1**, pp. 335–342.
[5] Rezaian, A., and Poulikakos, D., 1991, "Heat and Fluid Flow Process During the Coating of a Moving Surface," AIAA J. Thermophys & Heat Transfer, **5**, pp. 192–198.
[6] Mahmound, K. G., 1993, "Heat Transfer with Moving Boundary-Application to Transient Solidification of Warm Liquid on a Moving Cold Plate," Comput. Chem. Eng., **17**, pp. 705–715.
[7] Cheung, F. B., and Cha, S. W., 1987, "Finite-Difference Analysis of Growth and Decay of a Freeze Coat on a Continuous Moving Cylinder," Numer. Heat Transfer, **12**, pp. 41–56.
[8] Cheung, F. B., Pellizzari, R. O., and Cha, S. W., 1990, "An Experimental Study of Freeze Coating on a Chilled Axially Moving Wire," Exp. Therm. Fluid Sci., **3**, pp. 431–439.
[9] Stevens, R., and Poulikakos, D., 1991, "Freeze Coating of a Moving Substrate With a Binary Alloy," Numer. Heat Transfer, Part A, **20**, pp. 409–432.
[10] Krieger, I. M., 1972, "Rheology of Monodisperse Lactices," Adv. Colloid Interface Sci., **3**, pp. 111–126.
[11] Ni, J., and Beckermann, C., 1991, "A Volume-Averaged Two-Phase Model for Transport Phenomena During Solidification," Metall. Trans. B, **22B**, pp. 339–361.
[12] Fukusako, S., Yamada, M., Horibe, A., and Kawai, A., 1995, "Solidification of Aqueous Binary Solution on a Vertical Cooled Plate with Main Flow," Heat and Mass Transfer, **30**, pp. 127–134.
[13] Cheung, F. B., and Epstein, M., 1984, "Solidification and Melting in Fluid Flow," Advances in Transport Processes, **3**, pp. 35–117, Wiley Eastern, New Delhi.
[14] Voller, V. R., Brent, A. D., and Prakash, C., 1989, "The Modelling of Heat, Mass and Solute Transport in Solidification Systems," Int. J. Heat Mass Transf., **32**, pp. 1719–1731.
[15] Wang, C. Y., and Beckermann, C., 1996, "Equiaxed Dendritic Solidification With Convection: Part 1. Multi-Scale/-Phase Modeling," Metall. Mater. Trans. A, **27A**, pp. 2754–2764.
[16] Gao, J., and Wang, C. Y., 1999, "An Experimental Investigation Into the Effects of Grain Transport on Columnar-to Equiaxed Transition During Dendritic Alloy Solidification," ASME J. Heat Transfer, **121**, pp. 430–437.
[17] Yamada, M., Fukusako, S., Tago, M., and Horibe, A., 1993, "Freezing Characteristic Along a Horizontal Cooled Tube Immersed in Aqueous Binary Solution With Main Flow," ASME J. Eng. Mater. Technol., **115**, pp. 54–62.
[18] Paradies, C. J., Smith, R. N., and Glicksman, M. E., 1997, "The Influence of Convection During Solidification on Fragmentation of the Mushy Zone of a Model Alloy," Metall. Mater. Trans. A, **28A**, pp. 875–883.
[19] Kuznetsov, A. V., 1998, "Horizontal Continuous Casting of Thin Aluminum Strips-Numerical Modeling and Simulation," *Advances in Aluminum Casting Technology, Materials Solution Conference '98 on Aluminum Casting Technology*, M. Tiryakioglu and J. Campbell, eds., Rosemont, IL, pp. 251–258.
[20] Flemings, M. C., 1974, *Solidification Processing*, McGraw-Hill, New York.
[21] Einstein, A., 1906, "Eine neue Bestimmung der Molekuldimension," Ann. Physik., **19**, pp. 289–306.
[22] Krieger, I. M., and Daugherty, T. J., 1959, "A Mechanism of Non-Newtonian Flow in Suspensions of Rigid Spheres," Trans. Soc. Rheol., **3**, pp. 137–152.
[23] Barnes, H. A., Hutton, J. F., and Walters, K., 1989, *An Introduction to Rheology*, Elsevier, Amsterdam.

Measurement of Interstitial Convective Heat Transfer and Frictional Drag for Flow Across Metal Foams

J.-J. Hwang
Mem. ASME
e-mail: jjhwang@chu.edu.tw
Department of Mechanical Engineering,
Chung-Hua University,
Hsinchu, Taiwan 300, ROC

G.-J. Hwang
Fellow ASME

R.-H. Yeh

Department of Power Mechanical Engineering,
National Tsing Hua University,
Hsinchu, Taiwan 300, ROC

C.-H. Chao
Department of Electrical Engineering,
Ta-Hwa Institute of Technology,
Hsinchu, Taiwan 300, ROC

Convective heat transfer and friction drag in a duct inserted with aluminum foams have been studied experimentally. The combined effects of foam porosity (ε=0.7, 0.8, and 0.95) and flow Reynolds number (1900≤Re≤7800) are examined. Frictional drags for flow across the aluminum foam are measured by pressure taps, while interstitial heat transfer coefficients in the aluminum foam are determined using a transient single-blow technique with a thermal non-equilibrium two-equation model. Solid material temperature distribution is further measured for double check of the heat transfer results. To understand the frictional drag mechanisms, smoke-wire flow visualization is conducted in the aluminum-foam ducts. Results show that both the friction factor and the volumetric heat transfer coefficient increase with decreasing the foam porosity at a fixed Reynolds number. In addition, the aluminum foam of ε=0.8 has the best thermal performance under the same pumping power constraint among the three aluminum foams investigated. Finally, empirical correlations for pore Nusselt number are developed in terms of pore Reynolds number under various foam porosities. [DOI: 10.1115/1.1416690]

Keywords: Convection, Heat Transfer, Inverse, Non-Equilibrium, Porous Media

Introduction

Porous media have been widely used in industrial applications such as electronic cooling, thermal energy absorber, geothermal system and many others. They can be in the form of packed beds, sintered materials, or foam materials. In the past, a large amount of research works for packed beds and sintered materials has been done [1–10], and extensive data and empirical correlations for convective heat transfer coefficient and friction factor are available now, which cover a large range of particle diameters, Reynolds numbers and fluids. The heat transfer and friction in porous foam materials, however, has not been studied to the same extent as that of pack beds and sintered materials [11–14]. Thus, the related data and correlations are relatively sparse. It is inappropriate to use the data or correlations of packed beds and sintered materials to predict the convective heat transfer inside foam materials because their internal structures are quite different [13]. In addition, the porosity of foam materials (ε>0.7) is much larger than the porosity of the packed beds or sintered materials (ε <0.476) [15]. Therefore, substantial data about the fluid flow and heat transfer characteristics inside foam materials are required to develop and optimize the design of such advanced devices.

Two kinds of heat transfer coefficients are often employed to depict heat transfer characteristics in porous media for their own application purpose, i.e., wall heat transfer coefficient and interstitial heat transfer coefficient. The first one always illustrates the global extent of heat transfer augmentation from the wall surface where the porous medium attaches. These surface heat transfer data are useful in the design of heat sinks such as electronics cooling [8,10,11,16]. The second one describes the heat exchange between the fluid stream and the solid matrix of the porous medium. Technologic applications of these data include thermal energy absorbers, advanced burners or incinerators, compact heat exchangers, etc. [7,12,13,17]. The present paper focuses on the interstitial heat transfer characteristics of the aluminum foams. Several relevant studies related to the interstitial heat transfer characteristics in porous media are briefly reviewed below. Golombok et al. [17] employed the heat regenerator technique to measure the heat transfer coefficient between the flowing gas and the metal fiber of a burner. The porosity of the porous fibrous material was fixed at ε=0.8. Results showed that the heat transfer coefficient for laminar flows increased rapidly with increasing gas flow. Vafai and Sozen [6] analyzed the thermal-fluid characteristics for flow through a packed bed of spherical particles of a fixed porosity ε=0.39. They used the fluid-to-solid heat transfer coefficients from an empirical correlation established by Gamson et al. [18]. Results showed that the local thermal equilibrium condition was very sensitive to the particle Reynolds number and the Darcy number. Younis and Viskanta [12] utilized a single-blow method to determine the volumetric heat transfer coefficients between the air stream and ceramic foam under a small range of the porosity (0.83≤ε≤0.87). It was found that the volumetric heat transfer coefficients were significantly different from previous data for packed beds and sintered metals. Ichimiya [13] evaluated the convective heat transfer between the fluid and the solid material of an aluminum-ceramic foam (ε=0.87) by comparing the measured and predicted Nusselt number on the heated wall of a porous channel. In his prediction, the analysis was performed under the assumption that porous media was constructed by small spherical particles.

It is evident that the above studies related to the interstitial heat transfer in porous media were performed under a fixed porosity or a small range of porosity. Strictly speaking, the results concerning the effect of porosity on the interstitial heat transfer and friction of metal foam have not been reported yet. Therefore, the objective of this paper is to investigate the combined effects of porosity (ε =0.7, 0.8 and 0.95) of the aluminum foam and the flow Reynolds number (1900≤Re≤7800) on interstitial heat transfer and friction characteristics in an aluminum-foam channel. Several issues are discussed in the present paper. First, experiments are conducted to examine the effect of porosity on the pressure-drop for flow across the aluminum foam, which has not been studied before. To quali-

Contributed by the Heat Transfer Division for publication in the JOURNAL OF HEAT TRANSFER. Manuscript received by the Heat Transfer Division November 17, 2000; revision received May 15, 2001. Associate Editor: D. Poulikakos.

tatively understand the frictional drag mechanism in the channel inserted with different-porosity aluminum foams, flow visualization using a smoke-wire technique is undertaken. Then, the volumetric heat transfer coefficient between the gas and the aluminum foam is obtained by using a transient single-blow technique. It is hard to directly measure the interstitial heat transfer coefficient of the porous medium because of the difficulty in the measurement of the temperature difference between the gas and solid phases. Therefore, an inverse method of transient single-blow technique is used to determine the convective heat transfer coefficients between the fluid and solid phases of the aluminum foams. Subsequently, by quoting the friction and heat transfer data, a comparison of the thermal performance among the three aluminum foams is made under two constraints, i.e., constant pumping power and constant though flow rate. Finally, empirical correlations for pore Nusselt numbers are developed in terms of pore Reynolds number for the different-porosity aluminum foam, which may be helpful in the design of related devices such as compact heat exchanger and thermal energy absorber. In addition, the interstitial heat transfer and friction data presented can provide a reference of computational-fluid-dynamic-based studies relating the heat transfer in the foam materials.

Experimental Program

Apparatus. An experimental setup for the measurement of interstitial heat transfer characteristic in the aluminum foam is shown in Fig. 1. It consists of an airflow circuit, the test section, and instruments. Air from a 2 hp compressor first enters into a surge tank for the supply of airflow in the circuit. The compressed air released from the surge tank passes through two filters and a refrigeration dehydrator to remove oil, water and particulate material. It then flows into a settling chamber to reduce the possible noise and to attain a uniform axial velocity profile. Before entering the test section, airflow is heated by passing through a specially designed plate heater, which is formed by 30-μm thick stainless steel foil wound around in a bakelite frame. The hot air then traverses the aluminum-foam test section, and finally exits from the test section to the outside of the building via an exhaust system. A digital flow meter is situated at the downstream of the test section to measure the volumetric flow rate through the test section. The test channel as shown in Fig. 2 made of Plexiglas® plates has a rectangular cross section of 60×25.4 mm^2. The aluminum foam of size $60\times25.4\times60$ mm^3 is cut in the way that the sides are flush with the channel walls for a good contact. The aluminum foam is fitted into the channel, and subsequently the entire test section is bolted tightly from outside. Two pressure taps located at the inlet and the outlet of the test section measure the

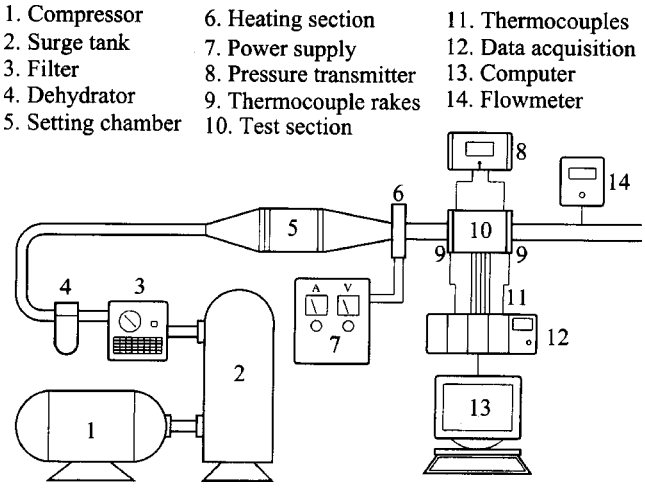

Fig. 1 Sketch of the experimental setup

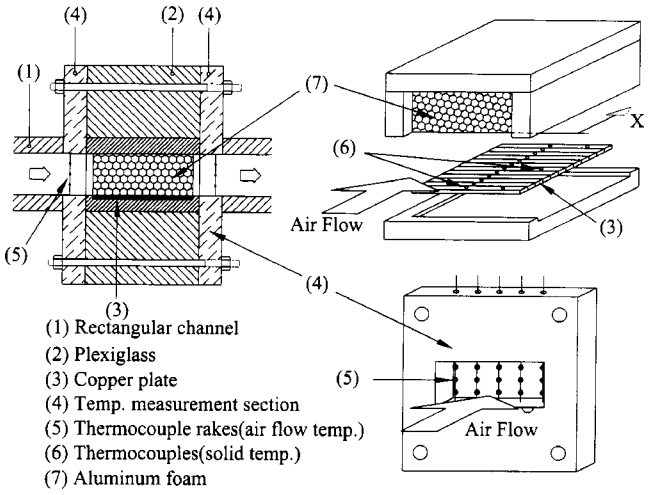

Fig. 2 Schematic drawing of the test section

static pressure differences across the test sample. They are connected to a micro-differential transmitter to display the pressure signals. At both the upstream and the downstream of the test section, five thermocouple rakes (each with three beads) are used to measure the averaged airflow temperature. The transient responses of temperature signals are transferred and subsequently recorded by a real-time hybrid recorder (YOKOGAWA DA100) with a sample rate of 2 Hz. Since it is difficult to measure directly the solid-phase temperature of the porous matrix, twelve segments of copper plate of size $60\times6\times2$ mm^3 are fixed on the bottom surface of the foam metal for the measurement of wall temperature (Fig. 2), which represents the solid-phase temperature of the porous matrix at the corresponding axial station. Using high-conductive epoxy at each interface between the aluminum fiber and copper plate minimizes the contact resistance. In addition, the copper segments are spaced by wood strips to minimize axial conduction between them. Twelve copper-constantan thermocouples are distributed along the span-center of each segment, and their junction beads are carefully embedded into the copper segments. In addition, to check the spanwise distribution of the wall temperature, the lateral wall temperature of the first, sixth, and twelfth segments are measured by three thermocouples located at 20 mm away from the span-center of the segment. Results show that the wall temperature difference between the span-center and lateral thermocouples is less than 0.2°C. To ensure that the wall temperature measured above can represent the corresponding solid-phase temperature in the porous matrix, an additional measurement of solid-phase temperature at the real face ($x=L$) of the foam material are conducted by infrared thermography. The infrared camera is focused on the exit plane of the porous medium from the channel outlet to view the solid-phase temperature distribution. Results show that the solid-phase temperature distribution is rather uniform, and the averaged solid-phase temperature compare well with the wall temperature with maximum deviation less than 2°C.

Porous Medium. Figure 3 is a photo showing the structure of aluminum foam (Duocel®, ERG Inc.) investigated, which is manufactured by directional solidification of metal from a superheated liquid state in an environment of overpressure and high vacuum. It has a reticulated structure of open, duodecahedronal-shaped cells connected by continuous, solid metal ligaments. The matrix of cells and ligaments is completely repeatable, regular, and uniform throughout the entirety of the material. The solid ligaments are made of aluminum alloy 6101-T6 that has a thermal conductivity of 218 W/m-K. Table 1 summarizes the properties of the three samples of the aluminum foams that are used in the experimental study. The effective thermal conductivity of the po-

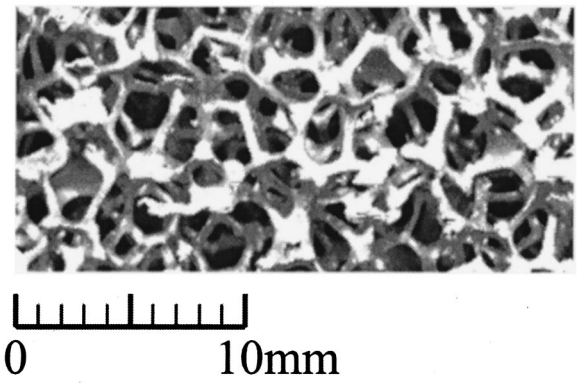

Fig. 3 Photograph of the aluminum foam matrix

rous matrix is expressed by a function of geometry and solid conductivity, i.e., $k_s^* = (1-\varepsilon)k_s$. The volume-based porosity (ε) provided by the manufacturer is determined using the weight of the sample with the density of the aluminum. It is rechecked by determining the void-to-total volume ratio of the sample, in which the sample total volume is measured by its geometry and the pore volume is determined by filling water inside the sample. It should be noted that, due to the manufacturing limitation, the aluminum foam produced by ERG has a small range of porosity about $0.88 \leqslant \varepsilon \leqslant 0.97$. In this study, the low-porosity samples of $\varepsilon = 0.7$ and 0.8 are obtained by slowly compressing the aluminum foam of $\varepsilon = 0.95$ (pore density 10 PPI) with identical compression ratio in all directions [19,20]. Measurements of pressure drop/thermal conductivity by rotating the porous matrix relative to flow/temperature gradient direction indicate that the matrix is hydraulically/thermally isotropic. In addition, visual inspections do not reveal any non-uniformity in the structure of matrix. As for the permeability and inertia coefficient of the three aluminum foams, they are determined by the fully developed pressure-drop across the porous sample together with the mean velocity in the porous channel under an isothermal condition. A rearranged version of modified Darcy equation [11] expresses the relationship between these two constants.

$$-\frac{dP}{dx}\cdot\frac{1}{\mu u} = \frac{1}{K} + \frac{F}{\sqrt{K}}\cdot\frac{\rho_f u}{\mu} \tag{1}$$

Figure 4 shows the relationship between $(\Delta P/L)/(\mu u)$ and $\rho_f u/\mu$ for three different porosities investigated. The straight lines are curve-fit results of these measured data with standard deviation less than 11 percent. The permeability K and inertial coefficient F are determined from the intercept together with the slope of the line [11]. According to the estimation method of Antohe et al. [19], the uncertainties of K and F are less than 6 percent and 9 percent, respectively. Note that the length of the present porous matrix should be long enough such that the value of $\Delta P/L$ can well represent the fully developed pressure gradient dP/dx in Eq. (1). To this end, experiments of longer porous matrices of $L = 90$ mm and 120 mm, are conducted to check the entrance and exit effects on the pressure gradient. Results show that in the range of flow velocity investigated the value of $\Delta P/L$ for $L = 60$ mm is about 5.6 percent and 5.3 percent higher than those of $L = 90$ mm and 120 mm, respectively, which represents the typical entrance and exit effects of the present porous matrix.

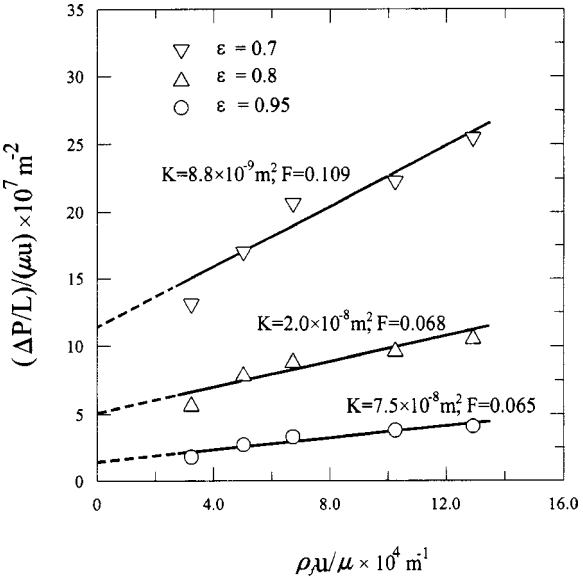

Fig. 4 Relation between $(\Delta P/L)/(\mu u)$ and $\rho_f u/\mu$

Theoretical Simulation

Heat transfer in a porous channel involves a complex thermal transport mechanism between the air and surface of solid matrix. It is difficult to find the exact solutions for the flow and temperature fields. The transient single-blow technique utilized in the present study offers a hot fluid to heat up the porous medium. The physical configuration considered is a rectangular channel filled with the aluminum foam. High temperature airflow passes through and transports energy to the porous medium. The heat transfer characteristic of the porous medium can be evaluated by the transient response of the outlet air temperature, and double rechecked by the wall temperature distribution. To establish a mathematical model, the following assumptions and simplifications are employed.

1 The inlet fluid temperature is uniform. Temperature variations of the solid and fluid in the porous channel depend only on the position along the flow direction and time; therefore, it is a one-dimensional transient problem.
2 The medium is isotropic and has a uniform porosity.
3 The fluid flow is steady and incompressible; its thermal physical properties are constant.
4 There is no local thermal equilibrium between air and solid.
5 The fluid velocity in the porous channel is uniform.

The governing equations are developed by application of the local volume-average technique. This averaging process may obscure local pore phenomena that contribute to the global transport. Energy equations for the solid and fluid phases are as follows:

Table 1 Physical properties of the aluminum foam

Porosity, ε	0.70	0.80	0.95
Average Ligament Diameter, L_d (mm)	0.36	0.36	0.36
Thermal Conductivity, k_s^* (W/m-K)	65.4	43.6	10.9
Mean Cell Size, d (mm)	1.84	1.92	2.03
Permeability, $K \times 10^8$ (m^2)	0.88	2	7.5
Inertial Coefficient, F	0.11	0.068	0.065

Table 2 Coefficients under various flow parameters

ε	Re	ζ_1	ζ_2
0.7	1900	8.2	4.0
	2800	8.8	4.7
	3800	8.1	3.2
	6100	8.8	2.1
	7800	9.5	1.8
0.8	1900	4.7	0.1
	2800	6.0	0.8
	3800	6.5	0.1
	6100	7.7	0.1
	7800	7.6	0.1
0.9	1900	11.1	0.2
	2800	13.9	1.6
	3800	12.1	1.3
	6100	18.2	0.5
	7800	16.0	1.6

$$(1-\varepsilon)(1+\zeta_1)(\rho c_p)_s\frac{\partial T_s}{\partial t}=h_v(T_f-T_s)+k_s^*\left(\frac{\partial^2 T_s}{\partial x^2}\right) \quad (2)$$

$$\varepsilon(\rho c_p)_f\left(\frac{\partial T_f}{\partial t}+\frac{U}{\varepsilon}\frac{\partial T_f}{\partial x}\right)=h_v(T_s-T_f)+(k_f^*+k_t^*)\left(\frac{\partial^2 T_f}{\partial x^2}\right) \quad (3)$$

In Eq. (2) ζ_1 is a constant to modify the time delay due to heat capacity and heat loss of the copper plate on the porous medium. k_f^* and k_s^* are the equivalent conductivity of the solid and fluid phases, respectively, and are represented as εk_f and $(1-\varepsilon)k_s$. Moreover, k_t^* is the transverse thermal dispersion conductivity due the fluctuating tortuous air motion in the solid matrix. According to the simple model reported by Hunt and Tien [11], the dispersion conductivity is expressed as $k_t^*=0.025(\rho c_p)_f\sqrt{K}U$.

The appropriate initial and boundary conditions are

$$T_s(0,x)=T_f(0,x)=T_r \quad (4)$$

$$(1-\varepsilon)k_s\frac{\partial T_s}{\partial x}(t,0)=(1+\zeta_2)h_vL[T_i(t)-T_s(t,0)] \quad (5)$$

$$\frac{\partial T_s}{\partial x}(t,L)=0 \quad (6)$$

$$T_f(t,0)=T_i(t) \quad (7)$$

$$\frac{\partial T_f}{\partial x}(t,L)=0. \quad (8)$$

ζ_2 is another constant to modify the inlet boundary condition due to the heat transfer enhancement by the random structure of the porous medium. These weighting factors could be determined by trial and error via comparing the measured and predicted wall temperature distributions. Table 2 summarizes the values of ζ_1 and ζ_2 selected for different flow and parameters in the present study. T_i is the inlet air temperature and is determined from the measurement. By introducing the following variables:

$$\theta=\frac{T-T_r}{T_{\text{final}}-T_r};\quad X=\frac{x}{L};\quad \tau=\frac{t}{(L/U)};$$

$$C_1=\frac{(\rho c_p)_f}{(\rho c_p)_s(1+\zeta_1)};\quad C_2=\frac{k_s(\rho c_p)_f}{k_f(\rho c_p)_s(1+\zeta_1)};$$

$$\text{St}=\frac{h_vL}{(\rho c_p)_fU};\quad \text{Re}=\frac{\rho_fUL}{\mu};\quad \text{Pr}=\frac{\mu(c_p)_f}{k_f};$$

$$\text{Pr}^*=\frac{\mu(c_p)_f}{(k_f^*+k_t^*)};\quad \text{Bi}=\frac{h_vL^2}{k_s},$$

the governing equations can be nondimensionalized as:

$$\frac{\partial\theta_s}{\partial\tau}=\frac{C_1\text{St}}{1-\varepsilon}(\theta_f-\theta_s)+\frac{C_2}{\text{Pr Re}}\frac{\partial^2\theta_s}{\partial X^2} \quad (9)$$

$$\frac{\partial\theta_f}{\partial\tau}+\frac{1}{\varepsilon}\frac{\partial\theta_f}{\partial X}=\frac{\text{St}}{\varepsilon}(\theta_s-\theta_f)+\frac{1}{\varepsilon\text{Pr}^*\text{ Re}}\frac{\partial^2\theta_f}{\partial X^2}. \quad (10)$$

The dimensionless forms of the initial and boundary conditions are as follows:

$$\theta_s(0,X)=\theta_f(0,X)=0 \quad (11)$$

$$\frac{\partial\theta_s}{\partial X}(\tau,0)+\frac{(1+\zeta_2)\text{Bi}}{1-\varepsilon}[\theta_i-\theta_s(\tau,0)]=0 \quad (12)$$

$$\frac{\partial\theta_s}{\partial X}(\tau,1)=0 \quad (13)$$

$$\theta_f(\tau,0)=\theta_i \quad (14)$$

$$\frac{\partial\theta_f}{\partial X}(\tau,1)=0. \quad (15)$$

Using a guessed value of volumetric heat transfer coefficient (h_v) together with the prescribed values of geometric properties, physical properties, measured inlet air temperatures, a volumetric flow rate, and proper choices of empirical constants of ζ_1 and ζ_2, the solid and fluid phase temperatures, i.e., θ_s and θ_f, can be solved from Eqs. (9) and (10). Then, the value of h_v is modified until the accuracy between predicted and measured exit air temperatures is satisfactory (typically with deviation less than 1.0×10^{-3}). The flowchart of the transient single-blow technique is showed in Fig. 5.

The methodology used to solve the above equations associated with the boundary and initial conditions is based on the control volume, finite-difference technique [21]. The transient finite-difference form of the energy equations is solved explicitly by a line-by-line iterative method. Stepping forward in time and retaining a converged solution at each time step handle the time dependence. The sensitivity studies of node number and time increment are performed to check the stability and accuracy of the numerical scheme. Five sets of node numbers, i.e., 40, 60, 100, 150, and 200, are tested to ensure that the results of the present study are grid independent. A comparison of θ_f between 100 nodes and 150 nodes reveals accuracy up to three significant figures, suggesting that 100 nodes ($\Delta X=0.01$) are sufficient to obtain grid independent results. In addition, the effect of time step on the results is examined by testing several time steps of $\Delta\tau=0.05$, 0.1, 0.2, and 0.5. The results indicate that there is no significant difference be-

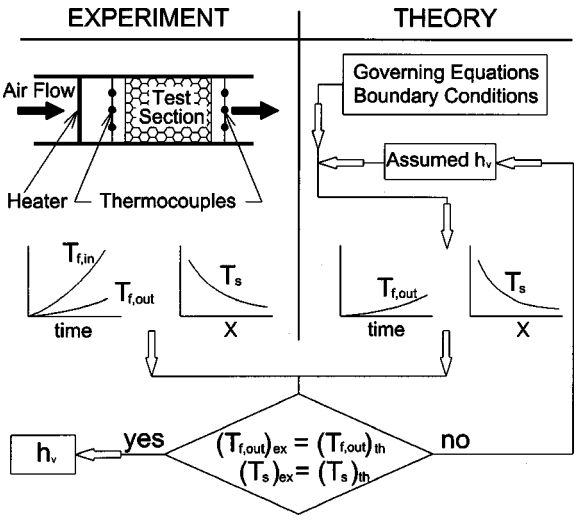

Fig. 5 Flow chart of the transient single-blow technique

tween the results using time increments of 0.05 and 0.1. Hence, the entire calculations are carried out with $\Delta X=0.01$ and $\Delta\tau=0.05$.

Data Analysis and Uncertainty

Friction Factors. The friction factor of the present foam channel is calculated from the pressure drop across the test channel and the bulk velocity of the air and expressed as

$$C_f=-2\Delta P/(\rho_f\cdot U^2). \tag{16}$$

Note that based on the heating level of this study, it is experimentally determined that the friction factor with heating is only about 2 percent higher than that without heating. Therefore, for time saving, the friction factor is based on the isothermal conditions without the tedious heating process. The individual uncertainties for ΔP and U are 5.5 percent and 3.0 percent, respectively. The maximum uncertainty of C_f is estimated to be less than 7.3 percent for Reynolds number greater than 1900 by the uncertainty estimation method of Kline and McClintock [22].

Interstitial Heat Transfer Coefficient. The errors of heat transfer coefficient are produced mainly due to the deviation of temperature measurement and the root-mean-square of the difference between the values of experiment and computation. The uncertainty in temperature measurement is about 3.3 percent. The maximum uncertainty in the root-mean-square of the temperature difference is less 14.0 percent. The combination of root-sum-square is employed to calculate the overall uncertainty of the volumetric heat transfer coefficient. As a result, the overall uncertainty of h_v is 14.0 percent.

Results and Discussion

Friction Factor. The effect of the Reynolds number (Re) on the friction factor (C_f) for the flow across the channel inserted with the aluminum foam is shown in Fig. 6. Three aluminum foams of different porosities are tested, i.e., $\varepsilon=0.7$, 0.8, and 0.95. The data points are the exact experiment and the lines passing through these points are least-square results. It is seen that the friction factor decreases with increasing Reynolds number for all porosities investigated. The aluminum foam of higher porosity has a lower friction factor due to the less channel blockage together with a smaller surface drag. To qualitatively understand the drag of flow across different-porosity foams, a comparison of the flow patterns around different-porosity aluminum foams is shown in Fig. 7, which is measured by a smoke-wire technique [23]. The

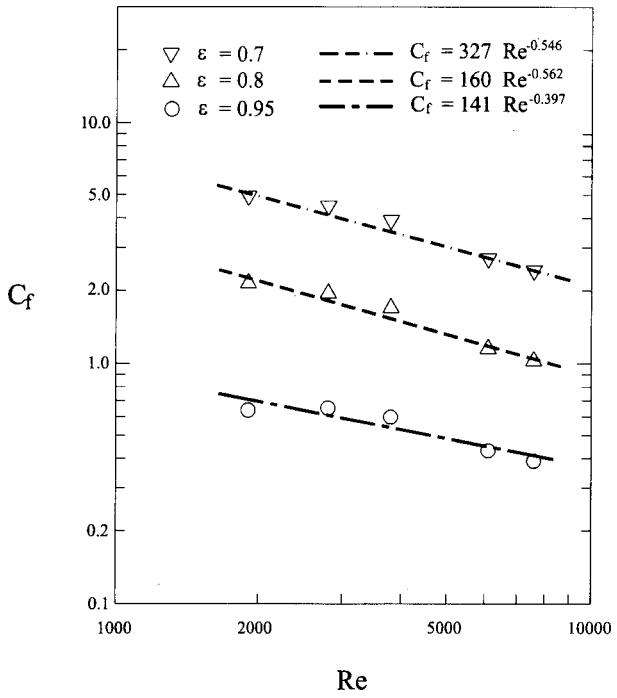

Fig. 6 Friction factor in the aluminum foam channel

smoke wire is placed vertically along the duct center on the axial station ahead of aluminum foam. Instead of the thick sample (60 mm) employed in the heat transfer experiment, a slender aluminum foam (10 mm) is used herein for easier permeable. The airflow is from left to right. Figure 6(*a*) shows the flow over a smooth plane channel without porous medium and serves as a reference. Figures 6(*b*) and (*c*) are the results of $\varepsilon=0.7$ and 0.95, respectively. For $\varepsilon=0.7$, it is seen that some smokes stay in front of the aluminum foam, meaning that the flow cannot easily penetrate the aluminum foam due to a large blockage. In contrast, the flow for $\varepsilon=0.95$ seems to pass smoothly through the aluminum foam. The above flow-structure comparison has reasonably illustrated the effect of porosity on the friction factor showing in Fig. 6. Another interesting observation by comparing Figs. 7(*b*) and (*c*) is that the flow structures behind the aluminum foam are different. A large amount of eddies is clearly observed behind the rear face of the aluminum foam for $\varepsilon=0.7$ and, however, the flow after the

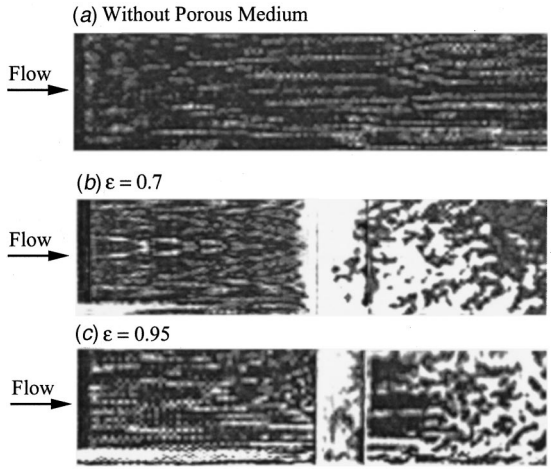

Fig. 7 Comparison of flow structure around the aluminum foams of different porosities

Table 3 Coefficients of friction factor correlations of the porous channel

ε	$C_f = a_1 \mathrm{Re}^{a_2}$			
	a_1	a_2	Deviations	Eq.
0.95	141	-0.397	4.2 %	(17-1)
0.80	160	-0.562	5.5 %	(17-2)
0.70	327	-0.546	3.4 %	(17-3)

high-porosity aluminum foam ($\varepsilon=0.95$) is relatively laminar. Therefore, we may extrapolate this fact to that the flow inside the foam material of $\varepsilon=0.7$ would be more turbulent than that of $\varepsilon=0.95$, which largely affects the heat transfer characteristics inside the porous medium and will be shown later. The data presented in Fig. 5 could be correlated as the following equations:

$$C_f = a_1 \mathrm{Re}^{a_2}, \tag{17}$$

where the coefficients a_1 and a_2 for various foam porosities are listed in Table 3. The maximum deviation between the equation above and the experimental data is only 5.5 percent.

Heat Transfer Characteristics. Typical examples of the histories of inlet and outlet air temperatures during the present experiment for the single-blow technique are shown in Fig. 8 under various ε and Re. The solid circles in each figure are the measured inlet air temperatures, while the solid lines passing through these circles are the curve-fitted results (by the 5th order polynomials) that serve as the inlet condition to the present theoretic model equations. The solid triangles are the measured outlet air temperatures, while the dashed lines are the calculating results from the present theoretic model using the volumetric heat transfer coefficient listed in each figure. In general, the theoretically simulated outlet air temperatures are in good agreement with the experimental ones, indicating the appropriate volumetric heat transfer coefficient selected in each case. It should be noted that in all tests the heat dissipated from the electric heater is controlled to be constant by adjusting the current through the resistance of the heater. Although the range of abscissa (time) displayed in each figure may be different, the histories of the inlet air temperatures under the same mass flow rate (Re) are essentially the same. As shown in Figs. 8(*a*)–(*c*) for Re=1900, with the same history of the inlet air temperature, the smaller the foam porosity is, the slower is the incremental rate of the outlet air temperature. For example, at time step of $\tau=100$, the outlet air temperatures are $\theta_o=0.027$, 0.016, and 0.008, respectively, for $\varepsilon=0.95$, 0.08, and 0.7. This means that the aluminum foam of a small porosity has a large heat capacity that reduces the incremental rate of the outlet air temperature. There is a significant heat exchange between the air and solid matrix for the small-porosity aluminum foam. Attention is now turned to the effect of the Reynolds number showed in Fig. 8(*c*), in which the difference between the inlet and outlet air temperatures is roughly the same for Re=1900 and 6100. It has clearly showed that the higher Reynolds number (Re=6100) requires more time to reach the same temperature difference than the lower Reynolds number (Re=1900). This is because a higher Reynolds number has a higher heat transfer coefficient inside the porous medium that removes more heat from the air to the porous medium, and thus requires more time to increase the difference of the inlet and outlet air temperatures. Figure 9 presents the temperature distribution of the solid material (the aluminum foam) along the streamwise direction. It is found that the theoretic curves agree fairly well with the experimental data. This confirms again the correctness of the predicted heat transfer coefficient.

There is a broad variety of constraints that may be utilized in evaluating the thermal performance of the channel with porous medium [24,25]. In this paper, thermal performance comparisons among the three aluminum-foam channels are made for two sets of constraints that are widely employed, namely, the same through flow rate and the same pumping power. The comparison of heat transfer coefficients for the same airflow rate constraint is made in Fig. 10, which shows the Nusselt number as a function of the Reynolds number for three different aluminum foams. The corresponding volumetric heat transfer coefficient (h_v) is also plotted on the right-hand side of ordinate of this figure. As shown in Fig. 10, the Nusselt number increases with increasing the Reynolds number. For a fixed Reynolds number, the heat transfer coefficient increases with decreasing the porosity due to an increase in local fluid velocity and, partly, the enhancement of turbulent transport inside the foam (Fig. 7). Attention is now turned to the same pumping power constraint. The pumping power required to drive a fixed volumetric flow rate ($\dot{V}$) in the foam duct can be written as $\Delta P \cdot \dot{V}$. As shown in Fig. 6, the pressure drop is higher for the foam channel of a lower porosity. Therefore, the use of low-porosity foam instead of high-porosity foam should reduce the through flow rate to keep the fluid pumping power constant in a porous channel, which lead to a reduction in the heat transfer coefficient. To implement this case, Fig. 11 shows the Nusselt number as a function of the nondimensional pumping power $C_f \cdot \mathrm{Re}^3$. From this figure, it is seen that the volumetric heat transfer coefficient increases with increasing the nondimensional pumping power for all aluminum-foam channels. Further inspection of this figure reveals that the aluminum-foam channel of $\varepsilon=0.8$ has the best thermal performance among the three aluminum-foam channels. This is because the aluminum-foam channel for $\varepsilon=0.8$ is accompanied by a moderate pressure-drop (Fig. 6) and produces a sufficiently high heat transfer, and thus yields the highest thermal performance.

Comparison With Previous Results. A comparison of the present and previous interstitial heat transfer results is made in Fig. 12. The volumetric heat transfer coefficient is expressed in dimensionless form in terms of the pore Nusselt number (Nu_d), which is plotted against the pore Reynolds number (Re_d) in Fig. 12. In general, the mean pore diameter appears to be a reasonable choice for the characteristic length in defining the Nusselt number and Reynolds number in the foam materials [12]. In this figure, the present data are presented by open symbols, and the straight lines passing through these symbols are least-square fits, and can be expressed as

$$\mathrm{Nu}_d = b_1 \mathrm{Re}_d^{b_2}. \tag{18}$$

The coefficients b_1 and b_2 for various porosities and the maximum deviation between the equation above and the experimental data are listed in Table 4. Note that the data of pore Nusselt numbers for $\varepsilon=0.7$ and 0.8 gather closely, and can be further correlated as a single equation with a reasonable deviation. As for the previous interstitial heat transfer results, the data band represents the results obtained from ceramic foams of $0.83 \leqq \varepsilon \leqq 0.87$ by using a single-blow technique [12], which consists of three correlations for various pore diameters $d=0.76$, 0.94 and 1.52 mm. The Reynolds-number dependence (Re_d^n) for these correlations ranges from $n=0.7$ to 0.96. In addition, The dashed line is the volumetric heat transfer coefficient inside a ceramic-aluminum foam for $\varepsilon=0.87$, which is obtained by comparing the measured and predicted Nusselt number on the heated wall of a porous channel [13]. A light irregularity of the curve at $\mathrm{Re}_d=20$ is because of the inconsistency of results obtained for $d=2.0$ and 4.2 mm at the same Reynolds number. Furthermore, the centerline is

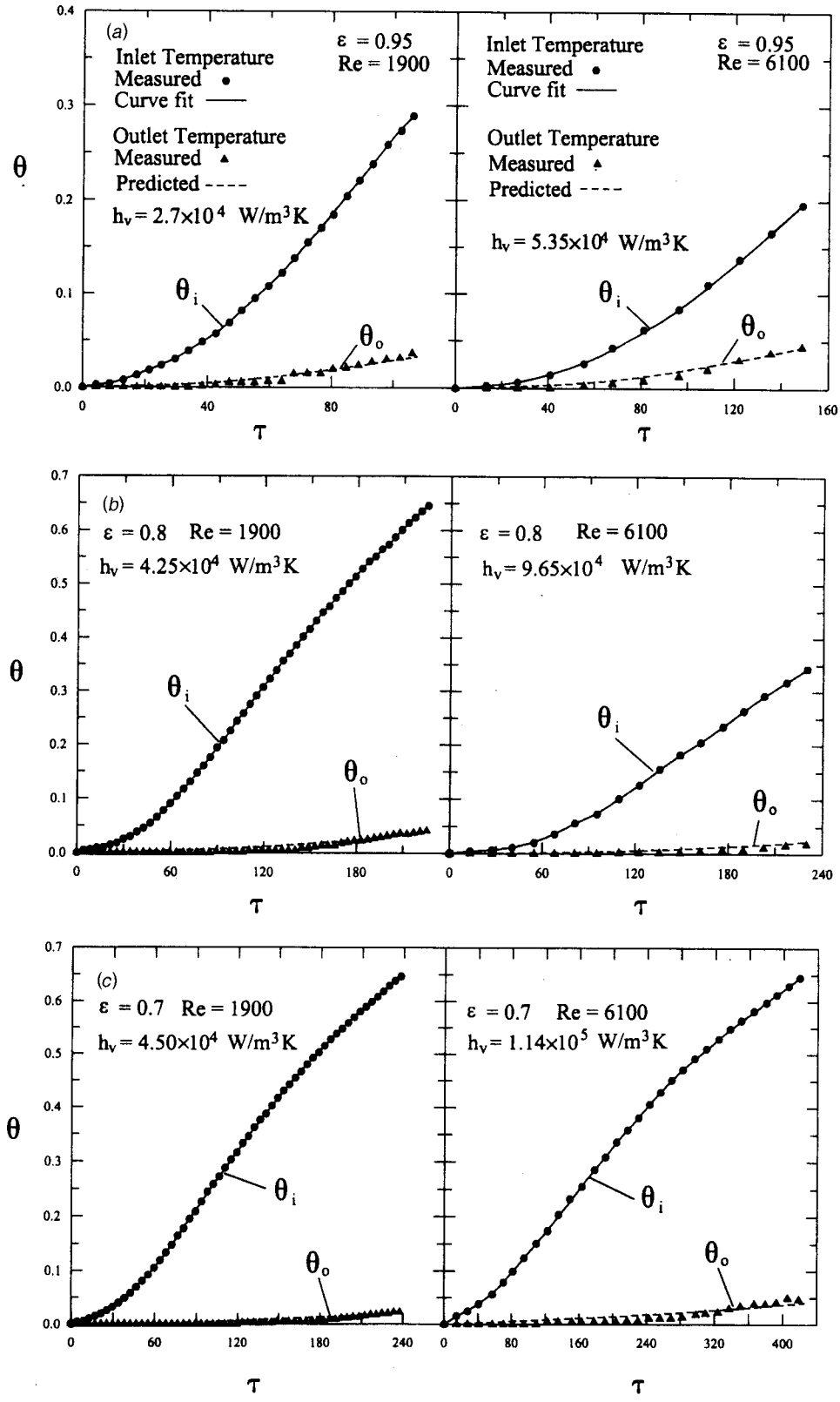

Fig. 8 Histories of the inlet and outlet air temperatures

an empirical correlation compiled from transient and steady state data of packed spherical particles. This correlation is unique and covers a broad range of porosity and Reynolds number [25].

It is seen from this figure that the Reynolds-number dependence (Re_d^n) of the present data ($n=0.6-0.83$) is largely similar to that of Younis and Viskanta [12]. Quantitatively, the present data for $\varepsilon=0.7$ and 0.8 can extrapolate well to those in low pore Reynolds numbers obtained by Ichimiya [13] but are slightly lower than those of Younis and Viskanta [12]. This discrepancy in heat transfer coefficient may be attributed to the different size (in stream-

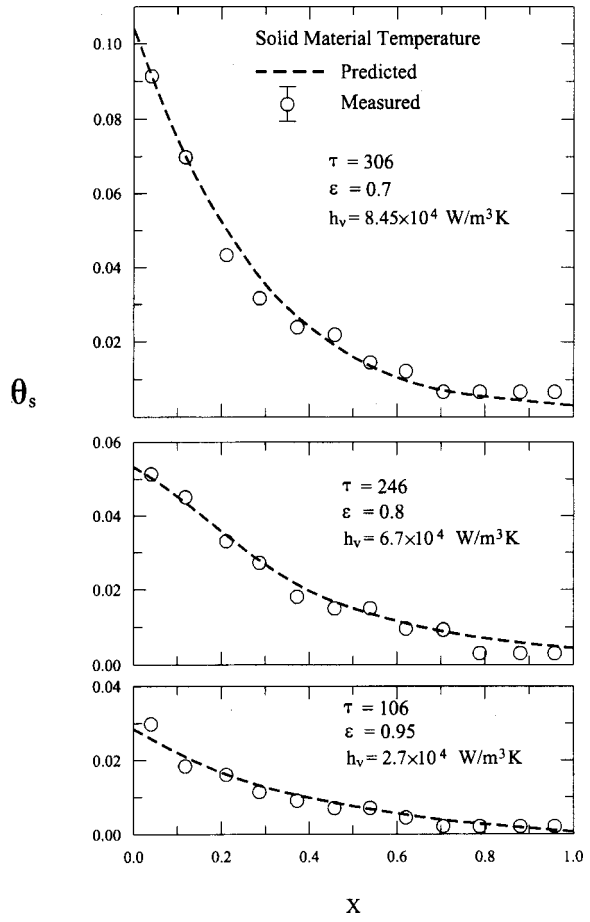

Fig. 9 Solid material temperature distributions along the streamwise direction

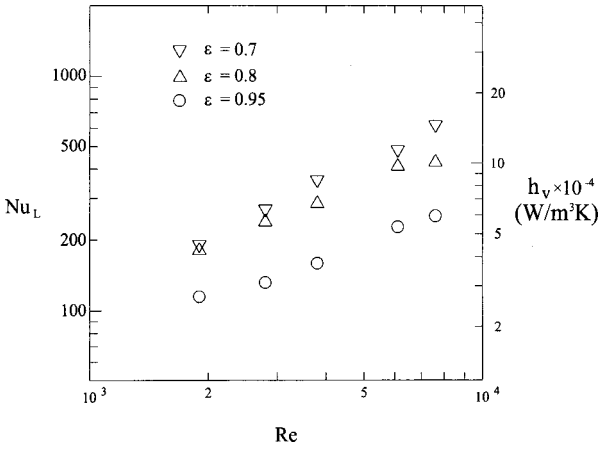

Fig. 10 Volumetric heat transfer coefficient as a function of the Reynolds number

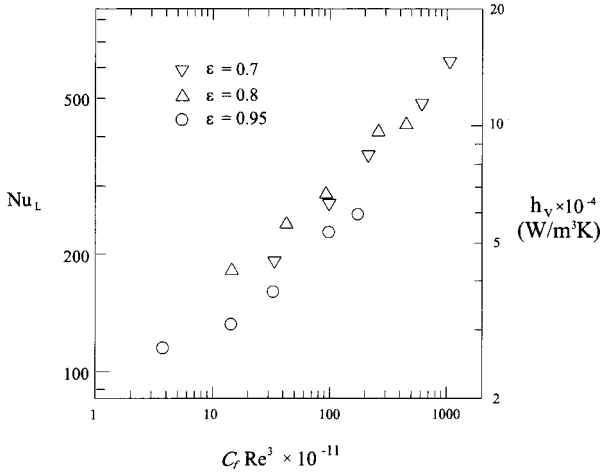

Fig. 11 Volumetric heat transfer coefficient as a function of the nondimensional pumping power

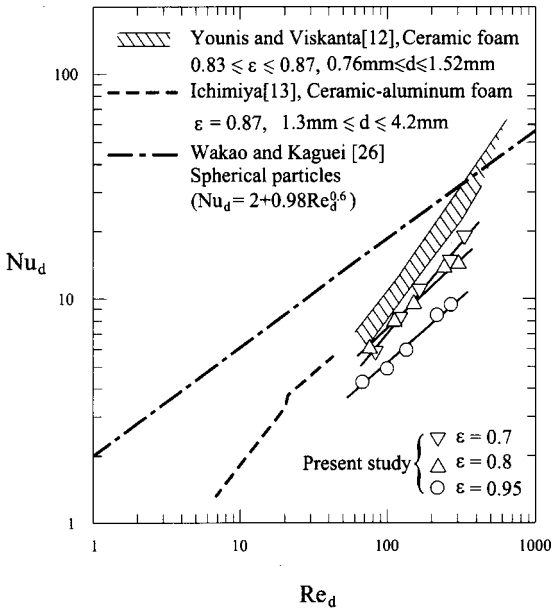

Fig. 12 Comparison of the pore Nusselt number between the present and previous works

wise direction) of foam used between Younis and Viskanta [12] and the present work. In Younis and Viskanta [12], a shorter ceramic porous medium (12–14 mm) than the present one (60 mm) will cause a more significant entrance effect that increases the length-mean heat transfer coefficient. Nevertheless, the above comparison between the present data with those by Younis and Viskanta [12] and Ichimiya [13] is satisfactorily in agreement. It is further seen that the correlation proposed by Wakas and Kaguei [26] seems to be invalid for the data presented, especially in the

Table 4 Coefficients of heat transfer correlations

ε	$Nu_d = b_1 Re_d^{b_2}$			
	b_1	b_2	Deviation	Eq.
0.95	0.3248	0.601	1.5 %	(18-1)
0.80	0.3760	0.644	1.0 %	(18-2)
0.70	0.1569	0.825	0.6 %	(18-3)
0.70 + 0.80	0.2396	0.737	2.4 %	(18-4)

low Reynolds number range. We attribute this to the fact that the porous structures of the present foam material are different from those of the packed beds, which has a large influence on the convective heat transfer through affecting the shape of the flow passages as well as the surface area per unit volume.

Conclusions

Interstitial heat transfer and friction characteristics for flow across a channel inserted with aluminum foams have been studied experimentally. The combined effects of foam porosity ($\varepsilon=0.70$, 0.80, and 0.95) and flow Reynolds number ($1900 \leqq Re \leqq 7900$) are examined in detail. A transient single-blow technique has been applied to the determination of the interstitial heat transfer coefficient of the aluminum foam. The results of numerical simulation coincide with those of experimental measurement by using the thermal non-equilibrium energy equations together with appropriate thermal boundary conditions and proper choices of the empirical constants ζ_1 and ζ_2. Main findings based on the data presented are as follows.

1 At a fixed Reynolds number, as the porosity of the aluminum foam increases from $\varepsilon=0.70$ to 0.95, the friction factor decreases due to the decrease in the channel blockage. The friction factor decreases with an increase of Reynolds number for all porosities investigated.

2 Under the same through flow rate and history of the inlet air temperature, the small-porosity aluminum foam has a slow incremental rate of the outlet air temperatures, meaning that the aluminum foam of a small porosity has a large heat capacity.

3 At a fixed Reynolds number, the volumetric heat transfer coefficient inside the aluminum foam increases with decreasing the porosity due to the increase in local fluid velocity and the enhancement of turbulence transport. In addition, the volumetric heat transfer coefficient increases with increasing the Reynolds number under a fixed value of foam porosity.

4 Among the three aluminum foams investigated, the foam channel of $\varepsilon=0.8$ appears the best thermal performance under constant pumping power constraint because it produces a satisfactorily high heat transfer and is accompanied by a moderate pressure drop.

5 Empirical correlations of pore Nusselt number for three aluminum foams under a specific length ($L=60$ mm) are developed in terms of pore Reynolds number for the first time, which can be helpful in the design of the related devices such as compact heat exchangers or thermal energy absorbers. Further efforts are required to conclude a unique correlation that covers a wide range of the flow and geometric parameters such as the porosity of foam metal, Reynolds number, etc.

Acknowledgments

This work was sponsored by the National Science Council of the Republic of China under contract No. NSC 85-2212-E-216-003.

Nomenclature

Bi = Biot number, $h_v L^2/k_s$
C_1 = constant $C_1=(\rho c_p)_f/[(\rho c_p)_s(1+\zeta_1)]$;
C_2 = constant $C_2=k_s(\rho c_p)_f/[k_f(\rho c_p)_s(1+\zeta_1)]$
C_f = friction factor, Eq. 16
c_p = isobaric specific heat, kJ/kg-K
d = mean pore diameter, m
F = inertia coefficient constant
h_v = volumetric heat transfer coefficient, W/m^3-K
K = permeability, m^2
k = thermal conductivity, W/m-K
L = test section length, m
Nu = Nusselt number based on porous matrix length, $h_v L^2/k_f$
Nu_d = pore Nusselt number, $h_v d^2/k_f$
P = pressure, N/m^2
Pr = Prandtl number $(\mu c_p)_f/k_f$
Re = Reynolds number, $\rho_f UL/\mu$
Re_d = pore Reynolds number, $\rho_f Ud/(\varepsilon\mu)$
St = Stanton number, $h_v L/[(\rho c_p)_f U]$
T = temperature, K
T_{final} = steady state fluid temperature at test section inlet, K
T_r = reference (room) temperature, K
t = time, s
U = mean velocity in the rectangular channel, m/s
u = pore velocity, m/s
X = dimensionless axial length, x/L
x = axial length, m
ε = porosity
θ = dimensionless temperature $(T-T_r)/(T_{final}-T_r)$
μ = viscosity, kg/m-s
ρ = density, kg/m^3
τ = dimensionless time, $U\cdot t/L$
ζ_1, ζ_2 = constants

Subscripts

d = pore
f = fluid
i = inlet value
s = solid

Superscripts

$*$ = equivalent value

References

[1] Koh, J. C. Y., and Stevens, R. L., 1975, "Enhancement of Cooling Effectiveness by Porous Medium in Coolant Passages," ASME J. Heat Transfer, **96**, pp. 309–311.
[2] Cheng, P., 1982, "Mixed Convection About a Horizontal Cylinder and a Sphere in Fluid Saturated Porous Medium," Int. J. Heat Mass Transf., **28**, pp. 1245–1247.
[3] Jones, D. P., and Krier, H., 1983, "Gas Flow Resistance Measurements Through Packed Beds at High Reynolds Number," ASME J. Fluids Eng., **105**, pp. 168–173.
[4] Cheng, P., and Zhu, H., 1987, "Effects of Radial Thermal Dispersion on Fully Developed Forced Convection in Cylindrical Packed Bed," Int. J. Heat Mass Transf., **30**, pp. 2373–2383.
[5] Renken, K. J., and Poulikakos, D., 1988, "Experimental and Analysis of Forced Convection Heat Transport in Packed Bed of Spheres," Int. J. Heat Mass Transf., **31**, pp. 1399–1408.
[6] Vafai, K., and Sozen, M., 1990, "Analysis of Energy and Momentum Transport for Fluid Flow through a Porous Bed," ASME J. Heat Transfer, **112**, pp. 690–699.
[7] Amiri, A., and Vafai, K., 1994, "Analysis of Dispersion Effect and Nonthermal Equilibrium, Non-Darcy Variable Porosity Incompressible Flow Through Porous Media," Int. J. Heat Mass Transf., **37**, pp. 939–954.
[8] Hwang, G. J., and Chao, C. H., 1994, "Heat Transfer Measurement and Analysis for Sintered Porous Channel," ASME J. Heat Transfer, **116**, pp. 456–464.
[9] Varahasamy, M., and Fand, R. M., 1996, "Heat Transfer by Forced Convection in Pipes Packed with Porous Media Whose Matrices Are Composed of Spheres," Int. J. Heat Mass Transf., **39**, pp. 3931–3947.
[10] Peterson, G. P., and Chang, S. W., 1998, "Two-Phase Heat Dissipation Utilizing Porous-Channels of High Conductivity Material," ASME J. Heat Transfer, **120**, pp. 243–252.
[11] Hunt, M. L., and Tien, C. L., 1988, "Effects of Thermal Dispersion on Forced Convection in Fibrous Media," Int. J. Heat Mass Transf., **31**, pp. 301–309.
[12] Younis, L. B., and Viskanta, R., 1993, "Experimental Determination of the Volumetric Heat Transfer Coefficient Between Stream of Air and Ceramic Foam," Int. J. Heat Mass Transf., **36**, pp. 1425–1434.
[13] Ichimiya, K., 1999, "A New Method for Evaluation of Heat Transfer Between Solid Material and Fluid in a Porous Medium," ASME J. Heat Transfer, **121**, pp. 978–983.
[14] Calmidi, V. V., and Mahajan, R. L., 2000, "Forced Convection in High Porosity Metal Foams," ASME J. Heat Transfer, **122**, pp. 557–565.
[15] Genetti, A. J., 1999, "Engineering and Design—Groundwater Hydrology," *USACE*, Washington DC.
[16] Hadim, A., 1994, "Forced Convection in a Porous Channel with Localized Heat Sources," ASME J. Heat Transfer, **116**, pp. 465–472.
[17] Golombok, M., Jariwala, H., and Shirvill, L. C., 1990, "Gas-Solid Heat Exchange in a Fibrous Metallic Material Measured by a Heat Regenerator Technique," Int. J. Heat Mass Transf., **33**, pp. 243–252.
[18] Gamson, B. W., Thodos, G., and Hougen, O. A., 1943, "Heat, Mass and

Momentum Transfer in the Flow of Gases Through Granular Solids,'' AIChE J., **39**, pp. 1–35.
[19] Antohe, B. V., Lage, J. L., Price, D. C., and Weber, R. M., 1997, ''Experimental Determination of Permeability and Inertia Coefficients of Mechanically Compressed Aluminum Porous Matrices,'' ASME J. Fluids Eng., **119**, pp. 404–412.
[20] Lage, J. L., Antohe, B. V., and Nield, D. A., 1997, ''Two Type of Nonlinear Pressure-Drop Versus Flow Rate Relation Observed For Saturated Porous Media,'' ASME J. Fluids Eng., **119**, pp. 700–706.
[21] Patankar, S. V., 1980, *Numerical Heat Transfer and Fluid Flow*, Hemisphere, New York.
[22] Kline, S. J., and McClintock, F. A., 1953, ''Describing the Uncertainties in Single-Sample Experiments,'' Mech. Eng. (Am. Soc. Mech. Eng.), pp. 3–8.
[23] Hwang, J. J., 1998, ''Heat Transfer-Friction Characteristic Comparison in Rectangular Ducts With Slit and Solid Ribs Mounted on One Wall,'' ASME J. Heat Transfer, **120**, pp. 709–716.
[24] Hwang, J. J., 1997, ''Turbulent Heat Transfer and Fluid Flow in a Porous-Baffled Channel,'' J. Thermophys. Heat Transfer, **11**, pp. 429–436.
[25] Hwang, J. J., and Chao, C. H., 2000, ''Passive Control of Convective Transport Phenomena Utilizing an Attached-Detached Rib-Array,'' J. Thermophys. Heat Transfer, **14**, pp. 579–583.
[26] Wakao, N., and Kaguei, S., 1993, *Heat and Mass Transfer in Packed Beds*, Gordon and Breach Science.

Jean-François Mercier[1]

Catherine Weisman[2]
e-mail: weisman@limsi.fr

Mouaouia Firdaouss
e-mail: firdaous@limsi.fr

Patrick Le Quéré
e-mail: plq@limsi.fr

LIMSI-CNRS, BP 133,
F-91403 Orsay Cedex,
France

Heat Transfer Associated to Natural Convection Flow in a Partly Porous Cavity

The object of this study is the heat transfer associated to a buoyancy-induced flow developing in a rectangular cavity, partly filled with porous medium, with given heat flux from the sides. Numerical experiments show the existence of a quasi parallel solution away from the top and bottom end walls, characterized by a linear vertical temperature profile. Analytical expressions are derived for the velocity and temperature which, combined with an energy balance, enable us to relate the stratification to the other governing parameters. Influence of the porous layer's permeability and width, and of the Rayleigh number on the flow structure and heat transfer is thoroughly investigated, and summarized in simple relationships. [DOI: 10.1115/1.1418372]

Keywords: Analytical, Heat Transfer, Natural Convection, Porous Media, Stratified

1 Introduction

Studies of flows developing in a system containing simultaneously a fluid and a porous layer are of both mathematical and practical interest. Such systems are important for instance in cooling or ventilation problems, and juxtaposition of porous and fluid layers is also involved in thermal insulation of buildings. Many numerical approaches have been applied to the study of these systems. Simulations were performed on flows developing in a rectangular cavity, either exclusively porous (Lauriat and Prasad [1]) or separated into a fluid part and a porous part. These last studies were lead for isothermal flows (Vafai and Kim [2]), natural convection flows (Beckerman et al. [3], Le Breton et al. [4]) and for thermal and solutal convection flows (Gobin et al. [5]). There is a thorough and up to date review of such studies in Nield and Bejan [6].

In this paper we focus on the buoyancy-induced flows created in a rectangular cavity partly filled with a porous layer, when natural convection is induced by imposing a given horizontal heat flux from the sides. We have not found any account of an experimental setup to ensure cooling under constant heat flux. However, although there are experimental setups with either constant temperature or constant heat flux on the hot side and constant temperature on the cold side, other boundary conditions may be used for modeling: Nield and Bejan [6] specified that in the field of thermal insulation engineering, a model including constant heat flux boundary conditions is more appropriate to describe the side heating of a porous layer. Moreover, in this paper we will perform a numerical-analytical study and we use these boundary conditions because they clearly lead to a quasi-parallel solution.

It is difficult to characterize the flow developing in a composite porous-fluid layer using a numerical approach because of the large number of independent parameters: there are physical parameters like the porous layer permeability and the thermal conductivity and heat capacity of both the porous medium and the fluid, geometrical parameters like the width of the porous layer or the aspect ratio of the cavity, and last the heat power injected in the cavity. Because numerical simulations are time consuming, exploration of the flow characteristics when all these parameters vary within a physical range is very difficult. Our purpose here is to use alternate means to direct numerical integration of Navier-Stokes and energy equations. This study is motivated by recent results obtained with numerical simulations of the two-dimensional flow produced in a cavity where the heat flux is imposed on the vertical boundaries (Weisman et al. [7]). The horizontal boundaries are maintained thermally insulated. Isothermal contour lines and streamlines are shown on Fig. 1.

The porous medium is adjacent to the heated wall and extends through a quarter of the cavity's width. It clearly appears that the two-dimensional flow becomes one-dimensional away from the horizontal boundaries, and that this approximation is valid on a large vertical extent. Also the temperature is found to vary linearly in the vertical direction. These flow properties allow us to seek an analytical form for the solution in the central part of the cavity.

The analytical form was found by solving the problem in a cavity of infinite vertical extent and finite width, partly filled with a porous layer (also of infinite vertical extent) adjacent to the hot wall. This calculation was analogous to the work previously done for a solely fluid cavity (Bergholz [8], Kimura and Bejan [9]) or a completely porous cavity (Trevisan and Bejan [10]). In all these studies, the analytical solution that was exhibited involves a stratification parameter γ, which in the case of a cavity of infinite vertical extent is a free parameter. But for a vertically bounded cavity, γ is a function of the characteristic parameters of the porous medium and of the Ra number. The value of γ appearing in the analytical solution can then be calculated by using an energy balance between conductive and convective heat transfer in the cavity. A similar method was first applied in the case of cavities with differentially heated walls, for a fluid cavity (Gill [11]) or a porous cavity (Weber [12]). Later the same method was used when the vertical walls are submitted to a heat flux, in the cases of fluid (Kimura and Bejan [9]) or porous (Trevisan and Bejan [10]) cavities.

After having presented the studied geometry, governing equations will be detailed and then the stationary analytical flow will be calculated. A full parameter study will be presented: the vertical velocity and temperature profiles will be shown and analyzed for a large range of the four independent parameters, the Rayleigh number, the Darcy number, the width of the porous medium *ep* and the vertical temperature stratification γ. Then, using the energy balance in the closed cavity to relate γ and *ep*, Ra and Da, thorough analysis of the hydrodynamic and thermal characteristics (and specifically Nusselt numbers) will be presented.

[1]Present address: Laboratoire de Simulation et de Modélisation des phénomènes de Propagation, Ensta, URA 853 du CNRS, Paris, France. E-mail: jmercier@ensta.fr

[2]Corresponding author.

Contributed by the Heat Transfer Division for publication in the JOURNAL OF HEAT TRANSFER. Manuscript received by the Heat Transfer Division September 26, 2000; revision received June 25, 2001. Associate Editor: H. H. Bau.

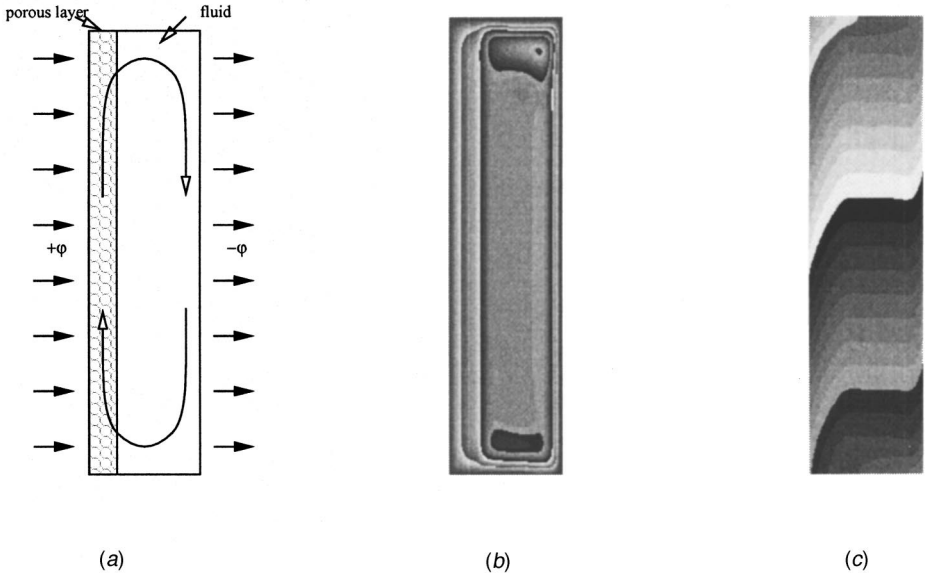

Fig. 1 Problem geometry (*a*) and steady flow in a cavity of aspect ratio 4, with heat flux imposed on the sides. A porous layer covers the heated wall and fills one quarter of the cavity. Ra=10^6, Da=10^{-4}: (*b*) streamlines, (*c*) isothermal lines.

2 Problem Geometry

We study the two-dimensional flow developing in a vertical rectangular cavity, as represented on Fig. 2. The cavity is of height H and of width L. The horizontal axis is noted x while the vertical axis is called z. The vertical wall located at $x=0$ is submitted to a horizontal heat flux density φ, constant and uniform. On the other vertical wall at $x=L$ is extracted the same heat flux density. The cavity is partly filled with a vertical porous layer of width d placed in contact of the heated vertical boundary. Before studying the heat transfer in the cavity, the first step consists in modelling the flow in the fluid and in the porous medium, which will be presented in the next paragraph.

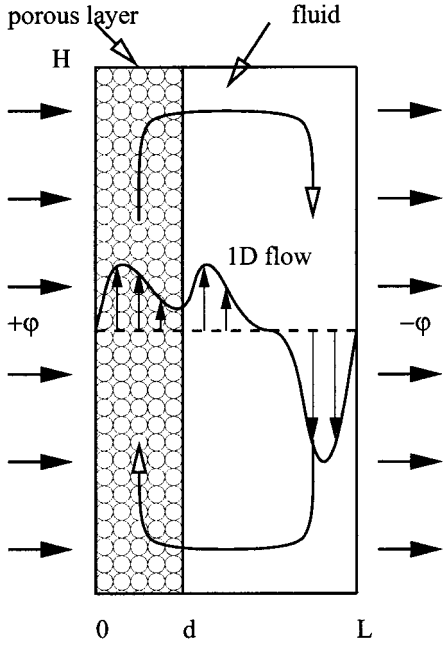

Fig. 2 Problem geometry and vertical flow $w_0(x)$ in the central part of the cavity

3 Generalized Navier-Stokes Equations in Partly Porous Cavities

3.1 Description of the Natural Convection Flow in a Partly Porous Medium. The flow in the cavity is induced by natural convection, and the fluid density ρ is assumed to vary linearly with respect to the temperature $\tilde{T}$, according to the law $\rho=\rho_c[1-\beta(\tilde{T}-T_c)]$. β is the thermal expansion coefficient, T_c and ρ_c are respectively the reference temperature and density. Outside the porous area the fluid is supposed to obey Navier-Stokes equations in the Boussinesq approximation.

In the porous medium the Navier-Stokes equations are modified using a Darcy-Brinkman formulation. The equations can be written in a unified form by using a parameter ϵ, equal to 1 in the porous medium, and equal to 0 in the fluid part.

$$\left(1-\epsilon+\frac{\epsilon}{\phi}\right)\frac{\partial\vec{U}}{\partial t}+(1-\epsilon)(\vec{U}.\vec{\nabla})\vec{U} = -\frac{1}{\rho_c}\vec{\nabla}P+\frac{\rho}{\rho_c}\vec{g}+\nu_{\text{eff}}\Delta\vec{U}-\epsilon\frac{\nu}{K}\vec{U} \tag{1}$$

$$\rho_c c_p\left(\frac{\partial}{\partial t}+\vec{U}.\vec{\nabla}\right)\tilde{T}=\lambda\Delta\tilde{T}, \tag{2}$$

$$\vec{\nabla}.\vec{U}=0. \tag{3}$$

In these equations, $\vec{U}$ is the fluid velocity and P is the pressure, K is the porous medium permeability, ϕ the porosity and ν is the fluid viscosity. The effective viscosity ν_{eff} takes into account the influence of the porous medium on the fluid flow and is assumed to be related to the fluid viscosity through the relation $\nu_{\text{eff}}=\nu/\phi$. The momentum Eq. (1), which makes use of ϕ, implicitly takes into account the distinction between Darcy velocity and intrinsic velocity (see Nield and Bejan [6] and Amiri and Vafai [13,14]). However, since the porosity only appears in the time-dependent term, the value of ϕ will have no influence on the steady-state solution. The Darcy term included in Eq. 1 induces a decrease of the fluid velocity due to the presence of the porous medium. In the

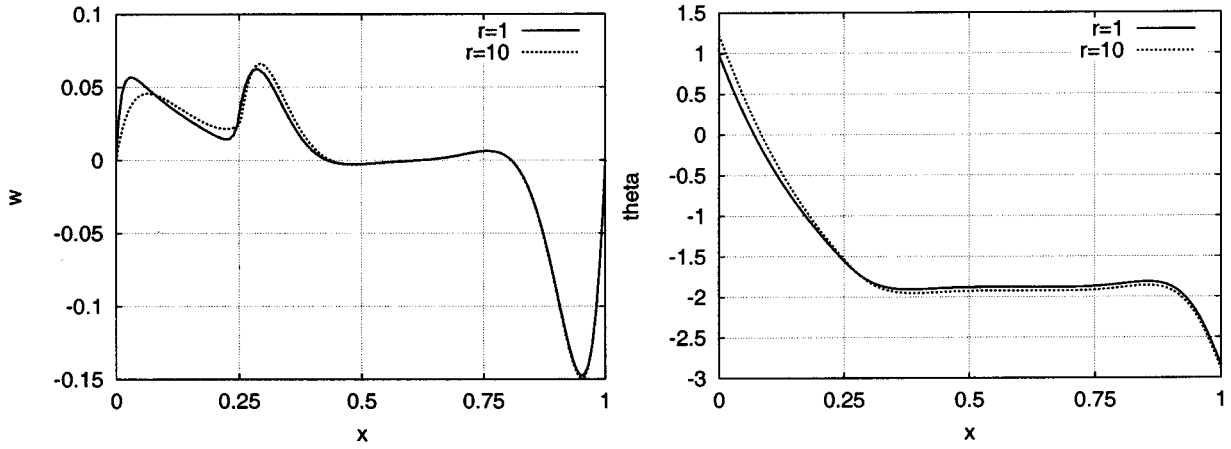

Fig. 3 Comparison of dimensionless vertical velocity profiles (left) and temperature profiles (right) at mid-height of the cavity for $r=1$ and $r=10$ for one given numerical setup, $A=4$, $\mathrm{Ra}=10^6$, $\mathrm{Da}=10^{-4}$, $ep=0.25$

porous medium only, the advective term $1/\phi^2 \vec{U}.\vec{\nabla}\vec{U}$ is excluded, which is consistent with the work of Beck [15]. Also in this equation, the Forchheimer term $c_f/K^{1/2}|\vec{U}|\vec{U}$, where c_f is a geometric function (Alazmi and Vafai [16]), is neglected, since all simulations are carried out for low values of the Reynolds number, typically $R_e \leqslant 1$. The Reynolds number can be calculated using the relation of the permeability (Cozeni-Karman formula) and of the geometric function c_f versus the porosity (Alazmi and Vafai [16]). This Darcy-Brinkman formulation is also used in Amahmid et al. [17] where low Reynolds number values are also found. Large values of the Reynolds number may be obtained for $\phi \to 1$. However, the Cozeni-Karman formula is not valid in this porosity limit. Moreover, there is some uncertainty about the validity of the Forchheimer law at large porosity (Nield and Bejan [6]). Therefore, this term will be omitted in the rest of this paper.

Givler and Altobelli [18] have estimated the ratio r of the effective viscosity to the fluid viscosity to be approximately 7.5 ± 3, for values of the Reynolds number comparable to ours. We have performed several numerical simulations with values of r ranging from 1 to 12. For a rather high ratio $r=10$, we observed small changes (see Fig. 3) in the flow in the porous part compared to the case of a ratio equal to 1, the maximum value of the stream function changing by 5.6 percent. The associated decrease of the vertical temperature stratification is small, of 0.4 percent. Also, for a given numerical setup, the vertical temperature stratification is found to vary almost linearly with r. The steady-state solutions obtained for $r=10$ are close to those obtained for $r=1$, i.e., $\nu_{\mathrm{eff}}=\nu$.

This ratio r should be varied in order to correctly describe several kinds of porous media, but based on these results, we will assume in the rest of this paper that $\nu_{\mathrm{eff}}=\nu$. Moreover since we cannot assess that our simulations would fit well with experimental data and because we do not pretend to cover all the experimental setups, we have chosen in our article to focus on the case of $r=1$. This assumption is commonly used when studying natural convection in a composite fluid-porous layer (Beckerman et al. [3], Lauriat and Prasad [1], Le Breton et al. [4]), and also when adding solutal convection (Gobin et al. [5]). It is also used in isothermal flows (Vafai and Kim [2]). Moreover the assumption $\nu_{\mathrm{eff}}=\nu$ has been found to be in good agreement with some experimental observations (Beckerman et al. [3]).

One main modeling issue is the choice of appropriate boundary conditions at the fluid-porous medium interface. In the numerical code, the viscosity coefficients are calculated in order to ensure the continuity of velocity and stress at the interface, which is in agreement with model number 2 in a recent study of Alazmi and Vafai [19]. The widest used condition is that of Beavers and Joseph (1967) relating the stress discontinuity to the difference between the fluid velocity at the interface and the velocity in the porous medium slightly away from the interface. This condition involves an empirical parameter, therefore requiring to be fitted with experimental data. Ochoa-Tapia and Whitaker [20,21] also provide an interface condition, introducing a stress discontinuity. Again their condition involves a parameter that needs to be fitted with experimental data. Such data are hard to find: in the experimental work of Le Breton [22], it is specified that they were able to measure the vertical velocity in a horizontally differentially heated cavity, but unable to access the velocity in the porous layer. Ochoa-Tapia and Whitaker also used a variable porosity model to continuously link the Darcy and Stokes equations, and then showed the complexity of the interface region. However, they still did not succeed in giving a representation model compatible with experimental observation. Therefore we have chosen to solve the motion equations without modifying the existing interface conditions in the numerical code. We will develop the appropriate conditions for the analytical solution in Section 4.

In the energy equation, we have considered the case of a porous medium of the same thermal conductivity λ_{eff} than the fluid conductivity λ. In this paper we also consider the special case where the porous medium heat capacity $(\rho c_p)_p$ is the same as the fluid's. Different models linking λ and λ_{eff} are available (Beckerman et al. [3]), but the previous assumptions are justified in the case of a porous medium porosity close to one (Le Breton et al. [4]). Although these assumptions may seem restrictive, they allow us to obtain a plan-parallel flow satisfying the generalized Navier-Stokes equations. Indeed these assumptions allow for the continuity of the temperature and of the heat flux through the fluid-porous interface, which is in agreement with model number I of Alazmi and Vafai [19]. Without these assumptions, the temperature would still be continuous, but no longer analytic.

3.2 Dimensionless Form of the Generalized Navier-Stokes Equations. Classical scaling analysis for the pure fluid buoyancy flow induced in a vertical plate heated with a given flux density leads to the following typical scales L, $\kappa \mathrm{Ra}^{2/5}/L$, $\Delta T^{\star} = \varphi L \mathrm{Ra}^{-1/5}/\lambda$, $L^2/\kappa \mathrm{Ra}^{2/5}$ and $\rho_c \nu \kappa \mathrm{Ra}^{2/5}/L^2$, respectively for length, velocities, temperature, time and pressure (Bejan [23]). One can note that the Rayleigh number appears with a power of 2/5 in this scaling analysis, which is directly related to the given heat flux boundary condition, as developed in Bejan [23] (see p. 131). Also, the non-dimensional parameters governing the problem are different when solely porous flow is considered (see for example Straughan [24]), as opposed to the fluid-porous flow considered here.

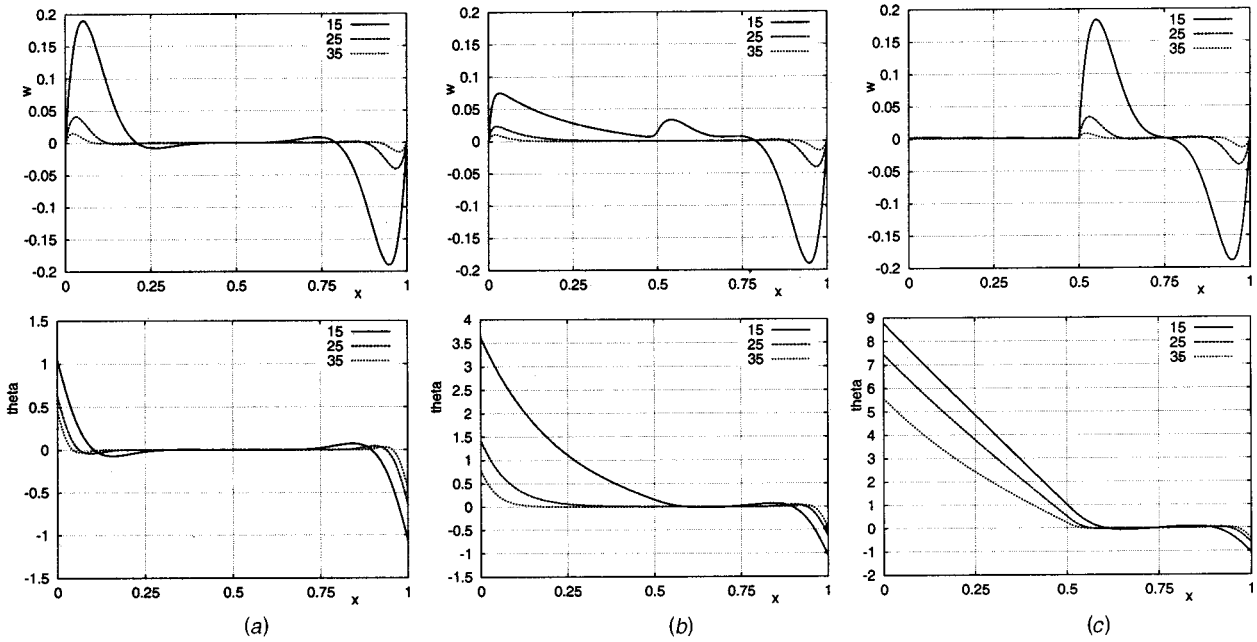

Fig. 4 Steady state profiles $w_0(x)$ and $\theta_0(x)$ for Ra$=10^6$, $ep=0.5$, and γ varying in the range [15,35]: (*a*) Da$=1$, (*b*) Da $=10^{-4}$, and (*c*) Da$=10^{-6}$

The Rayleigh number is defined as $\mathrm{Ra}=g\beta\varphi L^4/\lambda\nu\kappa$ where the thermal diffusivity is equal to $\kappa=\lambda/\rho_c c_p$. In a non-dimensional form, the governing Eqs. 1, 2, and 3 in the porous medium read:

$$\frac{\mathrm{Ra}^{2/5}}{\mathrm{Pr}}\left[\left(1-\epsilon+\frac{\epsilon}{\phi}\right)\frac{\partial}{\partial t}+(1-\epsilon)\vec{u}.\vec{\nabla}\right]\vec{u}$$

$$=-\vec{\nabla}p+\mathrm{Ra}^{2/5}(T-T_c)\vec{z}+\Delta\vec{u}-\frac{\epsilon}{\mathrm{Da}}\vec{u}, \qquad (4)$$

$$\mathrm{Ra}^{2/5}\left(\frac{\partial}{\partial t}+\vec{u}.\vec{\nabla}\right)T=\Delta T, \qquad (5)$$

$$\vec{\nabla}.\vec{u}=0, \qquad (6)$$

where the Prandtl number is defined as $\mathrm{Pr}=\nu/\kappa$ and the Darcy number as $\mathrm{Da}=K/L^2$.

4 Stationary Solution

In this paragraph we will determine analytically the one-dimensional flow created in a cavity of infinite vertical extent and finite width L, submitted to a given heat flux from the sides and partly filled with a porous layer of width d such that $ep=d/L$, adjacent to the heated wall. The stationary solution is a vertical velocity field depending only upon the horizontal coordinate $\vec{u}_0=w_0(x)\vec{z}$. The associated temperature field is made of two contributions $T-T_c=\delta z+\theta_0(x)$: a constant vertical temperature gradient δ, and a horizontal temperature distribution $\theta_0(x)$. δ is dimensionless and is deduced from the dimensional vertical temperature gradient α through the relation $\delta=\alpha L/\Delta T^\star=\alpha\lambda\mathrm{Ra}^{1/5}/\varphi$. The horizontal temperature distribution is due to the convective heat transport associated to the vertical temperature gradient δ through the vertical flow $w_0(x)\vec{z}$. Eq. 4 and Eq. 5 become for the stationary solution

$$\vec{0}=-\vec{\nabla}p_0+\mathrm{Ra}^{2/5}(\delta z+\theta_0)\vec{z}+D^2w_0\vec{z}-\frac{\epsilon}{\mathrm{Da}}w_0\vec{z}, \qquad (7)$$

$$\mathrm{Ra}^{2/5}\delta w_0=D^2\theta_0. \qquad (8)$$

Equation 8 can be integrated between $x=0$ and $x=1$, showing that $\int_0^1 w_0(x)dx=0$, and, therefore, this solution satisfies mass conservation. Projection on the x axis of Eq. 7 shows that p_0 is only a function of z. Equation 7 can then be projected onto the z axis, and variables can be separated. The stationary pressure field $p_0(z)$ is found to be a second order polynomial in z, and Eq. 8 can be used to eliminate the temperature, leading to a fourth order differential equation for $w_0(x)$. The new system is

$$D^4w_0-\frac{\epsilon}{\mathrm{Da}}D^2w_0+4\gamma^4w_0=0, \qquad (9)$$

$$\mathrm{Ra}^{2/5}(\theta_0-\theta_c)=\frac{\epsilon}{\mathrm{Da}}w_0-D^2w_0, \qquad (10)$$

where $D=d/dx$, θ_c is a free constant, and the parameter γ is given by

$$4\gamma^4=\mathrm{Ra}^{4/5}\delta=\alpha\lambda\mathrm{Ra}/\varphi. \qquad (11)$$

In the following the parameter δ will never appear again, and γ will be called the stratification parameter.

The boundary conditions on the left and right walls are zero velocity (no slip) and given dimensionless heat flux:

$$w_0=0 \text{ and } D\theta_0=-\mathrm{Ra}^{1/5}, \text{ at } x=0 \text{ and } 1. \qquad (12)$$

The boundary conditions at the interface between the fluid and the porous medium are the continuity of the velocity field, of the temperature and of their first derivative with respect to the x coordinate (Beckerman et al. [3]). These conditions are necessary to find a solution (w_0,θ_0) in the correct functional framework ($w_0 \in H^2(]0,1[)$, $\theta_0\in H^1(]0,1[)$).

A one-dimensional solution is found, taking the form of the sum of four complex exponential terms in each domain, the do-

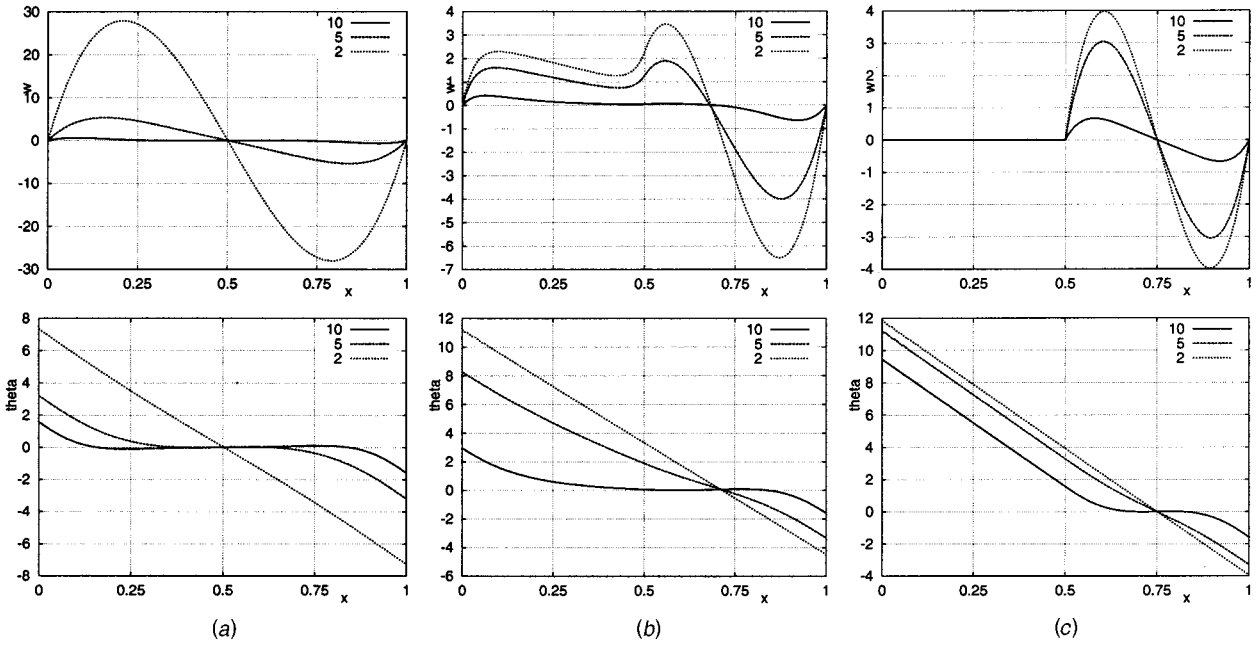

Fig. 5 Steady-state profiles $w_0(x)$ and $\theta_0(x)$ for Ra$=10^6$, $ep=0.5$, and γ varying in the range [2,15]: (*a*) Da$=1$, (*b*) Da $=10^{-3}$, and (*c*) Da$=10^{-6}$

main containing only fluid, and the one filled with the porous medium. Introducing $\Delta = 1/\mathrm{Da}^2 - 16\gamma^4$, when Δ is positive the solution reads

$$w_0(x) = A_1 e^{x\sqrt{1/2(1/\mathrm{Da}+\sqrt{\Delta})}} + A_2 e^{-x\sqrt{1/2(1/\mathrm{Da}+\sqrt{\Delta})}} + A_3 e^{x\sqrt{1/2(1/\mathrm{Da}-\sqrt{\Delta})}} + A_4 e^{-x\sqrt{1/2(1/\mathrm{Da}-\sqrt{\Delta})}}, \quad 0 < x < ep$$

$$w_0(x) = B_1 e^{(1+i)\gamma x} + B_2 e^{(1-i)\gamma x} + B_3 e^{(-1+i)\gamma x} + B_4 e^{(-1-i)\gamma x}, \quad ep < x < 1. \tag{13}$$

When Δ is negative, the previous formulas are still valid replacing $\sqrt{\Delta}$ with $i\sqrt{-\Delta}$. The temperature field $\theta_0(x)$ is obtained from the velocity field derivatives according to Eq. 10. Using the boundary conditions and the interfacial conditions, the eight constants are calculated by solving a 8×8 linear system. This analytical solution has been compared with a numerical solution obtained by direct simulation in a two-dimensional configuration, and excellent agreement has been obtained (Weisman et al. [7]). It is interesting to note that the stationary solution does not depend on the Prandtl number $Pr = \nu/\kappa$, which is not the case for the perturbations of this base flow for example.

Our results could be generalized to the case of a ratio $r(=\nu_{\mathrm{eff}}/\nu)$ different from 1, by changing equation (9) into

$$\alpha D^4 w_0 - \frac{\epsilon}{\mathrm{Da}} D^2 w_0 + 4\gamma^4 w_0 = 0, \tag{14}$$

where a new function $\alpha(\epsilon) = 1 - \epsilon + r\epsilon$ has been introduced. Then the interface condition would be the continuity of w_0 and of $\alpha D w_0$, keeping the continuity of temperature and heat flux.

The stationary velocity and temperature profiles depend on numerous parameters: the Rayleigh and Darcy numbers, the dimensionless width *ep* of the porous layer and also the parameter γ. In the case of a cavity of infinite vertical extent considered here, the stratification parameter γ is a free parameter. γ will be calculated in the next section in the case of a closed cavity. Before that, the influence of all four parameters previously mentioned on the velocity and temperature profiles will be discussed.

4.1 Influence of the Darcy Number. In order to illustrate the effect of the Darcy number, we will first consider the case Ra$=10^6$ and $ep=0.5$, i.e., the porous layer filling half of the cavity. The Darcy number used here, $\mathrm{Da}=K/L^2$, is defined using the macroscopic reference length L. A "microscopic" Darcy number, Da′ would be multiplied by a factor typically of $\approx 10^4$, since $\mathrm{Da}' = K/l^2 = (K/L^2).(L^2/l^2)$. Da′ should vary in the range $10^{-11} \leqslant \mathrm{Da}' \leqslant 10^5$ (values for fiber glass [25] p. 9, p. 26), corresponding to $10^{-15} \leqslant \mathrm{Da} \leqslant 10$. A porous medium characterized by a very low Darcy number is very impermeable, and should act like a solid medium. On the contrary, very high values of the Darcy number are characteristic of a very permeable medium, which should behave like a solely fluid phase. The effects of variation of the Darcy number upon the velocity and temperature profiles differ according to the range of γ, and two main ranges are presented:

Large Values of γ: $15 \leqslant \gamma \leqslant 35$. Variations of the velocity w_0 and of the temperature distribution θ_0 versus the horizontal coordinate x are represented on Fig. 4 for three values of the Darcy number belonging to the range $[10^{-6},1]$. As expected when the value of the permeability is large (Da$=1$), the porous layer behaves like a fluid medium and the flow develops in the whole width of the cavity. The flow takes the form of two separated boundary layer flows, one flow going upward near the heated wall and the return flow moving downward near the cooled wall. In the core between the two boundary layer flows, the velocity is nearly equal to zero. For larger Da numbers, the same curves are obtained. For intermediate values of the permeability (Da$=10^{-4}$), the upward flow splits into two flows: one developing in the porous part, the other one appearing in the fluid part in contact with the porous layer. Last in the case of a low value of the porous medium permeability (Da$=10^{-6}$ or smaller), the porous layer is equivalent to a solid layer and the flow just develops in the fluid part, $ep \leqslant x \leqslant 1$. Therefore we observe that the upward boundary layer becomes located next to the porous layer, which behaves like a solid boundary. We also observe that the effect of the decrease of the Darcy number is to bring the upward boundary layer

closer to the downward boundary layer, and thus to reduce the independence between the two boundary layers. The effect of the increase in γ is an increase of the absolute maximum velocity in the boundary layers.

Now for the horizontal temperature distribution $\theta_0(x)$, it must be stated that given the heat flux boundary conditions, the temperature field is defined except for one constant value θ_c. We take that constant to be zero in the middle part of the purely fluid layer. The temperature is then found to be constant (equal to zero) throughout the fluid, except in the boundary layers, and that holds for all values of Da or γ. In the purely fluid part, to the upward and downward boundary layer flows are associated small variations of θ_0. In the porous medium, the temperature variation is larger and increases continuously when the permeability decreases or when γ increases. In the case of a low value of the permeability of the porous medium ($Da=10^{-6}$), heat transfer in the porous layer is quasi conductive and the temperature consequently varies linearly.

It is useful to note that whatever the value of the Darcy number is, the same downward flow and associated temperature distributions are observed near the cooled vertical wall. This is due to the fact that the medium is still purely fluid in contact of the cold wall, and also that the two boundary layers do not interact. The temperature gradient over the fluid medium is the same for all permeability values.

Small Values of γ: $2 \leqslant \gamma \leqslant 15$. Profiles of the velocity w_0 and of the temperature distribution θ_0 versus the horizontal coordinate x are represented on Fig. 5 for three values of the Darcy number. The case $\gamma=5$ summarizes the effect of changes in the value of the Darcy number for small values of γ: it appears that the decrease in Da induces a transition from a double boundary layer regime to a conduction regime flow. This last flow is associated to a temperature profile varying linearly on the whole width of the cavity.

4.2 Influence of the Rayleigh Number. It should be noted that the widths of the boundary layers are independent of the Rayleigh number, once γ, *ep*, and Da are specified. The effect of varying the Rayleigh number is to modify the maximum value of the velocity and of the temperature. More precisely when the value of Ra is increased by a factor of 10, the maximum value of the velocity is multiplied by four and the maximum value of the temperature (at $x=0$) is multiplied by a factor close to 5/3. It should also be noted that this study focuses on stationary solutions, and that therefore these calculations only hold for Rayleigh numbers below the critical Ra number for the first bifurcation.

4.3 Influence of *ep* and of γ. The influence of the width of the porous layer *ep* and of the value of the vertical temperature stratification γ appears more clearly for a value of the Darcy number $Da=10^{-6}$. On Fig. 6 are represented the variations of the velocity profile for the following parameter values: $Ra=10^6$, $Da=10^{-6}$, $\gamma=15$, the value of the porous layer width varying between $ep=0.25$ and $ep=0.75$. It appears that an increase in the width of the porous layer induces a transition from a separated boundary layers flow to a dependent boundary layers flow and last to a conduction regime flow.

The same transitions take place when the stratification parameter γ decreases. This can be seen on Fig. 7, showing the variations of the velocity profile for $Ra=10^6$, $Da=10^{-6}$, $ep=0.25$, with γ increasing from $\gamma=5$ to $\gamma=20$.

As already mentioned in the introduction, the stratification parameter γ is a free parameter for the natural convection flow within an infinite vertical slot. But when dealing with a finite cavity, the vertical extent of the flow is bounded by horizontal walls, and that may be taken into account to determine the value of the stratification parameter, as shown in the next paragraph.

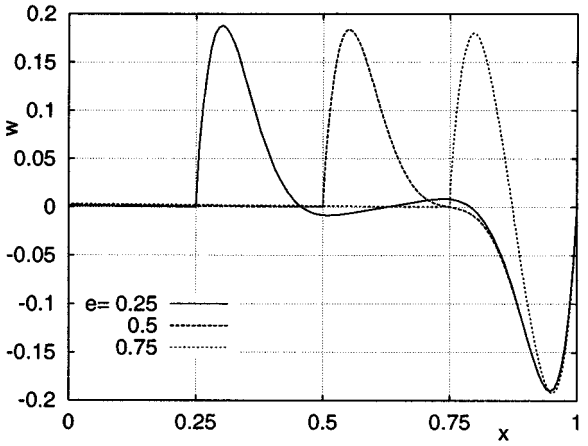

Fig. 6 Velocity profiles $w_0(x)$ for $Ra=10^6$, $Da=10^{-6}$, $\gamma=15$ and three values of *ep*: $ep=0.25$, $ep=0.5$, and $ep=0.75$

5 Determination of the Stratification Parameter

5.1 Energy Balance Method. The method, apparently first developed by Kimura and Bejan [9], consists in defining a control volume incorporating the upper horizontal boundary of the cavity, located at $z=H$, and part of the vertical walls, as represented on Fig. 8. Conservation of energy inside the control volume leads to equality between convective and conductive heat fluxes through the control volume surface S:

$$\int_S \rho_c c_p \tilde{T}\vec{U}.d\vec{S} = \int_S \lambda \vec{\nabla}\tilde{T}.d\vec{S}. \tag{15}$$

In a non-dimensional form Eq. 15 becomes

$$\mathrm{Ra}^{2/5} \int_S T\vec{u}.d\vec{S} = \int_S \vec{\nabla}T.d\vec{S}. \tag{16}$$

Replacing T with $T=T_c+\delta z+\theta_0(x)$ and using mass conservation through any horizontal plane

$$\int_0^1 w_0 dx = 0,$$

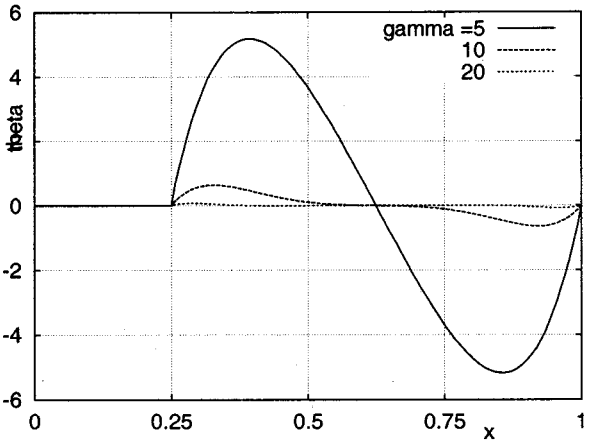

Fig. 7 Velocity profiles $w_0(x)$ for $Ra=10^6$, $Da=10^{-6}$, *ep* $=0.25$ and three values of γ: $\gamma=5$, $\gamma=10$ and $\gamma=20$

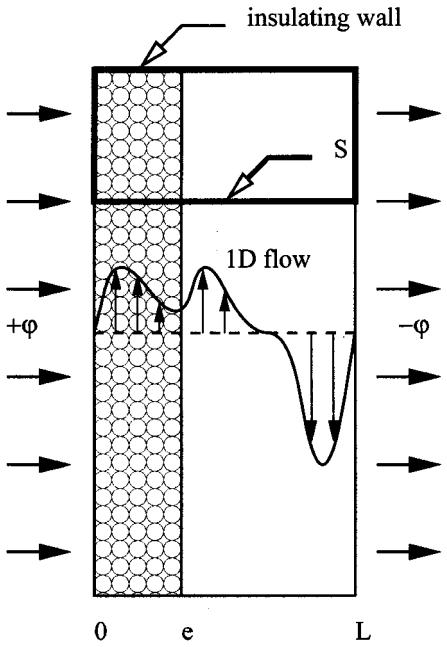

Fig. 8 Location of the control volume, with boundary *S* shown in bold line

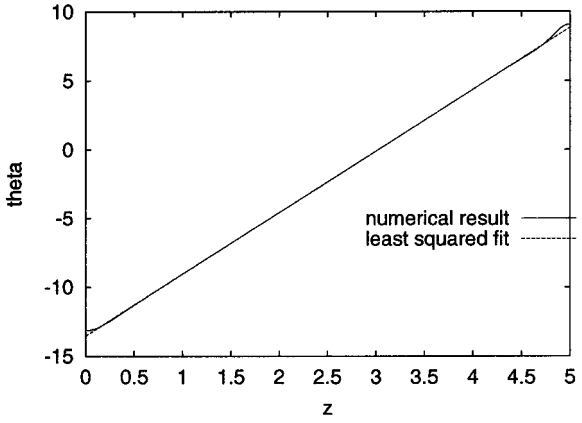

Fig. 9 Vertical temperature profile obtained from two-dimensional numerical simulations at mid-width of the cavity for Da$=10^{-4}$, $ep=0.25$, Ra$=10^6$, $A=5$. A least squared approximation for the central linear region is shown.

the left hand side of Eq. 16 can be simplified. Also the upper horizontal boundary is insulating, and the fluid velocity is zero on all cavity walls. Consequently, the following energy balance is obtained:

$$\int_0^1 w_0 \theta_0 dx = \frac{4\gamma^4}{\mathrm{Ra}^{6/5}}. \tag{17}$$

Once the Rayleigh and Darcy numbers are chosen, Eq. 17 is solved for γ using a bisection method. The solution for the vertical velocity and for the temperature is then completely determined using the analytical expressions for w_0 and θ_0 previously detailed.

5.2 Comparison With Numerical Simulations. The values of the stratification parameter γ obtained using the analytical expressions of Eqs. 10 and 13 and the energy balance method described in the previous paragraph were compared with those issued from direct integration of the two-dimensional time dependent Navier-Stokes and energy equations. For a given set of the aspect ratio $A=H/L$, the porous layer width ep, the Ra number and the Da number, the equations were integrated until a steady state was reached using a projection method and a second order backward Euler scheme, on a 128×256 regular mesh. The algorithm of march in time is based on a projection method, known as a modified fractional time step method and introduced by [26]. The algorithm involves implicit treatment of the viscous and Darcy penalty terms as well as explicit treatment of the convective term and the pressure gradient. The spatial discretization is based on a staggered mesh where the discrete equations are based on finite volume formulation. The resulting sparse pentadiagonal systems are solved by an ADI factorization. For solving the Poisson equation (in solving for the pressure field), a multigrid method is used. It was proven that the convergence of the numerical method is of order 2 in space and in time. The numerical results were examined by varying the number of grid points from 32×64 to 128×256. Refining the grid allowed to obtain grid independent results. In the case of a cavity filled with fluid (i.e., for $D_a>10$), results are in exact agreement with results of [27]. It should be noted that reaching truly steady state solution in the case of Neumann type boundary conditions (given heat flux on the boundaries) requires integrating the equations over very long times (typically one to two hours on NEC SX5 are needed). The calculation is much faster for Dirichlet boundary conditions (given temperature).

The vertical temperature profile (see the example shown in Fig. 9, corresponding to $A=5$, $ep=0.25$, Ra$=10^6$, and Da$=10^{-4}$) on the section $x=0.5$ was then plotted. For large enough aspect ratios ($A>1$), there is a large linear section away from the boundary coordinates ($z=0$ and $z=H/L=A$). The corresponding slope δ was calculated using a least squared error approximation, from which the value of the corresponding value of γ was calculated using Eq. 11, $\gamma=(\mathrm{Ra}^{4/5}\delta/4)^{1/4}$. The value found for γ does not depend on the vertical section selected for plotting the temperature profile.

Excellent agreement results from the comparison between values of γ determined numerically and semi-analytically using the energy balance: for a heating of the fluid corresponding to Ra $=10^6$, and a porous width $ep=0.25$ the values of the vertical temperature stratification found from the energy balance are $\gamma=14.787$, $\gamma=16.299$, and $\gamma=14.736$ for, respectively, the Darcy number values Da$=10^{-2}$, 10^{-4}, and 10^{-6}. From the two-dimensional temperature distributions numerically obtained, the values $\gamma=14.79$, 16.30, and 14.74 were determined for a fluid of Prandtl number Pr$=\nu/\kappa=0.71$ and for the same values of the Darcy number than previously. The agreement is convincing.

Relation (17) is independent of the cavity's height H. Therefore the stratification parameter γ is independent of the aspect ratio A of the cavity, as soon as H is large compared to the width L of the cavity. We verified this property on the solution obtained numerically. We performed a test on a completely fluid cavity (see Fig. 10(a)) as well as on a fluid-porous cavity (see Fig. 10(b)), for several aspect ratios ranging from 1 to 8. In both cases, the Rayleigh number was equal to 10^6. The vertical temperature profiles shown correspond to the $x=1/2$ section. On the figures the central linear portion of the profiles seem to be parallel for all shown aspect ratios. We calculated the corresponding values of γ. In the first case (fluid cavity, Ra$=10^6$) the values obtained are as follows: $\gamma=14.821$ (for an aspect ratio $A=1$), $\gamma=14.640$($A=2$), $\gamma=14.663$ ($A=4$), $\gamma=14.661$ ($A=6$), $\gamma=14.660$ ($A=8$). The value found analytically is $\gamma=14.659$. In the second case (Da$=10^{-4}$, $ep=0.25$, Ra$=10^6$), the obtained numerical values are $\gamma=16.301$ ($A=2$), $\gamma=16.301$ ($A=4$), and $\gamma=16.300$ ($A=6$), the analytical value being $\gamma=16.298$. The aspect ratio $A=1$ is too small to be able to neglect the effect of the horizontal boundaries. The result of these comparisons is clear and confirms

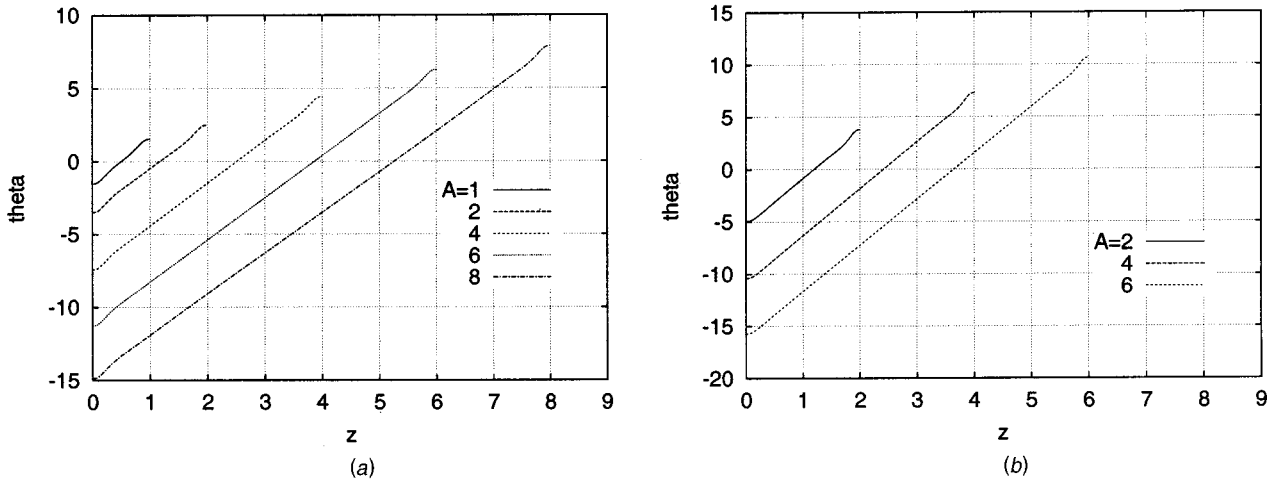

Fig. 10 Vertical temperature profile obtained from two-dimensional numerical simulations at mid-width of the cavity for several aspect ratios: (*a*) fluid cavity, Ra=10^6; (*b*) Da=10^{-4}, *ep*=0.25, Ra=10^6.

that γ is independent of the aspect ratio A. We next present a parameter study of the stratification parameter γ, calculated using the analytical solution and the energy balance.

5.3 Results for a Porous Layer of Width *ep*=0.5. On Fig. 11(*a*) and (*b*) are drawn the variations of the stratification parameter γ with respect to the Darcy number for several values of the Rayleigh number, and a constant width of the porous layer width $ep=0.5$.

First of all, one can note that for large Darcy number values γ is approximately constant: $\gamma(\mathrm{Da})\approx\gamma(1)$ for $\mathrm{Da}\geqslant 1$. This value of γ will be noted γ_f since the porous medium is then very permeable and behaves like a fluid. Similarly, for small Darcy number values, γ is also approximately constant: $\gamma(\mathrm{Da})\approx\gamma(10^{-9})$ for $\mathrm{Da}\leqslant 10^{-9}$. This value of γ will be noted γ_s, since the porous medium is then very impermeable and behaves like a solid. Therefore our results obtained for the range $10^{-9}\leqslant\mathrm{Da}\leqslant 1$ can be easily extended to the range $10^{-15}\leqslant\mathrm{Da}\leqslant 10^{6}$.

Furthermore looking at large values of the Rayleigh number in Fig. 11(*a*), one can see that $\gamma_f\approx\gamma_s$. This means that when the porous layer fills half of the cavity, the vertical temperature stratification does not change whether the flow develops either through the whole width of the cavity or only through only half of the cavity. This property remains true for all *ep* values. However when Ra decreases, differences between the values of γ for extreme values of the permeability appear (Fig. 11(*b*)). For Ra $>2.10^4$ we note that γ_s is slightly larger than γ_f, whereas for Ra$<2.10^4$, we note that γ_s is slightly smaller than γ_f. For instance when $ep=0.5$ and Ra=10^4, we obtained $\gamma_f=5.322$ and $\gamma_s=5.012$.

The transition between γ_s and γ_f takes place on a fairly narrow Da range. In that transition, γ increases and reaches a maximum value noted $\gamma_{\max}$ for a value of the Darcy number denoted by $\mathrm{Da}_{\max}$ (located roughly between Da=10^{-3} and Da=10^{-6}). Thus, the influence of the porous medium permeability on the vertical temperature gradient is concentrated around this point ($\gamma_{\max}$,$\mathrm{Da}_{\max}$). The two values $\gamma_{\max}$ and $\mathrm{Da}_{\max}$ just depend upon the Rayleigh number and the width of the cavity, and it appears that the location of the maximum $\mathrm{Da}_{\max}$ decreases when the Rayleigh number takes larger values.

Last we observe that when the heating strength, measured by the Rayleigh number, is increased, the value of the stratification parameter follows the same behavior. This can be understood considering the heat conservation equation Eq. 16, where it appears

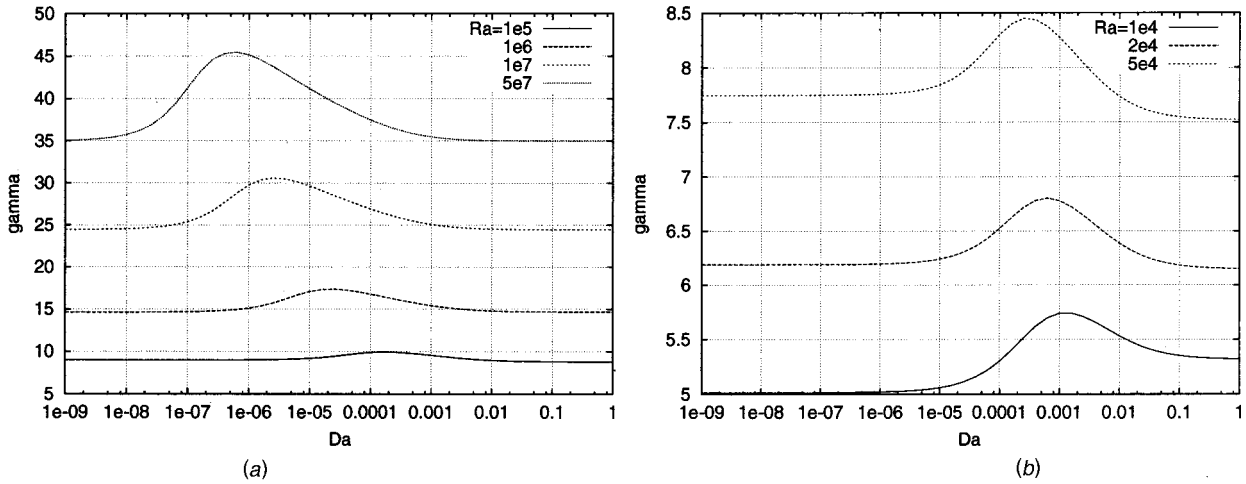

Fig. 11 Vertical temperature gradient γ versus the Darcy number Da for different heating strengths Ra, *ep*=0.5: (*a*) Ra $\in[10^5,5.10^7]$; and (*b*) Ra$\in[10^4,5.10^4]$.

that the vertical conductive heat transport term in the right hand side of the equation is proportional to a power law of the Rayleigh number.

The cavity studied here is characterized by parameters Ra and *ep*, and by the parameters γ_{max} and Da_{max} that we have just introduced. Useful relations between these four parameters can be found, and are presented in the following sections.

5.4 Case of a Purely Fluid Cavity Da=∞. The values of γ (denoted γ_f) for large values of the Darcy number are interesting, since in this case the cavity remains purely fluid, whatever the value of the width of the porous layer is. Thus this value depends only on the Rayleigh number.

Figure 12 shows the variations of $\log(\gamma_f)$ versus log(Ra) where log denotes the decimal logarithm, for twelve values of the Rayleigh number. γ_f is found to depend on the Rayleigh number according to the law

$$\gamma_f = 0.681 \ \mathrm{Ra}^{2/9}. \tag{18}$$

Also in the same case of a purely fluid cavity, Kimura and Bejan [9] have found a power law between the vertical temperature gradient in the core of the base flow, the Rayleigh number Ra_{KB} and the aspect ratio A of the cavity: $\partial T/\partial z = \mathrm{CA}^{4/9}\mathrm{Ra}_{KB}^{8/9}$. Contrary to us, their result depends on the aspect ratio because they have used a Rayleigh number depending on the height of the cavity. Using our definition of the Rayleigh number, their law becomes: $\partial T/\partial z = C'\mathrm{Ra}_{KB}^{2/9}$, as in Eq. 18.

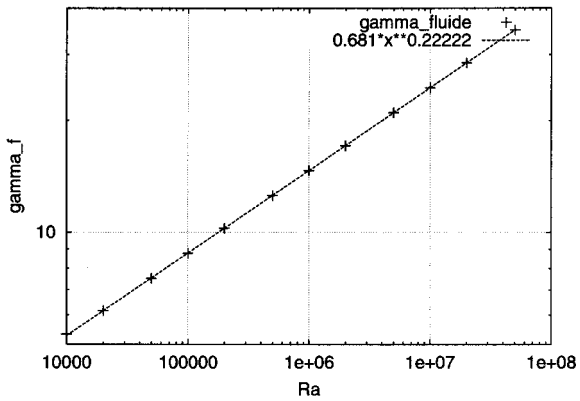

Fig. 12 log(γ_f) versus log(Ra), with 12 values of Ra shown

When the porous layer is no more perfectly permeable, there is a point of maximum γ called γ_{max}, with corresponding Da called Da_{max}. γ_{max} and Da_{max} are functions of Ra and *ep*. Expressions of these functions will be determined now.

5.5 Evolution of γ_{max} Versus Ra and *ep*. Figure 13(a) represents the variations of $\ln(\gamma_{max})$ versus the logarithm of the porous layer width for several values of the Rayleigh number. There

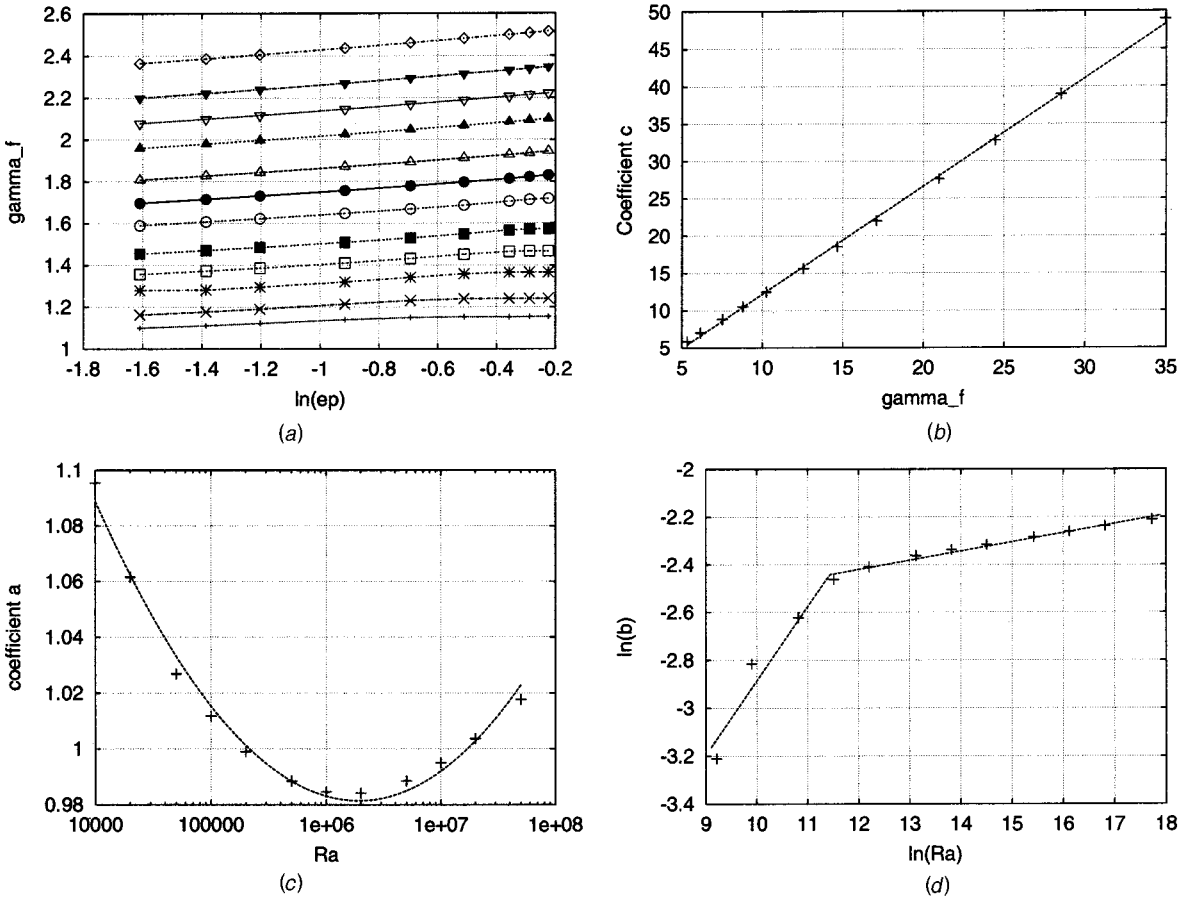

Fig. 13 (*a*) ln(γ_{max}) versus ln(*ep*). Each line corresponds to a value of Ra, and on each line, each point corresponds to a value of *ep*. There are twelve Ra values in the [10^4,5.10^7] range, and eight *ep* values in the [0.25,0.8] range; (*b*) *c*(γ_f) versus the stratification parameter γ_f in the entirely fluid layer, each point corresponds to one of the 12 Ra values of (*a*); (*c*) *a* versus ln(Ra), each point corresponds to one of the 12 Ra values of (*a*); (*d*) *b* versus Ra, each point corresponds to one of the 12 Ra values of (*a*).

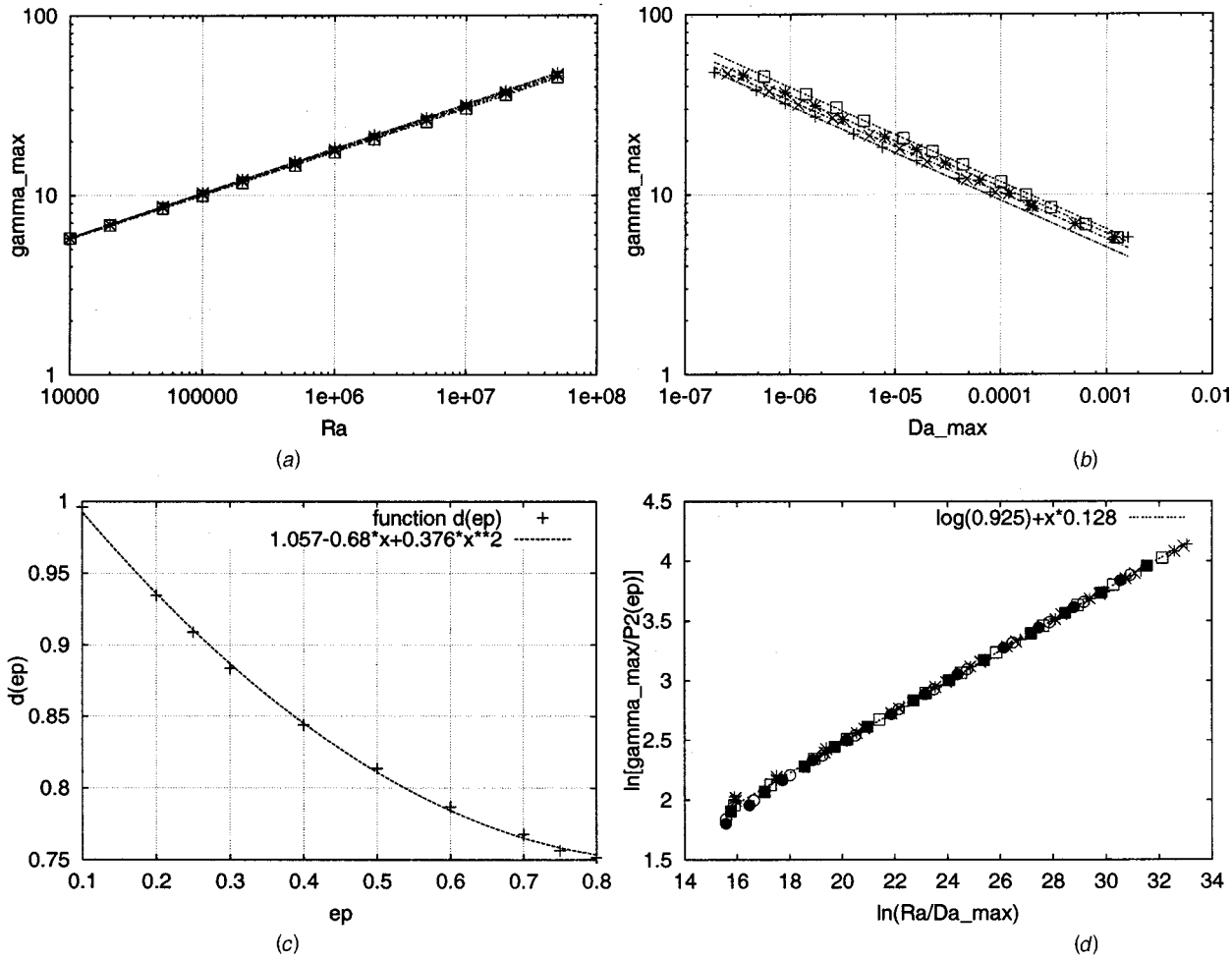

Fig. 14 (*a*) $\log(\gamma_{max})$ versus $\log(Ra)$. Each line corresponds to a value of *ep*, and on each line, each point corresponds to a value of Ra. There are twelve Ra values in the $[10^4,5.10^7]$ range, and five *ep* values in the [0.5,0.8] range; (*b*) $\log(\gamma_{max})$ versus $\log(Da)$, same *ep* values and Ra values as in (*a*); (*c*) function $d(ep)$ versus *ep*, all eight *ep* values in the [0.25,0.8] range; (*d*) $\ln(\gamma_{max}/P_2(ep))$ versus $\ln(Ra/Da_{max})$, all *ep* values and Ra values.

are twelve values of Ra: $Ra=10^4$, 2.10^4, 5.10^4, 10^5, 2.10^5, 5.10^5, 10^6, 2.10^6, 5.10^6, 10^7, 2.10^7, 5.10^7, and eight values of *ep*: $ep=0.25$, 0.3, 0.4, 0.5, 0.6, 0.7, 0.75, 0.8. At first glance, approximately parallel straight lines are obtained, leading to the law $\gamma_{max}=c(Ra)ep^{1/10}$. For each line the coefficient c was obtained using a least squared error fit. Instead of determining $c(Ra)$, variations of c versus the stratification parameter γ_f in the entirely fluid layer may be studied, since we have just shown that γ_f is linked to the Rayleigh number (Eq. (18). Figure 13(*b*) giving the variation of c versus γ_f, indicates that $c(Ra)=P_1(\gamma_f)$ where P_1 is a first order polynomial. More careful analysis showed that the straight lines observed on Fig. 13(*a*) are not perfectly parallel nor straight, and that $\gamma_{max}/c(Ra)$ is not exactly equal to $ep^{1/10}$. Writing the law in the form $\gamma_{max}/c(Ra)=a(Ra)ep^{b(Ra)}$, the functions $a(Ra)$ and $b(Ra)$ were fitted. Variations of a and $\ln(b)$ versus $\ln(Ra)$ are represented respectively on Fig. 13(*c*) and (*d*). The results are that function a takes the form of a second order polynomial of $\ln(Ra)$, and that b varies exponentially with Ra. As a summary, the analytical fit that found for evaluation of γ_{max} as a function of Ra and *ep* is

$$\begin{cases} \gamma_{max}=P_1(\gamma_f)a(Ra)ep^{b(Ra)}, \\ P_1(\gamma_f)=-2.27+1.44\gamma_f \\ a=1.769-0.113\ln(Ra)+3.891\ \ 10^{-3}(\ln(Ra))^2. \\ b=2.512\ \ 10^{-3}\times Ra^{0.310}\ \text{ for } Ra\leqslant 10^5 \\ \ \ =5.604\ \ 10^{-2}\times Ra^{0.0385}\ \text{ for } Ra>10^5 \end{cases} \quad (19)$$

The above expression uses γ_f, which is a function of Ra, as written in Eq. 18. In the following chapter, another fit is found for the expression of γ_{max} as a function of Ra, Da_{max}, and *ep*.

5.6 Evolution of γ_{max} Versus Ra, Da_{max}, and *ep*. On Fig. 14(*a*) are represented the variations of the decimal logarithm $\log(\gamma_{max})$ versus $\log(Ra)$ for different values of the width of the porous layer. The same twelve values of Ra as in the previous section are used, and only 5 values of *ep* are shown on Fig. 14(*a*) and (*b*): $ep=0.5$, 0.6, 0.7, 0.75, 0.8. It appears that γ_{max} varies like $Ra^{1/4}$. In addition Fig. 14(*b*) gives the evolution of $\log(\gamma_{max})$ versus $\log(Da_{max})$, still for different values of *ep*. Here γ_{max} is found to vary like $Da_{max}^{-1/4}$. Thus the maximum value of γ depends upon the ratio of the Rayleigh number to Da_{max}, according to the law $\gamma_{max}=d(ep)(Ra/Da_{max})^{1/8}$. Values of $d(ep)$ were obtained using a least squared fit using all Ra values for a given *ep* value. The function $d(ep)$, represented on Fig. 14(*c*), is found to be well fitted with a second order polynomial: $d(ep)=P_2(ep)$. Similarly to the previous section, the power of 1/8 may be improved. From Fig. 14(*d*), giving the variations of $\ln(\gamma_{max}/P_2(ep))$ versus $\ln(Ra/Da_{max})$ for all eight values of the porous layer's width, and all twelve values of Ra, we deduce the law $\gamma_{max}/P_2(ep)=0.925\times(Ra/Da_{max})^{0.128}$.

As a summary, the analytical fit found for the evaluation of γ_{max} as a function of Ra, Da_{max}, and *ep* is:

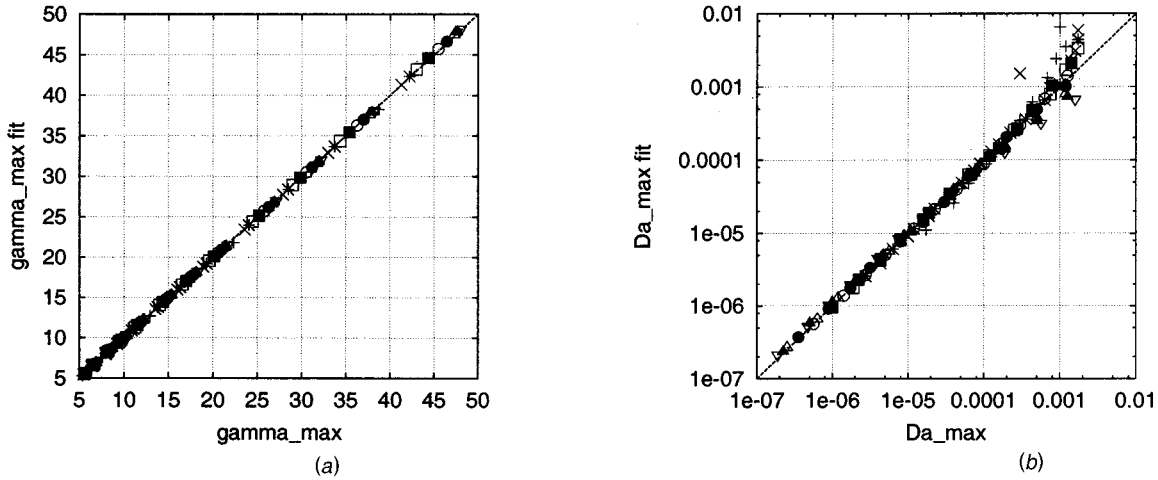

Fig. 15 γ_{max} (*a*) and Da_{max} (*b*) calculated from the analytical fit versus the same quantities calculated directly from the model equations. All points shown (12 values of Ra and 8 values of *ep*).

$$\begin{cases} \gamma_{max} = P_2(ep) \times 0.925 \times \left(\dfrac{Ra}{Da_{max}} \right)^{0.128} \\ P_2(ep) = 1.057 - 0.68 \times ep + 0.376 \times ep^2 \end{cases} . \quad (20)$$

From Eqs. 18, 19, and 20, the following law relating Da_{max} and the Rayleigh number and the porous layer's width may be deduced, where $P_1(\gamma_f)$, $P_2(ep)$, $a(Ra)$, and $b(Ra)$ are given in the referenced equations:

$$Da_{max} = Ra \times \left(\frac{P_2(ep) \times 0.925}{P_1(0.681 Ra^{2/9}) a(Ra) ep^{b(Ra)}} \right)^{7.8} . \quad (21)$$

This relation indicates which porous material must be used (more precisely which permeability should be chosen) in order to obtain maximum vertical heat transfer in the porous medium, for a given width of the porous layer (the width of the fiberglass layer in an insulating wall for example) and a given amount of energy supplied to the material.

According to the previous study, one can now determine γ_{max} and Da_{max} from the knowledge of Ra and *ep*, according to Eqs. 19 and 21 that summarize the fits that were performed. Figure 15 shows the quality of these fits for determining γ_{max} and Da_{max}. On the figure are shown on the *x* axes the values calculated from the analytical formulas giving $w_0(x)$ and $\theta_0(x)$ and from Eq. 17 for the energy balance, and on the *y* axes the values given from the fits of Eqs. 19 and 21. If the fits are correct, all points should fall on the $y=x$ line. Figure 15(*a*) shows the γ_{max} values and Fig. 15(*b*) shows the Da_{max} values. All points are shown (12 values of Ra and 8 values of *ep*). The fits seem to be correct, except for the estimate of Da_{max} for small Ra values (largest values of Da_{max}, for all *ep* values).

One interesting quantity is the ratio of γ_{max} versus γ_f: it measures the efficiency of the presence of a porous layer on the heat transfer in the cavity. On Fig. 16 are reported the variations of this ratio versus the Ra number or the Da_{max} number.

Results show that for a given porous width the presence of a porous layer improves the vertical heat transfer in the cavity in two specific situations: when external heating is intense (large Rayleigh number) or when the porous medium is more impermeable (small Da_{max}).

After having studied vertical transport of heat, the next paragraph will be devoted to the determination of horizontal heat transfer between the two vertical walls of the cavity, and the calculation of Nusselt numbers.

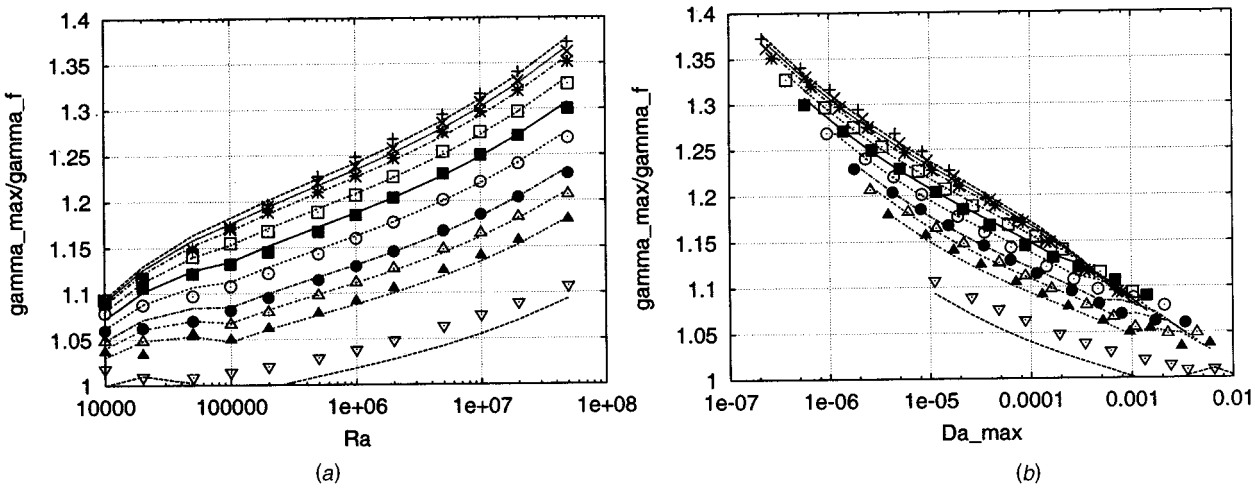

Fig. 16 γ_{max}/γ_f calculated from the analytical fit (solid curves) and calculated directly from the model equations (points) versus (*a*) Ra and (*b*) Da_{max}. All points shown (12 values of Ra and 8 values of *ep*, bottom *ep*=0.1 to top *ep*=0.8).

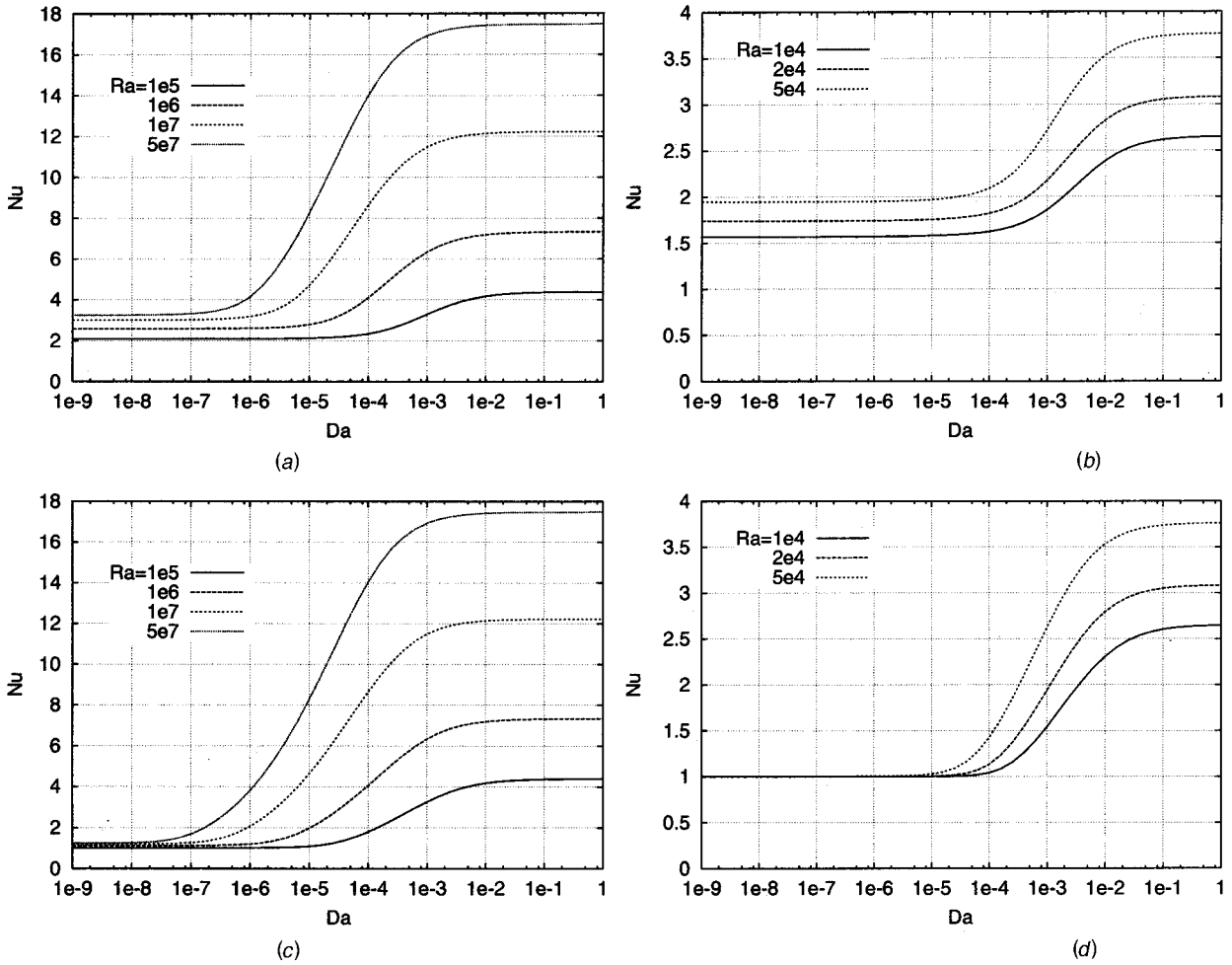

Fig. 17 Nusselt number Nu versus Da, top: $ep=0.25$, bottom: $ep=0.75$; (left) $Ra\in[10^5,5.10^7]$ (right): $Ra\in[10^4,5.10^4]$.

6 Nusselt Numbers

The cavity is submitted to a horizontal heat flux of density φ, and we saw in the previous paragraph that part of this injected energy is convected vertically. Now we are interested in the horizontal propagation of the energy through the width of the cavity. Once a horizontal heat flux φ is imposed, the horizontal heat transfer capacity of the cavity is characterized by the resulting horizontal temperature difference between the vertical boundaries $\Delta T=T(x=0)-T(x=L)$. As usual, the Nusselt number is defined as

$$\mathrm{Nu}=\frac{\varphi L}{\lambda \Delta T}, \tag{22}$$

which in dimensionless form, using $\Delta\theta_0=\theta_0(x=0)-\theta_0(x=1)$, is

$$\mathrm{Nu}=\frac{\mathrm{Ra}^{1/5}}{\Delta\theta_0}. \tag{23}$$

The efficiency of the horizontal heat transfer through the cavity is measured by the Nusselt number. When the width ep of the porous layer is fixed, variations of Nu versus the Darcy number for a fixed Rayleigh number are drawn on Fig. 17. In complement, when the Rayleigh number is fixed the variation of the Nusselt number versus Da for several porous layer thicknesses are presented on Fig. 18. From the two figures a predominant tendency in the behavior of the Nusselt number can be deduced: Nu increases with the Darcy and Rayleigh numbers, but decreases with ep. Therefore heat transfer is more efficient when the porous layer is permeable or thin, and when Ra is high. For small Da numbers, Nu is close to 1 (conductive heat transfer) and variation of Ra does not affect the value of Nu. This is especially true for larger porous layer widths ep (corresponding to an almost totally solid cavity).

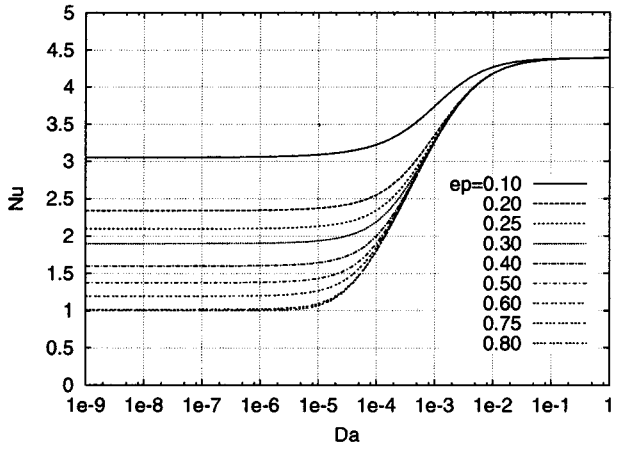

Fig. 18 Nusselt number versus Darcy number for various ep values, $Ra=10^5$

These results can be understood, looking back at the horizontal temperature profiles presented on Fig. 4 and Fig. 5. On these figures one can see the temperature difference $\Delta\theta_0$, which is inversely proportional to the Nusselt number through Relation 23. It clearly appears that the horizontal temperature distribution presents a large decrease essentially in the porous part. Moreover the temperature difference through the porous medium is proportional to the width of the porous layer, and is larger when the porous medium is impermeable (with a linear temperature variation): when strong vertical flow develops in the cavity, a large convective heat transport is induced, leading to a small horizontal temperature difference. Therefore horizontal heat transfer is essentially affected by the presence or the absence of flow. To strong vertical flow is associated large heat transfer. Then the influence of the Darcy number and of the porous part width previously described is directly deduced from the base flow characteristics, which are: the flow is stronger in the fluid layer, and is decelerated in the porous part as this layer becomes impermeable.

Concerning the influence of the Rayleigh number, one can look at the heat conservation equation Eq. 5 written in the case of a stationary flow $\Delta T = \mathrm{Ra}^{2/5}(\vec{u}.\vec{\nabla})T$. Thus an increase in the value of the Rayleigh number induces stronger vertical heat transport. Small horizontal temperature difference is then induced in the cavity.

7 Conclusion

We have presented the complete calculation of the one-dimensional buoyancy-induced flow developing in a rectangular cavity, where the vertical boundaries are submitted to a horizontal and uniform heat flux, and a vertical porous layer is placed close to the heated wall. Our aim was to improve the analytical determination of the one-dimensional flow (Weisman et al. [7]) by calculating the stratification parameter γ associated to the plan-parallel flow.

In the case of a vertically infinite cavity, γ is a free parameter and we have presented the influence of the characteristic parameters of the cavity (Da, Ra, *ep*, and γ) on the stationary flow. According to the values of these parameters, we can observe a transition from a double boundary layer flow (with boundary layers independent or linked) to a conductive regime flow.

In the case of a closed cavity, we have calculated the value for the stratification parameter. The method is based on the use of the balance between vertical convective and conductive heat transfer both in the fluid and in the porous medium. The obtained values of γ are also in perfect agreement with the values found with the two-dimensional numerical simulations. We have shown that the stratification parameter reaches a maximum value $\gamma_{\max}$ for an intermediate value of the porous medium permeability, $\mathrm{Da}_{\max}$. We have determined by fitting some simple relations between $\gamma_{\max}$, $\mathrm{Da}_{\max}$, *ep* and Ra. With these relations we can now determine the permeability of the porous material leading to maximal vertical heat transfer for a given heating strength, and a given porous layer width.

Moreover we have characterized the horizontal heat transfer through the cavity by calculating the temperature difference between the vertical walls of the cavity, once a given heat flux between the vertical boundaries is prescribed. This temperature difference is found to develop essentially in the porous part and therefore Nusselt numbers are larger when the porous layer becomes permeable or thin.

Now that we have completely characterized the base flow in the cavity, the linear stability analysis of this flow can be performed. This work, where perturbations are sought under the form of transverse propagating waves, is under progress.

Acknowledgments

Numerical simulations were performed on the SX5-NEC of the laboratory IDRIS-CNRS.

Nomenclature

A = aspect ratio$=H/L$
c_p = isobaric specific heat, J/kgK
Da = Darcy number$=K/L^2$
d = porous layer thickness, m
$\vec{dS}$ = surface vector
ep = dimensionless porous layer thickness
$\vec{g}$ = gravitational acceleration, m^2/s
H = cavity height, m
K = permeability of the porous medium, m^2
L = cavity width, m
Nu = Nusselt number$=\varphi L/\lambda\Delta T$
P = pressure, Pa
p = dimensionless pressure
Pr = Prandtl number$=\nu/\kappa$
r = ratio ν_{eff}/ν
Ra = Rayleigh number$=g\beta L^4\varphi/\lambda\nu\kappa$
t = time, s
$\tilde{T}$ = temperature, K
T = dimensionless temperature
T_c = reference temperature, K
ΔT = horizontal temperature difference, K
$\Delta T^{\star}$ = temperature difference scale$=\varphi L\,\mathrm{Ra}^{-1/5}/\lambda$, K
$\vec{U}$ = velocity vector, m/s
$\vec{u}$ = dimensionless velocity vector
u = dimensionless x component of the velocity
w = dimensionless z component of the velocity
x = horizontal coordinate
z = vertical coordinate
α = vertical temperature gradient, $\mathrm{K\,m^{-1}}$
β = fluid thermal expansion coefficient, $\mathrm{K^{-1}}$
δ = dimensionless vertical temperature gradient
$\Delta\theta_0$ = dimensionless horizontal temperature difference
ϵ = porous layer characteristic function
γ = stratification parameter$=(\mathrm{Ra}^{4/5}\delta/4)^{1/4}$
γ_s = stratification parameter for an almost solid porous medium
κ = thermal diffusivity$=\lambda/\rho_c c_p$, $\mathrm{m^2 s^{-1}}$
λ = fluid thermal conductivity, W/mK
μ = dynamic viscosity, $\mathrm{kg\,m^{-1}\,s^{-1}}$
ν = kinematic viscosity, $\mathrm{m^2\ s^{-1}}$
ρ = fluid density, $\mathrm{kg\,m^{-3}}$
ρ_c = fluid reference density, $\mathrm{kg\,m^{-3}}$
θ_0 = dimensionless horizontal temperature
θ_c = reference dimensionless temperature
φ = prescribed heat flux density, $\mathrm{W/m^2}$
ϕ = porosity

Subscripts

0 = refers to stationary state
eff = refers to effective properties for a fluid-saturated porous medium
f = refers to the fluid
p = refers to the porous medium

References

[1] Lauriat, G., and Prasad, V., 1987, "Natural Convection in a Vertical Porous Cavity: A Numerical Study for Brinkman-Extended Darcy Formulation," ASME J. Heat Transfer, **109**, pp. 688–696.
[2] Vafai, K., and Kim, S. J., 1990, "Fluid Mechanics of the interface Region Between a Porous Medium and a Fluid Layer—An Exact Solution," Int. J. Heat Fluid Flow **11-3**, pp. 254–256.
[3] Beckerman, C., Viskanta, R., and Ramadhyani, S., 1988, "Natural Convection in Vertical Enclosures Containing Simultaneously Fluid and Porous Layer," J. Fluid Mech., **186**, pp. 257–284.
[4] Le Breton, P., Caltagirone, J. P., and Arquis, E., 1991, "Natural Convection in a Square Cavity With Thin Porous Layers on its Vertical Walls," ASME J. Heat Transfer, **113**, pp. 892–898.
[5] Gobin, D., Goyeau, B., and Songbe, J.-P., 1998, "Double Diffusive Natural

Convection in a Composite Fluid-Porous Layer,'' ASME J. Heat Transfer, **120**, pp. 234–242.
[6] Nield, D., and Bejan, A., 1998, *Convection in Porous Media*, 2nd edition, Springer-Verlag, New York.
[7] Weisman, C., Le Quéré, P., and Firdaouss, M., 1999, ''Sur une solution exacte de la convection naturelle en cavité partiellement remplie d'un milieu poreux,'' C. R. Acad Sc. Paris, Vol. 327-II B, pp. 235–240.
[8] Bergholz, R. F., 1978, ''Instability of Steady Natural Convection in a Vertical Fluid Layer,'' J. Fluid Mech., **84**, pp. 743–768.
[9] Kimura, S., and Bejan, A., 1984, ''The Boundary Layer Natural Convection Regime in a Rectangular Cavity with Uniform Heat Flux from the Side,'' ASME J. Heat Transfer, **106**, pp. 98–103.
[10] Trevisan, O. V., and Bejan, A., 1986, ''Mass and Heat Transfer by Natural Convection in a Vertical Slot Filled With Porous Medium,'' Int. J. Heat Mass Transf., **29**, pp. 403–415.
[11] Gill, A. E., 1966, ''The Boundary-Layer Regime for Convection in a Rectangular Cavity,'' J. Fluid Mech., **26**, pp. 515–536.
[12] Weber, J. E., 1974, ''The Boundary-Layer Regime for Convection in a Vertical Porous Layer,'' Int. J. Heat Mass Transf., **18**, pp. 569–573.
[13] Amiri, A., and Vafai, K., 1994, ''Analysis of Dispersion Effects and Non-Thermal Equilibrium, Non-Darcian, Variable Porosity Incompressible Flow Through Porous Media,'' Int. J. Heat Mass Transf., **37**, No. 6, pp. 939–954.
[14] Amiri, A., Vafai, K., and Kuzay, T. M., 1995, ''Effects of Boundary Conditions on Non-Darcian Heat Transfer Through Porous Media and Experimental Comparisons,'' Numer. Heat Transfer, Part A, **27**, pp. 651–664.
[15] Beck, J. L., 1972, ''Convection in a Box of Porous Material Saturated With Fluid,'' Phys. Fluids, **15**, No. 8, pp. 1377–1383.
[16] Alazmi, B., and Vafai, K., 2000, ''Analysis of Variance Within the Porous Media Transport Models,'' ASME J. Heat Transfer, **122**, pp. 303–326.
[17] Amahmid, A., Hasnaoui, M., and Vasseur, P., 1999, ''Etude analytique et numérique de la convection naturelle dans une couche poreuse de Brinkman doublement diffusive,'' Int. J. Heat Mass Transf., **42**, pp. 2991–3005.
[18] Givler, R. C., and Altobelli, S. A., 1994, ''A Determination of the Effective Viscosity for the Brinkman-Forchheimer Flow Model,'' J. Fluid Mech., **258**, pp. 355–370.
[19] Alazmi, B., and Vafai, K., 2001, ''Analysis of Fluid Flow and Heat Transfer Interfacial Conditions Between a Porous Medium and a Fluid Layer,'' Int. J. Heat Mass Transf., **44**, pp. 1735–1740.
[20] Ochoa-Tapia, J., and Whitaker, S., 1995, ''Momentum Transfer at the Boundary Between a Porous Medium and a Homogeneous Fluid: I—Theoretical Development,'' Int. J. Heat Mass Transf., **38**, No. 14, pp. 2635–2646.
[21] Ochoa-Tapia, J., and Whitaker, S., 1995, ''Momentum Transfer at the Boundary Between a Porous Medium and a Homogeneous Fluid: II—Comparison With Experiment,'' Int. J. Heat Mass Transf., **38**, No. 14, pp. 2647–2655.
[22] Le Breton, P., 1991, ''Etude numérique et expérimentale de la convection naturelle laminaire et turbulente en cavité partiellement occupée d'un milieu poreux,'' Ph.D., Univ. Bordeaux.
[23] Bejan, A., 1984, *Convection Heat Transfer*, John Wiley and Sons, New York.
[24] Straughan, B., 2001, ''A Sharp Nonlinear Stability Threshold in Rotating Porous Convection,'' Proc. R. Soc. London, Ser. A, **457**, pp. 87–93.
[25] Kaviany, M., 1991, *Principles of Heat Transfer in Porous Media*, Springer-Verlag, New York.
[26] Temam, R., 1979, *Navier-Stokes Equations*, North-Holland, Amsterdam.
[27] Le Quéré, P., 1991, ''Accurate Solutions to the Square Differentially Heated Cavity at High Rayleigh Number,'' Comput. Fluids, **20**, pp. 19–41.

Effect of a Variable Gravity Field on Convection in an Anisotropic Porous Medium With Internal Heat Source and Inclined Temperature Gradient

Sherin M. Alex

Prabhamani R. Patil
Professor,
e-mail: prabha@annauniv.edu

Department of Mathematics,
Anna University,
Chennai 600 025, Tamil Nadu, India

The convective instability of a horizontal fluid-saturated anisotropic porous layer, with internal heat source and inclined temperature gradient, subject to a gravity field varying with distance in the layer, is investigated. A linear stability analysis is performed and the resulting eigenvalue problem solved using a Galerkin technique. In the absence of an inclined temperature gradient, an increase in the variable gravity parameter above -1 destabilizes the system. In its presence interesting developments occur. An increase in the heat generation destabilizes the system when the variable gravity parameter is nonnegative. When it is negative the opposite effect is seen. [DOI: 10.1115/1.1420711]

Keywords: Convection, Heat Transfer, Instability, Natural Convection, Porous Media

1 Introduction

The investigation of convective instability in a fluid-saturated porous medium due to an inclined temperature gradient is of relevance in the study of geothermal activities, underground transport of pollutants, gas reservoirs and crystal growth as noted by Manole and Lage [1]. Lage and Nield [2] have provided an excellent review of the literature on this problem.

Although the investigation of thermal instability due to a time-dependent gravity field has attracted the attention of several researchers [3–5], convection due to a gravity field varying with distance, has received little attention. However in studying large-scale flows in the Earth's crust it is imperative to consider the gravitational field of the earth as a variable quantity, varying with distance from the center, as pointed out by Pradhan and Samal [6]. The existence of elevated gravity levels varying with distance, during the formation of crystals grown from the molten phase in a furnace placed at the arm extremity of a centrifuge, have been reported by Rodot et al. [7]. Chen and Chen [8] have investigated the effect of such a gravity gradient on the onset of salt finger convection in a pure fluid. The thermal stability of a nonviscous fluid layer and that of a viscous fluid layer, subject to a gravitational field varying with distance in the layer, have been analyzed by Pradhan and Samal [6] and Straughan [9], respectively. The linear and nonlinear stability limits for convection in an isotropic porous medium with internal heat source under variable gravity fields have been obtained by Rionero and Straughan [10].

Kaloni and Qiao [11] and Alex and Patil [12] have investigated the convective instability of a horizontal fluid-saturated porous layer with inclined temperature gradient subject to a gravitational field varying linearly with distance in the layer. Alex and Patil [13] have studied the influence of a variable gravitational field on the thermal instability of a fluid-saturated porous medium with inclined temperature gradient and vertical throughflow.

When the fluid is heated internally by a uniform distribution of heat sources a thermally unstable situation arises, similar to that caused by the decay of radioactive matter in the earth's mantle. Hence the investigation of thermal convection in porous layers with internal heat generation is of importance in the extraction of geothermal energy, the enhanced recovery of oil by thermal methods and the use of aquifers for water storage, and has attracted the attention of several researchers.

Degan et al. [14] have noted that, as a consequence of a preferential orientation or asymmetric geometry of a grain, most porous media encountered in nature and in industry are anisotropic. Hence the aim of this article is to analyze the effect of a variable gravitational field on convective instability induced by an internal heat source and inclined temperature gradient in an anisotropic porous medium.

2 Mathematical Formulation

A horizontal fluid-saturated anisotropic porous layer of thickness d is considered. The layer extends to infinity in the x and y co-ordinate directions, and is bounded by rigid impermeable perfectly conducting planes at $z=0$ and $z=d$. The co-ordinate axes (x,y,z) are oriented parallel to the principal axes of the anisotropic porous medium and the z-axis points vertically upwards opposing the direction of gravity. Neale [15] has pointed out that, in many practical situations involving homogeneous anisotropic porous media, the macroscopic properties in two principal directions parallel to the bedding plane are equal. Hence isotropy can be assumed in the bedding plane, which leads to the horizontally isotropic case. Thus, taking the x-y plane to be the bedding plane, it has been assumed that the permeabilities are equal in the x and y directions, and so also the thermal diffusivities. That is, $K_x = K_y \neq K_z$ and $\kappa_x = \kappa_y \neq \kappa_z$. The boundaries are assumed to have a linear horizontal temperature gradient α_T in the x direction, and for a given x the lower plane is hotter than the upper by ΔT. Accordingly, for a system heated from below the boundary conditions following Nield [16] are,

$$\mathbf{q}\cdot\mathbf{k}=0 \quad \text{at } z=0 \quad \text{and} \quad z=d, \tag{1}$$

$$T=T_0+\Delta T/2-\alpha_T x \quad \text{at } z=0, \tag{2}$$

$$T=T_0-\Delta T/2-\alpha_T x \quad \text{at } z=d, \tag{3}$$

where the symbols have been defined in the Nomenclature. The medium is internally heated due to uniformly distributed heat sources of total strength Q.

Contributed by the Heat Transfer Division for publication in the JOURNAL OF HEAT TRANSFER. Manuscript received by the Heat Transfer Division November 27, 2000; revision received August 3, 2001. Associate Editor: C. Beckermann.

It is assumed that the Boussinesq approximation is valid, and that the flow in the porous medium is governed by Darcy's law. Accordingly the dimensional governing equations are

$$\nabla \cdot \mathbf{q} = 0 \tag{4}$$

$$\nabla p + (\mu/(K_x, K_x, K_z))\mathbf{q} - \rho \mathbf{g} = 0 \tag{5}$$

$$(\rho c)_m (\partial T/\partial t) + (\rho c_p)_f \mathbf{q} \cdot \nabla T = (\lambda_x, \lambda_x, \lambda_z)_m \nabla^2 T + Q \tag{6}$$

$$\rho = \rho_0 [1 - \beta_T (T - T_0)], \tag{7}$$

where, following Chen and Chen [8], it has been assumed that the gravity vector **g**, varies linearly with distance. That is,

$$\mathbf{g} = -g_0 (1 + \eta z)\mathbf{k}, \tag{8}$$

where η, the variable gravity coefficient, is assumed to be a constant.

Dimensionless variables (denoted by the superscript*) are introduced by choosing d, κ_z/d, $(\rho c)_m d^2/(\lambda_z)_m$, $\Delta T/R_T$, and $\rho_0 \nu \kappa_z/K_z$ as scales for length, velocity, time, temperature and pressure respectively, where $R_T = g_0 \beta_T \Delta T K_z d/(\kappa_z \nu)$ is the vertical thermal Rayleigh number. The governing equations in dimensionless form are

$$\nabla^* \cdot \mathbf{q}^* = 0 \tag{9}$$

$$\nabla^* p^* + \mathbf{q}_1^* - T^* (1 + \eta^* z^*)\mathbf{k} = 0 \tag{10}$$

$$(\partial T^*/\partial t^*) + \mathbf{q}^* \nabla^* T^* = \kappa_1 \nabla_1^{*2} T^* + \partial^2 T^*/\partial z^{*2} + R_T Q^*, \tag{11}$$

where the internal heat source parameter $Q^* = Q d^2/(\lambda_z)_m \Delta T$ and the variable gravity parameter $\eta^* = \eta d$.

The boundary conditions are now,

$$w^* = 0 \quad \text{at } z^* = 0 \quad \text{and} \quad z^* = 1, \tag{12}$$

$$T^* = R_T/2 - R_{HT} x^* \quad \text{at } z^* = 0, \tag{13}$$

$$T^* = -R_T/2 - R_{HT} x^* \quad \text{at } z^* = 1, \tag{14}$$

where $R_{HT} = g_0 \beta_T \alpha_T K_z d^2/(\kappa_z \nu)$ is the horizontal thermal Rayleigh number.

2.1 Basic State. Equations (9)–(14) permit a basic steady state solution of the form,

$$\mathbf{q}_b^* = U^*(z^*)\mathbf{i}, \quad T_b^* = \tilde{T}^*(z^*) - R_{HT} x^*, \quad p_b^* = p^*(x^*, z^*). \tag{15}$$

Here $U^*(z^*)$ and $\tilde{T}^*(z^*)$ satisfy,

$$D^* U^*(z^*) = R_{HT} K_1 (1 + \eta^* z^*), \tag{16}$$

$$D^{*2} \tilde{T}^*(z^*) = -R_{HT} U^*(z^*) - R_T Q^* \tag{17}$$

along with the boundary conditions,

$$\tilde{T}^*(0) = R_T/2, \tag{18}$$

$$\tilde{T}^*(1) = -R_T/2. \tag{19}$$

The solution of the system (16)–(19) is given by

$$U^*(z^*) = R_{HT} K_1 [-(1/2) - (\eta^*/6) + z^* + (\eta^* z^{*2})/2], \tag{20}$$

$$\begin{aligned} \tilde{T}^*(z^*) = {} & R_T/2 - R_T z^* + (R_T Q^*/2)[z^* - z^{*2}] - R_{HT}^2 K_1 \{([1/12] \\ & + [\eta^*/24]) z^* - ([1/2] + [\eta^*/6])(z^{*2}/2) + (z^{*3}/6) \\ & + (\eta^* z^{*4}/24)\}, \end{aligned} \tag{21}$$

where it is assumed that there is no net mass flow. That is,

$$\int_0^1 U^*(z^*) dz^* = 0 \tag{22}$$

2.2 Perturbed State. The basic state described by the system (15) is slightly perturbed, and the altered state is given by

$$\begin{aligned} \mathbf{q}^* &= \mathbf{q}_b^* + \hat{\mathbf{q}}^* \\ T^* &= T_b^* + \hat{T}^* \\ p^* &= p_b^* + \hat{p}^* \end{aligned} \tag{23}$$

Substituting (23) into the system (9)–(11) and linearizing, the equations governing the perturbed quantities become

$$\nabla \cdot \hat{\mathbf{q}} = 0 \tag{24}$$

$$\nabla \hat{p} + \hat{\mathbf{q}}_1 - \hat{T}(1 + \eta z)\mathbf{k} = 0 \tag{25}$$

$$(\partial \hat{T}/\partial t) + U(z)(\partial \hat{T}/\partial x) - \hat{u} R_{HT} + \hat{w} D\tilde{T} = \kappa_1 \nabla_1^2 \hat{T} + \partial^2 \hat{T}/\partial z^2 \tag{26}$$

subject to,

$$\hat{w} = \hat{T} = 0 \quad \text{at } z = 0 \quad \text{and} \quad z = 1, \tag{27}$$

where the asterisks have been dropped for simplicity (with the understanding that all the variables are dimensionless henceforth).

Expanding the perturbed quantities in terms of the normal modes as,

$$\begin{aligned} (\hat{u}, \hat{v}, \hat{w}, \hat{p}, \hat{T}) = {} & (u(z), v(z), w(z), p(z), \theta(z)) \\ & \times \exp[i(k_x x + k_y y - \sigma t)] \end{aligned} \tag{28}$$

the system (24)–(26) yields, on eliminating $u(z)$, $v(z)$, and $p(z)$, the following system of differential equations in $w(z)$ and $\theta(z)$:

$$(D^2 - K_1 k^2) w(z) + K_1 k^2 \theta(z)(1 + \eta z) = 0 \tag{29}$$

$$\begin{aligned} & (D^2 - \kappa_1 k^2 + i\sigma - i k_x U(z))\theta(z) + (i k_x R_{HT}/k^2) D w(z) \\ & - w(z) D\tilde{T}(z) = 0, \end{aligned} \tag{30}$$

where σ is the frequency of disturbance and $k = (k_x^2 + k_y^2)^{1/2}$ is the overall horizontal wave number. The disturbance with $k_x = 0$ is referred to as the longitudinal mode and that with $k_y = 0$ as the transverse mode. The problem is now reduced to that of solving the system (29) and (30) subject to the boundary conditions,

$$w(z) = \theta(z) = 0 \quad \text{at } z = 0 \quad \text{and} \quad z = 1. \tag{31}$$

The system (29)–(31) can be regarded as an eigenvalue problem in R_T with parameters k_x, k_y, K_1, κ_1, Q, R_{HT}, η, and σ.

3 Method of Solution

The eigenvalue problem formulated in the previous section has been solved using a Galerkin technique. Accordingly, we write the variables in a series of basis functions as

$$w = \sum_{j=1}^{N} a_j w_j \tag{32}$$

$$\theta = \sum_{j=1}^{N} b_j \theta_j, \tag{33}$$

where a_j and b_j are constants. The basis functions considered were the trigonometric functions,

$$w_j = \theta_j = \sin(j\pi z) \quad j = 1,2,3, \ldots \tag{34}$$

which satisfy the boundary conditions identically. The Galerkin method requires that

$$\det(A_{i,j}) = 0, \tag{35}$$

where for $i, j = 1,2, \ldots, N$

$$A_{i,j} = \langle D w_i D w_j + K_1 k^2 w_i w_j \rangle$$

$$A_{i,j+N} = -\langle K_1 k^2 (1 + \eta z) w_i \theta_j \rangle$$

$$A_{i+N,j}=\langle D\tilde{T}(z)\theta_i w_j - ik_x R_{HT}k^{-2}\theta_i Dw_j\rangle$$

$$A_{i+N,j+N}=\langle D\theta_i D\theta_j+(k^2\kappa_1 - i\sigma + ik_x U(z))\theta_i\theta_j\rangle.$$

Here $U(z)$ is given by Eq. (20) and

$$D\tilde{T}(z)=-R_T+(R_TQ/2)[1-2z]-R_{HT}^2K_1\{1/12+\eta/24 - ([1/2]+[\eta/6])z+(z^2/2)+(\eta z^3/6)\}. \quad (36)$$

The inner products are defined as

$$\langle FG\rangle=\int_0^1 F(z)G(z)dz. \quad (37)$$

For neutral stability σ is real.

3.1 Numerical calculations. At the second order of approximation ($N=2$), the determinant of order four in Eq. (35) was expanded algebraically, for the isotropic case ($K_1=\kappa_1=1$). The real and imaginary parts were then equated to zero to yield a pair of simultaneous equations (as explained by Nield [16]). For fixed values of R_{HT}, Q, and $\eta(K_1=\kappa_1=1)$, the critical Rayleigh number, which is its minimum as k is varied, was then obtained numerically for the various modes of disturbance; namely, stationary longitudinal mode ($\sigma=0$, $k_x=0$), stationary transverse mode ($\sigma=0$, $k_y=0$), oscillatory longitudinal mode ($\sigma\neq0$, $k_x=0$) and oscillatory transverse mode ($\sigma\neq0$, $k_y=0$). It was found that no unstable oscillatory longitudinal mode was possible. Further, it was seen that the stationary transverse modes were not possible in the absence of variable gravity field (as noted by Parthiban and Patil [17]), and that in the presence of variable gravity field also the stationary transverse mode is possible only for certain values of the internal heat source parameter and horizontal thermal Rayleigh number. As the critical Rayleigh number for the stationary longitudinal mode was found to be always less than that for the stationary transverse mode (when it is possible) and oscillatory transverse modes, the favored form of disturbance is the stationary longitudinal mode ($\sigma=0$, $k_x=0$) both in the presence and the absence of a variable gravity field, when $K_1=\kappa_1=1$. Parthiban and Patil [17] have reported that, in the absence of a variable gravity field, the stationary longitudinal modes are the favored modes at the onset of instability in an anisotropic porous medium. In the absence of variable gravity field the results obtained in the present analysis using the second order approximation coincide with that of Parthiban and Patil [17], when $K_1=\kappa_1=1$.

Accordingly at higher orders of approximation the determinant in Eq. (35) is expanded numerically with $\sigma=0$ and $k_x=0$. To avoid errors during numerical integration, the inner products involved are evaluated analytically rather than numerically. On fixing the values of R_{HT}, Q, K_1, κ_1 and η the lowest value of R_T as k is varied is obtained numerically using a search method. The results presented here are for twelve terms in the series expansions, and are accurate to within 0.03. That is, the absolute difference in the critical Rayleigh numbers obtained with eleven and twelve terms in the series expansions does not exceed 0.03.

4 Results and Discussion

At order $N=12$, numerical computations to find the critical Rayleigh number, $R_{T\text{crit}}$ have been carried out for various values of η, (following Chen and Chen [8]), Q, R_{HT}, K_1, and κ_1 (following Parthiban and Patil [17]). Since K_z is greater than K_x and κ_z is greater than κ_x (Neale [15]), K_1 and κ_1 have been varied subject to this restriction. That is, K_1 and κ_1 are both assumed to be less than unity. The results are presented graphically in Figs. 1–6.

Case 1. Isotropic Porous Medium ($K_1=\kappa_1=1$)

(a) $Q=0$.

1 Figure 1 reveals that, in the absence of internal heat source, an increase in the horizontal thermal Rayleigh number, R_{HT} (in the range considered) delays the onset of convective instability, that is, stabilizes the system for all values of the variable gravity parameter. A similar trend was observed by Nield [18] in the absence of a variable gravity field.

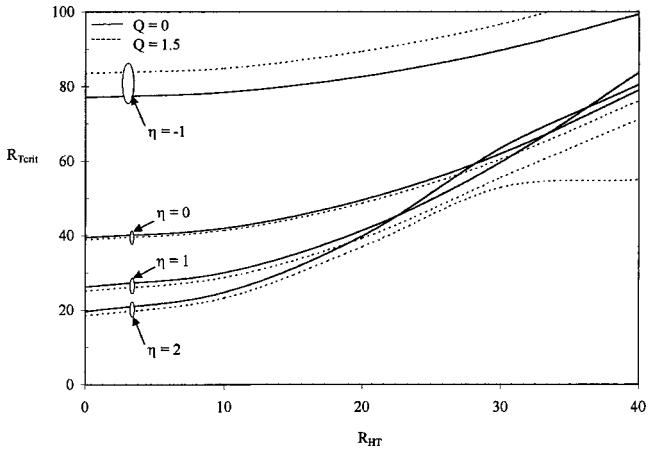

Fig. 1 Effect of a variable gravity field on the critical Rayleigh number in an isotropic porous medium ($K_1=\kappa_1=1$)

2 $R_{HT}=0$: From Fig. 1 it can be observed that, $R_{T\text{crit}}$ is maximum when the variable gravity parameter η takes the value -1, and as η increases above -1 $R_{T\text{crit}}$ decreases, when $Q=0$. Thus, when compared to the gravity field with $\eta=0$, the onset of convective instability is advanced when η is positive, and when it is negative the opposite effect is seen. This is because, as noted by Chen and Chen [8], when $\eta<0$, the buoyancy effects are maximum at the lower wall and decrease with height. Further, the critical Rayleigh number is based on the gravity level at the lower wall. Thus when $\eta<0$, the gravity level in the layer is decreased, which thereby causes an increase in the critical Rayleigh number. When η is positive the opposite effect is seen. That is, the critical Rayleigh number is less than that for the constant gravity case ($\eta=0$).

3 $R_{HT}\neq0$: It can be seen from Fig. 1 that, in the presence of horizontal temperature gradient, as in its absence, the system is most stable when η assumes the value -1, for all values of the horizontal thermal Rayleigh number, when $Q=0$. When R_{HT} ranges between 0 and 22, an increase in η above -1, advances the onset of convective instability, so that in this range the system is least stable when $\eta=2$. When R_{HT} exceeds 22 this trend is disturbed. As R_{HT} varies between 22 and 36 it is seen that $R_{T\text{crit}}$ is greater when $\eta=2$ than when $\eta=1$, implying that the system with

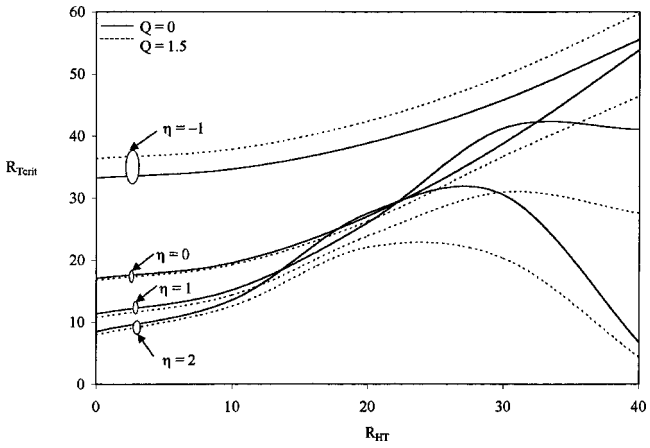

Fig. 2 Effect of a variable gravity field on the critical Rayleigh number in an anisotropic porous medium ($K_1=1$, $\kappa_1=0.1$)

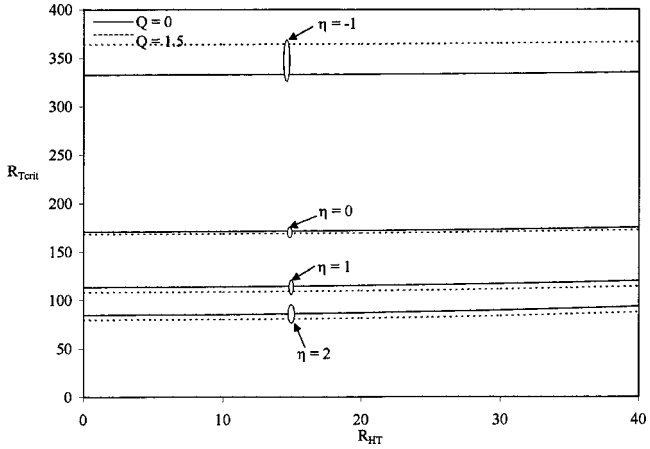

Fig. 3 Effect of a variable gravity field on the critical Rayleigh number in an anisotropic porous medium ($K_1=0.1$, $\kappa_1=1$)

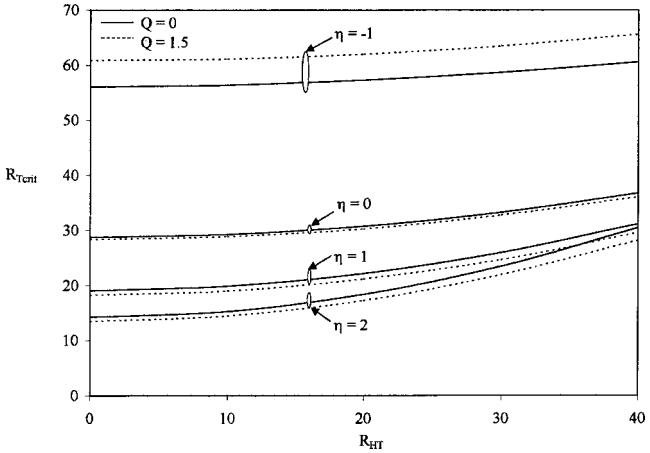

Fig. 5 Effect of a variable gravity field on the critical Rayleigh number in an anisotropic porous medium ($K_1=0.2$, $\kappa_1=0.1$)

$\eta=2$ is more stable than that with $\eta=1$, in this range. It is also seen that, when R_{HT} exceeds 28, the value of $R_{T\text{crit}}$ when $\eta=2$ exceeds that when $\eta=0$, so that the system with $\eta=2$ is more stable than that with constant gravitational field. Further, it can be seen that when R_{HT} exceeds 33, $R_{T\text{crit}}$ is greater when $\eta=1$ than when $\eta=0$, and when R_{HT} exceeds 36 $R_{T\text{crit}}$ is greater when $\eta=1$ than when $\eta=2$. Thus when R_{HT} varies between 22 and 33 the system is least stable when $\eta=1$, and thereafter the system is least stable when $\eta=0$. Therefore, it is seen that in the absence of internal heat source, an increase in the variable gravity parameter η above 0, plays a dual role (stabilizing in a certain range and destabilizing in another) on the stability of the system.

The trends seen when the variable gravity parameter is positive are possibly due to the interaction between the stabilizing effects caused by the increase in the horizontal temperature gradient, and the destabilizing effects of the elevated gravity fields. When η is negative, the stabilizing effect of the decreased gravity field, together with the stabilizing effect of the increase in the horizontal temperature gradient, may be additive, so that the system is the most stable when η is negative.

(b) $Q\neq 0$.

1 It can be noted from Fig. 1 that, in the presence of internal heat source ($Q=1.5$), an increase in R_{HT} stabilizes the system for all values of η. The same behavior was seen in the absence of internal heat source.

2 $R_{HT}=0$: As observed in the absence of internal heat source, in its presence too, the system is most stable when the variable gravity parameter η takes the value -1, and an increase in η above -1 advances the onset of convective instability.

3 $R_{HT}\neq 0$: From Fig. 1 it can be seen that, in the presence of internal heat source, unlike in its absence, an increase in the variable gravity parameter above -1, destabilizes the system for all values of the horizontal thermal Rayleigh number. Thus the dual role played by the increase in η above 0 in the absence of internal heat source is not observed in its presence. This may be due to the damping of the trends seen when $Q=0$, by the destabilizing effect of the increase in the heat generation.

(c) Comparison of the Cases $Q=0$ and $Q\neq 0$. From Fig. 1, it can be observed that when the variable gravity parameter η is nonnegative, the values of $R_{T\text{crit}}$ in the presence of internal heat source ($Q=1.5$) are less than the corresponding values in the absence of internal heat source ($Q=0$), for all values of the horizontal thermal Rayleigh number. This implies that an increase in the heat generation due to internal heat source always destabilizes the system when η is nonnegative. In the absence of variable gravity field ($\eta=0$), this is in concurrence with the conclusion of Parthiban and Patil [17], who have shown that an increase in the internal heat source parameter destabilizes the system for all values of the horizontal thermal Rayleigh number. Thus when $\eta>0$, the destabilizing effect of internal heat source, together with the destabilizing effect of the elevated gravity fields and stabilizing

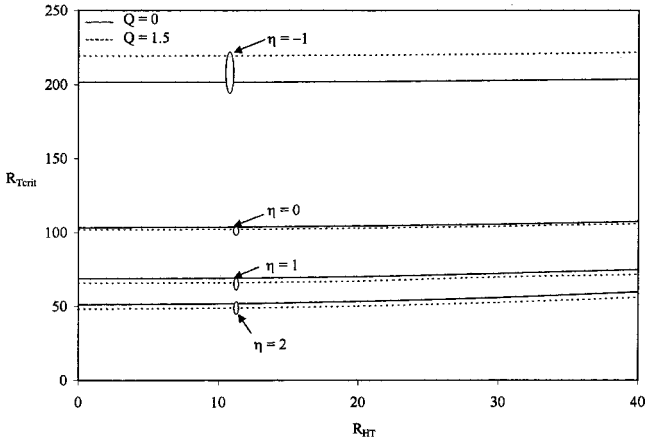

Fig. 4 Effect of a variable gravity field on the critical Rayleigh number in an anisotropic porous medium ($K_1=0.1$, $\kappa_1=0.5$)

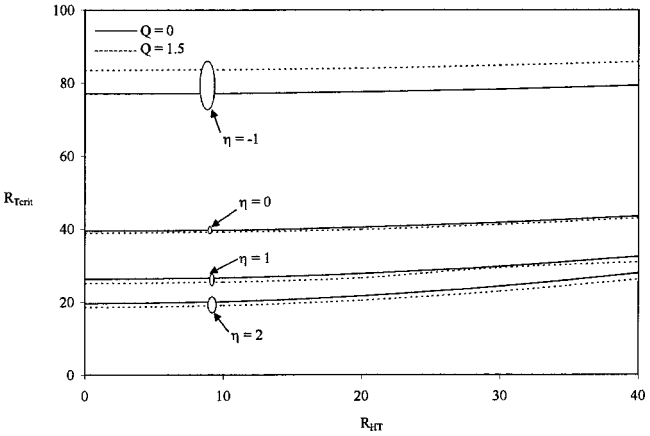

Fig. 6 Effect of a variable gravity field on the critical Rayleigh number in an anisotropic porous medium ($K_1=\kappa_1=0.1$)

effect of the increase in the horizontal temperature gradient, probably cause the trends that are seen. When η is negative it is seen that an increase in Q stabilizes the system for all values of R_{HT} considered. This may be because the stabilizing effect of the decreased gravity field dominates the destabilizing effect of internal heat source for all values of the horizontal temperature gradient.

Case 2. Anisotropic Porous Medium. The effect of fixing one of the anisotropy parameters at 1, and varying the other has been studied. The critical Rayleigh numbers for the anisotropic porous medium, for various values of the anisotropy parameters are given in Figs. 2–6. It should be noted that K_1 and κ_1 are both assumed to be less than unity.

(a) Effect of Anisotropy in Diffusivity.

1 A comparison of Figs. 1 and 2 reveals that, $R_{T\text{crit}}$ is greater when $K_1=\kappa_1=1$ than when $K_1=1$, $\kappa_1=0.1$, for all values of η, R_{HT} and Q. This implies that when the permeability is isotropic ($K_1=1$) and the parameter κ_1 is decreased the system is always destabilized. In the absence of a variable gravity field, this is in agreement with the conclusion of Parthiban and Patil [17]. Hence in the presence and absence of a variable gravity field, an increase in the vertical diffusivity (or a decrease in the horizontal diffusivity), promotes the onset of convective instability. Thus the effect of anisotropy in diffusivity is to destabilize the system for all values of the variable gravity parameter, when $\kappa_1<1$, that is, when the thermal diffusivity in the x co-ordinate direction is less than that in the z co-ordinate direction.

2 $Q=0$:

(i) It can be seen from Fig. 2 that an increase in the horizontal thermal Rayleigh number R_{HT} stabilizes the system when the variable gravity parameter is negative or zero, when $Q=0$, as in the isotropic case. However, when the variable gravity parameter is positive an increase in R_{HT} initially stabilizes the system and then destabilizes it. This may be due to the interaction of the destabilizing effects of the elevated gravity fields and anisotropy in diffusivity, with the stabilizing effect of the increase in R_{HT}.

(ii) $R_{HT}=0$: From Fig. 2 it is observed that as η increases above -1, $R_{T\text{crit}}$ decreases, implying that the system is destabilized. The same trend is seen when the medium is isotropic.

(iii) $R_{HT}\neq 0$: It can be seen from Fig. 2 that, when $Q=0$, the system is most stable when $\eta=-1$, and that an increase in the variable gravity parameter above -1 destabilizes the system when R_{HT} varies between 0 and 14 and when it exceeds 32. When R_{HT} ranges between 14 and 22, the system is the least stable when $\eta=1$. Thereafter the system is the most unstable when $\eta=2$. When R_{HT} assumes values between 22 and 32 the system is more stable when $\eta=1$ than when $\eta=0$. Thus trends similar to those seen in the isotropic case are seen at lower values of R_{HT} when $K_1=1$, $\kappa_1=0.1$. This may be due to the interaction of the destabilizing effects of the elevated gravity fields and anisotropy in diffusivity, with the stabilizing effect of the increase in R_{HT}.

3 $Q\neq 0$:

(i) In the presence of internal heat source ($Q=1.5$), as in its absence, an increase in the horizontal thermal Rayleigh number initially stabilizes the system and then destabilizes it, when η is positive, and stabilizes it when η is negative or zero. This trend is not seen when the medium is isotropic.

(ii) $R_{HT}=0$: In the presence of internal heat source, the system is most stable when the variable gravity parameter η takes the value -1, and an increase in η above -1 advances the onset of convective instability, as also seen when $Q=0$. The same behavior is observed when the medium is isotropic.

(iii) $R_{HT}\neq 0$: Figure 2 reveals that, in the presence of internal heat source, unlike in its absence, an increase in the variable gravity parameter above -1 destabilizes the system for all values of the horizontal thermal Rayleigh number. This pattern is seen when the medium is isotropic also.

(iv) Comparison of the cases $Q=0$ and $Q\neq 0$: It is seen from Fig. 2, that, as in the isotropic case, an increase in the internal heat source parameter destabilizes the system when the variable gravity parameter is nonnegative and stabilizes it when the variable gravity parameter is positive.

(b) Effect of Anisotropy in Permeability.

1 On comparing Figs. 1 and 3, it is seen that a decrease in K_1 to 0.1 when the diffusivity is isotropic ($\kappa_1=1$) results in an increase in $R_{T\text{crit}}$ for all values of η, R_{HT}, and Q in the ranges considered. Therefore, when the horizontal permeability is much less than the vertical permeability, the onset of convective instability is always delayed. Thus anisotropy in permeability stabilizes the system in both the presence and absence of a variable gravity field, when $K_1<1$, that is, when the permeability in the x co-ordinate direction is less than that in the z co-ordinate direction.

2 $Q=0$:

(i) It can be seen from Fig. 3 that, (as in the isotropic case), an increase in the horizontal thermal Rayleigh number imparts stability to the system for all values of η, when $Q=0$.

(ii) $R_{HT}=0$: From Fig. 3 it is observed that an increase in η above -1 destabilizes the system, in the absence of internal heat source. The same trend is seen when the medium is isotropic.

(iii) $R_{HT}\neq 0$: From Fig. 3 it is noted that, as in the absence of horizontal temperature gradient, the onset of convective instability is advanced as η increases above -1, when $Q=0$. The dual role played by the increase in η above 0 seen in the isotropic case is not observed here, possibly due to domination of the stabilizing effect of anisotropy in permeability.

3 $Q\neq 0$:

(i) In the presence of internal heat source ($Q=1.5$), as in its absence, an increase in the horizontal thermal Rayleigh number stabilizes the system for all values of the variable gravity parameter.

(ii) $R_{HT}=0$: As in the absence of internal heat source, the system is most stable when the variable gravity parameter η takes the value -1 and an increase in η above -1 advances the onset of convective instability. The same behavior is seen when the medium is isotropic.

(iii) $R_{HT}\neq 0$: When the medium is anisotropic in permeability (and when it is isotropic) an increase in the variable gravity parameter above -1 destabilizes the system for all values of the horizontal thermal Rayleigh number, when $Q\neq 0$.

(iv) Comparison of the cases $Q=0$ and $Q\neq 0$: It is seen from Fig. 3 that, as for an isotropic medium, an increase in the internal heat source parameter destabilizes the system when η is nonnegative and stabilizes it when η is positive.

Since the critical Rayleigh numbers for the isotropic porous medium are greater than that for Case 2(a) and less than that of Case 2(b), the effect of horizontal isotropy in permeability is to destabilize the system, whereas the effect of horizontal isotropy in diffusivity is to stabilize the system, in both the presence and absence of a variable gravity field (where it is assumed that K_1 and κ_1 are both less than 1).

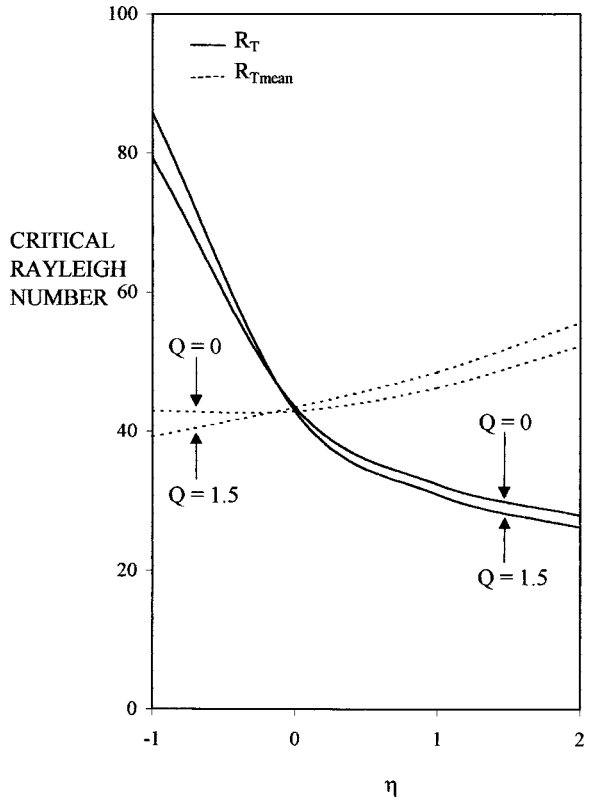

Fig. 7 Relationship between R_{Tmean} and R_T ($R_{HT}=40$, $K_1=0.1$, $\kappa_1=0.1$)

(c) Effect of Complete Anisotropy ($K_1 \neq 1, \kappa_1 \neq 1$). In the case of complete anisotropy, a comparison of Figs. 4 and 6 reveal that a decrease in κ_1 destabilizes the system, while Figs. 5 and 6 show that a decrease in K_1 stabilizes the system (except when $\eta=2$ and $R_{HT}=40$). Further, Figs. 4–6 show that the effect of the variable gravity field on the critical Rayleigh number when the medium is completely anisotropic is similar to that when the medium is horizontally isotropic in diffusivity.

In keeping with, and in order to compare with the current literature on convective instability under variable gravitational field (Chen and Chen [8] and Kaloni and Qiao [11]), the results obtained by considering the Rayleigh number based on the gravity level at the lower wall, have been discussed above. In the absence of inclined temperature gradient (and when $K_1=\kappa_1=1$, $Q=0$), the trends observed in the present analysis are in agreement with those reported by Chen and Chen [8], who investigated the onset of salt finger convection in a pure fluid under a variable gravity field. Further, the results obtained in the present analysis with $\eta=-1$, $Q=0$, $K_1=\kappa_1=1$ coincide exactly with the linear stability limits furnished by Kaloni and Qiao [11].

It may be argued that, in investigating the effect of one of the factors in a dimensionless parameter, its influence must be studied by considering its mean value in the dimensionless parameter. Here, if R_{Tmean} is the Rayleigh number based on the arithmetic mean of the gravitational acceleration in the layer, then it is seen that, when η is negative R_{Tmean} is less than R_T. When η is positive the opposite effect is seen. The relationship between R_{Tmean} and R_T, for typical values of η, Q, K_1, κ_1, and R_{HT} is shown in Fig. 7.

5 Conclusion

For the range of parameters under consideration (R_{HT} varying from 0 to 40, $Q=0$ and 1.5, $\eta=-1$, 0, 1, 2, $K_1=1$, 0.2, 0.1, and $\kappa_1=1$, 0.5, 0.1) it is seen that, in the absence of a variable gravity field, an increase in the horizontal thermal Rayleigh number delays the onset of convective instability, and an increase in the heat generation due to internal heat source advances it, for all values of the anisotropy parameters considered. When the variable gravity parameter takes positive values ($\eta=1$, 2) an increase in the horizontal temperature gradient always stabilizes the system, except when the medium is horizontally isotropic in permeability (when it initially stabilizes and then destabilizes it), and an increase in the internal heat source parameter always advances the onset of convective instability, in both isotropic and anisotropic porous media. When the variable gravity parameter is negative an increase in the horizontal temperature gradient imparts stability to the system, and an increase in the internal heat source parameter also stabilizes it.

In the absence and presence of internal heat source, an increase in the variable gravity parameter above -1 advances the onset of convective instability, in both isotropic and anisotropic porous media, when there is no inclined temperature gradient. However in the presence of an inclined temperature gradient, an increase in the variable gravity parameter above 0 plays a dual role in determining the stability of the system when there is no internal heat source, both when the porous medium is isotropic and when it is horizontally isotropic in permeability.

It is seen that a decrease in κ_1 destabilizes the system, while that in K_1 stabilizes it (except in the completely anisotropic case).

Acknowledgment

The authors thank Dr. K. S. Venkatakrishnan for his help in computational work. The authors are grateful to the reviewers for their valuable suggestions, which greatly helped in improving the quality of the article.

Nomenclature

c = specific heat
c_p = specific heat at constant pressure
d = depth of the porous layer
D = differential operator d/dz
∇ = $\partial/\partial x\mathbf{i}+\partial/\partial y\mathbf{j}+\partial/\partial z\mathbf{k}$
∇^2 = $\partial^2/\partial x^2+\partial^2/\partial y^2+\partial^2/\partial z^2$
∇_1^2 = $\partial^2/\partial x^2+\partial^2/\partial y^2$
$\mathbf{g}$ = gravity vector, $-g_0(1+\eta z)\mathbf{k}$
$\mathbf{i},\mathbf{j},\mathbf{k}$ = unit co-ordinate vectors, aligned with (x,y,z) directions, respectively
K_x, K_y, K_z = permeability in the x, y, and z co-ordinate directions
K_1 = anisotropy parameter, K_x/K_z
k_x, k_y = wave numbers in the x and y directions
k = overall horizontal wave number, $(k_x^2+k_y^2)^{1/2}$
N = order of Galerkin approximation
p = pressure
$\mathbf{q}$ = seepage velocity vector, (u,v,w)
$\mathbf{q}_1$ = $(u/K_1, v/K_1, w)$
Q = internal heat source parameter
R_T = vertical thermal Rayleigh number, $g_0\beta_T\Delta T K_z d/(\kappa_z\nu)$
R_{HT} = horizontal thermal Rayleigh number, $g_0\beta_T\alpha_T K_z d^2/(\kappa_z\nu)$
t = time
T = temperature
T_0 = standard temperature
ΔT = temperature difference between the lower and upper boundaries
$\tilde{T}(z)$ = vertical variation of the basic temperature
$U(z)$ = x component of basic velocity
x,y,z = co-ordinate directions

Greek Symbols

α_T = horizontal temperature gradient

β_T = coefficient of volume expansion
η = variable gravity parameter
θ = temperature perturbation
$\kappa_x, \kappa_y, \kappa_z$ = thermal diffusivity in the x, y, and z co-ordinate directions
κ_1 = anisotropy parameter, κ_x / κ_z
$\lambda_x, \lambda_y, \lambda_z$ = thermal conductivity in the x, y, and z co-ordinate directions
μ = coefficient of viscosity
ν = kinematic viscosity
ρ = density
ρ_0 = density at temperature T_0
σ = frequency of the disturbance
σ_r, σ_i = real and imaginary parts of σ

Subscripts

b = basic state
f = fluid
m = solid-fluid mixture

Superscripts

$*$ = dimensionless quantities
$\hat{}$ = perturbation quantities

References

[1] Manole, D. M., and Lage, J. L., 1995, ''Numerical Simulation of Supercritical Hadley Circulation, Within a Porous Layer Induced by Inclined Temperature Gradients,'' Int. J. Heat Mass Transf., **38**, No. 14, pp. 2583–2593.

[2] Lage, J. L., and Nield, D. A., 1998, ''Convection Induced by Inclined Gradients in a Shallow Porous Medium Layer,'' J. Porous Media, **1**, No. 1, pp. 57–69.

[3] Saunders, B. V., Murray, B. T., McFadden, G. B., Coriell, S. R., and Wheeler, A. A., 1992, ''The Effect of Gravity Modulation on Thermosolutal Convection in an Infinite Layer of Fluid,'' Phys. Fluids A, **4**, No. 6, pp. 1176–1189.

[4] Clever, R., Schubert, G., and Busse, F. H., 1993, ''Two-Dimensional Oscillatory Convection in a Gravitationally Modulated Fluid Layer,'' J. Fluid Mech., **253**, pp. 663–680.

[5] Rees, D. A. S., and Pop, I., 2000, ''The Effect of *g*-Jitter on Vertical Free Convection Boundary-Layer Flow in Porous Media,'' Int. Commun. Heat Mass Transfer, **27**, No. 3, pp. 415–424.

[6] Pradhan, G. K., and Samal, P. C., 1987, ''Thermal Stability of a Fluid Layer Under Variable Body Forces,'' J. Math. Anal. Appl., **122**, pp. 487–495.

[7] Rodot, H., Regel, L. L., and Turtchaninov, A. M., 1990, ''Crystal Growth of IV–VI Semiconductors in a Centrifuge,'' J. Cryst. Growth, **104**, pp. 280–284.

[8] Chen, C. F., and Chen, F., 1992, ''Onset of Salt Finger Convection in a Gravity Gradient,'' Phys. Fluids A, **4**, No. 2, pp. 451–452.

[9] Straughan, B., 1989, ''Convection in a Variable Gravity Field,'' J. Math. Anal. Appl., **140**, pp. 467–475.

[10] Rionero, S., and Straughan, B., 1990, ''Convection in a Porous Medium With Internal Heat Source and Variable Gravity Effects,'' Int. J. Eng. Sci., **28**, No. 6, pp. 497–503.

[11] Kaloni, P. N., and Qiao, Z., 2001, ''Non-Linear Convection in a Porous Medium With Inclined Temperature and Variable Gravity Effects,'' Int. J. Heat Mass Transf., **44**, No. 8, pp. 1585–1591.

[12] Alex, S. M., and Patil, P. R., 1999, ''Convection in a Porous Medium With Inclined Temperature Gradient in a Variable Gravity Field,'' J. Energy, Heat Mass Transfer, **21**, pp. 145–156.

[13] Alex, S. M., and Patil, P. R., ''Effect of Variable Gravity Field on Thermal Instability in a Porous Medium With Inclined Temperature Gradient and Vertical Throughflow,'' J. Porous Media, accepted for publication.

[14] Degan, G., Vasseur, P., and Bilgen, E., 1995, ''Convective Heat Transfer in a Vertical Anisotropic Porous Layer,'' Int. J. Heat Mass Transf., **38**, No. 11, pp. 1975–1987.

[15] Neale, G., 1977, ''Degrees of Anisotropy for Fluid Flow and Diffusion (Electrical Conduction) Through Anisotropic Porous Media,'' AIChE J., **23**, pp. 56–62.

[16] Nield, D. A., 1991, ''Convection in a Porous Medium With Inclined Temperature Gradient,'' Int. J. Heat Mass Transf., **34**, No. 1, pp. 87–92.

[17] Parthiban, C., and Patil, P. R., 1997, ''Thermal Instability in an Anisotropic Porous Medium With Internal Heat Source and Inclined Temperature Gradient,'' Int. Commun. Heat Mass Transfer, **24**, No. 7, pp. 1049–1058.

[18] Nield, D. A., 1994, ''Convection in a Porous Medium With Inclined Temperature Gradient: Additional Results,'' Int. J. Heat Mass Transf., **37**, No. 18, pp. 3021–3025.

Influence of Irradiation Time, Particle Sizes, and Initial Moisture Content During Microwave Drying of Multi-Layered Capillary Porous Materials

P. Ratanadecho

K. Aoki

M. Akahori

Department of Mechanical Engineering,
Nagaoka University of Technology,
1603-1, Kamitomioka, Nagaoka,
Niigata, 940-2188, Japan

The drying of capillary porous materials by microwave with rectangular waveguide has been investigated numerically and experimentally. Most importantly, it focuses on the investigation of the distributions of electric field, temperature and moisture profiles within the capillary porous materials. The measurements of temperature and moisture distributions within the capillary porous materials provide a good basis for understanding of the microwave drying process. The mathematical model gives qualitatively comparable trends to experimental data. The calculations of electromagnetic fields inside the rectangular waveguide and the capillary porous materials show that the variation of particle sizes and initial moisture content changes the degree of penetration and rate of microwave power absorbed within the sample. Further, the small particle size leads to much higher capillary pressure resulting in a faster drying time. [DOI: 10.1115/1.1423951]

Keywords: Electromagnetic, Heat Transfer, Microwave, Moisture, Numerical Methods, Packed Beds, Porous Media

1 Introduction

A convenient starting point of drying theory is a recent work by Whitaker [1], who derived locally volume averaged conservation equations for two-phase capillary flow in porous media. In the past decade, microwave technology has been applied to many processes. Microwave drying is one of the most interesting methods for drying materials. Unlike other heat sources such as conventional heating, where heat is applied externally to the surface of the material, microwave irradiation penetrates and simultaneously heats the bulk of the material. When properly designed, microwave drying systems have several advantages over conventional mechanical methods, such as reducing the drying times, high energy efficiency, and offer improvements in product quality for various industrial applications (Feng et al. [2] and Feng et al. [3]).

Microwave radiations have typical wavelengths and a penetration depth of roughly the same order of magnitude, commensurate with the size of the sample to be dried. For instance, the wavelength of an electromagnetic at frequency of 2.45 GHz is 12.4 cm and the penetration depth, that is the distance from the surface of the sample at which the power drop to e^{-1} from its initial value, is 2 cm of water at 60°C. Thus, a volumetric heat source is dissipated through the sample due to the characteristic of dielectric losses [4]. Further, the moisture and temperature distributions for microwave drying can appear to have uniform shapes, due to this phenomenon.

There are many successful examples of microwave application, including the drying of foods, drying of textiles, freeze drying process, and vulcanizations of rubber. Metaxas and Meredith [5] provide good introduction to heat and mass transfers in microwave processing. A number of other analyses of microwave heating processes have appeared in the recent literatures (Ayappa et al. [6], Li et al. [7] and Clemens et al. [8]). The one-dimensional analysis for heat and mass transport during microwave drying in porous material has been studied by Gori et al. [9], Perkin et al. [10] and Turner et al. [11].

Of all models above, the microwave power absorbed was assumed to decay exponentially into the sample following the Lambert's law. However, this assumption is valid for the large dimension samples (depth of bed, $d_P \approx 2.7\times$ penetration depth) [12,13]. For the small samples heat in a faster rate by microwave due to the resonance of standing waves whereas resonance is completely absent for greater length scales. In perspective, Lambert's exponential decay law cannot predict resonance. Therefore, the spatial variations of the electromagnetic field within small samples must be obtained by solution of the Maxwell's equations [14].

The two-dimensional models of interaction between electromagnetic field and dielectric materials have been used previously to study numerous heating processes in a variety of microwave applicator configurations such as rectangular waveguide and cavities ([14–16]). However, previous investigation considered only a single-layer sample. Indeed, little effort has been reported on the study of drying process of multi-layered materials in microwave fields, especially a complete comparison between mathematical. In this work, samples in a microwave cavity of 2.45 GHz and TE_{10} mode were packed beds of glass beads and water. The effects of the irradiation time, particle sizes and the variation of initial moisture content on microwave drying kinetics at long stages of drying process were clarified in detail. The result presented here provides a basis for fundamental understanding of microwave drying of capillary porous materials.

2 Experimental Apparatus

Figure 1 shows the experimental apparatus used. The microwave system was a monochromatic wave of TE_{10} mode operating

Contributed by the Heat Transfer Division for publication in the JOURNAL OF HEAT TRANSFER. Manuscript received by the Heat Transfer Division April 10, 2001; revision received September 10, 2001. Associate Editor: H. Bau.

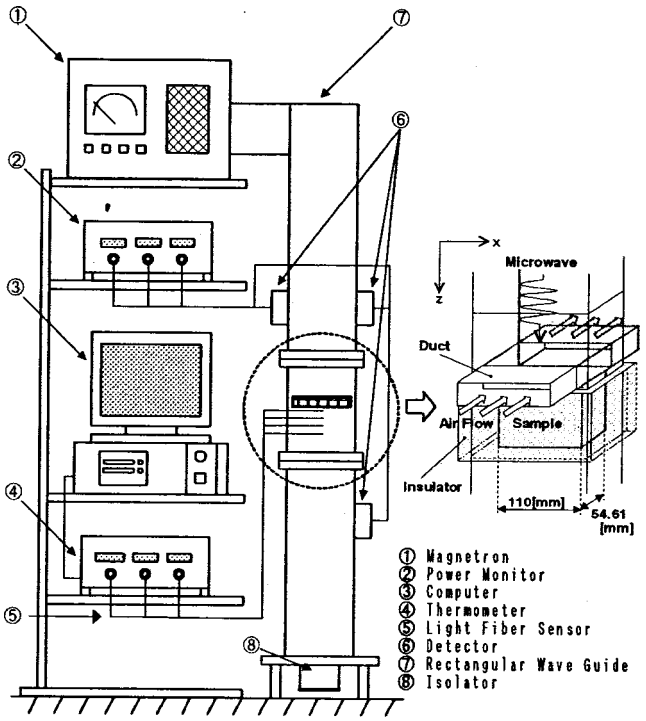

(*a*)

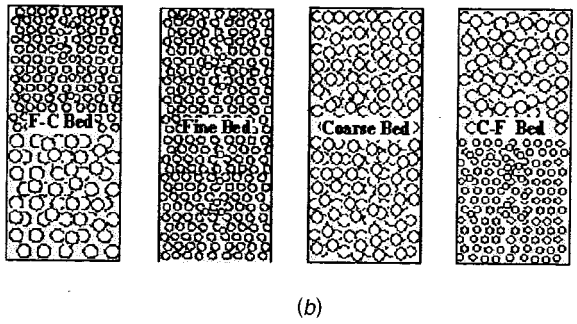

(*b*)

Fig. 1 Schematic of experimental facility: (*a*) equipment setup; and (*b*) multi-layered porous packed bed (Sample)

at a frequency of 2.45 GHz. Microwave energy was generated by magnetron (Micro Denshi Co., model UM-1500, Tokyo, Japan), it was transmitted along the *z*-direction of the rectangular waveguide with inside dimensions of 110 mm×54.61 mm toward a water load that was situated at the end of the waveguide. The water load (lower absorbing boundary) ensured that only a minimal amount of microwave was reflected back to the sample. Also, an isolator (upper absorbing boundary) was used to trap any microwave reflected from the sample to prevent it from damaging the magnetron. Output of magnetron was adjusted at 50 W. The powers of incident, reflected and transmitted waves were measured by a wattmeter using a directional coupler (Micro Denshi Co., model DR-5000, Tokyo, Japan).

As shown in Fig. 1(*b*), the samples were porous packed bed, which compose of glass beads and water. A sample container was made from polypropylene with a thickness of 0.75 mm, it did not absorb microwave energy. In this study, the voids occupy from a fraction up to 38 percent of the whole volume of packed beds. The samples were prepared in two configurations: a single-layered packed bed ($d=0.15$ mm, $d=1.0$ mm, and $d_P=50$ mm) and a two-layered packed bed, respectively. In the case of two-layered packed bed was classified in two configurations: F-C bed (attaching fine bed ($d=0.15$ mm, $d_P=12.5$ mm) on coarse bed ($d=0.4$ mm, $d_P=22.5$ mm)), and C-F bed (attaching fine bed ($d=0.15$ mm, $d_P=22.5$ mm) under coarse bed ($d=0.4$ mm, $d_P=22.5$ mm)), respectively. The sample of packed bed was inserted in the rectangular waveguide. The distributions of temperature within the sample were measured using fiberoptic (LUXTRON Fluroptic Thermometer, Model 790, Santa Clara, Canada, accurate to ±0.5°C), which were placed in the center of the sample at each 5 mm interval. An infrared camera was also used to measure the distributions of temperature within the sample in *x*-*z* plane. In each test run, the weight loss of the sample was measured by mass scale with high precision. The water saturations in the packed bed were defined as the fraction of the volume occupied by water to volume of the pores. They were obtained by weighing dry and wet mass of the sample which were cut out in volume (four positions) of about 110 mm×54.61 mm×12.5 mm at the end of each run. The water saturation formula can be described in the following form:

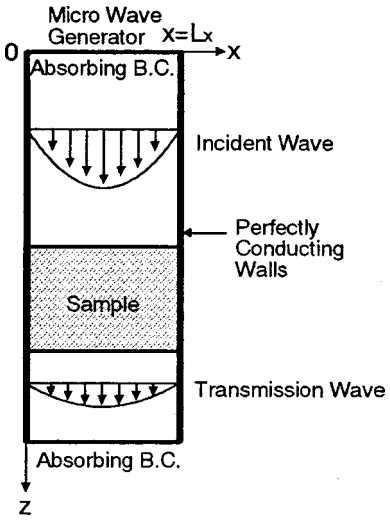

Fig. 2 Physical model

$$s=\frac{\rho_p(1-\phi)(m_w-m_d)}{\rho_l \phi m_d}, \tag{1}$$

where s is water saturation, m_w and m_d are wet and dry mass of the sample, respectively, ϕ is porosity, ρ_l and ρ_p are densities of water and particle, respectively. During the experimental microwave drying processes, the uncertainty of our data might come from the variations in humidity, room temperature and human errors. The uncertainty in drying kinetics was assumed to result from errors in the measured weight of the sample. The calculated drying kinetic uncertainties in all tests were less than 3 percent. The uncertainly in temperature was assumed to result from errors in measured input power, ambient temperature and ambient humidity. The calculated uncertainty associated with temperature was less than 2.85 percent.

3 Analysis of Mathematical Modeling

3.1 Analysis of Electromagnetic Model. Figure 2 shows the physical model used for analyzing microwave drying of capillary porous materials in a rectangular waveguide. The proposed model is based on the following assumptions: (1) since the microwave field in the TE_{10} mode has no variation of field in the direction between the broad faces, a two-dimensional model over the *x*-*z* plane is applicable to analysis of electromagnetic field inside a rectangular waveguide [14]; (2) the absorption of microwave energy by the cavity (including air) in the rectangular waveguide is negligible; (3) the walls of a rectangular waveguide are perfect

conductors; and (4) The effect of the sample container (made of polypropylene) on the electromagnetic field can be neglected because it did not absorb microwave energy.

Basic Equations. The basic equations for the electromagnetic field are based on the well-known Maxwell relations. For the microwave of TE_{10} mode [14], the governing equations can be written in term of the component notations of electric and magnetic field intensities:

$$\frac{\partial E_y}{\partial z}=\mu\frac{\partial H_x}{\partial t} \tag{2}$$

$$\frac{\partial E_y}{\partial x}=-\mu\frac{\partial H_z}{\partial t} \tag{3}$$

$$-\left(\frac{\partial H_z}{\partial x}-\frac{\partial H_x}{\partial z}\right)=\sigma E_y+\varepsilon\frac{\partial E_y}{\partial t} \tag{4}$$

where

$$\varepsilon=\varepsilon_0\varepsilon_r,\quad \mu=\mu_0\mu_r,\quad \sigma=2\pi f\varepsilon\tan\delta. \tag{5}$$

In this study, the effects on the overall drying kinetics are examined by selecting the dielectric properties as a function of moisture content and temperature. In order to determine the functional dependence of the combination of moisture content and temperature, the theory surrounding mixing formulas is used [17], in which the volume fractions (v) of water saturation, water vapor and glass particle were considered, as follows:

$$\varepsilon_r(s,T)=(\varepsilon_r'(s,T)-j\varepsilon_r''(s,T)) \tag{6}$$

where

$$[\varepsilon_r'(s,T)]^m=\sum_{i=1}^{3}v_i[\varepsilon_{ri}'(T)]^m=\phi s[\varepsilon_{rl}'(T)]^m+\phi(1-s)[\varepsilon_{ra}']^m+(1-\phi)[\varepsilon_{rp}']^m \tag{7}$$

$$[\varepsilon_r''(s,T)]^m=\sum_{i=1}^{3}v_i[\varepsilon_{ri}''(T)]^m=\phi s[\varepsilon_{rl}''(T)]^m+\phi(1-s)[\varepsilon_{ra}'']^m+(1-\phi)[\varepsilon_{rp}'']^m. \tag{8}$$

In above equations, the parameter m is likely to vary over the range 0–1, as suggested by Wang and Schmugge [17]. A value of $m=0.33$ has been used throughout in this study. The loss tangent coefficient can be expressed as follow:

$$\tan\delta=\frac{\varepsilon_r''(s,T)}{\varepsilon_r'(s,T)}. \tag{9}$$

Boundary Conditions. Corresponding to the physical model shown in Fig. 2, boundary conditions are given in the following list.

(a) Perfectly conducting boundaries; boundary conditions on the inner wall surface of a rectangular waveguide are given by using Faraday's law and Gauss' theorem:

$$E_t=0,\quad H_n=0. \tag{10}$$

(b) Continuity boundary condition; boundary conditions along the interface between different materials, for example between air and dielectric material surface, are given by using Ampere's law and Gauss' theorem:

$$E_t=E_t',\quad H_t=H_t',\quad D_n=D_n',\quad B_n=B_n'. \tag{11}$$

(c) Absorbing boundary condition; at both ends of the rectangular waveguide, the first order absorbing conditions proposed by Mur [18] are applied:

$$\frac{\partial E_y}{\partial t}=\pm v\frac{\partial E_y}{\partial z}. \tag{12}$$

Here, the symbol $\pm$ represents forward or backward waves and v is phase velocity of the microwave.

Oscillation of the electric and magnetic field intensities by magnetron; incident wave due to magnetron is given by the following equations:

$$E_y=E_{\text{yin}}\sin\left(\frac{\pi x}{L_x}\right)\sin(2\pi ft),\quad H_x=\frac{E_{\text{yin}}}{Z_H}\sin\left(\frac{\pi x}{L_x}\right)\sin(2\pi ft). \tag{13}$$

Z_H is the wave impedance defined as

$$Z_H=\frac{\lambda_g Z_I}{\lambda}=\frac{\lambda_g}{\lambda}\sqrt{\frac{\mu}{\varepsilon}}. \tag{14}$$

3.2 Analysis of Heat and Mass Transport Models. A schematic diagram of model is shown in Fig. 2. By conservations of mass and energy in the sample, the governing equation of mass and energy for all phases can be derived by using the volume average technique. The main transport mechanisms that enable moisture movement during microwave drying of sample are: liquid flow driven by capillary pressure gradient and gravity while the vapor is driven by the gradient of the partial pressure of the evaporating species. In this study, several simplifying assumptions are made in order to obtain a closed set of governing macroscopic equations: (1) the capillary porous material is rigid, no chemical reactions take place in the sample; (2) local thermodynamic equilibrium is assumed; (3) simultaneous heat and mass transport occurs at a constant pressure, where the dominant mechanisms are capillary transport, vapor diffusion and gravity: such is generally the case in drying of capillary porous medium at atmospheric pressure when the temperature is lower than the boiling point [19]; (4) the gas binary mixture of air and water vapor behaves like an ideal gas; and (5) corresponding to electromagnetic field, temperature and moisture profiles also can be assumed to be two-dimensional in the x-z plane.

Basic Equations. The governing equations based on a volume average approach led to the following conservation equations describing the drying process of capillary porous materials:

Mass Conservation.

$$\phi\frac{\partial}{\partial t}\{\rho_l s+\rho_v(1-s)\}+\frac{\partial}{\partial x}[\rho_l u_l+\rho_v u_v]+\frac{\partial}{\partial z}[\rho_l w_l+\rho_v w_v]=0 \tag{15}$$

Energy Conservation.

$$\frac{\partial}{\partial t}[(\rho c_p)_T T]+\nabla[\{\rho_l c_{pl}\mathbf{u_l}+(\rho_a c_{pa}+\rho_v c_{pv})\mathbf{u_g}\}T]+H_v\dot{n}=-\nabla q+Q, \tag{16}$$

where Q is the microwave power absorbed term, which is a function of the electric field and defined as [8]:

$$Q=2\pi\cdot f\cdot\varepsilon_0\cdot\varepsilon_r(\tan\delta)E_y^2 \tag{17}$$

Phenomenological Relations.

In order to complete the system of equations, the expressions for the superficial average velocity of the liquid and gas phases the generalized Darcy's law in the following vector form is used:

$$\mathbf{u_l}=-\frac{KK_{rl}}{\mu_l}[\nabla p_g-\nabla p_c-\rho_l\mathbf{g}],\quad \mathbf{u_g}=-\frac{KK_{rg}}{\mu_g}[\nabla p_g-\rho_g\mathbf{g}] \tag{18}$$

the velocity of vapor water and air phase the generalized Fick's law for a two-component gas mixture can be expressed in vector form as

$$\rho_v\mathbf{u_v}=\rho_v\mathbf{u_g}-\rho_g D_m\nabla\left(\frac{\rho_v}{\rho_g}\right),\quad \rho_a\mathbf{u_a}=\rho_a\mathbf{u_g}-\rho_g D_m\nabla\left(\frac{\rho_a}{\rho_g}\right), \tag{19}$$

where D_m is the effective molecular mass diffusion [20]:

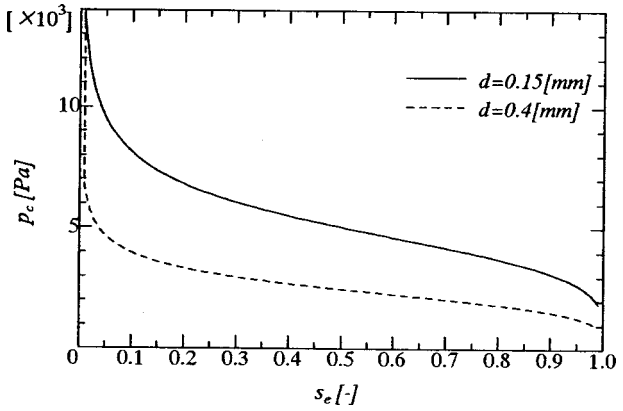

Fig. 3 Typical relationship between, p_c and s_e

$$D_m = \frac{2\phi}{3-\phi}(1-s)D_0. \tag{20}$$

Fourier's law is used to define the heat flux through the porous materials

$$q = -\lambda_{\text{eff}}\nabla T \tag{21}$$

Equilibrium Relations.

The system of conservation equations obtained for multiphase transport mode requires constitutive equation for relative permeabilities K_r, capillary pressure p_c, capillary pressure functions or Leverett functions $J(s_e)$, and the effective thermal conductivity λ_{eff}. A typical set of constitutive relationships for liquid and gas system given by [21]

$$K_{rl} = s_e^3, \quad K_{rg} = (1-s_e)^3, \tag{22}$$

where s_e is the effective water saturation considered the irreducible water saturation s_{ir} and defined by

$$s_e = \frac{s-s_{ir}}{1-s_{ir}}. \tag{23}$$

The capillary pressure p_c is further assumed to be a function of water saturation or Leverett functions $J(s_e)$ and surface tension $\xi(T)$. The Leverett functions $J(s_e)$ is dependent on the internal structure of the porous materials and defined by [22]:

$$J(s_e) = 0.325(1/s_e - 1)^{0.217}. \tag{24}$$

The relationship between the capillary pressure and the water saturation is defined by using Leverett functions $J(s_e)$:

$$p_c = p_g - p_l = \frac{\xi(T)}{\sqrt{K/\phi}}J(s_e). \tag{25}$$

Figure 3 shows the typical moisture characteristic curve for different particle sizes obtained from present experiments. It is seen that, in the case of the same water saturation, a smaller particle size corresponds to a higher capillary pressure.

Based on the experimental results of Aoki et al. [22] using a glass beads unsaturated with water, the effective thermal conductivity is further assumed to be a function of water saturation and defined by

$$\lambda_{\text{eff}} = \frac{0.8}{1+3.78e^{-5.95s}} \tag{26}$$

After some mathematical manipulations, the two-dimensional systems of two non-linear coupled partial differential equations which govern the microwave drying process are given by

Moisture Transport Equation.

$$\phi\frac{\partial}{\partial t}\{\rho_l s + \rho_v(1-s)\} + \frac{\partial}{\partial x}\left[\rho_l\frac{KK_{rl}}{\mu_l}\left(\frac{\partial p_c}{\partial x}\right) - D_m\frac{\partial \rho_v}{\partial x}\right] + \frac{\partial}{\partial z}\left[\rho_l\frac{KK_{rl}}{\mu_l}\left(\frac{\partial p_c}{\partial z}+\rho_l g_z\right) + \rho_v\frac{KK_{rg}}{\mu_g}(\rho_g g_z) - D_m\frac{\partial \rho_v}{\partial z}\right] = 0 \tag{27}$$

Heat Transport Equation.

$$\frac{\partial}{\partial t}[(\rho C_p)_T T] + \frac{\partial}{\partial x}[\{\rho_l C_{pl}u_l + (\rho_a C_{pa}+\rho_v C_{pv})u_g\}T] + \frac{\partial}{\partial z}[\{\rho_l C_{pl}w_l + (\rho_a C_{pa}+\rho_v C_{pv})w_g\}T] + H_v\dot{n} = \frac{\partial}{\partial x}\left[\lambda_{\text{eff}}\frac{\partial T}{\partial x}\right] + \frac{\partial}{\partial z}\left[\lambda_{\text{eff}}\frac{\partial T}{\partial z}\right] + Q, \tag{28}$$

where $(\rho C_p)_T$ is the effective heat capacitance of water-gas-matrix mixtures:

$$(\rho C_p)_T = \rho_l C_{pl}\phi s + \{(\rho C_p)_a + (\rho C_p)_v\}\phi(1-s) + \rho_p C_{pp}(1-\phi). \tag{29}$$

Also, the phase change term is given by

$$\dot{n} = \frac{\partial}{\partial t}\{\rho_v\phi(1-s)\} + \frac{\partial}{\partial x}\left[-D_m\frac{\partial \rho_v}{\partial x}\right] + \frac{\partial}{\partial z}\left[\rho_v\frac{KK_{rg}}{\mu_g}\rho_g g_z - D_m\frac{\partial \rho_v}{\partial z}\right]. \tag{30}$$

Boundary and Initial Conditions.

The boundary conditions proposed for the exchange of energy and mass at the open boundary can be described in the following form:

$$-\lambda\frac{\partial T}{\partial z} = h_c(T-T_a) + \dot{n}H_v \tag{31}$$

$$\rho_l w_l + \rho_v w_v = h_m(\rho - \rho_a). \tag{32}$$

Considering the boundary conditions at the closed boundary that no heat and mass exchange take place

$$\frac{\partial T}{\partial x} = \frac{\partial T}{\partial z} = 0, \quad \frac{\partial u}{\partial x} = \frac{\partial w}{\partial z} = 0. \tag{33}$$

The initial conditions are given by uniform initial temperature and moisture content.

4 Numerical Procedure

In order to predict the electromagnetic field (Eqs. (2)–(4)), a finite difference time domain (FDTD) method is applied. The system of nonlinear partial differential equations (Eqs. (27)–(33)) was solved by the method of finite differences based on the notion of control volumes as described by Patankar [23]. The Newton-Raphson method was employed at each iteration to quicken the convergence. Initially, the temperature and moisture profiles were set to be equal at all nodes at values corresponding to the measured capillary porous medium conditions. Considering the microwave drying in TE_{10} mode, it is the lowest mode of the supported microwave field for waves transmitted in the present rectangular waveguide without power dissipation. The type of wave mode is prescribed by the frequency and waveguide dimensions. Spatial and temporal resolution was selected to ensure of stability and accuracy. To insure stability of the time-stepping algorithm, Δt was chosen to satisfy the courant stability condition [15]:

$$\Delta t \leqslant \frac{\sqrt{(\Delta x)^2 + (\Delta z)^2}}{v} \tag{34}$$

Table 1 The electromagnetic and thermo physical properties used in the computations [25]

$\varepsilon_0 = 8.85419\times10^{-12}$[F/m]	$\mu_0 = 4.0\pi\times10^{-7}$[H/m]
$\varepsilon_{ra} = 1.0$,	$\varepsilon_{rp} = 5.1$
$\mu_{ra} = 1.0$,	$\mu_{rp} = 1.0$,
$\tan\delta_a = 0.0$,	$\tan\delta_p = 0.01$ $\mu_{rl} = 1.0$
$\rho_a = 1.205$[kg/m^3],	$\rho_p = 2500.0$[kg/m^3], $\rho_l = 1000.0$[kg/m^3]
$C_{pa} = 1.007$[kJ/(kg K)],	$C_{pp} = 0.80$[kJ/(kg K)], $C_{pl} = 4.186$[kJ/(kg K)]
$\varepsilon_{rl} = 88.15 - 0.414T + (0.131\times10^{-2})T^2 - (0.046\times10^{-4})T^3$	$\tan\delta_l = 0.323 - (9.499\times10^{-3})T + (1.27\times10^{-4})T^2 - (6.13\times10^{-7})T^3$

and the spatial resolution of each cell defined as

$$\Delta x, \Delta z \leq \frac{\lambda_g}{10\sqrt{\varepsilon_r}}. \tag{35}$$

Corresponding to Eqs. (34) and (35), the calculation conditions were as follows: (1) because the propagating velocity of microwave is very fast compared with the rate of heat transfer, different time steps of $dt=1$ [ps] and 0.1 [s] were used for the computation of the electromagnetic field and temperature profile: the spatial step size is $dx=dz=1.0$ [mm]; (2) number of grid: $N=110$ (width) $\times200$ (length); and (3) relative errors in the iteration procedure of 10^{-8} were chosen. One aspect of model verification was to compare drying data from experiments run under different conditions with mathematical simulations using parameter values obtained from Table 1.

5 Results and Discussion

5.1 Simulation of Electric Field Inside a Rectangular Waveguide. In the beginning, to understand the detailed structures of electric field developed inside a rectangular waveguide, the numerical simulation of the following three cases are conducted: (1) rectangular waveguide is empty, its dielectric constant is unity (which corresponds to that of air); (2) rectangular waveguide is filled with sample (single-layered packed bed) with drying times of 15 min (early drying times); and (3) rectangular waveguide is filled with sample (single-layered packed bed) with drying times of 540 min (long drying times).

Figures 4–6 are the numerical simulation of electric field in TE_{10} mode along the center axis ($x=54.61$ mm) of rectangular waveguide after 10,000 time steps. In the figures, the vertical axis represents the intensity of the electric field E_y, which is normalized to the amplitude of the input electromagnetic wave, E_{yin}.

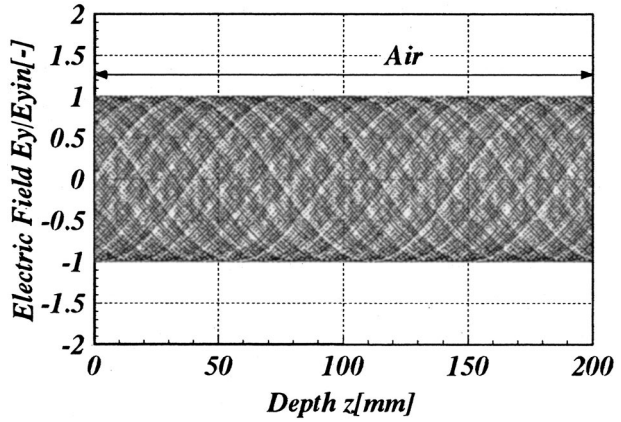

Fig. 4 Distribution of electric field for case of a rectangular waveguide is empty ($x=54.61$ mm)

Figure 4 shows the stationary wave inside the rectangular waveguide with completely absorbed power at the end of the rectangular waveguide (case 1). It is observed that a uniform wave is formed inside a rectangular waveguide. Figure 5 shows the wave distribution of the electric field when a dielectric material or sample is inserted in the rectangular waveguide (case 2). Within the sample, the electric field attenuates owing to energy absorption, and thereafter the absorbed energy is converted to the thermal energy, which increases the sample temperature. In the figure, the electric field with a small amplitude is formed within the sample waveguide. Furthermore, focusing attention of field pattern outside the sample (left hand side), a stronger standing wave with a larger amplitude is formed by interference between the forward wave and waves reflected from the surface of sample due to the different of dielectric properties of material (air and sample)

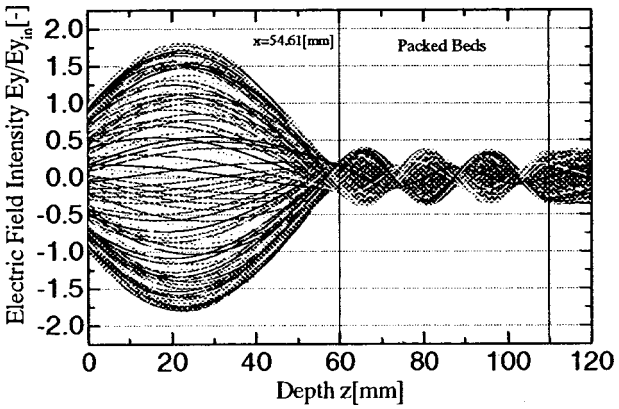

Fig. 5 Distribution of electric field for the sample inserted in the rectangular waveguide ($t=15$ min, $x=54.61$ mm)

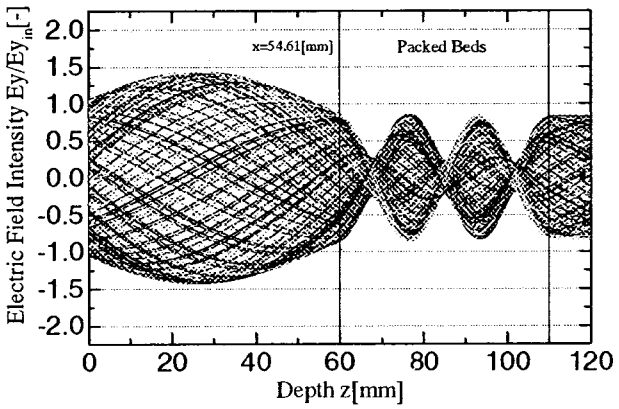

Fig. 6 Distribution of electric field for the sample inserted in the rectangular waveguide ($t=540$ min, $x=54.61$ mm)

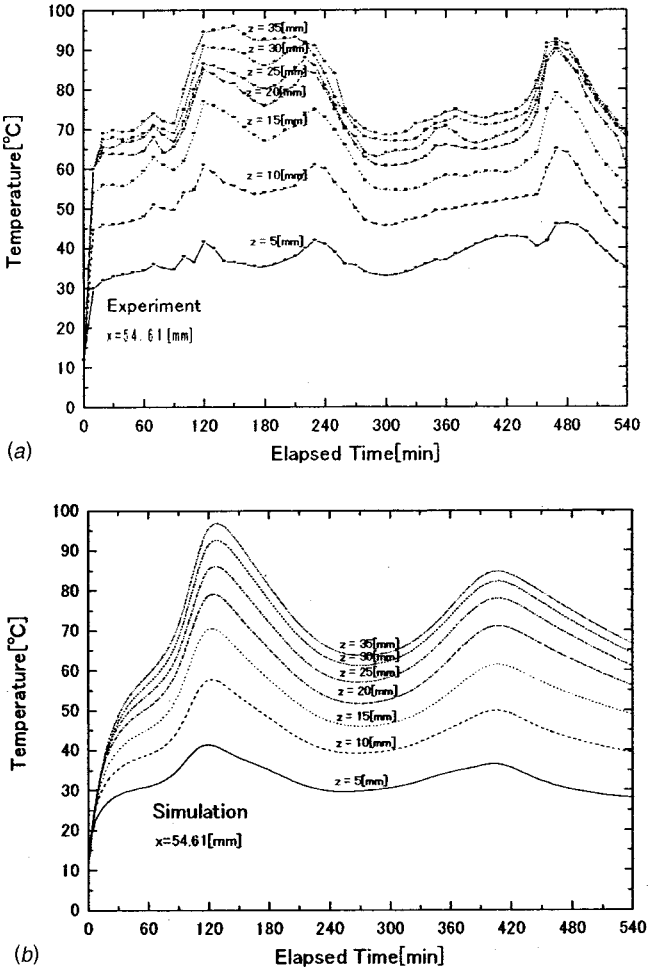

Fig. 7 Temperature profile in times at various depths ($P=50$ W, $d=0.15$ mm, $s_0=1.0$): (*a*) experiment; and (*b*) simulation

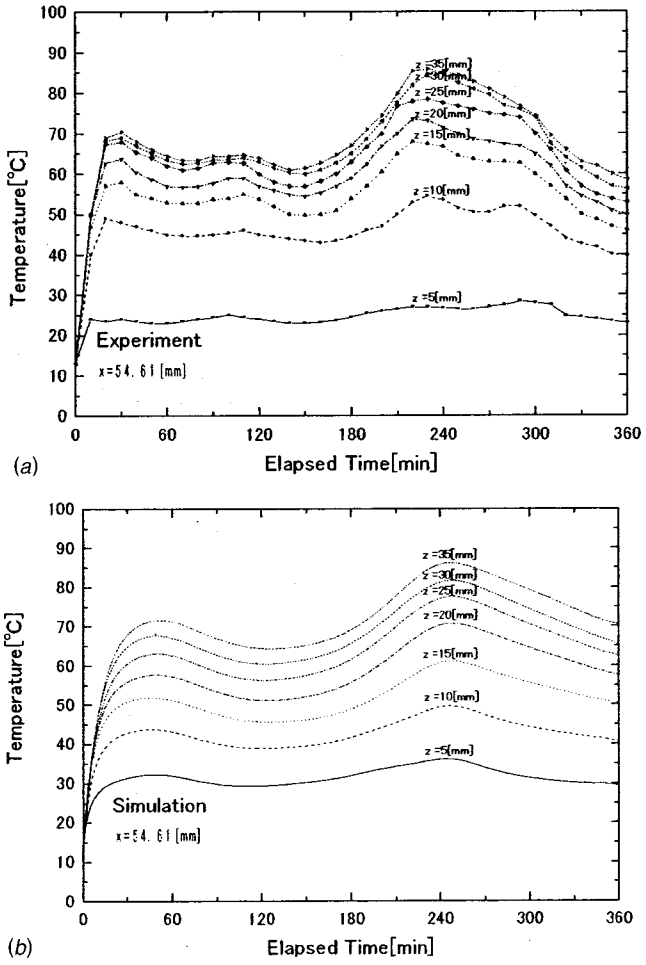

Fig. 8 Temperature profile in times at various depths ($P=50$ W, $d=0.15$ mm, $s_0=0.6$): (*a*) experiment; and (*b*) simulation

at this surface. Figure 6 shows the wave distribution of the electric field when a dielectric material or sample is inserted in the rectangular waveguide (case 3). In this case after a majority of the moisture level inside the sample has been removed, the effect of wave reflected from the surface of the sample is reduce which increases the large part of microwaves inside the sample. Consequently, the reflection and transmission components at each interface will contribute to the resonance of standing wave configuration with the larger amplitude and wave length inside the sample where the moisture content is small in comparison with previous cases.

5.2 Microwave Drying of Single-Layered Porous Packed Bed

The Distribution of Temperature Profiles Within the Sample. The predicted results are compared with experimental microwave drying data in Figs. 7–9, which corresponds to that of $T_0=10.4°C$, $T_a=10.4°C$, and $P=50$ W, along with the center axis ($x=54.61$ mm) of rectangular waveguide.

Figure 7(*a*) shows the temperature profiles measured by fiberoptic at various times and locations in the case of $s_0=1.0$ and $d=0.15$ mm ($\phi=0.385$). In contrast to that in conventional drying, microwave drying gives higher temperatures inside the drying sample while the surface temperature stays colder due to the cooling effect of surrounding air. At the same time the evaporation takes place at the surface of the sample at a lower temperature due to evaporative cooling. It is seen that the temperature profiles within the sample rise up steadily in the early stages of drying (about 90 min). Due to the large initial moisture content, the skin-depth heating effect causes a majority of microwave to be reflected from the surface during early irradiation stage (as referred to Fig. 5) resulting in a lower rate of microwave power absorbed in the interior (Fig. 10). As the drying process proceeds (about

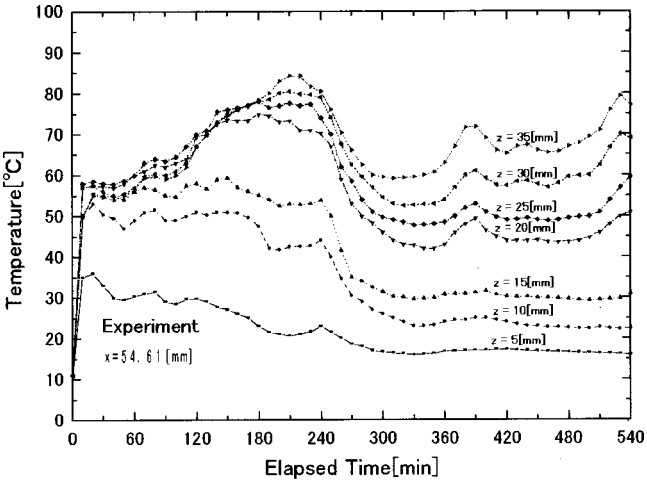

Fig. 9 Temperature profile in times at various depths (Experiment: $P=50$ W, $d=1.0$ mm, $s_0=1.0$)

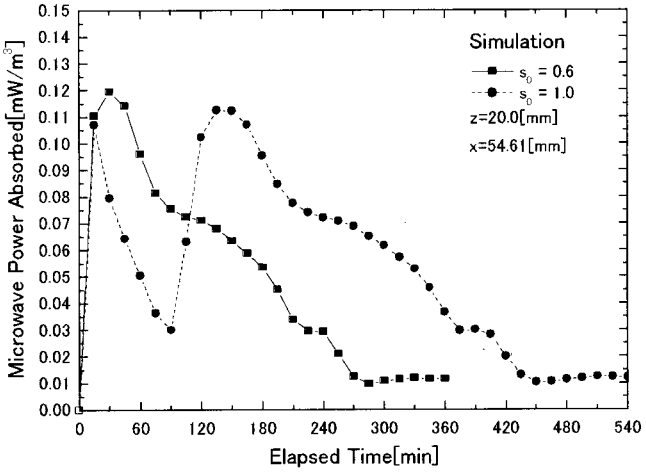

Fig. 10 Microwave power absorbed profile in times: (Simulation $P=50$ W, $d=0.15$ mm)

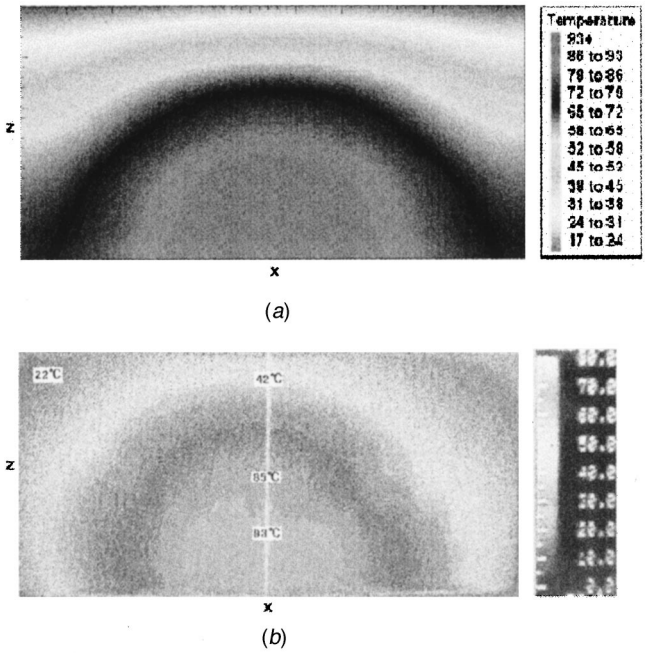

Fig. 11 Comparison between simulated results (*a*) and experimental results (*b*) of temperature distribution (°C) within the sample ($s_0=1.0$, $t=120$ min, $d=0.15$ mm, dimensions: 110 mm (x) ×50 mm (z))

90–240 min), after a majority of moisture content is removed from the sample, the microwave can penetrate further into the sample as material dries (as referred to Fig. 6) where the strength of the microwave power absorbed increases (Fig. 10). During this stage of drying, the behavior of dielectric properties is influenced primarily by that of moisture content, and heating becomes more volumetric. In time about 240 minutes, the temperature starts to drop, this is mainly due to fact that the moisture inside the sample is significantly reduced, reducing dielectric loss factor as well as microwave power absorbed (Fig. 10). However, at long stages of drying (about 480 min), the temperature increases rapidly due to the characteristic of dielectric loss factor, which becomes to dominant microwave drying at low moisture content where the stronger standing wave with a larger amplitude established within the sample [16], [24]. Nevertheless, near the end stages of drying as the majority of moisture content inside the sample is removed, this decreases the microwave power absorbed. Thus, equilibrium is reached between microwave drying and convective losses by lowering the sample temperature.

Figure 8(*a*) shows the temperature profiles measured by fiberoptic at various times and locations in the case of $s_0=0.6$ and $d=0.15$ mm ($\phi=0.385$). The temperature profiles within the sample rise up rapidly in the early stages of drying (about 27 min). This is because of the total rate of reflection wave is small in the early stages of drying, and a large part of microwave penetrates into the sample. Such pattern can lead to a much higher rate of microwave power absorbed in the interior compared with a previous case (Fig. 10). Later, the temperature starts to drop continuously since the rate of microwave absorption is lower after a majority of moisture content is removed from the sample. As the drying process proceeds (about 240 minutes) it would eventually cause the temperature level to increase again due to the characteristics of the dielectric loss factor that were explained in Fig. 7.

Figure 9 shows the temperature profiles measured by fiberoptic at various times and locations in the case of $s_0=1.0$ and $d=1.0$ mm. As the drying proceeds, the temperature profiles within the sample are different from those shown in Fig. 7. In this case, the temperature profiles have a rather unusual shape. This is because of the large particle size corresponding to a lower capillary pressure, the liquid water supply to surface by capillary action becomes insufficient to replace the liquid being evaporated. The latter arises from the fact that the drying layer took place on a front retreating from the surface into the interior of the sample. Furthermore, the combinations of hydrodynamic properties and dielectric properties cause a change in the location of the maximum temperature to occur, especially at the drying times about 45 min–180 min. This trend is more remarkable for large particle sizes having a lower capillary pressure. However, the vapor diffusion becomes strongly effective on the drying kinetics of the large particle sizes. Unfortunately, the lack of experimental data (permabilities and capillary pressure functions) for a large particle sizes so that, the drying kinetics predicted by the mathematical model were unrepresentative.

Additionally, it is evident from the results that the dielectric loss factor can become significant when microwave energy is utilized. The magnitude of this variable will directly affect the amount of microwave power absorbed within the sample during microwave drying process (Fig. 10). Further, for a more complete discussion on the evolution of the dielectric properties as a function of temperature and moisture content (Eqs. (6)–(9)), the reader is referred to Ratanadecho et al. [13].

The observation of temperature profiles depicted in Fig. 7 and Fig. 8 for the sample verify that the match between the experimental data (Fig. 7(*a*) and Fig. 8(*a*)) and simulated results (Fig. 7(*b*) and Fig. 8(*b*)) is qualitatively consistent, with the simulated results exhibiting the same overall trend of the experimental profiles. However, a fine wavy of the temperature distribution in the experimental results does not appear in the simulated results (Fig. 7(*a*) and Fig. 7(*b*)). The discrepancy may be attributed to uncertainties in the thermal and dielectric property database. Additionally, the discrepancy may be attributed from the nonuniformity of the microwave irradiation during experimental process.

Furthermore, the simulation and experimental data (measured by infrared camera) of temperature distributions within the sample in the vertical plane (x-z) are compared in Fig. 11 and Fig. 12. The results show the greatest temperature in the center of heating sample where the electric field is maximum for this standing wave configuration, while the outer edges display the lower temperature. It can be seen that the agreement between the two heating patterns is good, particularly concerning the location of the hot region.

The Distribution of Moisture Profiles Within the Sample. Figures 13 and 14 show the comparison between simulated results and experimental results (the method of measuring as referred to

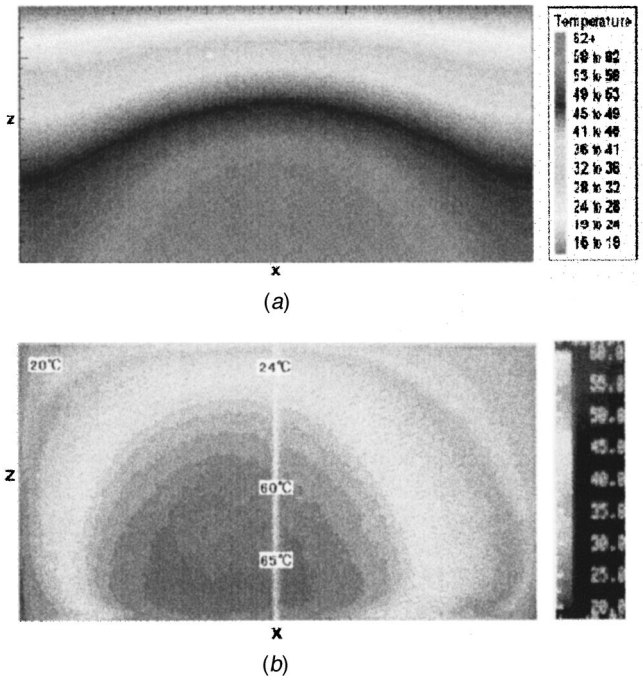

Fig. 12 Comparison between simulated results (*a*) and experimental results (*b*) of temperature distribution (°C) within the sample ($s_0=0.6$, $t=120$ min, $d=0.15$ mm, dimensions: 110 mm (x) ×50 mm (z))

section 2) of moisture profiles in the case of $s_0=1.0$ and $s_0=0.6$, respectively, which correspond to that of $T_0=10.7°C$, $T_a=10.7°C$, and $P=50$ W.

Figure 14 shows the moisture profile in the case of $s_0=1.0$ and $d=0.15$ mm. In the early stages of drying, the moisture content at the leading edge of the sample is lower than that inside the sample, where the moisture decreases due to the gravitational effect. Because of the higher moisture content within the sample, much larger reflected waves develop at the surface during the early stages of the drying. Later, the internal movement of moisture is due to liquid flow by capillary action and vapor flow by molecular diffusion. Liquid phase migration is related to capillary pressure gradient as well as temperature (which corresponds to that of surface tension, as referred to Eq. (25)), whereas in the vapor phase is driven by the gradient of the partial pressure of the

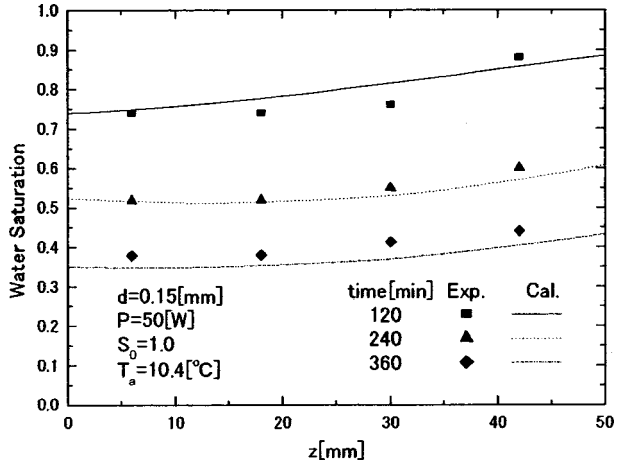

Fig. 13 Water saturation as a function of depth at various times ($P=50$ W, $d=0.15$ mm, $s_0=1.0$)

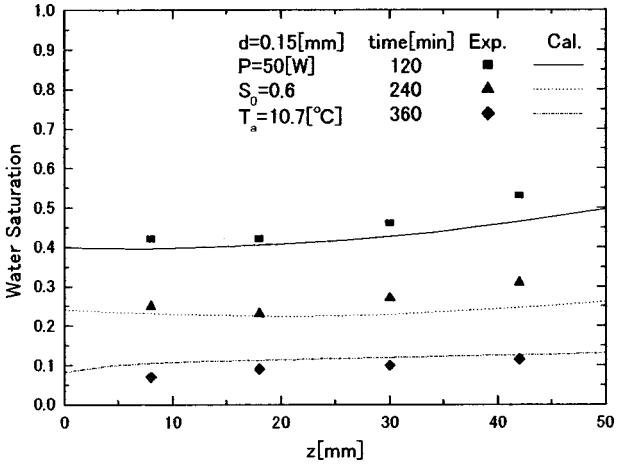

Fig. 14 Water saturation as a function of depth at various times ($P=50$ W, $d=0.15$ mm, $s_0=0.6$)

evaporating species. In this stage of drying, the capillary action plays an important role in the moisture migration mechanism, and maintains a good supply of liquid to the surface. Continued drying would cause the average moisture content inside the sample to decrease and leads to decrease microwave power absorbed (as referred to Fig. 10), reduced temperature (as referred to Fig. 7) and evaporation rate. Nevertheless, at the long stages of drying, the vapor diffusion effect plays an important role in the moisture migration mechanism because of the sustained vaporization that is generated within the sample. The simulated results are in agreement with the experimental results for microwave drying.

Figure 14 shows the average moisture profile along the sample depth in the case of $s_0=0.6$, $T_a=10.7°C$, $P=50$ W, and $d=0.15$ mm. It is evident from the figure that the sample dries quickly throughout. In particular, the bulk of this sample that receives the largest amount of microwave power absorbed (which corresponds to a small initial moisture content) in the early stages of drying process, due to the penetration depth of the microwave field (as referred to Fig. 10).

The simulations of moisture distribution within the sample in the vertical plane (x-z) are shown in Fig. 15 and Fig. 16. It is seen that the moisture content now appears to be high close to side walls of the sample, and the moisture content at lowering edge of the sample stays higher due to the hydrodynamic properties.

The variation of drying rate with respect to time obtained by measurement is shown in Fig. 17. It is seen that in the early stages of drying, the drying rate of the sample in the case of small particle sizes is nearly the same in that case of large particle sizes. However, at long stages of drying, the observed drying rate of sample in the case of small particle sizes is higher than that

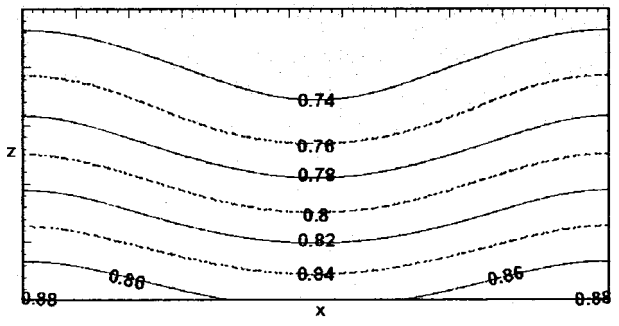

Fig. 15 The simulated water saturation distributions (dimensionless) within the sample ($s_0=1.0$, time=120 min, $d=0.15$ mm, Dimensions: 110 mm (x) ×50 mm (z))

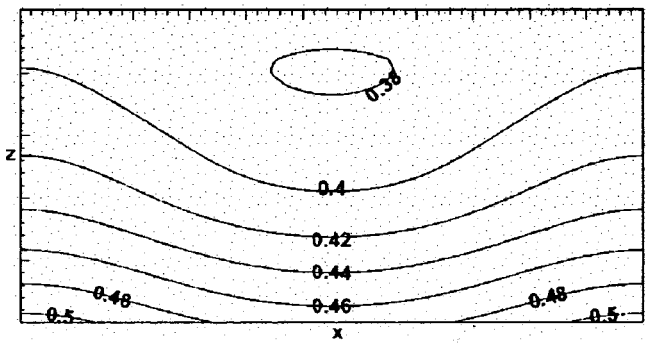

Fig. 16 The simulated water saturation distributions (dimensionless) within the sample, ($s_0=0.6$, time=120 min, $d=0.15$ mm, Dimensions: 110 mm (x) ×50 mm (z))

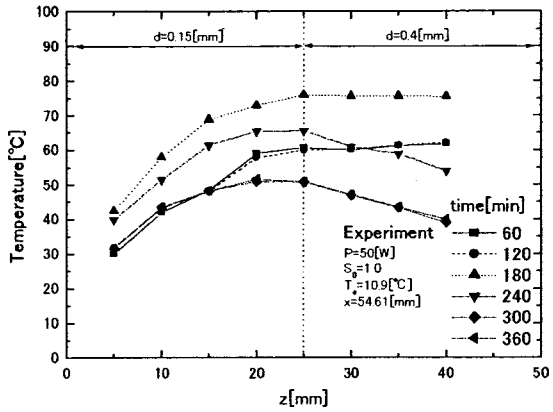

Fig. 19 Temperature as a function of depth at various times for F-C Bed (Experiment: $P=50$ W, $t=360$ min))

case of large particle sizes. This is because of the small particle sizes, however, leads to much higher capillary pressure resulting in a faster drying time.

5.3 Microwave Drying of Two-Layered Porous Packed Bed. Experimental results are shown in Figs. 18–21, which corresponds to that of $s_0=1.0$, $T_a=10.7$°C, and $P=50$ W, along with the center axis ($x=54.61$ mm) of rectangular waveguide. Figure 18 shows the moisture profile within F-C bed, from a macroscopic point of view for the hydrodynamic characteristic properties within two-layered porous packed bed, we will consider the liquid water transport at the interface between two beds where the difference of particle size is considered during microwave drying. As referred to Fig. 3, in the case of the same capillary pressure, a small particle size corresponds to higher water content. Now, consideration the case where two particle sizes having same capillary pressure and different particle sizes at the interface are justified. Since the capillary pressure has the same value at the interface between two beds, but the water saturation becomes discontinuous at the interface of two beds. This is because of the differences of the water characteristics between the two beds, the liquid water will be moved from the coarse bed to the fine bed (which corre

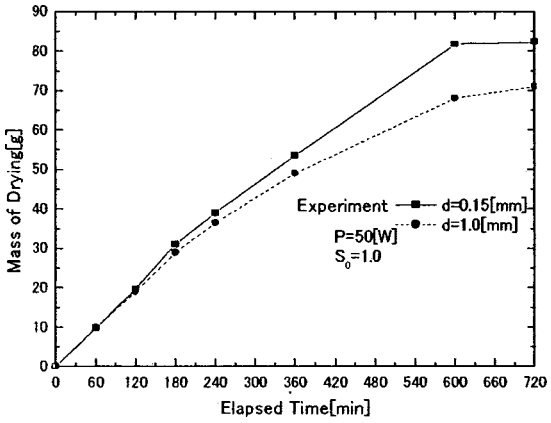

Fig. 17 The variation of drying rate with respect to time

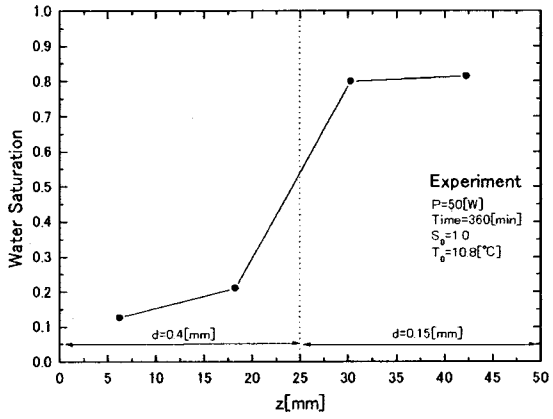

Fig. 20 water saturation as a function of depth for C-F Bed (Experiment: $P=50$ W, $t=360$ min))

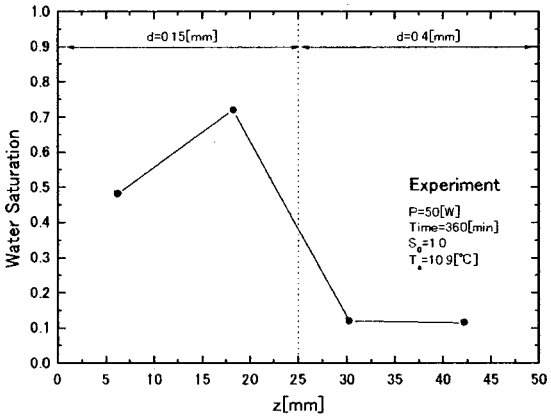

Fig. 18 water saturation as a function of depth for F-C Bed (Experiment: $P=50$ W, $t=360$ min))

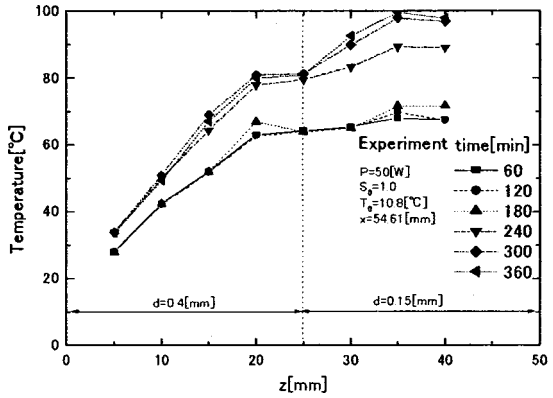

Fig. 21 Temperature as a function of depth at various times for C-F Bed (Experiment: $P=50$ W, $t=360$ min))

sponds to a higher capillary pressure) resulting in a faster drying time.

On the other hand, in the case of attaching fine bed under the coarse bed, called C-F bed is shown in Fig. 20. It is seen that the moisture content inside the fine bed displays very higher because a coarse bed set on the fine bed retards the upward migration of liquid water at the interface between two beds, while the moisture content inside the coarse bed stays lower due to the lower capillary pressure. Therefore, the efficiency of drying process in this case is the lowest.

The temperature profiles at various times and locations for both cases are shown in Fig. 19 and Fig. 21, respectively. Figure 19 shows that the temperature profile within the F-C bed rises up quickly in the early stages of drying process (about 10 min–60 min), However, its rise slows down after this stage. It is evident from the figure that near the end stages of drying as the moisture content inside the sample is reduced, this decreases the microwave power absorbed. Consequently, the temperature profiles are decreased in this stage of drying process. However, the temperature profile within the C-F bed (Fig. 21) corresponds to that of moisture content profile (as referred to Fig. 20) where the temperature continuously rises faster than that in the case of F-C bed. Further, the temperature remains high at the end of drying. This is because of a stronger standing wave with a larger amplitude is formed inside the C-F bed and having of dry layer-coarse bed (upper layer) protects the reflection of wave from the surface resulting in a higher rate of microwave power absorbed in the interior.

Additionally, microwave drying of C-F bed gives higher temperatures inside the fine bed (lower layer) while the temperature inside the coarse bed stays lower due to the behavior of the loss factor decreases significantly with decreasing moisture content and the cooling effect of surrounding air. The next steps in research in microwave drying of multi-layered porous packed bed are to develop a mathematical model for verifying the experimental data, and a study of the combined microwave and convective drying of capillary porous materials will be presented.

6 Conclusions

Experimental and predicted results of drying of capillary porous materials using a microwave energy as a heating source have been presented. The measurements of temperature and moisture distributions within the sample provide a good basis for understanding of the microwave drying process. The mathematical model gives qualitatively comparable trends to experimental data. The calculations of electromagnetic fields inside the rectangular waveguide and the sample show that the variation of particle sizes and initial moisture content changes the degree of penetration and rate of microwave power absorbed within the sample. Furthermore, the small particle size leads to much higher capillary pressure resulting in a faster drying time.

Acknowledgment

The authors gratefully acknowledge the financial support provided under the Science Research Grant of the Japanese Ministry of Education, for the development of the experimental and simulated facilities described in this paper.

Nomenclature

B = magnetic flux density [Wb/m^2]
C_p = specific heat capacity [J/kgK]
D = electric flux density [C/m^2]
D_0 = binary mass diffusion coefficient [m^2/s]
d = diameter [m]
d_P = deep of packed bed [m]
E = electric field intensity [V/m]
E_{yin} = the input value of electric field intensity [V/m]
f = frequency of incident wave [Hz]
g = gravitational constant [m/s^2]
H = magnetic field intensity [A/m]
h_c = heat transfer coefficient [W/m^{2}K]
h_m = mass transfer coefficient [m/s]
H_v = specific heat of vaporization [J/kg]
K = permeability [m^2]
L_x = the length of waveguide in x-direction [m]
$\dot{n}$ = volumetric evaporation rate [kg/m^{3}s]
P = microwave power input [W]
p = pressure [Pa]
Q = microwave power absorbed term [W/m^3]
q = heat flux [W/m^2]
s = water saturation
T = temperature [C]
$\tan \delta$ = loss tangent coefficient
t = time [s]
u,w = velocity [m/s]
Z_H = wave impedance [Ω]
Z_I = intrinsic impedance [Ω]

Greek Letters

ϕ = porosity [m^3/m^3]
ρ = density [kg/m^3]
ε = complex permittivity [F/m]
ε' = dielectric constant [F/m]
ε'' = dielectric loss factor [F/m]
λ = free space wave length [m]
λ_g = waveguide wave length [m]
λ_{eff} = effective thermal conductivity [W/mK]
μ = magnetic permeability [H/m]
μ_g = dynamic viscosity of gas [Pa s]
μ_l = dynamic viscosity of liquid [Pa s]
υ = velocity of microwave [m/s]
σ = electric conductivity [S/m]
ξ = surface tension [Pa m]

Subscripts

∞ = ambient
0 = free space
a = air
c = capillary
e = effective
g = gas
ir = irreducible
n = component of normal direction
p = particle
r = relative
t = component of tangent direction
v = water vapor
l = liquid water
x, y, z = coordinates

Superscripts

$'$ = interfacial position

References

[1] Whitaker, S., 1977, ''A Theory of Drying in Porous Media,'' Adv. Heat Transfer, **13**, pp. 119–203.
[2] Feng, H., and Tang, J., 1998, ''Microwave Finish Drying of Diced Apples in a Spouted Bed,'' J. Food. Sci., **63**, No. 4, pp. 679–683.
[3] Feng, H., Tang, J., and Cavalien, R. P., 1999, ''Combined Microwave and Spouted Bed Drying of Diced Apples: Effect of Drying Conditions on Drying Kinetics and Product Temperature,'' Drying Technol., **17**, No. 10, pp. 1981–1998.
[4] Constant, T., Moyne, C., and Perre, P., 1996, ''Drying with Internal Heat Generation: Theoretical Aspects and Application to Microwave Heating,'' AIChE J., **42**, No. 2, pp. 359–368.
[5] Metaxas, A. C., and Meridith, R. J., 1983, *Industrial Microwave Heating*, Peter Peregrinus, Ltd., London.
[6] Ayappa, K. G., Davis, H. T., Davis, E. A., and Gordon, J., 1991, ''Analysis of Microwave Heating of Materials with Temperature-Dependent Properties,'' AIChE J., **37**, No. 3, pp. 313–322.
[7] Li, W., Ebadian, M. A., White, T. L., and Grubb, R. G., 1993, ''Heat Transfer

Within a Concrete Slab Applying the Microwave Decontamination Process,'' ASME J. Heat Transfer, **115**, pp. 42–50.
[8] Clemens, J., and Saltiel, C., 1996, ''Numerical Modeling of Materials Processing In Microwave Furnaces,'' Int. J. Heat Mass Transf., **39**, No. 8, pp. 1665–1675.
[9] Gori, F., Gentili, G., and Matini, L., 1987, ''Microwave Heating of Porous Media,'' ASME J. Heat Transfer, **109**, pp. 522–525.
[10] Perkin, R. M., 1980, ''The Heat and Mass Transfer Characteristics of Boiling Point Drying Using Radio Frequency and Microwave Electromagnetic Fields,'' Int. J. Heat Mass Transf., **23**, pp. 687–695.
[11] Turner, W., and Ilic, M., 1991, ''Combined Microwave and Convective Drying of a Porous Material,'' Drying Technol., **9**, No. 5, pp. 1209–1269.
[12] Ayappa, K. G., Davis, H. T., Crapiste, G., Davis, E. A., and Gordon, J., 1991, ''Microwave Heating: An Evaluation of Power Formulations,'' Chem. Eng. Sci., **46**, No. 4, pp. 1005–1016.
[13] Ratanadecho, P., Aoki, K., and Akahori, M., 2001, ''Experimental and Numerical Study of Microwave Drying in Unsaturated Porous Material,'' Int. Commun. Heat Mass Transfer, **28**, No. 5, pp. 605–616.
[14] Aoki, K., Ratanadecho, P., and Akahori, M., 2000, ''Characteristics of Microwave Heating for Multi-layered Materials Using a Rectangular Wave Guide,'' *Proceeding of the 4 th JSME-KSME Thermal Engineering Conference*, October 1–6, Kobe, Japan, Vol. 2, pp. 191–196.
[15] Ratanadecho, P., Aoki, K., and Akahori, M., 2002, ''A Numerical and Experimental Study of Microwave Melting of Frozen Packed Bed Using a Rectangular Wave Guide,'' IEEE Trans. Microwave Theory Tech., accepted for publication.
[16] Perre, P., and Turner, W., 1997, ''Microwave Drying of Softwood in an Oversized Waveguide,'' AIChE J., **43**, No. 10, pp. 2579–2595.
[17] Wang, J., and Schmugge, T., 1980, ''An Empirical Model for the Complex Dielectric Permittivity of Soil as a Function of Water Content,'' IEEE Trans. Geosci. Remote Sens., **GE-18**, No. 4, pp. 288–295.
[18] Mur, G., 1981, ''Absorbing Boundary Conditions for the Finite-Difference Approximation of the Time-Domain Electromagnetic-Field Equations,'' IEEE Trans. Electromagn. Compat., **EMC-23**, No. 4, pp. 377–382.
[19] Bories, S. A., 1991, ''Fundamental of Drying of Capillary-Porous Bodies,'' in Kakac, S., Kilkis, B., Kulacki, F. and Arinc, F. eds., *Convective Heat and Mass Transfer in Porous Media*, NATO ASI series, Vol. 196, Kluwer Publishers, pp. 39–434.
[20] Kaviany, M., 1991, *Principle of Heat Transfer in Porous Media*, Springer, New York.
[21] Kaviany, M., and Mittal, M., 1987, ''Funicular State in Drying of Porous Slab,'' Int. J. Heat Mass Transf., **30**, No. 7, pp. 1407–1418.
[22] Aoki, K., Hattori, M., Kitamura, M., and Shiraishi, N., 1991, ''Characteristics of Heat Transport in Porous Media With Water Infiltration,'' *ASME/JSME Thermal Engineering Proceedings*, Vol. 4, pp. 303–308.
[23] Patankar, S. V., 1980, *Numerical Heat Transfer and Fluid Flow*, Hemisphere Publishing Corporation, New York.
[24] Feng, H., Tang, J., and Cavalien, R. P., 2001, ''Dielectric Properties of Dehydrated Apples as Affected by Moisture and Temperature,'' Trans. ASAE, (in press).
[25] Von Hippel, A. R., 1954, *Dielectric Materials and Applications*, MIT Press, Boston.

A Semi-Analytical Model to Predict the Capillary Limit of Heated Inclined Triangular Capillary Grooves

Ivan Catton[1]
Fellow ASME
e-mail: catton@ucla.edu

Gustave R. Stroes

Mechanical, Aerospace, and Nuclear Engineering Department,
University Of California, Los Angeles,
Los Angeles, CA 90095

This paper presents a one-dimensional, semi-analytical model for prediction of the wetted length supported by inclined triangular capillary grooves subject to heating from below. The model utilizes a macroscopic approach employing the concept of an apparent contact angle. Constant liquid properties are assumed and no specific account is taken of surface roughness. The concept of accommodation theory is introduced to account for the change in the radius of curvature of the liquid-vapor interface between the liquid reservoir and the groove proper. Empirical input is required in the form of the axial heat flux profile and the axial profile of the liquid height in the groove. To assist other researchers in the implementation of the model, this paper concludes with a series of design curves. These curves can readily be used to estimate the wetted length (capillary limit) in inclined heated triangular capillary grooves for a variety of operating conditions.
[DOI: 10.1115/1.1404119]

Keywords: Evaporation, Heat Transfer, Heat Pipes, Thin Films

Introduction

Grooved capillary structures find many applications where augmented heat removal is required. One familiar use of capillary grooves is wicking material in heat pipes. Although grooved capillary structures are commonly used in industry, the exact nature of liquid evaporation from heated grooves and the associated wicking power is not yet fully understood. A simple means of studying capillary channels is through the use of a grooved inclined plate heated from below. This setup is easy to implement experimentally, and also lends itself to simplified analytical modeling. Even so, there are few previous investigations dedicated specifically to the case of liquid flow and evaporation from inclined heated capillary grooves. The following is a summary of some of the more relevant recent works concerning grooved capillary evaporators.

Stephan and Busse [1] present a paper which deals with the interline region in capillary grooves—the axial flow of liquid along the grooves is not considered. The analysis is split up into two parts, the micro-region (what others call the interline region) and the macro-region (or intrinsic meniscus). Their result is a fourth order differential equation for the film thickness through the interline region which is solved numerically in conjunction with a two-dimensional sold-side conduction analysis.

A test case is examined for an aluminum groove filled with ammonia. By way of a series of graphs it is shown that the liquid approaches the micro region with a nearly constant slope. It is this slope, say the authors, that determines the ''apparent'' contact angle. Stephan and Busse calculate an apparent contact angle of 19.7 deg for this case. Many of the studies which examine the interline region in a liquid filled groove assume that the thin film extends all the way to the top of the groove. This is inaccurate for most cases since this precludes any capillary pumping in the axial direction, i.e., the groove is always full. Stephan and Busse allow for the evaporating film to terminate before the top of the groove.

Xu and Carey [2] developed a comprehensive picture of the flow of liquid in heated capillary channels. They construct a semi-analytical model to predict the heat transfer from grooves of triangular geometry. The liquid flow in the grooves is split into two parts, axial flow—in which capillary forces push liquid along the groove, and cross-sectional flow—where disjoining pressure drives liquid up the groove wall to the evaporating thin film region. In order to model the intrinsic meniscus a zero apparent contact angle is assumed. Thus a macroscopic approach is used to analyze the intrinsic meniscus (axial flow) before switching to a microscopic approach for the extended meniscus (cross-sectional flow).

Xu and Carey performed experiments in an attempt to validate their model. The working fluids were methanol and acetone, both on a copper substrate. The grooves in question were 25.4 mm long, 64 μm wide and 190 μm wide with a half-angle of 9.35 deg. This is a very small groove size which means that surface roughness will become important in relative magnitude. Difficulties were reported in that large heat flux values were required to bring the thermocouple heat flux meters into an accurate range. As a result dryout is reported to have occurred within the first 8 mm of the (25.4 mm) grooves. Thus only a small portion of the grooves supported thin film evaporation and only two of the heat flux meters fell within this zone, yielding a low number of data points.

Ha and Peterson [3] are the only previous researchers to take account of the way the liquid surface changes along the direction of the groove axis. In other words, the interline does not remain at the top edge of the groove but instead recedes towards the groove apex as the dryout point is approached. So where Xu and Carey assumed that evaporation occurs all the way up the groove wall, Ha and Peterson correctly introduce the fact that the groove wall is essentially adiabatic above the interline.

As described in earlier related work by Ha and Peterson [4], an axial momentum balance is used to relate the local radius of curvature of the liquid-vapor interface to the distance (x) along the groove axis. They do not fully account for the reservoir, or the singularity at the dryout point. They assume a quadratic profile for the heat flux $q''(x)$ in the axial direction. This was also done by

[1]Professor of Engineering, Department of Mechanical and Aerospace Engineering, University of California, Los Angeles, Los Angeles, CA 90095

Contributed by the Heat Transfer Division for publication in the JOURNAL OF HEAT TRANSFER. Manuscript received by the Heat Transfer Division March 21, 2000; revision received February 1, 2001. Associate Editor: G. P. Peterson.

Xu and Carey. The momentum balance can then be used to determine either the curvature profile or the maximum axial wetted length (i.e., the dryout point).

The main goal of Ha and Peterson was to find both the average heat transfer coefficient for, and the size of, the evaporating thin film region on the groove wall at each location x along the groove axis. This allows a determination of the profile of the extended meniscus at each axial position. The authors mention that when this is combined with the axial profile of the intrinsic meniscus that a fully three dimensional description of the liquid surface can be made.

In the paper presented here, the goal is to develop a model which will allow researchers to predict the distance to which liquid will flow up an inclined triangular channel heated from below. The resulting dryout point x_d is often lacking or overlooked in the existing literature. The triangular groove model is compared to previously obtained experimental data. To conclude, a pair of design curves is presented that can be used by future researchers to estimate the distance that liquid will be drawn up heated triangular capillary grooves for a variety of operational setups.

Development of the Triangular Groove Model

The model of a semi-analytical triangular groove is based on a one-dimensional momentum equation written along the groove axis (in the x-direction). A schematic of the groove and the orientation of the axes is shown in Fig. 1. Here the momentum equation is treated as a (body) force balance. Thus it must be determined which forces are relevant in the current situation. When liquid flows up an inclined triangular channel, whether heated or isothermal, there is an axial change in the radius of curvature of the liquid-vapor interface. This is most easily visualized from a macroscopic perspective. Here it is assumed that the liquid forms an apparent contact angle of $\theta=0$ deg at the groove wall. With a zero apparent contact angle, the radius of curvature of the liquid-vapor interface is directly dependent on the local height of the liquid in the groove $h(x)$. And as the liquid height decreases (which it must if dryout is to occur) the radius of curvature must also decrease (as shown in Fig. 1). Thus in the present analysis the radius of curvature of the liquid-vapor interface is perceived as a passive quantity—one which accommodates itself to the local groove geometry.

From the Young-Laplace equation it is known that the local radius of curvature of the liquid-vapor interface, $r(x)$, defines the difference in pressure between the liquid and the vapor phases. For this analysis, the pressure of the vapor above the liquid in the groove is assumed to be everywhere the same ($P_v=$constant). This allows an expression to be written for the local liquid pressure (P_l) as a function only of the local radius of curvature of the liquid-vapor interface $P_l(x)\sim r(x)$. Because $r(x)$ changes along the axis of the groove, the liquid pressure is forced to change also (any hydrostatic variation in liquid pressure in the z-direction is neglected since the grooves are small). Hence, one term which must appear in an axial force balance along the groove axis is the capillary force (i.e., capillary head).

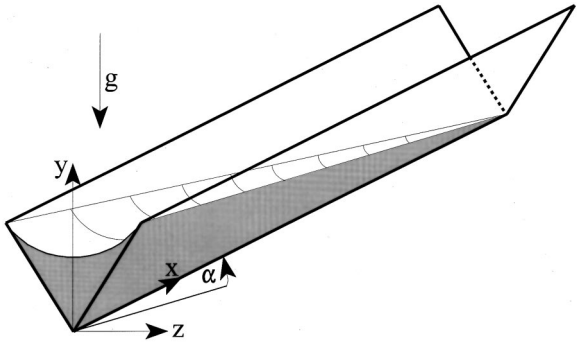

Fig. 1 Orientation of liquid in a triangular channel

Two additional terms which must be included in the one-dimensional force balance are gravity and friction. Gravity must be accounted for since, as the liquid flows up an inclined groove, it must overcome a component of the gravitational field. Friction is addressed because when an inclined groove is subject to a heat input from below because flow is induced by the considerable amount of liquid is lost to evaporative heat transfer. Replacement of this evaporated liquid requires a steady make-up flow rate, and this flow is subject to friction at the groove wall. Here, make-up flow is assumed to occur in two parts as proposed by Xu and Carey [2]. Axial flow takes place in the center of the groove where the liquid is thick and little evaporation occurs. Then, to drive liquid up onto the sides of the groove into the evaporating thin film region, there is cross-sectional flow. In the current development only axial forces are of interest. Thus only the axial flow rate is considered, and it is assumed to exist independently of any cross-sectional flow. The axial make-up flow rate creates a viscous friction force (F_v) at the groove wall in the opposite direction to the flow. The friction factor K, required to evaluate F_v is obtained from Ayyaswamy et al. [5]. Their work recommends $K=35.215$ for a groove half-angle of 40 deg (which is the half angle of the grooves used in the triangular groove experiment).

Up to this point in the development of the semi-analytical triangular model, the axial momentum equation contains a term describing capillary head, which drives liquid up the groove (F_{Ca}), and terms for gravity and friction (F_g and F_v), which both act to oppose positively directed flow.

The current groove model includes a fourth term which is a result of the physical layout of the inclined groove setup. At the beginning of the triangular channel, liquid flows from the reservoir into the groove, and there arises a special situation. In the reservoir the liquid surface is flat, therefore the radius of curvature of the liquid-vapor interface is equal to infinity. Theoretically, the liquid surface remains flat right up to the entry to the groove so that at $x=0$ the initial radius of curvature is $r(0^-)=\infty$. However, once the liquid is inside the groove, the situation is somewhat different. Here the liquid conforms to the channel geometry and assumes a radius of curvature which is dependent on both the height of the liquid in the channel $h(x)$, and the macroscopic contact angle θ. Thus, just inside the groove, the radius of curvature of the liquid vapor interface is given as $r(0^+)=r_o$. The combination of these two situations seems to indicate that the liquid-vapor interface undergoes a substantial change in its radius of curvature over an infinitesimal distance ($x=0^-\rightarrow x=0^+$). Both configurations of the liquid surface at the groove entry are shown in Fig. 2(b).

The circumstances just described amount to a singularity at $x=0$ for a triangular capillary groove. Existing triangular capillary groove studies have not had to cope with this singularity since in all cases the liquid reservoir has been neglected. However, all experimental data in the literature are developed using a liquid reservoir, thus any analytical model which is to be compared to the experimental data must take the reservoir into account.

It is difficult to imagine that the shape of the liquid surface could instantly ''accommodate'' itself to the groove geometry as it flows from the reservoir into the groove proper. What seems more reasonable is that the liquid-vapor interface accommodates itself to the groove shape in a gradual manner, over a finite axial distance. This is especially true in light of the following implication. From the Young-Laplace equation it is known that the pressure jump across the liquid-vapor interface is related to the local radius of curvature $r(x)$. Therefore, a finite change in the radius of curvature over zero axial distance creates a local pressure gradient equal to infinity.

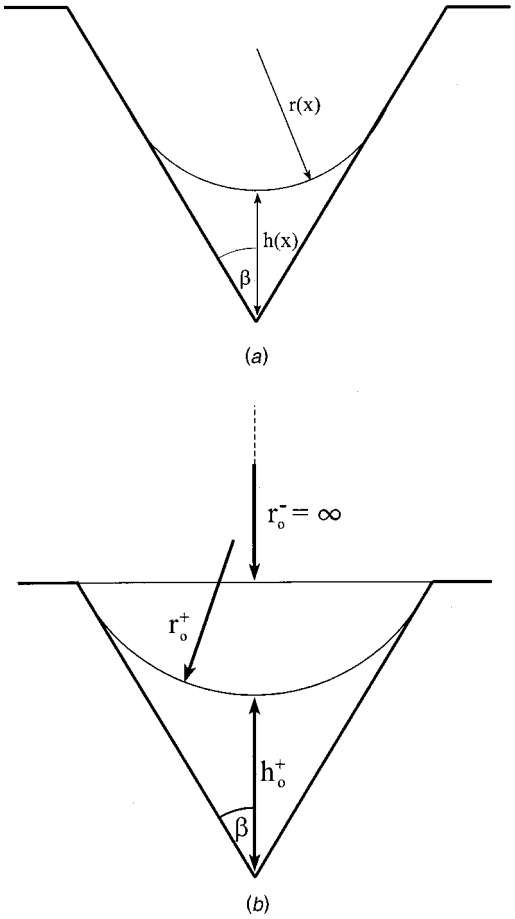

Fig. 2 (*a*) Radius of curvature and liquid height; and (*b*) liquid accommodation

$$P_v - P_l = \frac{\sigma}{r(x)} \Rightarrow -\left.\frac{dP_l}{dx}\right|_{x=0} = -\frac{\sigma}{r(x)^2}\left.\frac{dr}{dx}\right|_{x=0} \sim \frac{r(0^-) - r(0^+)}{\Delta x \ll 0} \sim \infty \tag{1}$$

Thus if the constraint of instant geometrical accommodation is enforced on the liquid surface at the groove entry, then this becomes a region of infinite capillary head. It is therefore proposed that the possibility of instant accommodation is unrealistic and that the liquid surface is more likely to take on the groove shape over some finite distance which is here defined as the "accommodation length (x_a)."

This idea is illustrated in Fig. 3. At the groove entry, $x=0$, the liquid surface is still flat due to the proximity of the liquid reservoir. At some distance farther up the groove, $x=x_a$, (see Fig. 4) the liquid surface is curved and has accommodated itself to the groove geometry. By accommodation it is meant that the slope of the groove walls (set by the groove half-angle β) in combination with a zero macroscopic contact angle ($\theta=0$ deg) forces the liquid-vapor interface to take on a particular radius of curvature compatible with the local groove geometry. The model assumes that this transformation occurs over an axial distance of x_a, the accommodation length. Note that the macroscopic contact angle does not reach its prescribed value of $\theta=0$ deg until $x=x_a$. Thus prior to this point, the apparent contact angle is greater than zero. Accommodation theory therefore implies that the macroscopic contact angle is variable over (at least) a portion of the axial wetted length.

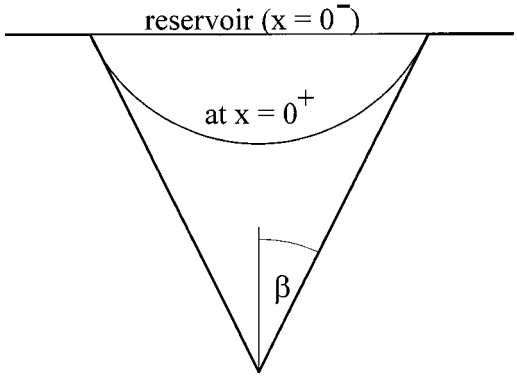

Fig. 3 Accommodation of liquid surface in a triangular channel

The semi-analytical triangular model also requires a value for the characteristic length x_a which is the result of accommodation theory. One potential choice for this characteristic length is developed in the following way. Suppose that an inclined flat plate were examined such that any effect between the liquid and the groove walls was eliminated. To what distance would liquid rise up this plate before it dried out? A schematic of the proposed scenario is portrayed in Fig. 4.

Using a second order polynomial for the shape of the liquid along with the following boundary conditions, an equation for the characteristic length x_a can be obtained. This offers a possible approach to determining the characteristic length x_a. In equation form

$$y(x) = ax^2 + bx + c$$

$$@x=0: \quad y(0) = c = h_o \quad \left.\frac{dy}{dx}\right|_{x=0} = b = -\tan\alpha \tag{2}$$

$$@x=x_a: \quad y(x_a) = 0 \quad \left.\frac{dy}{dx}\right|_{x=x_c} = 0 \Rightarrow x_a = \frac{2h_o}{\tan\alpha}.$$

This option, Eq. (2), was not satisfactory because it did not contain enough physics. The resulting accommodation length expression should show dependence on heat flux and groove characteristics.

If the accommodation length is assumed to be short relative to the overall wetted length, then a force balance can be used to estimate x_a. For x_a very short, the mass flow rate can be assumed to be equal to the total amount of liquid that is evaporated in the process of dissipating Q, the applied heat load. Thus, the entrance region is implicitly adiabatic because x_a is short, and the heat flux profile yields a negligible heat flux value over the first part of the

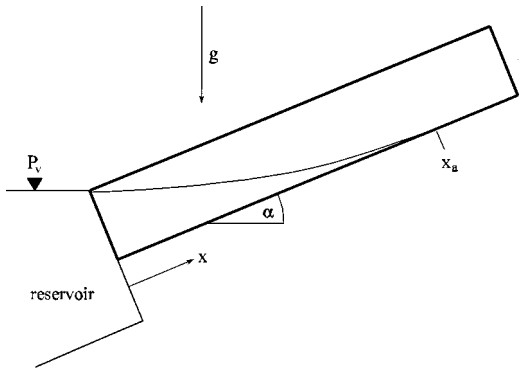

Fig. 4 Accommodation length in a triangular channel

groove. The capillary head generated as the radius of curvature of the liquid surface goes from $r=\infty$ to $r=r_o$ is balanced by friction and gravity. The friction term requires both the cross-sectional area of the liquid in the groove and the wetted perimeter be considered. Since both these quantities do not change markedly over the entrance region the current development assumes that the groove is ''full'' when calculating A_c and P. The resulting force balance for the entrance region is

$$F_a = F_v + F_g . \tag{3}$$

Substituting appropriate values for F_a, F_v, and F_g and solving for x_a results in the following expression:

$$x_a = \frac{\sigma}{r_o}\left(\frac{KQv_l P^2}{32h_{fg}A_c^3} + \rho_l g \sin\alpha\right)^{-1}. \tag{4}$$

The predicted results are better than those achieved with the simple geometric approximation but still need improvement.

Although the logic used in developing Eq. (4) to predict x_a is attractive, the results are not very promising. A better match to the experimental data is found by using a modified version of Eq. (4) to predict x_a

$$x_a = \frac{2\sigma}{r_o}\left(60\frac{KQv_l P^2}{32h_{fg}A_c^3} + \rho_l g \sin\alpha\right)^{-1}. \tag{5}$$

The problem in using Eq. (4) to predict x_a is that the effect of the friction term is under-represented. Thus it may not be appropriate to assume that the entrance region is very short. Accommodation is likely to occur gradually over a significant portion of the total wetted length. This would mean that the friction term cannot be evaluated as if the groove is ''full.'' Farther up the channel the liquid has receded significantly towards the apex of the groove. This results in a much smaller cross-sectional area for liquid flow and hence a much larger friction factor. Therefore, the factor of 60 in Eq. (5) has some physical explanation. It can be seen that the result is very good.

It now remains to combine the capillary head defined by accommodation theory with the remaining triangular capillary groove analysis. This is accomplished through superposition. An axial body force balance along the groove axis can be written as follows:

$$F_{Ca} + F_a = F_g + F_v . \tag{6}$$

In Eq. (6) the forces that drive the liquid up the axis of the channel are on the left. Positive head is created by capillary action F_{ca} and by accommodation theory F_a. The factors that inhibit liquid flow are on the right of Eq. (6). These are the axial component of gravity and the friction created at the groove wall. Each of these contributions is examined in detail below.

Capillary head (represented by F_{ca}) is a pressure gradient in the liquid caused by a changing radius of curvature at the liquid-vapor interface. As previously mentioned, the dependence of the liquid pressure on the radius of curvature is obtained through the Young-Laplace equation.

$$P_v - P_l = \frac{\sigma}{r(x)} \tag{7}$$

This is the one-dimensional version of Young-Laplace equation which accounts for the missing factor of 2 which is more commonly seen in the numerator of the right hand side. Now the first term in Eq. (6) becomes,

$$\frac{d}{dx}(P_v - P_l) = -\left.\frac{dP_l}{dx}\right|_{Ca} = \frac{d}{dx}\left(\frac{\sigma}{r(x)}\right) = -\frac{\sigma}{r(x)^2}\frac{dr}{dx}$$
$$F_{Ca} = -\left.\frac{dP_l}{dx}\right|_{Ca} = -\frac{\sigma}{r(x)^2}\frac{dr}{dx}. \tag{8}$$

The minus sign in front of the last term in Eq. (8) indicates that a liquid surface with a decreasing radius of curvature in the positive x-direction creates a positive capillary driving force.

The second term in the axial momentum balance (F_a in Eq. (6)) comes from accommodation theory and is developed as follows:

$$\text{at } x=0: \quad P_l(x) = P_v$$
$$\text{at } x=x_a: \quad P_l(x) = P_v - \frac{\sigma}{r_o} \tag{9}$$
$$F_a = -\frac{\Delta P_l}{\Delta x} = \frac{-[(P_v - \sigma/r_o) - P_v]}{x_a} = \frac{\sigma}{r_o x_a}.$$

Equation (9) represents the capillary head developed as the liquid surface accommodates itself to the groove geometry after having left the reservoir. In other words, F_a accounts for the capillary head generated as the liquid-vapor interface varies from $r=\infty$ in the reservoir to $r=r_o$ at the groove inlet, except that this variation is assumed to occur over a finite (versus infinitesimal) distance labeled x_a.

On the right hand side of Eq. (6) the first term is the component of gravity acting in the axial direction. This term is straightforward and is written as

$$F_g = \rho_l g \sin\alpha. \tag{10}$$

The friction term (F_v) is derived from the Darcy Weisbach equation for open channel flow.

$$F_v = \frac{K\dot{m}v_l}{2A_c(x)D_h(x)^2} \tag{11}$$

Here A_c is the cross-sectional area of the liquid in the groove, while D_h is the corresponding hydraulic diameter. As was previously pointed out, the friction factor K is obtained from Ayyaswamy, Catton and Edwards [5]. For a groove half-angle of $\beta=40$ deg and an apparent contact angle of $\theta=0$ deg, the value obtained for the friction factor is $K=35.215$. Using the geometry of the groove to calculate $A_c(x)$ and $D_h(x)$, Eq. (11) becomes

$$F_v = \frac{K\dot{m}v_l}{2C_3 r(x)^4}, \tag{12}$$

where

$$C_3 = C_1 C_2^2: \quad C_1 = \frac{1}{\tan\beta} - \left(\frac{\pi}{2} - \beta\right): \quad C_2 = 2C_1 \tan\beta. \tag{13}$$

The mass flow rate in Eq. (12) can be re-expressed in terms of the heat flux imposed on the groove

$$\dot{m}(x) = \frac{w}{h_{fg}}\int_x^{x_d} q''(x)dx \tag{14}$$

in combination with the latent heat of vaporization. The axial distribution of the heat flux at the wall $q''(x)$ is obtained from a two-dimensional conduction analysis [7],

$$q''(x) = 3q''_{\text{const}}\left(\frac{x}{x_d}\right)^2. \tag{15}$$

Substituting Eq. (15) into Eq. (14) and integrating yields an expression for the local mass flow rate of liquid along the groove axis

$$\dot{m}(x) = \frac{wq''_{\text{const}}}{h_{fg}x_d^2}(x_d^3 - x^3). \tag{16}$$

Equation (16) is the axial mass flow rate at any point along the channel, x, expressed in terms of the amount of liquid that will be evaporated beyond point x.

Substituting the relationships given by Eqs. (8), (9), (10), and (13) into Eq. (6) produces,

$$\frac{d}{dx}\left(\frac{\sigma}{r(x)}\right)=\rho_l g\sin\alpha-\frac{\sigma}{r_o x_a}+\frac{K\dot{m}v_l}{2C_3 r^4(x)}. \tag{17}$$

Equation (17) can be rearranged in the following manner

$$\frac{dr}{dx}=\left[\frac{1}{r_o x_a}-\frac{\rho_l g}{\sigma}\sin\alpha\right]r(x)^2-\frac{wKv_l q''_{\text{const}}}{2C_3\sigma h_{fg}x_d^2 r(x)^2}(x_d^3-x^3). \tag{18}$$

Defining the following constants:

$$A=\left[\frac{\rho_l g}{\sigma}\sin\alpha-\frac{1}{r_o x_a}\right]\quad B=\frac{wKv_l q''_{\text{const}}}{2C_3\sigma h_{fg}} \tag{19}$$

allows Eq. (14) to be simplified to

$$\frac{dr}{dx}=-Ar(x)^2-B\frac{(x_d^3-x^3)}{x_d^2 r(x)^2}. \tag{20}$$

Note that the capillary head generated by accommodation theory has been combined with the gravity term in constant *A*. Multiplying Eq. (20) by dx allows for subsequent integration along the x axis of the triangular capillary channel.

$$\int_{r_o}^{r_f}dr=-A\int_0^{x_d}r(x)^2dx-B\int_0^{x_d}\frac{(x_d^3-x^3)}{x_d^2 r(x)^2}dx. \tag{21}$$

At this point additional information is required before integration of Eq. (21) can proceed. First, the endpoint conditions on the radius of curvature of the liquid-vapor interface (r_o and r_f) must be defined. Integration begins at $x=0$ where the initial radius of curvature is r_o. It has been previously shown that the actual radius of curvature at the groove entry is likely to be very large due to proximity to the reservoir (where the liquid surface is flat). However, any capillary head generated by the liquid surface changing from flat to curved (as it adapts to the groove geometry) has already been accounted for as the accommodation theory term in constant *A*. The capillary head generated by accommodation is super-imposed on the traditional triangular groove analysis over the groove entry region. Thus the initial radius of curvature r_o in Eq. (21) is simply the radius that the liquid would assume if the groove were full and displayed a macroscopic contact angle of $\theta=0$ deg. Remember that in ''traditional'' triangular groove analyses the reservoir is neglected. A depiction of the initial radius of curvature of the liquid surface is shown in Fig. 2(*a*).

Next the final radius of curvature at the dryout point must be ascertained. Upon first examination, it would appear that the final radius of curvature must be zero ($r_f=0$). This would be the case if the triangular groove came to a perfectly sharp point at its apex. Since at $x=x_d$ the liquid height is zero ($h(x)=0$), then with a zero liquid height in a perfectly sharp apex, the radius of curvature would indeed be forced to approach zero. The problem with setting the final radius of curvature of the liquid surface equal to zero is that $r_f=0$ creates a singularity at $x=x_d$ in Eq. (21). However, the manufacturing tolerance on the method used to create grooved plates sets a minimum value for the final radius of curvature. For example, as was described in Stroes and Catton [8], for grooves formed with wire EDM the radius of the wire determines the sharpest corner that can be created. In that case the minimum radius was $r_{\min}=0.25$ mm. Thus the final radius of curvature of the liquid-vapor interface at the dryout point in the current triangular groove analysis is $r=r_f$, where r_f is finite and dependent on the manufacturing method used to produce the grooves.

With r_o and r_f thus defined, the LHS of Eq. (21) can be integrated. But to integrate the RHS a suitable expression for $r(x)$ is required. The axial rate of change of the radius of curvature of the liquid surface is not known a priori. Because the current model is purposely kept simple, an empirically determined profile for $r(x)$ is used. Experimental analysis of the liquid profile in triangular capillary grooves [7] has shown that a quadratic profile for the liquid height, $h(x)$, is appropriate. This knowledge can be used to ascertain the axial profile for $r(x)$. From Fig. 2(*a*) it is apparent that at any location x along the groove, the value for the liquid height $h(x)$ also determines the radius of curvature of the liquid-vapor interface $r(x)$. This is true so long as the macroscopic contact angle θ is constant.

Thus, to arrive at an expression for $r(x)$, the profile for the liquid height $h(x)$ must first be defined. The quadratic equation for the liquid height profile $h(x)$ and the associated boundary conditions used to calculate the constants are shown as follows:

$$h(x)=ax^2+bx+c$$

$$h(0)=h_o=c$$

$$h(x_d)=ax_d^2+bx_d+h_o=0.114h_o \tag{22}$$

$$\left.\frac{dh}{dx}\right|_{x_d}=2ax_d+b=0\quad(flat)$$

$$\frac{h(x)}{h_o}=0.886\left(\frac{x}{x_d}\right)^2-1.772\left(\frac{x}{x_d}\right)+1.$$

Note the second boundary condition $h(x_d)=0.114h_o$. Since the radius of curvature of the liquid surface does not go completely to zero, the liquid height also terminates with a value greater than zero relative to a perfectly shaped groove. The final radius of curvature and the final liquid height are directly related if the macroscopic contact angle is known. Here h_o is based on a final radius of curvature of $r(x_d)=0.25$ mm, which is appropriate for grooves manufacture using wire EDM. However, other manufacturing methods may yield a different value for r_f.

The quadratic profile for the liquid height given by Eq. (22) can be combined with the geometric relation between $h(x)$ and $r(x)$ which applies when the macroscopic contact angle θ equals zero

$$r(x)=h(x)\left[\frac{\sin\beta}{1-\sin\beta}\right]. \tag{23}$$

The resulting equation for the axial profile of the radius of curvature of the liquid surface in a triangular groove is

$$\frac{r(x)}{r_o}=0.886\left(\frac{x}{x_d}\right)^2-1.772\left(\frac{x}{x_d}\right)+1. \tag{24}$$

With this expression it is possible to analytically integrate the first term on the RHS of Eq. (21). The result is

$$\int_0^{x_d}r^2(x)dx=0.237(x_d r_o^2). \tag{25}$$

Integration of the second term on the RHS of Eq. (21) requires first a substitution and then application of a numerical integration routine. For this the trapezoidal method with 100 intervals is considered sufficiently accurate for the scope of the current model.

$$\text{let } u=\frac{x}{x_d},\ \text{then } \int_0^{x_d}\frac{(x_d^3-x^3)}{x_d^2 r(x)^2}dx$$

$$=x_d^2\int_0^1\frac{(1-u^3)}{r(u)^2}du=9.134\frac{x_d^2}{r_o^2} \tag{26}$$

Using these results for the integrals, Eq. (21) becomes

This is the final result of the current analysis. Equation (27) is a quadratic equation for x_d, the dryout point. A solution for x_d can be found through use of the well known quadratic equation. A recap of the inputs to the triangular groove model is as follows:

Inputs.

$$x_d^2 + bx_d + c = 0$$

$$b = 0.0259 r_o^4 \left(\frac{A}{B}\right) \tag{27}$$

$$c = 0.110 r_o^2 (r_f - r_o)\left(\frac{1}{B}\right)$$

(i) Groove dimensions including depth (d), width (w), and half-angle (β).
(ii) Angle of inclination with respect to gravity α.
(iii) Liquid properties evaluated at an appropriate reference temperature.
(iv) Axial profile for the wall heat flux $q''(x)$.
(v) Axial profile for the liquid height in the channel $h(x)$.
(vi) The characteristic length for accommodation x_a.
(vii) Macroscopic contact angle is set to θ=0 deg as part of model development.

Output. ▶ Dryout point x_d for the specified conditions.

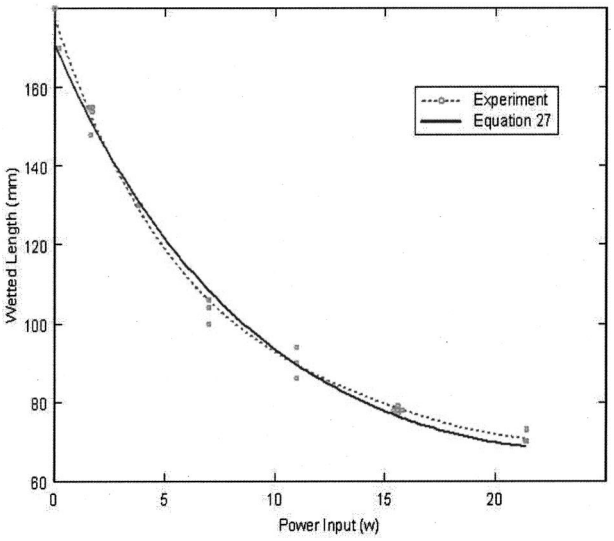

Fig. 5 The effect of power on wetted length: ethanol in a grove tilted at 4 deg

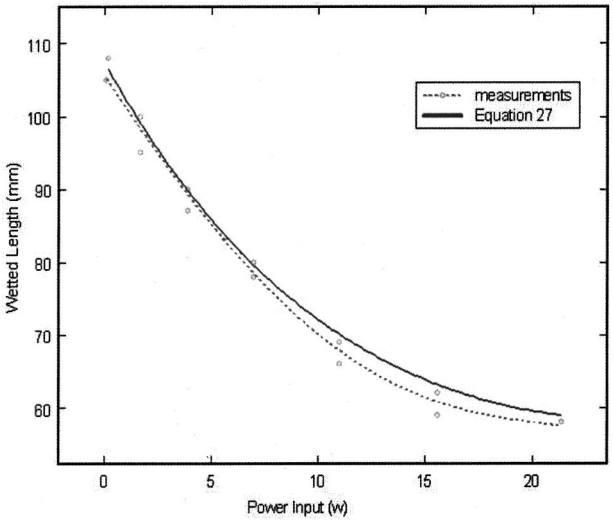

Fig. 6 The effect of power on wetted length; ethanol in a groove tilted at 6 deg

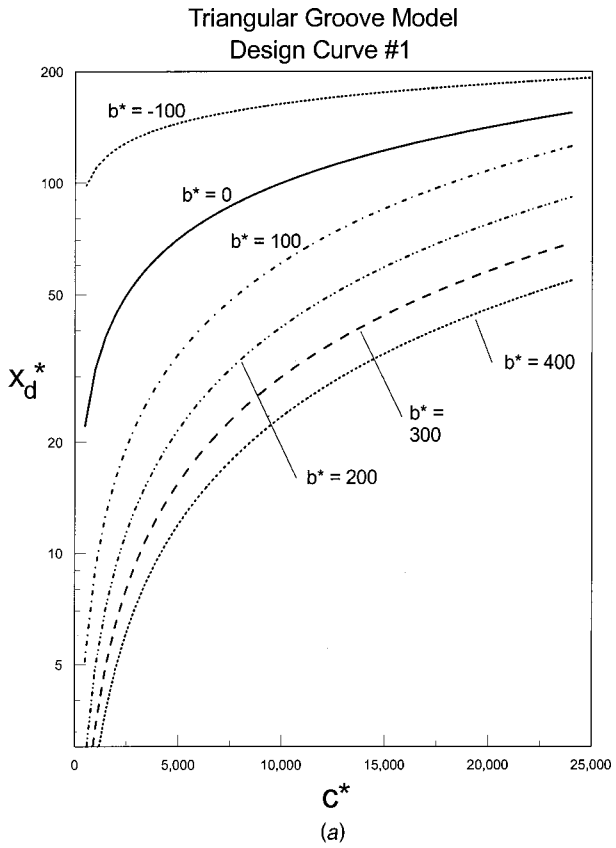

(*a*)

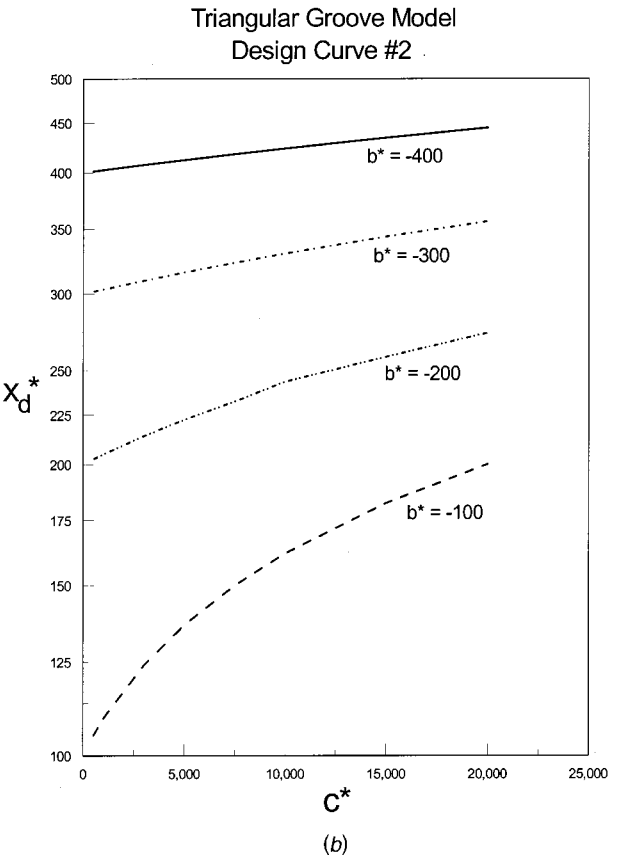

(*b*)

Fig. 7 (*a*) Triangular groove capillary limits; and (*b*) triangular groove cappilary limits

Comparison of predictions based on Eq. 27 with experimental data are shown in Figs. 5 and 6. These comparisons are for an ethanol filled groove tilted at either 4 or 6 degrees. As can be seen the comparisons are very good. Other fluids and tilt angles were extensively studied by Stroes [7]. Data is available for Methanol, Freon, Ethanol and water for a range of tilt angles and heating rates. Most of this data is as yet unexploited.

Implementation of the Triangular Groove Model

To assist future capillary groove researchers in using the current triangular model, a design curve is developed which can be used to estimate x_d for an inclined heated triangular channel under a variety of operational scenarios. After integration of the governing differential equation for a heated triangular capillary groove the following quadratic equation was arrived at for the axial wetted length (or dryout point),

$$x_d^2 + 0.0259 r_o^2 \left(\frac{A r_o^2}{B} \right) x_d + 0.110 r_o^2 (r_f - r_o) \frac{1}{B} = 0, \qquad (28)$$

where

$$A = \left[\frac{\rho_l g}{\sigma} \sin \alpha - \frac{1}{r_a x_a} \right] \quad B = \frac{w K v_l q''_{\text{ave}}}{2 C_3 \sigma h_{fg}}. \qquad (29)$$

Equation (28) is non-dimensionalized by dividing through by r_o^2 to yield

$$(x_d^*)^2 + b^*(x_d^*) + c^* = 0. \qquad (30)$$

The dimensionless parameters x_d^*, b^*, and c^* are given as follows:

$$x_d^* = \frac{x_d}{r_o} \quad b^* = 0.0259 r_o \left(\frac{A r_o^2}{B} \right) \quad c^* = 0.110 (r_f - r_o) \frac{1}{B}. \qquad (31)$$

Construction of a design curve involves graphing solutions of Eq. (30) for various values of b^* and c^*. Here this is done by forming curves of constant b^*. Thus with b^* held constant, c^* is varied along a realistic range (based on experimental data: $0 \leqslant c^* \leqslant 25{,}000$) and the solution for x_d^* is recorded. This is done for values of b^* ranging from $-400 \leqslant b^* \leqslant +200$. Note that negative values of b^* make sense, as this merely indicates that the capillary head due to accommodation theory outweighs the gravity term in the constant A.

The design curve for the triangular groove geometry based on the previous development is shown in Figs. 7(*a*) and 7(*b*). The graphs show c^* on the horizontal axis and x_d^* (on a logarithmic scale) along the vertical axis. The vertical axis is purposely stretched in order to facilitate the reading of data. To implement the triangular groove design curve, a researcher would first calculate the constants A and B from Eq. (29) based on the known operating parameters. These values are then used to calculate b^* and c^* from Eq. (31). With this data, Fig. 7(*a*) or 7(*b*) can be entered in order to yield the corresponding value for x_d^*, the dimensionless wetted length. Finally, based on the value for the initial radius of curvature r_o, the actual wetted length (dryout point) can be calculated.

Concluding Remarks

It is felt that the design curves should offer future researchers a reasonable engineering estimate of the wetted length produced in heated inclined capillary channels under a range of operating scenarios. However, it is recommended that the development of the triangular model be studied before using the curves. Specifically, an understanding of the limitations of the model is required. The concept of accommodation theory should also be clear. If exact information regarding wetted lengths is desired, then it may be more appropriate to redevelop the model for the case in question. However, for many situations Figs. 7(*a*) and 7(*b*) should offer the capillary groove researcher a good starting point in determining the wetted length in a triangular groove heated from below.

For application to heat pipes there is more work to be done. The condenser can be treated as a reservoir but the adiabatic section needs to be added. What we call the accommodation length will need a different treatment. It is our view, however, that what has been done could easily be extended to the more general case.

Acknowledgments

Early work on this project began under Grant NCC 2-374 from NASA Dryden Flight Research Center, Edwards AFB, California. Presently this work is supported by DARPA under project HERETIC award number DAAD19-99-1-0157;p00001.

References

[1] Stephan, P. C., and Busse, C. A., 1992, "Analysis of the Heat Transfer Coefficient of Grooved Heat Pipe Evaporator Walls," Int. J. Heat Mass Transf., **35**, No. 2, pp. 383–391.
[2] Xu, X., and Carey, V. P., 1990, "Film Evaporation from a Micro-Grooved Surface; An Approximate Heat Transfer Model and Its Comparison with Experimental Data," J. Thermophys. Heat Transfer, **4**, No. 4, pp. 512–520.
[3] Ha, J. M., and Peterson, G. P., 1995, "Interline Heat Transfer of Evaporating Thin Films Along a Micro Grooved Surface," *Proceedings of the 1995 ASME International Mechanical Engineering Congress and Exposition*, San Francisco, USA, ASME Paper no. 95-WA/HT-20.
[4] Ha, J. M., and Peterson, G. P., 1994, "Analytical Prediction of the Axial Dryout Point for Evaporating Liquids in Triangular Microgrooves," ASME J. Heat Transfer, **116**, pp. 498–503.
[5] Ayyaswamy, P. S., Catton, I., and Edwards, D. K., 1974, "Capillary Flow in Triangular Grooves," ASME J. Appl. Mech., **41**, No. 2, pp. 332–336.
[6] Catton and Edwards, 1974.
[7] Stroes, G., 1997, "An Experimental and Analytical Investigation of the Wetted Length Supported in Inclined Capillary Grooves Heated from Below," PhD thesis, UCLA, Los Angeles, CA.
[8] Stroes, G. R., and Catton, I., 1995, "An Experimental Study of the Heat Removal Capabilities of Triangular Versus Rectangular Capillary Channels," *Proceedings of the ASME/JSME Thermal Engineering Joint Conference*, May 20–25, Maui, Vol. 1, pp. 519–522.

M. Greiner
Professor of Mechanical Engineering,
University of Nevada,
Reno, Nevada 89557
e-mail: greiner@unr.edu

P. F. Fischer
Mathematician
Mathematics and Computer Science Division,
Argonne National Laboratory,
Argonne, IL 60637

H. M. Tufo
Assistant Computer Scientist
Mathematics and Computer Science Division,
Argonne National Laboratory,
Argonne, IL 60637

R. A. Wirtz
Professor of Mechanical Engineering,
University of Nevada,
Reno, Nevada 89557

Three-Dimensional Simulations of Enhanced Heat Transfer in a Flat Passage Downstream From a Grooved Channel

Spectral element simulations of three-dimensional flow and augmented convection in a flat passage downstream from a fully developed channel with symmetric, transverse grooves on opposite walls were performed for 405≤Re≤764. Unsteady flow that develops in the grooved region persists several groove-lengths into the flat passage, increasing both local heat transfer and pressure gradient relative to that in a steady flat passage. Moreover, the heat transfer for a given pumping power in the first three groove-lengths of the flat passage was greater than the levels observed in a fully developed grooved passage.
[DOI: 10.1115/1.1418371]

Keywords: Augmentation, Computational, Forced Convection, Heat Transfer, Three-Dimensional

Introduction

Engineering devices frequently employ enhanced heat transfer surfaces [1]. Fins are typically used to extend surface areas while offset strips are commonly used to promote thin boundary layers. In recent years, a number of configurations that increase fluid mixing by triggering flow instabilities have been considered. Transversely grooved channels [2–4], passages with eddy promoters [5,6] and communicating channels [7] all contain fairly large features whose sizes are roughly half the channel wall to wall spacing. These structures are designed to excite normally damped Tollmien-Schlichting waves at moderately low Reynolds numbers.

The current authors have presented a series of articles on heat transfer augmentation in rectangular cross section passages with transverse grooves cut into the walls. Flow visualizations in a long contiguously grooved passage exhibit two-dimensional waves at a Reynolds number of Re=350, followed by a rapid transition to three-dimensional mixing [8]. Heat transfer and friction factor measurements using air show that both the Nusselt number and friction factor are greater than the corresponding values for a flat channel with the same minimum wall to wall spacing [9,10]. A significant result is that fully developed heat transfer is enhanced relative to laminar flat channel flow by as much as a factor of 4.6 at equal Reynolds numbers and by a factor of 3.5 at equal pumping powers. Three-dimensional numerical simulations for Re≤2000 give results that are in good agreement with experimental measurements [11,12]. Moreover, *two*-dimensional simulations were inadequate to capture the transport processes in these configurations for Reynolds numbers greater than Re=570.

Investigations of external flow heat transfer on flat surfaces *downstream* from disturbances have also shown favorable performance characteristics. For example, measurements made on a flat plate downstream from different turbulence-generating grids show that the ratio of heat transfer to friction factor increases linearly with increasing turbulence intensity [13]. Maciejewski and Moffat [14] measured heat transfer from a flat plate subject to very high levels of free-stream turbulence. Their measured heat transfer coefficients, along with that of Blair, increase linearly with the maximum turbulence intensity of the flow.

Experimental measurements in a flat passage downstream of a grooved channel were performed to determine the effect of decaying unsteadiness in an internal flow for the Reynolds number range 1500≤Re≤5000 [15]. These measurements show that the heat transfer coefficient remained high for a substantial distance in the flat region. The pressure gradient, on the other hand, dropped back to the flat passage value much more rapidly, especially for Re>2500. As a result, the heat transfer for a given pumping power was even greater in the first five hydraulic diameters of the decay region than in the grooved passage itself. Moreover, this uncoupled heat/momentum transport behavior suggests that intermittently grooved passages, in which flat regions separate contiguous grooved sections, may have significant advantages in engineering heat transfer devices.

The current work is a numerical investigation of heat and momentum transport in a flat plate passage downstream from a fully developed, symmetrically grooved channel with constant temperature surfaces. This simulation employs two different three-dimensional sub-domains. The first represents one periodicity cell of a continuously grooved passage. It has periodic inflow/outflow boundary conditions in order to simulate fully developed flow. The second subdomain consists of a single groove cell coupled to a flat passage at its downstream end. The inflow conditions to the grooved/flat sub-domain are taken from the outflow of the fully developed domain. The variations of centerline velocity unsteadiness, heat transfer coefficient and pressure gradient with axial position are presented for the Reynolds number range 405≤Re≤764. Heat transfer results from the current work are directly compared to experimental data [10,16]. Finally, the heat transfer versus pumping power performance of the first few groove lengths of the flat passage is compared to that of a fully developed groove channel.

Numerical Method

Computational Domain. Figure 1 shows the pair of three-dimensional sub-domains employed in this work. The upper and lower boundaries are solid walls, and the fluid flows from left to right (in the positive *x*-direction). The domain shown in Fig. 1(*a*) represents one periodicity cell of a long, symmetrically grooved

Contributed by the Heat Transfer Division for publication in the JOURNAL OF HEAT TRANSFER. Manuscript received by the Heat Transfer Division May 17, 2000; revision received June 15, 2001. Associate Editor: J. G. Georgiadis.

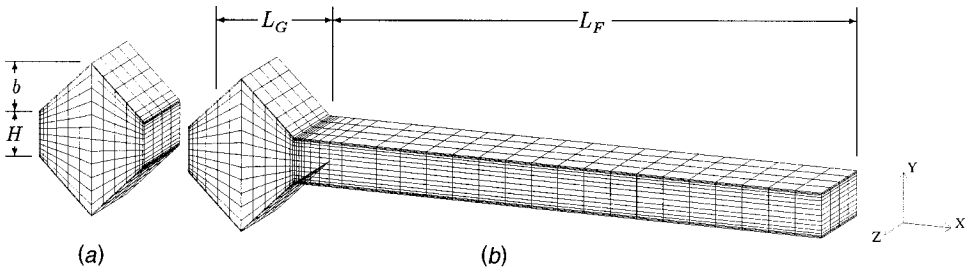

Fig. 1 Spectral element mesh. (*a*) Periodic groove domain. (*b*) Groove/flat domain. The *z*-direction width of both domains is *W*.

channel. The groove depth $b=1.2$ cm, groove length $L_G=2.4$ cm, and minimum wall-to-wall spacing $H=1.0$ cm are the same as those used in earlier experimental work [10,16]. These dimensions are chosen to be compatible with the wavelength of the most slowly decaying Tollmien-Schlichting waves of the outer channel flow [2]. This domain uses periodic inlet/outlet boundary conditions to model fully developed flow. Our earlier numerical simulations show that a single groove cell with periodic boundary conditions is sufficient to model heat transfer and pressure gradient to within 20 percent of experimentally measured values [12].

The sub-domain shown in Fig. 1(*b*) consists of a single groove coupled with a flat region at its downstream end. The flat region wall-to-wall spacing is $H=1.0$ cm and its length is $L_F=5L_G$. The conditions at the outlet of the periodic groove sub-domain (Fig. 1(*a*)) are used as the inlet conditions to the groove-flat domain. The outflow boundary condition for the groove-flat domain is the standard Neumann condition on velocity, $du/dx=0$. This condition produces a minimal flow-direction boundary layer having thickness and amplitude $O(1/\mathrm{Re})$ near the outlet. The grooved portion of the groove-flat domain is included so that the simulation models elliptic (upstream) effects caused by the flat passage. We refer to this region as the "final" or "last" groove since it represents the last groove before the flat passage. Periodic boundary conditions are imposed in the spanwise direction of both computational domains, for which the domain extent is $W=2.0$ cm.

The computational grids in both sub-domains consist of four levels in the *z*-direction. Each *z*-level of the periodic groove domain contains $K_P=196$ hexahedral spectral elements while the groove-flat domain has $K_{GF}=560$ elements in each *z*-level. In the spectral element method [17,18], the solution, data and geometric mapping are expressed as tensor-product polynomials of degree N in each spatial direction, corresponding to a total grid point count of roughly $4(K_P+K_{GF})N^3$. Numerical convergence is achieved by increasing the spectral order N.

The present simulations use consistent approximation spaces for velocity and pressure, with pressure represented as polynomials of degree $N-2$ [18,19]. The momentum equations are advanced by first computing the convection term, followed by a linear Stokes solve in which the velocity field is projected onto a divergence-free space. The scheme is second-order accurate in time. Further details on this method can be found in [19].

The Periodic Domain. In the periodic domain the flow is driven from left to right by a time-varying body force per unit mass f_x. This force is determined so that the mass flow rate through the domain is invariant with time [20]. The thermal problem for the periodic domain requires careful treatment. If one simply specifies zero-temperature conditions on the walls then the solution eventually decays to zero. To produce the desired spatially fully developed state requires that the temperature profiles at the inlet and outlet be self-similar, i.e.,

$$T(x=L_G,y,z,t)=CT(x=0,y,z,t),$$

with $C<1$. The solution technique for computing the fully developed temperature field for constant temperature boundary conditions follows the analysis of Patankar et al. [21]. The energy equation, and associated initial and boundary conditions are

$$\frac{\partial T}{\partial t}+\bar{U}\cdot\nabla T=\alpha\cdot\nabla^2 T \tag{1a}$$

$$T(x,y,z,t=0)=T_{\mathrm{init}}(x,y,z) \tag{1b}$$

$$T(x,y,z,t)=0 \quad \text{on the walls} \tag{1c}$$

$$T(x=L_G,y,z,t)=e^{-cL_G}T(x=0,y,z,t) \tag{1d}$$

Equation 1(d) corresponds to the fully developed and periodic condition where the temperature profile is self-similar from one cell to the next, i.e., $T(x+L_G,y,z,t)=e^{-cL_G}\cdot T(x,y,z,t)$ for all (x,y,z,t), where $e^{-cL_G}=C$. The constant c is unknown and is a parameter to be determined as part of the computation. The fact that each cell independently satisfies the homogeneous Eq. (1) and that we are considering fully developed solutions that are independent of T_{init} implies that the solution to (1) for each cell would yield the same value of c. Hence, c cannot be a function of x. Moreover, it is readily demonstrated from energy arguments that, under fully developed conditions, c cannot be a function of time even when the flow is itself unsteady.

Any function satisfying the above self-similar condition has the unique decomposition $T(x,y,z,t)=e^{-cx}\theta(x,y,z,t)$, where $\theta(x+L_G,y,z,t)=\theta(x,y,z,t)$ is a periodic function. Thus, the computation of T is reduced to the computation of a periodic function θ, and the constant c. Substituting this decomposition into Eq.(1) yields

$$\frac{\partial\theta}{\partial t}+\bar{U}\cdot\nabla\theta-\alpha\cdot\nabla^2\theta=(\alpha\cdot c^2+uc)\theta-2\alpha\cdot c\frac{\partial\theta}{\partial x} \tag{2a}$$

$$\theta(x,y,z,t=0)=\theta_{\mathrm{init}}(x,y,z) \tag{2b}$$

$$\theta(x,y,z,t)=0 \quad \text{on the walls} \tag{2c}$$

$$\theta(x=L_G,y,z,t)=\theta(x=0,y,z,t). \tag{2d}$$

Since the fully developed solution is independent of the initial condition we may arbitrarily set $\theta_{\mathrm{init}}=1$. Equation (2*a*) is solved using a semi-implicit time-stepping procedure similar to that for our Navier-Stokes solver. To avoid excessive time step restrictions, the diffusive terms are treated implicitly, while the convective terms are treated explicitly. In addition, all terms on the right of Eq. (2*a*) are treated explicitly using the latest available value for c.

In the steady state case $(\partial/\partial t=0)$, Eq. (2) constitutes an eigenproblem for the eigenpair (c,θ). The constant c corresponds to the decay rate of the mean temperature in the *x*-direction. As such, a larger value of c implies more rapid decay and more effective heat transfer. In the convection-dominated limit where the Peclet number $U_m D_h/\alpha$ is large, Eq. (2*a*) becomes a linear eigenvalue problem. In this case standard iterative methods for computing the lowest value of c (corresponding to the most slowly decaying

mode in x) can be used even when the nonlinear (c^2) term in Eq. (2a) is not identically zero. We find that this method accurately computes the decay rate and Nusselt numbers for steady flows in square and round ducts [22].

For steady periodic flows with period τ, the temperature is periodic in time, implying $T(x,y,z,t+\tau)=T(x,y,z,t)$. Since c is independent of time, this implies that $\theta(x,y,z,t+\tau)=\theta(x,y,z,t)$. If the value of c is not chosen correctly, this condition will not be satisfied. Unfortunately, τ is not known a priori but is a result of the hydrodynamic part of the calculation. A robust approach to compute c and θ is obtained by multiplying Eq. (2a) by θ, integrating over a single cell Ω, and simplifying to yield:

$$\frac{1}{2}\frac{d}{dt}\int_{\Omega}\theta^2 dV=\int_{\Omega}[(\alpha c^2+uc)\theta^2-\alpha\nabla\theta\cdot\nabla\theta]dV. \qquad (3)$$

While we do not expect the time derivative of the average temperature (represented by the left-hand side of Eq. (3)) to be identically zero, it will in general be less than the time derivative of θ at any one point in the domain. Moreover, if we integrate the right-hand side of Eq. (3) from time t to $t+\tau$, the resultant quantity must be zero due to the temporal periodicity.

This suggests a two-tier strategy for computing c in the unsteady case. Initially, we determine c such that the right hand side of Eq. (3) is identically zero at each time step. This will permit a relatively coarse but quick determination of c and θ. Subsequently, once τ is well established, we use this value of c to advance θ for one or more periods, and monitor the decay or growth of $\int\theta^2 dV$. At the end of each trial period, we adjust c until convergence is attained. Typical values of cL_G over the range of Re considered are 0.1039 to 0.1127, corresponding to 9.87 to 10.6 percent drops in mean temperature over a single groove length.

The periodic groove simulations were initialized using results from our work on contiguously grooved passages at Reynolds numbers of Re=405, 509, 640, and 764 [12]. To initialize the groove-flat computations, the periodic groove data was copied to the final groove, and plane Poiseuille flow of the same mass flux was used in the flat region. The combined simulations were then run for a sufficient length of time to flush the groove-flat region several times before collecting transport data.

The time and z-direction averaged temperature, velocity and pressure at each x,y-location are calculated after initial transients decay by averaging backwards from the final time t_F over successively longer intervals until the result converged. For example the average temperature field is

$$T_A(x,y)=\frac{1}{(t_F-t_1)W}\int_{t_l}^{t_F}\int_0^W T(x,y,z,t)dzdt.$$

In this expression t_l is a time after the flow has flushed through the domain several times but early enough so the results do not depend on its value.

The polynomial degree is $N=7$ for all calculations in this paper, corresponding to a grid point count of approximately 10^6. Our earlier work on contiguously grooved passages [11,12] established that $N=7$ and 9 give the same heat transfer and pressure gradient results at Re=950. Since the size of the smallest flow structures *increase* as the Reynolds number decreases, the results for Re<950 with $N=7$ were assumed to be spatially resolved and insensitive to higher spectral orders. Moreover, since the maximum Reynolds number for the current study is Re=764 there is no reason to believe that the current geometry contains smaller structures than the ones found in the earlier work. No additional spectral order sensitivity analysis was therefore seen as necessary for this geometry.

Our earlier work for a fully developed grooved channel used periodic boundary conditions in the z-direction and a domain width of $W=2$ cm [12]. That work showed that the transport results at Re=500 were not sensitive to the use of a wider domain ($W=3$ cm). The results for Re≥500 were assumed to be insensitive to the use of wider domains since the dominant flow modes were expected to *decrease* in size with increasing Reynolds numbers.

The domain width of $W=2$ cm was also used in the current study because it is twice the minimum wall-to-walls spacing H. However, due to the very large number of grid points and long time integrations involved in the current calculation, computational resources were not available to conduct a domain-width sensitivity study. This is unfortunate since the lowest Reynolds number of the current work (Re=405) is less than the value at which the width sensitivity analysis was performed in our earlier work. Moreover, small eddy structures exiting the grooved domain may possibly coalesce into larger structures as they move in the flat passage. However, the simulations at Re=509, 640, and 764 (Fig. 2) predict that the most energetic (most slowly decaying) structures have z-dimensions that are half the passage width or less.

The simulations were performed on $P=8$, 16, 32, and 64 processors of a 96 processor SGI Origin 2000. Each processor is a MIPS R10000 running at 250 MHz and shares 24 GB of memory. A typical three-dimensional simulation requires approximately fourteen seconds per time step ($\Delta t=0.00005$) for the groove ($P=16$) and for the groove-flat ($P=64$) simulations. The groove and groove-flat simulations were run concurrently with the outflow data from the groove used as the inflow boundary condition data of the groove-flat simulation.

Results

Velocity. Figure 2 shows the v-component of velocity in the passage center plane ($y=H/2$). These surfaces represent typical snapshots at four Reynolds numbers, Re=405, 509, 640, and 764. In this work the Reynolds number is $\mathrm{Re}=U_m D_H/\nu$, where the average velocity through the minimum channel cross section is $U_m=Q/WH$, the minimum channel hydraulic diameter is $D_H=2H$, ν is the fluid kinematic viscosity, and Q is the volume flow rate passing through the domain. The results in Fig. 2 are from the groove-flat sub-domain shown in Fig. 1(*b*).

Studies of transversely grooved passages have shown that Kelvin-Helmholtz instabilities of shear layers that span the groove openings destabilize two-dimensional Tollmien-Schlichting waves at Re=350 [2], and that three-dimensional flow structures develop as the Reynolds number increases [9]. Figure 2 shows that at Re=405 two-dimensional waves (with essentially no variation in the z-direction) travel through the groove region and decay downstream. At Re=509, the flow is three-dimensional with regular variations in the z-direction. This variation is much less regular as the Reynolds number increases to Re=640 and 764. Careful examination of the downstream edge of the surfaces at Re=509, 640, and 764 show that the most slowly decaying modes have two waves in the z-direction. Disturbances in flat passage flows generally decay for Reynolds numbers less than Re=2800 [23]. We see that unsteady flow structures that develop in the grooved regions dissipate in the flat section for all four Reynolds numbers considered in this work.

Figure 3 shows the unsteady component of fluid speed S_{rms} versus axial position and Reynolds number at the channel center plane ($y=H/2$). This unsteady speed is $S_{\mathrm{rms}}=(u_{\mathrm{rms}}^2+v_{\mathrm{rms}}^2+w_{\mathrm{rms}}^2)^{1/2}$ where u_{rms}, v_{rms}, and w_{rms} are the root mean squared averaged deviations of the x-, y- and z-components of velocity from their respective mean values. In Fig. 3, S_{rms} is normalized by the fully developed centerline velocity in a parallel plate passage, $U_{p,c}=1.5U_m$. The region $0\leq x/L_G\leq 1$ represents results from the periodic groove domain (Fig. 1(*a*)). The region $1\leq x/L_G\leq 2$ corresponds to the groove portion of the groove-flat domain, referred to as the "last groove." The region $2\leq x/L_G\leq 7$ represents the flat section.

We see that the level of unsteadiness in the grooves increases from roughly 8 percent at Re=405 to over 16 percent at Re=764.

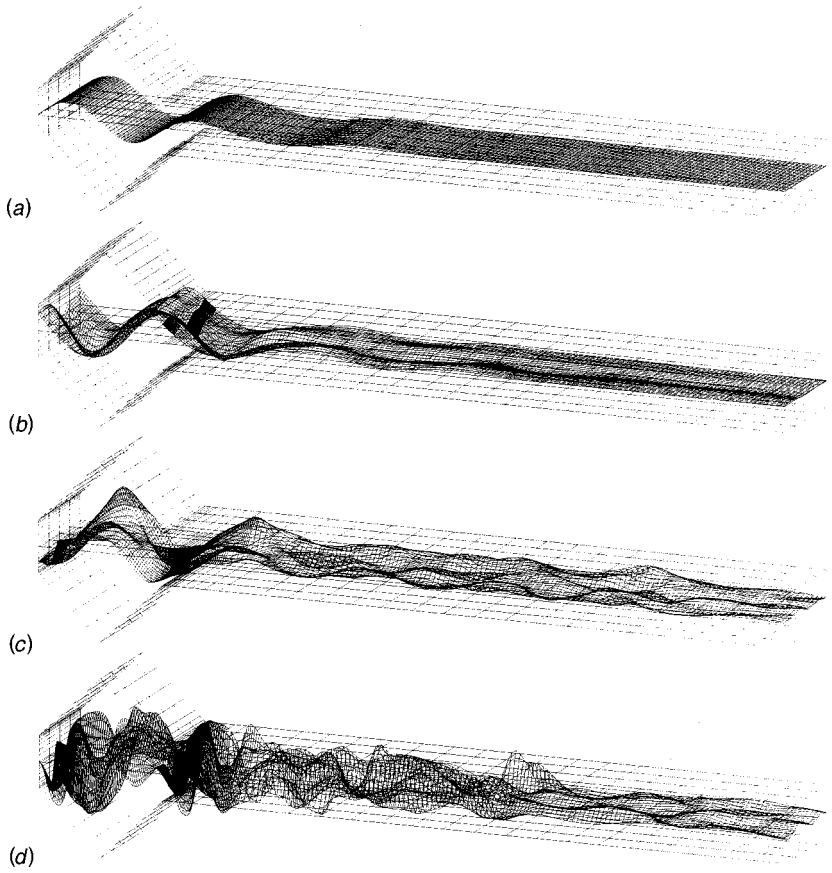

Fig. 2 Surfaces of *v*-velocity at $y=H/2$. (*a*) Re=405. (*b*) Re=509. (*c*) Re=640. (*d*) Re=764.

At each Reynolds number the profile shapes in the two grooves are similar. However, the values in the downstream three-quarters of the last groove ($x/L_G=1.25$ to 2) are somewhat different than those in the periodic groove ($x/L_G=0.25$ to 1). This is an elliptic effect caused by the presence of the downstream flat passage.

The unsteadiness that develops in the grooved regions dissipates in the flat section for all four Reynolds numbers, as discussed in connection with Fig. 2. The rate of axial decay is steep near $x/L_G=2$ and then decreases further downstream. At Re $=405$, the unsteadiness decays to essentially zero before the end of the flat passage. At the higher Reynolds numbers, however, unsteadiness is still present five groove-lengths after the end of the grooved passage.

Figure 4 is a plot of time average velocity in the channel center plane U_c versus axial position. This velocity is normalized by the fully developed centerline velocity in a parallel plate passage, $U_{p,c}$. Once again, while the profile shapes are similar in the two grooves, the flat passage does affect the centerline velocity in the downstream three-quarters of the last groove. We see that the centerline velocity experiences a substantial acceleration near $x/L_G=2$. This acceleration is caused by the development of

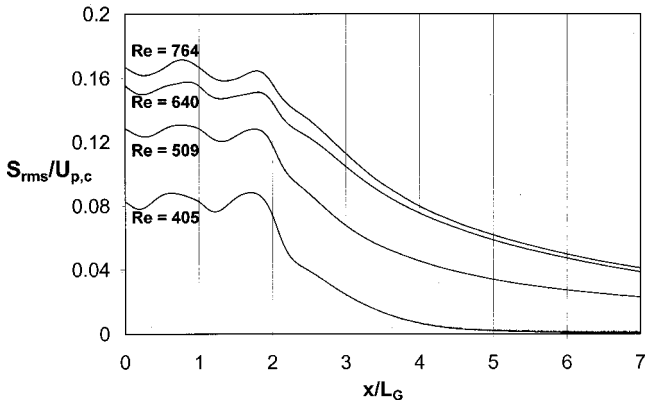

Fig. 3 Centerline unsteady velocity versus location and Reynolds number.

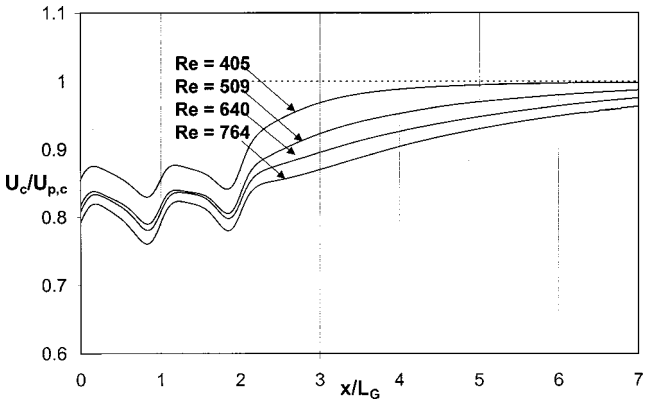

Fig. 4 Centerline velocity versus axial location and Reynolds number

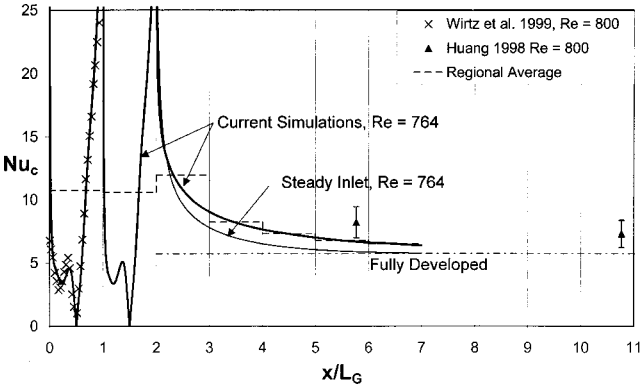

Fig. 5 Centerline Nusselt number versus axial location

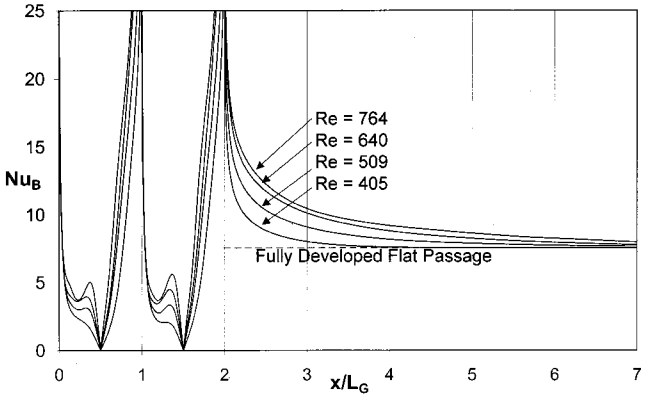

Fig. 6 Bulk Nusselt number versus axial location

boundary layers on the surfaces of the flat region. For Re=405 the centerline speed reaches the flat passage fully developed value at $x/L_G=7$. For higher Reynolds number however, the centerline speed does not reach the fully developed value before the end of the computational domain. Finally, comparing the profiles of average centerline velocity in Fig. 4 with the rms profiles in Fig. 3, we see that regions of accelerating flow ($dU_c/dx>0$) generally correspond to regions of rapidly decreasing unsteadiness ($dS_{\rm rms}/dx<0$).

Transport. Figure 5 shows measured and calculated centerline Nusselt numbers Nu_C versus axial position. The centerline Nusselt number is defined as $\mathrm{Nu}_C=q''D_h/(\Delta T_C k)$. In this expression the heat transfer to the fluid per unit *projected* surface area is $q''=-k(dT_A/dn)_{\rm wall}/m$, where T_A is the time and *z*-averaged temperature, *n* is the direction normal to the wall, *m* is the wall surface direction cosine, and the temperature gradient is evaluated at the wall. The direction cosine in the flat region is $m=1$, while it is $m=0.7071$ in the grooved region. The fluid thermal conductivity is *k*, and ΔT_C is the local, time and *z*-averaged difference between the surface temperature and the fluid temperature at the *centerline* of the passage $T_A(y=H/2)$ (rather than the bulk fluid temperature). The holographic measurement technique used in the experiments was better suited for measuring local centerline temperatures than it was for measuring bulk values [10,16].

Measurements made in a fully developed grooved channel at Re=800±57 (the reported uncertainly limit has a 99 percent confidence level) are shown using *x*-symbols [16]. Measurements in a flat passage downstream from the groove channel at the same Reynolds number are shown using up-pointing triangles [10]. The 99 percent confidence level uncertainty limits on the flat passage measurements are shown using error bars. Directly comparable center point Nusselt numbers calculated from the current simulation at Re=764 are shown using a heavy solid line (the value Re=764 was used so that the simulation could be initiated using earlier results from a fully developed groove passage simulation [12]. The thinner solid line is from a simulation that used steady inlet temperature and velocity profiles at $x/L_G=2$. Those profiles were equal to the time average profiles from the unsteady simulations at Re=764. Horizontal dashed lines represent arithmetic average values of Nu_C in the regions $0\leqslant x/L_G\leqslant 1$, $1\leqslant x/L_G\leqslant 2$, $2\leqslant x/L_G\leqslant 3$, etc. A dashed-dot line shows the fully developed center point Nusselt number for a laminar flat channel.

The experimental measurements in a fully developed groove show that the heat transfer on the downstream (windward) surface ($0.5\leqslant x/L_G\leqslant 1$) is significantly higher than the heat transfer on the upstream (leeward) side ($0\leqslant x/L_G\leqslant 0.5$). This is due to the direction of the re-circulating vortex flow in the groove. The upstream surface exhibits a local peak at $x/L_G=0.3$ due to the impingement of the vortex at that location. The experimental results in the flat passage show that the heat transfer is at least 25 percent higher than the fully developed flat passage value for $x/L_G<11$.

Figure 5 shows excellent agreement between the experimental and numerical results in the periodically fully developed grooved channel ($0\leqslant x/L_G\leqslant 1$). However, the numerical results decay more rapidly in the flat region than is expected from the measurements. We do not currently understand why this difference exists.

We note that while the numerical Nusselt number profile in the last groove ($1\leqslant x/L_G\leqslant 2$) has a different shape from that in the fully developed groove ($0\leqslant x/L_G\leqslant 1$), the regionally averaged values for these two grooves (horizontal dashed lines) are roughly equal. The average heat transfer over the first groove-length of the flat passage ($2\leqslant x/L_G\leqslant 3$) is somewhat larger than value in the groove regions. Subsequent regionally averaged values decrease as distance from the last groove increases. Finally, we note that the simulation that used steady inlet conditions at $x/L_G=2$ (thinner solid line) gave a Nusselt number profile that is roughly 20 percent below the results from the unsteady simulation. We see that at this Reynolds number, unsteadiness from the grooved channel increases the flat passage heat transfer for at least five groove-lengths.

Figure 6 shows local *bulk* Nusselt number versus axial location for 405≤Re≤764. The bulk Nusselt number is defined as $\mathrm{Nu}_B=q''D_h/(\Delta T_B k)$, where ΔT_B is the local, time averaged difference between the surface and bulk fluid temperatures. The bulk temperature at any axial location *x* and time *t* is defined as $T_B(x,t)=(\int uT dA)/(\int u dA)$, where both integrations are taken across the entire cross sectional area at the given *x*-location.

We see that the heat transfer level throughout the domain increases with Reynolds number. In the grooved region, the local peak heat transfer due to impingement of the vortices becomes more prominent with increasing Re. Moreover, while the Nusselt number profiles in the two grooves are similar, the local maximum is more prominent in the last groove than it is in the periodic groove. In the flat region, the Nusselt number is very high at the inlet and drops off in the axial direction. These Nusselt number values approach the value of a fully develop flat channel for large x/L_G. However, the decay rate decreases as the Reynolds number increases.

Figure 7 shows the log mean bulk Nusselt number versus Reynolds number and location. Each line represents a different region in the passage. The log mean Nusselt number is defined as $\mathrm{Nu}_{B,LM}=q''_R D_h/(\Delta T_{B,LM} k)$, where $\Delta T_{B,LM}$ is the log mean bulk temperature difference across each region, and q''_R is the total heat flux to the region divided by its total projected surface area. The fully develop bulk Nusselt number for a flat passage is shown using a dashed line.

The log mean Nusselt numbers in the periodic groove region (open squares) and the final groove (*x*-symbols) are essentially identical for all four Reynolds numbers considered in this work.

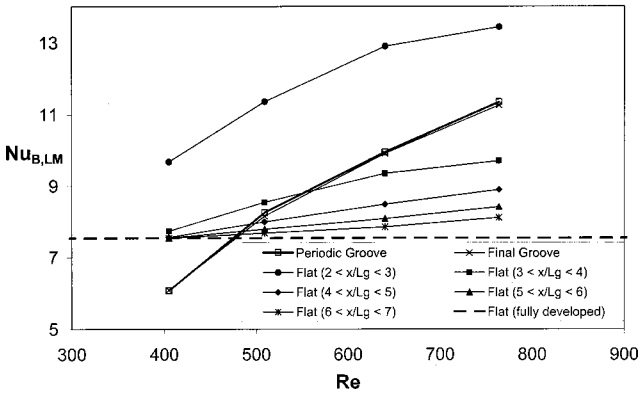

Fig. 7 Regionally averaged Nusselt number versus Reynolds number and location

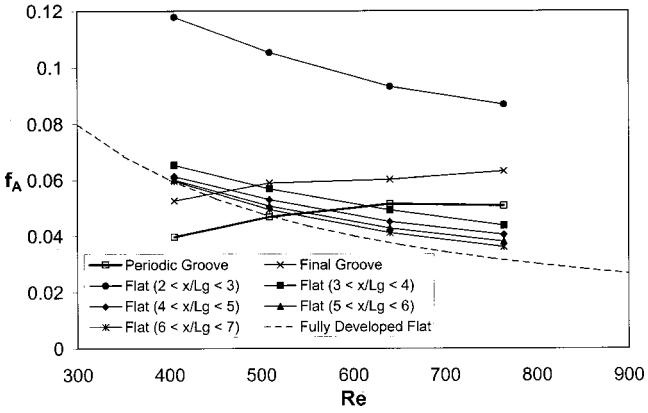

Fig. 9 Regionally averaged pressure gradient versus Reynolds number and location

At Re=405, the heat transfer coefficient in the groove region is actually lower than the level in a flat passage. The thermal resistance of the slowly turning groove vortices causes this. Even though the flow field is unsteady at this Reynolds number (see Figs. 2(*a*) and 3), the level of enhanced mixing is not sufficient to overcome this resistance. At Re=509, the level of three dimensional mixing exhibited in Figs. 2(*b*) and 3 is sufficient to slightly overcome the thermal resistance of the grooves. As the Reynolds number is increased to Re=640 and 764, the highly irregular three-dimensional mixing discussed earlier substantially increases heat transfer compared to a flat passage.

In the first groove-length of the flat passage ($2 \leqslant x/L_G \leqslant 3$, solid circles) the average heat transfer exceeds the grooved channel value for all Reynolds numbers considered. This increased heat transfer is due to the absence of the thermal resistance of the groove. The heat transfer decreases in each subsequent region and eventually approaches the fully developed flat passage value.

Figure 8 shows the local dimensionless pressure gradient f versus axial location and Reynolds number. The dimensionless gradient is defined as $f=(-dp_{A,c}/dx)[D_h/(2\rho U_m^2)]$, where $p_{A,c}$ is the time and z-averaged pressure in the center plane ($y=H/2$) and ρ is the fluid density. The profiles of f are in many ways similar in shape to the Nusselt number profiles seen in Fig. 6. However, while the Nusselt number profile represents the heat flux (temperature gradient) at the wall, the pressure gradient is a combination of wall shear stress (velocity gradient) and the axial gradient of the momentum flux. The converging and diverging regions of the grooved sections, as well as the developing boundary layer flow in the flat passage, cause the velocity profiles to vary in the axial direction. This variation may cause the axial gradient of the momentum flux to be significant.

The pressure gradient profiles in the two grooves are similar to each other. However, the flat passage affects the pressure gradient in the downstream three-quarters of the last groove. The pressure gradient at $x/L_G=2$ is substantially greater than the value at $x/L_G=1$. This is due to the acceleration of the flow at $x/L_G=2$, discussed in connection with Fig. 4.

Figure 9 shows the average dimensionless pressure gradient across different regions of the passage versus Reynolds number and location. The average gradient is defined as

$$f_A=\frac{1}{x_2-x_1}\int_{x_1}^{x_2} f\,dx=\frac{p_{A,1}-p_{A,2}}{x_2-x_1}\frac{D_h}{2\rho U_m^2},$$

where $p_{A,1}$ and $p_{A,2}$ are the time and z-average centerline pressures at locations x_1 and x_2, respectively. Each line corresponds to the average across a different region in the passage ($0 \leqslant x/L_G \leqslant 1$, $1 \leqslant x/L_G \leqslant 2$, $2 \leqslant x/L_G \leqslant 3$, etc). A dashed line shows the fully developed Fanning friction factor for a flat passage ($f=24/\mathrm{Re}$).

The dimensionless pressure gradient across the periodic groove (open squares in Fig. 9) increases with Reynolds number. At Re =405, this pressure gradient is actually smaller than the gradient in a flat passage. This is because the grooves effectively relax the no slip boundary conditions at $y=0$ and H. While the flow is unsteady at this Reynolds number, the level of mixing does not overcome the decrease in drag due to the grooves. As the Reynolds number increases to Re=509, the flow exhibits three dimensional mixing that brings the pressure gradient in the periodic

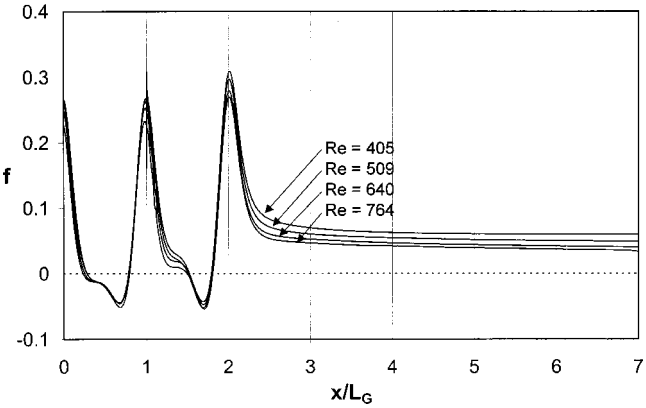

Fig. 8 Local dimensionless pressure gradient versus axial location and Reynolds number

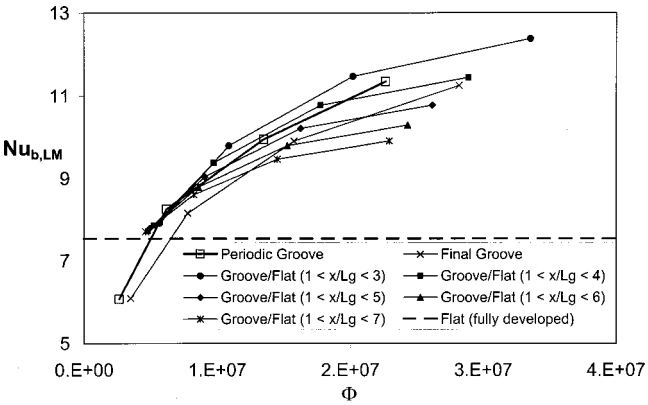

Fig. 10 Regionally averaged Nusselt number versus pumping power

groove to the same value as a flat passage. The pressure gradient increases beyond the level in flat passages at higher Reynolds numbers.

Unlike the heat transfer, the pressure gradient across the last groove is substantially larger than that across the periodic groove. This is partially due to the acceleration of the flow as it enters the flat passage. The dimensionless pressure gradient reaches its highest values in the first groove-length of the flat passage ($2 \leqslant x/L_G \leqslant 3$) and rapidly drops back to the fully developed flat passage values further downstream.

Figure 10 is a plot of the log mean bulk Nusselt number for different regions of the passage versus the dimensionless power required to pump fluid through the region. The dimensionless pumping power per unit length is

$$\Phi = \frac{p_{A,1} - p_{A,2}}{x_2 - x_1} \frac{Q}{W} \frac{D_h^3}{\rho \nu^3} = f_A \, \mathrm{Re}^3$$

In Fig. 10, different lines are used for the periodic groove (heavy line with open squares), the last groove (x-symbols), and regions that include the last groove *and* different lengths of the flat passage (i.e., $2 \leqslant x/L_G \leqslant 3$, $2 \leqslant x/L_G \leqslant 3$, etc.). The horizontal dashed line shows the performance of a fully developed flat passage. The purpose of this plot is to compare the performance of flat regions downstream from a fully developed grooved passage to the performance of the grooved passage itself. The last groove is included with the flat passage because the flat region always affects its performance.

The results for the fully developed groove (open squares) show that the heat transfer increases with the pumping power. Heat transfer in laminar parallel plate flow, on the other hand, is constant. Moreover, the curvature of this line indicates that at low pumping power levels, small increases in pumping power lead to large increases in heat transfer. However, the increase in heat transfer for a given increase in pumping power diminishes as the initial pumping power level increases. The final groove (x-symbols) gives lower levels of heat transfer for a given pumping power than in the fully developed groove. This is because the heat transfer levels in the two grooved regions are the same but the pressure gradient in the last groove is higher than that in the fully developed groove.

For the region that includes the last groove and the first groove-length of the flat passage (solid circles), the heat transfer for a given pumping power is roughly 5 percent higher than that in the fully developed groove. Alternately stated, the pumping power requirement for a given heat transfer level is decreased by approximately 25 percent. As the flat region length increases, its performance approaches that of a fully developed flat passage and its average heat transfer decreases. However, configurations with flat regions up to three groove-lengths long still exhibit higher heat transfer for a given pumping power than a fully developed grooved passage.

Conclusions

Navier-Stokes simulations of three-dimensional flow and augmented convection in a flat passage downstream from a fully developed channel with symmetric, transverse grooves on two opposite walls were performed for $405 \leqslant \mathrm{Re} \leqslant 764$ using the spectral element technique. Unsteady flow that develops in the grooved region persists several groove-lengths into the flat passage, increasing both local heat transfer and pressure gradient relative to steady flat passage flow. Moreover, the heat transfer for a given pumping power in a flat region up to three groove-lengths long is even greater than the high levels observed in a fully developed grooved passage.

This work suggests that the performance of intermittently grooved passages, in which flat regions separate contiguously grooved sections, may offer favorable heat transfer versus pumping power performance in engineering devices. However, the development of unsteady flow in short grooved regions and the decay of non-fully-developed grooved channel unsteadiness in flat regions must be investigated before these designs can be optimized.

Acknowledgments

National Science Foundation Grant CTS-9501502 supported this work. The work of P. F. Fischer was supported by the Mathematical, Information, and Computational Sciences Division subprogram of the Office of Advanced Scientific Computing Research, U.S. Department of Energy, under Contract W-31-109-Eng-38. The work of H. M. Tufo was supported by the Department of Energy under Grant number B341495 to the Center on Astrophysical Thermonuclear Flashes at University of Chicago, and by the University of Chicago.

Nomenclature

b = groove depth, Fig. 1
L_G = channel periodicity length, Fig. 1
c = decay constant
D_h = minimum hydraulic diameter, $2H$
f = fanning friction factor, $(dp/dx)[f_x/(2\rho U_a^2)]$
f_x = fluid body force per unit mass in the x-direction
H = minimum channel wall to wall spacing, Fig. 1
k = fluid thermal conductivity, 0.0263 W/m°C
K = number of spectral elements
N = spectral element order
Nu_b = bulk Nusselt number based on projected area
Nu_c = center point Nusselt number
Pr = fluid molecular Prandtl number, 0.70
Re = Reynolds number, $U_m D_h/\nu$
t = time
T = temperature
T_b = bulk temperature
T_c = center point temperature
u,v,w = velocity components in the x, y, and z directions
U_m = mean x-velocity at the minimum channel cross-section
V = volume
Q = volume flow rate, $V_r = (1/L)\int_\Omega u dV$
W = width of the computational domain, Fig. 1

Greek

α = thermal diffusivity, 2.63×10^{-5} m^2/s
ν = fluid kinematic viscosity, 1.84×10^{-5} m^2/s
θ = periodic temperature
ρ = fluid density, 1.006 kg/kg
τ = period of local time variations
Ω = computation domain

References

[1] Webb, R. L., 1994, *Principles of Enhanced Heat Transfer*, John Wiley & Sons, New York.
[2] Ghaddar, N. K., Korczak, K., Mikic, B. B., and Patera, A. T., 1986, "Numerical Investigation of Incompressible Flow in Grooved Channels: Part 1—Stability and Self-Sustained Oscillations," J. Fluid Mech., **168**, pp. 541–567.
[3] Greiner, M., 1991, "An Experimental Investigation of Resonant Heat Transfer Enhancement in Grooved Channels," Int. J. Heat Mass Transf., **24**, pp. 1383–1391.
[4] Roberts, E. P. L., 1994, "A Numerical and Experimental Study of Transition Processes in an Obstructed Channel Flow," J. Fluid Mech., **260**, pp. 185–209.
[5] Kozlu, H., Mikic, B. B., and Patera, A. T., 1988, "Minimum-Dissipation Heat Removal by Scale-Matched Flow Destabilization," Int. J. Heat Mass Transf., **31**, pp. 2023–2032.
[6] Karniadakis, G. E., Mikic, B. B., and Patera, A. T., 1988, "Minimum-Dissipation Transport Enhancement by Flow Destabilization: Reynolds Analogy Revisited," J. Fluid Mech., **192**, pp. 365–391.
[7] Amon, C. H., Majumdar, D., Herman, C. V., Mayinger, F., Mikic, B. B., and Sekulic, D. P., 1992, "Experimental and Numerical Investigation of Oscillatory Flow and Thermal Phenomena in Communicating Channels," Int. J. Heat Mass Transf., **35**, pp. 3115–3129.
[8] Greiner, M., Chen, R.-F., and Wirtz, R. A., 1989, "Heat Transfer Augmentation

Through Wall-Shaped-Induced Flow Destabilization,'' ASME J. Heat Transfer, **112**, pp. 336–341.
[9] Greiner, M., Chen, R.-F., and Wirtz, R. A., 1991, ''Enhanced Heat Transfer/Pressure Drop Measured From a Flat Surface in a Grooved Channel,'' ASME J. Heat Transfer, **113**, pp. 498–500.
[10] Wirtz, R. A., Huang, F., and Greiner, M., 1999, ''Correlation of Fully Developed Heat Transfer and Pressure Drop in a Symmetrically Grooved Channel,'' ASME J. Heat Transfer, **121**, pp. 236–239.
[11] Greiner, M., Spencer, G., and Fischer, P. F., 1998, ''Direct Numerical Simulation of Three-Dimensional Flow and Augmented Heat Transfer in a Grooved Channel,'' ASME J. Heat Transfer, **120**, pp. 717–723.
[12] Greiner, M., Faulkner, R. J., Van, V. T., Tufo, H. M., and Fischer, P. F., 2000, ''Simulations of Three-Dimensional Flow and Augmented Heat Transfer in a Symmetrically Grooved Channel,'' ASME J. Heat Transfer, **122**, pp. 653–660.
[13] Blair, M. F., 1983, ''Influence of Free-Stream Turbulence on Turbulent Boundary Layer Heat Transfer and Mean Profile Development: Part I—Experimental Data; Part II—Analysis of Results,'' ASME J. Heat Transfer, **105**, pp. 33–47.
[14] Maciejewski, P. K., and Moffat, R. J., 1992, ''Heat Transfer with Very High Free-Stream Turbulence: Part I—Experimental Data; Part II—Analysis of Results,'' ASME J. Heat Transfer, **114**, pp. 827–839.
[15] Greiner, M., Chen, R.-F., and Wirtz, R. A., 1995, ''Augmented Heat Transfer in a Recovery Passage Downstream From a Grooved Section: An Example of Uncoupled Heat/Momentum Transport,'' ASME J. Heat Transfer, **117**, pp. 303–308.
[16] Huang, F., 1998, ''Experimental Investigation of Fully-Developed Augmented Convection in a Symmetrically Grooved Channel,'' Masters of Science Degree thesis, University of Nevada, Reno.
[17] Patera, A. T., 1984, ''A Spectral Element Method for Fluid Dynamics; Laminar Flow in a Channel Expansion,'' J. Comput. Phys., **54**, pp. 468–488.
[18] Maday, Y., and Patera, A. T., 1989, ''Spectral Element Methods for the Navier-Stokes Equations,'' *State of the Art Surveys on Computational Mechanics*, A. K. Noor and J. T. Oden, eds., ASME, New York, pp. 71–143.
[19] Fischer, P. F., 1997, ''An Overlapping Schwarz Method for Spectral Element Solution of the Incompressible Navier-Stokes Equations,'' J. Comput. Phys., **133**, pp. 84–101.
[20] Fischer, P. F., and Patera, A. T., 1992, ''Parallel Spectral Element Solutions of Eddy-Promoter Channel Flow,'' *Proceedings of the European Research Community on Flow Turbulence and Computation Workshop*, Lausanne, Switzerland, Cambridge University Press, pp. 246–256.
[21] Patankar, S. V., Liu, C. H., and Sparrow, E. M., 1977, ''Fully Developed Flow and Heat Transfer in Ducts Having Streamwise Periodic Variations of Cross-Sectional Area,'' ASME J. Heat Transfer, **99**, pp. 180–186.
[22] Kays, W. M., and Crawford, M. E., 1993, *Convection Heat and Mass Transfer*, Third Edition, McGraw-Hill, New York.
[23] Fox, R. W., and McDonald, A. T., 1985, *Introduction to Fluid Mechanics*, 3rd Edition, John Wiley & Sons, New York, p. 338.

Performance of Horizontal Smooth Tube Absorber With and Without 2-Ethyl-Hexanol

Ick-Soo Kyung

Keith E. Herold
e-mail: herold@eng.umd.edu

Center for Environmental Energy Engineering,
Department of Mechanical Engineering,
University of Maryland,
College Park, MD 20742

Absorption of water vapor into aqueous lithium bromide is a fundamental step in absorption refrigeration. When the liquid film is laminar, the coupled heat and mass transfer process is controlled by mass transfer, resulting in low transfer coefficients. Significant augmentation of mass transfer, and hence of the coupled process, is achieved by introducing a trace amount (on the order of 100 ppm) of 2-ethyl-hexanol. The alcohol acts as a surfactant and drives Marangoni convection that effectively mixes the liquid providing a much higher effective mass diffusivity. The film flow in the presence of the alcohol is noticeably different with a complex, apparently unstructured appearance. The flow activity, which can be easily observed, has never been satisfactorily explained until the recent introduction of the Vapor Surfactant theory. This paper presents a series of experimental results of absorption in an actual chiller facility. The novel features of the work include measurement of the effect of inlet subcooling, discussion of the effect of droplets ejected from the tube bundle and an explanation of the importance of flux in the alcohol augmentation physics. [DOI: 10.1115/1.1418366]

Keywords: Absorption, Enhancement, Heat Transfer, Mass Transfer, Refrigeration, Surface Tension

Introduction

The motivation for the present study of absorber heat and mass transfer comes from the fact that the absorber is the largest and most expensive component in a water-lithium bromide absorption chiller. Although absorber heat and mass transfer has been considered previously, it was found that several aspects which prove important in design are missing from the literature treatments. These include: (1) an explanation of the physics of the mass transfer additive, (2) evaluation of the effect of solution inlet subcooling, and (3) evaluation of the effect of solution droplets ejected from the tubes (termed solution slinging in this work). These three new aspects are the focus of this paper.

Experimental studies of absorbers include the work of Nagaoka et al. [1], Cosenza and Vliet [2], Greiter et al. [3], Remec et al. [4], Beutler et al. [5], Hoffmann et al. [6], and Atchley et al. [7]. The field appears mature, but was found to include significant unanswered questions. Each of these studies contributed important parts to the current understanding of absorber design. However, none of these studies considered the effects of either solution inlet subcooling or solution slinging. Several of the studies included experiments involving a mass transfer additive but none of them provided a convincing explanation of the mechanism of additive action. The present study provides an explanation for all of these effects.

Experimental Setup

The experiments were conducted in a single-effect chiller constructed for absorber tube testing as shown in Fig. 1. This is in contrast to most of the other studies in the literature that were done in minisorber configurations consisting of only an absorber and a desorber, with associated support equipment. The advantage of the complete chiller configuration is that the conditions of the vapor flowing from the evaporator to the absorber are more realistic. In particular, the vapor temperature in a complete chiller is considerably lower than in a minisorber configuration. But the most important difference is the vapor concentration of the alcohol additive. This variable has not received much attention in the literature, but it is realized now to be the most critical variable in understanding Marangoni augmentation of absorption.

The chiller was driven by electric heaters (4 kW) in the desorber and cooled by a separate laboratory chiller. The cooling water was fed to the absorber and then condenser in series. A temperature-controlled heater provided the evaporator load. A subcooler at the inlet of the absorber was used to control the absorber solution inlet temperature using a heater and a temperature controller.

The absorber consisted of a set of 19.1 mm OD smooth horizontal copper tubes arranged in a vertical row with 180 deg return bends such that the cooling water flows in series. Two tube bundles were tested in this study; eight tubes of 0.46 m length and four tubes of 0.36 m length. The spacing between the tube walls is 25.4 mm in both bundles.

The solution distribution on the outside of the absorber tubes was accomplished with a header that provides a uniform series of streams spaced 12.7 mm apart. When these streams make contact with the first tube, they spread out and fully cover the top tube surface. However, coverage on the next and subsequent tubes is less complete as the flow tends to coalesce and drop down in larger streams. To improve distribution in the bundle, the vessel has a tilt of 0.45 deg which causes the solution film to flow slowly in the axial direction along the tubes. The result is that all tube surface throughout the bundle is supplied with liquid in a very uniform manner over a time interval of approximately 1.0 sec. Dry patches still form in the bundle but they are rewetted automatically. This tilted arrangement was observed to produce a very repeatable flow pattern in contrast to the poor wetting patterns observed in a closely horizontal alignment. A sight glass installed in the vessel wall enabled viewing of the falling film flowing over the absorber tubes for all experiments.

Experimental Method

The nominal operating conditions and specifications are listed in Table 1. For all tests other than the subcooling experiments, the absorber inlet subcooling was controlled within ± 0.1 K to mini-

Contributed by the Heat Transfer Division for publication in the JOURNAL OF HEAT TRANSFER. Manuscript received by the Heat Transfer Division April 26, 2000; revision received June 5, 2001. Associate Editor: S. Sadhal.

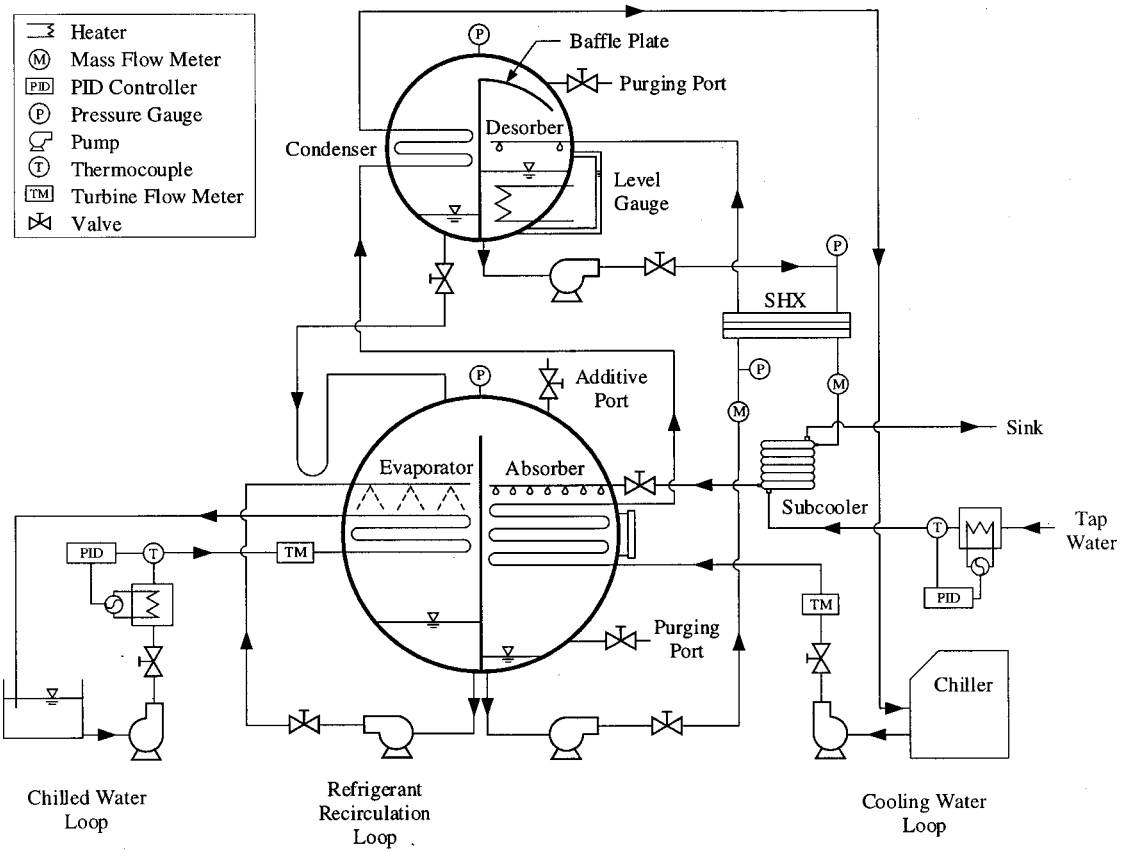

Fig. 1 Schematic diagram of absorber experiment facility

mize subcooling effects. The desorber heat input was set to obtain a particular absorber inlet mass fraction. However, due to disturbing variables, the value obtained was not always identical. For results grouped under a particular mass fraction value, the mass fraction varied in the range ±0.2 percent LiBr between tests.

Before installing a tube bundle in the absorber, the bundle was cleaned using a weak solution of citric acid in water (7 percent acid by weight). After rinsing, the treated surface was handled only with Neoprene gloves during installation of the tube bundle in the absorber.

The experimental setup was maintained at low pressure during the entire experiment schedule. Leakage of air into the system is a common problem in this type of system. The approach taken to address air leakage was to minimize it through careful technique and frequent purging to maintain low air concentrations. Air concentration was not directly measured. The rate of absorber pressure increase due to leakage was in the range 0.051~0.102 mmHg per hour corresponding to a decrease in solution side heat transfer coefficient of approximately 0.9~2.5 $W/m^2.K$ per hour. Prior to each experiment, the upper and lower vessels were purged while circulating the solution between desorber and absorber. When the experiment approached steady state, as judged by no measurable changes in absorber pressure and solution inlet/outlet mass fractions, the data were logged for approximately 20 minutes and average values were taken for analysis. When experimental conditions were changed, the lower vessel was again purged with the vacuum pump. Based on these measurements, it is estimated that the air mass fraction in the absorber during testing was less than 1 percent for all tests and that the presence of air does not interfere with the major conclusions of the study.

For introduction of the alcohol additive into the system, a port was installed in the center of the absorber vessel, just above the absorber tube bundle. The port was isolated from the vessel by a needle valve and a clear tube. After pouring liquid alcohol into the tube and carefully avoiding air bubbles, the alcohol was introduced into the absorber by opening the needle valve while monitoring the alcohol level in the clear tube to avoid introduction of air.

Table 1 Operating and geometry conditions

Parameters	Conditions
Inlet Mass Fraction	57 and 60 % LiBr
Solution Flow Rate	0.01~0.045 kg/s
Inlet Subcooling	-5.5 ~ 5.5 K
Cooling Water Flow Rate	$1.262\%10^{-4}$ m^3/s
Cooling Water Inlet Temp.	30.0 °C
Additive	2-ethyl-hexanol
Tube Number	4 and 8 without additive 4 with additive
Tube Length	0.36 and 0.47 m without additive 0.47 m with additive
Tube Spacing (wall to wall)	25.4 mm
Tube Inner/Outer Diameter	15.875 / 19.050 mm

Data Reduction and Analysis

A total of 34 data channels were recorded including temperatures, high and low pressures, mass flow rates and densities on each side of the solution loop, volume flow rates of the cooling and the chilled water, and the desorber power input. The temperatures were measured using thermocouples. The mass flow rates

and the densities of the rich and poor solutions were measured using two mass flow meters. The mass flow meters were accurate to ±0.10 percent for mass flow rate and ±0.0005 g/cc for density. The volumetric flow rates of the cooling and the chilled water were measured using turbine flow meters accurate to ±1 percent. The pressures in the vessels were measured using pressure transducers accurate to ±0.1 mmHg. The desorber power input was measured using a watt transducer accurate to ±0.2 percent.

The absorber heat transfer rate was calculated from the flow rate of the cooling water through the absorber tube and the temperature difference of the cooling water across the tube bundle according to

$$\dot{Q} = \dot{m}_{cw} c_{p,cw} (T_{cw,o} - T_{cw,i}). \quad (1)$$

The log mean temperature difference in the absorber (ΔT_{lm}) was calculated using the saturation temperatures of the solution at the absorber inlet and outlet and the cooling water inlet and outlet temperatures as

$$\Delta T_{lm} = \frac{(T^{\text{sat}}_{\text{sol},i} - T_{cw,o}) - (T^{\text{sat}}_{\text{sol},o} - T_{cw,i})}{\ln \dfrac{(T^{\text{sat}}_{\text{sol},i} - T_{cw,o})}{(T^{\text{sat}}_{\text{sol},o} - T_{cw,i})}}, \quad (2)$$

where the saturation temperatures were calculated from the measured absorber pressure and the corresponding mass fractions. The conductance for the absorber was calculated as

$$UA = \frac{\dot{Q}}{\Delta T_{lm}}. \quad (3)$$

From the conductance, the solution side heat transfer coefficient, h_{sol}, was calculated as

$$\frac{1}{h_{\text{sol}} A_o} = \frac{1}{UA} - \frac{1}{h_{cw} A_i} - \frac{\ln(d_o/d_i)}{2\pi kL}. \quad (4)$$

The uncertainty in the solution side heat transfer coefficient was estimated to be ±14.6 percent in accordance with a 95 percent confidence level.

The cooling water side heat transfer coefficient, h_{cw}, was measured for the smooth tube bundle (8 tube) through the Wilson plot technique [8] by varying cooling water flow rate from 1×10^{-4} to 3×10^{-4} m^3/s at the cooling water inlet temperature of 30.0°C. For the current cooling water flow rate of 1.26×10^{-4} m^3/s, the cooling water side heat transfer coefficient was determined to be 5368 W/m^2.K. This value was also used in the data analysis of the four-tube bundle.

The emphasis here on the heat transfer coefficient as a measure of the performance of the coupled heat and mass transfer process is a simplified view that is justified by the strong coupling that exists between heat and mass transfer in this system. The two processes are linked by the large energy release that accompanies absorption. Thus, the mass transfer and heat transfer coefficients provide largely redundant information. For laminar absorption (i.e., without the alcohol) the combined process on the tubes is strongly controlled by mass transfer but the mixing between tubes augments mass transfer such that the outlet state is close to a saturated condition. When the alcohol is driving significant surface convection, the outlet condition comes even closer to saturation.

Effect of Absorber Inlet Subcooling

Absorber performance was found to depend on the solution subcooling at the absorber inlet. Tests were run with fixed solution inlet flow rate and LiBr inlet mass fraction while the solution inlet temperature was varied. Figure 2 shows the dependence of the absorber heat transfer on the solution inlet subcooling. Solution side heat transfer coefficient and absorber heat transfer rate both decrease with an increase in subcooling. An increase in subcooling means more heat removal in the subcooler. It was found that

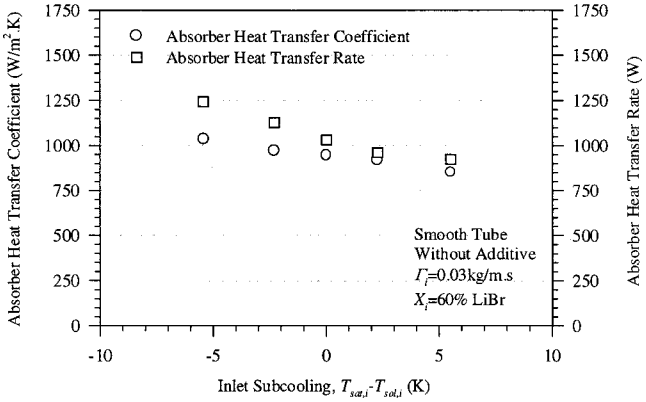

Fig. 2 Effect of inlet subcooling on absorber heat transfer coefficient and heat transfer rate

the absorber heat transfer rate decreased such that the sum of the heat rejection in the absorber and inlet subcooler stayed approximately constant. An increase in inlet subcooling causes a decrease in the mean temperature difference (in the absorber) between the solution and the cooling water, which results in a decrease of both the absorber heat transfer rate and the outlet temperature of the cooling water. This implies a larger temperature difference between the inlet saturation temperature and the cooling water outlet temperature and results in a larger absorber ΔT_{lm}. Thus, higher inlet subcooling causes both a lower absorber capacity and a higher absorber ΔT_{lm}, both of which lead to a smaller heat transfer coefficient.

Absorber Performance Without Additive

Figure 3 shows the comparison of solution side heat transfer coefficient and outlet subcooling for both 57 and 60 percent LiBr. For both conditions, the heat transfer coefficient rises from approximately 640 to 930 W/m^2.K as the specific film flow rate varies from 0.014 to 0.05 kg/m.s. The rate of increase of the heat transfer coefficient appears to level off at high flow rate. Above a specific film flow rate of 0.04 kg/m.s, the data exhibits a plateau heat transfer coefficient of approximate 930 W/m^2.K. This trend of heat transfer coefficient reaching an asymptotic value at high flow rate has been reported in previous studies [4–6,9]. Outlet subcooling of between 2.0 and 3.0 K was measured over the whole flow rate range.

Data on smooth tube absorption from the literature, based on the plateau value at high flow rate, are summarized in Table 2. In calculating ΔT_{lm}, saturated solution temperatures are used at the

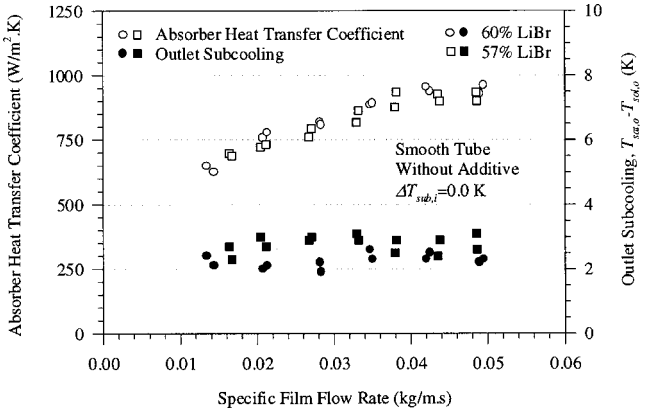

Fig. 3 Comparison of heat transfer coefficient and outlet subcooling

Table 2 Comparison of smooth tube data without additive

Reference	Solution Side Heat Transfer Coefficient ($W/m^2.K$)	Mass Fraction (% LiBr)	Tube Geometry
Current Study	930	57 and 60	4 and 8 Tubes 19.05 mm OD 25.4mm Spacing
Beutler et al. (1996)	800	56	24 Tubes 15.9 mm OD 6.0 mm Spacing
Hoffmann et al. (1996)	750	56	24 Tubes
Remec et al. (1996)	510	59	4 Tubes 18.0 mm OD 28.0 mm Spacing
Miller (1998)	900	62	28.6 mm OD

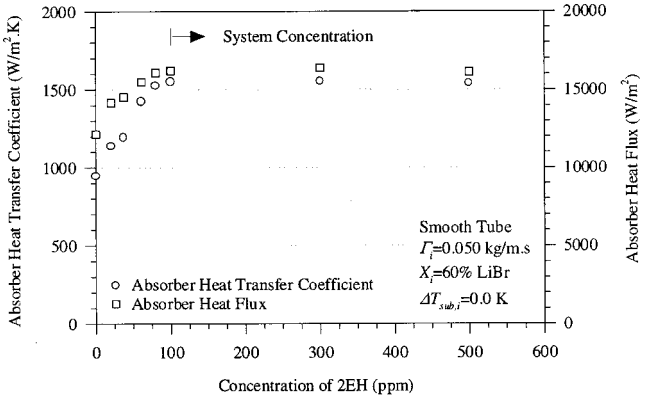

Fig. 4 Effect of 2EH concentration on absorber heat transfer coefficient and heat flux

absorber inlet and outlet except by Miller [9] who used measured solution temperature at the absorber outlet. The reason why the heat transfer coefficient in the current study is higher than values reported in the literature is considered to be due to the low leakage rate of the system, careful purging procedures and the slight tilt of tube bundle (0.45 deg from horizontal).

As shown in Fig. 3, it was found that the LiBr mass fraction had very little effect on the heat transfer coefficient. This seems to be in contrast to the results presented by Beutler et al. [5], Hoffman et al. [6] and Remec et al. [4], where it is reported that the heat transfer coefficient decreases with an increase in LiBr mass fraction, attributed to increases of both kinematic viscosity and surface tension. Hoffmann et al. [6] showed that the heat transfer coefficient decreases and levels off as both the kinematic viscosity and surface tension increase. In the current tests for 57 and 60 percent LiBr without additive, the absorber pressure was maintained at 8.0 and 8.2 mmHg, respectively, and corresponding kinematic viscosities are 2.72×10^{-6} and 3.14×10^{-6} m^2/s and surface tensions are 0.0864 and 0.0862 N/m, respectively. Thus, the kinematic viscosity is only slightly increased, and the surface tension is almost unchanged. Furthermore, these values of kinematic viscosity and surface tension fall in the plateau region in the analysis of Hoffmann et al. [6] so that the heat transfer coefficient is not particularly sensitive to the change of LiBr mass fraction in the current ranges. Thus, the trends exhibited by the present results are not inconsistent with those of Hoffmann et al. [6].

Effect of Alcohol Concentration

The alcohol used in this study is 2-ethyl-hexanol (2EH). This alcohol was chosen based on its widespread use in commercial absorption machines. It was observed through the sight glass that once the 2EH was introduced into the absorber, strong secondary flows, apparently driven by Marangoni convection, were present over the entire liquid film surface. The secondary flows cause the film thickness to be irregular and complex.

The experiments with alcohol were initially performed with an eight-tube bundle. However, the heat transfer with alcohol was found to be only 20 percent greater than the value without alcohol. For example, for the 57 percent LiBr case at a solution flow rate of 0.05 kg/m.s, the heat transfer coefficient increased from 930 (without alcohol) to 1110 $W/m^2.K$ with a system concentration of 500 ppm 2EH for an enhancement ratio of 1.2. The corresponding absorber heat fluxes were 6.17 kW/m^2 (without alcohol) and 7.06 kW/m^2 (with alcohol). To achieve higher flux, subsequent tests were run with a four-tube absorber bundle where the flux was found to range from 9.28 kW/m^2 without alcohol to 11.82 kW/m^2 with alcohol.

Figure 4 shows the results obtained using the four-tube bundle. The plot shows the 2EH concentration effect on heat transfer coefficient and absorber heat flux. These experiments were performed while both the solution flow rate and the inlet mass fraction were held constant. An amount of 2EH corresponding to 500 ppm based on the solution mass was initially added into the system and the data were obtained as the alcohol concentration decreased due to the purging process. As can be seen in Fig. 4, the heat transfer coefficient increases almost linearly from 930 $W/m^2.K$ at zero ppm to 1550 $W/m^2.K$ at 80 ppm where it levels off to a plateau value. The heat transfer coefficient at the plateau shows an enhancement of 1.67 times the value without alcohol under the conditions in Fig. 4. This is a similar enhancement ratio as obtained by Hoffmann et al. [6] although absolute values of heat transfer coefficient with and without alcohol are different.

The concentration of 2EH in Fig. 4 was inferred from surface tension measurements on the aqueous lithium bromide using the data shown in Fig. 5. The data shows that the surface tension reaches a plateau value as the 2EH concentration increases. The shape of the surface tension curve is thought to account for the shape of the heat transfer curve in Fig. 4. At concentrations above the solubility limit of the liquid, no variations in heat transfer are seen. This observation is in line with the mechanism described by the Vapor Surfactant theory.

Absorber Performance With Additive

Figure 6 is a plot of heat transfer coefficient versus solution flow rate with and without 2EH. As the specific film flow rate increases, the heat transfer coefficient increases (with and without alcohol). The heat transfer coefficient with 2EH reaches a plateau

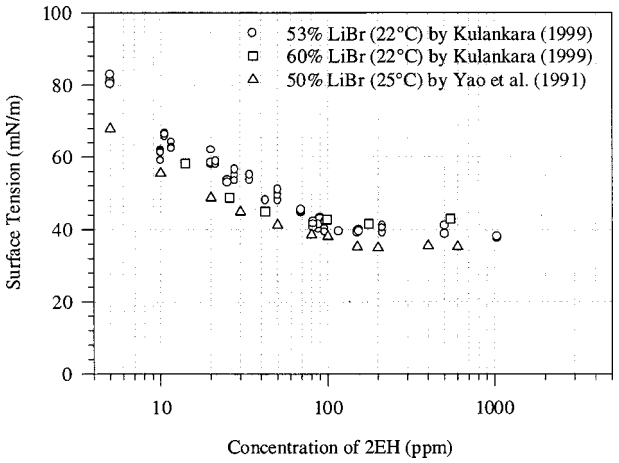

Fig. 5 Surface tension of aqueous lithium bromide solution with concentration of 2EH

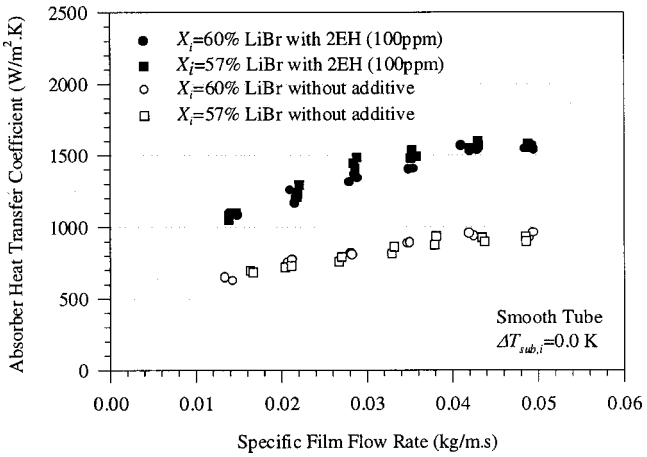

Fig. 6 Comparison of absorber heat transfer coefficient with and without additive

value of 1550 W/m^2.K at specific flow rates above 0.04 kg/m.s. The heat transfer coefficient increases from 930 W/m^2.K without alcohol to 1550 W/m^2.K when alcohol is present, which is an enhancement ratio of 1.67 times. The enhancement ratio is approximately constant over the flow rate range tested in this study. It is observed that the inlet mass fraction has little effect on the heat transfer coefficient. Figure 7 is a plot of absorber heat flux versus solution flow rate, with and without alcohol, for the same parametric cases considered in Fig. 6. As can be seen, the flux increases with flow rate. Also, the flux for the 60 percent LiBr cases is greater than that for the 57 percent cases. These data are important because the flux was found to play a strong role in the alcohol enhancement mechanism.

Solution Slinging

At high flow rate, the film flow around the tube becomes less stable and liquid droplets are observed to fly off the tubes such that they do not land on the next lower tube. This phenomenon is thought to be associated with unbalanced flow on the two sides of a tube. The droplets emerge on the side opposite of the larger flow and below the tube as if they were ejected from a sling attached to the tube as illustrated in Fig. 8. Thus, this phenomenon is termed ''solution slinging'' in the current study. Solution slinging is more severe at high solution flow rate and especially when 2EH is present.

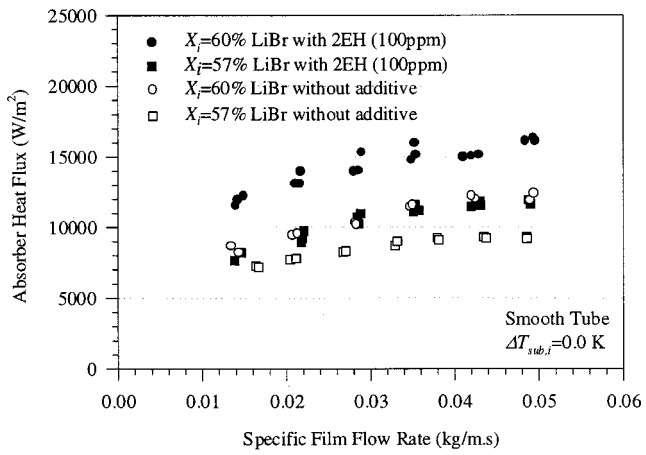

Fig. 7 Comparison of absorber heat flux with and without additive

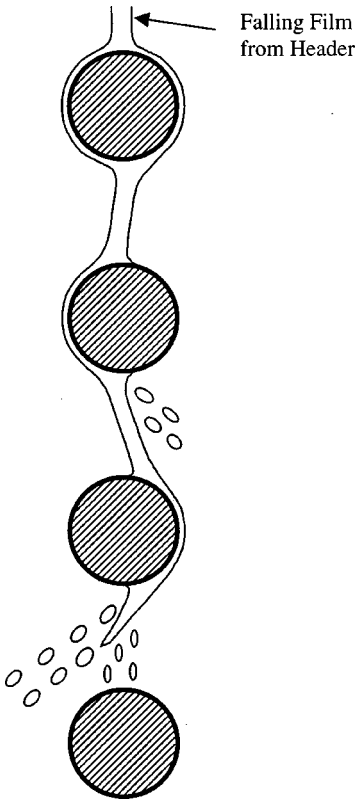

Fig. 8 Illustration of slinging at absorber tube bundle

Solution slinging causes the flow rate on the tubes to decrease and hence results in a decrease in the heat transfer coefficient. Although the liquid surface area of droplets is larger than the film surface area, the lack of cooling for the flying droplets results in a reduction in absorption [7]. The effect of slinging on the heat transfer coefficient can be estimated by the assumption that solution slinging ejects a certain fraction of solution from each tube. Figure 9 shows calculation results for the decrease of heat transfer coefficient versus the fraction of solution leaving each tube. The calculation was done using heat transfer coefficient data from Fig. 6. Figure 9 shows that the heat transfer coefficient is reduced almost linearly with an increase in solution slinging.

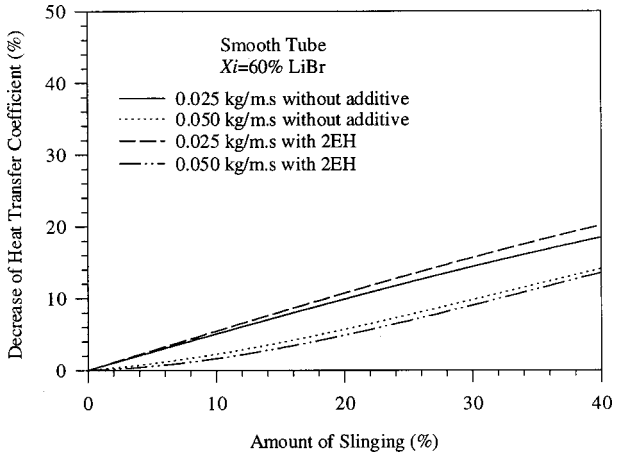

Fig. 9 Decrease of absorber heat transfer coefficient according to amount of slinging

Discussion

The physics of absorption enhancement due to alcohols such as 2-ethly-hexanol has been discussed since their introduction in the 1960's, but the details of the mechanism of action are only coming into focus today [10,11]. The new theory of the mechanism is called the Vapor Surfactant theory and it holds that the alcohol is a surfactant that provides enhancement to mass transfer by driving Marangoni convection. This piece of the mechanism has long been discussed but previously the theory was missing an explanation for how the alcohol gets to the surface. Recent experimental evidence clearly shows that the alcohol gets transported to the surface via bulk flow of the absorbing vapor [12]. Small amounts of alcohol that adsorb on the surface lead to dramatic reductions in surface tension. The absorption of water vapor is highly sensitive to mixing of the mass transfer layer on the liquid surface. Thus, the absorption flux in the presence of alcohol vapor is highly unstable spatially. In other words, a small local increase in absorption flux brings more alcohol to the surface, which then further augments absorption at that location. This instability has often been observed and is described in the literature listed previously.

The Vapor Surfactant theory is invoked here to help explain the experimental results presented in this paper. The importance of absorption flux in determining the heat transfer coefficient is only now becoming clear. The effect was clearly demonstrated in the current study when the enhancement factor increased significantly, from 1.2 to 1.7, when the area of the absorber was reduced 60 percent resulting in an increase in flux of approximately 50 percent. The explanation for this effect is that a higher flux delivers surfactant to the liquid surface at a higher rate and thus the stability of the liquid film is lower at high flux. Instability refers here to Marangoni flow that disrupts the saturated surface layer and brings subcooled liquid to the surface. The fact that the absorption heat transfer coefficient increases as flux increases is the opposite trend normally seen in condensation where increased flux leads to a thicker film and lower heat transfer coefficient. The main difference between these processes is that laminar absorption is strongly controlled by mass diffusion such that the thickness of the film is not the controlling factor in determining the flux. Instead, the mass diffusivity controls the flux. However, when mixing is present due to Marangoni convection, the effective mass diffusivity is much higher and the overall flux increases due to reduction of the mass transfer resistance.

The Vapor Surfactant theory implies that there is a circulation of alcohol throughout the entire absorption cycle. Alcohol arrives at the absorbing surface after passing through the condenser and evaporator. This mechanism means that a complete absorption cycle is needed for tests to determine the effect of alcohol on absorption. Minisorber testing (i.e., testing in a simplified reflux configuration) is likely to yield artificial 2EH vapor concentrations.

Conclusion

Absorption of water vapor into aqueous lithium bromide flowing over horizontal smooth tubes was revisited in the light of a new understanding of the physics of surfactant additives. The effects of solution inlet subcooling, solution inlet flow rate, solution inlet mass fraction, and additive (2-ethyl-hexanol) concentration on solution side heat transfer coefficient and absorber heat flux were examined. Inlet subcooling was found to significantly influence the heat transfer coefficient and thus the inlet subcooling was controlled within ± 0.1 K in this study. Solution slinging was observed and its effect on performance in a single row absorber was found to be relatively significant. In a full-scale absorber bundle, slinging is only an edge effect but in the interpretation of data from small absorber test bundles, slinging is a real issue that has not been properly addressed in the literature.

The effect of absorption flux on the heat transfer coefficient was observed and is described in the paper. The effect is explained in terms of the Vapor Surfactant theory. These observations are thought to be very significant for absorber bundle design. They imply a highly non-linear performance that is somewhat non-intuitive. If heat transfer coefficients continued to increase with flux, then one could expect a finite absorption rate in a very small device by rearranging the design to increase flux. This is an exciting prospect that has not been fully explored here. Unfortunately, it is expected that some limiting mechanism will intervene to provide an upper limit on performance. But there is no reason to expect that current machines operate near this limit. Thus, the work points toward an unexplored area of coupled heat and mass transfer that has exciting prospects.

Acknowledgments

This work was done under the Sorption Systems Consortium with support from Carrier Corp., Trane Co., Wolverine Tube Co., and York International. That support is gratefully acknowledged.

Nomenclature

A = area (m^2)
c_p = specific heat (J/kg.K)
d = tube diameter (m)
Γ = specific film flow rate ($=\dot{m}_{\mathrm{sol},i}/2L$) (kg/m.s)
h = heat transfer coefficient ($W/m^2.K$)
k = thermal conductivity of tube (W/m.K)
L = tube length (m)
$\dot{m}$ = mass flow rate (kg/s)
$\dot{Q}$ = heat transfer rate (W)
T = temperature (°C)
ΔT_{lm} = log mean temperature difference (K)
ΔT_{sub} = subcooling ($=T_{\mathrm{sat}}-T_{\mathrm{sol}}$) (K)
U = overall heat transfer coefficient ($W/m^2.K$)
X = LiBr mass fraction (percent)

Subscripts

cw = cooling water side
i = inlet or inner
o = outlet or outer
sol = solution or solution side

Superscript

sat = saturated

References

[1] Nagaoka, Y., Nishiyama, N., Ajisaka, K., and Nakamura, M., 1987, "Absorber of Absorption refrigerating Machine: Enhancement of Heat and Mass Transfer in Falling Film Absorbers by Surface Configuration," *17th Int. Congress of Refrigeration*, Vienna, Austria, International Institute of Refrigeration, pp. 990–995.

[2] Consenza, F., and Vliet, G., 1990, "Absorption in Falling Water/LiBr Films on Horizontal Tubes," ASHRAE Trans., **96**, Pt. 1, pp. 693–701.

[3] Greiter, I., Wagner, A., Weiss, V., and Alefeld, G., 1993, "Experimental Investigation of Heat and Mass Transfer in a Horizontal-Tube Falling-Film Absorber with Aqueous Solutions," *Proc. Int. Absorption Heat Pump Conf.*, Vol. 31, New Orleans, ASME, AES Vol. 31, pp. 225–232.

[4] Remec, J., Gjerkes, H., and Gaspersic, B., 1996, "Absorption of Vapor into Liquid Film on Horizontal Tubes," ASHRAE Trans., **102**, Pt. 1, pp. 973–979.

[5] Beutler, A., Hoffmann, L., Ziegler, F., Alefeld, G., Gommed, K., Grossman, G., and Shavit, A., 1996, "Experimental Investigation of Heat and Mass Transfer in Film Absorption on Horizontal and Vertical Tubes," *Proc. of Absorption 96*, Vol. I, Montreal, Canada, CANMET-EDRL, Natural Resources Canada, pp. 409–419.

[6] Hoffmann, L., Greiter, I., Wagner, A., Weiss, V., and Alefeld, G., 1996, "Experimental Investigation of Heat Transfer in a Horizontal Tube Falling Film Absorber with Aqueous Solutions of LiBr with and without Surfactants," Int. J. Refrig., **19**, No. 5, pp. 331–341.

[7] Atchley, J. A., Perez-Blanco, H., Kirby, M. J., and Miller, W. A., 1998, "An Experimental and Analytical Study of Advanced Surfaces for Absorption Chiller Absorbers," final report to the Gas Research Institute (GRI-95/0498).

[8] Bennett, C. O. O., and Myers, J. E., 1962, *Momentum, Heat, and Mass Transfer*, McGraw-Hill Book Co., Inc., pp. 409–411.
[9] Miller, W., 1998, personal communication (draft of chapter from report).
[10] Kulankara, S., 1999, ''Effect of Enhancement Additives on the Absorption of Water Vapor by Aqueous Lithium Bromide,'' Ph.D. dissertation, Univ. of Maryland at Baltimore, Baltimore, MD.
[11] Kulankara, S., and Herold, K. E., 2000, ''Theory of Heat/Mass Transfer Additives in Absorption Chillers,'' International J. Heating, Ventilating, Air-Conditioning and Refrigeration, **6**, No. 4, pp. 369–380.
[12] Yuan, Z., and Herold, K. E., 2001, ''Surface Tension of Aqueous Lithium Bromide with Controlled Vapor Concentration of 2-ethyl-hexanol,'' ASHRAE Trans., **107**, Pt. 1, pp. 463–468.

Evaporation-Combustion Affected by In-Cylinder, Reciprocating Porous Regenerator

Chan-Woo Park

Massoud Kaviany
e-mail: kaviany@umich.edu

Department of Mechanical Engineering,
The University of Michigan,
Ann Arbor, MI 48109-2125

An existing in-cylinder thermal regeneration concept for Diesel engines is examined for the roles of the porous insert motion and the fuel injection strategies on the fuel evaporation and combustion and on the engine efficiency. While the heated air emanating from the insert enhances fuel evaporation resulting in a superadiabatic combustion process (thus increasing thermal efficiency), the corresponding increase in the thermal NO_x is undesirable. A two-gas-zone and a single-step reaction model are used with a Lagrangian droplet tracking model that allows for filtration by the insert. A thermal efficiency of 53 percent is predicted, compared to 43 percent of the conventional Diesel engines. The optimal regenerative cooling stroke occurs close to the peak flame temperature, thus increasing the superadiabatic flame temperature and the peak pressure, while decreasing the expansion stroke pressure and the pressure drop through the insert. During the regenerative heating stroke, the heated air enhances the droplet evaporation, resulting in a more uniform, premixed combustion and a higher peak pressure, thus a larger mechanical work. [DOI: 10.1115/1.1418368]

Keywords: Engines, Heat Transfer, Heat Recovery, Porous Media, Regenerators

1 Introduction

A regenerative Diesel engine using an in-cylinder reciprocating, porous regenerator as shown in Fig. 1 has the potential to improve fuel-air mixing and combustion [1–3]. The porous insert is attached to a rod and moves in the cylinder, synchronized, but out of phase with the piston. During the regenerative heating stroke, the regenerator remains just beneath the cylinder head for most of the period and moves down to the piston (as it approaches the TDC position). During the regenerative cooling stroke, the regenerator moves up and remains in the original position until the next regenerative heating stroke. Following the combustion and expansion, the products of combustion (exhaust gases) retain an appreciable sensible heat. During the regenerative cooling stroke, the hot exhaust gas flows through the insert and stores part of this sensible heat by surface-convection heat transfer in the porous insert (with large surface area). While the external thermal regeneration, examined extensively, would reduce the volumetric efficiency (due to external heating of the intake air, before arrival in the cylinder), the internal thermal regeneration with the in-cylinder porous insert does not affect the volumetric efficiency significantly. This is because the intaked air arrives in the cylinder and is then heated by passing through the hot insert, after the intake valve is closed. The superadiabatic flame temperature (due to the thermal regeneration of the combustion heat) [4] and the fuel droplet-regenerator interaction, enhances the fuel evaporation. A uniform fuel vapor distribution is possible due to the deflection of fuel droplets by the air flow emanating from the porous regenerator and this can improve combustion. Here the fuel droplet-regenerator interaction is examined, i.e., aiming at an improved regenerative engine performance.

2 Analysis

The geometric parameters and variables of the regenerative Diesel engine with a side valve position are shown Fig. 2. The two gas zones of the top and bottom chambers are connected by the permeable regenerator. The regenerator is divided into N_r small volumes and each volume consists of the gas and solid phases. Considering the complexities and the transient behavior before a quasi-steady solution is reached, for the sake of computation economy, a lumped, multi gas zone model and a simplified chemical kinetic model are used. The multi-zone-first-order analysis of the regenerative engine performance is given below, followed by the analysis of the injected fuel droplet.

2.1 Heat Transfer. A multi-zone gas model and a one-dimensional model for the solid phases are used for the analysis of the regenerative Diesel engine. The mechanisms of the heat transfer considered include the surface-convection, conduction and surface/volume radiation. The prescribed temperature of the cooling water is used for the analysis of the conduction heat transfer through the cylinder walls. One-dimensional energy conservation equations with both uniform and nonuniform grids are used for solid phases of the regenerator, the piston, the cylinder head, and cylinder block. Since the fuel is injected into the top gas zone and the fuel vapor does not escape to the bottom gas zone under the conditions considered, it is assumed that the combustion occurs only in top gas zone. The heat release rate in the top gas zone is determined using a single-step, second-order combustion model and the empirical relation of the ignition delay. The species concentrations are calculated to determine the heat release rate and the NO_x production rate.

The gas is assumed to be an ideal gas

$$\rho_f = \frac{M_f}{V_f} = \frac{p_f}{\frac{R_g}{M_a} T_f}. \tag{1}$$

For the top gas zone above the regenerator, the energy conservation equation is given as

$$Q_{u,\mathrm{inj}} - (Q_{u,r})_{N_r} + \langle Q_{ku,t-ch} \rangle_{D_B} + \langle Q_{ku,t-cb} \rangle_{D_B} + \langle Q_{ku,t-r} \rangle_{D_B} = -\frac{d}{dt}(M_{f,t} c_{p,f} T_{f,t}) + \dot{S}_t, \tag{2}$$

where $Q_{u,\mathrm{inj}}$ is the heat transfer due to the fuel injection and $(Q_{u,r})_{N_r}$ is the heat transfer due to the gas influx through the

Contributed by the Heat Transfer Division for publication in the JOURNAL OF HEAT TRANSFER. Manuscript received by the Heat Transfer Division May 2, 2000; revision received May 20, 2001. Associate Editor: J. G. Georgiadis.

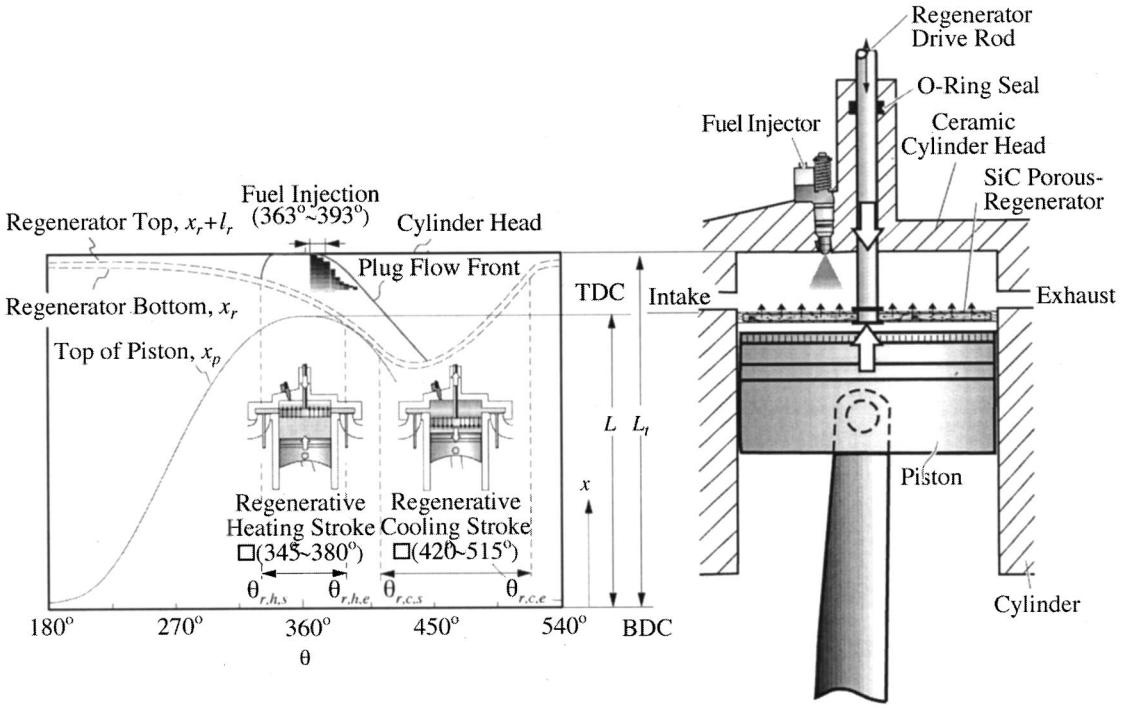

Fig. 1 Sequence of motion of the regenerator and piston and physical rendering of fuel injection and air blowing during the regenerative heating stroke

regenerator. $\langle Q_{ku,t-ch \text{ or } cb \text{ or } r}\rangle_{D_B}$ are the surface-convection heat transfer between the top fluid and surfaces (of the cylinder head, the cylinder block and the regenerator). The energy conversion in the top gas zone $\dot{S}_t$ is due to combustion (occurs only in the top gas zone) $\dot{S}_{r,c}$, gas expansion cooling/compression heating $\dot{S}_{m,p,t}$, fuel evaporation $\dot{S}_{F,lg}$, and radiation $(\dot{S}_{e,\epsilon}+\dot{S}_{e,\alpha})_t$, i.e.,

$$\dot{S}_t=\dot{S}_{r,c}+\dot{S}_{m,p,t}+\dot{S}_{F,lg}+(\dot{S}_{e,\epsilon}+\dot{S}_{e,\alpha})_t. \tag{3}$$

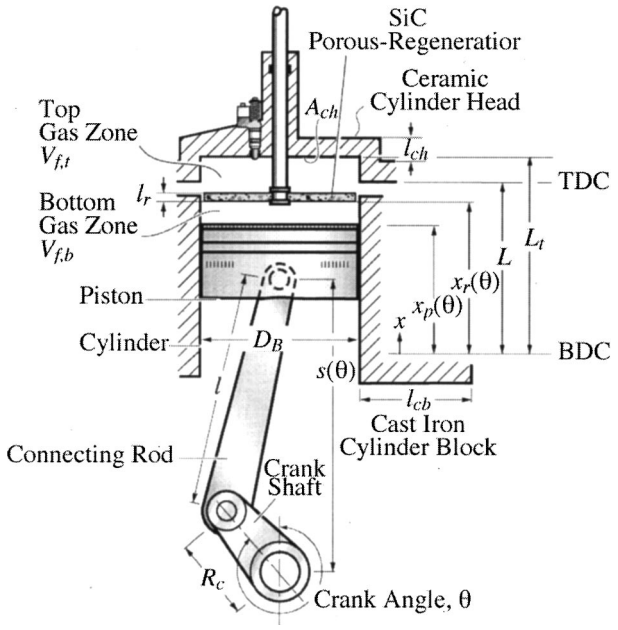

Fig. 2 Geometric parameters and variables of the regenerative Diesel engine

A more detailed description for each term of the energy conservation Eg. (2) is given in the Appendix.

Similarly, for the bottom gas zone the energy conservation equation is given as

$$-Q_{u,\text{int}}+Q_{u,\text{exh}}+(Q_{u,r})_0+\langle Q_{ku,b-cb}\rangle_{D_B}+\langle Q_{ku,b-p}\rangle_{D_B}$$
$$+\langle Q_{ku,b-r}\rangle_{D_B}=-\frac{d}{dt}(M_{f,b}c_{p,f}T_{f,b})+\dot{S}_b, \tag{4}$$

where $Q_{u,\text{int}}$, $Q_{u,\text{exh}}$ and $(Q_{u,r})_0$ are the convection heat transfer due to the intake, the exhaust, and the gas influx through the regenerator. Considering a combustion efficiency of 98 percent in top gas zone, under the conditions given in Table 1, it is assumed that the fuel is consumed completely in the top gas zone, and, therefore, no combustion occurs in the bottom gas zone. The energy conversion in the bottom gas zone $\dot{S}_b$ is due to gas expansion cooling/compression heating only, i.e.,

$$\dot{S}_b=\dot{S}_{m,p,b}=V_{f,b}\frac{dp_{f,b}}{dt}. \tag{5}$$

A more detailed description, for each term of the energy conservation Eq. (4), is given in the Appendix.

The porous regenerator is divided into N_r small volumes with uniform thickness $\Delta l_{r,i}$ and local thermal nonequilibrium is assumed between the gas and the solid phases. The energy equation for each volume of the solid phase is given by

$$-(Q_{k,r})_{(i-1)-i}+(Q_{k,r})_{i-(i+1)}+\langle Q_{ku,f-r}\rangle_i-Q_{d,i}$$
$$=-\rho_r\Delta l_{r,i}(1-\epsilon_r)A_r c_{p,r}\frac{dT_{r,i}}{dt}, \quad i=1,2,\ldots,N_r, \tag{6}$$

where $(Q_{k,r})_{i-(i+1)}$, $\langle Q_{ku,f-r}\rangle_i$ and $Q_{d,i}$ are the heat transfer due to the conduction in the solid phase, the surface-convection and the evaporation of the fuel droplet, respectively. Note that it is assumed that the heat transfer due to the evaporation of the fuel

Table 1 Operational characteristics of the engine

Parameter	Magnitude	Parameter	Magnitude
operating conditions:		intake valve:	
		$N_{v,i}$	1
V_d	1,718cm^3	$C_{D,i}$	0.75
V_c	245.4cm^3	$D_{v,i}$	0.044 m
r_c	$6 \sim 16.5$	$L_{v,i}$	$0.25D_{v,i}$
N	1,600 rpm	$\theta_{v,s,i}$	0°
$(A/F)_a$	30	$\theta_{v,e,i}$	224°
$(A/F)_s$	15.5	$p_{n,i}$	357 kPa
Φ	0.52	$T_{n,i}$	329 K
$T_{f,w}$	380 K	exhaust valve:	
fuel injection		$N_{v,e}$	1
$M_{F,o}$	0.216 g	$C_{D,e}$	0.7
N_d	50	$D_{v,e}$	0.042 m
D_{SM}	100 μ m	$L_{v,e}$	$0.25D_{v,e}$
$u_{d,o}$	100 m/s	$\theta_{v,s,e}$	474°
$T_{d,o}$	500 K	$\theta_{v,e,e}$	720°
$\theta_{F,s}$	363°	$p_{n,e}$	251 kPa
$\theta_{F,e}$	393°	$T_{n,e}$	800 K
regenerator schedule:			
$\theta_{r,c,s}$	345°		
$\theta_{r,c,e}$	380°		
$\theta_{r,h,s}$	420°		
$\theta_{r,h,e}$	515°		

droplet occurs in the solid phase of the regenerator. More detailed description, for each term of the energy conservation Eq. (6), is given in the Appendix.

The energy equation for the gas phase in the porous regenerator is given as

$$-(Q_{u,r})_{i-1}+(Q_{u,r})_i-\langle Q_{ku,f-r}\rangle_i = -\frac{d}{dt}(M_{f,r}c_{p,f}T_{f,r})_i+\dot{S}_{r,i}, \quad i=1,2,\ldots,N_r, \quad (7)$$

where

$$\dot{S}_{r,i}=(\dot{S}_{m,p})_{r,i}=V_{f,r,i}\frac{dp_{f,r,i}}{dt},$$

and the convection heat transfer $(Q_{u,r})_i$ and the surface-convection heat transfer $\langle Q_{ku,f-r}\rangle_i$ are given in Appendix in detail. The energy conservation equations at the top and bottom surfaces of the regenerator are also given in the Appendix.

The cylinder wall of the regenerative Diesel engine consists of the ceramic cylinder head and the cast iron cylinder block. The cylinder head and the cylinder block are assumed to be ideally insulated from each other. The cylinder head made of ceramic is used as a thermal barrier to reduce the heat loss. The cylinder head is divided into $N_{ch}-1$ small volumes with a uniform thickness $\Delta l_{ch,i}=l_{ch,1}/(N_{ch}-1)$ and a large volume with thickness $\Delta l_{ch,N_{ch}}=l_{ch,2}=l_{ch}-l_{ch,1}$. Then the energy equation for the solid phase is written as

$$(Q|_{A,ch})_i=-\rho_{ch}\Delta l_{ch,i}A_{k,ch}c_{p,ch}\frac{dT_{ch,i}}{dt}, \quad i=1,2,\ldots,N_{ch}, \quad (8)$$

where $(Q|_{A,ch})_i$ is heat transfer due to the conduction and is given in Appendix in detail. The energy conservation equations at the surface inside the cylinder head are also given in the Appendix.

The energy conservation equations for the cylinder block and the piston are given similarly.

The intake mass flow rate using the valve curtain area $A_{v,i}$, is given as

$$\dot{M}_{f,\mathrm{int}}=N_{v,i}C_{D,i}A_{v,i}\frac{p_o}{\left(\frac{R_g}{M_g}T_o\right)^{1/2}}f_{A,f}(p_T,p_o), \quad (9)$$

where

$$A_{v,i}=\pi D_{v,i}L_{v,i}f_{A,v}(\theta,\theta_{v,s,i},\theta_{v,e,i}).$$

Similarly, the exhaust mass flow rate $\dot{M}_{f,exh}$ is determined. Here $f_{A,f}(p_T,p_o)$ is obtained from a one-dimensional isentropic flow analysis for the compressible flow through a flow restriction [5].

The mass flow through the porous regenerator is determined by the Darcy law [6] and is given by

$$(\dot{M}_{f,r})_i=A_r\rho_{f,r}\frac{K_r}{\mu_f}\frac{(p_{f,r,i}-p_{f,r,i+1})}{\Delta l_{r,i}},$$

$$K_r=\frac{\epsilon_r^3D_p^2}{180(1-\epsilon_r)^2}, \quad i=0,1,\ldots,N_r, \quad (10)$$

where

$$\rho_{f,r}=\begin{cases}\rho_{f,r,i} & \text{for } (\dot{M}_{f,r})_i\geq 0 \quad \text{(the bottom to the top gas zone)}\\ \rho_{f,r,i+1} & \text{for } (\dot{M}_{f,r})_i<0\end{cases},$$

and $\rho_{f,r,0}=\rho_{f,b}$, and $\rho_{f,r,N_r+1}=\rho_{f,t}$.

The combustion reaction $\dot{M}_{r,F}$ in the top gas zone, using the single-step reaction model [7], is given by

$$\dot{M}_{r,F}=\rho_{f,t}a_r\rho_F^{a_F}\rho_O^{a_O}\exp^{\Delta E_a/R_gT_{f,t}}, \quad (11)$$

where a_r is the pre-exponential factor and ΔE_a is the activation energy (kJ/kmole-K). The ignition delay is determined using the empirical correlation of the Diesel engine and ranges 2~3 crank angles under the conditions considered [5].

2.2 Droplet Evaporation. The transient fuel evaporation and the fuel droplet fate are determined using a Lagrangian, droplet tracking model along with a porous-surface filtration submodel for the droplet-regenerator interaction. These allow for the analysis of the fuel droplet evaporation, accumulation and combustion. After the fuel is injected, the fuel spray is assumed to be divided into N_d homogeneous droplet parcels. It is assumed that each parcel has n_d droplet particles with the same properties (e.g., droplet diameter, speed and temperature) and does not interfere with other droplet parcels. The Sauter mean diameter D_{SM} is used as the initial droplet diameter [8].

The instantaneous location of a droplet is given by

$$\frac{d}{dt}\mathbf{x}_d=\mathbf{u}_d. \quad (12)$$

The instantaneous velocity is determined by the momentum equation of a droplet as

$$\frac{d}{dt}(M\mathbf{u})_d=\sum \mathbf{F}=\mathbf{F}_d+\mathbf{F}_{\Delta T}+\ldots, \quad (13)$$

and neglecting the thermophoresis force $\mathbf{F}_{\Delta T}$ and other forces, the momentum equation is given by

$$M_d\frac{d\mathbf{u}_d}{dt}=-\frac{\pi}{8}D_d^2\rho_{f,t}C_D|\mathbf{u}_d-\langle\mathbf{u}_f\rangle_{p,t}|(\mathbf{u}_d-\langle\mathbf{u}_f\rangle_{p,t}), \quad (14)$$

where

$$C_D=\begin{cases}27\,\mathrm{Re}_D^{-0.84} & \text{for } \mathrm{Re}_D<80\\ 0.271\,\mathrm{Re}_D^{0.217} & \text{for } 80<\mathrm{Re}_D<10^4,\end{cases}$$

where $\mathrm{Re}_D=\rho_{f,t}D_d|\mathbf{u}_d-\langle\mathbf{u}_f\rangle_{p,t}|/\mu_f$.

In order to account for the deflection of the fuel droplets by the air flow emanating from the regenerator, the gas flow in the top gas zone is assumed to be the plug flow and the gas velocity is given as

$$\langle u_f\rangle_{p,t}=\frac{(\dot{M}_{f,r})_{N_r}}{A_r\rho_{f,r}}+\frac{dx_r}{dt}. \tag{15}$$

From the uniform temperature model for the fuel droplet heat and mass transfer (only the composition of the bulk liquid remains at the injected condition while the surface composition varies as required by the local conditions. The temperature of the surface and the bulk liquid are the same and are known at each instant), the mass conservation for a droplet is given by [9]

$$\frac{dM_d}{dt}=-\dot{M}_d. \tag{16}$$

The corrected evaporation rate $\dot{M}_d$ for the convective ambient is expressed

$$\frac{\dot{M}_d}{\dot{M}_d(\mathrm{Re}_D=0)}=1+f(\mathrm{Re}_D,\mathrm{Sc}), \tag{17}$$

where the evaporation rate $\dot{M}_d(\mathrm{Re}_D=0)$ in the quiescent ambient is given in the Appendix and

$$f(\mathrm{Re}_D,\mathrm{Sc})=\frac{0.278\,\mathrm{Re}_D^{1/2}\mathrm{Sc}^{1/3}}{[1+1.232/\mathrm{Re}_D\mathrm{Sc}^{4/3}]^{1/2}}. \tag{18}$$

The droplet energy conservation equation based on the uniform temperature model is

$$+\frac{\mathrm{Nu}_{D,1}k_f}{D_d}A_d(T_d-T_{f,t})+\frac{\mathrm{Nu}_{D,2}k_f}{D_d}A_d(T_d-T_{r,i})$$
$$=-M_dc_{p,F}\frac{dT_d}{dt}-\dot{M}_d\Delta h_{lg}, \tag{19}$$

where $\mathrm{Nu}_{D,1}$ is due to single-phase (droplets in the gas) and $\mathrm{Nu}_{D,2}$ is due to phase change (film boiling) and surface convection (when the droplets are impinging on the regenerator) and the fuel droplet temperature T_d and $T_{r,i}$ is the temperature of the porous regenerator in contact with the droplets. The Nusselt number $\mathrm{Nu}_{D,2}$ is given in the Appendix in detail.

The corrected Nusselt number $\mathrm{Nu}_{D,1}$ in the convective ambient is expressed

$$\frac{\mathrm{Nu}_{D,1}}{\mathrm{Nu}_{D,1}(\mathrm{Re}_D=0)}=1+f(\mathrm{Re}_D,\mathrm{Pr}), \tag{20}$$

where $f(\mathrm{Re}_D,\mathrm{Pr})$ is the same as that given in Eq. (18), except Sc is replaced with Pr. The Nusselt number $\mathrm{Nu}_{D,1}(\mathrm{Re}_D=0)$ in the quiescent ambient.

For droplets colliding with the regenerator, the filtration efficiency is expressed as [10]

$$\alpha=\alpha_d\left[\frac{6(1-\epsilon_r)}{\pi}\right]^{1/3},\quad \alpha_d=0.093+0.387\mathrm{Sto}-0.054\mathrm{Sto}^2, \tag{21}$$

where

$$\mathrm{Sto}=\frac{\rho_{b,l}D_d^2\left|\mathbf{u}_d-\dfrac{d\mathbf{x}_r}{dt}\right|}{18\mu_f(d_s/2)},$$

where d_s is the particle diameter of porous regenerator and $\mathbf{u}_d$ is a droplet velocity.

Finally, the mass conservation equations for the gas phase, in the top and bottom gas zones, are given by

$$-(\dot{M}_{f,r})_{N_r}-\dot{M}_{F,\mathrm{evp}}=-\frac{dM_{f,t}}{dt} \tag{22}$$

$$-\dot{M}_{f,\mathrm{int}}+(\dot{M}_{f,r})_0+\dot{M}_{f,\mathrm{exh}}=-\frac{dM_{f,b}}{dt}, \tag{23}$$

where $\dot{M}_{F,\mathrm{evp}}=\sum_i^{N_d}(n_d\dot{M}_d)_i$.

The mass conservation equation for the gas phase, inside the regenerator, is given by

$$-(\dot{M}_{f,r})_{i-1}+(\dot{M}_{f,r})_i=-\frac{dM_{f,i}}{dt},\quad i=1,2,\ldots,N_r. \tag{24}$$

2.3 Regenerator Motion. The motion sequences of the piston and the bottom surface of the regenerator are given by

$$x_p=L_t-\frac{V_c}{A_{ch}}\left\{1+0.5(r_c-1)\left[1-\cos\left(\frac{\pi\theta}{180}\right)\right]\right\}, \tag{25}$$

$$x_r=a+b\theta+c\theta^2+d\theta^3+e\theta^4+f\theta^5, \tag{26}$$

where the constants *a*, *b*, *c*, *d*, *e*, and *f* are determined to satisfy the smooth transition of the velocity and the acceleration of the regenerator. Also, the minimum gaps, between the top surface of the regenerator and the cylinder head and between the bottom surface of the regenerator and the piston are needed due to the required tolerance.

The net indicated work per cycle $W_{c,\mathrm{in}}$ is given by

$$W_{c,\mathrm{in}}=\int\dot{W}_{c,\mathrm{in}}dt=\int\left[\oint\left(p_{f,t}\frac{dV_{f,t}}{dt}+p_{f,b}\frac{dV_{f,b}}{dt}\right)\right]dt. \tag{27}$$

The mechanical loss, due to the pressure drop $\Delta p=p_{f,t}-p_{f,b}$ across the porous regenerator, is expressed by

$$\dot{W}_{\mathrm{loss}}=-\oint(p_{f,t}-p_{f,b})A_{ch}\left(\frac{dx_r}{dt}-\frac{dx_p}{dt}\right). \tag{28}$$

The relevant indicators of the engine performance are the thermal efficiency η_T, the volumetric efficiency η_V, the net indicated mean-effective pressure $p_{\mathrm{mep,in}}$, the indicated specific fuel consumption sfc, and the fuel conversion efficiency η_F. The thermal efficiency η_T is defined as

$$\eta_T=\frac{W_{c,\mathrm{in}}}{-M_{r,F}\Delta h_{r,F}},\quad M_{r,F}=\int_{t_{F,s}}^{t_{F,e}}\dot{M}_{r,F}dt. \tag{29}$$

The volumetric efficiency η_V is

$$\eta_V=\frac{M_a(\theta_{v,e,i})}{M_{a,o}}, \tag{30}$$

where $M_a(\theta_{v,e,i})$ is the amount of mass of air in the cylinder when the intake valve closes and $M_{a,o}$ is the amount of air in the cylinder when charged under the inlet conditions of the intake valve.

The net indicated mean-effective pressure $p_{\mathrm{mep,in}}$, the specific fuel consumption sfc and the fuel conversion efficiency η_F are given by

$$p_{\mathrm{mep,in}}=\frac{W_{c,\mathrm{in}}}{V_d},\quad \mathrm{sfc}=\frac{M_{F,o}}{W_{c,\mathrm{in}}}\quad \eta_F=\frac{\mathrm{sfc}}{\Delta h_{r,F}}. \tag{31}$$

The energy and species conservation equations are solved with an IMSL solver (DIVPAG) capable of solving the stiff ordinary differential equations. The quasi-steady state (time periodic) solution is found when the overall energy balance error is less than 2~3 percent. The parameters used for the numerical simulation are listed in Table 2 and the operational characteristics are listed in Table 1.

Table 2 Characteristic dimensions and properties of the regenerative Diesel engine

Parameter	Magnitude	Parameter	Magnitude
cylinder:		fuel:	
D_B	0.125 m	M_F	142.3 kg/kmole
L	0.14 m	Δh_{lg}	116×10^3 J/kg-fuel
cylinder head:		$\rho_{b,l}$	853 kg/m^3
ρ_{ch}	5,200 kg/m^3	$c_{p,F}$	3,010 J/kg-K
$c_{p,ch}$	730 J/kg-K	$k_{F,v}$	54×10^{-3} W/m-K
k_{ch}	1.2 W/m-K	$\epsilon_{r,F}$	0.75
l_{ch}	2 cm	$D_{m,F}$	6×10^{-6} m^2/s
cylinder block:		T_c	617.6 K
ρ_{cb}	7,200 kg/m^3	p_c	2.096 MPa
$c_{p,cb}$	480 J/kg-K	reaction:	
k_{cb}	54 W/m-K	$\Delta h_{r,F}$	-42.5×10^6 J/kg-fuel
l_{cb}	2 cm	a_r	5.4×10^8
piston:		a_F	0.25
ρ_p	2,750 kg/m^3	a_O	1.0
$c_{p,p}$	915 J/kg-K	ΔE_a	1.256×10^8 J/kmole-K
k_p	155 W/m-K	NO formation:	
l_p	2 cm	a_r	5.74×10^{14} (cm^3/mol)$^{\frac{1}{2}}$/s
$\alpha_{r,ch/cb/p}$	0.7/0.5/0.5	ΔE_a	5.562×10^8 J/kmole-K
$\epsilon_{r,ch/cb/p}$	0.7/0.5/0.5	air:	
regenerator:		M_a	28.96 kg/kmole
ρ_r	200 kg/m^3	γ	1.4
$c_{p,r}$	1,300 J/kg-K	$c_{p,a}$	1,300 J/kg-K
k_r	63 W/m-K	gas mixture:	
$\alpha_{r,r}$	0.9	M_g	28.6 kg/kmole
$\epsilon_{r,r}$	0.9	$c_{p,f}$	1,600 J/kg-K
l_r	8 mm	k_f	0.0824 W/m-K
ϵ_r	0.7	μ_f	52.1×10^{-6} Pa-s
A_{sf}/V	11,602 m^2/m^3	Pr	1.0
d_s	150 μm	Sc	1.0
D_p	50 μm	$\alpha_{r,f}$	0.1
T_{sl}	2,700 K	$\epsilon_{r,f}$	0.1
$T_{r,max}$	1,600 K		

3 Results and Discussion

The results on engine performance, enhanced droplet evaporation, and superadiabatic combustion, and optimization of thermal regeneration are given below.

3.1 Thermal and Mechanical Performance. The $(p-V)_f$ diagram obtained from the analysis of the conventional and regenerative Diesel engines is shown in Fig. 3. The thermodynamic limit results, shown in Fig. 3, assume a constant volume process during thermal regeneration and a maximum regenerator temperature below $T_{r,\max}=1600$ K. The work gained due to thermal regeneration is denoted as A_1-A_2. Compared to the thermodynamic limit, the work loss due to insufficient thermal regeneration and the pressure drop through the regenerator (denoted as *B*), and the prolonged combustion of the Diesel engine (denoted as *C*), are detrimental to the thermal efficiency. The optimum performance should reduce the pressure drop and improve the combustion characteristics. Note that the compression ratio of the regenerative Diesel engine is lower than that of the conventional engine. This is due to the regenerator volume ($l_r=8$ mm), the gap (0.5 mm) between the regenerator top surface and the cylinder head, and the gap (1 mm) between the regenerator bottom surface and the piston.

Figure 4 shows the mass flow rate during the intake, $\dot{M}_{f,\text{int}}$, the mass flow rate during the exhaust stroke, $\dot{M}_{f,\text{exh}}$, the mass flow rate into the top gas zone from the regenerator, $(\dot{M}_{f,r})_{N_i}$, and the fuel evaporation rate, $\dot{M}_{F,\text{evp}}$. Note that the intake flow of $\dot{M}_{f,\text{int}}$ has a back flow due to the reversal of the pressure difference between the valve inlet and the bottom gas zone, and that there is a reciprocating flow of $(\dot{M}_{f,r})_{N_i}$ through the porous regenerator. The reciprocating flow is attributed to the pressure differences caused by the regenerator/piston motion, the heat transfer, and the combustion. This allows for the thermal regeneration of the flue gas heat resulting in a superadiabatic combustion.

Figure 5 shows the variations of the mass, volume, and temperatures of the top and bottom gas zones, and the top gas zone pressure during the cycle. Since thermal regenerative heating occurs after the intake valve is closed, the volumetric efficiency of the regenerative engine is not deteriorated by the thermal regeneration. The high volumetric efficiency of 92 percent is due to the surface temperature in the bottom gas zone (exposed to the intake air), which remains close to that of the conventional Diesel engine.

The temperature variations of the solid and gas phases during a cycle are shown in Fig. 6. Fuel evaporation and combustion occur during thermal regeneration resulting in a high peak gas temperature in the top gas zone and a relatively low peak gas temperature in the bottom gas zone. Note also that the ceramic cylinder head is insulated from the cylinder block (made of cast iron). The surface

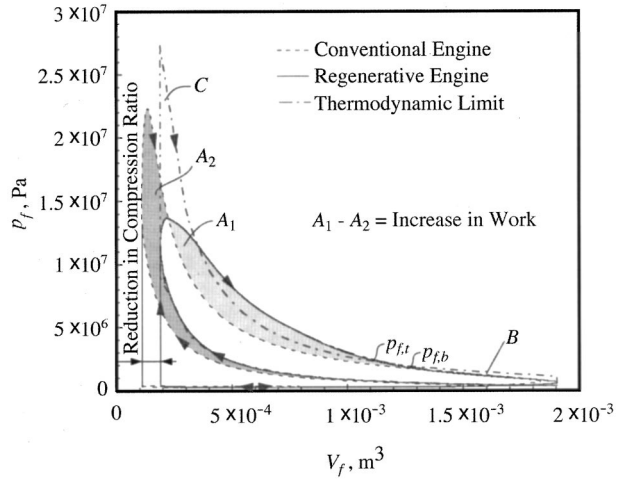

Fig. 3 Thermodynamic limit and predicted $(p-V)_f$ diagram from the start of cycle θ=0 deg to the end θ=720 deg, for the conventional and regenerative engines

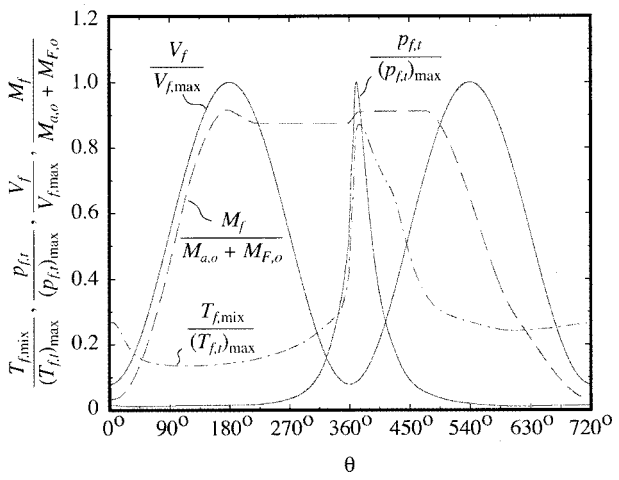

Fig. 5 Variations of dimensionless mass, volume, temperature (top and bottom gas zones), and pressure in top gas zone, during a cycle

temperature of the cylinder head $T_{ch,o}$ is higher than that of the conventional Diesel engine, but the surface temperatures of the cylinder block $T_{cb,o}$ and the surface temperature of the aluminum piston $T_{p,o}$ are lower. The surface temperature $T_{r,L}$ of the regenerator made of SiC, also has a large temperature variation.

The energy conversion, and surface heat transfer rates in the top and bottom gas zones are shown in Figs. 7(*a*) to (*c*). The heat release rate $\dot{S}_{r,c}$ is controlled only by fuel evaporation (due to the assumed perfect mixing). The heat transfer rate, Q_u, due to the thermal regeneration, shown in Figs. 7(*b*) and (*c*), enhances the fuel evaporation and leads to a superadiabatic combustion. Also the surface-radiation heat transfer $-(\dot{S}_{e,\epsilon}+\dot{S}_{e,\alpha})_t$ in the top chamber is comparable to the surface-convection heat transfer $\langle Q_{ku}\rangle_{D_B}$, due to the high surface temperature as shown in Fig. 7(*b*).

Under the baseline conditions (including $r_c=10$) given in Table 1, the predicted thermal efficiency of the regenerative engine is $\eta_T=53$ percent, the volume efficiency is $\eta_V=92$ percent, the indicated mean-effective pressure is $p_{\text{mep,in}}=2.82$ MPa, and the indicated specific fuel consumption is sfc=160 g/kW-hr.

3.2 Enhanced Evaporation. Since the fuel is injected toward the regenerator, which is located near the fuel injection nozzle, droplet impingement onto the regenerator is likely. The impinging droplets experience film boiling once in contact with the high temperature (above the Leidenfrost temperature) regenerator pore surface and are quickly vaporized. In addition to the high gas temperature (due to the thermal regeneration), the fuel impingement on the high temperature pore surface drastically reduces the evaporation time. Optimal fuel injection aims to achieve rapid fuel vaporization and uniform vapor distribution (in the top gas zone) with the least thermal impact on the porous regenerator, for the maximum performance.

The spray divergence angle θ_d is determined from the empirical correlation for a given nozzle geometry [5] and is given as

$$\tan\left(\frac{\theta_d}{2}\right)=\frac{4\pi}{4.9}\left(\frac{\rho_{f,t}}{\rho_{F,l}}\right)^{1/2}\frac{\sqrt{3}}{6}. \tag{32}$$

Figure 8(*a*) shows the penetration of the fuel spray into the top gas zone and the consequent impingement onto the moving regenerator. Figure 8(*b*) shows the fuel evaporation rate and the trajectories of the fuel droplet parcels (1st, 20th, 40th, and 50th of the 50 droplet parcels), the regenerator, and the piston. Once the fuel droplet makes contact with the porous regenerator, the fuel evapo-

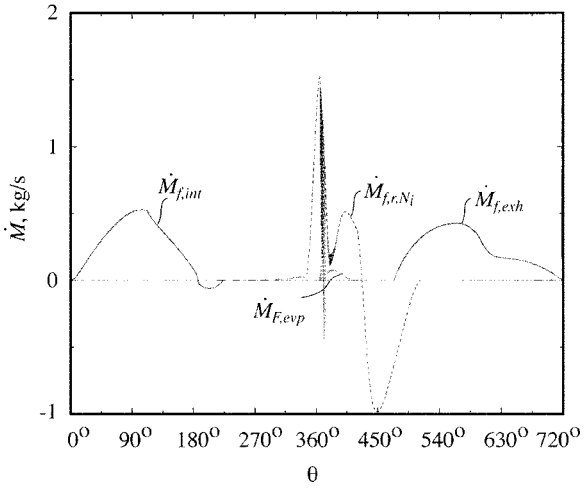

Fig. 4 Variation of mass flow rates during the intake and exhaust strokes, and the mass flow rate through the insert during the compression and expansion strokes, during a cycle

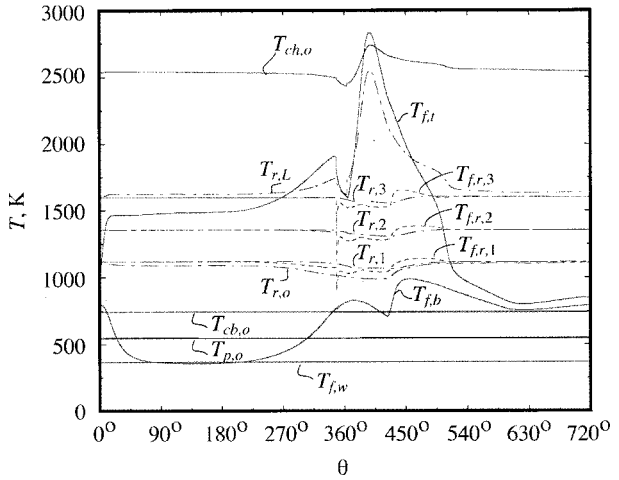

Fig. 6 Variations of the gas and solid temperatures during a cycle

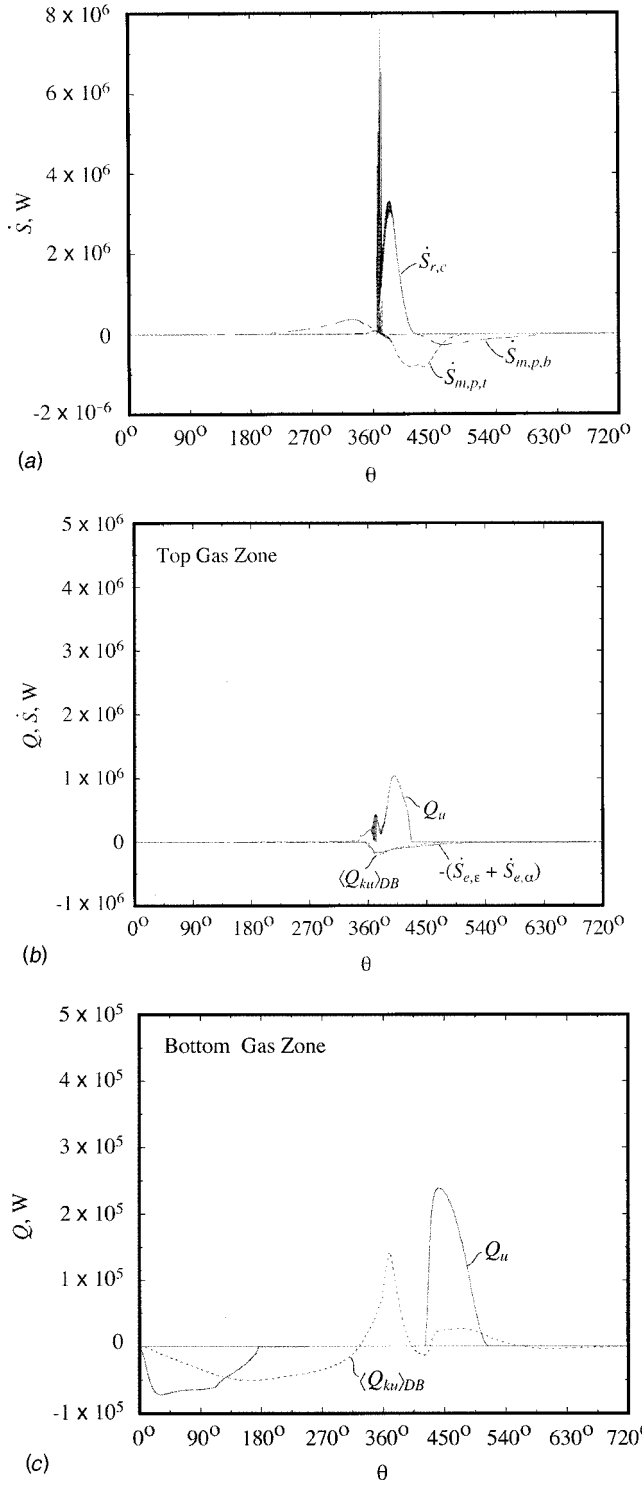

Fig. 7 Variation of the energy conversions (*a*) and heat transfer rates (*b*) and (*c*), during a cycle

ration rate $\dot{M}_{F,\mathrm{evp}}$ rapidly increases. The evaporation of the captured droplets helps to provide rapid fuel evaporation enabling intense premixed combustion, and increasing the peak pressure and the thermal efficiency. The air flow emanating from the regenerator deflects the droplets and helps to provide a uniform fuel-vapor distribution in the top gas zone. Using a plug flow model for this air flow, Fig. 8(*b*) shows that the front of the plug

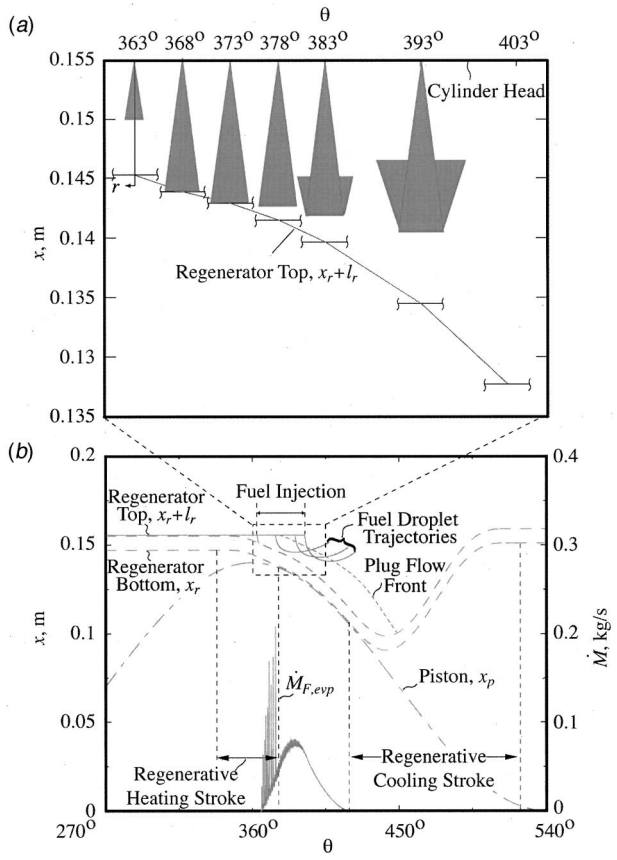

Fig. 8 (*a*) Penetration and surface impingement of fuel spray, and (*b*) the trajectories of the fuel droplets and the front location for plug gas flow in top gas zone

flow reaches the cylinder head for most of the fuel injection period and, therefore, ideal perfect mixing in the top gas zone can be justifiably used.

Since the regenerator moves with a high acceleration during the thermal regeneration, excess thermal stress due to the variation of the solid temperature should be avoided. To reduce the thermal stress, surface vaporization cooling due to the impinging fuel droplets should be distributed over a larger portion of the regenerator area, thus minimizing the temperature variation along the

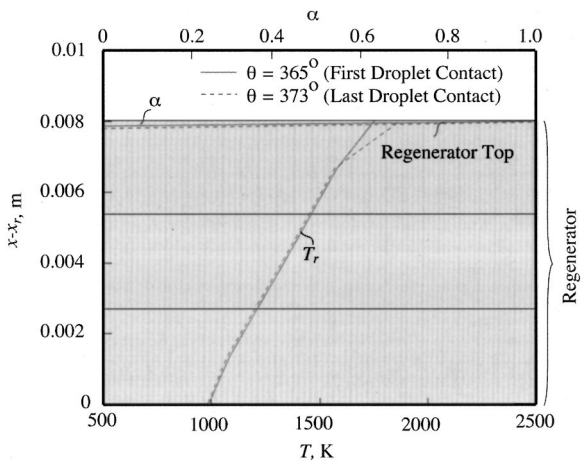

Fig. 9 The fuel droplet particle density of the first, impinging fuel droplet parcel and last parcel, and the temperature distribution within the regenerator insert

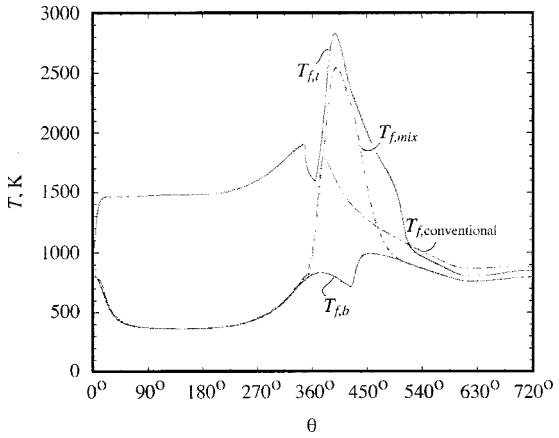

Fig. 10 Variations of gas temperatures in the regenerative and the conventional engines, during a cycle

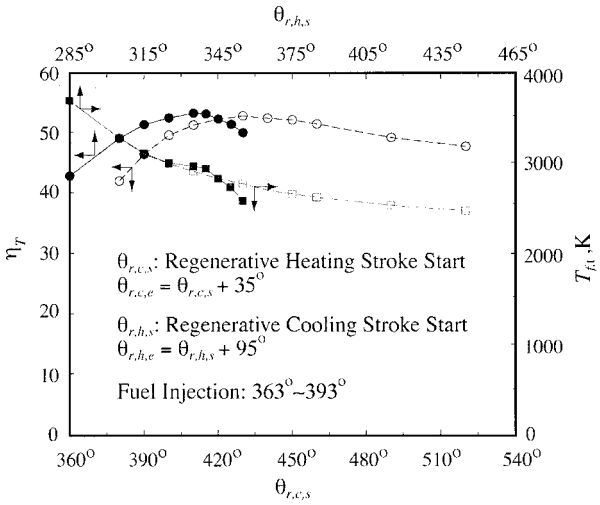

Fig. 11 Effect of the regenerative heating and cooling stroke periods on the thermal efficiency

regenerator surface. Figure 9 shows that the filtration efficiency α of the first and last impinging fuel droplet parcels captured within about 4 pores (<1 mm) for an 8 mm thickness regenerator. Also shown is that the temperature variation of the regenerator is rather small for the fuel impingement. Note that the temperature variation is affected by surface-convection, conduction, radiation, and fuel droplet evaporation.

3.3 Superadiabatic Combustion. The superadiabatic flame temperature, due to thermal regeneration of the combustion heat, increases the thermal efficiency. Figure 10 shows that the peak gas temperature $T_{f,t}$ in the top gas zone of the regenerative engine is higher than that of the conventional engine. The mixture gas temperature $T_{f,\mathrm{mix}}$ of the top and bottom gas zone is also higher than the gas temperature of the conventional engine, but only during the combustion period. The superadiabatic flame temperature during the fuel injection period enhances the fuel evaporation. The enhanced fuel evaporation assists the intense combustion resulting in an increase of the peak pressure and engine power.

The higher gas temperature, due to the superadiabatic combustion, will be beneficial in reducing the soot formation (because oxidation of the soot trapped in pores is enhanced). However, the higher gas temperature increases the thermal NO_x production. Lowering the peak flame temperature, by controlling the fuel injection timing, the thermal regeneration, and by using a fuel-lean mixture, would then become necessary to control NO_x emissions.

3.4 Optimization of Thermal Regeneration. The optimum motion schedule of the regenerator for a high thermal efficiency requires the maximum thermal regeneration and the minimum mechanical work loss due to the regenerator pressure drop.

Figure 11 shows that for the maximum thermal efficiency, the optimum regenerative heating and cooling strokes begin at 345 deg and 420 deg for prescribed stroke durations of 35 deg and 95 deg and the conditions given in Table 1, respectively (for the regenerative heating stroke, $\theta_{r,h,s} \sim \theta_{r,h,e}$, and for the regenerative cooling stroke, $\theta_{r,c,s} \sim \theta_{r,c,e}$). The optimum regenerative heating stroke would create a high gas temperature and more fuel impingement on the regenerator, and thus enhances evaporation. A retarded regenerative heating stroke decreases thermal regeneration period during the fuel injection and therefore does not achieve a higher super-adiabatic temperature.

The optimum regenerative cooling stroke using the high exhaust temperature optimizes the work gain by the thermal regeneration and the work loss by the pressure drop. An advanced regenerative cooling stroke recovers the combustion heat at a higher temperature, thus increasing the regenerator temperature and the superadiabatic flame temperatures. The retarded regenerative cooling stroke results in a higher expansion pressure due to higher exhaust gas temperature, thus increasing the work loss due to the regenerator pressure drop.

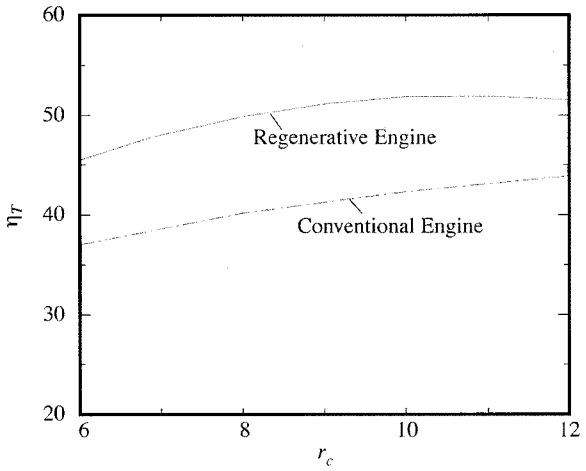

Fig. 12 Effect of compression ratio on the thermal efficiency of the regenerative and conventional engines

Figure 12 shows the effect of the compression ratio on the thermal efficiency. The maximum thermal efficiency of $\eta_T = 53$ percent is predicted at a compression ratio of $r_c = 10$. The maximum compression ratio r_c in the regenerative engine is limited to values below 14 due to the dead volume of the regenerator and the tolerance gaps. For maximum thermal efficiency, an optimum compression ratio of $r_c = 10$ is obtained.

4 Conclusion

The enhanced fuel evaporation, by droplet-regenerator interaction and air preheating, results in a more uniform fuel-vapor distribution and a dominant premixed combustion regime. The increase in the superadiabatic flame temperature enhances the fuel evaporation and increases the peak pressure, which correspondingly increases the thermal efficiency. Here the fuel-injection timing and the motion of the regenerator are optimized for a higher thermal efficiency. For the optimum compression ratio of $r_c = 10$, a thermal efficiency of $\eta_T = 53$ percent is predicted, compared to 43 percent of the conventional Diesel engine with a

Table 3 Comparison of results for conventional (non-regenerative) and regenerative Diesel engines

		Non-regenerative	Regenerative Engine
V_d	cm^3	1,718	1,718
V_c	cm^3	110.8	245.4
r_c		16.5	10
$M_{a,o}$	g	6.494	6.494
$M_{F,o}$	g	0.2165	0.2165
$(A/F)_a$		30	30
$p_{f,max}$	MPa	23.9	top: 30.3
	MPa		bottom: 30.3
$T_{f,max}$	K	1,619	top: 2,305
	K		bottom: 964
$\overline{T_{exh}}$	K	882	780
$W_{c,i,n}(720°)$	kJ	3.97	4.86
$P_{c,i}(720°)$	kW	53.0	64.8
$p_{mep,i,n}$	MPa	2.31	2.82
η_F		0.43	0.53
η_V		0.94	0.92
sfc	g/kW-hr	196	160

higher compression ratio. The performance comparison between the conventional (non-regenerative) and regenerative Diesel engines is listed in Table 3.

Acknowledgments

We are thankful to Mr. John M. Clarke at Caterpillar Inc. and Dr. Allan J. Ferrenberg at ReGen Inc. for the valuable comments on the simulation of the regenerative engine. We would also like to thank to Dr. Amir A. M. Oliveira for his start of simulation of the regenerative engine in our laboratory. The financial support of Caterpillar is greatly appreciated.

Nomenclature

a_r = frequency factor (s^{-1})
$a,b,\ldots f$ = coefficients of insert motion
A = area (m^2) or air
B_M = mass transfer number
c_p = specific heat capacity (J/kg-K)
C_D = drag coefficient
d = diameter (m)
D = diffusion coefficient (m^2/s) or diameter (m)
F = fuel
F_{i-j} = view factor
k = thermal conductivity (W/m-K)
K = permeability (m^2)
l = thickness (m)
L = length (m)
M = mass (kg) or molar weight (kg/kmole)
n = particle density per a parcel ($1/m^3$)
N = rpm (rot/min) or number of nodes or number of parcels
NTU = number of transfer units
Nu_D = Nusselt number based on D
p = pressure (Pa)
P = combustion product species
Pr = Prandtl number
q = heat flux (W/m^2)
Q = heat flow rate (W)
Q_k = conduction heat flow rate (W)
Q_{ku} = surface-convection heat flow rate (W)
Q_u = convection heat flow rate (W)
Q_r = surface radiation heat flow rate (W)
r = radial axis (m)
r_c = compression ratio
R = thermal resistance (K/W)
R_g = universal gas constant 8.3145 J/mole-K
Re_D = Reynolds number based on D
S = energy conversion rate (W)
Sc = Schmidt number
Sto = Stoke number
t = time (s)
T = temperature (K)
u = velocity (m/s)
V = volume (m^3)
W = work (J)
x = coordinate axes (m) or partial pressure

Greek

α = absorption coefficient or filtration efficiency
ΔE_a = activation energy (J/mole-K)
Δh_{lg} = heat of the phase change (J/kg)
$\Delta h_{r,F}$ = heat of reaction of fuel (J/kg-fuel)
Δl = nodal length (m)
Δp = pressure drop (Pa)
ϵ = emissivity or radiation or porosity
η_T = thermal efficiency, see Equation (25)
μ = viscosity (Pa-s)
ρ = density (kg/m^3)
θ = crank angle (degree)
σ_{SB} = Stefan-Boltzmann constant
Σ = summation
Φ = stoichiometric ratio

Subscripts

a = activation or air
A = surface or air
ad = adiabatic
b = bottom gas zone or bulk or blackbody
B = cylinder bore
c = combustion or compression or clearance or cooling
cb = cylinder block
ch = cylinder head
d = droplet or displacement or divergence
D = diameter or drag
e = exhaust or end or emission
exh = exhaust
evp = evaporation
f = fluid
F = fuel
g = gas phase
i = node index or porous insert or intake
id = ignition delay
in = indicated variable
inj = fuel injection
ins = porous insert
int = intake
k = conduction
ku = surface convection
l = liquid
loss = loss
lg = liquid-gas
n = ambient
m = mass diffusion or mass
max = maximum
mep = mean effective pressure
o = reference
O = oxidant species
p = pressure or piston or pore or plug flow
P = product species
r = radiation or reaction
R = reactant species
s = solid phase or start or particle stoichiometric
sfc = specific fuel consumption (g/kW-hr)
sl = solid-liquid

sg = saturation gas
sat = saturation
sf = solid-fluid interface
sfc = indicated specific fuel consumption
SM = Sauter mean diameter
t = top gas zone or thermal or total
T = thermal or isentropic
u = convection
v = vapor or valve
V = volume
w = cooling water
x = x-component

Other symbols

$\langle\ \rangle$ = local spatial averaged
$[\ ]$ = species concentration (mol/cm^3)

Appendix

Terms appearing in the energy conservation Eq. (2) of the top gas zone are given below. The heat transfer due to the fuel injection is

$$Q_{u,\mathrm{inj}} = -\dot{M}_{F,\mathrm{inj}} c_{p,F} T_{F,o}\,. \tag{A.1}$$

The surface-convection heat transfers between the top gas zone and surfaces of the cylinder head, the cylinder block, and the top regenerator surface $\langle Q_{ku}\rangle_{D_B}$, are

$$\langle Q_{ku,t-ch}\rangle_{D_B} = \frac{(T_{f,t}-T_{ch,o})}{\langle R_{ku,t-ch}\rangle_{D_B}}, \quad \langle Q_{ku,t-cb}\rangle_{D_B} = \frac{(T_{f,t}-T_{cb,o})}{\langle R_{ku,t-cb}\rangle_{D_B}},$$

$$\langle Q_{ku,t-r}\rangle_{D_B} = \frac{(T_{f,t}-T_{r,L})}{\langle R_{ku,t-r}\rangle_{D_B}}, \tag{A.2}$$

where the surface-convection resistance is given as

$$\langle R_{ku,t}\rangle_{D_B} = \frac{D_B}{\langle \mathrm{Nu}\rangle_{D_B,t} k_f A_{ku,t}}, \tag{A.3}$$

where $\langle \mathrm{Nu}\rangle_{D_B,t}$ is determined from the Woschni correlation using the average cylinder gas velocity and the cylinder pressure [11], as given below

$$\langle \mathrm{Nu}\rangle_{D_B,t} = 0.035\,\mathrm{Re}_{D_B,t}^{0.8}, \quad \mathrm{Re}_{D_B,t} = \frac{\rho_{f,t} D_B \langle u_f\rangle_t}{\mu_f}. \tag{A.4}$$

Here $\langle u_f\rangle_t$ is given by

$$\langle u_f\rangle_t = c_1 (\overline{u_{p,t}^2})^{1/2} + c_2 \frac{V_f (p_{f,t}-p_m)}{(M_{a,o}+M_{F,o})\dfrac{R_g}{M_g}}, \tag{A.5}$$

where

$$(\overline{u_{p,t}^2})^{1/2} = 2 L_d N \frac{2\pi(\mathrm{rad/rot})}{60(\mathrm{s/min})}, \quad p_m V_f = M_f \frac{R_g}{M_g} T_n \tag{A.6}$$

and $c_1 = 0.57$, $c_2 = 0$ m/s-K, and for only expansion, $c_1 = 0.57$, $c_2 = 0.00081$ m/s-K. Note that c_1 and c_2 are determined by the calibration of current simulation results against the Caterpillar's engine simulation code which has similar submodels to the current simulation code.

The energy conversion terms in the top gas zone are

$$\dot{S}_{r,c} = \dot{M}_{r,F} \Delta h_{r,F}, \quad \dot{S}_{m,p,t} = V_{f,t} \frac{dp_{f,t}}{dt}, \quad \dot{S}_{F,lg} = -\dot{M}_{F,\mathrm{evp}} \Delta h_{lg},$$

$$\begin{aligned}(\dot{S}_{e,\epsilon} + \dot{S}_{e,\alpha})_t = {} & (-\epsilon_{r,f}\alpha_{r,ch}\sigma_{\mathrm{SB}} T_{r,f,t}^4 + \epsilon_{r,ch}\alpha_{r,f}\sigma_{\mathrm{SB}} T_{ch,o}^4) A_{r,ch} \\ & + (-\epsilon_{r,f}\alpha_{r,cb}\sigma_{\mathrm{SB}} T_{r,f,t}^4 + \epsilon_{r,cb}\alpha_{r,f}\sigma_{\mathrm{SB}} T_{cb,o}^4) A_{r,cb,t} \\ & + (-\epsilon_{r,f}\alpha_{r,r}\sigma_{\mathrm{SB}} T_{r,f,t}^4 + \epsilon_{r,r}\alpha_{r,f}\sigma_{\mathrm{SB}} T_{r,L}^4) A_{r,r}\,.\end{aligned} \tag{A.7}$$

Note that the $T_{r,f,t}$ is the apparent flame temperature for the gas volumetric radiation [12] and the $T_{r,L}$ is the top surface temperature of the regenerator.

For the bottom gas zone, the convection heat transfer due to gas flow through the regenerator, the intake and the exhaust are

$$Q_{u,\mathrm{int}} = \begin{cases} -\dot{M}_{a,\mathrm{int}} c_{p,f} T_n & \text{for } \dot{M}_{a,\mathrm{int}} \geqslant 0 \\ \dot{M}_{a,\mathrm{int}} c_{p,f} T_{f,b} & \text{for } \dot{M}_{a,\mathrm{int}} < 0 \end{cases}$$

$$Q_{u,\mathrm{exh}} = \begin{cases} -\dot{M}_{a,\mathrm{exh}} c_{p,f} T_{f,b} & \text{for } \dot{M}_{a,\mathrm{exh}} \geqslant 0 \\ \dot{M}_{a,\mathrm{exh}} c_{p,f} T_e & \text{for } \dot{M}_{a,\mathrm{exh}} < 0\,. \end{cases} \tag{A.8}$$

Note that the intake and exhaust occurs in the bottom chamber. The surface-convection heat transfers $\langle Q_{ku,b-cb}\rangle_{D_B}$, $\langle Q_{ku,b-p}\rangle_{D_B}$, $\langle Q_{ku,b-r}\rangle_{D_B}$ are determined similarly as in the top chamber.

In the regenerator, the conduction heat transfer rate in the solid phase is given by

$$(Q_{k,r})_{i-(i+1)} = \frac{T_{r,i}-T_{r,i+1}}{(R_{k,r})_{i-(i+1)}}, \quad (R_{k,r})_{i-(i+1)} = \frac{\Delta l_{r,i}}{(1-\epsilon_r) A_r k_r}. \tag{A.9}$$

The surface-convection heat transfer between the porous regenerator and the gas is given by

$$\langle Q_{ku,f-r}\rangle_i = \frac{\langle \mathrm{Nu}\rangle_{D,p,i} k_f}{D_p} \frac{A_{sf}}{V} (\Delta l_{r,i} A_r)(T_{r,i} - T_{f,r,i}) \tag{A.10}$$

where

$$\langle \mathrm{Nu}\rangle_{D,p,i} = 2 + (0.4\,\mathrm{Re}_{D,p,i}^{1/2} + 0.2\,\mathrm{Re}_{D,p,i}^{2/3})\mathrm{Pr}^{0.4}$$

$$\mathrm{Re}_{D,p,i} = \frac{\dot{M}_{f,r,i} D_p}{(1-\epsilon_r) A_r \mu_f}, \quad D_p = 6(1-\epsilon_r)\frac{V}{A_{sf}}.$$

It is assumed that the heat transfer due to the fuel droplet-regenerator interaction occurs between the fuel droplet and the solid phase of the regenerator. The heat transfer due to the fuel droplet in contact with the regenerator is given by

$$Q_{d,i} = n_d \alpha_d \frac{\mathrm{Nu}_{D,2} k_f}{D_d} A_d (T_d - T_{r,i}), \tag{A.11}$$

where $\mathrm{Nu}_{D,2}$ is due to the film boiling heat transfer for the droplets colliding the porous regenerator over Leidenfrost temperature and is expressed as [13]

$$\begin{aligned}\mathrm{Nu}_{D,2} = \frac{D_d}{k_f}\Bigg[& \rho_{b,l}\Delta h_{lg,\infty} \frac{\langle \dot{m}_d\rangle}{\rho_{b,l}} \eta_d \left\{ 1 - \frac{\langle \dot{m}_d\rangle/\rho_{b,l}}{(\langle \dot{m}_d\rangle/\rho_l)_o} \right\} \frac{1}{T_{r,i}-T_d} \\ & + 1720 (T_{r,i}-T_d)^{-0.088} D_d^{-1.004} u_d^{-0.764} \frac{(\langle \dot{m}_d\rangle/\rho_{b,l})^2}{(\langle \dot{m}_d\rangle/\rho_l)_o} \Bigg],\end{aligned} \tag{A.12}$$

where

$$\eta_d \equiv \frac{3.68\times 10^4}{\rho_{b,l}\Delta h_{lg,\infty}} (T_{r,i}-T_d)^{1.691} D_d^{-0.062}$$

$$\Delta h_{lg,\infty} \equiv c_{p,l}(T_{lg}-T_d) + \Delta h_{lg}$$

$$\left(\frac{\langle \dot{m}_d\rangle}{\rho_l}\right)_o \equiv 5\times 10^{-3}\ \text{m/s}.$$

Note that the above correlation is based on experimental results for water droplet spray on a nickel-plated copper surface, in an otherwise stagnant air is used for $180°\mathrm{C} < T_{r,i} - T_{l,\infty} < 380°\mathrm{C}$. Although the regenerator surface condition is out of the range considered, it is assumed that the relation can be used for the analysis of the impinging droplets in the vapor-film regime.

In the regenerator, the convection heat transfer rate for the fluid phase is given by

$$(Q_{u,r})_i=\begin{cases}(\dot{M}_{f,r})_i c_{p,f} T_{f,r,i} & \text{for } (\dot{M}_{f,r})_i \geqslant 0\\ -(\dot{M}_{f,r})_i c_{p,f} T_{f,r,i+1} & \text{for } (\dot{M}_{f,r})_i < 0.\end{cases}$$
$$i=0,1,\ldots,N_r, \qquad (A.13)$$

where $T_{f,r,0}=T_{f,b}$ and $T_{f,r,N_r+1}=T_{f,t}$.

At the bottom surface of the porous regenerator $i=1$, the energy equation is

$$-\frac{(T_{f,b}-T_{r,o})}{\langle R_{ku,b-r}\rangle_{D_B}}+\frac{T_{r,o}-T_{r,1}}{(R_{k,r})_{o-1}}=0. \qquad (A.14)$$

At the top surface of the porous regenerator $i=N_r$, the energy equation is

$$-\frac{(T_{f,t}-T_{r,L})}{\langle R_{ku,t-r}\rangle_{D_B}}-\frac{\sigma_{SB}(T_{cb,o}^4-T_{r,L}^4)}{(R_{r,\Sigma})_{cb-r,t}}-\frac{T_{r,N_r}-T_{r,L}}{(R_{k,r})_{N_r-L}}$$
$$=-\dot{S}_{e,\epsilon,r}-\dot{S}_{e,\alpha,r}, \qquad (A.15)$$

where $(R_{r,\Sigma})_{cb-r,t}$ is the surface radiation resistance [14]

$$(R_{r,\Sigma})_{cb-r,t}=\frac{1-\epsilon_{r,cb}}{\epsilon_{r,cb}A_{r,cb}}+\frac{1}{F_{cb-r}(A_{r,cb})_t}+\frac{1-\epsilon_{r,r}}{\epsilon_{r,r}A_{r,r}}.$$

Note that the surface and volumetric radiation are neglected at the bottom chamber due to the low temperature.

In the energy conservation equation for the cylinder head, the heat transfer rates are given by $(Q|_{A,ch})_i$ is given for the volumes $i=1,2,\ldots N_{ch}-1$ as

$$(Q|_{A,ch})_i=-\frac{(T_{ch,i-1}-T_{ch,i})}{(R_{k,ch})_{(i-1)-i}}+\frac{(T_{ch,i}-T_{ch,i+1})}{(R_{k,ch})_{i-(i+1)}}, \qquad (A.16)$$

and for the inside surface of cylinder head, the energy equation is given by

$$-\frac{(T_{f,t}-T_{ch,o})}{\langle R_{ku,t-ch}\rangle_{D_B}}+\frac{\sigma_{SB}(T_{ch,o}^4-T_{r,L}^4)}{(R_{r,\Sigma})_{ch-r,t}}+\frac{\sigma_{SB}(T_{ch,o}^4-T_{cb,o}^4)}{(R_{r,\Sigma})_{ch-cb,t}}$$
$$+\frac{(T_{ch,o}-T_{ch,1})}{(R_{k,ch})_{o-1}}=-\dot{S}_{e,\epsilon,ch}-\dot{S}_{e,\alpha,ch}, \qquad (A.17)$$

and for the last volume $i=N_{ch}$, we have

$$(Q|_{A,ch})_{N_{ch}}=-\frac{(T_{ch,N_{ch}-1}-T_{ch,N_{ch}})}{(R_{k,ch})_{(N_{ch}-1)-N_{ch}}}+\frac{(T_{ch,N_{ch}}-T_{f,w})}{R_{k,ch-w}+(R_{ku,f})_w}, \qquad (A.18)$$

where $(R_{ku,f})_w$ is the thermal resistance for surface convection in the coolant jacket.

For the mass conservation equation, the fuel evaporation rate $\dot{M}_d(\mathrm{Re}_D=0)$ in the quiescent ambient is [9]

$$\dot{M}_d(\mathrm{Re}_D=0)=2\pi\rho_{f,t}D_d D_{m,F}\ln(1+B_M), \qquad (A.19)$$

where

$$B_M=\frac{Y_{F,sg}-Y_{F,\infty}}{1-Y_{F,sg}}.$$

The saturation fuel-vapor concentration $Y_{F,sg}$ is determined as

$$Y_{F,sg}=\frac{x_{sg}M_F}{(1-x_{sg})M_a+x_{sg}M_F}, \qquad (A.20)$$

where

$$x_{sg}=\frac{p_v}{p_{f,t}}, \quad p_v=p_{v,o}e^{(-M_v\Delta h_{lg}/R_g)(1/T_d-1/T_{lg,o})}.$$

From the mass conservation equation, the droplet diameter is given by

$$\frac{dD_d}{dt}=-\frac{4\rho_{f,t}D_{m,F}}{\rho_{b,l}D_d}\ln(1+B_M)[1+f(\mathrm{Re}_D,\mathrm{Sc})], \qquad (A.21)$$

where $D_{m,F}$ is the diffusion coefficient, D_d is the droplet diameter, and B_M are the mass transfer number.

For the energy conservation equation of the fuel droplet, Nusselt number $\mathrm{Nu}_{D,1}$ $(\mathrm{Re}_D=0)$ in the quiescent ambient is expressed

$$\mathrm{Nu}_{D,1}(\mathrm{Re}_D=0)=\frac{\dfrac{\dot{M}_d(\mathrm{Re}_D=0)c_{p,F}}{\pi D_d k_f}}{\exp\left(\dfrac{\dot{M}_d(\mathrm{Re}_D=0)c_{p,F}}{2\pi D_d k_f}\right)-1}. \qquad (A.22)$$

Species conservation equations in the top chamber are given by

$$-\dot{M}_{F,\mathrm{evp}}+\dot{M}_{r,F}=-\frac{dM_{F,t}}{dt} \qquad (A.23)$$

$$[-(\dot{M}_{f,r})_{N_r}+\dot{M}_{r,F}(A/F)_s]\left(\frac{O}{A}\right)-\frac{1}{2}\dot{M}_{NO,t}=-\frac{dM_{O,t}}{dt} \qquad (A.24)$$

$$-(\dot{M}_{f,r})_{N_r}\left[1-\left(\frac{O}{A}\right)\right]-\frac{1}{2}\dot{M}_{NO,t}=-\frac{dM_{N_2,t}}{dt}, \qquad (A.25)$$

where $M_{f,t}=M_{F,t}+M_{O,t}+M_{P,t}+M_{N_2,t}$ and $(A/F)_s=15.5$, $(O/A)_s=0.23$.

The mass of fuel injected $M_{F,o}$ is calculated as a function of the air to fuel ratio $(A/F)_a$ and the intake conditions by

$$M_{F,o}=\frac{M_{a,o}}{(A/F)_a}, \quad M_{a,o}=\frac{p_n V_d}{T_n\dfrac{R_g}{M_a}}. \qquad (A.26)$$

References

[1] Ferrenberg, A. J., 1988, "Regenerative Internal Combustion Engine," US Patent 4,790,284.

[2] Ferrenberg, A. J., 1990, "The Single Cylinder Regenerated Internal Combustion Engine," SAE Paper No. 900911.

[3] Ferrenberg, A. J., Williams B. E., and McNeal, S. R., 1995, "Low Heat Rejection Regenerated Diesel Engines for Shipboard Mechanical and Electrical Power (Part2)," Contract N00167-92-C-0020.

[4] Park, C.-W., and Kaviany, M., 2000, "Combustion-Thermoelectric Tube," ASME J. Heat Transfer , **122**, pp. 721–729.

[5] Heywood, J. B., 1988, *Internal Combustion Engine Fundamentals*, McGraw-Hill.

[6] Kaviany, M., 1999, *Principles of Heat Transfer in Porous Media*, Corrected Second Edition, Springer-Verlag, New York.

[7] Westbrook, C. K., and Dryer, F. L., 1984, "Chemical Kinetic Modeling of Hydrocarbon Combustion," Prog. Energy Combust. Sci., **10**, pp. 1–57.

[8] Hiroyasu, H., and Kadota, T., 1974, "Fuel Droplet Size Distribution in Diesel Combustion Chamber," SAE Paper No. 740715.

[9] Faeth, G. M., 1983, "Evaporation and Combustion of Sprays," Prog. Energy Combust. Sci., **9**, pp. 1–76.

[10] Martynenko, V. V., Echigo, R., and Yoshida, H., 1998, "Mathematical Model of Self-Sustaining Combustion in Inert Porous Medium With Phase Change Under Complex Heat Transfer," Int. J. Heat Mass Transf., **41**, No. 1, pp. 117–126.

[11] Woshni, G., 1967, "Universally Applicable Equation for the Instantaneous Heat Transfer Coefficient in the Internal Combustion Engine," SAE Paper No. 670931.

[12] Assanis, D. N., and Heywood, J. B., 1986, "Development and Use of Computer Simulation of the Turbocompounded Diesel System for Engine Performance and Components Heat Transfer Studies," SAE Paper No. 860329.

[13] Bernardin, J. D., and Mudawar, I., 1997, "Film Boiling Heat Transfer of Droplet Streams and Sprays," Int. J. Heat Mass Transf., **40**, pp. 2579–2593.

[14] Siegel, R., and Howell, J. R., 1992, *Thermal Radiation Heat Transfer*, Third Edition, Hemisphere, Washington, D.C.

Journal of Heat Transfer

Technical Notes

This section contains shorter technical papers. These shorter papers will be subjected to the same review process as that for full papers.

The Effect of Space-Dependent Thermal Conductivity on the Steady Central Temperature of a Cylinder

Louis C. Burmeister
e-mail: kume@mecheng.me.ukans.edu
Mem. ASME Department of Mechanical Engineering, University of Kansas, Lawrence, KS 66045

A transformation is presented that enables the center temperature of a cylinder to be expressed in terms of an integral of the peripheral temperature distribution for heat conduction with space-dependent thermal conductivity. Its predictions agree with exact answers and with numerical solutions obtained with finite difference methods for four test cases. The new result can be applied to a two-dimensional floating random-walk Monte Carlo procedure which previously was restricted to the case of constant thermal conductivity. [DOI: 10.1115/1.1418701]

Keywords: Conduction, Cylinder, Heat Transfer, Monte Carlo, Space

Introduction

Accurate prediction of the temperature distribution in a solid requires solution of the heat diffusion equation. This can be done either with boundary conditions specified or to determine them from measured temperatures at internal locations, the latter as done by Ganesa-Pillai and Haji-Sheikh [1]. Complex geometries and boundary conditions often necessitate numerical methods of solution whether or not thermal conductivity is constant. The boundary element (Brebbia [2]) and floating random-walk Monte Carlo numerical methods (Haji-Sheikh and Sparrow [3]) are among those that utilize information obtained from exact relationships. For these methods to be accurate when thermal conductivity varies with position, it is desirable that relationships for that case be found.

The same mathematical problem is encountered in related areas. In Turner's [4,5] two-dimensional applications of Monte Carlo techniques to prediction of unsteady piezometric potential in a water well, it was observed that variation of hydraulic transmissibility with location ought to be taken into account.

While many analytical solutions are known if thermal conductivity k is constant, few are known when it is space dependent. In their surveys of possibilities for that case, Bellman [6] and, especially, Luikov [7] point out that analytical solutions are generally possible only for restrictive cases, such as one-dimensional conductivity variation or conductivity constant in zones. For one-dimensional cases, transformation of the space coordinate x as $\omega = \int dx/k(x)$ is a useful simplification. In physical terms, it gives the thermal resistance in the x direction. Grigoriu [8] proposed a floating-random-walk Monte Carlo method based on properties of Brownian motion and Itô processes that is claimed to be applicable to space-dependent conductivity, but without examples.

Following a suggestion of Bellman [6], Munoz and Burmeister [9] utilized the substitution $y = k^{1/2}T$ to find that the steady heat diffusion equation is transformed into $\nabla^2 y = Fy$ in which $F = k^{-1/2}\nabla^2 k^{1/2}$. Then, analytical solutions can be obtained if F is a convenient function. This substitution was advanced by Clements and Budhi [10] who incorporated a Kirchoff transformation (Carslaw and Jaeger [11]) to obtain a boundary element method for numerical solution of a class of problems in which thermal conductivity is dependent upon space and temperature. Munoz and Burmeister [9] explored the use of their results for a Monte Carlo numerical procedure. They found that when F is a function of radius r alone in cylindrical coordinates, the center temperature T_c of a cylinder of radius R is related to the peripheral temperature $T_R(\theta)$ and thermal conductivity $k_R(\theta)$ at angular location θ as

$$T_c = \int_0^{2\pi} T_R(\theta) k_R^{1/2}(\theta)\, d\theta / \overline{k_R^{1/2}} \quad \text{with} \quad \overline{k_R^{1/2}} = \int_0^{2\pi} k_R^{1/2}(\theta)\, d\theta / 2\pi \tag{1}$$

The relationship in Eq. (1) between the center and peripheral temperatures, although correct for the stated condition, lacks generality. For example, the common case of thermal conductivity varying stepwise as in a layered anisotropic material violates the condition that F be continuous and depend only upon radius. In the following, another relationship will be derived and its predictions will be compared with those obtained by other means.

Formulation

The steady heat diffusion equation in cylindrical coordinates is

$$\frac{1}{r}\frac{\partial\left(kr\dfrac{\partial T}{\partial r}\right)}{\partial r} + \frac{1}{r^2}\frac{\partial\left(k\dfrac{\partial T}{\partial \theta}\right)}{\partial \theta} = 0. \tag{2}$$

Integration of Eq. (2) with respect to θ from 0 to 2π gives

$$\frac{1}{r}\frac{\partial\left(\int_0^{2\pi} kr\dfrac{\partial T}{\partial r}\, d\theta\right)}{\partial r} + \frac{1}{r^2}\left[k(2\pi)\frac{\partial T(2\pi)}{\partial \theta} - k(0)\frac{\partial T(0)}{\partial \theta}\right] = 0.$$

Since conditions at the beginning and end of an angular traverse are the same, it follows that

$$\frac{d\left(\int_0^{2\pi} kr\dfrac{\partial T}{\partial r}\, d\theta\right)}{dr} = 0.$$

Contributed by the Heat Transfer Division for publication in the JOURNAL OF HEAT TRANSFER. Manuscript received by the Heat Transfer Division September 25, 2000; revision received July 10, 2001. Associate Editor: D. B. R. Kenning.

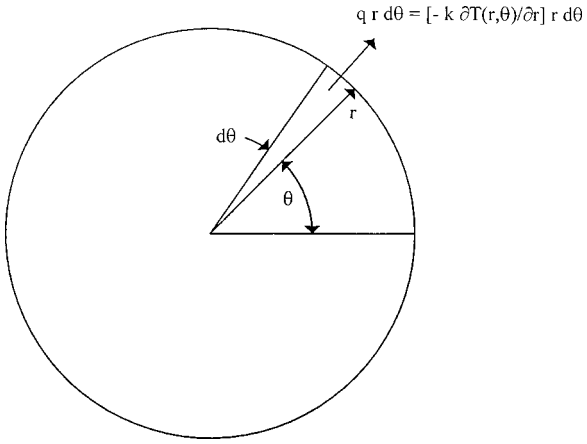

Fig. 1 Conductive heat flux q across a differential element of area $rd\theta$ on the periphery of a cylinder

Integration with respect to r from 0 to r gives

$$\int_0^{2\pi} k(r,\theta) r \frac{\partial T(r,\theta)}{\partial r} d\theta = 0. \tag{3}$$

Equation (3) represents the physical requirement that the sum of steady heat flows into and out of a circle be zero as shown in Fig. 1, and the current development could have started with it.

Recasting Eq. (3) as

$$\int_0^{2\pi} \frac{1}{k^{-1}} \frac{\partial T(r,\theta)}{\partial r} d\theta = 0$$

motivates the coordinate transformations

$$\eta = \int_0^r \frac{dr'}{k(r',\theta)} \Bigg/ \int_0^R \frac{dr'}{k(r',\theta)} \tag{4}$$

and

$$f = \int_0^\theta \frac{d\theta'}{\int_0^R dr'/k(r',\theta')} \Bigg/ \int_0^{2\pi} \frac{d\theta}{\int_0^R dr'/k(r',\theta)}. \tag{5}$$

With the transformations of Eqs. (4) and (5), Eq. (3) becomes

$$\int_0^1 \frac{\partial T(\eta,f)}{\partial \eta} df = 0.$$

Integration with respect to η from 0 to the outer radius of the cylinder gives the center temperature in terms of the specified peripheral temperature as

$$T_c = \int_0^1 T_R df. \tag{6}$$

Discussion

The functional form of $f(\theta)$ in Eq. (5) is consistent with the previously cited observations by Bellman [6] and Luikov [7]. It is also consistent with the use by Hameed and Lebedeff [12] of the space variable transformation $\omega = \int dx/k(x)$ in an application of the integral method to heat conduction in media in which thermal conductivity varies one-dimensionally with position. Patankar's [13] use of the harmonic mean of thermal conductivity k_{eff} between nodes in a finite difference numerical method as

$$2/k_{\text{eff},i} = 1/k_{i+1/2} + 1/k_{i-1/2}$$

is similar. Further support for the functional form of $f(\theta)$ is obtained from a finite difference formulation to determine the center temperature of a cylinder of specified peripheral temperature as depicted in Fig. 2. Use of only three control volumes around the central control volume for simplicity yields

$$T_c \left(\frac{1}{\frac{r_1}{k_o} + \frac{R-r_1}{k_{R1}}} + \frac{1}{\frac{r_1}{k_o} + \frac{R-r_1}{k_{R2}}} + \frac{1}{\frac{r_1}{k_o} + \frac{R-r_1}{k_{R3}}} \right) = \frac{T_{R1}}{\frac{r_1}{k_o} + \frac{R-r_1}{k_{R1}}} + \frac{T_{R2}}{\frac{r_1}{k_o} + \frac{R-r_1}{k_{R2}}} + \frac{T_{R3}}{\frac{r_1}{k_o} + \frac{R-r_1}{k_{R3}}}.$$

This finite difference expression suggests the continuous equivalent

$$T_c \int_0^{2\pi} \frac{1}{\int_0^R \frac{dr'}{k(r',\theta)}} d\theta = \int_0^{2\pi} T_R(\theta) \frac{1}{\int_0^R \frac{dr'}{k(r',\theta)}} d\theta,$$

which is consistent with Eq. (6). If interior control volumes are used between the central and the peripheral control volumes, a similar but more complex expression is obtained that contains additional, small terms that represent heat flow in the angular direction.

The first demonstration of the predictive ability of the formulation in Eq. (6) is for the one-dimensional case of a slab of two layers, each of thickness L. The temperature distribution is given by

$$\frac{d\left(k \frac{dT}{dx}\right)}{dx} = 0, \quad T(-L) = T_H, \quad T(L) = T_L,$$

$$k = \begin{cases} k_o(1+a), & x<0 \\ k_o & \text{otherwise} \end{cases}.$$

The solution is

$$T = \begin{cases} T_H - (T_H - T_L)(x/L+1)/(2+a), & x<0 \\ T_L - (T_H - T_L)(x/L-1)(1+a)/(2+a) & \text{otherwise} \end{cases}. \tag{7a}$$

The temperature T_c at $x=0$, the interface between the two layers, is

$$T_c = [(1+a)T_H + T_L]/(2+a). \tag{7b}$$

To compare the prediction of Eq. (6), it is first recognized that $x = r\cos(\theta)$ for a cylindrical coordinate system centered at $x=0$. Then, the peripheral temperature at a constant radial distance, equal to the layer thickness, from the interface between the two layers is obtained from Eq. (7a) to be

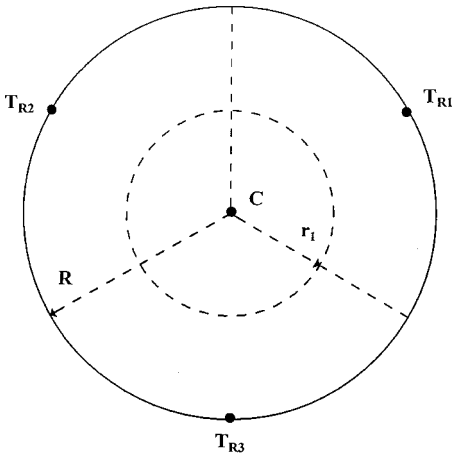

Fig. 2 Control volumes for determination of the central temperature of a cylinder in terms of the peripheral temperatures by a finite difference method

$$T_R=\begin{cases} T_H-(T_H-T_L)[1+\cos(\theta)]/(2+a), & \pi/2<\theta<3\pi/2 \\ T_L-(T_H-T_L)(1+a)[\cos(\theta)-1]/(2+a) & \text{otherwise} \end{cases}. \quad (8)$$

For this problem, Eq. (5) gives

$$f=\begin{cases} \theta/[(2+a)\pi], & 0\leqslant\theta<\pi/2 \\ [(1+a)\theta-a\pi/2]/[(2+a)\pi], & \pi/2\leqslant\theta<3\pi/2. \\ (\theta+a\pi)/[(2+a)\pi], & 3\pi/2\leqslant\theta<2\pi \end{cases} \quad (9)$$

Use of Eqs. (8) and (9) in Eq. (5) gives

$$T_c=\int_0^{2\pi} T_R(\theta)\frac{1}{\pi(2+a)}\begin{Bmatrix} 1, & -\pi/2\leqslant\theta<\pi/2 \\ 1+a, & \pi/2\leqslant\theta<3\pi/2 \end{Bmatrix} d\theta$$

$$=[(1+a)T_H+T_L]/(2+a),$$

which is identical to the exact answer in Eq. (7*b*). The earlier prediction of Eq. (1) is erroneous for this case in which F is not solely a function of radius.

The second case is one for which Eq. (1) is exact. In this case the thermal conductivity variation is $k=[2+(r/R)\cos\theta]^2$, for which $F=0$. Application of Eq. (5) results in $f=(2\theta+\sin\theta)/4\pi$ which, when used in Eq. (6) with $T_R(\theta)=100(2+\cos\theta)$, yields

$$T_c=\frac{25}{\pi}\int_0^{2\pi}[4+4\cos(\theta)+\cos^2(\theta)]d\theta=225.$$

Munoz and Burmeister demonstrated by comparison with a finite difference numerical solution that this is the correct value for the center temperature.

A third case for which F is not solely a function of radius has the thermal conductivity uniform in each of two zones as described by

$$k=\begin{cases} 1, & 0.3\leqslant r<0.5, \quad 0\leqslant\theta\leqslant\pi \\ 5 & \text{otherwise} \end{cases}$$

for which Eq. (6) gives

$$f=\begin{cases} 5\theta/14\pi, & 0\leqslant\theta\leqslant\pi \\ 5/14+9(\theta/\pi-1)/14 & \text{otherwise} \end{cases}.$$

With $T_R=100(2+\cos\theta)$ Eq. (6) then gives the center temperature as 200, agreeing exactly with the value obtained with a finite difference numerical method by Munoz [14].

Use in a Monte Carlo Procedure

The result of the present analysis is Eq. (6) which can be recast into the form

$$T_c=\int_0^{2\pi} T_R(\theta)[df/d\theta]d\theta. \quad (10)$$

In this form it can be seen that T_c is the expected value of a series of experiments for which the probability distribution function for an outcome $T_R(\theta)$ within the range $0\leqslant\theta\leqslant2\pi$ is $df/d\theta$. From this it follows that the cumulative distribution function is $f(\theta)$.

Equation (10) can be used in a two-dimensional floating random-walk Monte Carlo procedure.

In general, because the thermal conductivity dependence upon location would not be convenient, evaluation of the cumulative distribution function f in Eq. (5) would have to be accomplished numerically.

Conclusion

A transformation has been found that enables the center temperature of a cylinder to be expressed in terms of an integral of the peripheral temperature distribution for heat conduction with space-dependent thermal conductivity. The predictions of the new result agree with exact answers and with numerical solutions obtained with finite difference methods for four test cases. The new result can be applied to a two-dimensional floating random-walk Monte Carlo procedure which previously was restricted to the case of constant thermal conductivity.

Nomenclature

a = constant for conductivity variation, see Eq. (7)
f = transformed angular coordinate, see Eq. (5)
F = conductivity function
k = thermal conductivity
$\overline{k_R}$ = thermal conductivity at radius R averaged over a circle
L = slab thickness
q = radial conductive heat flux, $q=-k\partial T/\partial r$
r' = dummy radial coordinate and position
r = radial coordinate and position
R = cylinder radius
T = temperature
x = space coordinate and position

Greek Symbols

η = transformed space coordinate, see Eq. (4)
θ = angular coordinate and position
π = natural number, $\pi=3.1415\ldots$
ω = transformed space coordinate

Subscripts

c = at the center
eff = effective value
H = high
i = index
L = low
o = at the center
R = at radial distance R

References

[1] Ganesa-Pillai, M., and Haji-Sheikh, A., 1998, "A Critical Evaluation Of the Monte Carlo Method For Application To The Inverse Heat Conduction Problem," *Proc. ASME. Heat Transfer Div.-1998, Intl. Mech. Engr. Congr. And Exp*, Nov. 15–20, HTD-V. 361-5, pp. 95–107.

[2] Brebbia, C., 1984, *The Boundary Element Method For Engineers*, Pentech Press Ltd., Estover Road, Plymouth, Devon PL6 7PZ, Great Britain.

[3] Haji-Sheik, A., and Sparrow, E., 1967, "The Solution Of Heat Transfer Problems by Probability Methods," ASME J. Heat Transfer, **89**, pp. 121–131.

[4] Turner, J., 1978, "An Improved Monte Carlo Procedure For The Solution Of The Steady-State, Two-Dimensional Diffusion Equation With Application To Flow Through Porous Media," M. S. thesis, University of Kansas, Lawrence, KS.

[5] Turner, J., 1982, "Improved Monte Carlo Procedures For The Unsteady-State Diffusion Equation Applied To Water Well Fields," Ph. D. thesis, University of Kansas, Lawrence, KS.

[6] Bellman, R., 1952, *Stability Theory Of Differential Equations*, McGraw-Hill, p. 109.

[7] Luikov, A., 1971, "Methods Of Solving The Nonlinear Equations Of Unsteady-State Heat Conduction," Heat Transfer-Sov. Res., **3**, pp. 1–51.

[8] Grigoriu, M., 2000, "A Monte Carlo Solution Of Heat Conduction And Poisson Equations," ASME J. Heat Transfer, **122**, pp. 40–45.

[9] Munoz, A., and Burmeister, L., 1988, "Steady Conduction With Space-Dependent Conductivity," ASME J. Heat Transfer, **110**, pp. 778–780.

[10] Clements, D., and Budhi, W., 1999, "A Boundary Element Method For The Solution of a Class of Steady-State Problems for Anisotropic Media," ASME J. Heat Transfer, **121**, pp. 462–465.

[11] Carslaw, H., and Jaeger, J., 1959, *Conduction Of Heat In Solids*, Oxford University Press, p. 89.

[12] Hameed, S., and Lebedeff, S., 1975, "Application Of Integral Method To Heat Conduction In Nonhomogeneous Media," ASME J. Heat Transfer, **97**, pp. 304–305.

[13] Patankar, S., 1978, "A Numerical Method For Conduction In Composite Materials, Flow in Irregular Geometries and Conjugate Heat Transfer," *Proc. Sixth Int. Heat Transfer Conf.*, Toronto, Canada, Vol. 3, Paper No. CO-14, pp. 297–302.

[14] Munoz, A., 1984, "Variable Thermal Conductivity And The Monte Carlo Floating Random Walk," Master of Science thesis, University of Kansas, Lawrence, KS.

Effective Radiative Properties of a Cylinder Array

Chongshan Zhang

Abraham Kribus
e-mail: avi.kribus@weizmann.ac.il

Environmental Sciences and Energy Research Dept.,
Weizmann Institute of Science,
Rehovot 76100, Israel

Rami Ben-Zvi
Solar Facilities Unit, Weizmann Institute of Science,
Rehovot 76100, Israel

Fully anisotropic problems are found where the radiative interaction is due to small-scale elements that lack spherical symmetry, for example: fibrous insulation, finned heat sinks, plant canopies, and some solar energy absorbers. We present the effective bulk optical properties of a PM composed of small-scale opaque cylinders. The properties are derived from data generated by detailed Monte-Carlo numerical experiments. The data reduction procedure is relatively simple and does not require a full solution and optimization of the Radiative Transfer Equation. Benchmark cases are presented, comparing an exact solution (with geometric detail of the cylinder array) and an approximate solution using a continuous PM model with the effective volumetric properties.
[DOI: 10.1115/1.1423317]

Keywords: Cylinder, Heat Transfer, Modeling, Numerical Methods, Properties, Radiation

1 Introduction

Treatment of radiative transport in Participating Media (PM) is usually limited to semianisotropic media, i.e., volumetric absorption and scattering coefficients that are independent of direction, and a degenerate scattering phase function depending only on the angle between the incident and outgoing radiation. In a fully anisotropic medium, the volumetric absorption and scattering coefficients depend on the direction of incident radiation, and the scattering phase function depends separately on both the incident and outgoing directions. A fully anisotropic PM can be a useful model in problems of radiation transport through media containing small-scale interacting elements that lack spherical symmetry and are not randomly oriented, for example fibrous insulation [1], finned heat sinks [2], plant canopies [3], and solar absorbers [4,5].

Producing a useful PM model of such a system requires finding the bulk optical properties of the equivalent PM. The optical properties often cannot be predicted from first principles and need to be derived from experimental data. A sample of the medium is exposed to a known incident radiation, and outgoing radiation fluxes in several directions are measured. To analyze the results, a guess for the optical properties is provided; the direct problem is solved by some approximation of the Radiative Transfer Equation (RTE); and the outgoing flux results are compared to the experimental measurement. The optical properties are then adjusted and the computation is repeated within an optimization process, until reasonable agreement is reached [6]. This can be a resource-consuming process due to the need to solve the RTE repeatedly.

Fully anisotropic media require a large number of parameters to describe the optical properties, and a large optimization problem with an embedded RTE solver may become prohibitively expensive. In a recent contribution [7] we have proposed an alternative method requiring only the direct solution of algebraic equations. In the current paper, this procedure is applied to a specific example of a complex medium modeled as an anisotropic PM. The model problem is a volume containing a regular array of cylinders [2,3,5]. The anisotropy is due to the difference between the direction along the cylinders and the directions in the plane perpendicular to the cylinders. The effective optical properties of this medium were derived from the results of a numerical experiment. The effective properties were then used to simulate a benchmark problem, and the results were compared to a reference solution.

2 Numerical Experiment

The sample was a cube containing a section of the cylinder array (Fig. 1). The array pitch is three cylinder diameters in both directions. The cylinders can be black, ideal diffuse reflectors, or gray absorbing (surface absorptivity 0.4) and diffusely reflecting.

The approach is based on the division of directional space into discrete solid angle intervals, following the Finite Volume method [8,9]. For convenience, we refer to these solid angle intervals as ordinates (although they are not identical to the classical definition from the Discrete Ordinate Method). Each of the optical properties has a distinct value within each ordinate, so that the number of unknowns is related to the number of ordinate directions chosen. The polar and azimuthal angles were divided into equal intervals. The directional grid resolution varied between 4×4 and 16×8 (16 division in ϕ, 8, in θ). The experiments were performed numerically, using a Monte Carlo ray tracing procedure. Simulated incident light was introduced within a single ordinate direction, and outgoing radiation was measured for each outgoing ordinate. The procedure was repeated with the incident light coming within other ordinates.

The analysis method of the experimental results was presented in detail in [7]. The general Finite Volume formulation of Fiterman et al. [10] was used, producing a coupled set of ordinary differential equations. The discrete RTE was integrated over the volume of the sample to produce integral energy balance equations. This volume averaging required several simplifying assumptions as described in [7]. The transmitted and the scattered contributions to the outgoing radiation were separated, and the extinction coefficient for each ordinate direction was found from an approximate equation involving only the transmitted contribu-

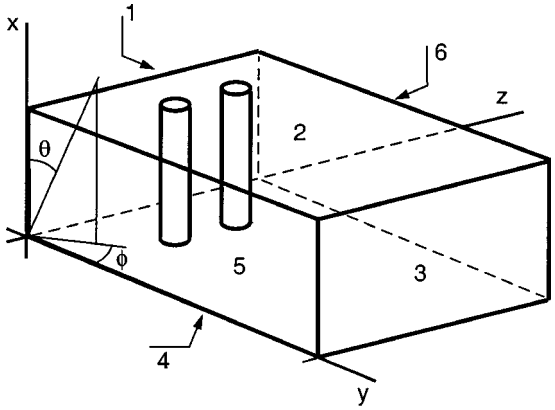

Fig. 1 Geometry of the cylinder array

Contributed by the Heat Transfer Division for publication in the JOURNAL OF HEAT TRANSFER. Manuscript received by the Heat Transfer Division September 1, 2000; revision received August 20, 2001. Associate Editor: D. A. Kaminski.

tion. The phase function was eliminated next by summing equations for all outgoing directions and using the energy conservation property of the phase function. This elimination produced equations for the scattering coefficient in each of the ordinate directions. Finally, given the extinction and scattering coefficients, a set of equations for the phase function can be solved. This procedure required solution of sets of algebraic equations, without the need for sophisticated solution methods of the RTE, and without iterative optimization.

3 Properties of the Cylinder Array

Figure 2 shows the distribution of the extinction coefficient of the array for a coarse and a fine directional grid. Each rectangle corresponds to the solid angle range of an ordinate. The extinction is low in directions along the cylinders' axis (small and large polar angle θ), and high in directions perpendicular to the axis (intermediate θ). The variations with the azimuthal angle ϕ, visible in the high-resolution solution, correspond to the angles where the cylinders are aligned (minimal extinction) and staggered (maximum extinction). Each ordinate in the coarse grid solution is close to the average of the corresponding ordinates in the fine grid solution, with an average error of 0.5 percent. The optical properties at different resolutions are then consistent. The distribution of the scattering coefficient is similar to that of the extinction coefficient. The scattering albedo (ratio of scattering coefficient to extinction coefficient) is nearly constant over all ordinates, with an average value of 0.63, which is very close to the real surface reflectivity of 0.6.

Figure 3 presents selected distributions of the phase function. High phase function values are found in the azimuthal direction opposite to the incident direction, representing strong backward scattering. There is no "memory," however, of the incident polar angle since reflection from the cylinders is diffuse. Therefore, the medium is not truly backward scattering and cannot be modeled as a semi-anisotropic medium. The minima of the phase function are negative. This is clearly unphysical, and can be an artifact of the simplifications made in order to model the average scattered flux [7].

The statistical error of the Monte Carlo process is the analog of measurement errors in a physical experiment. The number of rays was changed between 10^4 and 10^6 for the case of 16 ordinates (4×4). The largest error in the optical properties with 10^4 rays was 4 percent. 10^5 rays were used in the results presented here, with errors of at most 1 percent.

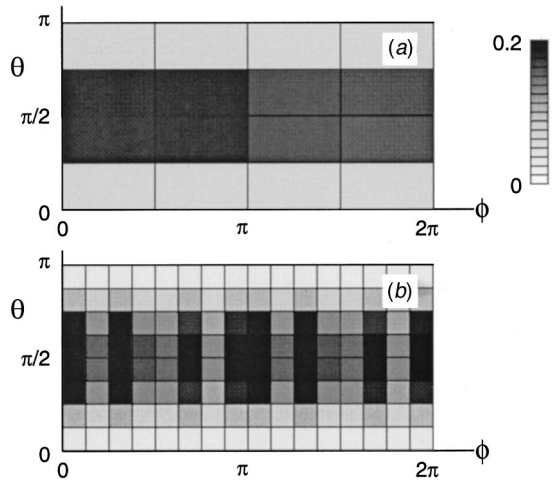

Fig. 2 Anisotropic extinction coefficient as a function of polar and azimuthal angles: (*a*) ordinate resolution 4×4 and (*b*) ordinate resolution 16×8.

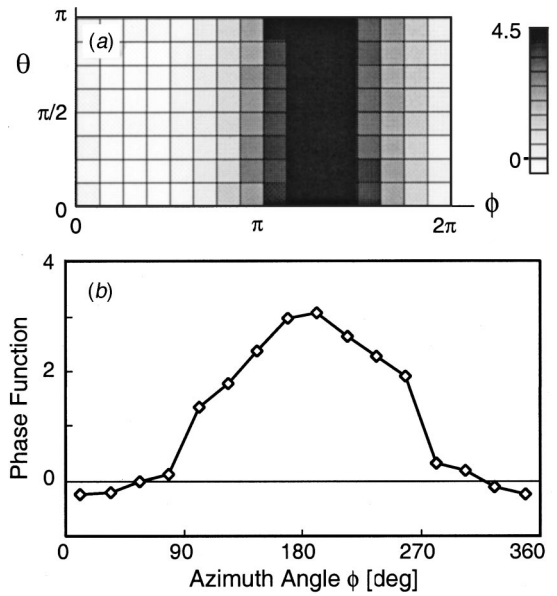

Fig. 3 (*a*) Phase function of incident ordinates $3\pi/8<\theta<\pi/2$, $\pi/4<\phi<3\pi/8$, ordinate resolution 16×8; and (*b*) cross-section in the outgoing direction $3\pi/8<\theta<\pi/2$.

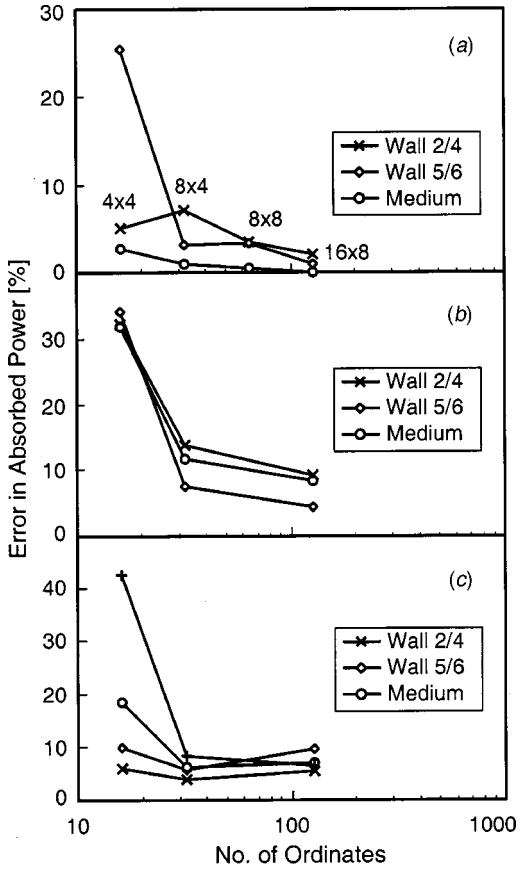

Fig. 4 Benchmark results: convergence of errors in absorbed power with number of ordinates, for (*a*) absorbing cylinders, (*b*) reflecting cylinders (scattering medium), and (*c*) absorbing and reflecting cylinders

The effective optical properties should be independent of the size of the sample if the PM model is valid. The size of the sample was increased by changing the number of cylinder rows between 3 and 6. The optical properties showed very little variation, indicating that even three rows produce a good representation of the behavior of the entire medium.

4 Benchmark Results and Discussion

The benchmark case is defined as a cubic box containing twelve rows of cylinders for an overall size of 36 diameters. Wall 1 of the cube at $y=0$ (Fig. 1) is hot, while all other walls and the cylinders are cold. All walls are black. We measure the distribution of the radiation emitted from wall 1 that is absorbed in the other walls and in the cylinders (i.e., the medium filling the box). The top and bottom (walls 2 and 4) are symmetric and are counted together. The sidewalls 5 and 6 are also symmetric. A reference solution was computed by detailed ray tracing of the full geometry of the cylinder array. The PM model results were computed by defining a continuous PM in the same volume as the cylinder array, using the effective optical properties that were presented in the previous section, and then performing ray tracing through the effective continuous medium.

Figure 4 shows the results for three cases: black cylinders (absorbing medium), reflective cylinders (scattering medium), and cylinders that are both absorbing and reflecting. The error is defined as the difference between the approximate solution (PM model using the effective properties) and the reference solution. The errors show convergence as a function of the number of ordinates in all three cases. Convergence is best for the absorbing case, but not as good for the two cases with a scattering component. Nevertheless, the errors for a 16×8 directional resolution were less than 10 percent even in the presence of scattering, indicating that the solutions are useable even though not very accurate.

The representation of scattering seems to cause larger errors, as well as some negative values of the phase function. This is probably due to the simplifying assumptions that were used in the derivation of the scattering coefficients and the phase function [7]. Additional work is needed on improving the procedure for deriving the scattering properties. Nevertheless, as a first attempt to solve a complex problem that was not previously treated, the present results are a reasonable approximation.

References

[1] Lee, S. C., 1990, ''Scattering Phase Function for Fibrous Media,'' Int. J. Heat Mass Transf., **33**, pp. 2183–2190.
[2] Sparrow, E. M., and Vemuri, S. B., 1985, ''Natural Convection/Radiation Heat Transfer From Highly Populated Pin-Fin Arrays,'' Journal of Heat Transfer, **107**, pp. 190–197.
[3] Mann, J., Curry, G., Demichele, D., and Baker, D., 1980, ''Light Penetration in a Row Crop With Random Plant Spacing,'' Agron. J., **72**, pp. 131–142.
[4] Thynell, S. T., and Merkle, C. L., 1989, ''Analysis of Volumetric Absorption of Solar Energy and Its Interaction With Convection,'' Journal of Heat Transfer, **111**, pp. 1006–1014.
[5] Karni, J., Kribus, A., Rubin, R., and Doron, P., 1998, ''The *Porcupine*: A Novel High-Flux Absorber for Volumetric Solar Receivers,'' ASME J. Sol. Energy Eng., **120**, pp. 85–95.
[6] Özisik, M. N., and Bokar, J. C., 1995, ''Inverse Problems of Radiative Transfer in Absorbing, Emitting and Scattering Media,'' *1st Int. Symp. Radiative Transfer*, M. P. Menguc, ed., Kusadasi, Turkey, Begell House, pp. 507–520.
[7] Zhang, C., Kribus, A., and Ben-Zvi, R., 2001, ''Volumetric Optical Properties of Fully Anisotropic Participating Media,'' J. Quant. Spectrosc. Radiat. Transf., **69**, pp. 27–42.
[8] Chui, E. H., and Raithby, G. D., 1993, ''Computation of Radiant Heat Transfer on a Nonorthogonal Mesh Using the Finite-Volume Method,'' Numer. Heat Transfer, Part B, **23**, pp. 269–288.
[9] Chai, J. C., Lee, H. S., and Patankar, S. V., 1994, ''Finite-Volume Method for Radiation Heat Transfer,'' J. Thermophys. Heat Transfer, **8**, pp. 419–425.
[10] Fiterman, A., Ben-Zvi, R., and Kribus, A., 1999, ''DOTS: Pseudo-Time-Stepping Solution of the Discrete-Ordinate Equations,'' Numer. Heat Transfer, Part B, **35**, pp. 163–183.

Viscous Dissipation in Finite Thin-Gap Couette Devices

Michael C. Wendl
Research Associate and Affiliate Professor, School of Medicine and Department of Mechanical Engineering, Washington University, 4444 Forest Park Blvd., Box 8501, Saint Louis, MO 63108
e-mail: mwendl@watson.wustl.edu

Ramesh K. Agarwal
The William Palm Professor, Department of Mechanical Engineering, Washington University, 1 Brookings Drive, Box 1185, Saint Louis, MO 63130

An analytical solution is reported for the temperature distribution in finite span thin-gap Couette devices which accounts for viscous dissipation. Taken in conjunction with an established solution for the stable velocity profile, this result describes the standard experimental configuration where no external heat fluxes are applied. We discuss physical aspects as well as conditions for which classical one-dimensional theory should be replaced by the present result. [DOI: 10.1115/1.1418373]

Keywords: Analytical, Conduction, Flow, Heat Transfer, Laminar

1 Introduction

Couette flow devices [1] utilize the concept of two coaxial cylinders enclosing a working fluid. Motion is sustained via shear forces generated by rotating one of the cylinders. In ''thin-gap'' configurations, the ratio of gap size to inner cylinder radius is vanishingly small and fluid response is independent of which cylinder functions as the rotor. The basic design has been used in many practical applications, including viscometry [2] and fluid processing [3]. Moreover, it has evolved as a standard platform for studying fundamental phenomena, such as laminar transition [4–6] and viscous heating [7–10].

Couette devices are typically modeled using an idealized geometry where cylinder spans are considered infinite [4–11]. Spanwise effects imparted on the ends are neglected and the task of determining stable base flow and temperature distributions, i.e., the Couette problem, is reduced to one dimension. Here, velocity profiles assume the classical linear ''constant shear'' form and temperature profiles are parabolic if viscous heating is considered [11]. This treatment represents a significant theoretical simplification. Yet it is well-known that spanwise effects are appreciable in devices having small to moderate cylinder spans. This has been shown by numerous experimental investigations using aspect ratios on the order of 10 or less [12–14]. Thus, there exists a class of instruments for which idealized theory is clearly not sufficient [2,12].

An analytical solution for the Couette velocity profile in thin-gap devices having finite aspect ratios has long been available [15]. In the absence of viscous dissipation, the thermal problem is trivial since temperature can be inferred directly from the velocity profile. However, for non-trivial dissipation, e.g., Brinkman numbers in the 10^{-1} to 10^{2} range [7], heat generation terms in the temperature equation prevent leveraging the existing model. We

Contributed by the Heat Transfer Division for publication in the JOURNAL OF HEAT TRANSFER. Manuscript received by the Heat Transfer Division, July 27, 2000; revision received June 25, 2001. Associate Editor: J. Georgiadis.

present here an analytical solution for this case. In light of previous studies of viscous dissipation [7–10], we consider the implementation in which there are no externally applied heat fluxes.

2 Problem Formulation

Let gap size and total span be H and L, respectively (where L is finite). Also, define the translation velocity of the inner cylinder surface as u_w and take T_w to be a reference temperature. Fluid properties are constant density ρ, kinematic viscosity ν, and thermal conductivity k. Pertinent non-dimensional parameters are the aspect ratio $\phi = L/H$ and the Brinkman number $\mathrm{Br} = [(\rho \nu u_w^2)/(kT_w)]$. The Reynolds number is relevant only to the extent that it is below a critical value for the onset of flow instability, a prerequisite for the existence of stable Couette flow. The seven parameter dimensional system therefore reduces to a two parameter dimensionless one defined by parameter space (Br, ϕ). The parallel Couette flow model applied to the Navier-Stokes equations yields [16]

$$\nabla^2 u = 0, \tag{1}$$

and

$$\nabla^2 T = -\mathrm{Br}\left[\left(\frac{\partial u}{\partial y}\right)^2 + \left(\frac{\partial u}{\partial z}\right)^2\right], \tag{2}$$

where u and T are the non-dimensional streamwise velocity component and the temperature distribution in the cross-section, respectively. These variables have been non-dimensionalized as $u = u^*/u_w$ and $T = (T^* - T_w)/T_w$, where u^* and T^* are corresponding dimensional quantities. Independent variables are non-dimensionalized using H as a length scale. The dimensionless Laplacian operator ∇^2 has the form $\partial^2/\partial y^2 + \partial^2/\partial z^2$, where y and z represent the directions normal and tangential to the moving surface, respectively. Boundary conditions governing the flow profile are

$$u = 0 \quad \text{at} \quad z = 0, \quad z = \phi, \quad y = 1 \quad \text{and} \quad u = 1 \ \text{ at } \ y = 0. \tag{3}$$

Boundary conditions for temperature are

$$T = 0 \quad \text{at } z = 0, \quad z = \phi, \quad y = 0, \quad \text{and } y = 1, \tag{4}$$

that is, all surfaces of the instrument remain at the reference temperature T_w. Equation (4) represents the standard case in which no external heat fluxes are applied [7–10].

The exact solution for Eqs. (1) and (3) can be written for the present coordinate system as [15]

$$u(y,z) = \frac{4}{\pi}\sum_{m=1}^{\infty} \frac{\sin(2m-1)\pi z/\phi \, \sinh(2m-1)\pi(1-y)/\phi}{(2m-1)\sinh(2m-1)\pi/\phi}. \tag{5}$$

Using Eq. (5), $\partial u/\partial y$ and $\partial u/\partial z$ are determined and their squares are used to obtain the viscous dissipation source term in Eq. (2). This procedure yields

$$\begin{aligned}\nabla^2 T = &-\frac{16\ \mathrm{Br}}{\phi^2}\sum_{m=1}^{\infty}\sum_{n=1}^{\infty}\frac{1}{\sinh\ \gamma_m \sinh\ \alpha_n} \\ &\times[\sin\ \gamma z_m \sin\ \alpha z_n \cosh\ \gamma_m(1-y)\cosh\ \alpha_n(1-y) \\ &+\cos\ \gamma z_m \cos\ \alpha z_n \sinh\ \gamma_m(1-y)\sinh\ \alpha_n(1-y)],\end{aligned} \tag{6}$$

where $\gamma_m = (2m-1)\pi/\phi$ and $\alpha_n = (2n-1)\pi/\phi$. Equations (4) and (6) govern the viscous dissipation problem we desire to solve.

3 Solution Procedure

Equation (6) is not readily separable. We therefore employ the integral transform [17,18]

$$\overline{T}(y,\beta_j) = \int_0^{\phi} Z(\beta_j, z')T(y,z')dz' \tag{7a}$$

and

$$T(y,z) = \sum_{j=1}^{\infty}\frac{Z(\beta_j,z)\overline{T}(y,\beta_j)}{\int_0^{\phi} Z^2(\beta_j,z')dz'}, \tag{7b}$$

where the overbar notation represents a transform in z, eigenvalues are given by β_j, and $Z(\beta_j, z)$ are corresponding eigenfunctions. As boundary conditions are of the Dirichlet type, eigen-related quantities can be obtained explicitly [19] and are specified by the expressions $\beta_j = j\pi/\phi$ and $Z(\beta_j, z) = \sin\ \beta_j z$.

Equation (6) is transformed using Eq. (7*a*). Regarding the Laplacian operator, $\partial^2 T/\partial y^2$ and $\partial^2 T/\partial z^2$ transform, respectively, as $d^2\overline{T}/dy^2$ and $-\beta_j^2 \overline{T}$. It is necessary to transform the right hand side of the equation on a term-by-term basis. Constants and terms that depend only on y can be moved outside the transformation integral and the equation can be written

$$\begin{aligned}\frac{d^2\overline{T}}{dy^2} - \beta_j^2\overline{T} = &-\frac{16\ \mathrm{Br}}{\phi^2}\sum_{m=1}^{\infty}\sum_{n=1}^{\infty}\frac{1}{\sinh\ \gamma_m \sinh\ \alpha_n} \\ &\times\Big[\cosh\ \gamma_m(1-y)\cosh\ \alpha_n(1-y) \\ &\times\int_0^{\phi} Z_j' \sin\ \gamma_m z' \sin\ \alpha_n z' dz' \\ &+\sinh\ \gamma_m(1-y)\sinh\ \alpha_n(1-y) \\ &\times\int_0^{\phi} Z_j' \cos\ \gamma_m z' \cos\ \alpha_n z' dz'\Big],\end{aligned} \tag{8}$$

where Z_j' represents a shorthand notation for $Z(\beta_j, z')$. Evaluating the integrals, we find

$$\begin{aligned}\frac{d^2\overline{T}}{dy^2} - \beta_j^2\overline{T} = &-\frac{16\ \mathrm{Br}\,[1-(-1)^j]j}{\phi\pi} \\ &\times\sum_{m=1}^{\infty}\sum_{n=1}^{\infty}\frac{1}{\cosh\ b_{mn}\pi/\phi - \cosh\ a_{mn}\pi/\phi} \\ &\times\left[\frac{\cosh\ b_{mn}\pi(1-y)/\phi}{j^2 - a_{mn}^2} - \frac{\cosh\ a_{mn}\pi(1-y)/\phi}{j^2 - b_{mn}^2}\right],\end{aligned} \tag{9}$$

where $a_{mn} = 2(m-n)$ and $b_{mn} = 2(m+n-1)$. Boundary conditions transform as $\overline{T} = 0$ at $y = 0$ and $y = 1$.

The problem is now posed in terms of non-homogeneous ordinary differential equations for $\overline{T}$. Since coefficients are constant, the method of partial fractions may be used to solve for $\overline{T}$ as the sum of a homogeneous solution T_H and a particular solution $\overline{T_P}$ [20]. The homogeneous component is of the form $T_H = c_1 \cosh\ \beta_j y + c_2 \sinh\ \beta_j y$. If $f(y)$ and D are taken to represent the right hand side of Eq. (9) and d/dy, respectively, the equation for the particular solution may be written symbolically as $(D^2 - \beta_j^2)\overline{T_P} = f(y)$. Applying the method of partial fractions results in $T_P = [(D-\beta_j)^{-1} - (D+\beta_j)^{-1}]f(y)/(2\beta_j)$. Integrating this expression and handling evaluation once again on a term-by-term basis for the double series embedded in $f(y)$, we obtain after considerable derivation the particular solution

$$\overline{T}_p = \frac{16\ \mathrm{Br}\,[1-(-1)^j]j\phi}{\pi^3}\sum_{m=1}^{\infty}\sum_{n=1}^{\infty}\frac{\cosh b_{mn}\pi(1-y)/\phi - \cosh a_{mn}\pi(1-y)/\phi}{(\cosh b_{mn}\pi/\phi - \cosh a_{mn}\pi/\phi)(j^2-b_{mn}^2)(j^2-a_{mn}^2)}. \tag{10}$$

Reconstructing the general solution as $\overline{T}=\overline{T}_H+\overline{T}_P$, the integration constants c_1 and c_2 can be evaluated using the transformed boundary conditions. The result can be written as

$$\overline{T}(y,\beta_j) = \frac{16\ \mathrm{Br}\,[1-(-1)^j]j\phi}{\pi^3}\sum_{m=1}^{\infty}\sum_{n=1}^{\infty}\frac{1}{(j^2-b_{mn}^2)(j^2-a_{mn}^2)} \times\left[\frac{\cosh b_{mn}\pi(1-y)/\phi-\cosh a_{mn}\pi(1-y)/\phi}{\cosh b_{mn}\pi/\phi-\cosh a_{mn}\pi/\phi} - \frac{\sinh j\pi(1-y)/\phi}{\sinh j\pi/\phi}\right]. \tag{11}$$

To obtain the physical solution $T(y,z)$, the inverse transform in Eq. (7*b*) is applied to Eq. (11), yielding

$$T(y,z) = \frac{64\ \mathrm{Br}}{\pi^3}\sum_{j=1,3,5,\ldots}^{\infty} j\ \sin j\pi z/\phi \times\sum_{m=1}^{\infty}\sum_{n=1}^{\infty}\frac{1}{(j^2-b_{mn}^2)(j^2-a_{mn}^2)} \times\left[\frac{\cosh b_{mn}\pi(1-y)/\phi-\cosh a_{mn}\pi(1-y)/\phi}{\cosh b_{mn}\pi/\phi-\cosh a_{mn}\pi/\phi} - \frac{\sinh j\pi(1-y)/\phi}{\sinh j\pi/\phi}\right]. \tag{12}$$

Trivial modes represented by $j=2,4,6,\ldots$, have been removed.

4 Results

The Brinkman number appears simply as a scaling factor for the magnitude of T in Eq. (12), while the aspect ratio is embedded within the series. The ratio T/Br therefore describes the topology of all possible temperature profiles associated with stable flow. Figure 1 shows several examples. Small values of ϕ yield asymmetries where maxima are shifted toward the moving surface. This behavior arises in response to the fact that velocity gradients, especially $\partial u/\partial y$, increase near $y=0$ and decrease near $y=1$ as ϕ is reduced. These gradient shifts have a commensurate effect upon the dissipation source term in Eq. (6). The degree of asymmetry lessens as the aspect ratio is increased. In the limit $\phi\to\infty$, a parabolic profile is obtained about $y=1/2$ as predicted by standard one-dimensional theory [11].

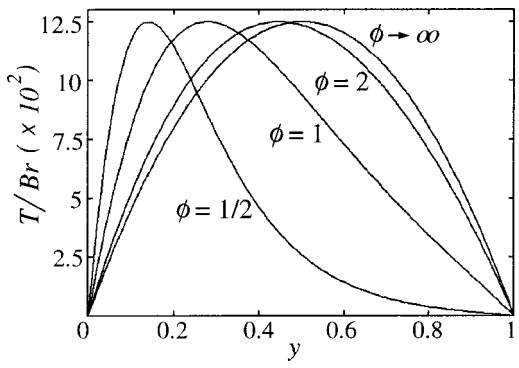

Fig. 1 Thermal shape profiles (T/Br) at the device centerline ($z=\phi/2$) for aspect ratios 1/2, 1, 2, and ∞

While Fig. 1 suggests rapid convergence to idealized behavior, it does not quantify error for finite values of ϕ when the span is approximated as being infinite. Here, we define an error measure ε in terms of r.m.s. differences between the idealized profiles [11], $u=1-y$ and $T=\mathrm{Br}\cdot y(1-y)/2$, and their two-dimensional counterparts in Eqs. (5) and (12). Figure 2 shows that both u and T converge logarithmically as functions of ϕ to their one-dimensional forms. Notice that contours for u and T coincide at $\mathrm{Br}=5.5$. The hydrodynamic component governs error for $0\leqslant\mathrm{Br}\leqslant 5.5$ because it represents the lower bound for error. Thermal curves for $\mathrm{Br}<5.5$ therefore have no physical significance. Conversely, increased dissipation governs the error for $\mathrm{Br}>5.5$. To a good approximation ($L_\infty\approx 3.5\%$), results in Fig. 2 are described by

$$\varepsilon = 0.16\ \ \mathrm{Br}\ e^{-1.568\phi}, \tag{13}$$

where $\phi\geqslant 1/2$ and e is the Euler number. That is, Eq. (13) describes the r.m.s. error when using the idealized thermal profile to approximate Eq. (12) and further describes the error when applying the corresponding hydrodynamic idealization to approximate Eq. (5) if Br is set to 5.5.

Because of its logarithmic nature, the actual error will never identically vanish. However, one can choose an appropriate error tolerance below which application of idealized theory is reasonably justified. Strictly speaking, the selected tolerance applies to stable flow only. Any case involving additional higher-order flow modes would likely add a numerical approach and formalized benchmarking would then be required [21]. One can err conservatively by choosing a sufficiently low tolerance, for example, $\varepsilon=10^{-5}$. A neutral curve can then be found which separates the one and two-dimensional models by plotting the locus of points in (Br,ϕ) space for this value. This procedure results in the map shown in Fig. 3. The vertical line represents the lower error bound, which is valid for Brinkman numbers up to 5.5. Here, one-dimensional modeling is justified for approximately $\phi\geqslant 7.3$. For $\mathrm{Br}>5.5$, thermal effects govern the problem and the one-dimensional simplification may only be applied at progressively larger aspect ratios. The thermal curve has a steeply increasing slope implying that the required value of ϕ is only a weak function of the Brinkman number. This can also be inferred from the close spacing of thermal contours in Fig. 2.

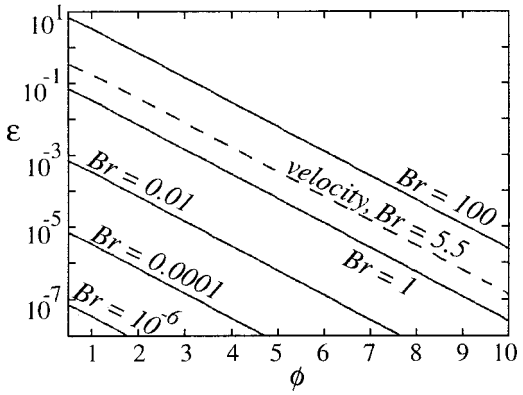

Fig. 2 Convergence rate of velocity and temperature profiles at the device centerline ($z=\phi/2$) to their one-dimensional forms. Dashed line represents coincident contours for temperature at Br=5.5 and velocity

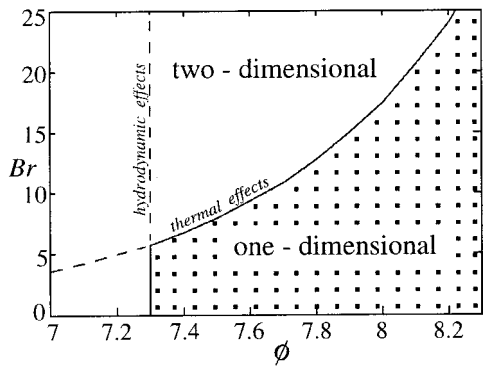

Fig. 3 Map of parameter space denoting shaded region where idealized theory is permitted within bounds of a 10^{-5} r.m.s. error tolerance

Equations (5) and (12) are predicated upon constant fluid properties. Since the maximum dimensionless temperature rise shown in Fig. 1 is identical for both finite and infinite configurations, the range of applicability of the current model is essentially the same as that for one-dimensional theory [11]. Properly extending the map in Fig. 3 to significantly higher values of Br would require one to consider variable properties, especially viscosity. This would introduce additional material parameters to the problem. Work based upon idealized theory has focused on this issue [7–10], however, we are not aware of any corresponding studies relating to finite devices.

5 Conclusion

We have derived the dissipation-dependent temperature distribution for thin-gap Couette flow and used it to analyze finite instruments. This solution can be applied in ways beyond what is discussed here, for example as a numerical test case and/or initial condition for codes designed to simulate heat generating flows.

Br = Brinkman number $[(\rho \nu u_w^2)/(kT_w)]$
H = gap size [m]
L = cylinder span [m]
T = dimensionless temperature
T_w = reference temperature [K]
Z = eigenfunction
j,m,n = eigenmodes
k = thermal conductivity [W/mK]
u = dimensionless velocity component
u_w = translation speed of rotor surface [m/s]
y,z = dimensionless Cartesian coordinates
β_j = eigenvalues
ε = r.m.s. error
ϕ = aspect ratio $[L/H]$
ν = fluid kinematic viscosity [m^2/s]
ρ = fluid density [$\mathrm{kg/m}^3$]

References

[1] Taylor, G. I., 1923, "Stability of a Viscous Liquid Contained Between Two Rotating Cylinders," Philos. Trans. R. Soc. London, Ser. A, **223**, pp. 289–343.
[2] Kobayashi, H., Nashima, T., Okamoto, Y., and Kaminaga, F., 1991, "End Effect in a Coaxial Cylindrical Viscometer," Rev. Sci. Instrum., **62**, pp. 2748–2750.
[3] Ameer, G. A., Barabino, G., Sasisekharan, R., Harmon, W., Cooney, C. L., and Langer, R., 1999, "Ex Vivo Evaluation of a Taylor–Couette Flow, Immobilized Heparinase I Device for Clinical Application," Proc. Natl. Acad. Sci. U.S.A., **96**, pp. 2350–2355.
[4] Criminale, W. O., Jackson, T. L., Lasseigne, D. G., and Joslin, R. D., 1997, "Perturbation Dynamics in Viscous Channel Flows," J. Fluid Mech., **339**, pp. 55–75.
[5] Nagata, M., 1997, "Three-Dimensional Traveling-Wave Solutions in Plane Couette Flow," Phys. Rev. E, **55**, pp. 2023–2025.
[6] Waleffe, F., 1997, "On a Self-Sustaining Process in Shear Flows," Phys. Fluids, **9**, pp. 883–900.
[7] Yueh, C.-S., and Weng, C.-L., 1996, "Linear Stability Analysis of Plane Couette Flow With Viscous Heating," Phys. Fluids, **8**, pp. 1802–1813.
[8] Davis, S. H., Kreigsmann, G. A., Laurence, R. L., and Rosenblat, S., 1983, "Multiple Solutions and Hysteresis in Steady Parallel Viscous Flows," Phys. Fluids, **26**, pp. 1177–1182.
[9] Johns, L. E., and Narayan, R., 1997, "Frictional Heating in Plane Couette Flow," Proc. R. Soc. London, Ser. A, **453**, pp. 1653–1670.
[10] Caridis, K. A., Louwagie, B., and Papathanasiou, T. D., 1997, "Viscous Heating in Planar Couette Flow: Series Solutions for Temperature-Sensitive Fluids," J. Chem. Eng. Jpn., **30**, pp. 123–136.
[11] Bird, R. B., Armstrong, R. C., and Hassager, O., 1977, *Dynamics of Polymeric Liquids*, Wiley, New York.
[12] Benjamin, T. B., 1978, "Bifurcation Phenomena in Steady Flows of a Viscous Fluid II. Experiments," Proc. R. Soc. London, Ser. A, **359**, pp. 27–43.
[13] Benjamin, T. B., and Mullin, T., 1981, "Anomalous Modes in the Taylor Experiment," Proc. R. Soc. London, Ser. A, **377**, pp. 221–249.
[14] Aitta, A., Ahlers, G., and Cannell, D. S., 1985, "Tricritical Phenomena in Rotating Couette-Taylor Flow," Phys. Rev. Lett., **54**, pp. 673–676.
[15] Berker, R., 1963, "Intégration des équations du mouvement d'un fluide visqueux incompressible," in *Handbuch der Physik*, Vol. VIII/2, S. Flügge, ed., Springer-Verlag, Berlin, pp. 1–384.
[16] Schlichting, H., 1979, *Boundary Layer Theory*, McGraw-Hill, New York.
[17] Cotta, R. M., 1993, *Integral Transforms in Computational Heat and Fluid Flow*, CRC Press, Boca Raton.
[18] Wendl, M. C., 1999, "General Solution for the Couette Flow Profile," Phys. Rev. E, **60**, pp. 6192–6194.
[19] Özişik, M. N., 1980, *Heat Conduction*, Wiley, New York.
[20] Sokolnikoff, I. S., and Sokolnikoff, E. S., 1941, *Higher Mathematics for Engineers and Physicists*, McGraw-Hill, New York.
[21] Roache, P. J., 1997, "Quantification of Uncertainty in Computational Fluid Dynamics," Annu. Rev. Fluid Mech., **29**, pp. 123–160.

Natural Convection in a Cylindrical Enclosure Filled With Heat Generating Anisotropic Porous Medium

M. R. Dhanasekaran

Sarit Kumar Das

S. P. Venkateshan
e-mail: spv35@hotmail.com

Heat Transfer and Thermal Power Laboratory,
Department of Mechanical Engineering,
Indian Institute of Technology Madras,
Chennai-600036, India

A numerical study has been made to analyze the effects of anisotropic permeability and thermal diffusivity on natural convection in a heat generating porous medium contained in a vertical cylindrical enclosure with isothermal wall and the top and bottom perfectly insulated surfaces. The results show that the anisotropies influence the flow field and heat transfer rate significantly. The non-dimensional maximum cavity temperature increases with increase in permeability ratio. For aspect ratio greater than or equal to two, the nondimensional maximum cavity temperature increases with an increase in the thermal diffusivity ratio. For aspect ratio equal to unity, there exists a critical value of thermal diffusivity ratio at which the maximum cavity temperature is a minimum. This critical value increases with an increase in the value of anisotropic permeability ratio. Based on a parametric study correlations for maximum cavity temperature and average Nusselt number are presented. [DOI: 10.1115/1.1418700]

Contributed by the Heat Transfer Division for publication in the JOURNAL OF HEAT TRANSFER. Manuscript received by the Heat Transfer Division December 15, 2000; revision received May 30, 2001. Associate Editor: C. Beckerman.

Introduction

Convective heat transfer in volumetrically heated porous enclosures is of fundamental importance in a number of technological applications such as storage of agricultural products, fermentation process in food industries, packed-bed chemical reactors, nuclear reactor assembly and is also of interest in environmental sciences and geophysics. Much of the work on this topic has been concerned with an isotropic porous medium. Notable among them are the works of Haajizadeh et al. [1] and Prasad [2], on vertical rectangular cavities, Stewart and Dona [3], Prasad and Chui [4] and Rao and Wang [5] on vertical cylinders.

However, in many applications, porous materials are anisotropic, for example, drying of preferentially oriented food grains, columnar dendritic structures formed during solidification of multi-component mixtures, tubular packed bed reactors and rod bundles in a nuclear reactor core. Due to the preferential orientation of the porous matrix in the above applications the permeability and equivalent thermal conductivity of the porous matrix are different in different directions. Only recently, researchers have started investigating natural convection in heat generating anisotropic porous media. Royer and Flores [6] considered natural convection in an anisotropic porous layer inter-bedded horizontally into a homogeneous impermeable medium enclosed in a rectangular enclosure. Parthiban and Patil [7] studied onset of convection in a horizontal layer of heat generating anisotropic porous medium.

The objective of the present work is to study natural convection in a vertical cylindrical enclosure filled with a heat generating porous medium, which is both hydrodynamically and thermally anisotropic. A porous medium is said to be hydro-dynamically anisotropic when it has different permeabilities in different directions whereas it is said to be thermally anisotropic when it has different thermal diffusivities in different directions.

Mathematical Formulation

The physical system under consideration is a vertical cylinder filled with a porous medium. The wall of the cylinder is considered to be isothermally cooled at T_c while the horizontal surfaces are adiabatic. The porous matrix is both hydrodynamically and thermally anisotropic, and is saturated with an incompressible fluid. The principal directions of the permeabilities (K) and effective thermal conductivities (k) coincide with the horizontal (r) and vertical (z) coordinate axes and hence the flow is assumed to be two-dimensional. The thermophysical properties of the fluid and solid matrix are constant except for the fluid density variation in the body force term, i.e., the Boussinesq approximation is employed. The convecting fluid and the porous matrix are in local thermodynamic equilibrium. Darcy's law is assumed to be valid. The heat is generated by a uniformly distributed energy source.

The governing equations for axisymmetric, steady-flow through the porous medium then are

$$\frac{\partial}{\partial r}(ru') + \frac{\partial}{\partial z}(rv') = 0 \tag{1}$$

$$u' = -\frac{K_r}{\mu}\left(\frac{\partial p}{\partial r}\right) \tag{2}$$

$$v' = -\frac{K_z}{\mu}\left[\frac{\partial p}{\partial z} - g\beta(T - T_c)\right] \tag{3}$$

$$u'\frac{\partial T}{\partial r} + v'\frac{\partial T}{\partial z} = \alpha_r\left[\frac{1}{r}\frac{\partial}{\partial r}\left(r\frac{\partial T}{\partial r}\right)\right] + \alpha_z\frac{\partial^2 T}{\partial z^2} + \frac{q'''}{\rho c}, \tag{4}$$

where K_r and K_z are the permeability of the porous medium respectively along the r and z directions; $\alpha_r = k_r/\rho c$ and $\alpha_z = k_z/\rho c$ are the thermal diffusivity of the porous medium respectively along the r and z directions. As ρ and c are assumed to be constant, α_r and α_z are essentially the ratios of thermal conductivities in the r and z directions. In the above $u' = -1/r\partial\psi'/\partial z$ and $v' = 1/r\partial\psi'/\partial r$. By eliminating the pressure term from the momentum equations by cross-differentiation, the governing Eqs. (1)–(4) may be rewritten in the non-dimensional stream-function-temperature form as

$$K^*\frac{\partial}{\partial R}\left[\frac{1}{R}\frac{\partial\psi}{\partial R}\right] + \frac{1}{A^2}\frac{\partial}{\partial Z}\left[\frac{1}{R}\frac{\partial\psi}{\partial Z}\right] = \mathrm{Ra}^*\frac{\partial\theta}{\partial R} \tag{5}$$

$$\frac{\partial\psi}{\partial R}\frac{\partial\theta}{\partial Z} - \frac{\partial\psi}{\partial Z}\frac{\partial\theta}{\partial R} = A\frac{\partial}{\partial R}\left(R\frac{\partial\theta}{\partial R}\right) + \frac{1}{\lambda A}\frac{\partial}{\partial Z}\left(R\frac{\partial\theta}{\partial Z}\right) + 2AR. \tag{6}$$

The dimensionless variables used in writing the above equations are: $R = r/r_0$, $Z = z/H$, $A = H/r_0$ and $\psi = \psi'/\alpha_r r_o$. Since there is no obvious reference temperature difference available, the temperature is non-dimensionalized using the volumetric heat generation rate as $\theta = (T - T_c)/(q''' r_0^2/2k_r)$. As a result of symmetry about the axis of the cylinder, $r = 0$, Eqs. (5) and (6) are solved with the following hydrodynamic and thermal boundary conditions:

$$R = 0,\ \psi = 0,\ \frac{\partial\theta}{\partial R} = 0; \quad R = 1,\ \psi = 0,\ \theta = 0;$$

$$Z = 0,\ \psi = 0,\ \frac{\partial\theta}{\partial Z} = 0; \quad Z = 1,\ \psi = 0,\ \frac{\partial\theta}{\partial Z} = 0.$$

Equations (5) and (6) are solved by the finite volume method as outlined by Gosman et al. [8]. The discretization in this scheme is equivalent to central differences for all terms except the convective term in the energy equation, for which second upwind differencing has been employed. To solve the system of algebraic equations thus obtained, SOR point iterative solver is used that makes use of the new values as soon as they are available. A non-uniform grid field, varying in the form of geometric progression, with very fine grids near the central line and the wall is employed. The adequacy of the grid is verified by comparing the results computed with a 101×101 grid with those obtained using a 151×151 grid. The difference in maximum non-dimensional temperature and in maximum stream function value for the two grid sizes is within 1 percent. Hence grid size of 101×101 has been used for the parametric study. The energy equation is under relaxed at high Rayleigh numbers. A convergence criterion of 10^{-3} percent change in both ψ and θ at all nodes in the domain has been selected to terminate the iterative scheme.

Results and Discussion

Numerical results for the streamlines, isotherms and Nusselt numbers are obtained for $0.1 \leq K^* \leq 10.0$, $0.1 \leq \lambda \leq 10.0$, $1 \leq A \leq 5$ and $10^2 \leq \mathrm{Ra}^* \leq 10^4$. The range of permeability and thermal diffusivity ratios are chosen based on the work of Neale [9].

Validation. The results obtained by the present computational scheme are compared with the results of Rao and Wang [5] and Prasad and Chui [4] in Tables 1 and 2 respectively, which are for an isotropic porous medium. The present results are found to be in good agreement with them.

Streamlines and Isotherms. For the case of anisotropic heat generating porous medium representative streamlines and isotherms are shown in Figs. 1 and 2 for $A = 2$ and $\mathrm{Ra}^* = 500$. The flow consists of an asymmetric single cell rotating slowly in the clockwise direction. Figure 1 brings out the effect of permeability ratio on the flow pattern. Figure 1(b) illustrates the streamlines

Table 1 Comparison of results with those of Rao and Wang [9]

A	Ra^*	θ^*_{max}		Ψ_{min}	
		Rao and Wang [9] (81 x 81)	Present work (151 x 151)	Rao and Wang [9] (81 x 81)	Present work (151 x 151)
4	10	0.263	0.264	-0.157	-0.157
	1×10^4	0.080	0.079	-25.000	-24.414

Note: $Ra^* = Ra^*/2$, $\theta^*_{max} = \theta_{max}/2$

Table 2 Comparison of results with those of Prasad and Chui [8]

A	Ra^*	θ_{max}	
		Present work (151 x 151)	Prasad and Chui [8] (41 x 61)
1	1×10^2	0.400	0.398
	1×10^3	0.185	0.180
	1×10^4	0.082	0.078
5	1×10^2	0.541	0.556
	1×10^3	0.277	0.277
	1×10^4	0.128	0.128

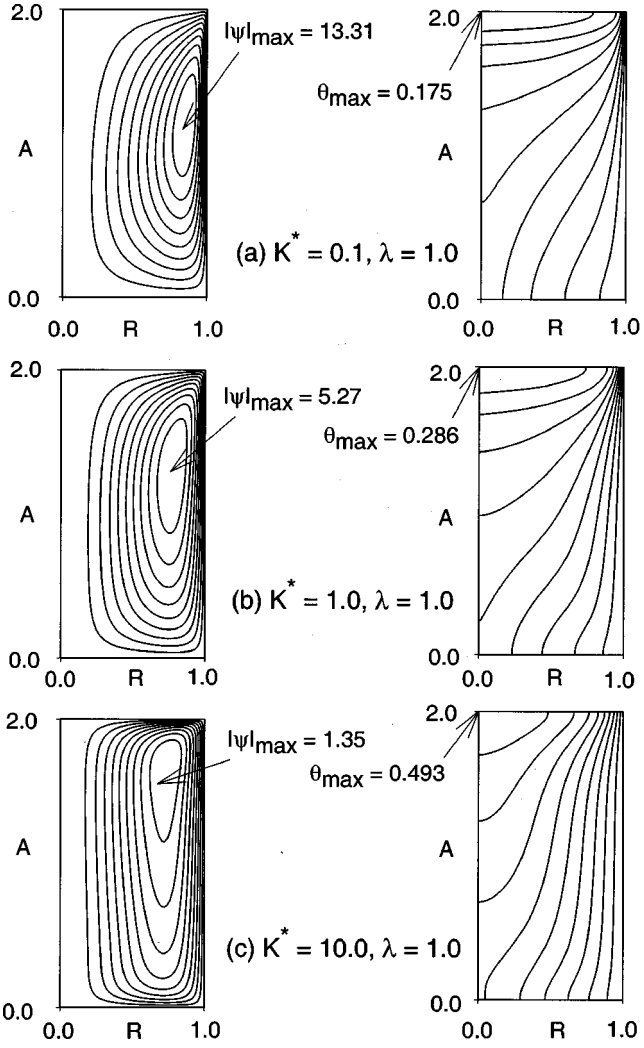

Fig. 1 Streamline and isotherm plots for different permeability ratios keeping the thermal diffusivity ratio constant at λ=1

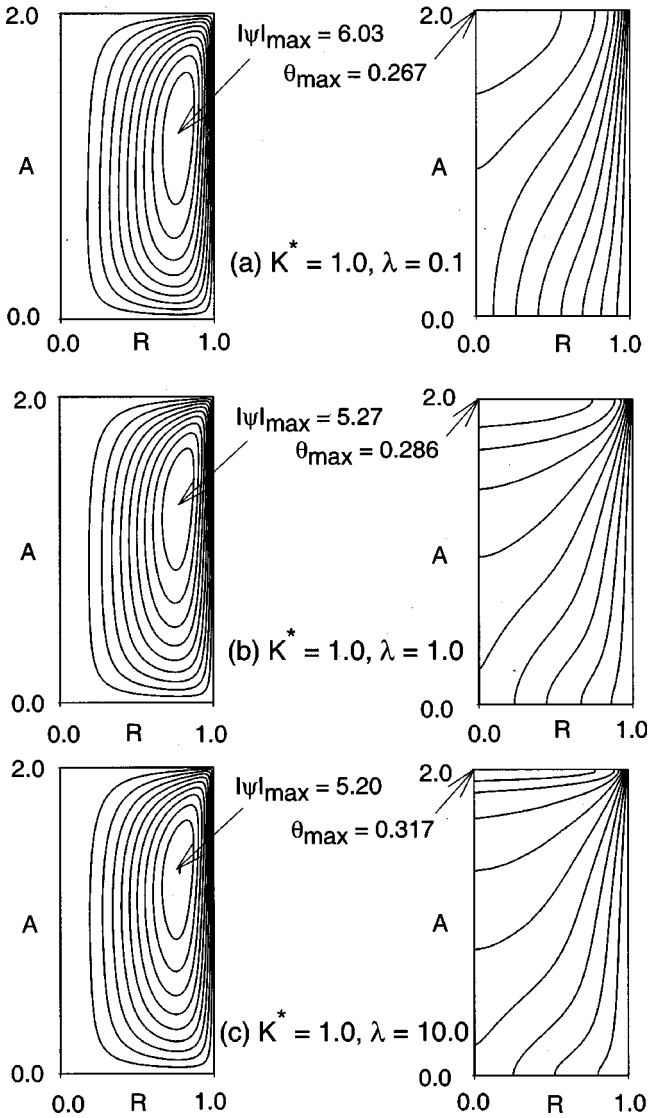

Fig. 2 Streamlines and isotherms for different thermal diffusivity ratios keeping the permeability ratio constant at $K^*=1$

and isotherms for the isotropic case (i.e., $K^*=\lambda=1.0$). Sharp gradients in velocity and temperature are observed near the isothermally cooled side wall. Temperature stratification is observed in the upper portion of the cylinder. Figure 1(*a*) shows the streamlines and isotherms for $K^*=0.1$ and $\lambda=1.0$ (i.e., the permeability in the vertical direction is greater than that in the horizontal direction). The buoyancy induced flow along the isothermal cold wall is much stronger for this case than for $K^*=1.0$. The flow channels along the side wall. When compared to isotropic case the extent of thermally stratified zone increases.

The opposite extreme is shown in Figure 1(*c*). For $K^*=10.0$ and $\lambda=1.0$, no sharp gradients in velocity and temperature are observed near the side wall, while the horizontally flowing fluid channels along the top and bottom adiabatic walls. This practically induces the so called ''plug flow'' in the fluid. Due to the relatively low permeability in the vertical direction, the intensity of natural convection flow is very weak as compared to isotropic permeability case. Also the flow outside the ''horizontal channels'' is very nearly parallel to the vertical wall. Once the fluid reaches the top or bottom adiabatic wall, it bends sharply and merges into

the fast flowing fluid in the horizontal channels. Consequently, the isotherms are almost vertical, indicating that heat transfer across the enclosure is mostly by conduction.

Figure 2 shows the effect of thermal diffusivity ratio via streamline and isotherm plots for $K^*=1.0$. For $\lambda=0.1$ (Fig. 2(*a*)), the thermal diffusivity is much higher in the vertical direction than in the horizontal direction. Hence the temperature gradient in the vertical direction is observed to be smaller than that for $\lambda=1.0$ case. However, the flow intensity is slightly higher than that for $\lambda=1.0$. As shown in Fig. 2(*b*) and 2(*c*), increase in thermal diffusivity ratio has virtually no effect on the flow pattern. Due to the relatively low thermal diffusivity in the vertical direction, the temperature stratification in the vertical direction is stronger for $\lambda=10.0$ than that for $\lambda=1.0$.

Centerline Temperature Distribution. Figure 3 presents the temperature distribution on the centerline of the cylinder for three different permeability ratios while keeping the diffusivity ratio constant at $\lambda=1$ and also for three different thermal diffusivity ratios while keeping the permeability ratio constant at $K^*=1.0$. As the permeability ratio decreases (i.e., the permeability in the vertical direction is larger than that in the horizontal direction), the dimensionless temperature θ_o is observed to be less than that in the isotropic case due to stronger buoyancy. As the permeability ratio increases (i.e., the permeability in the horizontal direction is larger than that in the vertical direction), the dimensionless temperature θ_o is found to be higher than the isotropic case. Also, the larger the permeability ratio, the larger is the temperature gradient $\partial\theta_o/\partial Z$ at any height Z.

When the thermal diffusivity ratio is above unity, the dimensionless temperature θ_o is observed to be less than the isotropic case everywhere except in a small region near the top adiabatic wall. Due to the relatively smaller thermal diffusivity in the vertical direction, there exists a very large temperature gradient, which results in the temperature exceeding that of the isotropic case, near the top adiabatic wall. As the thermal diffusivity ratio is reduced below unity, the centerline temperature is observed to be higher than the isotropic case everywhere except in a small region close to the top adiabatic wall. Due to the relatively larger thermal diffusivity in the vertical direction, a smaller temperature gradient exists in the vertical direction such that the temperature falls below the isotropic value near the top adiabatic wall.

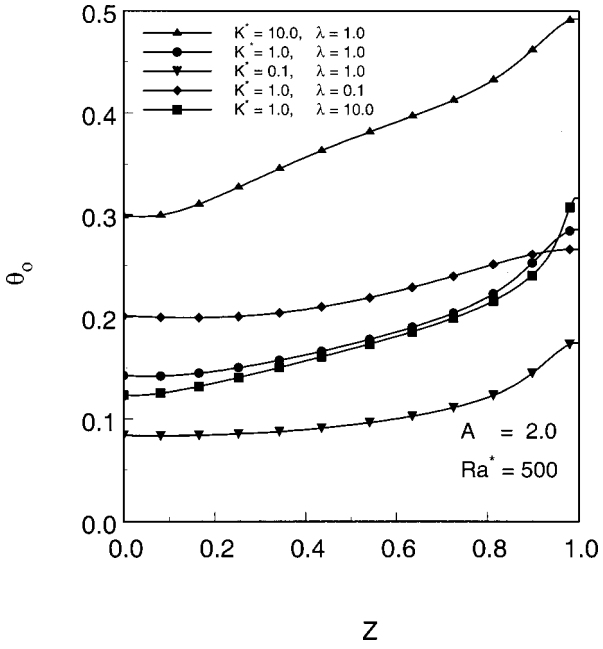

Fig. 3 Effect of permeability ratio and thermal diffusivity ratio on centerline temperature distribution

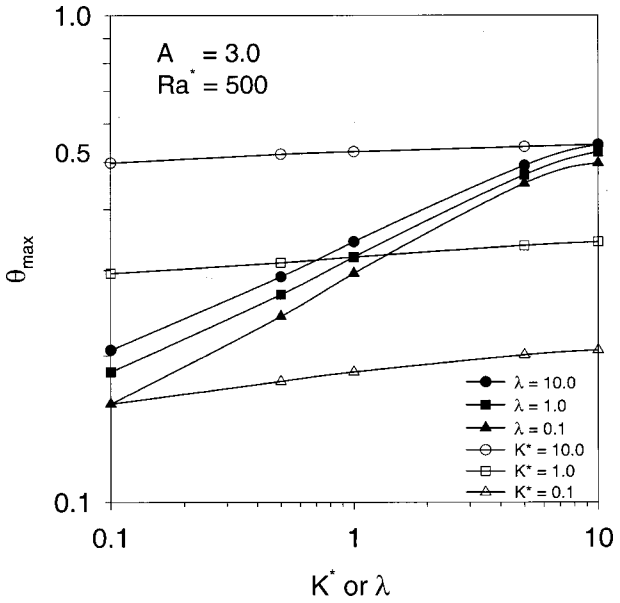

Fig. 4 Effect of permeability ratio and thermal diffusivity ratio on the maximum temperature for $A\geq 2$

Maximum Temperature. Figure 4 shows the effect of permeability ratio and thermal diffusivity ratio on non-dimensional maximum temperature $\theta_{\max}$. For the entire range of aspect ratios, $\theta_{\max}$ increases with an increase in permeability ratio because of fluid flow channeling along the horizontal walls and also because of reduced flow velocity everywhere in the cavity. (Refer to Fig. 1 also). $\theta_{\max}$ varies linearly with the permeability ratio for the range of permeability ratio considered in the present work. When $K^* \rightarrow 10$, $\theta_{\max}$ is observed to approach the pure conduction value. For $A\geq 2$, $\theta_{\max}$ is observed to increase linearly with thermal diffusivity ratio. However, it is evident that the effect of thermal diffusivity ratio on $\theta_{\max}$ is not as severe as that of permeability ratio. Effect of permeability ratio and thermal diffusivity ratio on $\theta_{\max}$ presented in Fig. 5 for $A=1$ shows an interesting feature. Though $\theta_{\max}$ increases with an increase in permeability ratio, the variation is non-linear. However, the variation is linear for higher aspect ratios ($A\geq 2$) as shown in Fig. 4. For a given permeability ratio, there exists a critical value of λ at which $\theta_{\max}$ becomes a minimum. However the difference between the maximum and minimum is within ± 10.0 percent of the mean value for the range of λ considered in the present study. This critical value of λ increases with an increase in K^*. Existence of a critical value of λ with respect to the variation of Nusselt number has been reported earlier by Chang and Lin [10] for anisotropic porous medium without heat generation.

The maximum temperature can be correlated in terms of aspect ratio, Rayleigh number and for the first time, permeability ratio and thermal diffusivity ratio as

$$\theta_{\max}=1.778\mathrm{Ra}^{*-0.325}A^{0.259}K^{*0.271}\lambda^{0.028} \tag{7}$$

for the range $1\times 10^3\leq \mathrm{Ra}^*\leq 1\times 10^4$, $2\leq A\leq 5$, $0.1\leq K^*\leq 10.0$, and $0.1\leq\lambda\leq 10.0$. The correlation coefficient and the average error for the correlation are 0.998 and ± 3.23 percent respectively, which show the goodness of the fit.

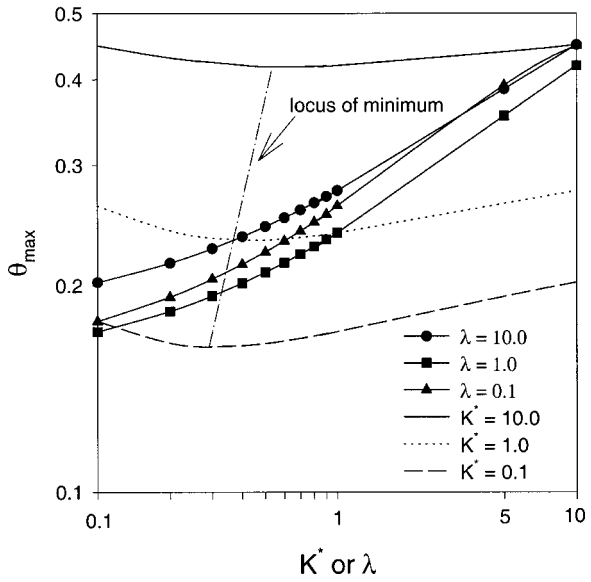

Fig. 5 Effect of permeability ratio and thermal diffusivity ratio on the maximum temperature for $A=1.0$

Overall Heat Transfer. For the problem considered here, there is no well-defined characteristic temperature difference to express the heat transfer coefficient. However, one can define an overall Nusselt number based on the mean temperature on the centerline. When the heat transfer coefficient is defined in terms of $(T_m - T_c)$, the overall Nusselt number is obtained as $\mathrm{Nu}_{av} = h_{av} r_o / k_r = 1/\theta_m$. The overall Nusselt number can thus be correlated as

$$\mathrm{Nu}_{av} = 0.556 \mathrm{Ra}^{*0.396} A^{-0.233} K^{*-0.338} \lambda^{0.032}, \qquad (8)$$

for the range $1\times10^3 \leq \mathrm{Ra}^* \leq 1\times10^4$, $2 \leq A \leq 5$, $0.1 \leq K^* \leq 10.0$, and $0.1 \leq \lambda \leq 10.0$. The correlation coefficient and the average error for the correlation are 0.998 and ± 3.34 percent respectively, which show the goodness of the fit.

Conclusions

A numerical study has been performed of natural convection in a cylindrical cavity filled with a heat generating anisotropic porous medium. A low permeability ratio ($K^*<1$) causes channeling of the flow along the isothermal vertical wall and a higher flow intensity in the enclosure. A large permeability ratio ($K^*>1$) causes channeling of the flow along the horizontal adiabatic walls and a lower flow intensity in the enclosure. A low thermal diffusivity ratio ($\lambda<1$) causes a slightly higher flow intensity in the enclosure. A large thermal diffusivity ratio ($\lambda>1$) has little effect on the flow pattern or flow intensity in the enclosure. As permeability ratio increases maximum cavity temperature increases, for the entire range of aspect ratio studied. For $A \geq 2$, larger the thermal diffusivity ratio, larger is the maximum cavity temperature. For $A=1$, there exists a critical value of thermal diffusivity ratio at which the maximum cavity temperature is minimum. This critical value increases with an increase in permeability ratio. General correlations for maximum cavity temperature and average Nusselt number are presented in terms of Rayleigh number, aspect ratio, permeability ratio and thermal diffusivity ratio.

Nomenclature

A = aspect ratio, H/r_o
g = acceleration due to gravity, m/s^2
H = cylinder height, m
h = heat transfer coefficient, W/m^{2}K
K = porous medium permeability, m^2
K^* = anisotropic permeability ratio, K_r/K_z
k = porous medium effective thermal conductivity, W/mK
Nu = Nusselt number based on cylinder radius, hr_o/k_r
p = pressure, Pa
q''' = volumetric heat generation rate, W/m^3
r = radial co-ordinate, m
R = dimensionless distance in radial direction, r/r_o
r_o = cylinder radius, m
Ra* = Darcy modified Rayleigh number, $g\beta K_r r_o (q''' r_0^2/2k_r)/\nu\alpha_r$
T = temperature, K
u', v' = fluid velocity in the r and z directions, m/s
z = axial co-ordinate, m
Z = dimensionless distance in the axial direction, z/H

Greek Symbols

α = thermal diffusivity, m^2/s
β = isobaric coefficient of volumetric thermal expansion, 1/K
λ = anisotropic thermal diffusivity ratio, α_r/α_z
θ = dimensionless temperature, $(T-T_c)/(q''' r_o^2/2k_r)$
μ = dynamic viscosity, Ns/m^2
ν = kinematic viscosity, m^2/s
ρ = fluid density, kg/m^3
ψ' = stream function, m^3/s
ψ = dimensionless stream function, $\psi'/\alpha_r r_o$

Subscripts

av = average
c = cold vertical wall
m = averaged along the line of symmetry
max = maximum
o = line of symmetry ($r=0$)
r, z = radial and axial directions
z = axial direction

References

[1] Haajizadeh, M., Ozgue, A. F., and Tien, C. L., 1984, "Natural Convection in a Vertical Porous Enclosure With Internal Heat Generation," Int. J. Heat Mass Transf., **27**, pp. 1893–1902.
[2] Prasad, V., 1987, "Thermal Convection in a Rectangular Cavity Filled With a Heat Generating, Darcy Porous Medium," ASME J. Heat Transfer, **109**, pp. 697–703.
[3] Stewart, W. E., Jr., and Dona, C. L. G., 1988, "Free Convection in a Heat Generating Porous Medium in a Finite Vertical Cylinder," ASME J. Heat Transfer, **110**, pp. 517–520.
[4] Prasad, V., and Chui, A., 1989, "Natural Convection in a Cylindrical Porous Enclosure With Internal Heat Generation," ASME J. Heat Transfer, **111**, pp. 916–925.
[5] Rao, Y. F., and Wang, B. X., 1991, "Natural Convection in Vertical Porous Enclosures With Internal Heat Generation," Int. J. Heat Mass Transf., **34**, pp. 247–252.
[6] Royer, J. J., and Flores, L., 1994, "Two-Dimensional Natural Convection in an Anisotropic and Heterogeneous Porous Medium With Internal Heat Generation," Int. J. Heat Mass Transf., **37**, pp. 1387–1399.
[7] Parthiban, C., and Patil, P. R., 1997, "Thermal Instability in an Anisotropic Porous Medium With Internal Heat Source and Inclined Temperature Gradient," Int. Commun. Heat Mass Transfer, **24**, pp. 1049–1058.
[8] Gosman, A. D., Pun, W. M., Runchal, A. K., Spalding, D. B., and Wolfshtein, M., 1969, *Heat and Mass Transfer in Recirculating Flows*, Academic Press, London.
[9] Neale, G., 1977, "Degrees of Anisotropy for Fluid Flow and Diffusion Through Anisotropic Porous Media," AIChE J., **23**, pp. 56–62.
[10] Chang, W. J., and Lin, H. C., 1994, "Natural Convection in a Finite Wall Rectangular Cavity Filled With an Anisotropic Porous Medium," Int. J. Heat Mass Transf., **37**, pp. 303–312.

Application of Differential Transform Method to Heat Conduction in Tapered Fins

Charles W. Bert
School of Aerospace and Mechanical Engineering, The University of Oklahoma, Norman, OK 73019-1052
e-mail: cbert@ou.edu

This paper analyzes steady-state heat conduction in a triangular-profile fin using a relatively new, exact series method of solution known as the differential transform method. This method converges with only six terms or less for the cases considered. Its advantage is that, unlike many popular methods, it is an exact method and yet it does not require the use of Bessel or other special functions. [DOI: 10.1115/1.1423316]

Keywords: Computational, Finned Surfaces Heat Transfer, Temperature, Heat Conduction

Introduction

Zhou [1] introduced a method, based on Taylor series expansion, for solving initial-value problems of electrical circuits. He named the method *differential transformation*. Later, Chen and Ho [2] applied the differential transformation (DT) method to solution of second-order eigenvalue problems. Recently Malik and Dang [3] first applied the DT method to vibration analysis, specifically the fourth-order system for vibration of prismatic beams.

After completing the present work, the author learned, from one of the reviewers, of previous work by Yu and Chen [4]. They dealt with determination of the optimal length for circular fins of rectangular profile. They considered thermal conductivity varying with temperature, heat transfer coefficient varying with radial position and nonlinear conducting-convecting-radiating heat transfer. Solution was by a domain version of the differential transformation method, although few details were given regarding accuracy.

The present paper considers steady-state heat transfer in a triangular-profile fin with constant properties and gives details of application of the method as well as a convergence study.

The Boundary-Value Problem

Let x be the position coordinate along the axis of the fin (normalized by the length L) and θ dimensionless temperature above ambient. The cross-sectional area of the fin varies linearly with x, measured from the apex. Then the governing differential equation is the following second-order equation with varying coefficients (Arpaci, [5])

$$x\frac{d^2\theta}{dx^2}+\frac{d\theta}{dx}-m^2\theta=0, \tag{1}$$

where θ is the temperature measured above ambient and normalized by the base temperature, and m^2 is a fin parameter given by

$$m^2=(h_1+h_2)AR/k.$$

Here AR is the plate aspect ratio (length /depth), h_1 and h_2 are the convective heat transfer coefficients of the top and bottom surfaces, and k is the thermal conductivity.

The boundary conditions are no heat flux at the tip

$$\lim_{x\to 0}\left(x\frac{d\theta}{dx}\right)=0, \tag{2}$$

and a dimensionless temperature of unity at the base ($x=1$), i.e.,

$$\theta(1)=1. \tag{3}$$

Differential Transformation Method

An arbitrary function $f(x)$ can be expanded in a Taylor series about a point $x=0$ as

$$f(x)=\sum_{k=0}^{\infty}\frac{x^k}{k!}\left[\frac{d^k u}{dx^k}\right]_{x=0}. \tag{4}$$

The differential transformation of $f(x)$ is defined as

$$F(k)=\frac{1}{k!}\left[\frac{d^k u}{dx^k}\right]_{x=0}. \tag{5}$$

Then the inverse differential transformation is

$$f(x)=\sum_{k=0}^{\infty}x^k F(k). \tag{6}$$

Before taking the differential transformation of each term in Eq. (1), we note that

$$x\to\delta(k-1)=\{1 \text{ if } k=1 \text{ otherwise } 0$$

$$\frac{d^n\theta}{dx^n}\to\frac{(n+k)!}{k!}T(n+k),$$

where $T(k)$ is the differential transform (DT) of $\theta(x)$.

$$f(x)\theta(x)\to\sum_{l=0}^{k}F(l)T(k-l),$$

where $F(k)$ is the DT of $f(x)$.
For the first term in Eq. (1), $f(x)$ is simply x and $n=2$. Thus,

$$x\frac{d^2\theta}{dx^2}\to\sum_{l=0}^{k}\delta(l-1)(k-l+1)(k-l+2)T(k-l+2).$$

For the second term in Eq. (1),

$$\frac{d\theta}{dx}\to(k+1)T(k+1),$$

and for the third term,

$$-m^2\theta(x)\to-m^2T(k).$$

Thus, the transformed version of Eq. (1) is

$$\sum_{l=0}^{k}\delta(l-1)(k-l+1)(k-l+2)T(k-l+2)$$
$$+(k+1)T(k+1)-m^2T(k)=0. \tag{7}$$

The transformed boundary conditions are

$$\sum_{l=0}^{k}\delta(l-1)(k+1)T(k+1)=0 \tag{8}$$

$$\sum_{l=0}^{k}T(k)=1. \tag{9}$$

Expanding the boundary condition Eq. (8) for various k values, one can obtain all the $T(k)$ values as zero which is a trivial solution. However, the solution as given by DT method Eq. (6) automatically satisfies this boundary condition as $x\to 0$. In other words, the physical significance is that as $x\to 0$, all the coefficients of $d\theta/dx$ should be finite. As there are no negative powers

Contributed by the Heat Transfer Division for publication in the JOURNAL OF HEAT TRANSFER. Manuscript received by the Heat Transfer Division January 12, 2001; revision received August 15, 2001. Associate Editor: G. S. Dulikravich.

of x in Eq. (6) the coefficients $T(k)$ are indeed finite and the boundary condition is automatically satisfied. For the case of tapered fins having both ends of finite thickness, this boundary condition is necessary to solve the problem completely.

Successive applications of Eq. (7) yield

$$k=0: \quad T(1)-m^2T(0)=0 \quad \text{or} \quad T(1)=m^2T(0)$$

$$k=1: \quad 2T(2)+2T(2)=m^2T(1).$$

Thus,

$$T(2)=(m^2/4)T(1)=(m^4/4)T(0)$$

$$k=2: \quad 6T(3)+3T(3)=m^2T(2).$$

Thus,

$$T(3)=(1/9)m^2T(2)=(m^6/36)T(0).$$

Inserting the above expressions for $T(0)$ through $T(3)$ into Eq. (9) and solving for $T(0)$ yields

$$T(0)=\frac{1}{1+m^2+(m^4/4)+(m^6/36)}. \tag{10}$$

Numerical Results

For $m^2=1$, Eq. (10) yields $T(0)=0.439024$, which is only 0.079 percent higher than 0.4386734, the exact Bessel function solution.

Once the various values of $T(k)$ are known, the dimensionless temperature distribution is given by Eq. (6) converted to the notation of the present problem:

$$\theta(x)=\sum_{k=0}^{\infty} x^kT(k). \tag{11}$$

For the present case, up to third order,

$$\theta(x)=T(0)+xT(1)+x^2T(2)+x^3T(3).$$

For the case of $m^2=1$, the dimensionless temperature at the midpoint ($x=1/2$) is 0.6874993, which is 0.0717 percent higher than the exact solution. Fin efficiency η is defined as the ratio of the actual heat transfer rate through the base of a fin to that of an ideal fin having a uniform temperature equal to the base temperature of the actual fin. Fin efficiency is probably a better measure of the accuracy of the method than the temperature values mentioned above. For $m^2=1$, the *DT* method gives $\eta=69.5$ percent or 0.372 percent lower than the exact value.

Table 1 Root and mid-point temperatures and fin efficiency as a function of parameter *m* using only three terms (% error in parentheses)

m	0.25	0.5	0.75	1.0	1.5	2.0
T(0)	0.9403 (0.0)	0.7898 (0.0)	0.6073 (0.016)	0.439 (0.079)	0.2069 (1.025)	0.09278 (4.95)
T(1/2)	0.9699 (0.0)	0.8916 (0.0)	0.7904 (0.0)	0.6874 (0.0717)	0.5133 (0.864)	0.3917 (4.12)
Fin Efficiency, %	96.99 (-0.01)	89.26 (-0.022)	79.41 (-0.088)	69.51 (-0.372)	52.7 (-2.389)	40.2 (-6.892)

Table 2 Exact values and the number of terms required to obtain them, as a function of parameter *m*

m	0.25	0.5	0.75	1.0	1.5	2.0
T(0)	0.9403	0.7898	0.6072	0.4386	0.2048	0.0884
T(1/2)	0.9699	0.8916	0.7904	0.6868	0.5089	0.3765
Fin Efficiency %	96.99	89.26	79.48	69.74	53.98	43.13
Number of Terms	3	3	4	4	5	6

Table 1 summarizes the end and mid point temperatures along with fin efficiency for various values of m with three terms and Table 2 gives the number of terms required to converge to an exact solution up to five significant digit accuracy.

Conclusion

The advantage of the *DT* method over other methods, such as the ordinary and variational heat balance integral method, the ordinary and improved Rayleigh method, and the mean-square error method [6], is that the *DT* method is exact. Nevertheless it is rather straight forward to apply.

Acknowledgment

The author acknowledges the computations performed by Krishna K. Devarakonda.

References

[1] Zhou, J. K., 1986, *Differential Transformation and its Application for Electrical Circuits* (in Chinese), Huazhong University Press, Wuhan, P. R. China.

[2] Chen, C. K., and Ho, S. H., 1996, "Application of Differential Transformation to Eigenvalue Problems," Appl. Math. Comput., **79**, pp. 173–188.

[3] Malik, M., and Dang, H. H., 1998, "Vibration of Continuous Systems by Differential Transformation," Appl. Math. Comput., **96**, pp. 17–26.

[4] Yu, L. T., and Chen, C. K., 1999, "Optimization of Circular Fins with Variable Thermal Parameters," J. Franklin Inst., **336B**, pp. 77–95.

[5] Arpaci, V. S., 1966, *Conduction Heat Transfer*, Addison-Wesley, Reading, MA, p. 150.

[6] Bert, C. W., 1986, "Improved Approximate Methods for Analyzing Steady Heat Conduction," Commun. Appl. Numer. Methods, **2**, pp. 587–592.

Laminar Mixed Convection Adjacent to Three-Dimensional Backward-Facing Step

A. Li and B. F. Armaly

Department of Mechanical and Aerospace Engineering and Engineering Mechanics, University of Missouri-Rolla, Rolla, MO 65409

Simulations of three-dimensional laminar buoyancy-assisting mixed convection adjacent to a backward-facing step in a vertical rectangular duct are presented to demonstrate the influence of Grashof number on the distributions of the Nusselt number, and the reverse flow regions that develop adjacent to the duct's walls. The Reynolds number, and duct's geometry are kept constant: heat flux at the wall downstream from the step is kept uniform but its magnitude varied to cover a Grashof number range of 0–4000; all the other walls in the duct are kept at adiabatic condition; and the flow, upstream of the step, is treated as fully developed and isothermal. Increasing the Grashof number results in increasing the Nusselt number; the size of the secondary recirculation flow region adjacent to the stepped wall; the size of the reverse flow region adjacent to the sidewall and the flat wall; and the spanwise flow from the sidewall toward the center of the duct. On the other hand, the size of the primary recirculation flow region adjacent to the stepped wall decreases and detaches partially from the heated stepped wall as the Grashof number increases. Details are presented and discussed. [DOI: 10.1115/1.1423909

Keywords: Convection, Finite Volume, Mixed Convection, Separated, Three-Dimensional

Contributed by the Heat Transfer Division for publication in the JOURNAL OF HEAT TRANSFER. Manuscript received by the Heat Transfer Division March 27, 2001; revision received October 5, 2001. Associate Editor: M. Faghri.

Introduction

Separated and reattached flow occurs in many heat-exchanging devices, such as electronic and power generating equipment and dump combustors. A great deal of mixing of high and low energy fluid occurs in the separated and reattached flow regions, thus impacting significantly the heat transfer performance of these devices. Studies have been conducted extensively during the past decade, and the backward facing step geometry received most of the attention [1–3]. The majority of published work dealt with the two-dimensional isothermal flow behavior, and comparatively little is published about the three-dimensional non-isothermal case. Forced convection results have been reported for a duct with an aspect ratio of 16 by Iwai et al. [4], with an aspect ratio of 12 by Pepper and Carrington [5], and with an aspect ratio of 8 by Armaly et al. [6]. The numerical study of Iwai et al. [7] established that an aspect ratio greater than 16 is needed to maintain a small two-dimensional region near the centerline of the duct with expansion ratio of 2 at Reynolds number of 250, and for higher Reynolds number the flow becomes three-dimensional throughout the duct. To the authors' knowledge the work of Iwai et al. [8] on the effects of inclination angle on the heat transfer for a duct with aspect ratio of 16, and the work of Li and Armaly [9] on mixed convection in a duct with aspect ratio of 8 are the only published three-dimensional results that incorporate the buoyancy force in the analysis.

Model Description and Simulation

Three-dimensional laminar buoyancy-assisting convection flow in a heated duct with a backward-facing step is numerically simulated and the computation domain is shown in Fig. 1. The upstream height of the duct (h) is 0.01 m, its downstream height (H) is 0.02 m, and its width is (W) is 0.08 m. This geometry provides a backward facing step height of $S=0.01$ m, an expansion ratio of $ER=H/(H-S)=2$, and an aspect ratio of $AR=W/S=8$. By exploiting the symmetry of the flow field in the spanwise direction, the width of the computation domain was reduced to half of the actual width of the duct ($L=0.04$ m). The length of the computation domain is 0.02 m and 0.5 m upstream and downstream of the step respectively, i.e., $-2\leqslant x/S\leqslant 50$. The origin of the coordinate system is located at the bottom corner of the step as shown in Fig. 1. The governing equations for laminar buoyancy assisting mixed convection flow (with gravity, g, in the streamwise direction) with constant properties under steady conditions are formulated for continuity, momentum and energy conservation. Thermal buoyancy effects are modeled using the Boussinesq approximation. The full elliptic three-dimensional coupled governing equations are solved using finite volume method to simulate the thermal and the flow field (where T is temperature and u, v, w are velocity components in coordinate direction x, y, and z as shown in Fig. 1) in this geometry. Details of the formulation are given by Li and Armaly [9]. The physical properties are treated as constants in the simulations and evaluated for air at the inlet temperature of $T_0=20$°C (i.e., density (ρ) equals to 1.205 kg/m^3, dynamic viscosity (μ) is 1.81×10^{-5} kg/m·s, thermal conductivity (k) is 0.0259 W/m·°C, specific heat (C_p) is 1005 J/kg°C, and volumetric coefficient of thermal expansion (β) is 0.00341 1/K). The boundary conditions are treated as no slip conditions at the solid walls, and adiabatic at all the walls with the exception of the downstream stepped wall ($y/S=0.0$ m, for $0.0\leqslant x/S\leqslant 50$, and all z) that was treated as having a uniform heat flux ($q_w=-k\partial T/\partial y|_{y=0}$). The uniform heat flux at the downstream stepped wall is varied while keeping the flow rate constant (Reynolds number, $\mathrm{Re}=2\rho u_0 h/\mu=200$, where u_0 is the average inlet velocity in the upstream section of the duct) in order to investigate the effects of the buoyancy force (the Grashof number, $\mathrm{Gr}=\rho^2 g\beta q_w S^4/\mu^2 k$, and $0.0\leqslant \mathrm{Gr/Re}^2\leqslant 0.1$) on the flow and heat transfer behavior. Symmetry conditions were imposed at the center width of the duct ($z/L=1$, for all x and y), and fully developed conditions were imposed at the outlet ($x/S=50$, for all y and z) and inlet planes ($x/S=-2$, $1\leqslant y/S\leqslant 2$, for all z) of the computation domain.

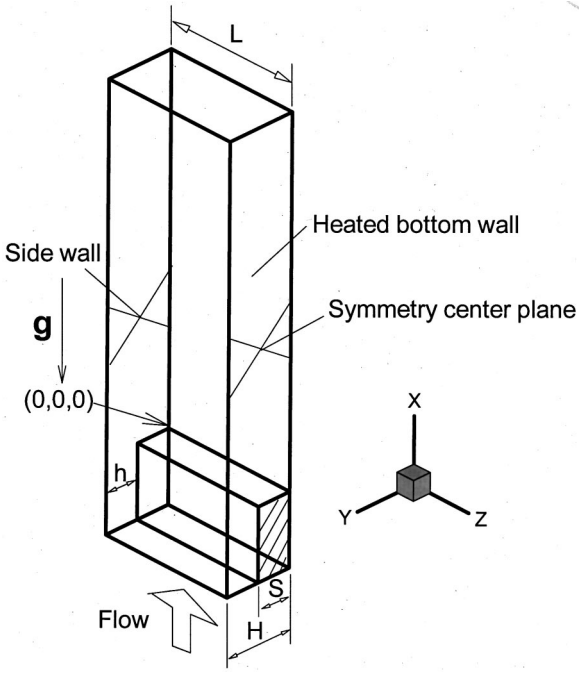

Fig. 1 Schematic of the computation domain

Hexahedron volume elements are used in the simulations. The convergence criterion required that the scaled residuals be smaller than 10^{-4} for the continuity and the momentum equations and smaller than 10^{-6} for the energy equation. All of the calculations were performed on HP Visualine C200 workstations, and the CPU time for converged solution is approximately five hours. Detailed descriptions of the CFD code and the solution procedure can be found in the FLUENT manual. The grid was generated to insure high density close to the walls and the step, where high gradients are expected, in order to insure the accuracy of the simulation. Grid independence tests were performed for the case with Reynolds number of Re=400, and wall heat flux of $q_w=21.19$ W/m^2. Comparisons of the results for the minimum and maximum temperature on the downstream stepped wall, reattachment length at the center of the duct and the minimum reattachment length are conducted for different grid densities downstream of the step, $100(x)\times20(y)\times20(z)$, $125\times25\times25$, $150\times30\times30$, and $180\times35\times35$, respectively. The results show that for the larger grid ($180\times35\times35$), the differences are less than 1 percent for the temperature and reattachment length. A grid of $150\times30\times30$ downstream of the step and a grid of $20\times15\times30$ upstream of the step are selected for this simulation.

Results and Discussion

The present study is an extension to the one reported by Armaly et al. [6], dealing with the forced convection in the same duct geometry. The "jet like" flow that develops near the sidewall within the separating shear layer, and the reverse flow that develops adjacent to the sidewall are the major three-dimensional flow features in this geometry. These features also dominate the flow and heat transfer behavior in mixed convection. The focus of this study is on examining and quantifying the effects of the buoyancy force (Gr) on the flow and heat transfer characteristics.

Impingement of the "jet like" flow on the stepped wall is responsible for creating a minimum in the spanwise distribution of the reattachment line, along with a maximum in the Nusselt num-

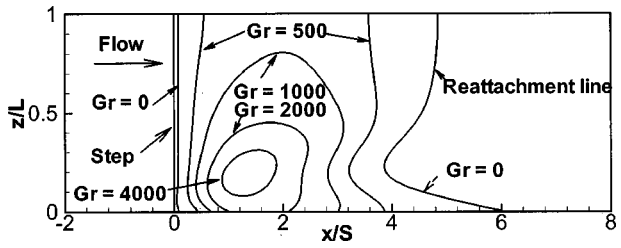

Fig. 2 Effects of Grashof number on the distribution of the reattachment line

ber distribution near the sidewall. Spanwise distributions of reattachment line (as defined by the locations where $\partial u/\partial y|_{y=0}$) for the primary and secondary recirculation flow regions are presented in Fig. 2 for different Grashof numbers. The minimum that occurs in that distribution near the sidewall can be seen clearly for Gr=0 and 500. The maximum length of the primary recirculation flow region occurs at the sidewall and not, as expected, at the center of the duct. As the Grashof number increases, i.e., Gr=500, the primary reattachment line moves closer to the step, and the secondary reattachment line moves away from the step. This means that the size of the secondary and the primary recirculation flow regions increase and decrease, respectively, as the Grashof number increases. The figure shows that the primary recirculation flow region is partially lifted away from the heated stepped wall and the secondary recirculation flow region is vented to the main flow at the center of the duct for Gr=1000. The size of that lifted region increases with increasing Grashof number. The figure shows that only a small portion of the separating shear-layer is reattached to the stepped wall for the case where the Grashof number is 4000, while the rest of the region that is close to the step is vented directly to the main flow.

The effect of the Grashof number on the size of the reverse flow region that develops adjacent to the sidewall is shown Figs. 3 and 4. Results in Fig. 3 represent the linked points (a line) that identify the locations where the streamwise velocity component (u) is zero on a plane that is near the sidewall ($z/L=0.01$). Each one of the lines represents the downstream and the upstream boundaries of the reverse flow region that develops adjacent to the sidewall. At the downstream boundary the flow reverses its direction and starts flowing upstream toward the step, and at the upstream boundary that flow reverses its direction again to move in the downstream direction with the main flow. For low Grashof number, Gr<700, the reverse flow region adjacent to the sidewall develops at the upper corner of the sidewall and that region is separated from the primary recirculation flow region. As the Grashof number increases, Gr>700, the reverse flow region that develops adjacent to the sidewall merges with the primary recirculation flow region as shown in Fig. 3. These results also demonstrate that the primary recirculation flow region is vented to the main flow at the plane of $z/L=0.01$ for Grashof number equals to 4000, but the reverse flow region adjacent to the sidewall remains connected with the primary recirculation flow region at that plane. Results in Fig. 4 represent the linked points (a line) that identify the locations where the streamwise u-velocity component is zero on a plane near the flat wall of the duct at $y/S=1.99$. Each one of these lines represents the downstream and the upstream boundaries of the reverse flow region that develops adjacent to that wall, similar to what was described in Fig. 3. The depth of that region in the spanwise direction extends to approximately 15 percent of the duct's half width at Gr=0, but extends to approximately 40 percent of the duct's half width at Gr=4000.

Due to space limitations, graphical results for the effects of the Grashof number on velocity distributions are not presented in this Note. Results for the streamwise u-velocity component indicate that a "jet like" flow develops in the separating shear layer near the sidewall and the magnitude of the peak velocity decreases and moves closer to the sidewall with increasing Grashof number. Results for the transverse v-velocity component indicate that its magnitude is mostly negative due to sudden expansion in geometry with its peak increasing in absolute value as the Grashof number increases, and that peak develops at approximately the same height as the step. In the neighborhood of the sidewall, however, that trend is reversed and the magnitude of that velocity component decreases in absolute value and becomes positive as the Grashof number increases due to the reverse flow that develops in that region. A "jet like" flow develops in the spanwise distribution of that velocity component near the sidewall, and the magnitude of the peak in these distributions increases with increasing Grashof numbers. Results for the spanwise w-velocity component indicate that the flow is moving mostly from the wall toward the center of the duct, but in the corner near the sidewall and the stepped wall, the flow moves toward the sidewall to support the reverse flow that develops in that region. That reverse flow region increases in size as the Grashof number increases.

Distributions of Nusselt number ($\mathrm{Nu}=q_w S/k(T_w-T_0)$, where T_w is the wall temperature and T_0 is the inlet fluid temperature) on the heated stepped wall are presented in Fig. 5 for different Grashof numbers. The maximum that occurs near the sidewall can be clearly seen in that figure. The development of this peak in the Nusselt number distribution near the sidewall is due to the "jet like" flow that develops in that region. The peak Nusselt number

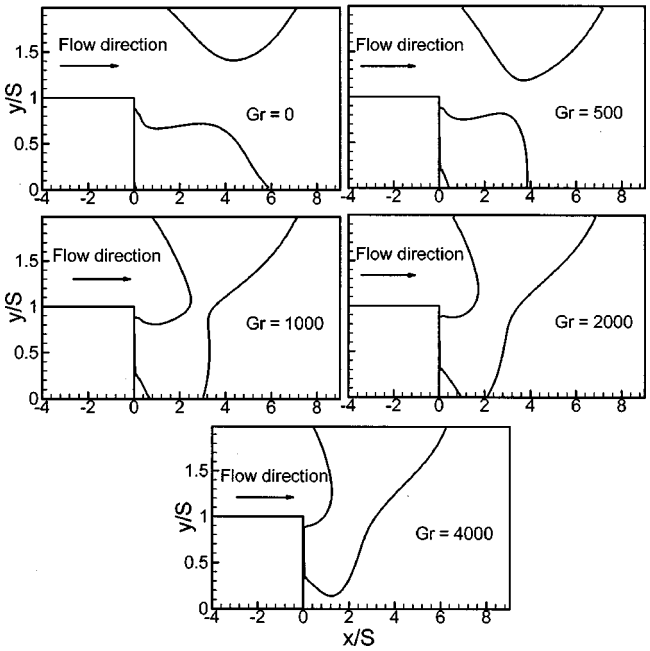

Fig. 3 Effects of Grashof number on size of reverse flow region at a plane $z/L=0.01$

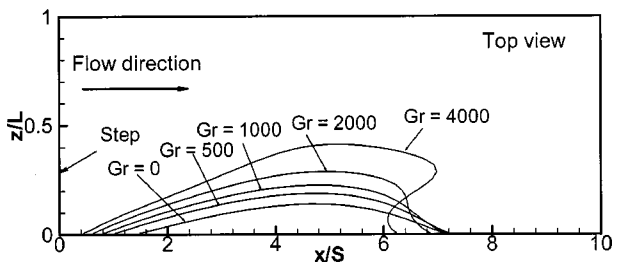

Fig. 4 Effects of Grashof number on size of reverse flow region at a plane $y/S=1.99$

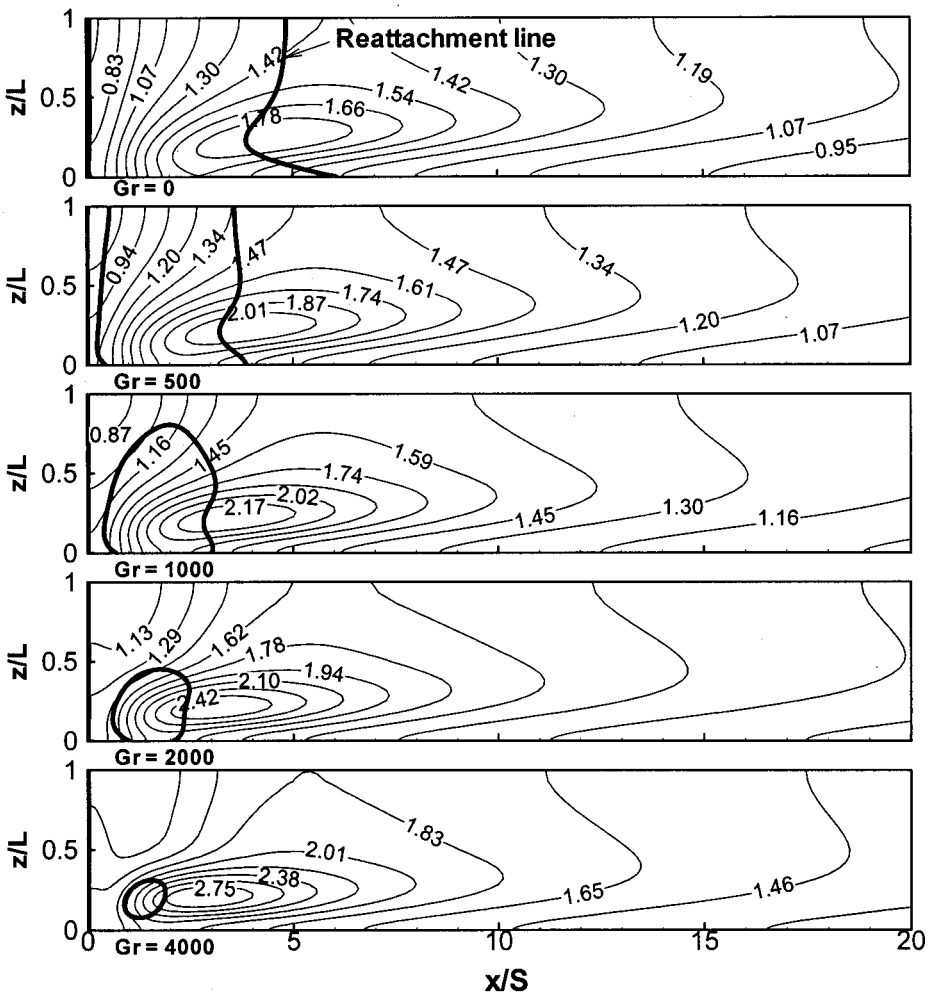

Fig. 5 Effects of Grashof number on the Nusselt number distribution

occurs in the same general region where the reattachment length is minimum, and it is downstream from the reattachment line. Reattachment lines are included in this figure for comparisons of relative positions. The maximum in that distribution moves upstream toward the step and closer to the sidewall as the Grashof number increases. The maximum Nusselt number increases from 1.85 at Gr=0, to 2.8 at Gr=4000.

Conclusions

Numerical simulations of three-dimensional laminar buoyancy-assisting mixed convection flow adjacent to a backward-facing step in a duct are presented to demonstrate the influence of the Grashof number on the distributions of the Nusselt number, and the reverse flow regions that develop adjacent to the duct's walls in this geometry. Increasing the Grashof number results in increasing the Nusselt number; the size of the secondary recirculation flow region adjacent to the stepped wall; the size of the reverse flow region adjacent to the sidewall and the flat wall; and the spanwise flow from the sidewall toward the center of the duct. On the other hand, the size of the primary recirculation flow region adjacent to the stepped wall decreases and detaches partially from the heated stepped wall as Grashof number increases. The locations of the maximum Nusselt number move upstream toward the step and closer to the sidewall as the Grashof number increases. The ''jet like'' flow that develops near the sidewall is responsible for developing a minimum in the spanwise distributions of the reattachment length and a maximum in the spanwise distributions of Nusselt number near the sidewall. The reverse flow region that develops adjacent to the sidewall is not connected to the primary recirculating flow region for the cases of low Grashof number (Gr=0.0, and 500) but becomes connected to that region at higher Grashof numbers.

Acknowledgments

This work was supported in part by the National Science Foundation (NSF) under grants No. CTS-9906746, and CTS-9818203.

References

[1] Armaly, B. F., Durst, F., Pereira, J. C. F., and Schonung, B., 1983, ''Experimental and Theoretical Investigation of Backward-Facing Step Flow,'' J. Fluid Mech., **127**, pp. 473–496.
[2] Simpson, R. L., 1996, ''Aspects of Turbulent Boundary-Layer Separation,'' Prog. Aerosp. Sci., **32**, pp. 457–521.
[3] Eaton, J. K., and Johnson, J. P., 1981 ''A Review of Research on Subsonic Turbulent Flow Reattachment,'' AIAA J., **19**, pp. 1093–1100.
[4] Iwai, H., Nakabe, K., and Suzuki, K., 1999, ''Numerical Simulation of Buoyancy-Assisting, Backward-Facing Step Flow and Heat Transfer in a Rectangular Duct,'' Journal of Heat Transfer—Asian Research, **28**, pp. 58–76.
[5] Pepper, D. W., and Carrington, D. B., 1997, ''Convective Heat Transfer Over a 3-D Backward Facing Step,'' *Proceedings of the ICHMT Int. Symp. on Advances in Computational Heat Transfer*, G. de Vahl Davis and E. Leonardi, eds., pp. 273–281.

[6] Armaly, B. F., Li, A., and Nie, J. H., 2001, ''Three-Dimensional Laminar Forced Convection Adjacent to a Backward-Facing Step,'' J. Thermophys. Heat Transfer, in press.
[7] Iwai, H., Nakabe, K., and Suzuki, K., 2000, ''Flow and Heat Transfer Characteristics of Backward-Facing Step Laminar Flow in a Rectangular Duct,'' Int. J. Heat Mass Transf., **43**, pp. 457–471.
[8] Iwai, H., Nakabe, K., Suzuki, K., and Matsubara, K., 2000, ''The Effects of Duct Inclination Angle on Laminar Mixed Convective Flows Over a Backward-Facing Step'' Int. J. Heat Mass Transf., **43**, pp. 473–485.
[9] Li, A., and Armaly, B. F., 2000, ''Mixed Convection Adjacent to 3-D Backward-Facing Step,'' *Proceedings of the ASME-IMECE Conference*, ASME HTD, 366-2, pp. 51–58.